

Association of Metallurgical Engineers of Serbia

# 1<sup>st</sup> MME SEE 2013

Metallurgical & Materials  
Engineering Congress  
of South-East Europe

## **PROCEEDINGS & BOOK OF ABSTRACTS**

May, 23<sup>rd</sup>-25<sup>th</sup> 2013, Belgrade, Serbia

[www.mme-see.org](http://www.mme-see.org)



**Association of Metallurgical Engineers of Serbia (AMES)  
University of Belgrade - Faculty of Technology and Metallurgy Belgrade (TMF)**

**First Metallurgical & Materials Engineering  
Congress of South-East Europe  
(MME SEE 2013)**

---

**PROCEEDINGS AND  
BOOK OF ABSTRACTS**

---

Editors:

Endre Romhanji  
Milan T. Jovanović  
Nenad Radović

May 23-25, 2013  
Belgrade, Serbia

**Editors:**

**Dr Endre Romhanji**

*Faculty of Technology and Metallurgy, University of Belgrade*

**Dr Milan T. Jovanović**

*Institute for Nuclear Sciences »Vinča«, Belgrade*

**Dr Nenad Radović**

*Faculty of Technology and Metallurgy, University of Belgrade*

**Technical editor:**

Department of Printing Engineering

*Faculty of Technology and Metallurgy, University of Belgrade*

**Published by:**

*Association of Metallurgical Engineers of Serbia (AMES)*

**Circulation:** 150 copies

**Printed by:**

Department of Printing Engineering

Faculty of Technology and Metallurgy

Karnegijeva 4, POB 35-03

11 120 Belgrade, Serbia

Tel: +381 11 3370 492

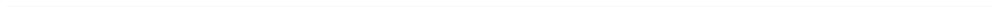
ISBN 987-86-87183-24-7

---

**Supported by:**

---

Ministry of Science and Technological Development  
Republic of Serbia





### **Supported by**

- SEE Associations of Metallurgical Engineers
- Balkan Union of Metallurgists
- Chambers of Commerce of SEE Countries

### **Organized by**

- Association of Metallurgical Engineers of Serbia
- Serbian Foundrymen's Society
- Metallurgical Academic Network of SEE Countries

### **Congress represent fusion of following scientific events**

- Balkan Conference of Metallurgy
- Processing and Structure of Materials
- Light metals and Composite materials
- International Foundrymen Conference

### **International Scientific Committee**

- Endre Romhanji, Serbia, Chairman
- Vanja Asanović, Montenegro
- Avram Avramov, Bulgaria
- Mirjam Jan Blažič, Slovenia
- Peter Cvahte, Slovenia
- Sveto Cvetkovski, Macedonia
- Martin Debelak, Slovenia
- Kemal Delijić, Montenegro
- Sorin Dimitriu, Romania
- Aleksandar Dimitrov, Macedonia
- Mile Djurdjevic, Austria
- Bernd Friedrich, Germany
- Nenad Gubelj, Slovenia
- Sebahattin Gürmen, Turkey
- Milan T. Jovanović, Serbia
- Željko Kamberović, Serbia
- Nikola Majinski, Serbia
- Srđan Marković, Serbia
- Jožef Medved, Slovenia
- Sulejman Mehmedagić, Bosnia and Herzegovina
- Primož Mrvar, Slovenia
- Dimitrios Pnias, Greece
- Miljana Popović, Serbia
- Nenad Radović, Serbia
- Karlo Raić, Serbia

- Srećko Stopić, Germany
- Nadežda Talijan, Serbia
- Faruk Unkić, Croatia
- Srećko Manasijević, Serbia

### **Organizing Committee**

- Nenad Radović, Serbia
- Marija Korać, Serbia
- Olivera Blagojević, Serbia

## **PREFACE**

*The First Metallurgical & Materials Engineering Congress of South-East Europe is a meeting of scientists, professionals and specialties working not only in the field of processing of metals and materials, but also those engaged in research related to the production, structure and property relationship and applications of modern materials.*

*Time has shown a strong need for interdisciplinary research in metallurgical and materials engineering. Therefore, in order to cover all research fields, Congress represents fusion of following scientific events: Balkan Conference of Metallurgy, Processing and Structure of Materials, Light metals and Composite materials and International Foundrymen Conference. Regional significance is supported by South East Europe Associations of Metallurgical Engineers, Balkan Union of Metallurgists and Chambers of Commerce of SEE Countries, and organized by Association of Metallurgical Engineers of Serbia, Serbian Foundrymen's Society and Metallurgical Academic Network of SEE Countries*

*The Conference and Proceedings bring together a wide range of related topics and present the views from both academia and industry. Future of metal industry in South-East European countries, geology and minerals potentials for metallurgy production, new industrial achievements, developments and trends in extractive metallurgy, ferrous and nonferrous metals production, metal forming, casting, powder metallurgy, new and advanced materials, coating, galvanizing, corrosion and protection of materials, process control and modeling, recycling and waste minimization, nanotechnology, sustainable development, solvothermal synthesis, physical metallurgy and structure of materials, welding, environmental protection and education are all covered in the Proceedings.*

*The Editors hope that the Conference will help to improve the knowledge on the symbiotic topics as processing and materials properties.*

*The Editors would like to thank the Scientific and the Organizing Committee, the Conference Secretariat - CONGREXPO d.o.o. and all those who helped in making the Conference a success.*

*The Conference is organized jointly by the Association of Metallurgical Engineers of Serbia and the Faculty of Technology and Metallurgy at the Belgrade University. The Conference was sponsored by PRIZMA Kragujevac and TST Tesic, Germany.*

*Special thanks are due to the Ministry of Education, Science and Technological Development of the Republic of Serbia for the financial support of the Conference,*

*Editors*



## Content

Plenary lecture .....	1
W. Huaiwen, Z. Hongwei, J. Hongwei	
DIGITAL SPECKLE CORRELATION METHOD AND ITS APPLICATIONS IN MATERIALS DEFORMATION MEASUREMENT .....	3
H.W. Wang, H. W. Zhou, L. Mishnaevsky Jr, V. Rajković	
MECHANICAL BEHAVIORS SIMULATION OF COPPER MATRIX REINFORCED WITH Al <sub>2</sub> O <sub>3</sub> .....	17
V. Kevorkijan	
PROGRESS IN THE DEVELOPMENT OF RECYCLING-FRIENDLY WROUGHT ALUMINIUM ALLOYS.....	18
R. Rudolf, I. Anzel, S. Stopić, B. Friedrich, M. Čolić	
GOLD NANOPARTICLES- PROPERTIES, SYNTHESIS AND APPLICATION .....	25
M. Radivojević	
THE RISE OF METALLURGY IN EURASIA: BALKAN PERSPECTIVE .....	35
V. Krstic	
TOUGHENING AND STRENGTHENING IN ADVANCED CERAMICS AND THEIR COMPOSITES.....	37
M. Djurdjevic	
PRESENT AND FUTURE APPLICATION OF THE THERMAL ANALYSIS IN ALUMINUM CASTING INDUSTRY .....	47
P.Mrvar, B.TALJAT, J.Medved, A.Mahmutović	
PASSIVE AND ACTIVE CHAMBERS FOR DIE CASTING WITH COLD AND HOT CHAMBER MACHINES .....	63
Oral Presentations.....	83
E. Balomenos, C. Kemper, P. Diamantopoulos,D. Panias, I. Paspaliaris, B. Friedrich	
NOVEL TECHNOLOGIES FOR ENHANCED ENERGY AND EXERGY EFFICIENCIES IN PRIMARY ALUMINIUM PRODUCTION INDUSTRY .....	85
A. Ćosović, V. Ćosović, Lj. Balanović, D. Živković, T. Žák, N. Talijan	
NANOCRYSTALLINE NiFe <sub>2</sub> O <sub>4</sub> SYNTHESIZED BY MODIFIED PRECIPITATION METHOD .....	92
B. Yolcu, Y. Kılıç, G. Kartal, S. Yılmaz, S. Timur	
ELECTROLYTIC DESULFURIZATION OF LEAD-ACID BATTERY PASTES .....	99

J. M. Vázquez-Rodríguez, P. J. Herrera-Franco, P. I. González-Chi, A.del C. Lizardo-Pérez, S.G. Gómez-Jiménez	
PRINCIPAL PHOTOELASTIC STRESS DIRECTIONS AND ISOCLINIC FRINGES.....	107
M. Pouranvari, S. P. H. Marashi, Z. Salimi	
FAILURE MODE OF DUAL PHASE STEELS RESISTANCE SPOT WELDS .....	115
S. Markovic, N. Korolija, E. Romhanji, S. Manasijevic, M. Stakic	
SIMULATING FORMATION OF CRACKS DURING COOLING ALUMINIUM ALLOY BILLETS IN A DIRECT CHILL ELECTROMAGNETIC CASTING PROCESS.....	121
S. Pocajt, V. Pocajt, K. Raić	
DEVELOPMENT OF A DATABASE OF ADVANCED MATERIAL PROPERTIES.....	129
S. Pocajt, V. Pocajt, K. Raić	
NEW MODEL FOR COMPARISON AND CROSS-REFERENCING OF ENGINEERING METAL ALLOYS.....	135
F. Rögener, C. Dittrich	
RECOVERY OF NICKEL FROM STAINLESS STEEL WASTE STREAMS .....	141
J. Ferčec, R. Rudolf, I. Anžel, I. Pulko, E. Marković, D. Stamenković, B. Glišić	
METHODS OF INVESTIGATION OF THE STRESS-INDUCED MARTENSITE IN ORTHODONTIC WIRE FROM THE SHAPE MEMORY ALLOY NiTi UNDER DIFFERENT STRESS STATES .....	147
P.Terek, L.Kovačević, A.Miletić, D.Kakaš, B.Škorić, D.Kukuruzović	
ADHESION OF LOW TEMPERATURE TIN COATING GOVERNED BY INTERFACIAL LAYER THICKNESS AND SURFACE ROUGHNESS .....	154
J. C. Sturm, J. Pristavec, G. Busch	
"CAST IRON - A PREDICTABLE MATERIAL" NEW CAPABILITIES IN CASTING PROCESS SIMULATION TO ASSESS IRON CASTING PRODUCTION AND PROPERTIES.....	162
G. Gojsević Marić, D. Žveglić, B. Dikić, K. Terzić, F. Unkić	
INFLUENCE OF WALL THICKNESS ON PROPERTIES OF DUCTILE IRON FOR AUSTEMPERING.....	169
G. Gojsević Marić, D. Žveglić, B. Dikić, K. Terzić, F. Unkić	
THE ROLE OF HYDROMETALLURGY IN THE PRODUCTION OF THE CRITICAL METALS .....	187
A. Halap, M. Popović, V. Vaščić, T. Radetić, E. Romhanji	
EXFOLIATION AND PITTING CORROSION SUSCEPTIBILITY IN A MODIFIED 5083 TYPE ALUMINIUM ALLOY.....	194
A. Fadel, D. Glišić, N. Radović, D. Drobňak	
NUCLEATION STAGES OF ISOTHERMAL TRANSFORMATION IN MEDIUM CARBON V-MICROALLOYED STEELS.....	202
N. Stöhr, B. Baudrit, P. Heidemeyer, M. Bastian, M. Nase	
WELDABILITY OF PLASTICIZED POLYLACTID ACID FILMS.....	207

Pavel Hanzl, Siniša Srdić	
LIME AND LIME-BASED SOLUTIONS FOR ENVIRONMENTAL IMPACTS OF NON-FERROUS MINING AND METAL PROCESSING .....	215
Poster session.....	227
M. Kozic, S. Polic-Radovanovic, S. Ristic	
ANALYSIS OF AIR POLLUTION DISPERSION FROM THE STEEL PLANT IN THE REGION OF SMEDEREVO FORTERESS BY NUMERICAL SIMULATION (CFD) .....	229
V. M. Maksimović, M. M. Stoilković, A. D. Čairović	
CHANGES OF Co-Cr BASED DENTAL ALLOY INDUCED BY MULTIPLE CASTING .....	236
V. Matković, V. Manojlović, M. Sokić, B. Marković, Z. Gulišija, Ž. Kamberović	
PRODUCTION OF HIGH GRADE PURE MAGNESIUM USING VACUUM DISTILLATION PROCESS .....	241
B. Marković, D. Živković, D. Manasijević, N. Talijan, M. Sokić	
PHASE EQUILIBRIA INVESTIGATION AND CHARACTERIZATION OF THE ALLOYS IN THE Bi-Cu <sub>0.75</sub> Ni <sub>0.25</sub> SECTION OF THE Bi-Cu-Ni SYSTEM.....	248
M. Sokić, A. Mitovski, N. Štrbac, I. Mihajlović, J. Stojanović, V. Andrić	
PHYSICAL AND CHEMICAL CHANGES DURING HYDROMETALLURGICAL TREATMENT OF NON-STANDARD COPPER CONCENTRATE.....	255
Z. Avramovic, M. Antonijevic, M. Avramovic	
CHARACTERISTICS OF MATERIALS USED FOR CORROSION PROTECTION OF METAL AND CONCRETE STRUCTURES IN AGGRESSIVE ENVIRONMENT .....	262
V. Ćosović, A. Ćosović, M. Pavlović, A. Kostov, D. Živković, N. Talijan	
NANOCOMPOSITE Ag-SnO <sub>2</sub> ELECTRICAL CONTACTS PREPARED BY TEMPLATE METHOD .....	267
Z. Aćimović-Pavlović, Lj. Andrić, A. Terzić, G. Šekularac, M. Pavlović	
DEVELOPMENT OF MODERN TECHNOLOGIES OF COPPER ALLOYS CASTING .....	274
G. Slavkovic,R. Markovic ,M. Bugarin	
COPPER ECONOMIC PROJECTION FROM OSTRELJ WASTE DUMPS AND OLD FLOTATION TAILING DUMP LOCATION BOR, SERBIA.....	281
S. Butković, M. Oruč, E. Šarić, M. Mehmedović, S. Muhamedagić	
INVESTIGATION OF HARDENING OF THE NIOBIUM MODIFIED HEAT RESISTANT STAINLESS STEEL GX40CrNiSi25-20 DURING SINTERING PROCESS .....	289
Z. Karastojković, R. Perić, Z. Janjušević, N. Bajić, A. Sedmak	
SURFACE ROUGHNESS CHANGES AROUND TIG WELDS OF AlMg <sub>5</sub> SHEETS .....	297
Z. Karastojković, R. Perić, M. Jovanović, M. Srećković, Z. Janjušević, G. Radoš	
ELLIPSOMETRIC MEASURINGS OF tan(ψ) AND cos(Δ) AT ANNEALED AND COLD ROLLED STRIPS MADE FROM GOLD ALLOY 585 .....	304

L. Kovačević, P. Terek, D. Kakaš, A. Miletić, D. Kukuruzović DETERMINATION OF METAL-MOLD HEAT TRANSFER COEFFICIENT DURING CO <sub>2</sub> SAND CASTING.....	312
J. Ružić, D. Božić, J. Stašić, V. Rajković, Karlo Raić THE INFLUENCE OF SYNTHESIS PARAMETERS ON STRUCTURAL AND MECHANICAL PROPERTIES OF Cu-ZrB <sub>2</sub> ALLOY.....	320
S. Manasijevic, S. Markovic, R. Radisa MICROSTRUCTURE OF ALUMINUM PISTON ALLOYS.....	326
S. Dimitrijević, M. Rajčić-Vujasinović, R. Jančić-Hajneman, V. Trujić, D. Trifunović CURRENT DENSITY AND TEMPERATURE EFFECTS ON MICROHARDNESS OF DECORATIVE GOLD COATINGS OBTAINED FROM THE AURI-MERCAPTOTRIAZOLE- COMPARISON WITH CYANIDE .....	334
G. Kokeza, K. Raić ECONOMIC ASPECTS OF ENERGENTS CONSUMPTION IN COPPER MELTING AND REFINING PLANTS .....	341
R. Rudolf, K. Raić, Z. Aleksić, V. Lazić, A. Todorović, D. Stamenković, V. Jokanović CHARACTERIZATION OF HYDROXYAPATITE-COATED Ti SURFACE MICROSTRUCTURE PREPARED BY PLASMA SPRAYING .....	349
M. Kos, I. Anžel, R. Rudolf, M. Gilić, M. Romčević, M. Petrović Damjanović, U. Ralević, B. Hadžić, M. Mitrić, N.a Romčević DETERMINATION OF MICROSTRUCTURAL CHANGES BY SEVERELY PLASTICALLY DEFORMED OXIDE DISPERSION STRENGTHENED COPPER ALLOY.....	355
M. Mihailović, A. Patarić, T. Volkov-Husović, K. Raić AN ATOMIC-SCALE WETTING MODEL OF THE LIQUID METAL/CERAMIC INTERFACE.....	362
R. Perić, Z. Karastojković, Z. Kovačević, D. Gusković THE THERMIC HARDENING OF Au-Ag-Cu ALLOYS IN JEWELRY PRODUCTION – AGE- HARDENING .....	368
A. Efremov OPTIMIZATION OF THE MINERAL RESOURCES VALORIZATION IN NON-FEROUS METALLURGY OF THE REPUBLIC OF MACEDONIA.....	380
G.Bakić, V. Šijački-Žeravčić, M. Đukić, V. Maksimović, B. Rajčić MATERIAL CHARACTERIZATION OF 1Cr0.25Mo0.25V POWER PLANT STEEL AFTER PROLONGED SERVICE .....	387
V. Maksimović, A. Došen, I.Bobić, T.Volkov-Husović CAVITATION EROSION RESISTANCE OF HYPOEUTECTIC ALUMINUM ALLOY .....	394
I. Radovic, V. Radojević, D. Trifunovic, P. Uskoković, D. Stojanović, M. Dramićanin, R. Aleksić OPTICAL POLYMER NANOCOMPOSITES PMMA – NANOPHOSPHORS .....	399

V. Obradović, D. Stojanović, M. Grković, I. Živković, V. Radojević, P. Uskoković, R. Aleksić DYNAMIC MECHANICAL PROPERTIES OF ARAMID FABRICS IMPREGNATED WITH CARBON NANOTUBE/POLY (VINYL BUTYRAL)/ETHANOL SOLUTION.....	406
V. Nikolić, Ž. Kamberović, Z. Anđić, M. Korać, M. Sokić J. Stojanović SYNTHESIS OF CATALYTIC MATERIALS BASED ON SYSTEM Ni/ $\alpha$ -Al <sub>2</sub> O <sub>3</sub> SUPPORTED ON MONOLITH CERAMIC FOAMS.....	414
M. Filipović, Z. Kamberović and M. Korać CARBIDE PHASES IN Fe <sub>19</sub> Cr <sub>2.9</sub> C <sub>3.3</sub> V ALLOY IN AS-CAST CONDITION.....	421
<b>Book of abstract.....</b>	<b>429</b>
B. Markoli, K. Delijić, I. Naglič, N. Štrekelj, T. Bončina, F. Zupanić DEVELOPMENT OF HIGH-STRENGTH Al-Alloys Reinforced With Quasicrystals .....	431
K. Miłkowska-Piszczek, M. Korolczuk-Hejnak THE INFLUENCE OF THE VISCOSITY VALUE AND THE METHOD OF ITS IMPLEMENTATION IN THE NUMERICAL MODEL OF THE STEEL CONTINUOUS CASTING PROCESS ON THE DISTRIBUTION OF THE SOLIDIFYING STRAND TEMPERATURE.....	432
K. Ozel, S. Cetinarslan, M. Sahin WELDING OF 5083 ALUMINUM ALLOYS WITH FSW METHOD .....	433
D. Ivšić-Bajčeta, Ž. Kamberović, J. Rogan, M. Ćirković, T. Pavlović ANALYSIS OF COPPER LOSSES THROUGHOUT WEAK ACID EFFLUENT FLOWS GENERATED DURING OFF-GAS TREATMENT IN THE NEW COPPER SMELTER RTB BOR.....	434
B. Katavić, B. Gligorijević, A. Alil, Z. Odanović THE EFFECTS OF AGING ON THE PRECIPITATION OF THE W-RICH PHASE IN THE MATRIX OF THE 92.5W-5Ni-2.5Fe POWDER METALLURGY HEAVY ALLOYS.....	435
M. Tokár, J. Dúl, G. Fegyverneki, V. Mertinger ANALYSIS OF INTERMETALLIC COMPOUNDS In Al-Si FOUNDRY ALLOY .....	436
V. Najati PREVENTION OF SURFACE DEFECTS IN LOST FOAM CASTINGS.....	437
V. Cvetković, J. Jovičević ALLOY FORMATION BY UNDERPOTENTIAL DEPOSITION OF Mg ON Al FROM NITRATE MELTS .....	438
Martins, C.E.L., Veloso, A.C.R., Gomes, R.M., Melo, T.A.A., Lima, S.J.G. Cavalcanti, E.B., Figueiredo, R.T. THERMOMECHANICAL ANALYSIS OF CU-Al-Be ALLOY USED AS COUPLINGS OF OIL AND GAS PIPES .....	429
D. Petković, G. Radenković, M. Miljković A FAILURE ANALYSIS OF A HIP STAINLESS STEEL IMPLANT: CASE REPORT .....	440

B. Zlaticanin, M. Filipovic THERMODYNAMIC MODELLING OF THE MATERIAL PROPERTIES FOR Al-Cu-Mg ALLOYS .....	441
R. Markovic, J. Stevanović, G. Slavković CHARACTERIZATION OF COPPER POWDER OBTAINED ON ALLUMINIUM CATHODE BASE .....	442
M. Rimac, M. Oruč, S. Muhamedagić, S. Butković INVESTIGATIONS OF STRUCTURE OF NICRALY METALLIC COATING APPLIED BY DIAMOND JET PROCESS ON IRON-BASED SUPERALLOY A286 .....	443
J.M. Vázquez-Rodríguez, A.del C. Lizardo-Pérez, S.G. Gómez-Jiménez NATURAL FIBERS-WASTE COMPOSITES: MECHANICAL PROPERTIES PROFILES ...	444
V. Kevorkijan THE INCREASING OF WROUGHT ALUMINIUM ALLOYS SUSTAINABILITY TOWARD HIGHER CONSUMPTION OF COST BENEFICIAL GRADES OF EXTERNAL SCRAP .....	445
S. Šešlija, J. Stevanović, S. Veličković THE INFLUENCE OF THE TYPE AND CONCENTRATION OF METALS ON THE ELECTRICAL CONDUCTIVITY OF PECTIN HYDROGELS.....	446
R. Ashiri STUDY OF STRUCTURE-CHEMISTRY RELATIONSHIP IN THE SYNTHESIS OF BARIUM TITANATE NANOSCALE PARTICLES THROUGH A NEWLY DEVELOPED PROCESS...	447
A.M. Al-Mukhtar CALCULATION OF THE LOADING AND RESIDUAL STRESS INTENSITY FACTOR .....	448
V. Cvetković, N. Mitković, N. Vukićević, G. Zebić ELECTROCHEMICAL BEHAVIOR OF NIOBIUM IN SOME ACID WATER SOLUTIONS.....	449
RVSM. Ramakrishna, P. Pramod Kumar STRAIN INDUCED MELT ACTIVATION (SIMA) OF AA2014 ALLOY .....	451
S. Perisic, N. Aleksic, M. Zrilic, D. Trifunovic, D. Stojanovic, V. Radojevic, R. Aleksic MICROMECHANICAL PROPERTIES OF WOOD HYBRID COMPOSITES.....	452
S. Mousavizade, H. Fuji EFFECT OF CRYSTALLOGRAPHIC ORIENTATIONS ON THE LIQUATION CRACKING TENDENCY IN LASER WELDED IN738 .....	453
Dj. Veljović, Z. Radovanovic, E. Palcevskis, A. Dindune, A. Krumina, R. Petrović, Dj. Janačković PROCESSING OF NANOSTRUCTURED Mg DOPED HAP/TCP BIOCERAMICS BY MICROWAVE SINGLE- AND TWO-STEP SINTERING .....	454
M. Nikačević, R. Ljubica, B. Jordović THE INFLUENCE OF Mg CONTENT AND IMPURITIES OF AA5083 ALLOY ON THE PROPERTIES OF FLOW FORMED TUBES .....	456

M. Ćosić, M. Dojčinović, Z. Aćimović-Pavlović	
THE POSSIBILITY OF ALUMINUM PISTON ALLOY OBTAINED BY RHEOCASTING AND COMPOCASTING PROCESS APPLICATION IN CAVITATION CONDITIONS .....	457
N. Tomić, M. Dimitrijević, J. Zec, M. Zrilić, I. Živković, R. Jančić Heinemann, R. Aleksić	
FINITE ELEMENT MODELING OF HYDRIDE COMPOSITE MATERIAL SUBJECTED TO BALLISTIC IMPACT .....	458



# Plenary lecture



# DIGITAL SPECKLE CORRELATION METHOD AND ITS APPLICATIONS IN MATERIALS DEFORMATION MEASUREMENT

Wang Huaiwen<sup>1,2</sup>, Zhou Hongwei<sup>2</sup>, Ji Hongwei<sup>1</sup>

<sup>1</sup> *Tianjin Key Laboratory of Refrigeration Technology, Tianjin University of Commerce, Tianjin 300134, China*

<sup>2</sup> *Institute of Rock Mechanics and Fractals, China University of Mining and Technology (Beijing), Beijing 100083, China*

## Abstract

The digital speckle correlation method (DSCM), or alternatively digital image correlation method (DICM), has become an accepted method for measuring the surface displacements and displacement gradients in materials under elastic deformation. In this review article, basic concepts and applications of digital speckle correlation method are discussed. The digital speckle correlation method is overviewed and illustrated by reference to seminal publications describing both the developments and applications of digital speckle correlation method. Some conclusions and prospects of the method are given at the end of the paper

*Keywords: Digital Speckle Correlation Method; Fundamental Principles; Applications; Deformation Measurement*

## Introduction

The digital speckle correlation method is a rapidly developing photomechanical technique with advantages including (1) sufficient sensitivity, (2) full-field and non-contact measurement, (3) simple system setup, (4) potential for use in both large and small viewing fields, (5) avoidance of interferometric fringe treatment, etc. As such, it has been fertile ground for experimental mechanics analysis in various engineering problems. The basic idea of DSCM was developed at the beginning of 1980s for experimental stress analysis. Subsequently it was employed to determine the centre-line displacements of a cantilever beam [1] and to analyze the rigid body deformations of a body undergoing two-dimensional motion [2]. During the following three decades, the potential of DSCM for the solution of different types of applied science and engineering problems was recognized. Research to date on DSCM has resulted in the publication of a great deal of new information and has led to improvements in design and measurement practices. Publications in a wide range of journals have attracted the attention of both researchers and practitioners with backgrounds in the mechanics of solids, applied physics, mechanical engineering and materials science.

It is a general understanding that DSCM originated in the early 1980s. Several publications of that time might be considered as the initial work of the DSCM. For example, Paters and Ranson utilized digital imaging techniques as a measure of surface displacement components in laser speckle metrology [3]. They used a vidicon-type television tube to scan the object's images before and after

load. These image data were stored in a PDP-8/E mini-computer through analog-to-digital conversion. Then, the basic problem of surface displacement measurement was to correlate the two images. Yamaguchi proposed a non-contact, automatic method of measuring surface strain using speckle displacement detected by cross-correlating the signals from a photodiode array, naming the method a laser-speckle strain gauge [4]. After that, computer-based analysis for deformation measurement increased rapidly, the theory of the digital speckle/image correlation method became more and more sophisticated, and the applied fields of the method increasingly broadened. These aspects are discussed in the following sections in detail.

## Two-Dimensional Digital Speckle Correlation Method

The two-dimensional digital speckle correlation method, which is also called digital speckle correlation method, includes recording, digitizing and processing two speckle patterns (or images) of an object in different deformation states, one before and the other after deformation, to yield in-plane displacement components and in-plane displacement gradients. Two speckle images of the object's surface are captured, usually before and after loading. Speckle images in the two states are known as reference and deformed speckle patterns, respectively. A small speckle area in the undeformed speckle pattern is defined as a reference subset and the speckle area corresponding to the reference subset in the deformed speckle pattern is defined as the target subset. In this case, there is a need to identify the corresponding relation between the two subsets. The difference between the two subsets includes the translation and distortion information of the object. The deformation measurement is performed at two different deformation stages and comparison is made for subsets between the two digital patterns. The experimental measurement process also entails a process of mathematical calculation.

### *Basic Principles*

Consider an object that is illuminated by a light source. The light-intensity patterns  $f(x, y)$  and  $\hat{f}(x^*, y^*)$  correspond to the reflected light from the undeformed and deformed object configurations respectively. One of the basic assumptions of DSCM is that  $f(x, y)$  and  $\hat{f}(x^*, y^*)$  are assumed to be in unique, one-to-one correspondence with the respective object surfaces and the grey value of a material point is a constant before and after deformation. Therefore, the deformations of small subsets of the image can be measured and thereby the deformations of small subsets of the actual object surface can be evaluated.

Further, consider a small subset of the object, as shown as Fig. 1, centered at  $P(x, y)$  before deformation. The subset centre moves to a new point  $P^*(x^*, y^*)$  after deformation. The intensity values at positions  $P$  and  $P^*$  can be written as

$$\begin{aligned} f(P) &= f(x, y) \\ g(P^*) &= g(x^*, y^*) = g[x + u(P), y + v(P)] \end{aligned} \quad (1)$$

where  $f$  and  $g$  are the grey level distributions of undeformed and deformed speckle patterns respectively. Similarly, for a point  $Q$  at position  $(x+dx, y+dy)$  of the object prior to deformation, the intensity values of  $Q$  and  $Q^*$  can be written as:

$$\begin{aligned} f(Q) &= f(x+dx, y+dy) \\ g(Q^*) &= g[x+u(Q)+dx, y+v(Q)+dy] \end{aligned} \quad (2)$$

Noting that the intensity pattern may deform but does not alter its local value due to deformation, we have

$$\begin{aligned} f(P) &= g(P^*) \\ f(Q) &= g(Q^*) \end{aligned} \quad (3)$$

i.e.

$$\begin{aligned} f(x, y) &= g[x+u(P), y+v(P)] \\ f(x+dx, y+dy) &= g[x+u(Q)+dx, y+v(Q)+dy] \end{aligned} \quad (4)$$

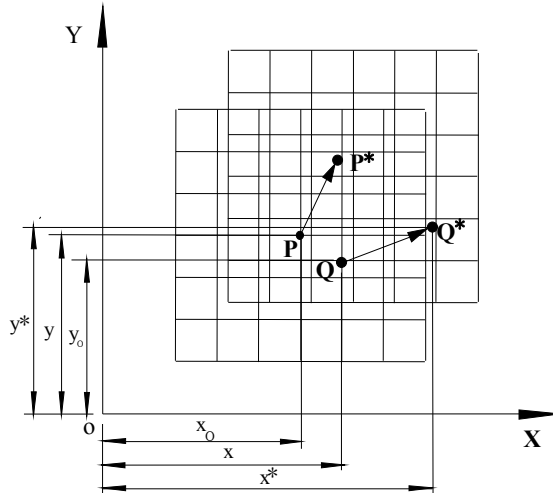


Fig. 1 Illustration of a subset before and after deformation

If the subset is sufficiently small that straight lines remain straight after deformation, then Eq. (4) can be rewritten as

$$\begin{aligned} f(x, y) &= g[x+u(P), y+v(P)] \\ f(x+dx, y+dy) &= g\left[x+u(P) + \frac{\partial u}{\partial x} dx + \frac{\partial u}{\partial y} dy, y+v(P) + \frac{\partial v}{\partial x} dx + \frac{\partial v}{\partial y} dy + dy\right] \end{aligned} \quad (5)$$

Therefore, if the displacement of the central point P of a subset and the displacement derivative terms (such as  $\frac{\partial u}{\partial x}(P)$ , etc.) are known, the position of any nearby point Q\* is determined. Conversely, once the values of  $u(P)$ ,  $v(P)$ ,  $\frac{\partial u}{\partial x}(P)$ ,  $\frac{\partial u}{\partial y}(P)$ ,  $\frac{\partial v}{\partial x}(P)$ , and  $\frac{\partial v}{\partial y}(P)$  are assumed, one can estimate the positions of points P\* and all points Q\* which are within the small subset surrounding P\*. This statement forms the foundation for the numerical computation of local deformation.

Accurate values for the six variables mentioned above can be obtained by comparing the difference between subsets of the intensity pattern at different stages of deformation. To this end, two subsets M and M\* taken from the digitized intensity pattern of the undeformed and deformed object surface centred at point P and point P\* respectively are chosen, and then the six variables can be determined by analyzing the difference between the two selected subsets. In order to estimate the degree of similarity between the reference and target subsets, a criterion is required. The criterion for comparing the two subsets can be established by way of a correlation coefficient (also sometimes called correlation function):

$$C(u, v, \frac{\partial u}{\partial x}, \frac{\partial u}{\partial y}, \frac{\partial v}{\partial x}, \frac{\partial v}{\partial y}) = C[f(x, y)_{|(x, y) \in M}, g(x^*, y^*)_{|(x^*, y^*) \in M^*}] \quad (6)$$

where  $(x, y)$  and  $(x^*, y^*)$  are Cartesian coordinates of a material point in the two subsets,  $f(x, y)$  and  $g(x^*, y^*)$  are grey levels of these points in the corresponding subsets, respectively. The correlation coefficient is a quantitative assessment of the strength of relationship between the two subsets, i.e. it shows how closely the two subsets are related. In general, an extremum of C is considered as the coincidence of the assumed displacement and strain values with the actual deformation components. Here, a maximum or a minimum is chosen by selecting the form of Eq. (6). For example, maximizing C is equivalent to minimizing 1-C (or -C). The detailed forms of Eq. (6) are discussed in the following subsection.

### Correlation Equations

Since the correlation coefficient is used as a criterion for matching two subsets chosen from undeformed and deformed speckle patterns, respectively, its properties directly affect the accuracy and the searching speed of DSCM. The definition of correlation coefficient is, therefore, of great importance for the development and application of DSCM.

Generally, the frequently used correlation coefficient can be written as:

$$S(u, v, \frac{\partial u}{\partial x}, \frac{\partial u}{\partial y}, \frac{\partial v}{\partial x}, \frac{\partial v}{\partial y}) = 1 - \frac{\Sigma[f(x, y) \cdot g(x^*, y^*)]}{\sqrt{\Sigma f^2(x, y) \cdot \Sigma g^2(x^*, y^*)}} \quad (7)$$

where  $(x, y)$  and  $(x^*, y^*)$  are Cartesian coordinates of a material point in the two subsets,  $f(x, y)$  and  $g(x^*, y^*)$  are grey levels of these points in the corresponding subsets, and  $\bar{f}$  and  $\bar{g}$  are the mean values of  $f_i(x, y)$  and  $g_i(x^*, y^*)$ , respectively.

### Reconstruction of Intensity Patterns

It is well known that the digital speckle pattern obtained by a digitizer (also called 'image board' or 'image grabber' in some publications) is in discrete form. The intensity values are recorded as 'pixels'. Due to the discrete nature of the digital image, a pixel in the undeformed image may map to a position between pixels in the deformed image. To obtain a continuous intensity pattern for accurate measurement of deformation at arbitrary locations at subpixel level, an interpolation method is required. Several kinds of interpolation formula are used in the literature, such as the bilinear interpolation method, the polynomial interpolation method and the bi-cubic spline interpolation method. Hou and Qin [5] proposed a fractal interpolation method which seems to be effective in this field. Among the above methods the bilinear interpolation method is the simplest one. With this method, the grey level of an arbitrary location  $(x, y)$ , which is between the sampled pixels  $(i, j)$ ,  $(i+1, j)$ ,  $(i, j+1)$ ,  $(i+1, j+1)$  is calculated by the formula

$$g(x, y) = ax + by + cxy + d \quad (8)$$

where

$a = g(i, j+1) - g(i, j)$ ,  $b = g(i+1, j) - g(i, j)$ ,  $c = g(i+1, j+1) - g(i+1, j) - g(i, j+1) + g(i, j)$ ,  $d = g(i, j)$  and  $g(i, j)$  is the intensity value at the sampled point  $(i, j)$ . In this way a continuous intensity pattern can be obtained. The grey distributions of a subset with dimensions of  $10 \times 10$  pixels<sup>2</sup> before and after bilinear interpolation method are shown in Fig. 2. The first order and second order derivatives of the intensity function  $g(x, y)$  within a subset are continuous except for points located on the mesh lines.

### 2.4 Correlation Search Method

In the analysis above, we mentioned that an extremum of  $C$  is considered as the coincidence of the assumed displacement and strain values with the actual deformation components. Therefore, to the manner of determining the extremum of  $C$ , through use of the correlation search method, is one of the keys to DSCM. As the correlation search method is time-consuming, it is important to select an appropriate algorithm for determining the extremum of  $C$ . In the evolution of DSCM, several methods and techniques have been employed to improve convergent performance, such as double-parameters method, coarse-fine search

method, optimized mathematical model, newton-raphson iterative method, quasi-newton method and self-adaptive search method etc.

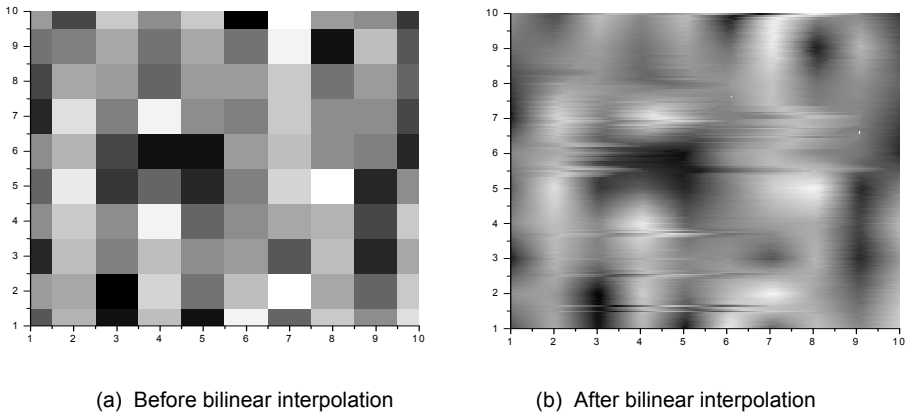


*Fig. 2 Gray distributions of a subset with dimensions of  $10 \times 10$  pixel<sup>2</sup> before and after bilinear interpolation method*

### *Experimental Process and Computer Vision System*

DSCM starts by creating a random black-and-white dot pattern on the specimen surface. In order to obtain a high contrast, black and white random speckle pattern and improve the sensitivity and accuracy of measurement, the speckle may be created artificially. For example, a light spray of black and white paint can be used. A speckle pattern obtained by this method is shown in Fig. 3. Sometimes the natural texture of the specimen surface can also be used as an information carrier. Then two speckle images of the object's surface are captured, usually before and after loading. Finally, the two image patterns are compared with each other and the deformation measurement is performed at two different deformation stages and comparison is made for subsets between the two digital patterns. The experimental measurement process results in a process of mathematical calculation.

The output from application of the theory depends largely on the quality or the performance of hardware used, among which of the greatest concern is the SNR (signal-to-noise ratio) of CCD (charge coupled device) recording. However, in choosing a CCD camera for the system, cost is often the first consideration. A slow scan camera or a so-called scientific grade CCD camera has higher quality in terms of pixel numbers, grey levels, SNR, etc., but it is usually much more expensive. Besides, a higher performance camera must be matched by a large frame buffer and computer memory as well as longer recording and processing time, in short, higher performance computer facilities. On the other hand, a video camera combined with a frame grabber and a PC provides an inexpensive system with satisfactory performance. The testing system we used in our study, as shown schematically in Fig. 3, comprised an 8 bit video CCD camera, an OK\_M40 image grabber, a Pentium 4 PC, and a normal incandescent lamp.

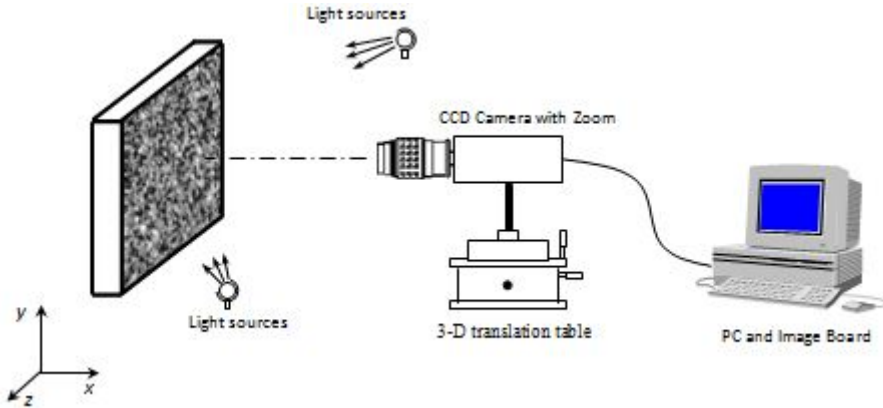


Fig. 3 Schematic of computer vision system for two-dimensional DSCM

In general, calibration of the measurement system is required before a real experiment is undertaken. Though there are several parameters that need to be determined, the major parameter is the magnification factor relating the size of the region being imaged to the pixel dimensions of the sensor plane, for  $x$  and  $y$  direction in pixels/mm. A simple method to determine them is to use a coordinate paper attached to the surface of a planar object. By performing edge detection to locate the pixel position of two lines having known spacing, magnification factors can be obtained with sufficient accuracy.

### Recent Developments

Fast Fourier transforms (FFT) have been shown to be a viable alternative for applications where in-plane strains and rigid body rotations are relatively small. The FFT method uses discrete Fourier transforms of the intensity pattern in both deformed and undeformed sub-regions to determine the cross-correlation function. The displacement of the deformed sub-regions is then estimated by locating the peak of the cross-correlation function. Calculation using the FFT approach has been found to be fast for some applications [6]. However, the method does not allow subset deformation and hence experiences a loss of accuracy.

Recently, some researchers have continued to improve DSCM and gain a deeper understanding of it with advances such as the introduction of wavelet transform theory [7] and some other algorithms [8] into DSCM.

By expanding information in both the spatial and frequency domains, the wavelet transform is efficient for multi-resolution local analysis of signals. Because of its edge enhancement property and noise filtering function, image matching based on wavelet transform produces a sharper and narrower distribution of correlation coefficients than that obtained by convenient correlation computed directly on grey values.

In addition to the artificial neural networks and genetic algorithms mentioned earlier, some other fast-search strategies and full-field DSCM procedures have emerged. Zhang et al. [8] proposed a fast-search approach that combined a multi-

step search with a maximum gradient vector finder to find the maximum of the correlation coefficient.

More recently, some other optical techniques related to correlation theory have been proposed and developed. For instance, Voloshin et al. [9] developed a displacement measurement method based on analysis of the three colors of the image. Qian et al. [10] evaluated a binary speckle correlation by computer simulation. He et al. [11] used quartz optical fibers and digital image technique for measuring local deformation at high temperature. Smith et al. [12] described a digital volume correlation method using computed tomography (CT) images.

In addition, Wang et al. [13] proposed a marker identification method for non-contact optical measurement of in-plane displacement based on correlation analysis. In this marker identification process the information carrier are dots marked on the surface of the specimen or the object, as shown as in Fig. 4. Several dots were marked on the specimen and sometimes the natural texture on the specimen surface also can be used as those dots. Before and after loading, two patterns of the specimen were recorded by a CCD camera and stored in computer as data files. A subset, whose center is one marked dot, is selected as the reference subset in the undeformed image. The next step is to find the target subset, i.e. finding the location where the reference subset moves to. In order to find the best possible estimation of the deformation values a must be established mathematically. In this processing, a zero-order displacement shape function is used, i.e. pure translation is considered. Using the obtained displacements information, the normal strain and the shear strain can be determined according to the theory of linear elasticity. As shown in Fig. 5, considering a point  $P$  on the object surface and two small segments  $PA$  and  $PB$  along  $x$ -axis and  $y$ -axis, linear elastic material response and small deformations provided:

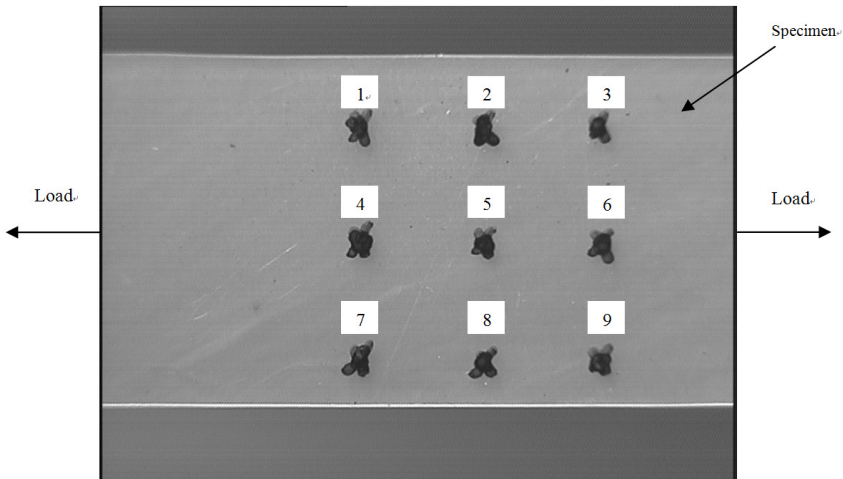


Fig. 4 Marked dots on the specimen (No.  $i$  stands for the  $i$ th dot.  $i=1, 2, \dots, 9$ )

$$\begin{aligned}\varepsilon_x &= \frac{(u_A - u_P)}{\overline{PA}}, \\ \varepsilon_y &= \frac{(v_B - v_P)}{\overline{PB}}, \\ \gamma_{xy} &= \alpha + \beta \approx \tan \alpha + \tan \beta = \frac{(v_A - v_P)}{\overline{PA}} + \frac{(u_B - u_P)}{\overline{PB}}\end{aligned}\quad (9)$$

where

$$u_i = x_i' - x_i, \quad v_i = y_i' - y_i \quad (i=P, A, B), \quad \overline{PA} = x_A - x_P, \quad \overline{PB} = y_B - y_P.$$

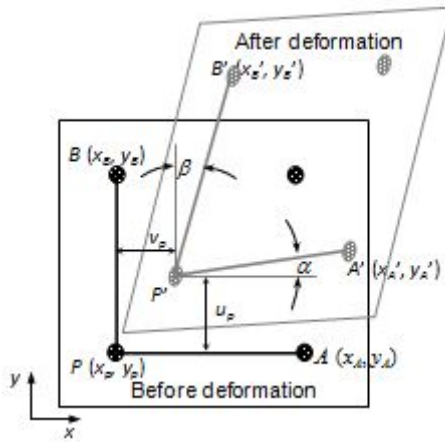


Fig. 5 Markers and its deformation kinematics

If the loading force  $F$  and the cross-section area  $A$  in the unloaded state are given, assuming linear elastic material response the stress-state is known, then Eq's (41) yield the Young's modulus  $E$  and either Poisson's ratio  $\nu$  or the shear-modulus  $G$ .

$$\begin{aligned}\nu &= -\frac{\varepsilon_y}{\varepsilon_x} \\ A(\varepsilon) &= b \cdot d(1 - \nu \cdot \varepsilon_x)^2 = b \cdot d(1 + \varepsilon_y)^2 \\ \sigma_x &= \frac{F_x}{A(\varepsilon)} = \frac{F_x}{b \cdot d}(1 + \varepsilon_y)^{-2} \\ E &= \frac{F_x}{b \cdot d} \times \varepsilon_x^{-1} \times (1 + \varepsilon_y)^{-2} \\ (G &= \frac{E}{2(1 + \nu)})\end{aligned}\quad (10)$$

## Applications of Two-Dimensional DSCM

### *Measurement in the Field of Fracture Mechanics*

Two-dimensional DSCM has been used extensively in fracture mechanics studies, including crack-tip opening displacement (CTOD) during crack growth and strain measurements near crack-tips.

In the field of fracture mechanics, recent studies have shown that a critical CTOD is a viable parameter for predicting crack growth and predicting the residual life of the structural components in engineering applications. Two-dimensional DSCM has been used successfully in measuring the in-plane deformations of thin aerospace materials under mixed-mode I/II loading. Specifically, CTOD, surface displacement and strain field measurement were all acquired through the use of the two-dimensional DSCM by Amstutz et al. [14]. In these studies, in-plane mixed-mode CTOD was measured both at initiation and during crack growth progress in thin 2024-T3 aluminum specimens. The effects of material grain orientation and mixed mode I/II loading on crack initiation and stable tearing of the material were investigated. The CTOD was found to be a strong function of crack orientation relative to the rolling direction. Mode I/II CTOD increased rapidly during initial increments of crack growth and then decreased towards a constant value as the growth continued.

Wang and Kang [15] measured the deformation of fields in the region of the crack-tip in thin copper foil material. Subsequently, they [16] studied the size effects on fracture behavior of the same material. The  $J$  integral and fracture toughness  $J_C$  were evaluated directly from the strain fields around the crack tip. The results indicated that  $J_C$  depends on foil thickness within a certain range of thickness (the thickness varied from 20 micron to 1 millimeter in that work). The schematic illustration of  $J_C$  evaluating processing is shown in Fig. 6. Wang et al. [17] studied the fracture behaviors of modified high polymer material.

### *Measurement in Micro-Scale Fields*

One asset of DSCM is that the measurement range extends from macro- to meso-scale, even to micro-scale fields. Recently, the method has been successfully extended to the study of meso-mechanics, measurement of micro-scale fields for deformations from scanning tunneling electron microscopy images [18]. Lockwood and Reynolds [18] presented a technique that utilized DSCM to provide a method of digitally reconstructing fracture surfaces from stereo pairs produced in the scanning electron microscope (SEM), for characterizing the three-dimensional geometry of fracture surfaces. Pascal et al. [19] applied DSCM to determine the local strain field in a heterogeneous material with a SEM.

In addition, DSCM has been applied in the micro-scale field using an optical microscope. Sun et al. [20] described a feasibility study of a high magnification full field deformation measurement using DSCM and found that the method could determine in-plane surface deformations at magnifications up to 2000 pixels/mm.

### Measurement in Non-Destructive Inspection

With the development of modern industry, non-destructive testing (NDT), which is designed to detect defects in components before they become critical under load, has become a well-established technique to ensure the safe and economical operation of components. DSCM also has some application in this field [21, 22, 23].

Coburn and Slevin [22] used DSCM system to evaluate the thermo-mechanical properties of two slightly different silicon nitride-based ceramic materials, yttria and neodymia. Russell and Sutton [23] observed the localized strain fields on the surface of a  $0^\circ/90^\circ$  glass-epoxy composite specimen with prefabricated flaws (inclusions or slits across the fibres) during a tension test.

Thermo-mechanical diagnostic techniques are required for the characterization and reliability engineering of electronic packaging. In this field, Lu et al. [24] measured thermo-mechanical strain using DSCM in an area encompassing the solder-copper interface near the corner of an outermost solder ball in a chip scale package and found that higher level constraints play a large part in solder joint deformation. Zhou and Goodson [25] studied the thermo-mechanical deformation of solder-joints in a cross-sectioned ball grid array thermal test package.

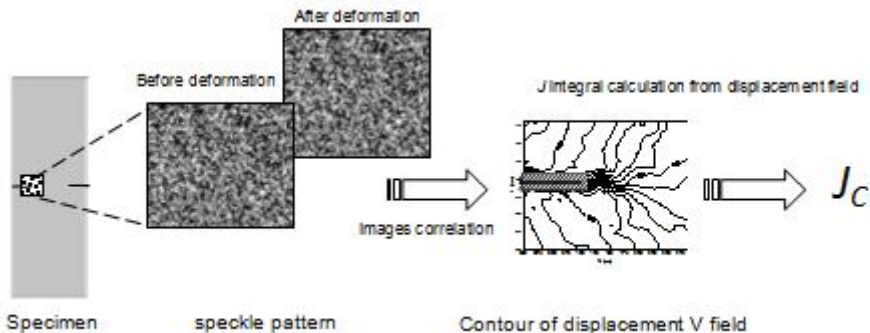


Fig. 6 Schematic illustration of  $J_C$  evaluating processing

### Essential Mechanical Properties Testing

One of the tasks of solid mechanics is to investigate and explore the mechanical behavior of materials. There are many applications of DSCM in study of the mechanical behaviors of many kinds of material such as polymeric materials, biomaterial, low-dimensional material and wood, paper, forest products, etc.

Chevalier et al. [26] used DSCM to discriminate models describing the mechanical behavior of polymeric materials under a biaxial loading condition through evaluating the heterogeneous strain field observed during those tests. Zhang et al. [27] adopted DSCM to examine the mechanical behaviour of arterial tissue from the bovine aorta, the results showing that the Poisson's ratio of the arterial sections increased with the magnitude of axial strain. Wang and Cuitino

[28] measured the heterogeneous deformation fields appearing during compression of ultralight open-cell polymeric foams.

## **Conclusions and Future Development**

DSCM/DICM is an efficient full-field photomechanics technique for both in-plane deformation measurement (two-dimensional DSCM) and three-dimensional deformation measurement (three-dimensional DSCM). The versatility and robustness of the method have been illustrated through numerous application examples from diverse areas during the past decades. On the basis of the preceding discussion, the following conclusions can be drawn:

1. Developing trends in DSCM are (1) the theory of the method is becoming increasingly sophisticated, (2) the convergence speed of the method is continually increasing, (3) the precision of the method is further increasing, and (4) the mathematical foundation employed has moved from classical mathematical theory to modern mathematical theory.

2. Application trends of the method are extending (1) from macro-field to meso-field and even micro-field, (2) from general materials to some novel materials, (3) from general surrounding conditions to severe surrounding conditions, such as high temperature, high pressure etc., (4) from laboratory conditions to engineering sites.

It is recognized that DSCM has become increasingly popular as an efficient optical measurement tool in experimental mechanics since its initiation in the early 1980s. However, there are still many possible extensions and areas in need of further development. Among those developments the following could be listed:

1. DSCM based on various theories used in the correlation search process has advantages and disadvantages. Further study is required to coordinate these theories ingeniously, to improve the performance of DSCM. It is possible that they might be combined in such a way that a global search followed by a local search achieves higher convergence speed and higher precision of the results.

2. Hardware with higher precision could be employed to improve DSCM, such as using CCD and a higher quality image board to improve precision; employing a higher speed PC to increase processing speed

3. Hybrid method combined by DSCM results and numerical method. For example, the experimental result obtained by DSCM can be used as the boundary condition of boundary element method (BEM).

4. Combine with SEM, STM, AFM and some other high resolution, high magnification factor device to micro-scale, even nano-scale measurement and MEMS measurement. Employ two-dimensional DSCM to measure surface profiles from multiple SEM images. Combine with high-speed photography for quasi-dynamic measurement or dynamic measurement.

## **Acknowledgement**

This work is supported by Program of International S&T Cooperation, MOST (Grant No. 2010DFA64560). The support by the National Natural Science Foundation of China (Grant No. 11072176, No. 11002100) and Tianjin Natural Science Foundation (No. 11JCYBJC26800) are also greatly acknowledged.

## **Reference**

- [1] Sutton MA, Wolters WJ, Peters WH, Rason WF, and McNeill SR (1983), Determination of displacements using an improved digital correlation method. *Image and Vision Computing* 1(3), 133-139.
- [2] Peters WH, Rason WF, Sutton MA, Chu TC, and Anderson J (1983), Application of Digital Correlation Methods to rigid body Mechanics, *Opt. Eng.* 22(6), 738-742.
- [3] Peters WH and Rason WF (1982), Digital imaging techniques in experimental stress analysis. *Opt. Eng.* 21(3), 427-431.
- [4] Yamaguchi I (1981), Laser-speckle strain gauge, *J. of Physics E: Scientific Instruments* 14 (11), 1270-1273.
- [5] Hou ZD, Qin YW(2002). A study of fractal interpolation method, in 3rd international conference on experimental mechanics, Xiaoping Wu, Yuwen Qin, Jing Fang, Jingtang Ke, , *Proceedings of SPIE Vol. 4537*, pp 386-389.
- [6] Chiang FP, Wang Q, Lehman F(1997), *New Developments in Full Field Strain Measurements Using Speckles*, ASTM Special Technical Publication, v 1318, p156-169.
- [7] Jin GC, Wu Z, Bao NK, and Yao XF(2003), Digital speckle correlation method with compensation technique for strain field measurements, *Optics and Lasers in Engineering* 39(4), 457-464.
- [8] Zhang D, Arola D, and Read D (2002), Fast-search strategy for digital image correlation, *Proceedings of the 2002 SEM annual*, p 80-82.
- [9] Voloshin A and Jose L. F. Freire (2000), Displacement Measurement using RGB. In *Proceedings of the 2000 SEM IX international congress on experimental mechanics*, Orlando, Florida. p140-143.
- [10] Qian KM, Soon SH, and Asundi A(2002), Evaluation of binary speckle correlation. In *Proceeding of optical technology and image proceeding for fluids and solids diagnostics*, Sept. 3-6, 2002, Beijing.
- [11] He XY, Xia J, Quan C, Tay CJ, and Tu SD(2001), Creep deformation measurement using quartz optical fiber. *Optics Communications* 190(1), p79-86.
- [12] Smith TS, Bay BK, and Rashid MM (2002), Digital volume correlation including rotational degrees of freedom during minimization, *Exp. Mech.* 42(3), 272-278.
- [13] Wang HW, Kang YL, Laermann KH, Zhang ZF, and Fu DH, Marker identification technique for deformation and strain testing, submitted to *Exp. Mech.*
- [14] Amstutz BE, Sutton MA, Dawicke DS, and Boone, ML (1997), Effects of mixed mode I/II loading and grain orientation on crack initiation and stable tearing in 2024-T3 aluminum, *ASTM Special Technical Publication v 1296*, 105-125.
- [15] Wang HW and Kang YL (2001), Digital Speckle Correlation Test for Fracture of Thin Film, in 10th international conference on fracture, Honolulu, Oahu, Hawaii, USA.
- [16] Wang HW, Kang YL, Zhang ZF, and Qin QH(2003), Size effect on fracture toughness of thin metallic foil, *International Journal of Fracture*, 123(3-4):

- 177-185.
- [17] Wang DM, Ji HW, and Qin YW (1999), Studies on fracture behaviors of the modified high polymer material by using digital image correlation method, *Journal of Tongji University* 27(3), 278-281.
  - [18] Lockwood WD and Reynolds AP (1999), Use and Verification of Digital Image Correlation for Automated 3-D Surface Characterization in the Scanning Electron Microscope, *Materials Characterization* 42(2), 123-134.
  - [19] Pascal D and Michel B(2000). Micromechanical Application of Digital Speckle Correlation Techniques. In *Interferometry in Speckle Light: Theory and Applications*, Springer, 67-74.
  - [20] Sun ZL, Lyons JS, and McNeill SR(1997), Measuring microscopic deformations with digital image correlation, *Optics and Lasers in Engineering* 27 (4), 409-428.
  - [21] Chan YC, Fan Y, Jin GC, Bao NK, and Chung PS (1995), Nondestructive Detection on Miniaturial Meltlayer Ceramic Capacitors Using Digital Speckle Correlation Techniques, *IEEE Transaction Components, Packaging and Manufacturing Technology* 18(3), 677-682, 1995.
  - [22] Coburn D and Slevin J (1995), Digital Correlation System for Nondestructive Testing of Thermally Stressed Ceramics, *App Op* 34(26), 5977-5986.
  - [23] Russell SR, Sutton MA, and Chen HS (1989), Image Correlation Quantitative NDE of Impact and Fabrication Damage in a Glass fiber Reinforced Composite System, *Materials Evaluation* 47(5), 550-558.
  - [24] Lu H, Yeh CP, and Dai JB(1999), Experimental evaluation of effect of global to local interaction on HDI solder joint deformation, *Proceeding of Electronic Components and Technology Conference*, 469 -474.
  - [25] Zhou P and Goodson K(2000), Thermomechanical diagnostics of BGA packages using digital image/speckle correlation, *Proceeding of Thermal and Thermomechanical Phenomena in Electronic Systems* 2, 240 -245.
  - [26] Chevalier L, Calloch S, Hild, F, and Marco, Y (2001), Digital image correlation used to analyze the multiaxial behavior of rubber-like materials, *European Journal of Mechanics - A/Solids* 20(2), 169-187.
  - [27] Zhang DS, Eggleton CD, Arola DD(2002), Evaluating the mechanical behavior of arterial tissue using digital image correlation, *Exp. Mech.* 42 (4), 409-416
  - [28] Wang Y, Cuitino AM(2002), Full-field measurements of heterogeneous deformation patterns on polymeric foams using digital image correlation, *International journal of solids and structures* 39 (13-14), 3777-3796.

## MECHANICAL BEHAVIORS SIMULATION OF COPPER MATRIX REINFORCED WITH $Al_2O_3$ \*

H.W. Wang<sup>1</sup>, H. W. Zhou<sup>2</sup>, L. Mishnaevsky Jr.<sup>3</sup>, V. Rajković<sup>4</sup>

<sup>1</sup>Tianjin Key Laboratory of Refrigeration Technology, Tianjin University of Commerce, Tianjin 300134, China

<sup>2</sup>State Key Laboratory of Coal Resources and Safe Mining, China University of Mining and Technology, Beijing 100083, China

<sup>3</sup>Department of Wind Energy, Technical University of Denmark, P.O. Box 49, Frederiksborgvej 399, DK-4000 Roskilde, Denmark

<sup>4</sup>Materials Science Laboratory, Institute of Nuclear Sciences "Vinca", University of Belgrade, P.O. Box 522, 11001 Belgrade, Serbia  
wanghw@tjcu.edu.cn

### Abstract

Nanostructured copper matrix, formed by addition of small amount of nanoparticles, such as  $Al_2O_3$  particles, have much better mechanical properties than the common copper matrix. A computational study of the effect of structures of nanocomposites on their elastic properties is presented. A special program code for the automatic generation of 3D multiparticle unit cells with/without overlapping interface layers around particles is developed for nanocomposite modeling in ABAQUS. The effects of the interface properties, particle sizes and volume fraction of nano-reinforcement on the mechanical properties of nanocomposites are studied in numerical experiments. Results indicate that the higher degree of particle clustering leads to lower Young's modules of the nanocomposites. The stiffness of the composite increases with increasing the particle volume fraction. With increasing the interface stiffness, the positive effect of the reinforcement increases. Smaller particle size causes higher Young's modules of the nanocomposites.

*Keywords: Copper matrix; Nano composites; Mechanical properties; Numerical Modeling; Finite element analysis; Elastic properties*

---

\* This work is supported by the Sino-Serbian inter-governmental S&T cooperation (No. 1-12).

## **PROGRESS IN THE DEVELOPMENT OF RECYCLING-FRIENDLY WROUGHT ALUMINIUM ALLOYS**

Varužan Kevorkijan, Impol R in R d.o.o., Partizanska 38,  
2310 Slovenska Bistrica, Slovenia

### **Abstract**

The purpose of this paper is to present activities for further increase in the sustainability of wrought aluminium alloys, mostly focused on formulation of wrought alloys with broader compositional tolerance limits for the desired properties. The main technological challenges in attaining these goals are development and implementation of: (i) more effective prior-to-melt scrap sorting and mixing procedures for achieving the appropriate metallurgical composition of the low grade scrap-based inputs with minimal addition of alloying elements and primary aluminium, as well as (ii) advanced processes for more reliable detection and removal of inclusions. Further steps in the compositional formulation of recycling-friendly aluminium alloys toward unification, - possibly by reducing their number, and the impact of such modifications on the global aluminium industry are also discussed.

### **Introduction**

Increasing the recyclability of wrought aluminium alloys through higher consumption of cost beneficial grades of external scrap (post-consumed scrap with organics) is technologically very demanding. In spite of the significant progress made in recent decades in the development of pre-melt, melt and refining technologies, the recyclability of commercial wrought alloys of standard quality remains far below the level already established in cast alloys. The main reasons for this are: (i) the existence of very narrow upper limits for the maximally allowed concentrations of alloying and tramp elements in wrought aluminium alloys, which significantly reduces possibilities for using less-defined scrap as the raw material; and (ii) the fundamental thermodynamic barrier to the removal of most elements from the melt, in practice limiting the refining procedures for wrought aluminium alloys to lowering the content of magnesium and calcium, as well as the removal of inclusions and hydrogen [1].

The expected benefits of using lower scrap grades instead of clean scrap are mostly in improved added value, as well as in the much better scrap availability and flexibility in supply. On that account, producers of wrought aluminium alloys are interested in technological restructuring, replacing new industrial with post – consumed scrap. The predominant objective in recycling wrought aluminium alloys is to achieve a standard chemical composition selected for strength, at the same time keeping the cost of raw materials and the overall production costs to the minimum. To achieve these two goals simultaneously, it is necessary to minimize the consumption of primary aluminium and new industrial scrap, replacing it with scrap of lower quality. However, to open such a “compositional window” for lower quality scrap it would be necessary to reformulate the composition of wrought

alloys, introducing broader compositional tolerance limits in a way which would not influence the selected combination of alloy properties.

The best existing recycling practice for wrought aluminium alloys is focused on implementation of the state-of-the-art **pre-melt physical separation**. This is combined with: (i) **scrap mixing technologies** for achieving the prescribed composition and the required compositional tolerance limits with the minimal addition of primary Al and alloying elements, (ii) **melt-technologies**, enabling the processing of scrap contaminated with various additives, as well as (iii) **modern removal techniques for inclusions and hydrogen** for assuring a standard quality of the melt.

Recent efforts toward further, more significant increases in the recyclability of wrought aluminium alloys are based on formulation of alternative (“recycling friendly”) wrought alloy compositions possessing broader compositional tolerance limits, but still capable of providing a suitable mix of commercially defined structural properties, and on development of new concepts of alloy recycling.

Thus, the purpose of this paper is to present activities for further increasing the sustainability of wrought aluminium alloys, mostly focused on formulation of wrought alloys with broader compositional tolerance limits for the desired properties. The future trends in the compositional formulation of recycling friendly scrap-intensive aluminium alloys toward unification and reduction in their number, as well as the impact of these factors on the global aluminium industry are also discussed.

### **Development of alternative wrought compositions for desired (numerically predicted) properties**

Generally, the selected properties of a wrought aluminium alloy (e.g. yield strength-YS, ultimate strength – US, elongation-L and hardness, H) can all be expressed as different (usually polynomial) functions of the alloy composition [2]:

$$YS = F (X_1, X_2, X_3, \dots, X_n) \quad (1)$$

$$US = G (X_1, X_2, X_3, \dots, X_n) \quad (2)$$

$$L = L (X_1, X_2, X_3, \dots, X_n) \quad (3)$$

$$H = H (X_1, X_2, X_3, \dots, X_n) \quad (4)$$

Here,  $X_1, X_2, X_3, \dots, X_n$  represent the concentrations of particular alloying elements. In addition, the concentrations of alloying elements in wrought aluminium alloys, especially in recycled ones, are usually selected for achieving maximal strength. To assure the proper combination of properties (not only mechanical but also electrical, thermal, corrosion resistant etc.), the concentrations of alloying elements should be inside the standard tolerance limits. The required standard compositional tolerance limits can be routinely attained by using raw materials of standard quality (primary aluminium and alloying elements) and also by replacing a certain amount of primary aluminium (typically less than 30%) with compositionally well defined, clean scrap (usually new industrial scrap - single alloy from well established closed loops). However, in compositions with a prevailing proportion of incoming scrap (even blended from different compositionally well-defined fractions

of sorted scrap), compositional degradation cannot be avoided [3]. Although the level of degradation depends on the total amount of scrap involved in the blended mixture, the number of sorted scrap fractions involved in blending the mixture for melting is also very significant. More sorted scrap fractions are combined, the higher is the possibility for compositional deviations in the final mixture, and consequently the more difficult it is to keep the concentrations of alloying elements inside the standard compositional tolerance limits. Therefore, producers of recycled wrought alloys try to develop compositions with broader tolerance limits, which at the same time do not significantly influence the selected (usually some of the mechanical) properties of the alloys. Statistically, in the real blend for melting obtained by such mixing of different fractions of sorted scrap, the concentrations of some of the alloying elements will be higher than prescribed by the standard, the concentrations of others will be lower, and there will also be some alloying elements whose concentrations will fit the standard requirements. The situation is illustrated in Fig. 1 where the concentration  $X_1$  of the alloying element 1 in the scrap mixture prepared for melting is inside the standard interval of concentrations, the concentration  $X_2$  of the alloying element 2 is higher and the concentration  $X_3$  of the alloying element 3 is lower. However, all three concentrations are inside the alternative interval of concentrations formulated for the “recycling-friendly” composition.

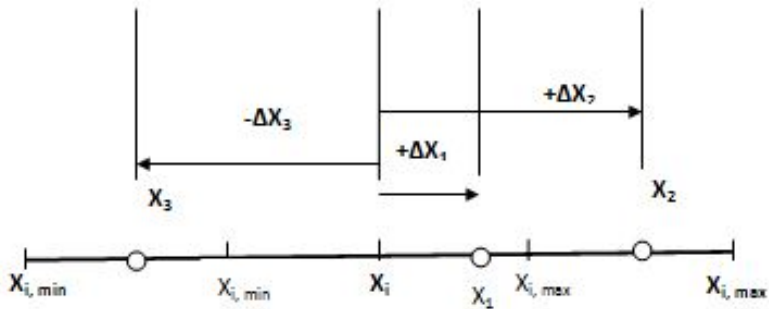


Fig. 1: Examples of standard and non-standard tolerance limits with the relevant denotations used in the model.

The mathematical condition for “recycling friendly” alloy compositions under which the selected alloy properties will all remain the same is expressed by Eqs. (5) - (8):

$$dYS = (\partial YS/\partial X_1)dX_1 + (\partial YS/\partial X_2)dX_2 + (\partial YS/\partial X_3)dX_3 + \dots + (\partial YS/\partial X_n)dX_n = 0 \quad (5)$$

$$dUS = (\partial US/\partial X_1)dX_1 + (\partial US/\partial X_2)dX_2 + (\partial US/\partial X_3)dX_3 + \dots + (\partial US/\partial X_n)dX_n = 0 \quad (6)$$

$$dL = (\partial L/\partial X_1)dX_1 + (\partial L/\partial X_2)dX_2 + (\partial L/\partial X_3)dX_3 + \dots + (\partial L/\partial X_n)dX_n = 0 \quad (7)$$

$$dH = (\partial H/\partial X_1)dX_1 + (\partial H/\partial X_2)dX_2 + (\partial H/\partial X_3)dX_3 + \dots + (\partial H/\partial X_n)dX_n = 0 \quad (8)$$

where  $(\partial YS/\partial X_1)dX_1$ ,  $(\partial YS/\partial X_2)dX_2$ ,  $(\partial YS/\partial X_3)dX_3$  ...  $(\partial YS/\partial X_n)dX_n$ ,  $(\partial US/\partial X_1)dX_1$ ,  $(\partial US/\partial X_2)dX_2$ ,  $(\partial US/\partial X_3)dX_3$  ...  $(\partial US/\partial X_n)dX_n$ ,  $(\partial L/\partial X_1)dX_1$ ,  $(\partial L/\partial X_2)dX_2$ ,  $(\partial L/\partial X_3)dX_3$  ...  $(\partial L/\partial X_n)dX_n$  and  $(\partial H/\partial X_1)dX_1$ ,  $(\partial H/\partial X_2)dX_2$ ,  $(\partial H/\partial X_3)dX_3$  ...  $(\partial H/\partial X_n)dX_n$  are the partial differentials of the functions YS, US, A and H where  $\pm dX_1$ ,  $\pm dX_2$ ,  $\pm dX_3$ , ... ,  $\pm dX_n$  correspond to the infinitesimal tolerance limits. Here and in what follows, the symbols presented in bold correspond to values inside the standard tolerance limits, whereas symbols not in bold represent values outside the tolerance limits. For practical (numerical) application, the infinitesimal values of the tolerance limits should be substituted by the **real** deviations,  $\pm \Delta X_i$ , of the concentrations of the individual alloying elements from the prescribed standard average values,  $x_i$ :

$$x_i = (x_{i,max} - x_{i,min})/2 \quad (9)$$

Note that  $x_{i,max}$  and  $x_{i,min}$  correspond to the upper and lower values of the standard tolerance interval of concentration for the appropriate alloying element, as schematically represented in Fig. 1. In this way, the numerical solution of the system of Eqs. (5) – (8) gives the combination of non-standard and standard tolerance limits ( $\Delta X_i$ ) under which the selected alloy's properties YS, US, A and H remain the same. However, it is important to note that under the above conditions is possible to create alternative alloy compositions which enable selected alloy properties to remain the same (e.g. the tensile strength, elongation, hardness), whereas some others will be definitely changed (e.g. thermal or electrical conductivity, corrosion resistance etc.).

### Quality of recycled alloys

Considering that "quality is the measure of the ability to fulfil defined and presumed demands" as defined by the German Institute of Standardisation, the following two measures of the quality of recycled aluminium alloy are particularly important for production of wrought alloys : (i) **compositional deviations** caused by replacing well-defined raw materials (primary aluminium and pure alloying elements) with wastes - metallurgically not pure enough and/or compositionally non-compatible ("unfit for purpose") incoming scrap, having an incorrect combination and/or content of major, minor and trace elements (impurities); and (ii) **the amount of inclusions**, enhanced by substituting primary aluminium with lower grades of scrap containing organics.

### Solutions for dealing with compositional deviations

In all recycled and especially in wrought aluminium alloys, the accumulation of unwanted chemical elements (trace elements – i.e. elements occurring naturally but not added in the production process) is a growing problem. The main reason for that lies in the quite large thermodynamic barrier to the removal of unwanted elements from molten aluminium, limiting the efficiency of refining procedures (selective melting, fluxing, Hoppes process, low temperature electrolysis, segregation and distillation technologies[1]), and also making them expensive.

Except for fluxing, all the other refining procedures are not part of industrial practice. Hence, continuous accumulation of unwanted elements, directly proportional to the number of recycling cycles performed on the initial alloy, appears as a kind of “recycling entropy”, resulting in increasing and uncontrolled concentrations of minor and unwanted (trace) elements in the recycled streams.

The most effective way of reducing the compositional deviations of recycled wrought aluminium alloys is to achieve the proper chemical composition before melting by combining the appropriate qualities and quantities of scrap, primary aluminium and alloying elements. Nowadays, significant removal of unwanted elements is assured in industry by physical separation of aluminium scrap into metallurgically clean fractions with proper chemical composition. The processes frequently used in industry are magnetic separation, air separation, eddy current separation, sink float/heavy media separation, colour sorting by hand, spectrographic technologies and hot crush [1].

### **Detection and removal of inclusions**

Inclusions are solid particles suspended in molten aluminium which are generally divided in two main classes [4]: (i) **exogenous** - already existing as a separate phase before melting (e.g. oxides on the surface of aluminium scrap, materials from refractory linings, salts, incompletely dissolved alloy elements) and (ii) **endogenous** or in-situ formed by chemical reactions taking place in the melt. Most inclusions can be classified as: (i) non-metallic, (ii) metallic and (iii) oxide films.

The most common sources of inclusions are: (i) **impurities in scrap**, particularly various non-metallic inorganic phases, among which exogenous oxides are predominant, as well as organics (paints, oils, lacquers, paper, inks, vinyls, phenolic resin, polymers, thermolacquers, etc.); and (ii) practically all the **different stages of alloy processing** – starting from scrap thermal processing (decoating, pyrolysis of composite packaging, paint removal), scrap melting technologies, holding and casting.

During thermal processing and melting of scrap, aluminium can be oxidised forming endogenous aluminium oxide of different morphology (skins, films or particles). However, it is important to note that endogenous aluminium oxide can also be formed by chemical reactions of various additives (e.g. pigments, paint fillers etc.) with molten aluminium. Additional sources of endogenous inclusions are compositional degradations caused by significant deviations from the specified amounts of major, minor and trace elements, grain refiners ( $\text{TiB}_2$ ), reaction products with graphite components, etc.

In industry, the detection of inclusions in molten metal is performed in two general modes: (i) off-line (by the **Porous Disc Filtration Apparatus - PoDFA**) and (ii) on-line (by the **Liquid Metal Cleanliness Analyzer - LiMCA**). Other methods are the **Pressure Filtration Melt Cleanliness Analyzer - PreFil** and more recently the **Optical Emission Spectroscopy (OEA)**. PoDFA, which is the proprietary technology for melt cleanliness evaluation, provides off-line information on the composition and concentration of the inclusions in molten aluminium. PoDFA samples can be routinely analysed by optical and scanning electron microscopy (SEM-EDS),

providing qualitative and quantitative information about the inclusions concentrated in the filter cake. On-line inclusion monitoring is possible by several methods, among which the most sophisticated is LiMCA II, based on a Coutler counter, which detects the total concentration and size distribution of inclusions by their impact on the electrical conductivity of aluminium flowing through a small tube. The inclusions are registered separately and counted per unit mass of metal.

PreFil, which is another proprietary inclusion analyser, is the only method that provides immediate information about the concentration of inclusions in the melt and, at the same time, a sample for further metallographic analysis, as performed on PoDFA samples. Fast detection of inclusions in aluminium alloys by optical emission spectrometry (OES) is an easy to use and cost-effective analytical technique, which in future, with some additional software development and more experience in the aluminium industry, might be a very useful tool for both quantitative and qualitative investigation of inclusions.

Industrial methods of inclusions removal involve (1) sedimentation, (2) flotation, and (3) filtration. Sedimentation is the process of settlement of inclusion particles at the bottom of the furnace melt. The process is governed by Stokes law, therefore the smaller the inclusions, the slower they will settle to the bottom of the furnace. Flotation is caused by the attachment of inclusions to bubbles rising in the melt from an injected chlorine and argon gas mixture, promoting migration of low density inclusions of the corresponding size to the surface of the molten aluminium.

The most effective method for inclusion removal, especially for finer fractions of particulates, is filtration [4]. The two main types of industrial filtrations are cake filtration (capturing inclusions at the surface of the filter), and deep bed filtration (entrapping particles inside ceramic filter pores by friction, confinement, electrostatic forces and chemical bonding). The significant progress made in deep bed filtration of molten aluminium in the last 20 years is one of the main reasons why recycled aluminium is able to compete with primary, even in very demanding wrought Al applications.

Particularly effective in filtering recycled molten aluminium for production of wrought alloys are the current generations of cartridge filters with tubes consisting of controlled size alumina particulate and a proprietary molten aluminium resistant binder, assembled into nitride-bonded refractory end plates.

## **Further steps in development of recycling-friendly wrought aluminium alloys**

Further developments in the recycling of wrought aluminium alloys will most probably result in (i) a significant reduction of the number of wrought alloys, and (ii) in replacing the existing recycling technologies based on extractive metallurgy with more advanced (so-called “recycling-friendly”) ones. In that sense, it is important to note that in future the term “**recycling-friendly**” will not necessarily mean just the broader tolerance limits of alloying elements, but the development of wrought alloys with **advanced chemical composition and physical properties** making them “recycling-friendly”. All these trends/factors will certainly create a significant impact on the entire aluminium chain and a complete revolution in the demands of end-users. The proposed reduced number of wrought aluminium alloys should be

able to provide a satisfactory range of mechanical, tribological and corrosion resistant properties, combined with (i) satisfactory formability (forming, forging, extrusion), (ii) excellent capabilities for productive and precise machining, (iii) good welding, brazing and soldering capabilities, and (iv) high capabilities for cleaning, finishing and coating.

## Conclusion

Because of the high cost and shortages of raw materials (primary aluminium and clean scrap), the main challenge facing producers of wrought aluminium alloys and semis are: (i) running production with alternative, cost-effective sources of aluminium; and (ii) with sources of metal which are more easily available. However, recent developments in recycling technology and inside the global recycling industry, together with the actual global economic crisis, started to change this traditional framework toward a new mentality among remelters. Following the opportunities for creating new added value in their niche business, remelters refocused on production of wrought alloys from less clean, so-called **metallurgically** clean scrap, which could be contaminated even with high amounts of various non-metallic (e.g. organic) impurities. In addition, they became familiar with achieving the proper composition of scrap batches before loading the scrap into the furnace (through the sorting of scrap), avoiding the more expensive dilution of impurities by primary aluminium addition during melting. To this end, several pre-melting operations (scrap sorting and separation, as well as in-house scrap batch compositional blending) were integrated into the production chain, together with some post-melting operations, such as traditional molten metal refining. With all these changes, contributing essentially to the creation of new added value, **a new mentality in remelters closer to recycling** production practice was established, increasing the importance of contaminated scrap as a long term source of aluminium for wrought alloys.

## References

- [1] G. Gaustad, E. Olivetti, R. Kirchain. Resources, Conservation and Recycling 58 (2012) 79-87.
- [2] J. T. Staley, R. E. Sanders, Jr., In: Handbook of Aluminum, Vol. 2, Eds.: G. E. Totten, D. S. MacKenzie, CRC Taylor & Francis, 2003, p. 319.
- [3] J. B. Hess, Metallurgical Transactions A, 14A (1983) 323-327.
- [4] M. E. Schlesinger, Aluminium Recycling, CRC Press, Broken Sound parkway, NW, 2007.

## **GOLD NANOPARTICLES- PROPERTIES, SYNTHESIS AND APPLICATION**

<sup>1</sup>Rebeka Rudolf, <sup>1</sup>Ivan Anzel, <sup>2</sup>Srečko Stopić, <sup>2</sup>Bernd Friedrich, B.,  
<sup>3</sup>Miodrag Čolić

<sup>1</sup>*Rebeka Rudolf E-Mail: rebeka.rudolf@um.si*

<sup>1</sup>*Faculty of Mechanical Engineering, Maribor, Slovenia*

<sup>2</sup>*IME Process Metallurgy and Metal Recycling, RWTH Aachen University, Germany*

<sup>3</sup>*Military Medical Academy, Institute of Medical Research, Belgrade, Serbia.*

### **Abstract**

Gold is a noble metal that is inert and shows little reactivity. The resistance of gold to corrosion has been known to humans for millennia and is reflected in the use of gold in jewellery and currency. Nanosized gold particles are used as a catalyst in important chemical reactions, such as the oxidation of hydrogen and carbon monoxide. The release of gold for metallurgical recovery from gold deposits is dependent on the nature and particle size of the gold-bearing mineral, the textural association of gold with gangue and economically recoverable sulphides. Lately, gold nanoparticles have been of high interest because of their potential application in electrochemistry, in medicine and in some nanodevices. The reasons for the high reactivity of gold nanoparticles are assumed to be hidden in their atomic structure. Different synthesis methods for preparation of nanosized gold particles have been used, such as photoreduction, chemical reduction in aqueous solutions and thermal decomposition in organic solvents. Chemical synthesis of gold nanoparticles with well-controlled shapes, sizes and structures is becoming a practical reality by using colloid chemistry. This study provides the newest information regarding the synthesis of gold nanoparticles via the ultrasonic spray pyrolysis method and reduction in aqueous solution. Ultrasonic spray pyrolysis (USP) is the mostly used method for the synthesis of particles with controlled and uniform particle size because of easy powder morphology control and the availability of cheap precursor solutions. In the USP process a metal-containing solution is cold atomized forming an aerosol. Special attention is given in this paper to the formation of Gold nanoparticles from gold auric acid solution using sodium citrate as the reducing agent in an aqueous solution under atmospheric and high pressure.

A key feature of the non-spherical nanoparticles is that their optical properties vary dramatically with their physical dimensions. In contrast to gold nanospheres, their resonance frequency is tuneable over a wide range from blue to near-infrared and enables one to set the surface plasmon resonance to a wavelength or spectral region specific to a particular application. Together with the high degree of biocompatibility of gold, these structures show potential in a wide variety of biological applications. It is confirmed that gold nanoparticles play a role in cancer diagnosis and therapy. To improve early cancer detection, researchers

are developing in vivo biomedical imaging techniques with a resolution which can distinguish between healthy and malignant tissue.

*Keywords: gold, nanoparticles, synthesis, ultrasonic spray pyrolysis*

## **Introduction**

The word “Nano” (symbol n) is derived from the Greek meaning dwarf, and was firstly officially confirmed as standard in 1960. This prefix in the metric system denotes a factor of  $10^{-9}$  or 0.000000001. It is encountered frequently in science and electronics for prefixing units of time and length. Nanostructured materials have shown an explosion of scientific and industrial interest over the last few decades [1].

Gold is known to be a noble metal which means that it is inert in air and shows little reactivity. The resistance of gold to corrosion has been known to humans for millennia and is reflected in the use of gold in jewellery and currency. Gold nanoparticles (GNPs) have attracted increasing attention due to their unique properties in multidisciplinary research fields. They are available with diameters ranging from a few to hundreds of nanometres. Remarkably, novel emerging applications bring a huge growth of the global demand for GNPs. For example, GNPs are used largely as bio delivery vehicles in medicine [2]. GNPs are developed as catalysts in new usages [3, 6]. To meet the enlarging demand for GNPs, more attention should be paid to effective synthesis methods, which should also be environmentally friendly and energy saving. From our previous work [4, 5], GNPs were synthesized by Ultrasonic Spray Pyrolysis (USP). The results suggest that USP enables the synthesis of pure GNPs with a size of a hundred nanometres. The reduction in aqueous solution using a sodium citrate offers a new way for obtaining a decrease in particle size.

## **Properties of gold nanoparticles**

Due to their attractive electronic, optical, and thermal properties; gold nanoparticles (GNPs) have emerged with great interest, as well as catalytic properties, in the fields of physics, chemistry, biology, medicine, material science and some interdisciplinary fields. The optical properties of gold are conferred by the interaction of light with electrons on the gold nanoparticle surface. At a specific wavelength of light, collective oscillation of electrons on the gold nanoparticle surface causes a phenomenon called surface plasmon resonance, resulting in strong extinction of light [7]. The particular wavelength of light is strongly dependent on the gold nanoparticle size (as shown in Fig. 1):

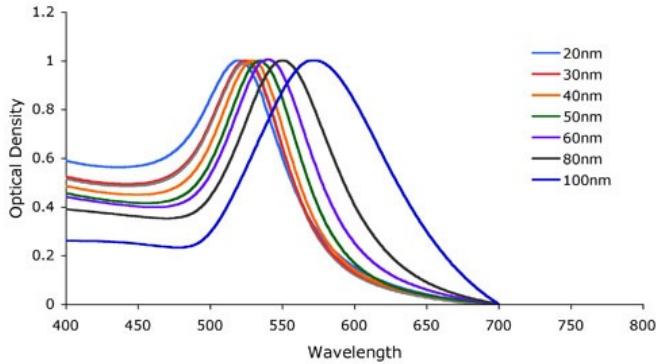


Figure 1: Gold nanoparticle size dependent surface plasmon resonance [7]

The influence of gold nanoparticle size on the surface plasmon resonance is shown in Figure 1 above, where the absorption maximum ( $\lambda_{max}$ ) increases from 520 nm to 570 nm for spherical gold nanoparticles between 20 and 100 nm, respectively. As a comparison, gold nanoparticles of sizes below 2 nm do not exhibit surface plasmon resonance.

The shape of gold nanoparticles has a big importance on their optical properties. Cytodiagnosics spherical colloidal gold have absorbance maxima between 515-570 nm, while irregular shaped particles such as gold nanorods, and “gold nanostars” have absorption maximum in the near-infrared region of the spectra [7]. The difference in absorption properties between spherical and irregular-shaped gold nanoparticles of the same average size is caused by an anisotropic distribution of the surface electron layers.

These nanostructure materials are distinguished from conventional polycrystalline micron materials by their fine crystallite sizes. A significant higher fraction of atoms are located at the surface of nanosized particulates as compared to conventionally prepared powders. The shape of gold nanoparticles is very different (spherical, cylindrical, prismatic, .), as shown in Figure 2. These particles show good biocompatibility without any cytotoxicity

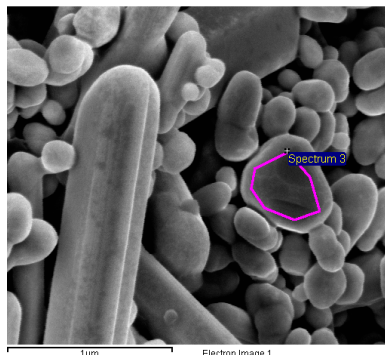


Figure 2: Nanogold produced from gold jewellery scrap by USP –method [3]

This structural characteristic is responsible for the enhanced reactivity of nanoparticles compared to conventional materials. Changes in properties at the nanosized level are shown especially in the following cases: Electrical (higher electrical conductivity in ceramics), magnetic (increase of magnetic coercivity down to a critical grain size), mechanical (enhanced ductility, toughness, and formability of ceramics), optical (increase in luminescent efficiency of semiconductors).

As shown in Figure 3, a decrease of particle radius leads to a smaller melting point of nanosized gold, which gives a new characteristic for some applications in medicine and catalysis. Modification of the rate of evaporation at the melting point was considered by Buffat and Borel [8].

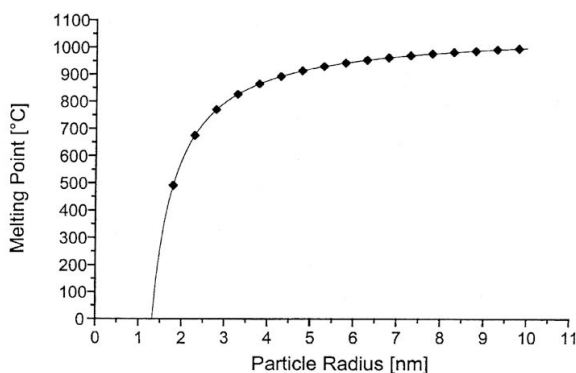


Figure 3: The change of melting point depends on gold particle radius [8]

The reasons for the high reactivity of these nanoparticles, so-called clusters, are assumed to be hidden in their atomic structure. As the active nanoparticles are smaller than the wavelength of visible light their structure cannot be inspected using an optical microscope.

Strong Paramagnetism of Gold Nanoparticles Deposited on a *Sulfolobus acidocaldarius* S Layer was reported by Bartolomé et al. [9]. X-ray magnetic circular dichroism and superconducting quantum interference device magnetometries demonstrate that the gold nanoparticles are strongly paramagnetic, without any indication of magnetic blocking down to 16 mK.

## Synthesis of gold nanoparticles

Chemical synthesis of gold nanoparticles with well-controlled shapes, sizes and structures is the subject in many investigations. The development of a colloid chemistry route continues to be essential for the synthesis and manipulation of anisotropic gold nanoparticles, with major requirements already demonstrated by Treguer-Delapierre et al. [10], such as the control of the nuclei shape and the growth on specific facets. In this review paper the presented preparation of nanosized gold particles by the ultrasonic spray pyrolysis method and reduction in water solution were done at the Institute for Process Metallurgy and Metal Recycling of the RWTH Aachen University, Germany. SEM analysis was performed at the Central Unit for Electron Microscopy of the RWTH Aachen

University. A Transmission Electron Microscope JEOL JEM-2100(HR) with attached Energy Dispersive X-ray Spectrometer EDS (JEOL JED-2300 Series) was used at the Faculty of Mechanical Engineering in Slovenia. Biocompatibility and cytotoxicity of gold nanoparticles were investigated at the Institute of Medical Research, Belgrade Military Medical Academy, Serbia. The cytotoxicity of gold nanoparticle fractions was tested using a standard method for measurement of mitochondrial succinic dehydro genase (SDH) activity in rat thymocytes and L929 mouse fibroblasts. Further microstructural analysis and biocompatibility studies are necessary for their selection from more toxic gold nanoparticles, which are contaminated with other microelements.

### *Ultrasonic Spray Pyrolysis*

Chloroauric acid  $\text{HAuCl}_4$  was used as precursor for the synthesis of gold nanoparticles by ultrasonic spray pyrolysis using the equipment shown schematically in Figure 4. The precursor was dissolved in water in order to prepare the solution for an aerosol production in an ultrasonic atomizer. The most important part of the set up contains: the ultrasonic atomizer, a small reactor, two bottles with water and alcohol for nanoparticle collection. Atomization of the obtained solution based on a water solution of gold chloride took place in an ultrasonic atomizer (Gapsol 9001, RBI/ France) with one transducer to create the aerosol. With regard to our previous results the resonant frequency was selected to be between 0.8 and 2.5 MHz.



*Figure 4: Experimental setup for the USP-synthesis of gold nanoparticles at IME, RWTH Aachen*

The most important components: Ultrasonic generator, thermostat, reaction tube, furnace, a bottle with water and alcohol, bottle with hydrogen. Nitrogen was firstly flushed from a bottle to remove air from the system. Under spray pyrolysis conditions hydrogen was overpassed continuously through the quartz tube ( $l= 1.0$  m,  $b= 20$  mm) at a flow rate of the 1 l/min. Then, atomized droplets of the solution based on gold were transported further by hydrogen to the furnace for hydrogen reduction at a different reaction temperature. After thermal decomposition and reduction of the transported aerosol in the furnace the formed gold nanoparticles were collected in a reaction tube and a bottle.

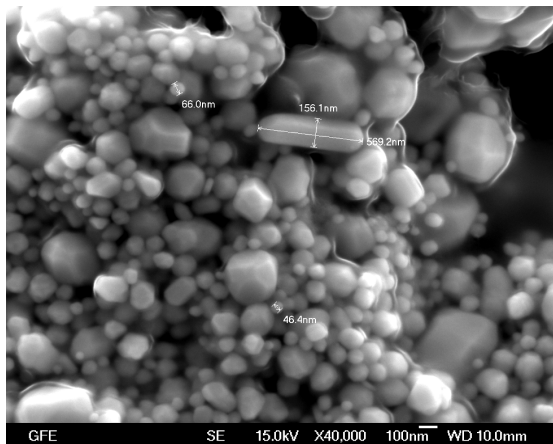


Figure 5: SEM analysis of Gold- Nanoparticles obtained by the USP-Process [5]

Two ultrasonic sources of 0.8 and 2.5 MHz, acting on the water solution of the  $\text{HAuCl}_4$  formed aerosols with constant droplet sizes between 2.26 and 4.79  $\mu\text{m}$ . The real size of droplet depends on the characteristics of the solution (surface tension, viscosity, and density) and the frequency of the ultrasound. In order to produce gold nanoparticles a subsequent thermal decomposition of the aerosol droplets was performed in a hydrogen atmosphere between 260 °C and 500 °C. SEM and EDS analysis have confirmed the presence of gold with different morphological forms (spherical, cylindrical and triangular), which is of great importance for some medical applications.

#### Reduction from aqueous solutions

Trisodium citrate (Alfa Aesar, 99.999%),  $\text{HAuCl}_4 \cdot 3\text{H}_2\text{O}$  (Alfa Aesar, 99,0 %min), Dialysis membrane(Spectrum Laboratories, Inc.) and Ultrapure deionized water were used for all solution preparations. All glassware was cleaned with aqua regia. To produce size controlled gold nanoparticles between 20 nm and 50 nm, through the chemical reduction ( $\text{Na}_3\text{C}_6\text{H}_5\text{O}_7$ ) method as described by Turkevich and Frens [11, 12], GNPs were prepared by the water bathed citrate reduction method. We set up easy reaction equipment like sets of beakers, which is more convenient and it is also possible to obtain uniform temperature distribution.



Figure 6: Synthesis of GNPs by citrate reduction and TEM analysis of GNPs

At first GNPs were synthesized from a 10mg Au in 100ml  $\text{HAuCl}_4$  solution increasing the volume of 1% trisodium citrate solution. In detail, 0.5ml, 1ml, 1.5ml, 2ml, 2.5ml of 1% trisodium citrate solution were preheated and added quickly into the  $\text{HAuCl}_4$  solution while stirring and heating for 15min. Then we kept stirring until the nanogold solution cooled down.

Sample 1, with 10mg Au/100ml of  $\text{HAuCl}_4$  solution and 1ml 1%  $\text{Na}_3\text{C}_6\text{H}_5\text{O}_7$ , water based method dialysis experiment for 48h, has been characterized by induced coupled analysis and TEM. The chemical analysis results, as Table 1 shows below, demonstrate here that, experimentally, gold nanoparticles' solution can be purified using the dialysis method. Considering the concentration changes of  $\text{Cl}^-$ , dialysis duration should be longer than 48h to get a more purified nanogold solution. Fig. 8 shows the TEM images of Sample 1. The size distribution of these GNPs ranges from 10nm to 50nm, the morphologies of these particles is inhomogeneous.

Table 1: Chemical analysis results for sample1 dialysis for 48h

Samples	Au	$\text{Na}^+$	$\text{Cl}^-$
	ppm	ppm	mg/L
Sample 1 (before dialysis)	117	90	≈95
Sample 1 (dialysis 48h)	94	≤1	≈16

For further purification dialysis Sample 2 and Sample 3 were prepared with 10mg Au/100ml of  $\text{HAuCl}_4$  solution while 0.5ml and 2.5ml 1%  $\text{Na}_3\text{C}_6\text{H}_5\text{O}_7$  water based method dialysis experiment for 144h, which was then characterized by chemical analysis and TEM. It was found that dialysis for 144h could obtain purified nanogold solutions by reduction from trisodium citrate and that a relatively large volume of trisodium citrate will help obtain GNPs with smaller size, which is indicated in Fig 7 (right). These findings are consistent with the results reported by Frens in Ref. 12.

#### Synthesis of GNPs under higher temperature and pressure

The concentration of  $\text{HAuCl}_4$  solution and trisodium citrate solution were fixed to 10 mg Au/100ml and 1ml 1%  $\text{Na}_3\text{C}_6\text{H}_5\text{O}_7$ . The water based method could always keep the reaction temperature below  $100^\circ\text{C}$ . To get more stable GNPs we used the autoclave to make the reaction temperature  $150^\circ\text{C}$  (about 0.5 MPa), 2h, and prepare 5 samples during this procedure for different durations (as shown in

Fig. 7). We expected that an increase of temperature and pressure in the system would lead to a decrease of particle size.



Figure 7: Synthesis in autoclave at 150°C, from 40min to 120min and TEM Analysis

The colour of the obtained gold nanoparticles can be compared with commercial ones from STREM Chemicals, INC gold nanoparticles.

### Application

Gold nanoparticles supported on ceria are excellent general heterogeneous catalysts for the aerobic oxidations of alcohols in organic solvents [13]. Amongst catalysts with different supports, but similar gold particle size and content, nanogold on ceria exhibits the highest activity.

Interaction between gold nanoparticles and biological species found in aqueous solution are being used as a basis for the development of biosensors. As reported by Baker and his colleagues at the University of Michigan [14] by combining chemical and physical therapy, gold nanoparticles with branching polymers could attack tumours in multiple ways. The nanoparticles are gathered inside cancer cells. Once that concentration is high enough, gold nanoparticles are heated up by laser or infrared light in order to destroy the cancer cells like a “thermal scalpel”.

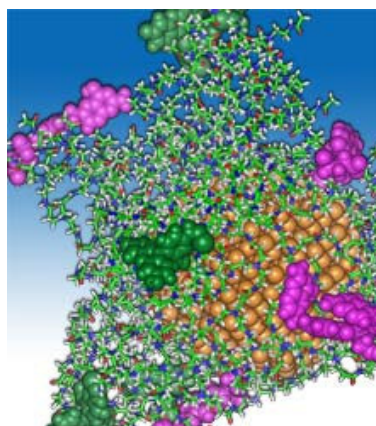


Figure 8: Gold nanoparticles with branching polymers [14]

Because of their good biocompatibility gold nanoparticles enveloped in treelike polymer branches could act as a multipurpose tool for fighting cancer. Folic acid (pink) and fluorescent dye (green) were attached to the nanoparticle in order to target and image tumours. Then tumour cells could be killed with cancer drugs, which are attached to the particle, and with lasers that heat up the gold nanoparticles. GNPs are conjugated readily to antibodies and other proteins due to the affinity of sulfhydryl (-SH) groups for the gold surface, and gold-biomolecule conjugates have been incorporated widely into diagnostic applications, where their bright red color is used in home and point-of-care tests such as lateral flow assays.

The gold plasmon resonance is the basis for the enhanced spectroscopy method such as Surface Enhanced Raman Spectroscopy (SERS) which can be used for detection with ultrahigh sensitivity.

## **Conclusion**

Gold Nanoparticles GNPs are of high interest because of their potential application in electrochemistry, the automotive industry, and medicine. The reasons for the high reactivity of gold nanoparticles are assumed to be hidden in their atomic structure. As the active nanoparticles are smaller than the wavelength of visible light their structure cannot be inspected using an optical microscope. Especially in recent years an important use of GNPs is available in the field of medicine for the diagnosis of and fight against cancer. The interaction of nanoparticles with biomolecules and microorganisms is an expanding field of future research. Within this field an unexplored area is the interaction of metal nanoparticles with different viruses. As relatively inexpensive and quite versatile techniques ultrasonic spray pyrolysis and reduction from aqueous solutions were tested by the IME Process Metallurgy and Metal Recycling of the RWTH Aachen University in order to prepare nanosized gold particles with different shapes. The smaller particles were obtained using a reduction from aqueous solutions (10-40 nm) in comparison to the ultrasonic spray pyrolysis method. Medical investigation has confirmed the good biocompatibility of gold nanoparticles.

## **References**

- [1] Rittner, M.N, Abraham, T: Nanostructured Materials: An Overview and Commercial Analysis, *Journal of Metals* (1998), 1, 37 – 47
- [2] Sperling RA, Rivera Gil P, Zhang F, Zanella M, Parak WJ: Biological applications of gold nanoparticles. *Chem Soc Rev* (2008), 37:1896.
- [3] Zhou XC, Xu WL, Liu GK, Panda D, Chen P: Size-dependent Catalytic Activity and Dynamics of Gold Nanoparticles at the Single Molecule Level. *J Am Chem. Soc* 2010, 132:138.
- [4] Rudolf, R., Friedrich, B, Stopić, S, Anzel, I, Tomic, S, Čolić, M: Cytotoxicity of Gold Nanoparticles Prepared by Ultrasonic Spray Pyrolysis, *Journal of Biomaterials Applications* 26 (2012) 1, 595 – 612.
- [5] Dittrich, R., Stopic, S., Friedrich B: Mechanism of nanogold formation by ultrasonic spray pyrolysis, *Proceeding of European Metallurgical Conference 2011, Volume 3: Resources efficiency in the non-ferrous metals industry-optimization and improvement*, 2011, 1065-1076.

- [6] Bond, G, Early History of Catalysis by Gold, *Gold Bulletin*, (2008): 41, 235-241
- [7] [http://www.cytodiagnosics.com/gold\\_nanoparticle\\_properties.php](http://www.cytodiagnosics.com/gold_nanoparticle_properties.php)
- [8] Buffat, Ph, and Borell, J: Size effect on the melting temperature of gold particles, *Physical Review A*, (1976) 13, 6, 2287-2297.
- [9] Bartolomé et al., Strong Paramagnetism of Gold Nanoparticles Deposited on a *Sulfolobus acidocaldarius* S Layer, *Phys. Rev. Lett.* (2012) 109, 24, 7203
- [10] Treguer-Delapierre, M., Majimeö, J, Mornet, S, Duguet, E., Ravaine, S: Synthesis of non-spherical gold-nanoparticles, *Gold Bulletin*, (2008) 41/2, 195-207.
- [11] Turkevich J, Stevenson PC, Hillier J: A Study of the Nucleation and Growth processes in the synthesis of Colloidal Gold. *Discuss Faraday* 1951, 55.
- [12] Frens G: Controlled nucleation for Regulation of particle-Size in monodispersed Gold Suspensions, *Nature- Physical Science* (1973), 241, 20.
- [13] Abad A, Corma, A, García, H.: Controlled nucleation for regulation of particle-size in monodispersed gold suspensions, *Chemistry* (2008), 14, 212-222.
- [14] <http://www.technologyreview.com/Nanotech/18999/>

## THE RISE OF METALLURGY IN EURASIA: BALKAN PERSPECTIVE

Miljana Radivojević

*UCL Institute of Archaeology*  
*m.radivojevic@ucl.ac.uk*

The synergy of metallurgical and archaeological methods in studying the knowledge past societies had about metals has thus far yielded very important results about the evolution of technological knowledge in humankind. One of the most significant technological achievements in human history is the invention of metallurgy, humankind's power to substantially *transform matter*. This invention triggered a whole new era of fundamental economic, social and cultural changes.

The early beginnings of experimentation with copper minerals, which turned ores during the extraction process, have been particularly attracting scholarly attention worldwide. The crafting of metal objects was traditionally considered a unique expertise, and interpreted as having been discovered only once in the Old World (wertime, 1964 and literature therein). Renfrew (1969) challenged this model by advocating multiple inventions, based on the trajectory of metallurgy in the Balkans. The debate on single vs. multiple origins of metallurgy has continued ever since, and recently gained renewed interest (Roberts et al., 2009; and Radivojević et al., 2010 for opposing views).

Despite these debates on the *when* and *where*, there has been no research specifically addressing *how* and *why* metallurgy emerged and evolved. Usually, the origins of metallurgy have been studied in isolation and detached from their technological, social and environmental context. A systematic and interdisciplinary approach using sites and assemblages of a high archaeological and archaeometallurgical resolution is needed to provide answers to these questions.

For several years, the Serbian *Archaeology in the Vinča Culture Project* has investigated on a small scale three crucial sites for early metal production, Jarmovac, Belovode and Pločnik, the latter two dated to c. 5400- 4600 BC (Šljivar et al., 2006; Borić, 2009). The recent application of modern archaeometallurgical techniques on technological debris from Belovode has transformed our understanding of early metallurgy and yielded the world-wide earliest known evidence for copper smelting, at c. 5000 BC (Radivojević et al., 2010).

Here I present results of an interdisciplinary approach using assemblages of high archaeological and archaeometallurgical resolution in order to address the initial stage of the pyrometallurgy in three Vinča culture sites in Serbia. I identified and sampled well-contextualised archaeometallurgical materials coming from the sites of Belovode, Vinča and Gornja Tuzla, all dated to the first half of the 5<sup>th</sup> millennium BC. Microstructural, chemical and isotope analyses of slags, slagged sherds and copper ores gave unprecedented insight into which ore minerals were chosen for metal making. Our results indicated that early copper smiths were indiscriminately sourcing different kinds of weathered minerals, mostly carbonates,

sulphates, arsenates and phosphates, apparently basing their decision primarily on distinctive colours in the shades of green and black.

The smelting of these distinctively coloured minerals for the first time demonstrates the long-postulated experimental approach to the diversity of choices available and applied at this very early stage in metal extraction. Significantly, this included smelting unsuitable minerals as well as relatively complex ores, shedding new light on our understanding of the role of experimentation in the emergence and development of metallurgy.

The application of material science methods in studying the earliest known pyrometallurgical debris worldwide helped archaeologists understand the evolution of metallurgical skills in early civilisations, and enrich our knowledge of the first ever engineers, who happen to have lived in the territory of the modern day Serbia.

## **References**

- [1] Borić, D. 2009. Absolute dating of metallurgical innovations in the Vinča culture of the Balkans. In: Kienlin, T. L. & Roberts, B. W. (eds.) *Metals and Societies. Studies in honour of Barbara S. Ottaway*. Bonn: Verlag Dr. Rudolf Habelt GmbH. p. 191-245.
- [2] Radivojević, M., Rehren, T., Pernicka, E., Šljivar, D., Brauns, M. & Borić, D. 2010. On the origins of extractive metallurgy: new evidence from Europe. *Journal of Archaeological Science*, 37, 2775-2787.
- [3] Renfrew, C. 1969. The autonomy of the south-east European Copper Age. *Proceedings of the Prehistoric Society* 35, 12-47.
- [4] Roberts, B. W., Thornton, C. P. & Pigott, V. C. 2009. Development of metallurgy in Eurasia. *Antiquity*, 83, 1012-1022.
- [5] Šljivar, D., Jacanović, D. & Kuzmanović-Cvetković, J. 2006. New contributions regarding the copper metallurgy in the Vinča culture. In: Tasić, N. & Grozdanov, C. (eds.) *Homage to Milutin Garašanin*. Belgrade: Serbian Academy of Sciences and Arts and Macedonian Academy of Sciences and Arts. p. 251-266.
- [6] Wertime, T. A. 1964. Man's first encounters with metallurgy. *Science*, 146, 1257-1267.

## TOUGHENING AND STRENGTHENING IN ADVANCED CERAMICS AND THEIR COMPOSITES

Vladimir D. Krstic

*Advanced Ceramics and Nanomaterials*  
Queen's University, Nicol Hall  
Kingston, Ontario, Canada  
K7L 3N6

### Executive summary

Over the last number of years, there has been a continuous effort to fabricate ceramics with high fracture toughness and strength, comparable to those of metals and their alloys. Many new ceramic materials have been manufactured which offer high resistance to crack propagation approaching that of fiber reinforced composites. So far three different toughening and strengthening mechanisms were identified which offer the possibility to fabricate super strong and tough ceramics. These are:

- i) Crack bridging by elongated grains randomly or uniformly distributed in a matrix of equiaxed or slightly elongated grain matrix, often called *in-situ* toughening.
- ii) Crack deflection (change of crack direction by weak interface), and
- iii) Bridging by ductile ligaments left behind the advancing crack.

This paper discusses toughening and strengthening in a selected number of systems where significant progress has been made in enhancing fracture toughness and strength to the levels found only in metals.

### Toughening by crack bridging In $\text{Si}_3\text{N}_4$ and SIC ceramics

One of the powerful mechanisms of toughening in monolithic ceramics such as silicon nitride and silicon carbide is the crack bridging by elongated grains oriented at an angle ranging from  $0^\circ$  to  $90^\circ$  relative to the direction of applied stress. The schematic representation of the structure most favorable for crack bridging is shown schematically in Fig. 1. As the crack propagates through the structure it hits the interface between the elongated grains and the matrix where it is deflected and forced to propagate along the weak interface. The deflection of the crack along the interface reduces the stress intensity factor which forces the elongated grains to pull out thus producing bridging of the faces of the advancing crack, as illustrated in Fig. 1. These bridging grains impose close tractions on the crack surfaces and contribute to toughening of the ceramics. The overall toughness of the system containing elongated grains is given by the expression [1]:

$$K_{IC} = K_m \cdot (1 - V) + \left\{ \frac{4E\tau Vu}{(1 - \nu^2)K_m} \right\} \cdot \frac{l}{d} \quad (1)$$

where  $K_{IC}$  is the fracture toughness of the system,  $K_m$  is the fracture toughness of the matrix,  $V$  is the volume fraction of the elongated grains,  $E$  is the elastic modulus,  $\tau$  is the interfacial friction stress,  $\nu$  is the Poisson's ratio,  $u$  is the pull out length and  $l/d$  is the aspect ratio, where  $l$  is the grain length and  $d$  is the grain diameter.

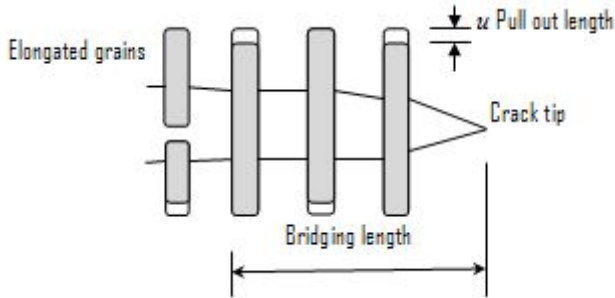


Fig. 1 Schematics of crack bridging by elongated grains oriented parallel to the externally applied stress.

Equation 1 shows that the key factors which control the level of toughening are the aspect ratio of the grains and their volume fraction. The role of aspect ratio and their volume fraction in toughening and strengthening of silicon nitride is shown in Fig. 2 and 3[2].

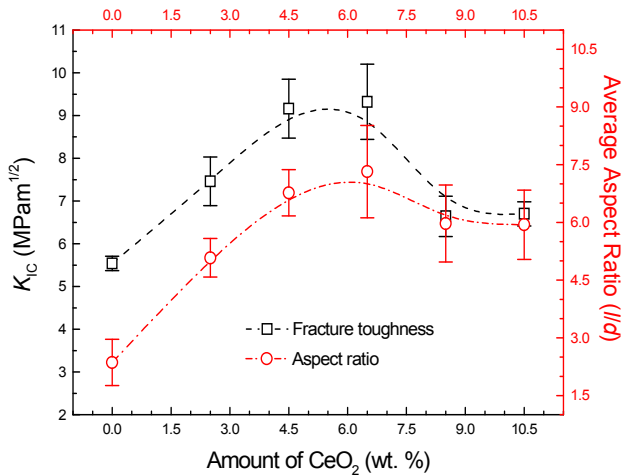


Fig. 2 Change of fracture toughness and an average aspect ratio with ceria content in silicon nitride ceramics [2].

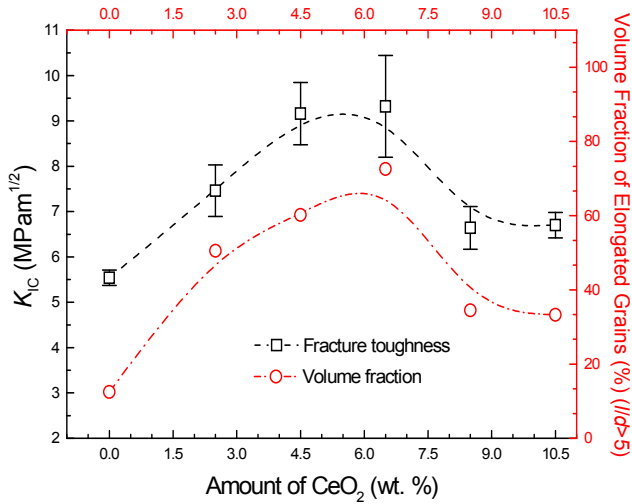


Fig. 3 Change of fracture toughness and volume fraction of elongated grains with ceria content in silicon nitride ceramics.

Both figure 2 and 3 show that there is a direct correlation between the volume fraction of elongated grains, their aspect ratio and the level of toughness as expressed by the eq. (1).

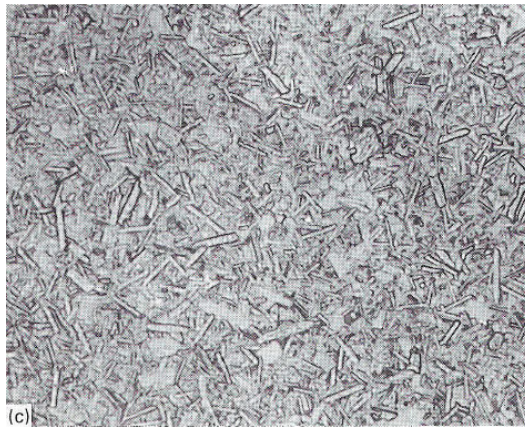


Fig. 4 Polished and etched microstructure of whisker-like elongated  $\alpha$ -SiC grains in a matrix of SiC with equiaxed or slightly elongated grains (x2000)

Although the other factors such as interfacial friction stress and pull out length play equally important role in toughening by crack bridging, the volume fraction and aspect ratio are the two microstructural features that can be controlled most effectively. In addition to aspect ratio, proper orientation of the elongated grains can significantly increase the level of toughening. For example, if all grains were oriented parallel to the applied stress the contribution of crack bridging to the overall toughness of the system can be increased by 50-60%.

Another example of elongated grain structure that offers increased fracture toughness is shown in Fig. 4 for *in-situ* toughened SiC ceramics [3]. In this ceramics the elongated  $\alpha$ -SiC grains are in the form of tiny small needles resembling whiskers rather than plates normally found in classical silicon carbide ceramics.

### Toughening by crack deflection-laminated structure

Over the last decade, most of the effort on the development of laminated structures have been centered on plate-form laminates where large increases in the apparent fracture toughness have been achieved. Two examples of laminated structures are SiC with weak graphite interfaces [4] and SiC with weak SiC interfaces where the apparent fracture toughness of over  $14\text{MPa m}^{1/2}$  [5] have been achieved. High fracture toughness [6] and work of fracture ( $\sim 8000\text{ J/m}^2$ ) were also measured in hot-pressed  $\text{Si}_3\text{N}_4/\text{BN}$  laminates [7]. Although in the early stage of the development most of the work on planar laminates was centered on SiC laminates, in the later stages the effort was centered on silicon nitride due to its inherently higher fracture toughness and strength [8].

Despite large increases in fracture toughness, planar laminates did not find wide spread use in structural applications, due mainly to the fact that they possess direction of easy crack propagation which makes it difficult incorporate it into the structure. To eliminate this problem a new concept of laminated structure was recently designed and fabricated, one that involves concentric ring structure. In this concentric ring structures all directions of easy crack propagation are eliminated which makes them considerably more attractive for structural applications [9]. Figure 5 illustrates the transformation of planar laminates to concentric ring laminates.

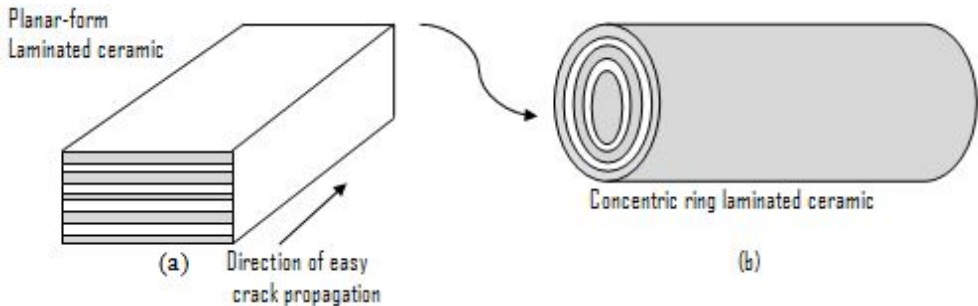


Fig. 5 Illustration of (a) planar laminate and (b) concentric ring laminate

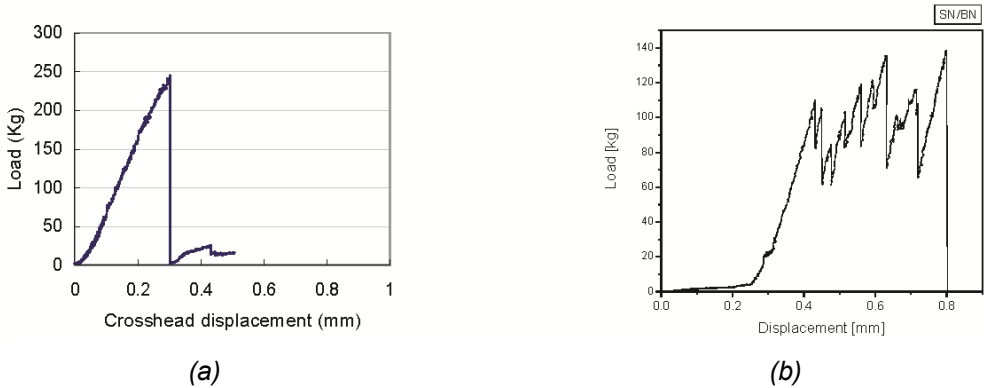


Fig. 6 Typical load-displacement curves for a) monolithic ceramics and b) laminated ceramics

Another advantage of the concentric ring laminated structure is the manner in which they fracture. This is best illustrated in Fig. 6 which shows the load-displacement curves for monolithic ceramic and for concentric ring laminated structure. While monolithic ceramic exhibits linear-elastic behavior (Fig. 6(a)) all the way to fracture, laminated structure exhibits graceful fracture (Fig. 6(b)) resembling that of fiber reinforce composites.

There are many factors which influence the mechanical properties of concentric ring structure. The most important of them are the number of layers and the layer thickness. In the case of silicon nitride ( $\text{Si}_3\text{N}_4$ ) concentric ring structures, it was found that minimum of 6 to 7 layers is required before maximum fracture toughness can be achieved (Figure 7). Similarly, there is an optimum silicon nitride layer thickness for which maximum in fracture toughness and fracture strength is achieved (Fig. 8).

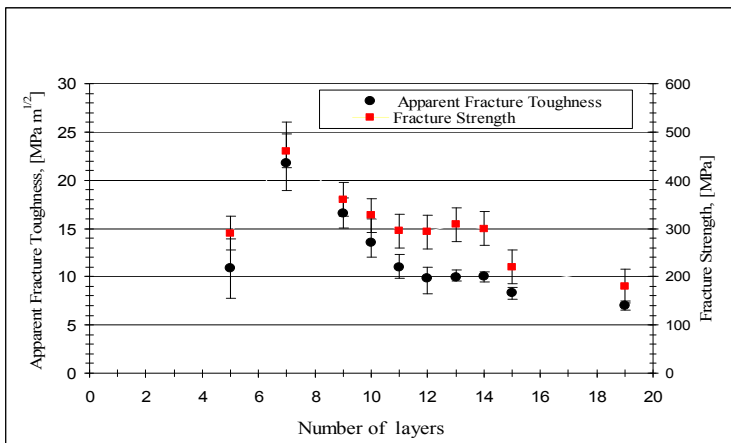


Fig. 7 Change of apparent fracture toughness and flexural strength with number of layers in silicon nitride concentric ring structure [9]

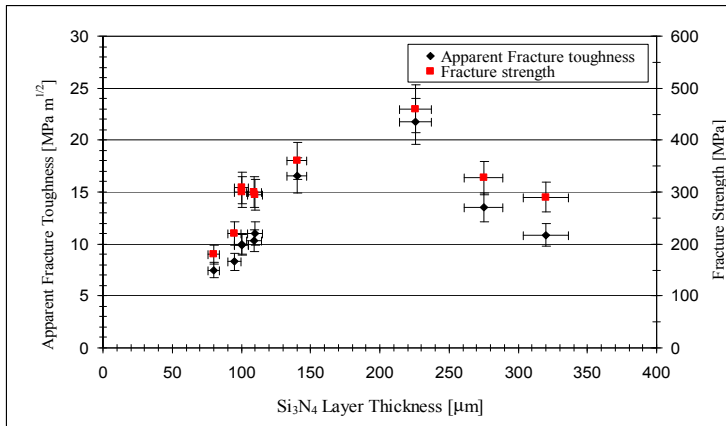


Fig. 8 Change of apparent fracture toughness and fracture strength with silicon nitride layer thickness in silicon nitride concentric ring structure [9]

It is interesting to note that both fracture toughness and strength show a maximum at the same number of layers and at the same silicon nitride layer thickness. This behavior is not surprising as both fracture toughness and fracture strength are controlled by the same mechanism which is the crack initiation at the next silicon nitride layer. After moving through the first layer, the crack deflections at the weak interface and move some distance before it stops. Further propagation of fracture requires initiation of a new crack at the next layer which requires higher stress than that required for propagation of the existing crack. The relation between fracture toughness, the strength of the silicon nitride layer and the critical stress for failure of the next layer is presented by the equation [10]:

$$G_{IC} = \sigma_c \frac{\delta}{18E} \left[ N - \left( \frac{(N-1)^3}{N^2} \right) \right] \quad (2)$$

where  $G_{IC}$  is the critical strain energy release rate,  $\sigma_c$  is the critical stress for failure of the next layer,  $\delta$  is the layer thickness,  $E$  is the elastic modulus and  $N$  is the number of layers. The initiation of the crack at the next silicon nitride layer is found to be high as the thin silicon nitride layers have structure with lower level of defects such as pores and cracks known to be responsible for lowering the strength of bulk (thick) ceramics.

### Bridging by ductile ligaments

Another powerful mechanism of toughening which can lead to large increases in fracture toughness is the ceramic-metal composites in which the metallic phase forms a continuous network that binds the ceramic particles together. This structure is schematically illustrated in Fig. 9 for the case of irregular shape hard ceramic particles (dark filed) randomly distributed in a ductile binder phase (gray filed).

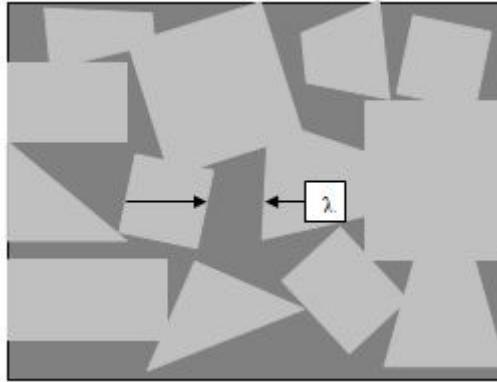


Fig. 9 Schematic illustration of the composite consisting of particles (gray field) bonded together by metallic binder phase (dark phase) forming continuous network

The difference in crack opening displacement between the brittle particle and the ductile binder phase allows the propagating crack to be blunted and forced to circumvent the ductile phase leaving unbroken ligaments behind. The unbroken ligaments generated behind the crack tip impose closure tractions on the crack surfaces and enhance the fracture toughness of the system. The contribution of ligaments to fracture toughness is expressed by the equation of the form [11]:

$$K_L = K_p(1 - V_b) + \frac{E_m l \sigma_b^2}{(1 - \nu_p^2) K_p E_b} \left\{ 1 - \frac{\pi}{4[(\lambda / D) + 1]} \right\} \quad (3)$$

where  $K_p$  is the fracture toughness of the particulate phase,  $V_b$  is the volume fraction of the metal phase,  $l$  is the length of the ligament that undergoes elongation,  $E_m$  is the elastic modulus of the metal phase,  $E_p$  is the elastic modulus of the particulate phase,  $\sigma_b$  is the strength of the ligament,  $\nu_p$  is the Poisson's ratio of the particulate phase,  $\lambda$  is the thickness of the ligament/binder phase and  $D$  is the average diameter of the particulate phase. Figure 10 shows the predicted change of fracture toughness of the composite as a function of binder phase volume fraction for three different particle diameters. The key result of Fig. 10 is that very larger increases in fracture toughness are possible at binder thicknesses above 1  $\mu\text{m}$ .

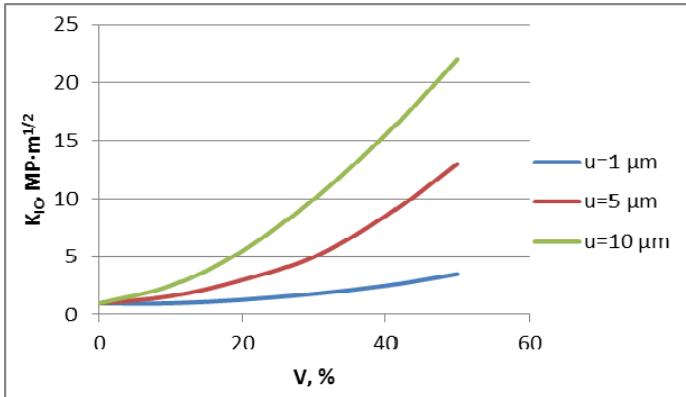


Fig. 10 Predicted variation of fracture toughness of ceramic-metal composite with metal volume fraction for three different particle diameters

One of the systems where ligaments fracture operates most successfully is the WC-Co composites where the metallic Co forms continuous network bonding together WC particles. Figure 11 shows the side view of WC-Co composite with the crack propagating through the WC particles and the Co binder phase [12]. The micrograph in Fig. 11 also shows the unbroken ligaments left behind the propagating crack which is a typical mode of fracture in this composite. Fracture toughness measurements revealed these composites have fracture toughness as high as  $20 \text{ MPa}\cdot\text{m}^{1/2}$  which is considered to be very high considering that the volume fraction of Co phase does not exceed 12-15 vol%. In order to achieve the toughness of  $15\text{-}20 \text{ MPa}\cdot\text{m}^{1/2}$  the strength of the ligaments must be at the order of 4-6 GPa. This level of strength is an order of magnitude larger than the strength of a bulk Co and is only found in whiskers and small fibers. Their high strength comes from the perfect structure which typically does not contain large defects in the form of pores and cracks which are known to control the strength of bulk/thick materials [11].

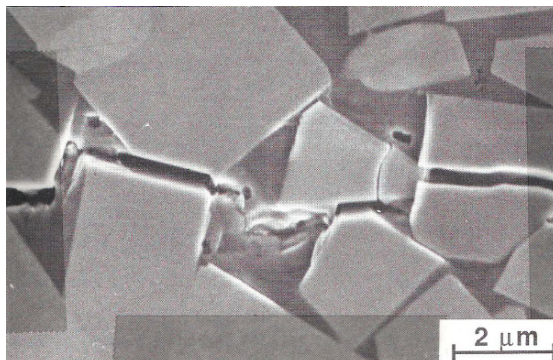
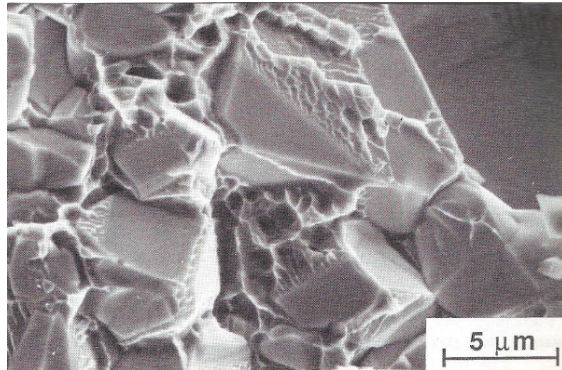


Fig. 11 Path of the crack propagation through the composite showing transgranular brittle fracture of the WC grains and deformation of the intergranular binder phase in the form of unbroken ligaments left behind the crack tip [Ref. 12].

Figure 12 shows the fracture surface of the WC-Co composite where extensive fracture of the binder phase (Co) takes place even though the constraint imposed by the rigid WC grains suppresses plastic deformation.



*Fig. 12 Fracture surface of the WC-Co composite (known as cemented carbide) showing brittle fracture of WC phase and typical ductile fracture of cobalt phase [Ref. 12].*

The theoretical analysis conducted in this and previous works [11] suggest that properties of the bulk metals and ceramics have quite different microstructural and mechanical properties from their counterparts but manufactured in thin forms (small thickness and /or small diameter). The present work predicts that if the cobalt can be manufactured in a highly porous, continuous network form, with wall thickness of the network not exceeding 1-2  $\mu\text{m}$ , the material will exhibit much larger strength compared to their bulk counterparts. Based on the ligament fracture mechanism of toughening, in which the strength of metallic ligaments determines the fracture toughness of the composites and not its plasticity at the crack tip, it can be concluded that the toughness of these type of composites will not decrease as the temperature is lowered below room temperature (even at liquid nitrogen temperatures) where plasticity of the metal is greatly reduced. Metallic cobalt and many other metals show an increase in strength at lower temperature which implies that fracture toughness of the system may remain high as long as the mechanism of fracture is the one involving ligament fracture. (see eq. (3)).

## References

- [1] V. D. Krstic, Development of high toughness ceramics by microstructural control, *Proceedings of International Conference on Engineering and Technological Science 2000-ISAM*, ed. J. Song and R. Yin, Chinese Academy of Engineering, Beijing, China, 1, (2000) pp. 83-88.
- [2] C. R. Zhou, Ph. D. Thesis, Queen's University, 2005.
- [3] M. Mulla and V. D. Krstic, *Acta metal. Mater.*, 42, No. 1, 303-308 (1994).
- [4] W.J.Clegg, K. Kendall, N.M. Alford, D. Birchall and T.W.Button, *Nature*, 347, 455-457(1990).
- [5] L. Zhang and V. D. Krstic, *Theoretical and Applied Fracture Mechanics* 24, 13-19 (1995).

- [6] C.Wang, Y. Huang, Q. Zang, L, Zou and S. Cai, J. Am. Ceram. Soc., 85,2457-2461 (2002).
- [7] D. Kovar, M. D. Thouless and J. W. Holloran, J. Am. Ceram. Soc., 81, 1004-1012 (1998).
- [8] Z. Krstic and V.D.Krstic, Silicon Nitride: the engineering material of the future, Invited Anniversary Review Paper, Journal of Materials Science, 47:535-552, 2012.
- [9] Z. Krstic and V.D.Krstic, J. European Ceramic Society, 29, 1825-1829 (2009).
- [10] A. J. Phillips, W. J. Clegg and T. W. Clyne, Acta Metall. Mater., 41(3), 805-817 (1993).
- [11] V.D.Krstic and M. Komac, Philosophical Magazine, A, Vol. 51, 191-203 (1985)
- [12] L.S.Sigl and S. Schmauder, Int. J. of Fracture, 36, 305-317 (1988).

## **PRESENT AND FUTURE APPLICATION OF THE THERMAL ANALYSIS IN ALUMINUM CASTING INDUSTRY**

Mile B. Djurdjevic,

*Nemak Linz GmbH, Zeppelinstrasse 24, 4030 Linz, Austria*

*E mail: mile.djurdjevicnemak.com*

### **Abstract**

The solidification process of a metal or alloy is accompanied by the evolution of heat the magnitude of which depends on the various phases that form during the solidification. Recorded temperature-time data can yield quantitative information about the alloy solidification process. Such a plot is called a cooling curve and the general name given to the technique is thermal analysis. Thermal analysis has been long time applied in aluminum casting plants as a quality control tool. Recently it has been recognized that cooling curve analysis and its first derivative offer some other parameters that can be successfully used in simulation software programs in order to improve their accuracy. The newest development in the cooling curve analysis related to application of its higher order derivatives has shown that this technique can be applied even to calculate the amount of precipitated phases. The aim of this paper is to gives short overview of the cooling curve application in the aluminum casting plants and to briefly indicate its potential application in the future.

*Key words: Thermal analysis, aluminum alloys, cooling curve, casting quality, simulation.*

### **Introduction**

Aluminum casting plants are using significant amounts of primary, secondary and master alloys in order to produce automotive parts of high quality. The quality of cast products depends directly on the quality of molten metal from which the products are cast. Comprehensive understanding of the melt quality is of vital importance for the control and prediction of actual casting characteristics. Any defect added or created during the melting stage will be carried to the final microstructure, and certainly, affect the quality of cast products. Therefore it is apparent that the control of the quality of the cast products begins with the control of the quality of the melt. If one is able to act in a proactive rather than a reactive manner in respect to melt and casting quality control, one can reduce cost downtime and scraps levels. Thermal analysis can provide such capabilities and therefore has important advantages over its post-process counterparts which are often destructive in nature.

Application of the thermal analysis technique in the ferrous and non-ferrous casting industry has been already many years successfully employed. Cooling curve analysis has been used for many years to determine binary phase diagrams and for fundamental metallurgical studies. In using this technique, binary alloys of varying composition were studied as they cooled and the arrest points were

recorded and plotted on a temperature - composition (phase) diagram. Utilization of the thermal analysis as a quality control tool in the cast iron plants has been recognized for more than seventy years. In the aluminum casting industry, the application of thermal analysis to study the development of the test sample structure was reported in early publications by Cibula [1] and Mondolfo [2]. In the late 1980's, this process control technology started to be regularly used in aluminum foundries [3-7]. The procedure to get the cooling curve plot is very simple. The liquid aluminum melt preheated to approximately 100°C above its liquidus temperature, is poured into a thermal analysis cup made from ceramic, steel, graphite or sand. One, two or more thermocouples are immersed into the melt, connected to data loggers. Collected signals from thermocouples are transferred into temperatures. The representation of the temperature versus time is identified as cooling curve and has been used to describe the solidification path of investigated alloys. Some thermally weak events, which are not visible on the cooling curve, can be only detected using its derivative curve. Recently Bäckerud and Sparkman [3,8] start to applied first, second or higher order derivatives of the cooling curves in order to identify more accurately the solidification characteristic temperatures and recognized some other features of solidified alloys. Short time ago, Bäckerud [3] introduced the application of two thermocouples; one located in the center and the other close to the wall of the thermal analysis cup. Calculating the difference in measured temperatures ( $\Delta T = T_{\text{wall}} - T_{\text{center}}$ ) and plotting it versus time he was able to detect the dendrite coherency point/temperature at which dendrites start to impinging each other during their growth. In most aluminum casting plants thermal analysis equipment has been presently used to control the efficiency of master alloys additions. Measuring the depressions by primary solidification of  $\alpha$ -Aluminum ( $\Delta T = T^{\alpha\text{-Al}}_{\text{MAX}} - T^{\alpha\text{-Al}}_{\text{MIN}}$ ) or depression of AlSi eutectic plateau temperature by precipitation of AlSi eutectic phase ( $\Delta T = T^{\text{AlSi}}_{\text{PLATEAU without Sr}} - T^{\text{AlSi}}_{\text{PLATEAU with Sr}}$ ) the efficiency of master alloys additions can be evaluated in advance [9-11]. Easy to handle, inexpensive, simple, accurate with high repeatability and reproducibility are some of properties that qualify this equipment to be often employed at aluminum foundry floor [12-14].

Beside quality control, cooling curve analysis recently starts to be interesting as a source of input data for simulation software packages. Available simulations software packages have data banks for few generic aluminum alloys. In real production, chemical compositions of aluminum alloys have significant variations regarding suggested contents of alloying elements, which considerably affect all solidification parameters (solidification characteristic temperatures, solid fraction, latent heat and many others). Therefore, application of the cooling curve analysis in providing a new set of input data for simulation purposes should be an additional challenge for thermal analysis. The main aim of this paper is to demonstrate the present ability of thermal analysis as a process and quality control equipment and to indicate its potential future application providing input data for simulation software packages.

## Present application of Thermal Analysis in aluminum casting industry

A typical cooling curve obtained using a center thermocouple ( $T_C$ ) and its first derivative for an AlSi5Cu1 alloy is presented in Figure 1.

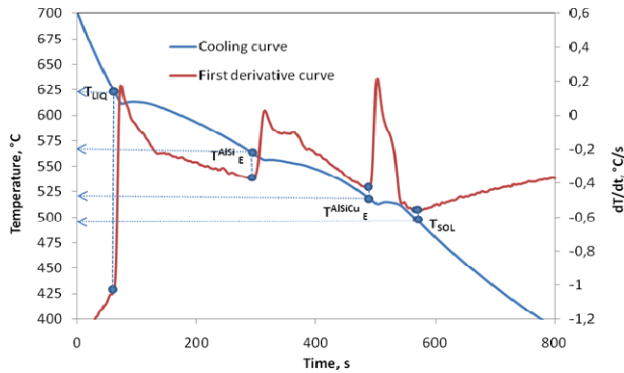


Figure 1. The cooling curve of AlSi5Cu1 alloy and its first derivative curve.

Solidification of any Aluminum alloys starts at the liquidus temperature with the formation of small solid pieces of  $\alpha$ -Al nucleus. This temperature delineates the transformation between liquid and solid condition. Further cooling of the melt, sometimes supported with addition of some foreign particles (grain refiners), allows the formation of millions of other nucleus which start to grow with a dendritic form. At the certain temperature below liquidus, these dendrites start to touch each other and form the solid skeleton in the residual melt. The temperature at which this happen is called dendrite coherency temperature and it is very important for many metallurgical and mechanical properties of cast parts. Cooling down to a lower temperature, the primary AlSi eutectic phase starts to precipitate. In the alloys with higher content of Si, this precipitation will take longer time releasing significant amount of latent heat. The presence of other alloying elements such as Cu, Mg, Fe and specially Sr and Na depress the start of precipitation significantly towards a lower temperature. Close to the end of solidification in some alloys with a minimum Cu concentration, Copper rich phases start to precipitate. Depending on the amount of Cu and the presence of other alloying elements Copper phase can appear in several forms (blocky, eutectic and fine eutectic form) [15, 16]. The temperature at which last drop of liquid is transformed into solid is called solidus temperature. In aluminum alloys with a minimum concentration of Mg and Fe, their corresponding intermetallics also start to precipitate. The temperatures at which these intermetallics appear depend on their concentration and process parameters.

### Assessment of Grain Size and Modification of Al-Si eutectic morphology

Aluminum alloys, like alloys of other light metals, will normally, without addition of grain refinement, form coarse, equiaxed and columnar crystals during solidification. Grain refinement may be achieved through a number of different methods such as: increasing cooling rate, the dynamic techniques like vibration and stirring, constitutional undercooling and the addition of grain refiners [1, 3, 5,

10, 11]. Addition of grain refiners (AlTi and AlTiB) is at the present the most common method used in the aluminum casting industry. Many years the cooling curve has been successfully used as a quality control tool for the assessment of the efficiency of added grain refiners. The shape of the cooling curve at the beginning of the solidification process gives a good indication of the number of nuclei present in the melt. When there are a great number of nuclei, the curve exhibits little undercooling, (as illustrated in Figure 2 by the dotted line). When there are few nuclei, there is more undercooling, which is illustrated in the Figure 2 by the solid line. Undercooling parameter  $\Delta T$  ( $\Delta T = T_{MAX} - T_{MIN}$ ) from the cooling curve has been routinely used for quality process control giving prompt information about efficiency of grain refining additions into aluminum melt. Smaller  $\Delta T$  parameter means higher potency of master alloys leading to smaller casting grains in as cast structure.

Aluminum hypoeutectic alloys have been developed to provide a range of properties and characteristics to meet the needs of wide variety of applications mostly in automotive industry. In order to increase their properties the as cast Silicon structure of these alloys have been modified by adding different amount of modifiers (Sr or Na). Strontium has been widely used in aluminum casting plant as a modifier of hypoeutectic aluminum-silicon cast alloys. Addition of Sr change coarse Silicon structure to fine fibrous improving mechanical and metallurgical properties of these alloys. For each Al-Si alloys there is an optimal amount of Strontium additions that can be control by using cooling curve analysis.

Figure 3, shows the effect of modification on the aluminum-silicon eutectic plateau temperature ( $T^{Al-Si}$ ). The depression of the aluminum-silicon eutectic plateau temperature, ( $\Delta T$ ), represents the temperature difference between the unmodified and modified aluminum-silicon eutectic growth temperatures [6]. The larger the magnitude of  $\Delta T$  the higher the level of modification (it means the smaller size of silicon particles). The advantage of Thermal Analysis in compare to classical chemical analysis is in fact that cooling curve measured only impact of active Strontium. It means that only free Strontium that is not bonded in some intermetallics can be used to change Silicon morphology.

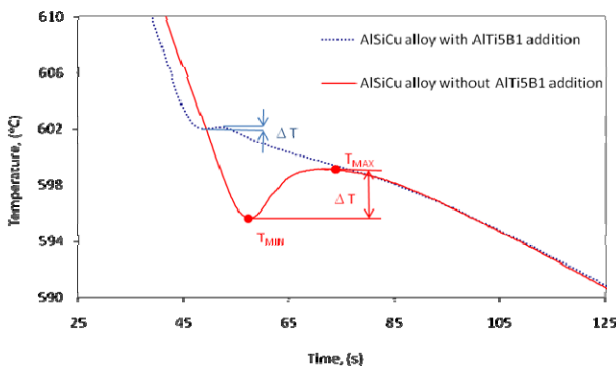


Figure 2. Part of the cooling curve related to the primary solidification of aluminum alloys.

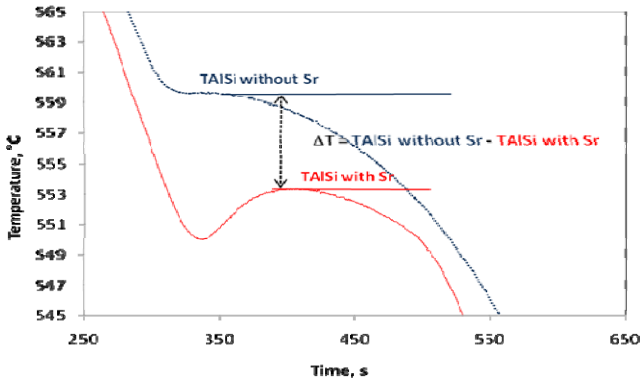


Figure 3. Part of the cooling curve related to Al-Si eutectic region

#### Precipitations of AlSiCu rich phase(s)

Immediately before the end of solidification of AlSiCu alloys the Copper rich eutectic phase starts to precipitate. Depending on the amount of Copper and some other alloying elements such as Sr, Pb and Sn [17, 18, 19] the start and the end solidification temperatures of this phase can vary, as well as the amount of latent heat released during its solidification.

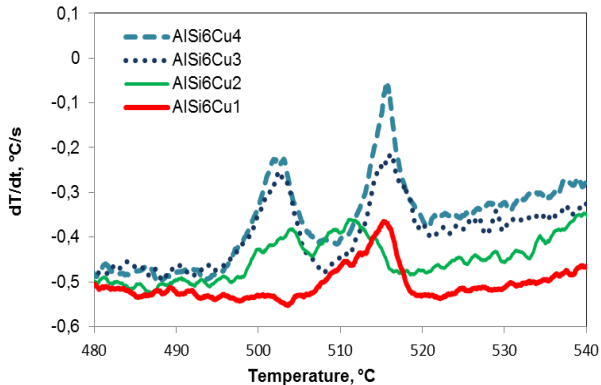


Figure 4. Copper rich area of precipitation; First derivative of the AlSi6Cu(1-4) cooling curves related to copper enriched region

The number and shape of the peaks visible in the Cu enriched region of the first derivative curves plotted versus temperature, show a strong relationship with the amount of Cu present in the alloy (for more details see Fig. 4). According to F.H. Samuel [15] the Cu phases precipitate in three distinct forms: two eutectics (Al-Al<sub>2</sub>Cu eutectic and ultra-fine Al<sub>5</sub>Mg<sub>8</sub>Cu<sub>2</sub>Si<sub>6</sub> copper eutectic) and blocky phase (Al<sub>2</sub>Cu). Samuel [15] as well as the other researchers [16] found that the increase in the Strontium content increases the proportion of blocky-Al<sub>2</sub>Cu and ultra-fine Al<sub>5</sub>Mg<sub>8</sub>Cu<sub>2</sub>Si<sub>6</sub> copper phases versus Al-Al<sub>2</sub>Cu eutectic Cu. Increasing the content

of Magnesium (some authors [15] suggested greater than 0.5 wt. % Mg), results in the precipitation of  $Al_5Mg_8Cu_2Si_6$  copper eutectic (occurring as a branched crystals or fine eutectic strings growing out from  $Al_2Cu$  blocky or  $Al-Al_2Cu$  eutectic types during the final stage of solidification). Some other elements (Pb, Sn, Bi, Ca, P, Sb and P) present in  $AlSiCu$  alloys in small amounts (ppm range) can also have significant impact on the  $AlSi$  and  $AlSiCu$  eutectic temperatures and precipitation morphology of copper rich phases. The nucleation temperature of the Cu enriched phases can be accurately read from the first derivatives of the cooling curves and used to define the maximum temperatures that the castings can be exposed to during the conventional solution treatment process.

*Precipitations of Low Melting Point Elements (Sn and Pb)*

Many aluminium casting plants have experienced sudden not expected high reject rates of as cast products due to the high level of shrinkage porosity. In most cases attention is often directed towards procedure parameters that can influence the solidification process and metal quality. Regarding the process parameters there are in any casting plants already very well defined routines and any variation from proposed values can be easily identified and corrected sometimes even automatically. Confusion occurs when alloy itself starts to be blame for a cause of problem. Major and minor alloying elements are for most of commercial alloys very well defined. Therefore, it should be no problem to check quickly if some of those elements are out of defined range. Unfortunately, the main problem appears regarding trace elements. There is no consensus in the literature and practice regarding the tolerable levels of these elements present in aluminum alloys.

Recently few of them have been identified (Sn and Pb) and recognized as increasingly more significant and problematic in the aluminum melt [18, 19, 20]. Both Sn and Pb elements are not dissolved in pure Al and Sn is only partly dissolved in pure Cu. During solidification Pb solidified in the form of pure particles while Sn precipitates either in the form of constituents together with other elements like Cu or as pure particles.

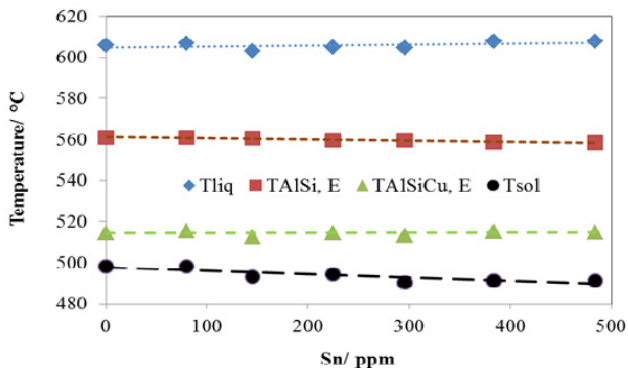


Figure 5. The impact of various content of Sn on characteristic solidification temperature of  $AlSi_6Cu_4$  alloy. Note that total solidification range,  $\Delta T (T_{LIQ} - T_{SOL})$  is larger with increased Sn content.

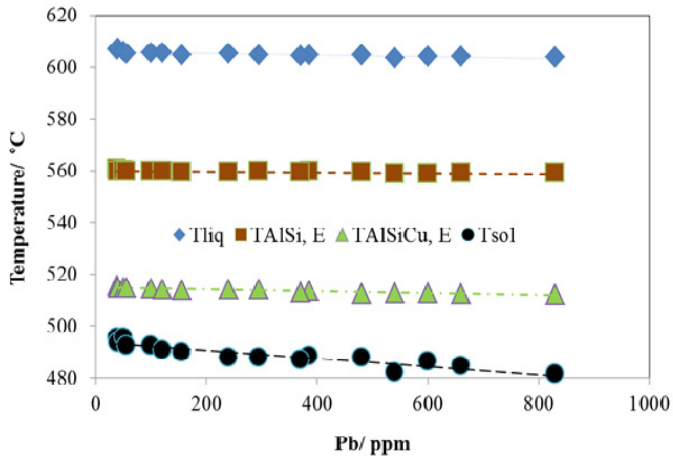


Figure 6. The impact of various content of Pb on characteristic solidification temperatures of AlSi6Cu4 alloy. Note that increase in the content of Pb significantly depress the solidus temperature.

The similar behaviour, as Figure 6 shows, has been recognized with various content of Pb dissolved in AlSi6Cu4 alloys. The cooling curve analysis can be used to predict such behaviour and suggest the operator to take some in advance action to eliminate later defect in as cast structure. This extended solidification could cause at least two problems by the AlSiCu cast alloy. From the literature and foundry practice it is well know that alloys with longer solidification interval are prone to shrinkage formation. Extended solidification will definitely overemphasize feeding problem by this alloy, carrying out formation of shrinkage porosity and as a consequence having lower mechanical properties of end product. Limited research indicates that low melting point elements (Sn and Pb) could be detrimental to the heat treated casting structural integrity due to its non-solid solubility in the aluminum matrix. Exceed of the  $T_{SOL}$  temperature during heat (solution) treatment cause dissolution of  $\theta - Al_2Cu$  phase(s) along grain boundaries well known as incipient melting. This is second very important point that cannot be ignore during heat treatment of this type of alloy. Using cooling curve analysis the impact of low melting point elements on the extended solidification can be easily recognized and prevented by adding elements (e.g., Mg, Sr..) that have high affinity to Pb and Sn.

#### Precipitations of Iron rich phase(s)

In all aluminum alloys, iron is always present as an impurity. Iron has limited solubility in solid aluminum (at 655 °C maximal solubility is 0.05 %), reacts with aluminum and silicon to form a thermodynamically stable intermetallic compounds; platelets like  $\beta-Al_5FeSi$  more harmful than so called script  $\alpha-Al_{15}(Fe, Mn)_3Si_2$ . The size and number of such needle phases in the microstructure of a casting is difficult to determine without using tedious metallographic work which is time consuming and costly. In additions aluminum foundries need a fast and accurate method of quantifying iron content on line. Thermal analysis has potential to be used as a

quality tool for detection of detrimental iron content in AlSi alloys. Figure 7 shows two first derivative curves of an AlSi8Cu3 alloy with two various content of iron. Both derivative curves clearly reveal peaks that are related to Iron rich phases. The peak related to higher content of Iron (0.8 wt. %) is more distinct than the peak revealed in the alloy with lower content of Iron (0.6 wt.%, dotted line). No noticeable peak in the alloy with lower Iron content is due to small amount of the latent heat released during solidification of iron rich phase. It is also interesting that the minor increase in the iron content significantly increase the precipitation temperature of Iron rich intermetallic moving it to the temperature even higher than AlSi eutectic temperature. Iron intermetallic particles that form prior the precipitation of AlSi eutectic tend to grow much larger than those that form after AlSi eutectic solidification. The larger particles are more detrimental for the feeding ability of the melt and could initiate defects in the as cast products. Therefore, the quality of aluminum cast parts need to be more closely control if the aluminum foundries are going to be competitive. Thermal analysis has potential to be used as quality tool for detection of detrimental iron content in AlSi alloys even at the foundry floor.

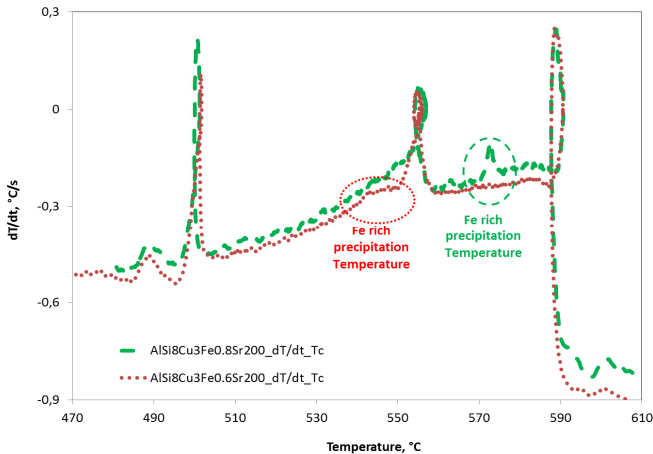


Figure 7. Iron rich phases detected using first derivative curves of AlSi8Cu3Fe0.6 and AlSi8Cu3Fe0.8 alloys modified with 200ppm Sr.

## Future application of Thermal Analysis in aluminum casting industry

### Simulation in aluminum casting industry

Last forty years the Thermal (cooling curve) analysis has been intensively used in aluminum casting industry. As has been previously shown, this technique is a good choice for drawing fundamental relationships between cooling curve characteristics and melts. A state-of-the-art thermal analysis system should be able to quantify parameters such as: grain size, level of silicon modification, low melting point of secondary eutectic(s) and other solidification characteristic temperatures. Modern casting industries which require more application of various simulation software packages open some extra field for thermal analysis. The

interest in simulation applied in the aluminum casting industry has extended significantly in the last few decades. Three main reasons are responsible for that: (i) the necessity to improve productivity and quality of cast products (ii) to speed up the design process and (iii) to investigate the influence of different process parameters without the need of expensive experimental trials. The accuracy of casting simulation depends in great deal on the quality of the available physical and thermophysical material properties provided by the software's database. Available databases presently used by commercial simulation software packages for the casting industry usually come with material properties for only a few selected standard alloys. In the case of more sophisticated alloys with differing chemical compositions, refinement and/or modification treatments, thermal analysis can be a very useful tool in order to collect the missing parameters or more accurate thermophysical data for investigated alloys. Here will be presented some of these parameters that can be detected using cooling curve analysis and incorporate in existing simulation software packages in order to improve their accuracy.

#### *Dendrite coherency point and rigidity temperature*

For all Aluminum cast alloys, the transformation from liquid to solid state is accompanied by a decrease in volume in the ranges between 4 to 8 %, dependent on the type of alloy. In order to fulfill the volume deficit, the cast parts during solidification need to be feed with extra volume of liquid melt. The main intention in this case is to prevent shrinkage formation by maintain a path for fluid flow from the higher heat mass and the pressure of the riser to the isolated liquid pool. Campbell [21] summarized the five characteristic feeding mechanisms that can occur during solidification of aluminum cast alloys. They are: liquid feeding, mass feeding, interdendritic feeding, burst feeding and solid feeding.

Characteristic solidification temperatures such as liquidus, dendrite coherency point, rigidity and solidus temperature have been recognized as an important parameters of solidify aluminum alloys because they mark transitions between several types of feeding mechanisms. Liquidus, DCP and solidus temperatures of aluminum alloys can be easily determined using thermal analysis technique (for detection of DCP it is necessary to apply two thermocouples techniques developed by Bäckerd at all. [3]). Rigidity is a physical phenomenon; however its direct detection is virtually impossible. Bäckerd used a mechanical (or rheological) method to detect this temperature. As Figure 8 shows, using rotation impeller immersed into the solidifying alloy it was possible to record the torque as a function of melt temperature. A small increase in torque is associated with the point at which the dendrites start to touch each other, reducing the rotation speed of impeller. Further coarsening and ripening of dendrites will increase the strength of solid network raising the torque to that point to stop rotation of impeller. Bäckerd named this point as rigidity point.

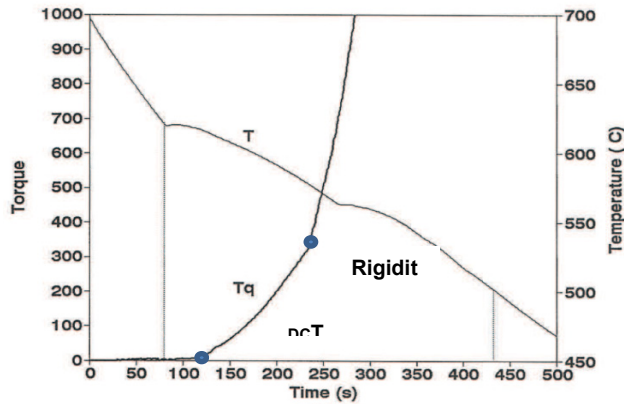


Figure 8. Cooling ( $T$ ) and torque ( $Tq$ ) curves collected from the sample of  $AlSi5.5Cu1.5Mg0.6$  alloy during the solidification at a cooling rate of  $1^{\circ}C/s$  [3].

Reading rigidity temperature from torque measurement and using other characteristic solidification temperatures obtained from the cooling curve all five feeding regions can be easily marked as it shown in Figure 9. Between pouring and liquidus temperature the melt has very low viscosity and flow through the mold following the liquid feeding. Before the melt reach the dendrite coherency temperature the mass feeding of mixture of slurry and melt is possible. At the coherency temperature the mass feeding becomes restricted and the melt start to flow through the solid skeleton of  $\alpha$ -aluminum dendrites. Interdendritic feeding occurs between dendrite coherency and rigidity temperature. After rigidity point further interdendritic flow is restricted and must be supported either by positive pressure from riser or negative pressure caused by volume deficit and capillarity forces. Between rigidity and solidus temperature occurs so called burst feeding. Solid feeding happens below solidus temperature where the yield strength of solidified material is very low.

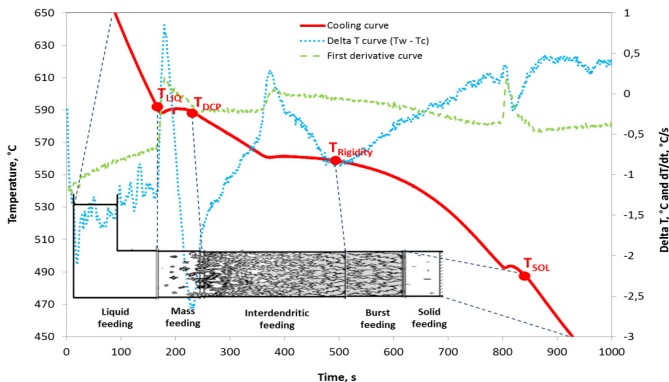


Figure 9. Bordering five feeding mechanisms using characteristic solidification temperatures determined from the cooling curve.

Dendrite coherency point and rigidity temperature have not been often used in aluminum foundry daily activities. But these temperatures are a very important parameter for simulation, because it defines the temperature range where feeding is possible by melt flow through interdendritic channels initiated by gravity force (so called interdendritic feeding).

According to Figure 9, the first minimum at the Delta T curve corresponds to dendrite coherency temperature. The Rigidity temperature is determined as a second  $\Delta T$  minimum identify in the region of primary precipitation of Al-Si eutectic. The different thermal conductivity in the liquid and the solid state is the main reason why at these points appear a larger difference in the measured temperatures using two thermo elements located in the center and close to wall of thermal analysis cup. Both temperatures are very dependent on the cooling rates and chemical compositions of aluminum alloys.

#### *Determination of fraction solid using cooling curve analysis*

Beside characteristic solidification temperatures, the thermal analysis is often used to calculate solid fraction distribution between liquidus and solidus temperatures. A critical requirement for the solid fraction calculation applying cooling curve analysis is determination of, what is called a base line [22, 23]. The base line is in principle the first derivative of the cooling curve measured by the thermocouple(s), inserted in the alloy test sample, assuming that the metal doesn't undergo any phase transformation during the solidification process. In other words the base line overlaps the first derivative of the cooling curve in single phase parts of the sample cooling process, for temperatures higher than T-liquidus and for temperatures lower than T-solidus. In the literature are known two methods, Newtonian [22, 23, 24] and Fourier [24, 25], that have been successfully used to calculate latent heat and solid fraction distribution using cooling curve analysis. Accurate information concerning fraction solid is necessary to perform computer simulations of casting feedability and characterization of the solidification process as well as to make predictions concerning casting structure.

The shape of the cooling curve is a result of the heat lost to the surroundings by the cooling test sample and the heat evolved in the cup during the phase transformation. The amount of heat evolved from a solidifying test sample can be calculated as the integrated area between the first derivative curve ( $FD = dT/dt$ ) and the base line (hypothetical cooling curve without phase transformations- BL) (Figure 10). Fraction solid can be calculated by numerically integrating the cumulative area between the first derivative of the cooling curve (FD), and the base line (BL). Figure 11 shows fraction solid curve calculated applying Newtonian base line for AlSi6Cu4 alloy.

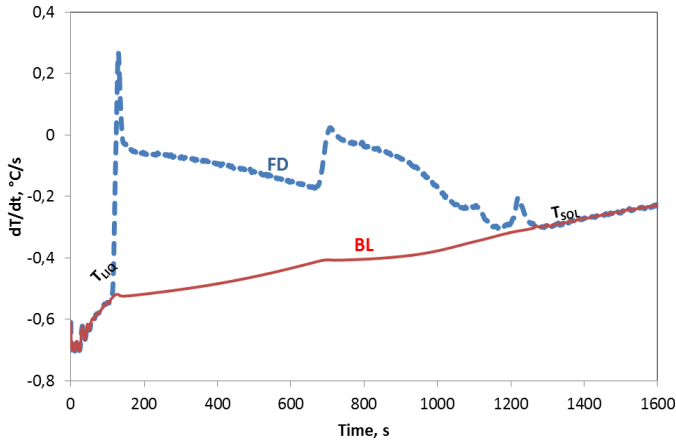


Figure 10. First derivative curve and its Newtonian base line for AISi5Cu1 alloy

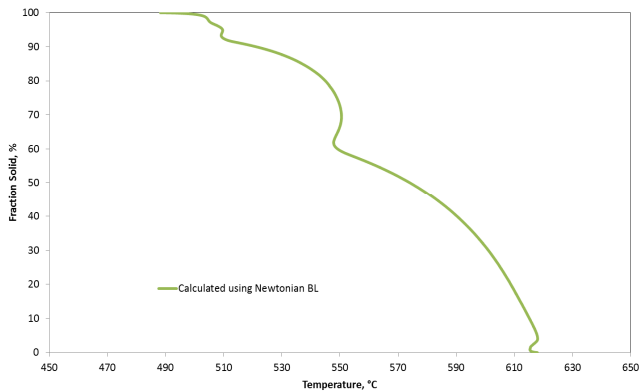


Figure 11. Fraction solid curve calculated using Newtonian base line for AISi5Cu1 alloy

### Terminal freezing range

Another useful criterion that can be extracted from the calculated fraction solid curve is the non-equilibrium partial freezing range near termination of solidification that according to [25] has been abbreviated as terminal freezing range (TFR). The TFR has significant impact on the hot tearing formation. In general as the freezing range increases the hot tearing susceptibility also increases. The chemical composition is the main influencing factor on the freezing range. Unfortunately, it is not yet established a range in which this criterion has to be calculated. In this paper has been used a range between 95 % and 99.5% fraction solid recently proposed by Schumacher et al [26]. Beside this criterion in the literature there are others theoretical models [27, 28, 29, 30] for the calculation of

the hot cracking tendencies. The most commonly used is the cracking susceptibility coefficient (CSC) model from Clyne and Davies [27]. The CSC model correlates the susceptibility-composition relationship based on the consideration of the time during which processes related to crack production may take place and the structure is most vulnerable to cracking (critical time interval during solidification). The CSC is defined as  $\text{CSC} = t_v / t_R$ ; where  $t_v$  is the vulnerable time period and is calculated as the time difference between mass fraction of liquid 10% and mass fraction of liquid 1%.  $t_R$  is the time available for stress relief processes and is calculated as the time difference between mass fraction of liquid 60% and mass fraction of liquid 10%.

Table 1. SCS and TFR values for evaluated alloys calculated using fraction solid curves

	AlSi8Cu1	AlSi8Cu2	AlSi8Cu3	AlSi8Cu4
SCS	0.478	0.416	0.379	0.234
TFR <sub>(fS = 95 – 99.5 %)</sub>	36.34	23.40	12.37	9.43

Table 1 summarized terminal freezing range (TFR) and cracking susceptibility coefficient (CSC) values that have been calculated using data from fraction solid distribution curves of investigated alloys. From both results it is evident that copper contents have significant impact on the hot tearing formation. Experimental evaluation of hot tearing tendency by aluminum alloys is very complex. With these two calculations it has been shown that cooling curve analysis has potential these criterions to quantify.

#### Derivative curves plotted versus temperature

Several researchers are even looking to extend the benefits of cooling curve analysis. One of them is D. A. Sparkman [8] that proposed next logical steps in utilization of thermal analysis introducing the application of higher order derivatives in order to measure the energy signatures of different microstructures. Higher order derivatives (up to fifth) offer the possibility of opening up the thermal analysis to become much more than just a quick chemistry/inoculant check. With this information, according to Sparkman, using thermal analysis it should become possible to calculate the amounts of different phases and defects (f.e. shrinkage porosity) that appear in as cast structure of aluminum alloys.

### **Conclusions**

A comprehensive understanding of melt quality is of paramount importance for the control and prediction of actual casting characteristics. Thermal analysis is already used tool for melt quality control in aluminum casting plant. It has been used routinely for assessment the master alloys addition into aluminum melt. This work has demonstrated that recording applying cooling curve analysis the following

characteristics of AlSiCu alloys can be determined/calculated: characteristic solidification temperatures (liquidus, dendrite coherency temperature, rigidity temperature, AlSi and AlSiCu eutectic temperatures and solidus temperature), fraction solid distribution, latent heat of solidification and terminal freezing range under equilibrium and non-equilibrium conditions. The data collected using cooling curve analysis should be applied in existing simulation software in order to improve accuracy of simulation. Intricate aluminum automotive cast parts contain different cross section thicknesses that solidified under different cooling rates, which in turn affect as-cast structure. In order to be able to produce such complex cast products it is necessary a deeper understanding of the melt flow through semi solid cast structure of cast parts. Thermal analysis in synergy with simulation software packages is a useful tool to help gauge the lack of knowledge regarding the understanding feeding mechanisms during solidification of aluminum cast alloys. The TA apparatus is capable to collect the cooling curves that solidified under various process parameters and calculated all characteristic solidification temperatures. Recorded data can be used as an input database for simulation in order to more accurately predict the quality of very complex cast parts. The data necessary for simulation of casting processes can be gathered either using experiments or calculated using commercial simulation software packages. Both approaches have advantages and disadvantages and need to be used on comparative basis. Experiments are expensive, time consuming but sometimes only possible source for thermo physical and physical properties. In contrary to them simulation is very fast, can be repeat many time and provide consistent results. The industrial interest is of course to be able to make simulation and optimization based on more realistic database in order to be able to predict the quality of very complex cast parts. A thermal analysis has such opportunity, and has to be used more often in providing simulation engineers with all necessary data for simulation of course in synergy with commercial software packages.

## **Literature**

- [1] A.Cibula "The Mechanism of Grain Refinement of Sand Castings in Aluminum Alloys", J.Ins. Metals vol. 76, p. 312 (1949/50).
- [2] P.B. Crossley and L.F. Mondolfo, "The Modification of Aluminum Silicon Alloys", Modern Casting vol. 49, p. 53/64, (1966).
- [3] L. Bäckerud et al. "Solidification Characteristics of Aluminum Alloys" Volume 1 to 3, AFS/SKANALUMINIUM, Oslo, (1986).
- [4] B. R. Krohn, "Thermal analysis: Metallurgical Thumbprinting", Modern Casting, March 1985, pp.1-7.
- [5] J. E. Gruzleski and B. M. Closset, " The treatment of liquid aluminum-silicon alloys" American Foundryman's Society, Inc. Des Plaines, Illinois, USA, (1990).
- [6] N. Tenekedjiev, H. Mulazimoglu, B. Closset and J. Gruzleski, "Microstructures and Thermal Analysis of Strontium-Treated Aluminum-Silicon Alloys", American Foundryman's Society, Inc. Des Plaines, Illinois, USA, p. 40-41, (1995).
- [7] L. Ananthanarayanan, and J. E. Gruzleski, "Thermal Analysis Studies on the

- Effect of Cooling Rate on the Microstructure of the 319 Aluminium Alloy” AFS Transactions, No.141, p. 383-391, (1992).
- [8] D. A. Sparkman; “ Microstructure by Thermal Analysis”, AFS Transactions 2011, Paper 11-068, pp. 1-8.
- [9] K.G. Upadhy, D.M. Stefanescu, K. Lieu, and D. P. Yeager, “Computer-Aided Cooling Curve Analysis: Principles and Applications in Metal Casting” AFS Transactions, Vol. 47, p. 61/66, (1989).
- [10] B. Apelian, G.R.Sigworth, K.R.Wahler, “Assessment of Grain Refinement and Modification of Al-Si Foundry Alloys by Thermal Analysis”, AFS Transactions, No.161, p. 297-307, (1984).
- [11] D. Apelian and J.A. Cheng, “Al-Si Processing Variables: Effect on Grain Refinement and Eutectic Modification” AFS Transactions, No 147, p. 797-808, (1986).
- [12] H. Beumler, A. Hammerstad, B. Wieting and R DasGupta, “Analysis of Modified 319 Aluminum Alloy” AFS Transaction No. 54, p. 1-12, (1988).
- [13] [13] M. Garat, et al. “State of the Art Use of Sb, Na and Sr-Modified Al-Si Casting Alloys” AFS Transactions No. 146, p. 821-832, (1992).
- [14] L. Wang and S. Shivkumar, “Strontium Modification of Aluminum Alloy Casting in the Expendable Pattern Casting Process” Journal of Materials Science 30, p. 1584-1594, (1995).
- [15] H. W. Doty, A. M. Samuel and F. H. Samuel; “Factors Controlling the Type and Morphology of Copper-Containing Phases in the 319 Aluminum Alloy”, *100<sup>th</sup> AFS Casting Congress*, Philadelphia, Pennsylvania, USA, April 20-23, 1996.
- [16] Djurdjevic M. B., Odanovic Z. and Talijan N. “Characterization of the Solidification Path of AlSi5Cu(1-4 wt.%) Alloys Using Cooling Curve Analysis”, J. of Metals Vol. 63 Issue: 11 pp.51-57, 2011.
- [17] M. B. Djurdjevic, W. Kasprzak, C. A. Kierkus, W. T. Kierkus and J. H. Sokolowski, “Quantification of Cu Enriched Phases in Synthetic 3XX Aluminum Alloys Using the Thermal Analysis Technique”, *AFS Transactions*, 2001 (ISBN 0-87433-248-6) vol. 24, pp.1-8.
- [18] D. Emadi, L. Whiting and R.Schmid-Fetzer, Influence of Sn on Solidification Characteristics and Properties of AlSiCuMg Cast Alloys: Experimental and Thermodynamic Approaches”, ICCA 11, Aachen, Germany 2008, pp. 328-335.
- [19] A. M. Mohamed, F. H. Samuel, ..A. M. Samuel and F. W. Doty “Effects of Individual and Combined Additions of Pb, Bi and Sn on the Microstructural and Mechanical Properties of Al-10.8Si-2.25Cu-0.3Mg Alloy” *Met Trans* 2009 Jan, Vol 40A, pp.240-254.
- [20] S.P. Ringer, K. Hono, T. Sakurai, “ The Effect of Trace Additions of Sn on Precipitation in Al-Cu Alloys; An Atom Probe Field Ion Microscopy Study”, *Metallurgical and Materials Transactions*, 26A (1995), pp. 2207-2217.
- [21] J. Campbell., *Feeding Mechanisms in Castings*. AFS Cast Metal Research Journal, 1969. 5: pp. 1-8.
- [22] E. Fras, W. Kapturkiewicz, A. Burbielko and H.F. Lopez, “A New Concept in Thermal Analysis of Castings”, AFS Transactions, Vol. 101, 1993, 505-511

- [23] Jiang H, Kierkus WT, Sokolowski JH. Dendrite coherency point determination using thermal analysis and rheological measurements. In: proceedings of the international conference on thermophysical properties of materials (TPPM 99), Singapore, 17–19 Nov 1999
- [24] Emadi D., Whiting L.V. and Nafisi S. “Applications of thermal analysis in quality control of solidification processes”, J. of Therm. Anal. and Calorim., Volume: 81 Issue: 1 pp. 235-241. 2005.
- [25] Djurdjevic M. B. and Schmid-Fetzer R. “Thermodynamic Calculation as a Tool for Thixoforming Alloy and Process Development”, Mat. Sci. and Eng. A, 2006, A 417, pp.24-33.
- [26] Pabel T., Bozorgi S., Kneissl C., Haberl K. and Schumacher P. “Einfluss von Kupfer und Magnesiumgehalt auf die Warmrissneigung bei AlSi7MgCu Legierungen“, Giesserei Praxis Nr. 12 2010, p. 388-394
- [27] Clyne T.W. and Davies G.J. “The influence of composition on solidification cracking susceptibility in binary alloy systems,” The Br. Foundrym., 74 (1981), 65-73.
- [28] Feurer U. “Mathematisches Modell der Warmrissneigung von binären Aluminium Legierungen“, Giesserei Forschung 28, 1976, pp. 75-80.
- [29] Katgerman L. “A Mathematical Model for Hot Cracking of Aluminum Alloys During D.C.Casting,” J. of Metals (1982), 46-49.
- [30] Rappaz M., Drezet J.M. and Gremaud M., „A New Hot-Tearing Criterion,“ Met. and Mat. Trans. A, 30A (1999), pp. 449-455.

## PASSIVE AND ACTIVE CHAMBERS FOR DIE CASTING WITH COLD AND HOT CHAMBER MACHINES

P.MRVAR\*, B.TALJAT\*\*, J.MEDVED\*, A.Mahmutović\*\*\*

*\*Univerza v Ljubljani, Naravoslovnotehniška fakulteta, Oddelek za materiale in metalurgijo,*

*\*\* HTS IC, Ljubljana, Inštitut za livarstvo in toplotne obdelave, Ljubljana,*

*\*\*\* TC livarstvo, Ljubljana*

Univerza v Ljubljani



### Abstract:

In examination witch discuss the problems of casting of Al in Mg alloys on high pressure die casting with cold and hot chamber machine the possibility of increasing the efficiency of working chamber. This is related on decreasing the solidification of molten alloy in chamber, pouring at lower temperature, increasing the life time of sleeve and piston and increasing of yield of molten metal.

For this purposes the examination study was done. It involves the check of ideas and innovative solutions what are connected with materials of sleeve and technology of production of it with computer simulation of casting process. The concept of passive and active chamber for high-pressure die-casting will be presented. According to problems which are connect with solubility of iron in Al alloys it is find out that currently used systems can be essence renew with new concept which have active working and contain also new gradient materials on a "in situ" composite base.

*Key words: high pressure die casting, sleeve, simulation*

### Introduction

Die-casting is important procedure for the last 30 years and has evolved to degree, where in industry has very wide applicative value.

Production of castings from alloys with low melting point (Al, Mg, Zn, Cu) is still steadily increasing and is largely tied to the automotive industry. Usually we have permanent mold, which is produced from tool steel. With the die casting technology we cast alloys with low melting point (aluminum, magnesium, zinc and copper alloys). Quantitative the largest share for die casting represent the aluminum alloy. But because Al alloy soluble Fe alloy we are limited to manly a cold chamber machine. Technology is continuously improving and their innovations relating using primarily the casting technology (manufacture of tools), as well as automation of the process of die-casting, which is in connection with the machine

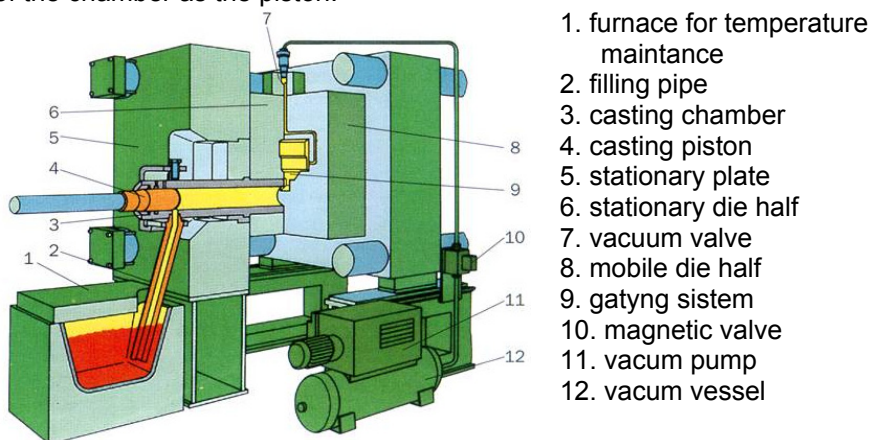
and the surrounding-cell. Since the casting of Al alloys in volume production is in the foreground and in the first place by quantity, a lot of research work focused in the field of die casting Al-alloy, which is only possible with the use of cold-chamber machine. In the last 20 years has resulted in some new concepts for die casting Al-alloys authored by prof. Dr.. Frederic Klein from the Hochschule Aalen, but unfortunately this new concept has not yet occurred (as far as we know).

Cold-chamber machine's design to date has not experienced revolutionary change; limiting cold-chamber machine is primarily concerned with the problems that are related to the dissolution of Fe in the molten Al. Because of the aforementioned characteristics has so far not been possible for chamber to operated at higher temperatures.

In Figure 1a presents a crushing machine manufacturer Muller Weigartner (now O. Frech) with vacuuming system of the molding cavity by the procedure Vacural.

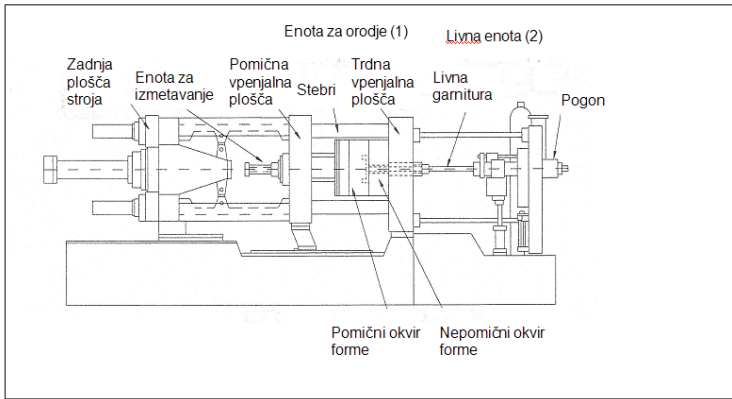
The existing system of the molding set, which includes a casting chamber and piston (Figure 1b) is a so-called passive chamber, which is usually made from tool steel, while the piston is made of copper alloy. Since the chamber is clamped unilaterally cantilever and rests on the flange of the fixed part of the basic clamping plates.

Steels that are used are relatively low heat conduction, during the cyclic operation of the die machine (chamber) takes place, that the chamber is very unevenly heated by the axial cross-section as well as the longitudinal axis (Fig. 2, 3). Bottom layer of the chamber is at a higher temperature level then the lower layer. As a result of the unevenly heated filed is stress and strain generated in the chamber. The chamber is to blame in the direction of "z" (top), while the inner bore of the chamber deforms as dictated by the temperature field and consequently bore chamber is no longer perfectly round. In this respect, it is also an increased wear of the chamber as the piston.



1. furnace for temperature maintenance
2. filling pipe
3. casting chamber
4. casting piston
5. stationary plate
6. stationary die half
7. vacuum valve
8. mobile die half
9. gatyng sistem
10. magnetic valve
11. vacum pump
12. vacum vessel

a)



b)

Figure 1: Pressure machine with cold chamber

Depending on the solidification chamber, which has already been said above it is necessary to quickly perform casting. In the phase of zero should melt transported from the casting furnace in a casting chamber, in that there is a partial oxidation and the formation of oxides, which during this phase is slowly comes to the surface. Followed by the first stage, which is necessary for the transport of liquid alloy to the element, and the gating feeder system. It is necessary to ensure the right rate of displacement of the piston in such a way that the light of the current viscosity of the cast, which is dependent on the chemical composition, the temperature and nucleation potential occurs cogging wave, wherein the oxide film is not mixed with the cast, as it floats on the surface and protects the weld pool before further oxidation (Figure 2).

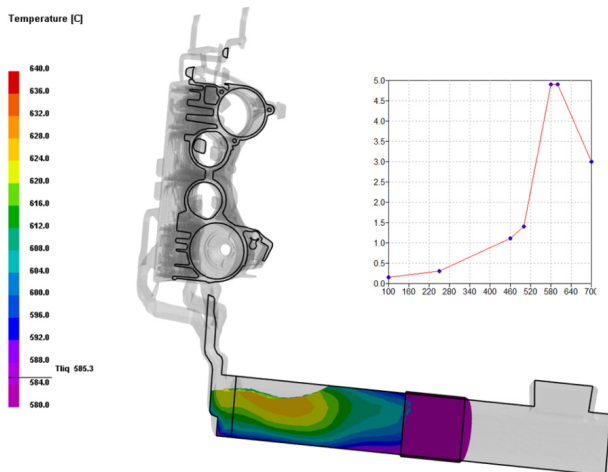


Figure 2: Moving the piston in the casting chamber (velocity as a function of the way)

The first phase is continuously continued in the second stage of the acceleration piston being made directly filling the casting melt in an extremely short period of time amounting to 8-60 ms. Such high-speed filling cavity resulting in significant turbulence, atmosphere vent cavity is difficult, first cool and relatively oxidized melt carrying ahead the release agent to collect the last places to fill in the dressing. Once the complete mold cavity is filled, the piston abruptly stops, since the melt is virtually incompressible. By means of the system to increase the pressure (intenzificator) the pressure of the third stage increases with a view to solidification is carried out at elevated pressure.

Only this is set on a process computer machine. In doing so, the trapped atmosphere cavity compresses the pressure at less volume. Typical pressures of the third stage are between 400 and 1,400 bars.

In the described event casting tool is particularly tempered as required by the casting technology in order to directional solidification and / or reduced bending of the casting. Even the chamber and piston are cooled.

The central event-casting is repeated, and the system is operating in a steady state, in this respect, due to the uneven temperature field in the chamber only deflects so that it comes to a decrease in roundness of the internal bore of the casting chamber, which results in relatively poor fitting between the piston and chamber. It is also according to the changed temperature field chamber deform in the vertical direction, the highest temperature load is in place the flow of melt in the casting chamber. These events due to the relative increase in friction conditions in the piston chamber system cause life-limited parts. Our analysis and studies is focused on o the molding chamber, which is a vital part of each die of the machine.

### **Preparation of the design solution and the creation of 3D models for innovative chamber**

In order to reduce deformation of the unilaterally cantilever fixture chamber to sway the tools both in the axial as well as in the transverse direction were made different geometry of casting chamber, wherein was maintained all through the dimension of the inner bore. With the implementation of passive tempering in order to minimize deformation during operation, were constructed models with integrated copper inlay of different thicknesses and lengths.

The first calculation is the chamber which does not have a copper insert figure 3a, the second model, which is shown in Figure 3b has an integrated copper insert over the entire length of the chamber is 10 mm thick and is located 10 mm below the surface of the bore. In the third model, which is shown in Figure 3c is implemented thicker sheet having a thickness of 15 mm is also 10 mm below the surface of the bore but at a distance of 350 mm from the edge of the chamber on the side where the charging takes place in the casting chamber (phase zero).

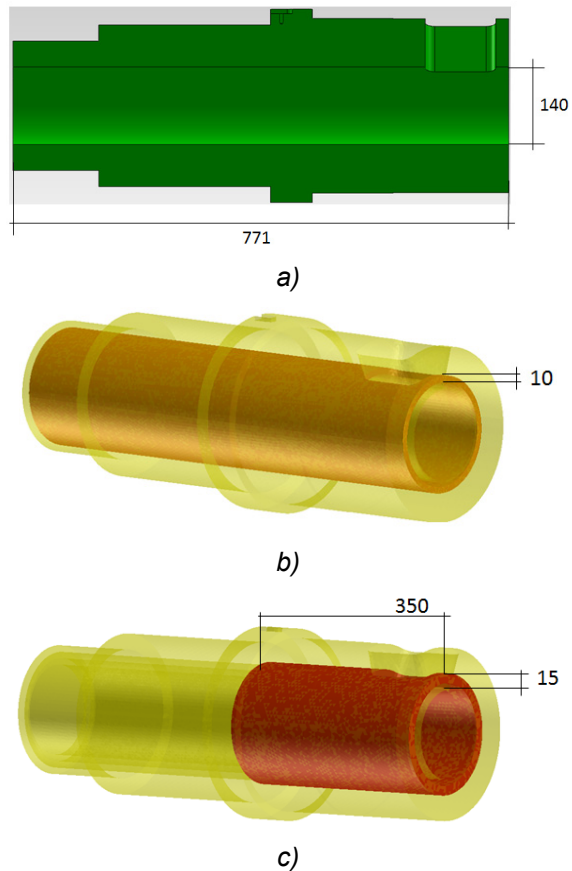
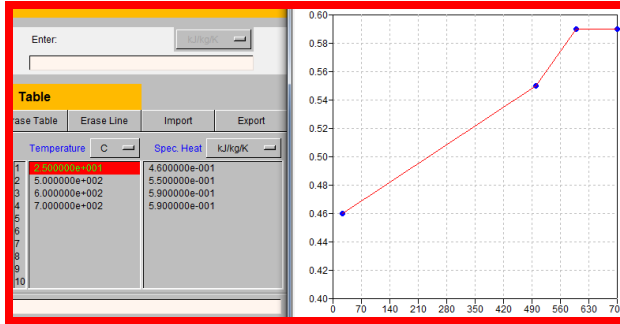
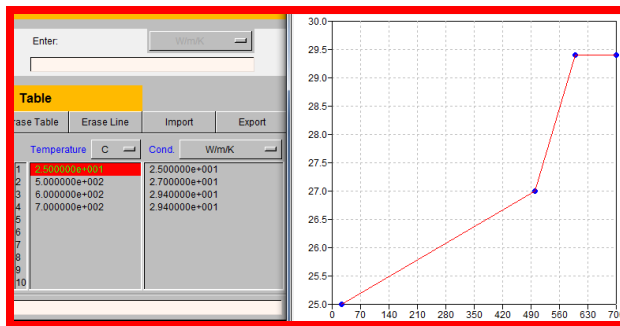


Figure 3: Models with integrated copper inlay

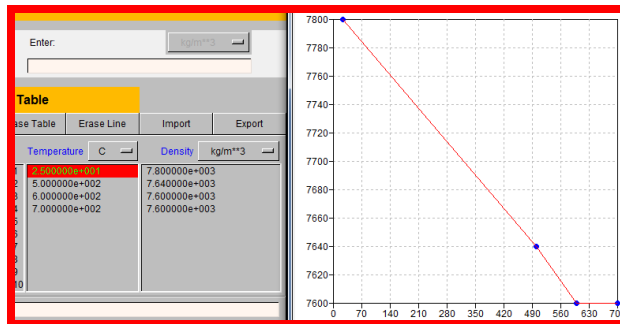
Figure 4 shows a model in the programme environment ProCAST where we used thermo mechanical properties of the chamber. We used the data were calculated by the program of dynamic thermal Computerterm for tool steel H11, the chemical composition of said steel consists of iron base, carbon 0.405 wt%, manganese 0.35 wt%, silicon 1.0 wt%, chromium 5.125 % by weight of molybdenum, 1.425 wt% vanadium and 1.0% by weight. The applied properties depending on the temperature of the selected material are necessary for the calculation of the temperature and stress field the pressure chamber.



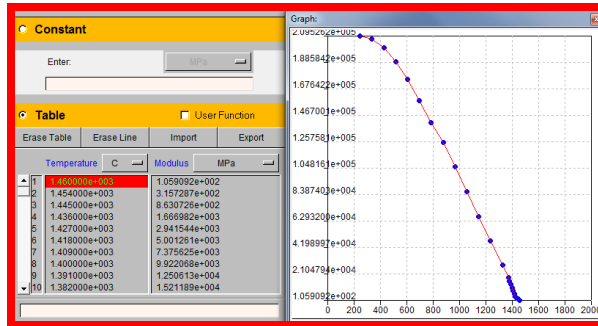
a) Thermal conductivity



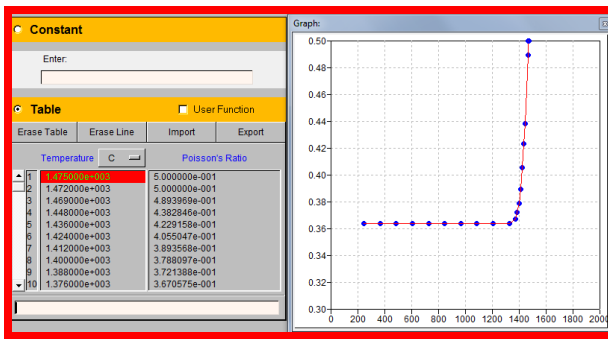
b) Specific heat (Cp)



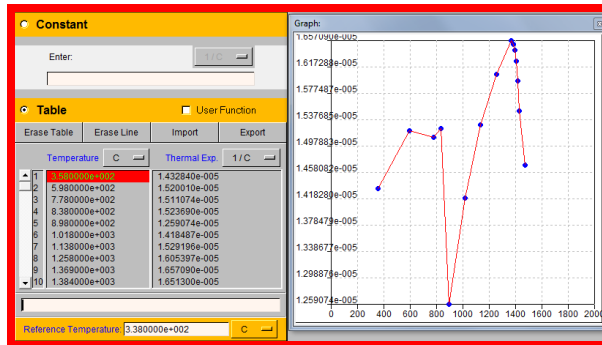
d) Young's modul



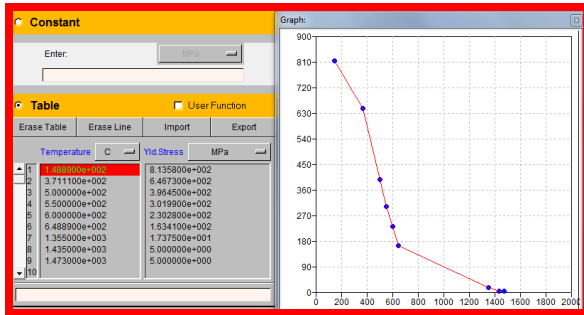
d) Young's modulus



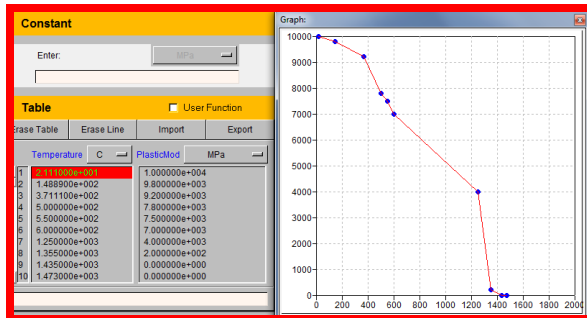
e) Poisson's ratio



f) Thermal expansion



g) Yield stress



h) Plastic modul

Figure 4: The material properties of the steel as a function of temperature

Contact of copper to steel is defined as a tight fit, so no air gap between the elements. Baker has a very good heat conductivity and copper inlay in the oppressive chamber is to ensure an even distribution of heat in the chamber and reduce its deformation. In Figure 5 we can see a diagram and a table showing a thermal conductivity of copper, depending on the temperature.

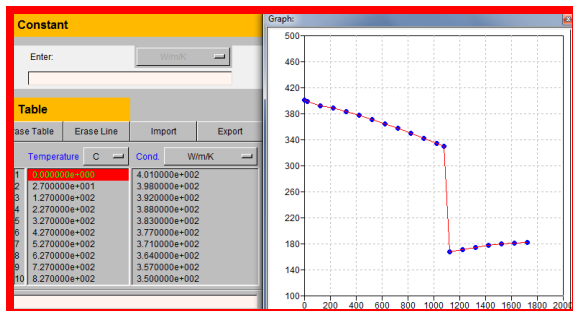


Figure 5: Thermal conductivity of copper

Other boundary conditions that define the heat transfer between the chamber and a tool (fixed part of the tool) are defined by the transfer of heat for that

interface is 1000 W/m<sup>2</sup> K for the ambient temperature (the average temperature of the tool) is defined as 150 °C (Figure 6).

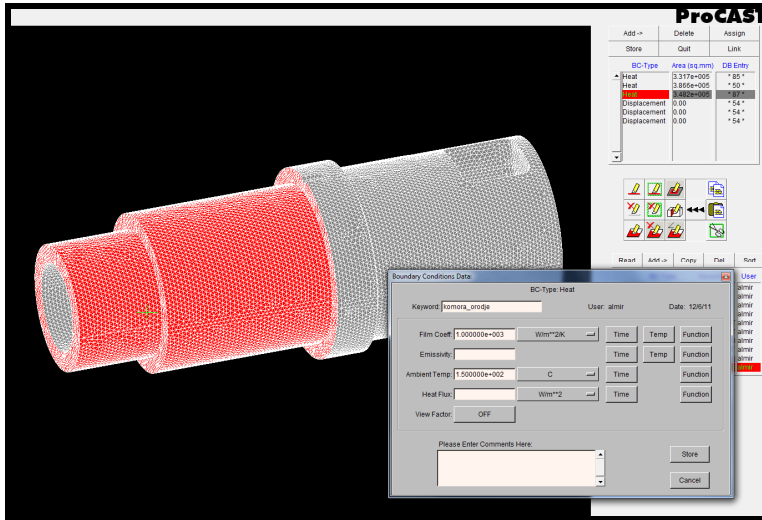


Figure 6: Heat transfer chamber - tool

Cyclic definition filling chamber was carried out with the function that described with the help of the program C++ and is shown in Figure 7

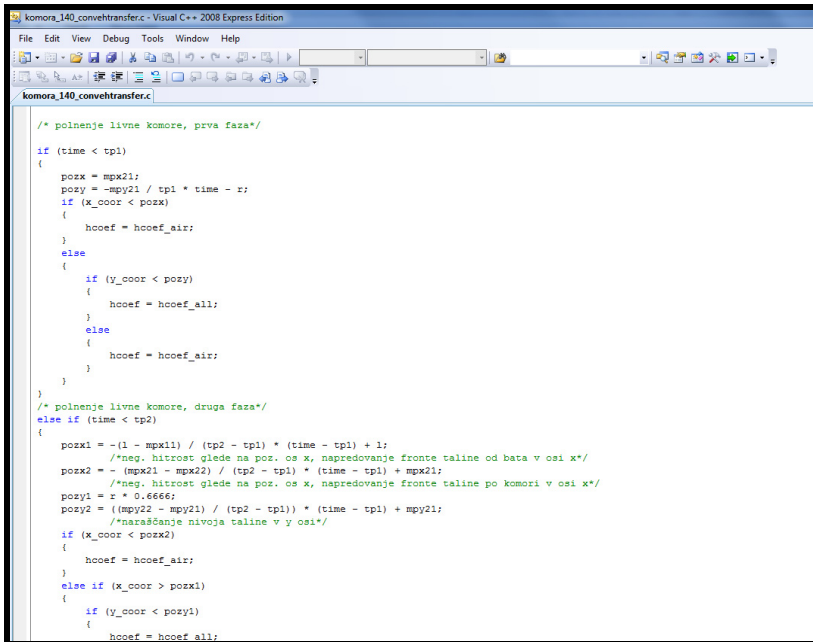


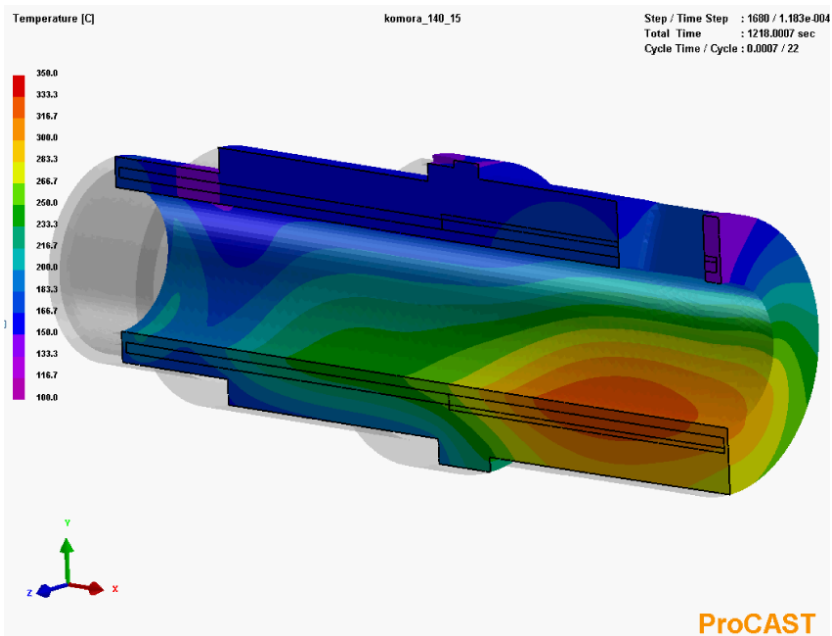
Figure 7: Cyclic description by means of functions in C++

## Optimization of geometry and virtual testing of innovative chamber

For the execution of casting was used as the average of the parameters, which are:

- Melt inflow at an angle of  $90^\circ$ ,
- The chamber is 37% filled with the liquid cast,
- alloy casting temperature is  $640^\circ\text{C}$ ,
- the alloy is alloy 226 - AlSi9Cu3
- temperature of the atmosphere in the chamber is  $250^\circ\text{C}$ ,
- Bat is tempered at  $100^\circ\text{C}$ ,
- thickness of residual alloy in the casting chamber is 30 mm,
- time flowing liquid alloy in the chamber is 4.5 s,
- the stabilization and calibration of liquid alloy in the chamber is 1.5 s,
- time of implementation of the first phase is 1.32 s,
- solidification time (time for the opening tool) 16,5 s,
- cycle lasts 58 s,
- the calculation was performed for 40 cycles (40 consecutive filled casting chamber).

Figure 8 shows that model was analyzed and investigate in the chamber without integrated passive copper deposit temper overall analysis of the individual sequences is widely given in electronic form in the form of a film.



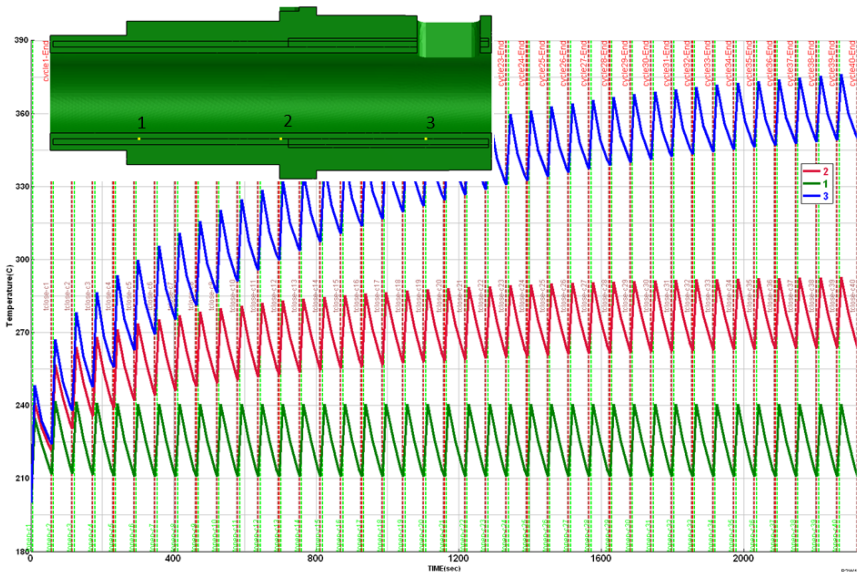


Figure 9: Temperature dependence of the time for 40 cycles

After 40 cycle's we can see test points (1,2,3) from which we can see results given in Figure 9. It can be seen that the steady state at point 3 up very late while in point 2 a little earlier.

For the calculations which were performed for the first time, such as a copper-free, the second time with 10 mm copper (Cu-10) and the third with 15 mm copper (Cu-15) the temperature field after 20 cycles is shown in Figure 10. Where we can see strong overheating of working directly under "inlet-om" for example, when there was no system used passive tempering, while in the case of a derivative tempering temperature field more homogeneous in a way that is entered with the current cast heat more evenly distributed the direction of the tool and the upper part of the chamber. Thus, the temperature on the surface directly below the "inlet-om" copper-free 300 ° C, with a copper Cu-10 260 ° C and with copper Cu-15, 255 ° C.

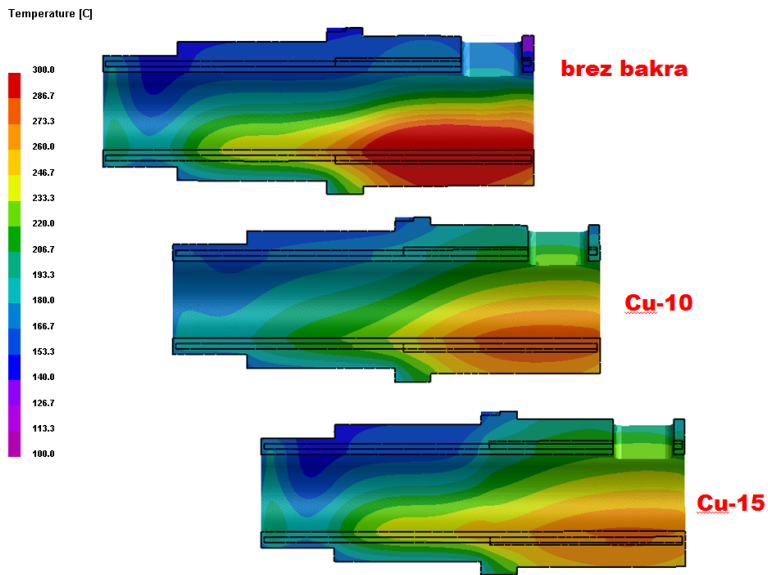


Figure 10: Temperature field at 20-th cycle

Temperature field over the area of site as shown in Figure 11. The comparison shows that the passive tempering with copper is quite successfully for transport of heat from the lower part to the higher parts. In the analysis model we wish to achieved, that the heat at which causes curvature shall be distributed evenly over the surface of the chamber.

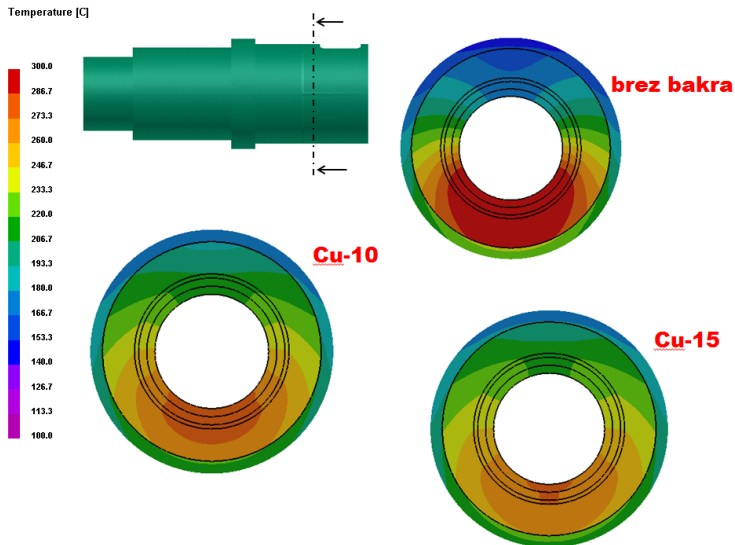


Figure 11: Temperature field at layers after 20 cycle

Temperature field after 40-cycle is shown in Figure 12 and it is obvious that in the case of more massive copper inserts Cu-15 does not result in significant changes in the temperature field comparatively speaking to the chamber with insert of material Cu-10.

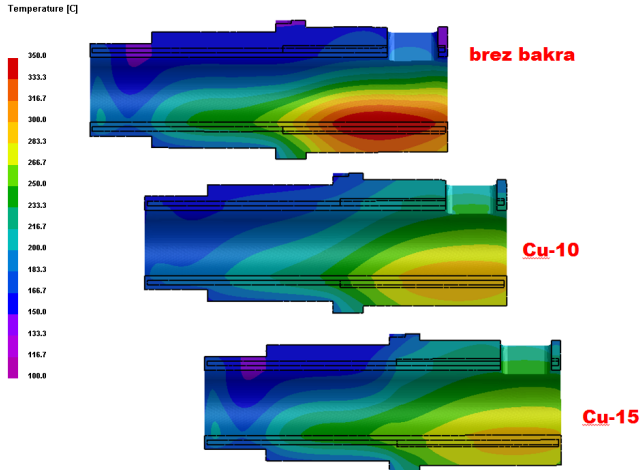


Figure 12: Temperature field after 40 cycle

It is well evident from the cross-section of a temperature field, as shown in Figure 13. The area under inlet the maximum temperature in the case of Cu-15 is slightly smaller. As can be seen from Figure 13, the maximum temperature on the surface under inlet for example, a copper-free after the 40-th cycle was 354 ° C, for example, with a copper Cu-10 298° C and with copper Cu-15 289°C.

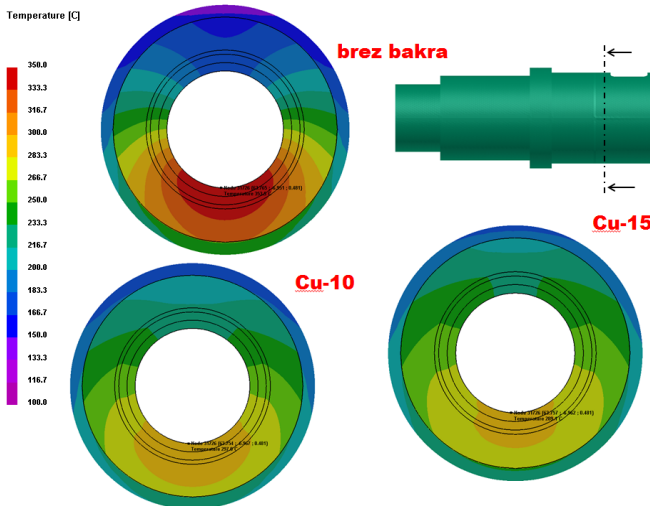


Figure 13: Temperature field at layers after 40 cycle

Temperature dependence of the individual analyzing the geometry of the copper-free, Cu-10 and Cu-15 to 40 cycles and location as shown in Figure 14 shows the effect of intensive system for reducing the maximum temperature on the surface of the chamber. It can be seen that the element with the largest dimension of the (Cu-15) due to the maximum heat capacity of the largest ability to reduce the maximum temperature on the surface of the chamber under inlet.

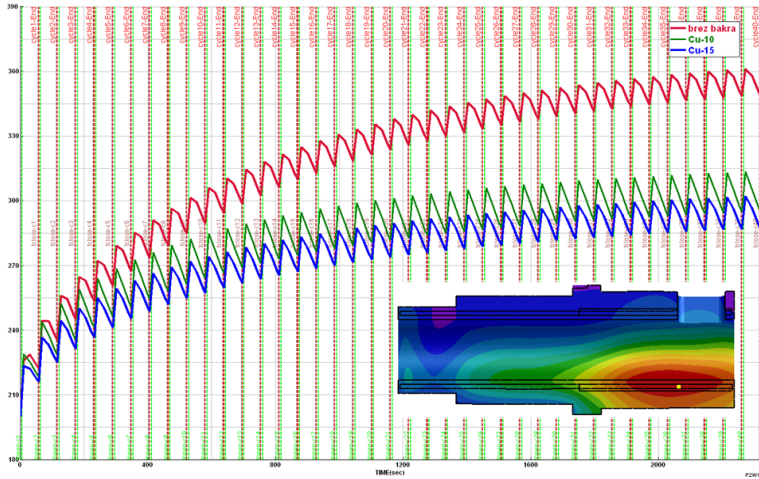


Figure 14: Temperature dependence of the individual models chambers

The effect of copper element is visible on the upper part of the chamber. From Figure 15 can be seen that the heat is relatively successfully transferred also to the upper part of the chamber, and from there we can see that the temperature gradient between the top and bottom is the lowest in the case of chamber with Cu-15 countries.

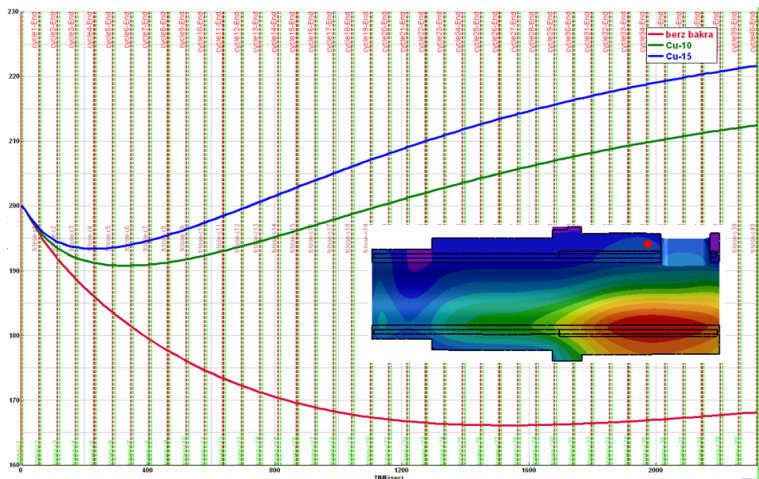


Figure 15: Temperature dependence of the individual models chambers

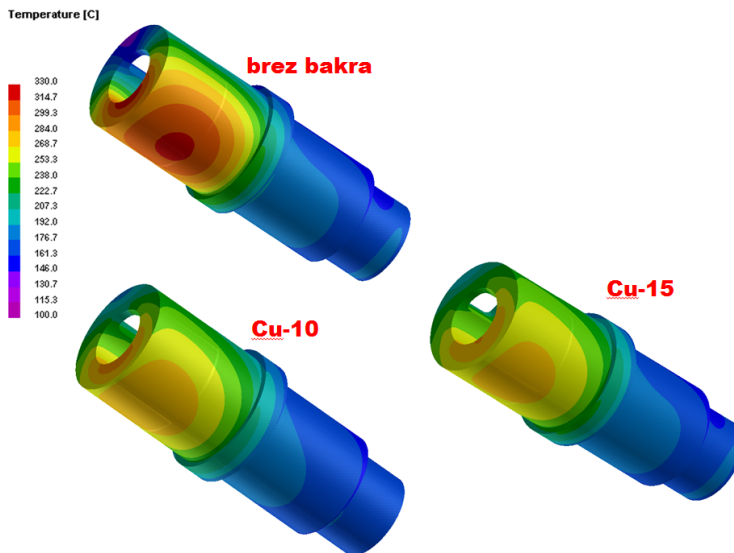


Figure 16: Temperature field outside of the chambers

### Deformation analysis of chamber

Deformation of all the three geometries of chambers in dependence on each cycle was calculated for the boundary conditions, which are presented in the first part of the report. We can see the results in the electronic versions where it was used to demonstrate a 30x magnification deformation. It also can be seen that the chamber is in accordance with the temperature field deforms so that the lower parts of the chamber "inlet" spread on the contrary, but the upper parts of chamber object, because of the lower temperature level. The resulting tensions thus chamber bend in the Y direction up. Deformation of the chamber in the Y direction, for each geometry (without copper, Cu-10 Cu-15) are shown in Figure 17, sees a very large deformation of chamber without the copper while the case Cu-10 and Cu-15 with passive tempering effectively reducing the deformation in the Y direction. It is interesting that the geometry of the Cu-15 deformation in the Y direction a little higher the extreme right corner above, as the geometry of the Cu-10.

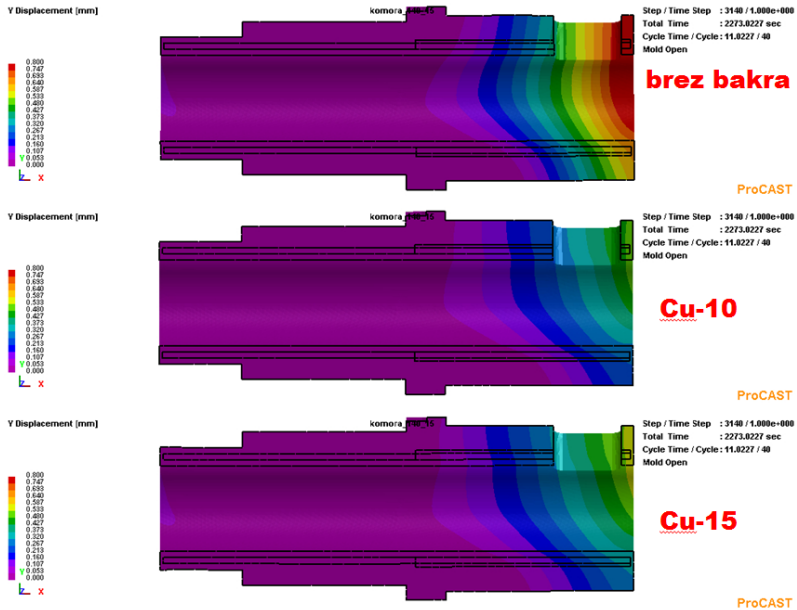


Figure 17: Deformation of the chamber in the Y direction

Due to the presentation of curvature was made comparison deformation network as shown in Figure 18.

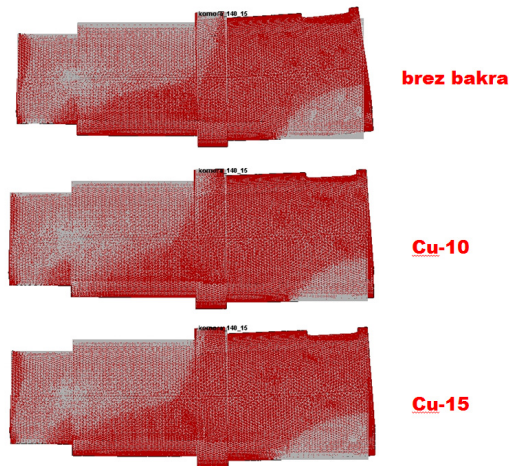


Figure 18: Deformation of mesh geometry for each model

Results for selected geometry deformation and the points from 1 to 5, which are located on the outer surface of the upper chamber were quantitatively determined and are presented with graph of curvature as a function of distance. Depending on the position of point 5 as shown in Figure 19, a minimum

deformation showing the geometry of Cu-10, which quantitatively is 0.49 millimeters, followed by deformation of chamber Cu-15, to the point 5 is 0.55 mm and, finally, the geometry of the chamber without copper, where the position 5 is 0.82.

Thus, the correlation reducing source deformation for point 5 of the 40 cycle were observed between the chamber without copper and Cu-10 represents a 40% reduction of the source deformation in Y direction. For all the analyzed point of the results are presented in Table 1.

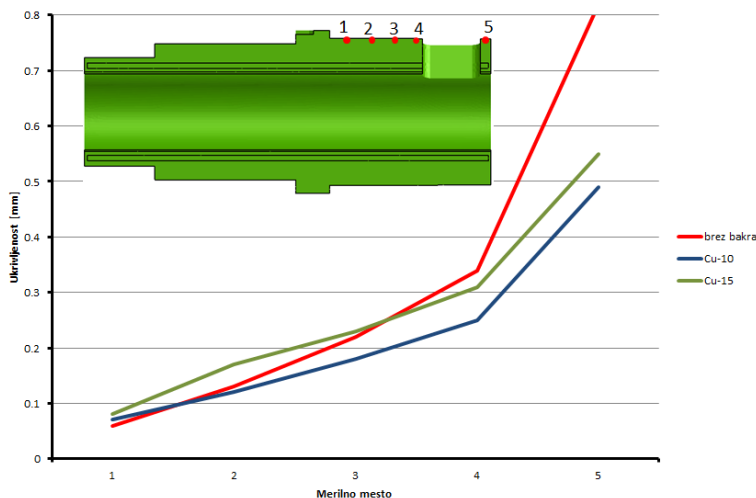


Figure 19: The curvature in dependence of the analyzed site

Table 1: Quantifying curvature for 1 to 5

Meritev	1	2	3	4	5
Brez bakra	0,06	0,13	0,22	0,34	0,82
Cu-10	0,07	0,12	0,18	0,25	0,49
Cu-15	0,08	0,17	0,23	0,31	0,55

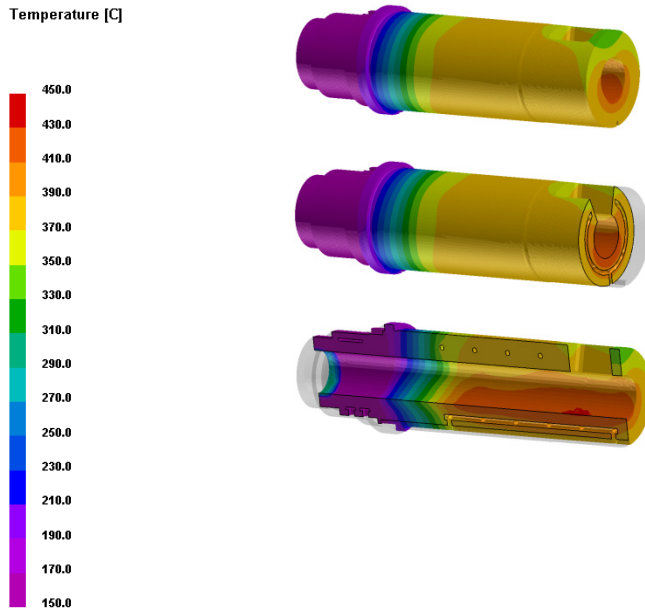


Figure 20: Example of calculation of the temperature field of the active chamber after 20 cycle (start casting)

## Conclusion

According to the results conclusions can be summarized in the following facts:

- Deformation of the chamber is strongly depend on the effectiveness of the redistribution of heat from the lower chamber to the upper part of the chamber (seen from Y direction).
- The result for geometry of the chamber with an integrated passive temperature control element, which has a 10 mm wall, resulting in a minimum deformation.
- The maximum surface temperature of the chamber under "inlet" is effectively reduced by using more massive Cu-15 passive cooler element.
- In the case of the existing system and technology of cold chambers for integrated passive tempering can be carried out some more optimizations, which relate to a slightly modified geometry of the copper elements.
- In view of the result of the calculation would be reasonable to make the concept of the active cold chamber with new materials and integrated diffusion barrier to prevent the dissolution of iron in the Al alloy.

**Reference**

- [1] M. Petric, J. Medved, P. Mrvar, *Metalurgija*, 50 (2011) 2, 127–131
- [2] W. Thorpe, V. Ahuja, M. Jahedi, P. Cleary, N. Stokes, *Trans. 20th int. die casting cong. & expo NADCA*, Cleveland, 1999, T99-014
- [3] F. Klein, *Fachhochschule Aalen, Seminar Ljubljana*, 13. March 2003, DLS
- [4] M. Trbižan, P. Mrvar, *Novosti tlačnega litja, TECOS-Development center of tooling Slovenia*, 2005



# **Oral Presentations**



## NOVEL TECHNOLOGIES FOR ENHANCED ENERGY AND EXERGY EFFICIENCIES IN PRIMARY ALUMINIUM PRODUCTION INDUSTRY

E. Balomenos<sup>\*</sup>, C. Kemper<sup>#</sup>, P. Diamantopoulos<sup>\*,#</sup>, D. Pantias<sup>\*</sup>, I. Paspaliaris<sup>\*</sup>, B. Friedrich<sup>#</sup>

<sup>\*</sup> *Laboratory of Metallurgy, School of Mining and Metallurgical Engineering, NTUA, Athens, Zografou 15780, Greece, Email: thymis@metal.ntua.gr*

<sup>#</sup> *IME Process Metallurgy and Metal Recycling, RWTH Aachen University, 52056 Germany*

### Abstract

The EC funded research project “ENEXAL” develops and demonstrates novel technologies for increasing the energy and exergy efficiency of the primary aluminium industry, which is currently amongst the most energy intensive industries in the world. In this paper a presentation of novel technologies for the red mud treatment and the carbothermic reduction of alumina are presented. Accordingly, the red mud by-product of the Bayer process is transformed into valuable products such pig-iron and mineral wool fibers through reductive smelting in a dust treating EAF. Aluminium and aluminium-silicon alloy are being produced through carbothermic reduction in EAF.

*Keywords: Red Mud, Bauxite residues, Carbothermic reduction of alumina, Al-Si alloy.*

### Introduction

The primary aluminium production industry is the world’s larger industrial consumer of energy and is ranked among the most CO<sub>2</sub> intensive industries. It also generates enormous quantities of wastes that further decrease the exergy efficiency of its production process. However, this industry is one of the most vital sectors from an economic and a social point of view, not only for Europe but also for the entire world. In order to remain viable and competitive, primary aluminium industry has to operate in a smarter way, be more energy efficient and meet the environmental requirements of our times. This can be achieved only through radical new technologies and novel business strategies, which will enable the industry to maintain its competitiveness and fasten its viability in the world’s markets, and explore new business opportunities.

The main goal of the EC funded ENEXAL project is to provide primary aluminium industry with “green” innovative technological and economical solutions, focusing on the (i) *significant improvement of energy and exergy efficiencies of the production process*, (ii) *substantial reduction of GHG emissions and (iii) complete elimination of its solid wastes*.

In this paper three technologies developed in the above framework are presented.

### The red mud treatment

On average the Bayer process requires 2.65 kg of bauxite ore to produce 1 kg of alumina, while the slurry containing the remaining bauxite ore, which is removed from the thickeners during the liquor clarification stage, is by far its greatest environmental problem. This by-product, called bauxite residue or “red mud”, on a dry basis is produced in almost a 1 to 1 mass ratio to alumina and consists from various metal oxides of Fe, Al, Ti, Si, K, Na, V (depending on the initial chemical composition of the bauxite ore) along with inclusions of unwashed sodium aluminate solution.

Utilizing modern Electric Arc Furnace reduction smelting technology today it is feasible to process dry fine red mud directly without the need for a costly agglomeration pre-treatment step. The pig-iron produced in such a way amounts to approximately to 35% of the initial red mud charge, while the remaining amount of the red mud is transformed into a viscous slag. The latter, through slag engineering, can be transformed into inorganic fibers suitable for the production of a variety of marketable products commonly known as mineral (or slag, rock) wool products

To establish the process, batch scale tests were conducted in NTUA's semi-industrial scale 400kVA dust treating EAF. The red mud used was supplied by ALUMINIUM SA, the Greek aluminum producer plant, and it was dried in a stationary electric dryer before feeding to the EAF. The optimal feed recipe used in the experiments, consisted of mixing dry red mud with coke fines and appropriate silica and lime bearing fluxes, so that the C to Fe atomic ratio was set at 2.4 and the basicity ratio of the feed ( $\text{CaO} + \text{MgO}/\text{SiO}_2$ ) was set at 0.94.

Each batch experiment consisted of a furnace pre heating stage (app 1 hour long), followed by the feeding of the material which was done at approximately 3kg/min rate, through a feeder tube at the top of the furnace. The temperature at the surface of the melt produced was measured with an optical pyrometer at 1540°C (average value). In the end of the batch feeding, two distinct phases were poured from the furnace, slag and pig iron, their weights and chemical analyses of which are presented in Table 1.

Table 1: EAF Experimental Results

<b>Pig iron wt. %</b>	<b>Fe</b>	<b>C</b>	<b>S</b>	<b>P</b>	<b>Si</b>	<b>Ti</b>	<b>V</b>	<b>Cr</b>	<b>Mn</b>
	87.093	4.047	0.050	0.202	1.705	0.455	0.281	4.427	0.115
<b>Pig iron phase weight</b>			120 kg		<b>Fe recovery in pig iron</b>			97.31%	
<b>Slag wt. %</b>	<b>Al<sub>2</sub>O<sub>3</sub></b>	<b>SiO<sub>2</sub></b>	<b>CaO</b>	<b>TiO<sub>2</sub></b>	<b>MgO</b>	<b>Fe<sub>2</sub>O<sub>3</sub></b>	<b>Na<sub>2</sub>O</b>	<b>Cr<sub>2</sub>O<sub>3</sub></b>	<b>-SO<sub>3</sub></b>
	24.226	32.624	29.650	6.786	4.646	1.106	1.890	0.409	1.090
<b>Slag phase weight</b>			280 kg		<b>Slag Basicity Ratio</b>			1.05	

The pig iron chemical analysis shows that the metal produced has concentrated practically all the iron and the vanadium content of the red mud, while also small amounts of silicon and titanium metal have also been reduced. Sulfur,

originating from the red mud and the coke, and phosphorous originating only from the coke, where kept at minimum values, thus producing a metal which can be easily used in secondary steel production. Carbon content has the typical pig iron value of 4wt.%. The chromium metal presence in the pig iron is not attributed to the feed material, but rather to magnesium chromite furnace refractory lining which was partially dissolved during the carbothermic reduction.

The slag phase contains the remaining metals of the red mud in form of oxides, in an overall neutral melt (basicity ratio = (mass of CaO + MgO) / (mass of SiO<sub>2</sub>) = 1.05). The chemical composition of the slag is within the empirical limits set by the mineral wool industry, as reported in [1]. During the slag phase pouring part of the slag was fiberized using a high speed air/water jet. The inorganic fibers produced from the slag were examined with scanning electron microscopy, in order to assess the physical qualities of the fibers. As seen in Figure 1, fibers with diameters less than 20µm were mostly formed, along with some substantially thicker fibers. Such imperfections, caused by the slag freezing prior to the completion of the fiber formation, can be attributed to the lack of an automated system during these preliminary experiments. In general, it is apparent that the slag from the red mud treatment process can be fiberized.

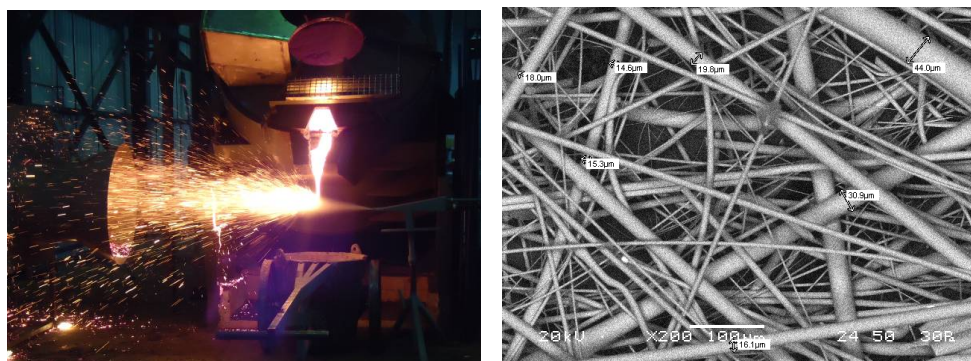


Figure 1: Photos of air/water jet slag fiberization test (left) SEM photograph of inorganic fibers produced (right).

## Carbothermic production of Aluminium

A recent thermodynamic study of the carbothermic reduction of alumina presented in [2], demonstrated the major thermodynamic role of aluminium volatilization phenomena in reducing liquid aluminum yields at high temperatures. Accordingly, to achieve an efficient one-step reduction process either one has to reduce the liquid aluminum activity or move to conditions favoring complete gaseous aluminum production. Both routes are investigate in the ENEXAL project

### Gaseous Aluminum production

As seen in Figure 2, for the systems Al<sub>2</sub>O<sub>3</sub> + 3C at atmospheric pressures temperatures above 2500°C thermodynamically one can achieve aluminum reduction yields above 90%. To test this process a custom hollow electrode DC-EAF, depicted in Figure 3, located at IME, RWTH Aachen was used, capable of

achieving temperatures above 2400°C in the arc zone between the tip of the hollow electrode and the bottom electrode. Through the use of the hollow electrode the material feed can be directly fed in the arc zone, allowing thus for fast reactions at high temperatures. The lid of the EAF is water cooled and was fitted with a customized copper condenser, in order to directly solidify gaseous aluminum products.

Following an optimization experimental campaign the optimum feeding rate of alumina carbon pellets (at stoichiometric ratio), condenser cooling rate, as well as the optimum Ar overpressure in the furnace (in order to avoid back-reactions with oxygen) was established. Accordingly the dusty material retrieved from the condenser, shown in figure 3, contained practically only metallic Al, with minimal amounts of  $\text{Al}_2\text{O}_3$ ,  $\text{Al}_4\text{C}_3$ , and  $\text{Al}_4\text{O}_4\text{C}$  (figure 4).

Quantitatively, the total mass of the material pellets which was fed during the experiment was 30g and at end of the experiment 16g of dusty material were retrieved from the condenser. In accordance with the chemical composition of the pellets and the XRD analysis presented above, one can deduce that approximately 77% of all Aluminium was retrieved in the condenser in the metallic state.

Therefore the process is proved successful both in quality of produced condensate and in quantity of Aluminium recovery. With an improved condenser design (e.g. by eliminating the lid condensation surface and further improving cooling rates) one should be able to achieve practically full aluminum recovery.

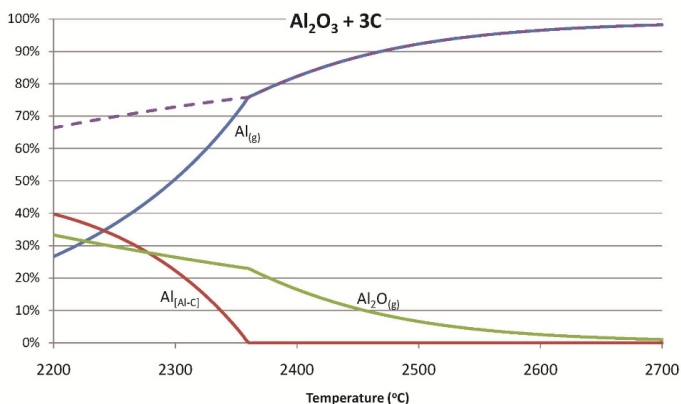


Figure 2: Factsage calculated distribution of aluminum species at thermodynamic equilibrium for various temperatures at atmospheric pressure in a system with initial molar composition of 1  $\text{Al}_2\text{O}_3$  + 3 C. The dashed line signifies the total alumina to metallic aluminum reduction yield (Al-C alloy and  $\text{Al}_{(g)}$ ). The [Al-C] subscript denotes the liquid aluminum alloy metal phase.



Figure 3: Schematic drawing and photograph of the EAF used. On the right picture of the reaction zone during operation (the graphite crucible is seen in the bottom while the hollow electrode tip is directly above it). No liquid melt formation is observed.

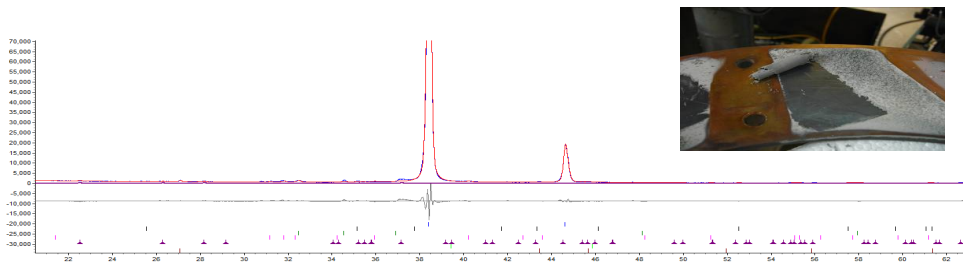


Figure 4: XRD analysis of the dust collected from the condenser. Both major picks correspond to metallic aluminium (2theta 38,10 and 44.37). Rietveld-method analysis shows at least 76.91% metallic Al, followed by cubic Alumina 9.37%, 4% or less in  $Al_2OC$ ,  $Al_4C_3$  and  $Al_4O_4C$ . Cubic alumina is the result of metallic aluminum re-oxidation after the end of the experiment. Inlet Picture: Dust collected from copper condenser surface.

#### Direct Al-Si master alloy production

An alternative process developed in ENEXAL is the carbothermic co-reduction of alumina and silica in EAF in order to produce directly an Al-Si master alloy. Al-Si alloys are used in casting application which approximately account for 30% of all Aluminium utilization.

Small addition of silicon in the aluminum melt reduces the activity of the melt thereby hindering volatilization phenomena and increasing liquid aluminum metal yields as shown in figure 5 calculated using FactSage.

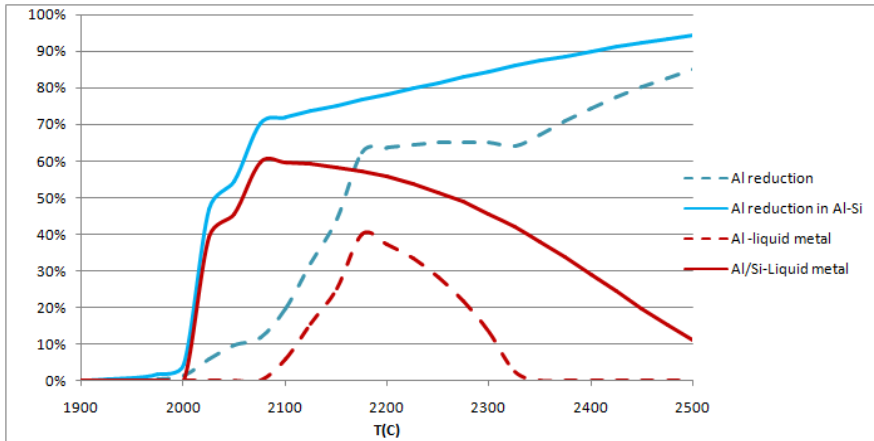


Figure 5: Prediction of aluminium overall reduction rate and aluminium liquid metal recovery rates for the system  $2 Al_2O_3 + 1 SiO_2 + 8 C$  (solid lines) and the system  $Al_2O_3 + 3 C$  (dashed lines).

Experiments were conducted in laboratory EAF in IME at RWTH Aachen utilizing as feed material pellets from technical grade alumina and silica combined with ca. 7% corn starch as binder and lignite coke or wood charcoal as reducing agent. The experiments took place in carbon crucible which was filled with feed pellets and heated for approximately 1 hour to achieve the full melting of the charge. Optimum results were achieved for a feed molar ratio of Si to Al of 0.26, as shown from the chemical analysis of the metal products received through different experiments (table 2). In all cases shown the crucible was removed from the furnace below a temperature of 1000°C and cast in a mould, resulting in Al-Si block shown in Figure 7.

Table 2: Chemical analysis of obtained Al - Si samples from co-reduction EAF trials in Aachen, measured by Optical Emission Spectrometry and C and O<sub>2</sub> Analysis

Identification Number	Al wt. %	Si wt. %	Fe wt. %	Mn wt. %	Ti wt. %	O <sub>2</sub> wt. %	C wt. %
Si/Al 0.26 A	72.53	25.58	1.62	0.028	0.032	0.03	0.06
Si/Al 0.26 B	71.37	25.95	2.32	0.034	0.032	0.06	0.34
Si/Al 0.35 A	68.85	30.79	0.11	0.017	0.042	0.43	0.11
Si/Al 0.35 B	61.79	>33.60	0.21	0.029	0.051	0.07	0.57
Si/Al 0.35 C	59.87	>33.60	0.26	0.030	0.050	0.03	0.27

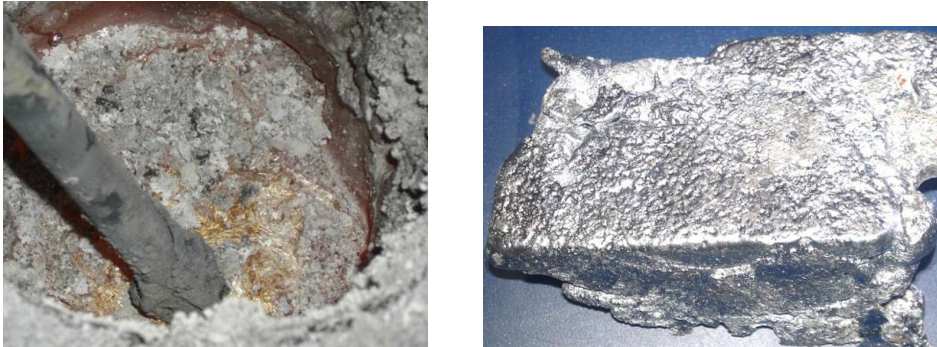


Figure 6 - Left: Visible aluminium melting “skin” during solidification process of the melt, Right: Picture of the casted carbothermally produced Al-Si alloy.

## Conclusions

The ENEXAL project has researched and developed three new technologies which have a direct potential for application in the primary aluminum production industry, greatly improving its sustainability.

The red mud process can remove completely the bauxite residues of the Bayer process for alumina production in a zero waste process which yields commercially valuable products. The process is ready for pilot scale industrial application, which will take place in the ALUMINIUM SA, plant in Greece.

The gaseous aluminum production is an innovative approach in producing a one-stage process for replacing the energy intensive Hall-Herlout electrolytic process. However the process requires further development until it can be considered for pilot scale industrial application.

Finally the Al-Si direct production represents an interesting alternative, for producing directly a commercial master alloy with an industrially mature technology (EAF), which is expected to have a significantly lower energy and carbon footprint than the currently established process for producing separately metallic Al and Si.

## Acknowledgements

The research leading to these results has received funding from the European Union Seventh Framework Programme ([FP7/2007-2013]) under grant agreement n° ENER/FP7/249710/ENEXAL ([www.labmet.ntua.gr/ENEXAL](http://www.labmet.ntua.gr/ENEXAL))

## References

- [1] Balomenos E. and Panias D., Iron Recovery and Production of High added Value Products from the Metallurgical By-products of Primary Aluminum and Ferronickel Industries, 3rd International Slag Valorization Symposium - The transition to sustainable materials management, Leuven, Belgium (2013)
- [2] Balomenos E., Panias D., Paspaliaris I., Theoretical Investigation of the Volatilization Phenomena Occurring in the Carbothermic Reduction of Alumina, World of Metallurgy – ERZMETALL 64(6):312-320 (2011).

## NANOCRYSTALLINE NiFe<sub>2</sub>O<sub>4</sub> SYNTHESIZED BY MODIFIED PRECIPITATION METHOD

A. Ćosović<sup>1</sup>, V. Ćosović<sup>2</sup>, Lj. Balanović<sup>3</sup>, D. Živković<sup>3</sup>, T. Žák<sup>4</sup>, N. Talijan<sup>2</sup>

<sup>1</sup> Institute for Technology of Nuclear and Other Mineral Raw Materials,  
Franseska ulica 86, 11000 Belgrade, Serbia

<sup>2</sup> Institute of Chemistry, Technology and Metallurgy, University of Belgrade,  
Njegoševa 12, 11000 Belgrade, Serbia

<sup>3</sup> Technical Faculty in Bor, University of Belgrade, Vojske Jugoslavije 12,  
19210 Bor, Serbia

<sup>4</sup> CEITEC IPM, Institute of Physics of Materials AS CR, v.v.i., Žitkova 22,  
CZ-616 62 Brno, Czech Republic

### Abstract

Nanosize Ni-ferrite was synthesized via precipitation process in which soluble starch is used as dispersing agent and Na<sub>2</sub>CO<sub>3</sub> as a precipitating agent. NiSO<sub>4</sub> was used as precursor for NiO, and Fe(NO<sub>3</sub>)<sub>3</sub> as precursor for Fe<sub>2</sub>O<sub>3</sub>. Considering that the magnetic properties of nanocrystalline NiFe<sub>2</sub>O<sub>4</sub> ferrites are directly related to their structure and phase composition, obtained reaction products were analyzed and discussed through structural, compositional and magnetic characterization. Formation of pure nanosized NiFe<sub>2</sub>O<sub>4</sub> phase has been confirmed by the subsequent X-Ray diffraction analysis (XRD), Fourier transform infrared spectroscopy (FTIR) and <sup>57</sup>Fe Mössbauer phase (MS) analyses. Average crystallite size of 21 nm was determined by XRD and material's nanocrystalline structure was additionally supported by results of field-emission and conventional scanning electron microscopy FE-SEM/SEM. The obtained room temperature magnetic hysteresis loop, measured on vibrating sample magnetometer (VSM), exhibits characteristic "S" shape with values of magnetic properties within expected range for this type of material.

*Keywords: nanocrystalline NiFe<sub>2</sub>O<sub>4</sub>, precipitation method, structural analysis, phase composition, magnetic properties*

### Introduction

As one of the most commonly used soft magnetic materials Ni-ferrites represent very important group of materials. Latest developments in nanotechnology have broadened their already wide range of application opening investigations for their use in hydrogen production, as catalysts, as photo reactive materials and for gas sensing [1-3]. Taking into consideration that functional properties of Ni-ferrites heavily depend on morphology, phase composition, crystal and particle sizes, applied synthesis method plays very significant role. Thus, despite the numerous synthesis techniques that have already been developed, investigation of alternative and innovative processing routes is still in progress.

In the present study, common method of synthesis of nanosized  $\text{NiFe}_2\text{O}_4$  has been modified by introduction of soluble starch. The studied synthesis route is essentially a precipitation process in which soluble starch is used as dispersing agent and sodium carbonate as a precipitating agent. Nickel sulfate was used as precursor for nickel oxide, and ferric nitrate as precursor for ferric oxide. Although, typically sodium hydroxide is used for precipitation, in the present study it was replaced with less aggressive sodium carbonate, often used for nickel removal and recovery processes. The obtained ferrite powder was analyzed and discussed through structural, compositional and magnetic characterization.

## **Experimental**

The studied nanocrystalline  $\text{NiFe}_2\text{O}_4$  powder was prepared using analytical grade inorganic salts  $\text{NiSO}_4 \cdot 6\text{H}_2\text{O}$  and  $\text{Fe}(\text{NO}_3)_3 \cdot 9\text{H}_2\text{O}$ , soluble starch  $(\text{C}_6\text{H}_{10}\text{O}_5)_n$  and anhydrous  $\text{Na}_2\text{CO}_3$ . Theoretically,  $\text{Na}_2\text{CO}_3$  and  $\text{NiSO}_4$  react in solution to give  $\text{NiCO}_3$  and/or  $\text{Ni}(\text{OH})_2$ . As  $\text{NiCO}_3$  precipitation occurs in competition with  $\text{Ni}(\text{OH})_2$  precipitation, solid phase is usually a mixed complex of nickel hydroxy-carbonates [4]. Since, when heated they both transform to  $\text{NiO}$ , it is not that important which phase will be dominant. pH range from 9 to 11 was maintained during synthesis since, according to literature [4,5], in this range maximal precipitation is achieved. Moreover, in reaction with  $\text{Fe}(\text{NO}_3)_3$  in solution,  $\text{Na}_2\text{CO}_3$  should give the same precipitate as  $\text{NaOH}$ , ferric hydroxide or hydrated ferric oxide. When heated, it transforms to  $\text{Fe}_2\text{O}_3$ , which in reaction with  $\text{NiO}$  at high temperature ( $>700^\circ\text{C}$ ) produces  $\text{NiFe}_2\text{O}_4$ .

The amounts of used chemicals were calculated according to possible reactions. In addition, soluble starch reacts with sodium in alkalization reaction [6] due to which certain amount of  $\text{Na}_2\text{CO}_3$  is lost. The lost amount of  $\text{Na}_2\text{CO}_3$  in this secondary reaction can be determined using the degree of substitution (DS) [6]. The DS is defined as the average number of substituents per anhydro glucose unit (AGU) and can have values between zero and three. In order to make process simpler, the scenario in which starch reacts with sodium up to level when  $\text{DS}=1$  was selected. Using chosen value for DS and number of moles of AGU units in added amount of starch, molar intake of  $\text{Na}_2\text{CO}_3$  was calculated.

In the first step of preparation process solution of starch in water was prepared which was further heated to boiling point, where it was kept for 15 min, and then cooled down to  $50\text{--}70^\circ\text{C}$ .  $\text{NiSO}_4 \cdot 6\text{H}_2\text{O}$  and  $\text{Fe}(\text{NO}_3)_3 \cdot 9\text{H}_2\text{O}$  were slowly added into the starch/water solution under stirring. Mixture was kept at  $50\text{--}70^\circ\text{C}$  and mixed constantly for next 10 minutes.  $\text{Na}_2\text{CO}_3$  was added to the mixture, which was then further stirred for another 10 minutes, and then dried at  $80^\circ\text{C}$ . In the final step, obtained solid composite was combusted and subsequently calcinated in muffle furnace at  $900^\circ\text{C}$ , for 5h. Prepared material was additionally rinsed few times with distilled water and centrifuged in order to remove any excess  $\text{Na}_2\text{CO}_3$ .

Microstructure and morphology of the obtained Ni-ferrite powder was analyzed by scanning electron microscopy (SEM) and field emission scanning electron microscopy (FE-SEM). Fourier transform infrared attenuated total reflection spectroscopy (FTIR-ATR) analysis was carried out at room temperature using Nicolet 380 spectrophotometer. Phase composition and structure were

analyzed by PANalytical X'Pert PRO MPD X-ray diffractometer (XRD) using  $\text{CoK}_\alpha$  radiation. Sample analysis, XRD pattern fitting and mean crystallite size  $d_{\text{XRD}}$  calculations were carried out using commercial software and database [7].  $^{57}\text{Fe}$  Mossbauer spectroscopy (MS) was used for additional phase composition analysis. MS spectra were taken in a standard transmission geometry at ambient temperature using  $^{57}\text{Co}(\text{Rh})$  source. The calibration was done against  $\alpha$ -iron foil data and for fitting and decomposition of the obtained spectra CONFIT [8] software package was used. Room temperature hysteresis loops were recorded using vibrating sample magnetometer (VSM) with magnetic field strength of  $1000 \text{ kAm}^{-1}$ .

## Results and Discussion

Morphology and structure of the obtained Ni-ferrite powder is illustrated by corresponding SEM and FE-SEM images given in Fig. 1.

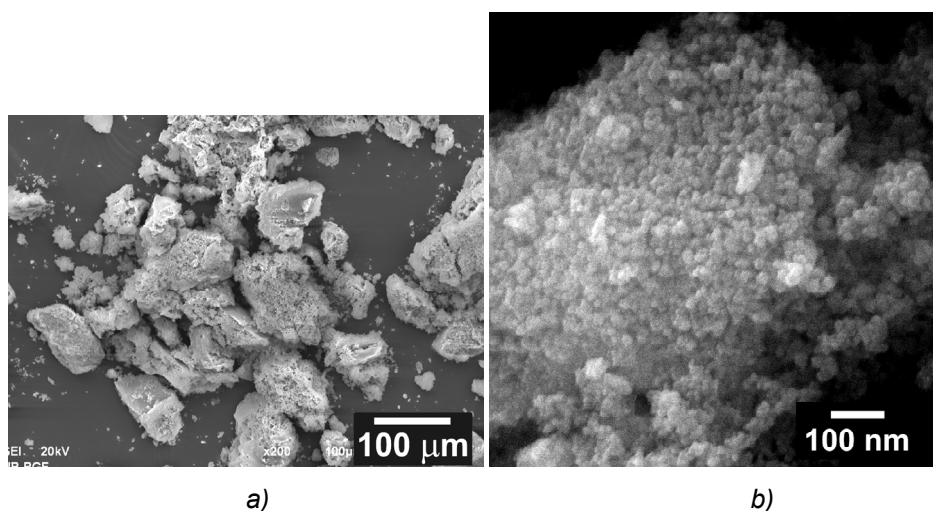


*Fig. 1 – Morphology of the prepared  $\text{NiFe}_2\text{O}_4$  powder:  
a) SEM image and b) FE-SEM image*

SEM image of the prepared Ni-ferrite powder (Fig. 1a) illustrates microstructure consisting of porous agglomerates of very fine particles. In addition, FE-SEM image (Fig. 1b) taken at higher magnification reveals fine-grained texture of the network structures with particles of about 20 nm.

The obtained FTIR spectrum of the studied ferrite material is given in Fig. 2.

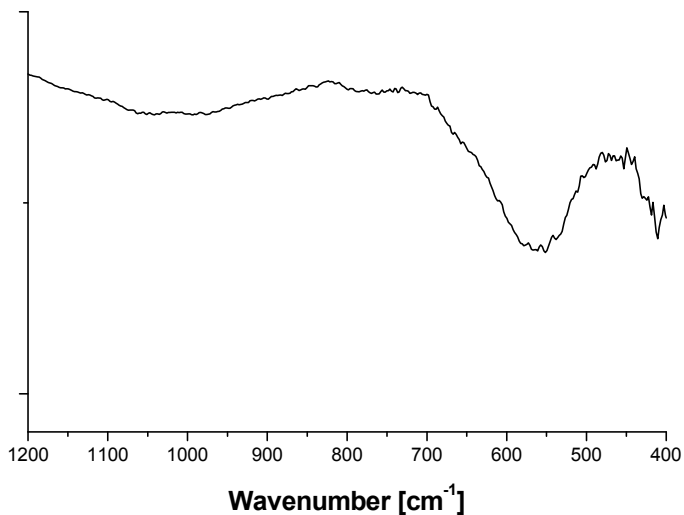


Fig. 2 – FTIR spectrum of the prepared Ni-ferrite powder

The presented FTIR spectrum (Fig. 2) demonstrates characteristic intrinsic stretching vibrations of the metal at the tetrahedral site ( $\text{Fe} \leftrightarrow \text{O}$ ) which are generally observed in the range of  $620\text{--}550\text{ cm}^{-1}$  as well as octahedral-metal stretching vibrations ( $\text{Ni} \leftrightarrow \text{O}$ ), that are generally observed in the range of  $450\text{--}385\text{ cm}^{-1}$  [9].

The obtained X-ray diffractogram of the prepared Ni-ferrite is shown in Fig.3.

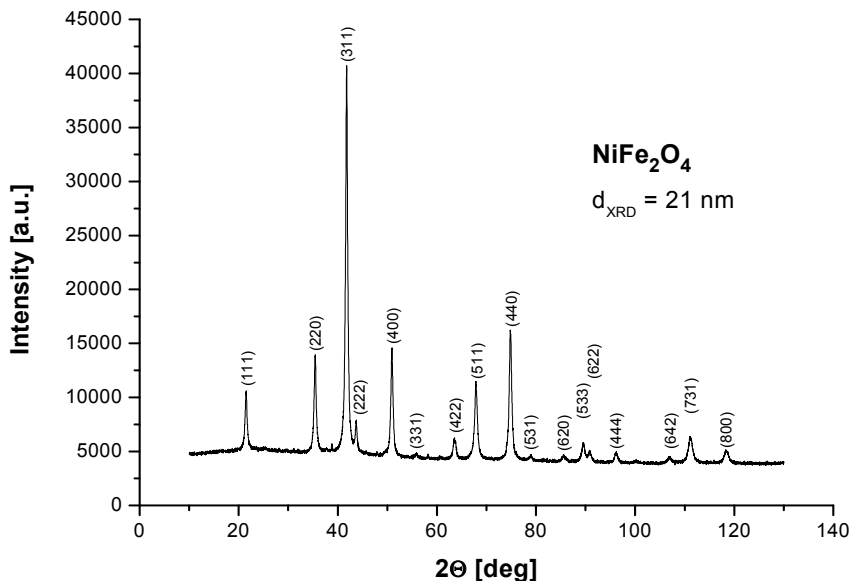


Fig. 3 – X-ray diffractogram of the studied Ni-ferrite powder

The presented X-ray diffraction diagram (Fig. 3) demonstrates monophasic composition of the obtained ferrite powder, consisting of pure  $\text{NiFe}_2\text{O}_4$  phase (ICSD #158834). Moreover, the calculated crystallite size of 21 nm confirms its nanocrystalline structure and additionally supports the results of FE-SEM analysis.

Further analysis of the prepared nanocrystalline Ni-ferrite powder was carried out by means of  $^{57}\text{Fe}$  Mössbauer spectroscopy and the obtained spectrum is given in Fig. 4.

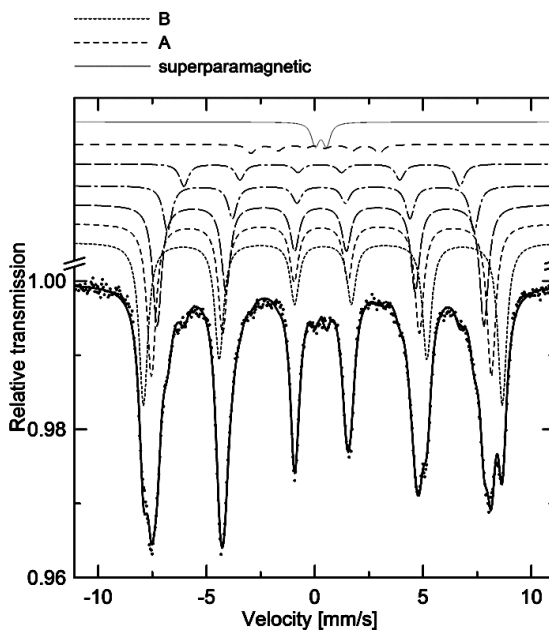


Fig. 4 – Mössbauer spectra of the prepared nanosize Ni-ferrite powder

The obtained results of MS analysis (Fig. 4) support the findings of the microstructural and XRD analysis as the presented spectrum is characteristic of Ni-ferrite material. Nonetheless, since MS technique is capable of identifying only iron containing phases, the obtained results can be discussed with having this in mind. Given that the values of Mössbauer parameters i.e. isomer shift (IS) and hyperfine field ( $B_{\text{hf}}$ ) were found to be in very good agreement with the values for  $\text{NiFe}_2\text{O}_4$  from the literature [10,11], corresponding spectral components were assigned to tetrahedral (A) and octahedral (B)  $\text{Fe}^{3+}$  atom sites.

The observed decrease in sextet intensity (Fig. 4) and rather small superparamagnetic doublet point to a distribution of crystallite sizes of  $\text{NiFe}_2\text{O}_4$  phase and can be ascribed to nanocrystalline structure of the material, as determined by XRD. The doublet in Mössbauer spectra can be associated with presence of superparamagnetic fraction of  $\text{NiFe}_2\text{O}_4$  phase, having size of the order of 10-13 nm or less [12,13]. In addition, with the decrease of the particle size the portion and influence of surface or interface atoms as well as atoms at some irregular positions increases [14].

Magnetic properties of the studied nanocrystalline Ni-ferrite powder are illustrated by the recorded room temperature hysteresis loop presented in Fig. 5.

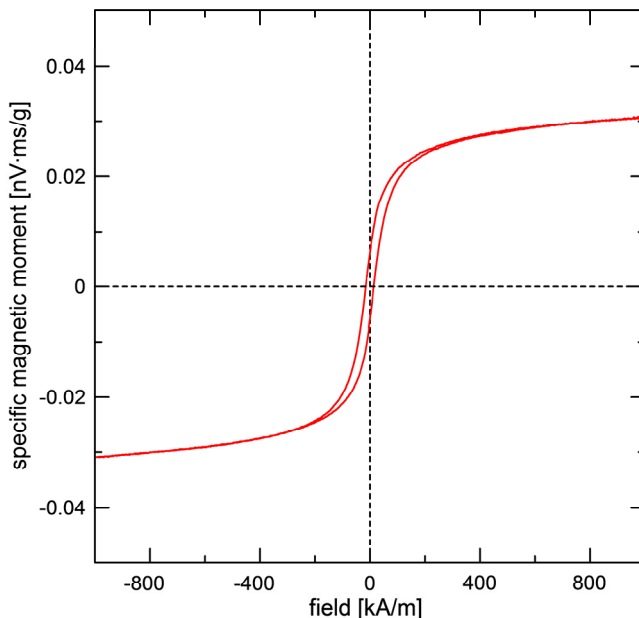


Fig. 5 – Room temperature hysteresis loop of the studied Ni-ferrite powder

Generally speaking, magnetic properties of nanocrystalline Ni-ferrites strongly depend on microstructure and morphology i.e. particle size and crystallinity. The obtained room temperature magnetic hysteresis loop exhibits characteristic “S” shape of the soft magnetic material. Measured values of magnetic properties e.g. coercivity of about  $10^1$  kA/m and the specific moment up to  $40 \text{ Am}^2/\text{kg}$  are comparable and within the expected range for this type of material.

## Conclusion

The use of soluble starch in precipitation synthesis route of nanosized  $\text{NiFe}_2\text{O}_4$  was investigated. The results of SEM/FE-SEM microstructural analysis of the prepared Ni-ferrite powders revealed porous agglomerates of very fine-grained network structures with particle size of about 20 nm. The FTIR spectrum exhibited characteristic bands that correspond to tetrahedral and octahedral sites in the ferrite structure. According to the obtained XRD results it was found that the obtained powder consist of pure  $\text{NiFe}_2\text{O}_4$  phase with mean calculated crystallite size of 21 nm.

The additional sample characterization by means of  $^{57}\text{Fe}$  Mössbauer spectroscopy supported the findings of the microstructural and XRD analysis as the studied material produced characteristic spectra of Ni-ferrite material. The observed decrease in sextet intensity and rather small superparamagnetic

component were ascribed to the nanocrystalline structure of the material and thus stronger influence of interfaces.

The obtained room temperature hysteresis loop and measured magnetic properties are comparable and within the expected range for this type of material.

### **Acknowledgement**

This work has been supported by the Ministry of Education, Science and Technological Development of the Republic of Serbia (Projects OI 172037 and TR 34023) and by grant Nr. GAP108/11/1350 of the Grant Agency of the Czech Republic. This work was realized in CEITEC – Central European Institute of Technology with research infrastructure supported by the project CZ.1.05/1.1.00/02.0068 financed from European Regional Development Fund.

### **References**

- [1] F. Fresno, T. Yoshida, N. Gokon, R. Fernandez-Saavedra, T. Kodama, *Int. J. Hydrogen Energ.*, 35 (2010) 8503.
- [2] K.-S. Lin, A.K. Adhikari, Z.-Y. Tsai, Y.-P. Chen, T.-T. Chien, H.-B. Tsai, *Catalysis Today*, 174 (2011) 88.
- [3] S.L. Darshane, S.S. Suryavanshi, I.S. Mulla, *Ceramics International*, 35(5) (2009) 1793.
- [4] D. Guillard, A.E. Lewis, *Ind. Eng. Chem. Res.*, 40 (2001) 5564.
- [5] J.W. Patterson, H.E. Allen, J.J. Scala, *Water Pollution Control Federation*, 49(12) (1977) 2397.
- [6] X'Pert High Score Plus 2.0a, PANalytical BV, Lelyweg 1, Almelo, the Netherlands. ICSD Database release 2010/2, FIZ Karlsruhe, Germany.
- [7] T. Žák, Y. Jirásková, *Surf. Interface Anal.*, 38 (2006) 710.
- [8] M. Santi, M. Chivaalrat, B. Banjong, S. Supapan, *Scripta Materialia*, 56 (2007) 797.
- [9] V. Šepelák, D. Baabe, D. Mienert, D. Schultze, F. Krumeich, F.J. Litterst, K.D. Becker, *J. Magn. Magn. Mater.*, 257(2-3) (2003) 377.
- [10] J. Jacob, M.A. Khadar, *J. Appl. Phys.* 107 (2010) 114310-1.
- [11] H. Yang, L. Zhao, X. Yang, L. Shen, L. Yu, W. Sun, Y. Yan, W. Wang, S. Feng, *J. Magn. Magn. Mater.*, 271(2-3) (2004) 230.
- [12] T. Komatsu, N. Soga, *J. Appl. Phys.*, 51(1) (1980) 601.
- [13] J.-M. Grenèche, M. Migliorini, in *Mössbauer Spectroscopy in Materials Science*, Eds. (M. Migliorini, D. Petridis), Kluwer, Dordrecht, 1999.

## ELECTROLYTIC DESULFURIZATION OF LEAD-ACID BATTERY PASTES

B. Yolcu<sup>a,\*</sup>, Y. Kılıç<sup>a</sup>, G. Kartal<sup>a</sup>, S. Yılmaz<sup>b</sup>, S. Timur<sup>a,\*\*</sup>

<sup>a</sup> *Istanbul Technical University, Metallurgical and Materials Department, Istanbul, TURKEY*

<sup>b</sup> *Inci Aku San. Tic. A.S. (R&D Centre), Manisa, TURKEY*

### Abstract

Disposal of lead-acid batteries is strictly restricted due to their hazardous substances; hence, so far several recycling processes have been adapted to recover such harmful and valuable components. The electrolyte of used lead-acid batteries (ULAB) is generally discarded after neutralization process. During recycling of ULAB, many problematic issues take place by reason of high sulfate contents. However, desulfurization is not always preferred owing to waste treatment problems generated by utilized chemicals. The novelty of our approach is to the elimination of chemical usage by suggesting an environmentally friendly alternative process in which regenerating of waste electrolyte is also possible. Basically, in this study both desulfurization and acid regeneration processes are accomplished in the same stage. The effects of electrolyte temperature, applied current density and acid concentration were examined to idealize the condition of developed electrolysis.

*Keywords: used lead-acid batteries (ULAB), desulfurization of battery paste, electrolytic desulfurization*

### Introduction

Approximately 80% of the lead produced in worldwide is currently used in lead-acid battery manufacture [1]. The recycling of used lead-acid batteries (ULAB) is apparently essential by taking the huge amounts of lead usage in batteries and toxic effects of lead into account.

There is an increasing research trends focusing on the recycling of batteries, and correspondingly numerous new techniques have been adapted for the reprocessing of ULAB. These studies can be categorized into two separate classes: pyrometallurgical and hydrometallurgical based methods. The hydrometallurgical approach was developed to figure out a solution in the environmental concerns related to lead smelting in pyrometallurgical processes. However, both methodologies have major problems on their own, owing to the characteristic properties of lead, such as its volatility and low solubility [2,3]

In pyrometallurgical processes, the main idea is to feed the battery paste into smelting furnace. In some processes desulfurization is preferred whereas in some of them direct reduction is applied. If paste is fed into furnace without desulfurization, many environmental problems are faced due to high sulfate content. Although melting point of lead is relatively low (327°C), furnace must be

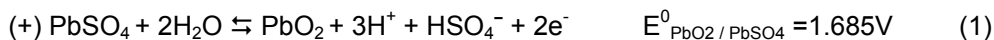
operated at much higher temperatures, over 1000°C, in order to reduce PbSO<sub>4</sub> [1,2,4]. Consequently, pyrometallurgical battery recycling processes encounter many issues; for instance, high operating costs caused by high furnace temperatures and formations of non- disposable Fe slag used in reduction of SO<sub>4</sub> as well as generation of fume carrying lead oxides and SO<sub>2</sub> gases [2,4].

Hydrometallurgical based techniques have been recently built up to get over mentioned environmental issues experienced in the pyrometallurgical route. In hydrometallurgical way, desulfurization is carried out during leaching process. However, solutions such as HBF<sub>4</sub>, HCl+NaCl, H<sub>2</sub>SiF<sub>6</sub> must be used for leaching as a result of low solubility of lead [4,5,6]. Typical desulfurization chemicals are given in Table.1, apparently hazardous wastes generated.

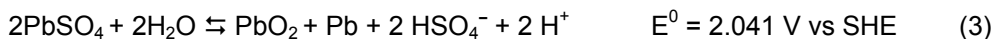
Table.1: Desulfurization chemicals

Desulfurization Chemical	Converted Into	
Na <sub>2</sub> CO <sub>3</sub> , NaOH	Na <sub>2</sub> SO <sub>4</sub>	[6,7,8]
K <sub>2</sub> CO <sub>3</sub>	K <sub>2</sub> SO <sub>4</sub>	
Ca(OH) <sub>2</sub>	CaSO <sub>4</sub>	4

The aim of this study is to not only minimize SO<sub>2</sub> emissions, but also to diminish waste of the battery recycling process near zero. To achieve the mentioned goals, the desulfurization takes place according to the charge principle of lead-acid batteries based on the reactions in Eq. 1-3.



+



## Experimental

### Experimental setup and equipment

Raw materials, such as waste battery paste, lead oxide and meshes were provided from different local companies. Chemical composition of waste battery paste is given in table.2:

Table. 2: Chemical composition of waste battery paste

Content	PbSO <sub>4</sub> [%wt.]	PbO [%wt.]	PbO <sub>2</sub> [%wt.]
Waste Battery Paste	48,36	29,5	23

The schematic depiction of the electrochemical cell made of plexiglass and consisted of two chambers is illustrated in fig.1. The two chambers of the cell were separated by a membrane with the active area of 189cm<sup>2</sup>. MA-3475 (manufactured by IONAC), anion exchange membrane was utilized. During electrolysis, the electrolyte was circulated separately in both chambers by using acid circulation pumps. Cathodic and anodic polarizations were measured versus Hg/HgCl<sub>2</sub> saturated calomel electrodes (E<sup>0</sup>=241mV) and collected by data acquisition system; Coda Locomotive Data Collector.

### Experimental procedures

Experiments were conducted in the electrolysis cell illustrated in Fig.1. Two main sets of experiments were carried out: the first one was the investigation of optimum conditions for sulfate removal and the next step was the examination of acid regeneration conditions in the light of previous ideal outputs.

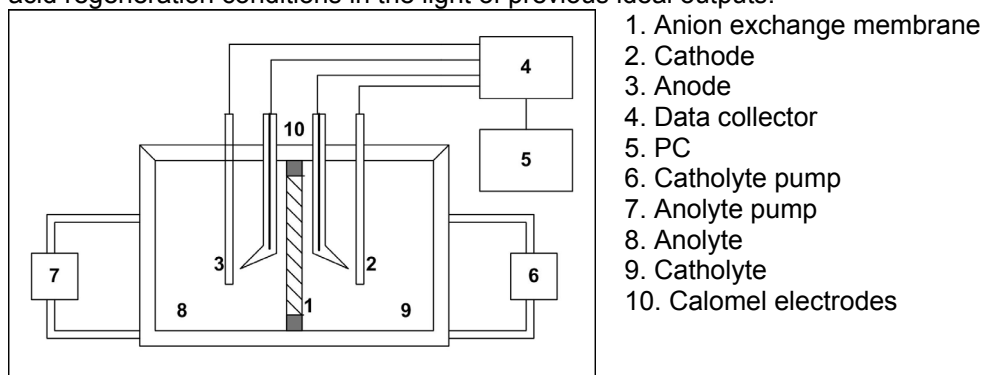


Figure.1: Schematic depiction of the electrochemical cell

The designed process followed in this study is demonstrated in Fig.2 as a flow chart.

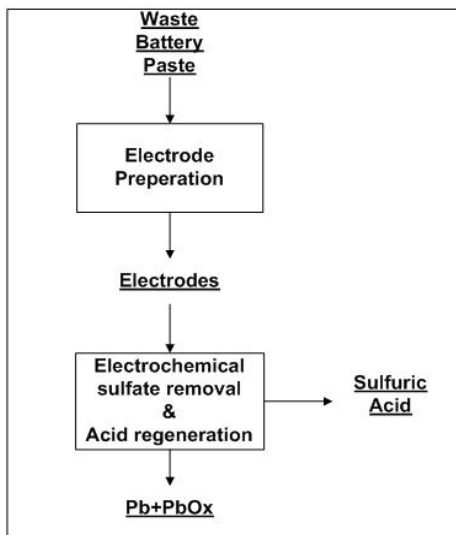


Figure. 2: Flow chart of the process

In the first stage (electrolytic desulfurization), electrodes (anode & cathode) were prepared by pressing the waste battery paste onto the lead meshes with the additions of 5-30wt.% lead oxide, 0,1-2wt.% fiber glass, 10-40wt.% deionised water. At the end of each experiment, electrodes were withdrawn from the electrolyte under polarization to prevent re-sulfurization, and then immediately soaked into diluted caustic solution to remove residual electrolyte.

#### Sulfate removal experiments

The same electrochemical cell was utilized for the sulfate removal experiments, but without the usage of membrane. During this serial investigation, electrolyte temperature, current density and electrolysis time as well as acid concentration parameters were examined in detail.

#### Electrochemical acid regeneration experiments

Waste electrolyte is illustrated with solutions prepared using MERCK acid (purity=95%). Solutions were poured into the anolyte and catholyte chambers; having equal volume of 2400 ml. The acid concentration in the anolyte compartment was held constant, 4g/L  $H_2SO_4$ ; whereas, acid concentrations in the catholyte compartment was the variable parameter in this set of experiments.

The distance between anode-cathode was increased to 5 cm due to the practical obstacles. The schematic view of the ion transfer between chambers and electrode reactions is simulated in fig.3.

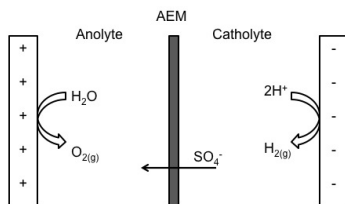


Figure.3: Schematic view of ion transfers

## Results and Discussion

### Electrochemical desulfurization

#### Effect of current density on sulfate removal

According to Faraday's law the amount of substance converted per unit time increases with increasing current. In other words, the higher current density is applied, the faster electrochemical reaction occurs. As expected, the removal of sulfate was completing in shorter periods at higher current densities (fig.4).

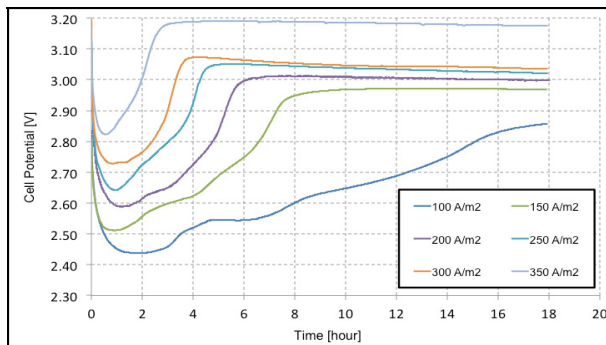


Figure.4: Variations of cell potential as a function of electrolysis time at different current density

[Room temperature, 2.5cm anode-cathode distance, 0.5 M  $H_2SO_4$ , 18 hours]

However, the residual sulfate in paste after desulfurization did not meet theoretical expectations as given in table.3. Even though at high current densities such as 300-350A/m<sup>2</sup>, the transformation was completed in much shorter time, residual sulfate gave the highest value of all. The reason of this could be the remaining electrolyte on the deformed surface formed by hydrogen gas evolution. Most probably electrolyte could not be cleaned completely on the damaged electrode surface and hence remaining electrolyte led to re-sulfuration.

Another negative side of working at high current densities could be the extra costs attributable to the energy losses caused by ohmic resistances and hydrogen evolution. Based on the obtained data (table.3 and fig.4) it could be deduced that the current density of 250A/m<sup>2</sup> gave the most desired results.

Table 3: Variation of residual sulfate with respect to electrolysis parameters

Residual Sulfate [% wt.]	Parameter	Experiment
0.35	100	
0.33	150	
0.22	200	Current Density [A/m <sup>2</sup> ]
0.3	250	[0.5 M H <sub>2</sub> SO <sub>4</sub> , 25°C, 18 hours, 2.5 cm anode-cathode distance]
0.37	300	
0.57	350	
0.35	0.1	
0.55	0.3	Acid Concentration [M]
0.32	0.5	[0.5 M H <sub>2</sub> SO <sub>4</sub> , 25°C, 18 hours, 2.5 cm anode-cathode distance]
0.46	1	
0.72	2	
0.89	3	
0.3	25	Electrolyte Temperature [°C]
0.38	40	[0.5 M H <sub>2</sub> SO <sub>4</sub> , 25°C, 18 hours, 2.5 cm anode-cathode distance]
0.12	55	
0.9	5	Electrolysis Time [hours]
0.79	6	[0.5 M H <sub>2</sub> SO <sub>4</sub> , 25°C, 18 hours, 2.5 cm anode-cathode distance]
0.3	8	
0.3	18	

#### Effect of acid concentration on sulfate removal

Electrolyte is of important factor determining the ohmic resistance of the electrochemical systems. Although 3M of sulfuric acid concentration could be considered as an ideal value for the conductivity of the electrolyte, the measured residual sulfate value was relatively bigger which was likely due to the fast re-sulfurization of the paste triggered at the high ion concentration.

The effect of acid concentration on sulfate removal is almost neglected (see table 3), and this consequence ensures that acid regeneration is possible without having an adverse influence on sulfate removal.

#### Effect of electrolyte temperature on sulfate removal

It was found that the chosen electrolyte temperature did not have a major effect on sulfate removal (table 3). According to Nernst equation; 1°C increase in temperature, results in 0.059V potential drops [ [HYPERLINK \l "Bag06" 10](#) ] which provides a significant advantage on process cost. However, considering an additional expenditure of heating cell, the benefit of higher temperature working is negligible. Therefore, operating at room temperature was decided to be an ideal for desulfurization.

#### Effect of time on sulfate removal

It is essential to determine the exact duration required to the completion of reactions in a continuous system. For this reason, the effect of process time on sulfate removal was investigated systematically. At idealized conditions, the all reaction terminated in 8 hours as seen in fig. 5. Plus, the residual sulfate in paste did not change after 8 hours of electrolysis (see Table 3). For that reason, it could be concluded that 8 hours was enough to complete all sulfate removal reactions.

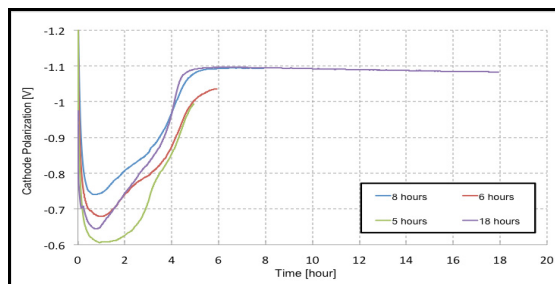


Figure.5: Variation of cell potential versus electrolysis time

[25°C, 2.5cm anode-cathode distance, 0.5 M H<sub>2</sub>SO<sub>4</sub>, 250A/m<sup>2</sup> current density]

### Electrochemical acid regeneration

Effects of catholyte concentration on acid regeneration efficiency were examined in laboratory scale.

The following formula used in the calculation of acid regeneration efficiency (%E):

$$\% E = \frac{\text{Final anolyte concentration } (C_2) - \text{Initial anolyte concentration } (C_1)}{\text{Initial catholyte concentration } (C_1)}$$

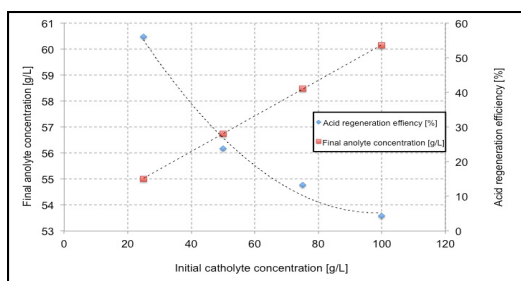


Figure.6: Effect of initial catholyte concentration on acid regeneration

[Initial anolyte concentration: 4g/L H<sub>2</sub>SO<sub>4</sub>, 25°C, 5cm anode-cathode distance, 24 hours]

As seen in fig.6, the final anolyte concentration increases in a significant way with increasing catholyte concentration. However in battery recycling process catholyte concentration is not a controllable parameter due to the close circulation of battery electrolyte. Still, waste battery electrolyte is known to be around 50g/L, and the experimental results with 50g/L H<sub>2</sub>SO<sub>4</sub> catholyte concentration revealed that %56 of waste battery electrolyte could be regenerated in 24 hours (see fig.6) without a noticeable dependence of the variations in the initial acid concentration of waste electrolyte.

### Summary

Both sulfate removal of waste battery pastes and regeneration of waste electrolyte could be achievable at the same stage with in this developed

electrochemical system. Regeneration of waste electrolyte and paste desulfurization without using any chemical were the virtues of this technology. Under optimum parameters (2.5 cm anode-cathode distances, 250A/m<sup>2</sup>, 25°C, 8 hours) sulfate content in the battery paste was able to be eliminated up to %0.9. Furthermore, more than 50% of waste electrolyte was regenerated in 24 hours.

### **Acknowledgements**

"Republic of Turkey Ministry of Science, Industry and Technology" and "Inci Akü" are gratefully acknowledged for funding the project Zero Waste Principled Recycling Process for Scrap Batteries (STZ.00829-2011\_1).

### **References**

- [1] M.A. Kreuzsch et al., "Technological improvements in automotive battery recycling," *Resources, Conservation and Recycling*, vol. 52, pp. 368-380, 2007.
- [2] M. Ş. Sönmez and R.V. Kumar, "Leaching of waste battery paste components. Part 1: Lead citrate synthesis from PbO and PbO<sub>2</sub>," *Hydrometallurgy*, vol. 95, pp. 53-60, 2009.
- [3] Z. Vaysgant, A. Morachevsky, A. Demidov, and E. Klebanov, "A low-temperature technique for recycling lead/acid battery scrap without wastes and with improved environmental control ," *Journal of Power Sources*, vol. 53, pp. 303-306, 1995.
- [4] C. Frias, M. Garcia, and G. Diaz, "New Clean Technologies to Improve Lead-Acid Battery Recycling," in *Lead-Zinc 2000*, 2000, pp. 791-801.
- [5] M. V. Ginatta, "Method for the Electrolytic Production of Lead," 4,451,340, 1983.
- [6] R. D. Prengaman and H. Mcdonald, "RSR's Full Scale Plant to Electrowin Lead from Battery Scrap," in *Lead-Zinc '90*, 1990, pp. 1045-1056.
- [7] N.K. Lyakov, D.A. Atanasova, V.S. Vassilev, and G.A. Haralampiev, "Desulphurization of damped battery paste by sodium carbonate and sodium hydroxide," *Journal of Power Sources*, vol. 171, pp. 960-965, 2007.
- [8] Ramus K. and P. Hawkins, "Lead/Acid Battery Recycling and the New ISASMELT Process," 1992.
- [9] V. P. Yanakieva, G. A. Haralampiev, and N. K. Lyakov, "Desulphurization of the Damped Lead Battery Paste with Potassium Carbonate," *Journal of Power Sources*, vol. 85, pp. 178-180.
- [10] V.S. Bagotsky, *Fundamentals of Electrochemistry*. Moscow: John Wiley & Sons, Inc., 2006, pp. 8,15-18, 41-42, 353.

## PRINCIPAL PHOTOELASTIC STRESS DIRECTIONS AND ISOCLINIC FRINGES

J. M. Vázquez-Rodríguez<sup>1</sup>; P. J. Herrera-Franco<sup>2</sup>, P. I. González-Chi<sup>2</sup>,  
A.del C. Lizardo-Pérez<sup>1</sup>, S.G. Gómez-Jiménez<sup>1</sup>

<sup>1</sup> *Universidad Juárez Autónoma de Tabasco. División Académica de Ingeniería y Arquitectura.*

<sup>2</sup> *Centro de Investigación Científica de Yucatán, A.C. Unidad de Materiales*

### Abstract

The interpretation of the single-fiber pull-out test still has a common problem: the complex stress state at the plane in which the fiber exits the resin block. A photoelastic technique was used to locate the principal stresses by tracing out the isoclinic fringe pattern of this geometry.

The two-dimensional in-plane problem for stress reconstruction from data on principal directions is somewhat similar to photoelasticity, where the concept of stress trajectories comes from. Photoelasticity techniques for the separation of principal stresses are based on a relatively dense set of uniformly distributed data, which allows one to determine the stress field with high accuracy.

Images of the isoclinic fringes from 0° to 90° showed that the load is symmetrically distributed in the pull-out specimen. The principal stress directions  $\sigma_1$  and  $\sigma_2$  converge at the plane in which the maximum shear stress is located close to the edge of the resin block.

*Keywords: Photoelasticity, isoclinic fringe, principal stress, pull-out.*

### Introduction

The single-fiber pull-out test had been employed to model the failure of fiber-reinforced composite and many experimental and mathematical interpretations had been presented and discussed in the literature [1-6]. Also, a thorough description of the pull-out experiment has been presented via the critical release rate of strain energy for crack initiation and crack propagation. However, the interpretation of the single-fiber pull-out test still has a common problem; the complex stress state at the plane in which the fiber exits the resin block [5]. This stress state can be analyzed with a photoelastic technique.

Photoelasticity is an optical method for stress analysis in materials which present birefringence when they are deformed [7]. These materials can resolve an incident polarized normal light beam into two orthogonal components. These orthogonal components could coincide with the direction of the principal stresses acting over the sample. A photoelastic sample, placed between two crossed polarizers and litten with white light, will generate two photoelastic responses. A dark fringe called isoclinic fringe and a superposed colored lobes corresponding to the isochromatic pattern.

An isoclinic fringe appears when the plane of the incident polarized light coincides with a stress direction within the sample. The second stress direction is then located in the perpendicular plane to the incident polarized light. Therefore, any isoclinic fringe is a set of planes in which each stress has a parallel direction, keeping an orthogonal direction among both.

A loaded pull-out specimen generates around the embedded fiber a full set of isoclinic fringes. Nevertheless, to locate each isoclinic fringe is necessary to rotate simultaneously both polarizers from  $0^\circ$  to  $90^\circ$  maintaining them crossed. The rotation angle  $\theta$  is known as the isoclinic parameter or simply the parameter. For each isoclinic parameter an isoclinic fringe is located and the angle of the corresponding stress direction coincides with the isoclinic parameter [7-9].

Since the two principal stresses at any plane of a two-dimensional stress system are mutually perpendicular, a pattern of stress trajectories will consist of two families of orthogonal curves. One of these families indicates the direction of the  $\sigma_1$  principal stresses (algebraically greater) and the other the  $\sigma_2$  principal stresses.

Analyzing the propagation of light through a plane polariscope sketched at figure 1, it is convenient to assume that the electric vector  $\mathbf{E}$ , incident on the model, splits in to two orthogonally polarized components  $\mathbf{E}_x$  and  $\mathbf{E}_y$ . The expression for the light emerging from the second polarizer of a plane polariscope (figure 1), is given by [10]:

$$I = E_x^2 \cos^2 \frac{R}{2} + (E_x \cos 2\alpha + E_y \sin 2\alpha)^2 \sin^2 \frac{R}{2} \quad (1)$$

where:

$R$  = relative retardation (stress-induced) in radians at the stressed model.

$\alpha$  = angle between the  $x$  direction and first principal stress direction at the model.

$\beta$  = angle between the  $x$  direction and the plane of polarization of the analyzer.

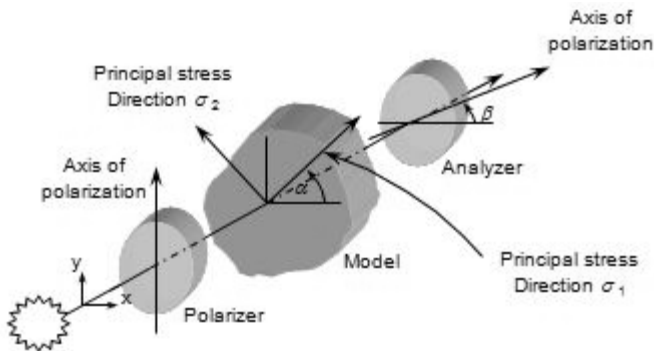


Figure 1 Plane polarization sketch for a stressed model.

The plane polariscope can be specially arranged to have the polarizer and the analyzer with their axes crossed. This yields to the basic plane dark-field polariscope. With  $\beta = 0$ , the expression for the light emerging from a plane polariscope transforms to:

$$I = E^2 \sin^2 2\alpha \sin^2 \frac{R}{2} \quad (2)$$

According to Eq. (2), the intensity of the emerging light from the dark-field of a plane polariscope is a function of the principal stress directions  $\alpha$  and the relative retardation  $R$  induced by the stress in the model. There are two conditions for the intensity of the emerging light to be  $I = 0$ ; for the first case:

$$\alpha = 0, \pi/2, \pi, 3\pi/2, \dots \text{ radians}$$

The polarizing axes of the polariscope coincide with the directions of the two in plane principal stress in the model. For any orientation of the model, the planes at which  $I = 0$ , lie along a continuous black curve (extinction curve) called isoclinic fringe. Elsewhere,  $I$  is not equal to zero and the isochromatic pattern is present. The second condition for the intensity of the emerging light to be  $I = 0$  is:

$$R/2 = 0, \pi, \dots \text{ radians} \quad \text{or} \quad R = 0, 2\pi, \dots N(2\pi)$$

Where  $N$  is an integer, which take values from 0 to  $\infty$ .  $N$  is known as isochromatic order [9]. Similarly to the isoclinic fringes, these planes lie along a continuous black curve (extinction curve) of principal stress difference, called isochromatic fringe.

## Materials

The thermoplastic polyester fiber used was from KIRSCHBAUM with a diameter of 1.3 mm. The Pull-out specimens were manufactured using a bisphenol-A epoxy resin DER 331 from DOW Chemical. The crosslinking agent was an aliphatic diamine ANCAMINE 1784 from Air Products and Chemicals Inc. The mol ratio between the epoxy resin and the curing agent was of 0.6 (g mol epoxy resin/g mol aliphatic diamine) [8].

## Experimental

The pull-out specimen had the following dimensions: the resin block was 4 cm wide, 6 cm long and 1.1 cm thick. The fiber was longitudinally embedded at the center of the block, and the embedded length was 4 cm. The free length of the fiber was 3 cm long. The curing process took place in eight days under controlled humidity conditions at room temperature. No contraction or residual stresses were found after curing.

The polarization instrument was arranged to conform a plane polariscope, with two polarization elements crossed  $90^\circ$  and a white light source. The load was transmitted to the specimen using a load frame with a cantilever system. The photoelastic method of stress trajectory reconstitution was as follows. During a

photoelastic experiment, the samples were subjected to a constant tension load of 367.9 N between two crossed polarizers which can rotate simultaneously to permit the isochromatic fringes to be observed within the samples. A  $5^\circ$  rotation of the polarizers was chosen and the specimen was tested from  $0^\circ$  to  $90^\circ$ . The images for each rotation angle (isoclinic parameter  $\theta$ ) were recorded using a camera, and each isoclinic fringe was then traced plane by plane from the images obtained. Finally, the set of stress trajectories consisting of two stress families were drawn using the method described previously.

### Results and discussion

The images for the isoclinic parameter of  $0^\circ$ ,  $20^\circ$  and  $45^\circ$  are shown at figure 2. The trajectory for an isoclinic fringe was individually traced out from the isochromatic pattern (figure 3a). Then along each observed isoclinic fringe (i.e.  $0^\circ$  isoclinic parameter figure 3a), several planes of same principal stress directions were drawn and finally linked (Figure 3b).

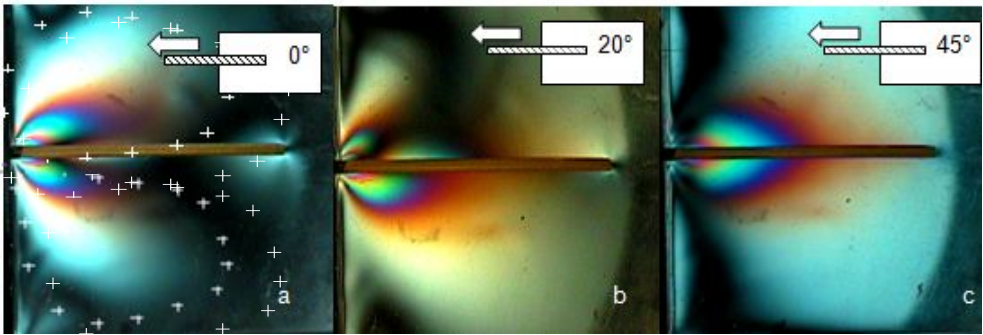


Figure 2 Photoelastic experiment showing the isoclinic fringes for the parameters a)  $\theta = 0^\circ$ , b)  $\theta = 20^\circ$  and c)  $\theta = 45^\circ$ .

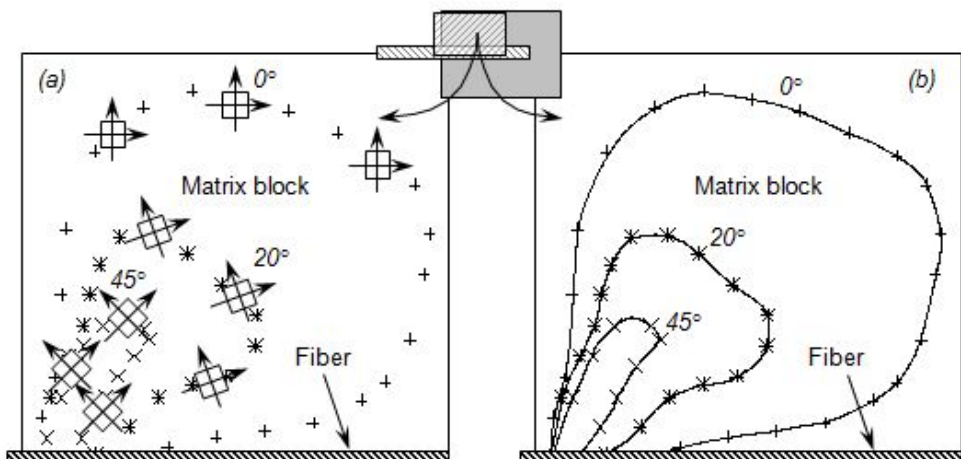


Figure 3 Isoclinic planes for the parameter  $\theta = 0^\circ$ ,  $20^\circ$  and  $45^\circ$

When the polarizers are rotated from  $0^\circ$  to  $90^\circ$ , symmetrical isoclinic fringes are obtained above and below the fiber embedded in the pull-out specimen. Taken the fiber as the symmetric axis, for a rotation from  $0^\circ$  to  $45^\circ$  the isoclinic fringes appear at the upper part of the pull-out specimen. For the polarizers rotation from  $45^\circ$  to  $90^\circ$ , the isoclinic fringes will appear at the lower part of the specimen.

The pairs of isoclinic fringe images from figure 4 (i.e. Isoclinic fringe for  $10^\circ$  and  $80^\circ$ ) show that the load is symmetrically distributed in the pull-out specimen. Figure 5 shows the set of isoclinic fringes for a pull-out specimen.

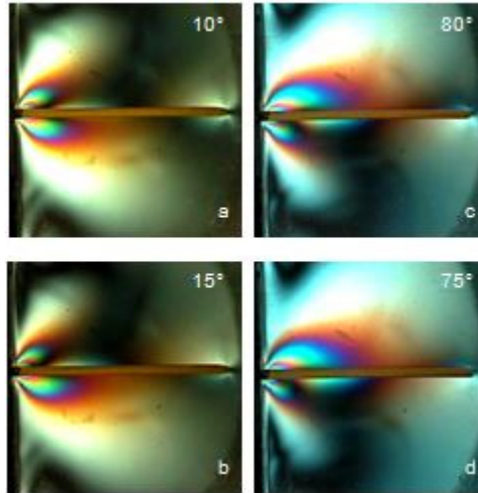


Figure 4 Photoelastic experiment showing the isoclinic images for a)  $10^\circ$ , b)  $15^\circ$ , c)  $80^\circ$  and d)  $75^\circ$ .

The principal stress trajectories are lines whose direction corresponds to the direction of one of the principal stresses in a material subject to load [6]. However, these lines cannot be located experimentally but they certainly can be determined theoretically or by a set of isoclinic fringes from a photoelastic model. The set of stress trajectories correspond to the principal stress  $\sigma_1$  and in the perpendicular direction the orthogonal component the principal stress  $\sigma_2$ .

Figure 5 shows the upper part of the pull-out specimen in which the fiber is the axis of symmetry to the stress trajectories and to the applied load. The inspection of the stress directions at figure 5 shows that they converge at a plane perpendicular to the fiber in which the maximum shear stress is located as it was found in previous works [8, 9]. The stress directions extend from this common plane and are distributed to the whole body of the pull-out specimen from the fiber (axis of symmetry) to the block's border. The orthogonal directions of  $\sigma_1$  and  $\sigma_2$  cover the space between the border-lines defined by the edge of the fiber and the resin.

Principal stress  $\sigma_1$  will act with a small angle to the horizontal axis. It can be assumed that the components along the x axis will act in shear and the

components along the  $y$  axis in tension. The principal stress  $\sigma_1$  is algebraically bigger than  $\sigma_2$  so the shear component will be always the main stress acting in this point. As we move towards the fiber embedded tip the stress direction will align to the fiber and the point 1 will be on the interphase, then the stress  $\sigma_1$  will act as a pure shear stress between the fiber and the resin while the tension stress along the  $y$  axis will disappear. The failure mechanism related to the precedent stress system can be associated to yielding in a ductile interphase through mode II when the shear stress exceeds the shear strength of the interphase.

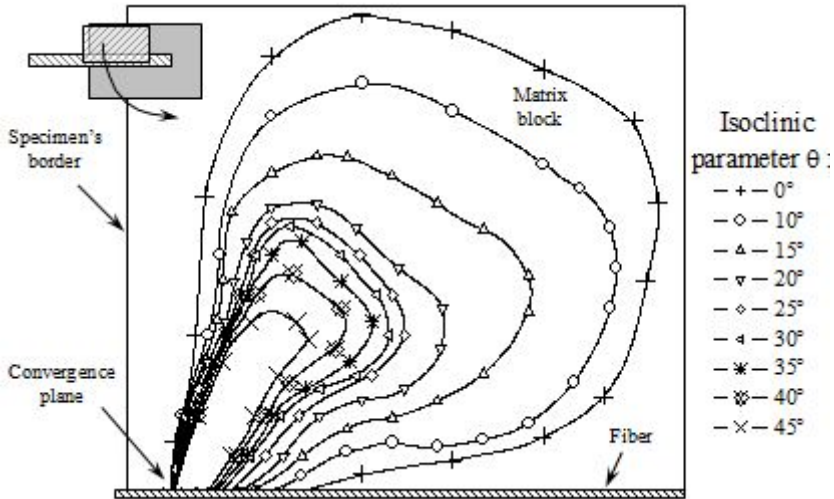


Figure 5 Set of isoclinic fringes for a pull-out specimen.

At the point located at the convergence plane; the stress system has mainly two opposite stress vectors on the  $y$  direction. One of the stresses corresponds to the principal stress  $\sigma_1$  acting on the resin block, the other one in the opposite direction is the stress corresponding to the fiber contraction.  $\sigma_1$  acts at  $90^\circ$  to the  $x$  axis so the load system is compound only by this principal stress which acts in a radial direction in a transversal plane to the fiber at the convergence plane. This transversal plane also coincides with the location of the maximum shear stress on the fiber matrix interphase.

From the convergence plane to the edge of the resin block there is a vague set of isoclinic fringes which leads to a distribution of principal stress directions which balances the principal stress directions located from the convergence plane towards the fiber tip. The vagueness of the isoclinic fringes means that the shear stresses  $\tau_{xy}$  vanish on all planes because the stresses at  $x$  and  $y$  directions are equal for all directions.

When the angle in which the principal stress  $\sigma_1$  acts is bigger than  $90^\circ$ , the load system will act in an area at the left of the convergence plane. This area covers from the convergence plane to the border of the resin block. In this area the directions of the principal stresses will be distributed in a similarly to the right of the convergence plane (embedded fiber area) but in a more restricted area. The

complex load system is then composed by the stress directions distributed from  $0^\circ$  to  $90^\circ$  and  $90^\circ$  to  $180^\circ$  at both sides of the convergence plane in which the direction of the principal stress  $\sigma_1$  converge and the maximum interfascial shear stress is located.

## **Conclusion**

The isoclinic fringes from  $0^\circ$  to  $90^\circ$  showed that the load is symmetrically distributed in the pull-out specimen where the fiber is the symmetric axis.

The isoclinic fringes for a pull-out specimen were used to locate the direction of the principal stresses acting in a pull-out specimen. The orthogonal directions  $\sigma_1$  and  $\sigma_2$  covers the space between the fiber surface and the edge of the resin block. They extend from a common plane on the fiber surface which coincides with the location of the maximum shear strength. The maximum shear strength is located at 2.5 fiber diameter times from the edge of resin block [8].

Analyzing the load system of the pull-out geometry, it is possible to make the following observations. The convergence plane is the result of the load system generated around a plane in which the maximum interfascial shear stress is located. The resultant of the load system in both sides the convergence plane generates a zero shear stress leading to areas with vague isoclinic fringes.

The failure mechanism in a pull-out specimen will begin at the plane in which the fiber emerges from the epoxy-resin block with a failure mode I. Close to this plane there is a stress concentration plane where the combined modes I and II will promote a failure along the fiber-resin interphase.

The plane, in which the stress directions converge, can be identified as a singular or isotropic plane where at least two isoclinic fringes of different parameters intersect. At this plane a maximum tension stress and maximum shear stress are acting at the same time generating a concentration plane. In this plane the resulting stress of the loading system becomes zero, which means that the shear stresses vanish on all planes. The stresses  $\sigma_x$  and  $\sigma_y$  are equally balanced in all directions but the shear or tension stresses are not zero. Then at this plane two systems act at the same time. One of them is producing a maximum tension stress and the other a shear stress generating a plane of stress concentration that would give place to the interfascial failure.

Two failure modes can be associated for the pull-out specimen based on the principal stress directions system. The failure mechanism in a pull-out specimen will begin at the plane in which the fiber emerges from the epoxy-resin block with a failure mode I then the failure mechanism continues as a combined failure modes I and II along the fiber-resin interphase.

## Bibliography

- [1] Molleda F., Moraa J., Molleda F.J., Carrilloa E., Mellorc B.G. "Stress trajectories for Mode I fracture" *Materials Characterization* **2005**, 54, 9– 12
- [2] Herrera Franco P. J., Rao Venkatesh, Drzal Laurence T. "Bond Strength measurement in composites analysis of experimental techniques" *Composites* **1992**, 23, 2-27
- [3] Laurence, P. "Some theoretical considerations of fiber pull out from an elastic matrix" *Journal of Materials Science* **1972**, 7, 1-6
- [4] Vázquez-Rodríguez J. Herrera-Franco M., P. J., González-Chi P. I. "Micromechanical Analysis of Thermoplastic-Thermoset Interphase" *Macromol. Symp.* **2004**, 216, 117-129
- [5] de Joussineau Ghislain, Petita Jean-Pierre, Gauthierb Bertrand D.M. "Photoelastic and numerical investigation of stress distributions around fault models under biaxial compressive loading conditions" *Tectonophysics* **2003**, 363,19– 43
- [6] Pisanova E., Zhandarova S., Mäder E., Ahmad I., Young R.J. "Three techniques of interfacial bond strength estimation from direct observation of crack initiation and propagation in polymer–fiber systems" *Composites: Part A* **2001**, 32, 435–443
- [7] [Frocht Max Mark, Ph. D. "Photoelasticity"Vol. I John Wiley and Sons, Inc. New York, **1947**
- [8] Vázquez-Rodríguez J. M., Herrera-Franco P. J., González-Chi P. I. "Analysis of the interphase between a thermoplastic fiber and thermosetting matrix using photoelasticity". *Composites Part A* 38, **2007**; 819–27.
- [9] E.A. Flores-Johnson, J.M. Vázquez-Rodríguez, P.J. Herrera-Franco, P.I. González-Chi. "Photoelastic evaluation of fiber surface-treatments on the interfacial performance of a polyester fiber/epoxy model composite". *Composites: Part A* 42 **2011**, 1017–1024

## FAILURE MODE OF DUAL PHASE STEELS RESISTANCE SPOT WELDS

M. Pouranvari<sup>1</sup>, S. P. H. Marashi<sup>2</sup>, Z. Salimi<sup>3</sup>

<sup>1</sup>Dezful Branch, Islamic Azad University, Dezful, Iran  
(mpouranvari@yahoo.com)

<sup>2</sup>Amirkabir University of Technology, Tehran, Iran

<sup>3</sup>South Tehran Branch, Islamic Azad University, Dezful, Iran

### Abstract

Quasi-static tensile-shear mechanical properties of resistance spot welds (**RSWs**) of three dual phase grades including DP600, DP780 and DP980 are investigated. Results showed that low hardness ratio of DP RSWs in respect to low carbon steel RSWs due to their higher **base metal (BM)** hardness, coupled with the fact that dual phase steels are more prone to solidification shrinkage can explain their higher tendency to fail in interfacial mode. Pronounced HAZ softening in DP980 resulted in reducing its tendency to fail in interfacial failure mode in comparison to DP780.

*Keywords: Resistance spot welding, Dual phase steel, Failure mode*

### Introduction

Ferrite-martensite dual-phase (DP) steel is one of the most common **advanced high-strength steels** (AHSS) steels which is currently used in automotive industry. Weldability of DP steel is one of the key factors governing its application in auto industry. Resistance spot welding is the predominant process in sheet metal joining, particularly in automotive industry. Vehicle crashworthiness, which is defined as the capability of a car structure to provide adequate protection to its passengers against injuries in the event of a crash, largely depends on the integrity and the mechanical performance of the spot welds [1,2].

According to the **literature**, problems associated with the resistance spot welding of DP steels can be summarized as follows [3-6]:

- i) high susceptibility to failure in interfacial failure mode,
- (ii) high susceptibility to expulsion,
- (iii) sensitivity to the formation of shrinkage voids,
- (iv) high hardness of the fusion zone due to martensite formation, this can have an adverse effect on the failure mode during some loading conditions (e. g. peel test)

Considering the development and commercialization of new DP steels for application in automotive bodies, there is an increasing need to study the spot welding behavior of these materials. Considerable works are focused on the spot welding behavior of DP600, but there are only limited published works regarding the weldability of higher grades of dual phase steels such as DP780 and DP980. This paper presents a comparative study on the failure mode of three DP grades,

DP600, DP780 and DP980. Key factors affecting the failure mode of spot welds are discussed.

Table 1: Chemical composition and mechanical properties of investigated DP steels

Steels	Chemical Composition (wt%)						Tensile Properties	
	C	Mn	Si	Cr	Mo	CE	UTS (MPa)	EL (%)
DP600	0.10	1.4	0.14	0.16	0.18	0.40	610	23
DP780	0.12	1.3	0.18	0.10	0.13	0.38	790	18
DP980	0.14	1.7	0.08	0.25	0.16	0.50	995	12

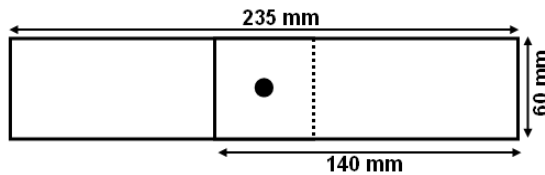


Figure 1. The tensile-shear test sample dimensions

### Experimental Procedure

Three DP steel grades including DP600, DP780 and DP980 steels were chosen for this study. The thickness of the sheets is 1.5mm. The chemical composition and mechanical properties of investigated steels are given in Table 1. The carbon equivalent was calculated based on the IIW formula.

Spot welding was performed using a 120kVA AC pedestal type resistance spot welding machine operating at 50 Hz, controlled by PLC. Welding was conducted using a 45-deg truncated cone RWMA Class 2 electrode with an 8-mm face diameter. To study the effects of weld (**fusion zone**) FZ size on mechanical properties, spot welding was performed in 20 different welding conditions. Electrode force and holding time were selected based on the thickness of the base material and were kept constant at 4 kN and 10 cycles, respectively. Welding current was changed step by step from 7 to 11.5 kA at two levels of welding times (0.2 and 0.3 s).

Four samples were performed per welding condition including three samples for the tensile-shear test and one sample for weld size measurement. The quasi-static tensile-shear test samples were prepared according to ANSI/AWS/SAE/D8.9-97 standard. 140×60 mm samples were sheared and a single spot weld was made at the center of an overlapped area that measured 45 mm (Fig.1). Vickers microhardness test was used to determine the hardness profile parallel to the sheets interface (20 μm away from the weld centerline), using a **Buehler** microhardness tester.

## Results and discussion

### Failure Mode

Two main failure modes were observed during the tensile-shear testing: interfacial failure mode and pullout failure mode, as shown in Fig. 2 (a and b). Some of the specimens failed in partial interfacial failure mode (i.e. fracture propagates along the interface and redirects perpendicularly to the centerline towards the sheet surface, resulting in partial interfacial failure), as shown in Fig.2c. Note that spot welds that failed in partial interfacial fracture are categorized as interfacial fracture during data processing (according to their first failure path).

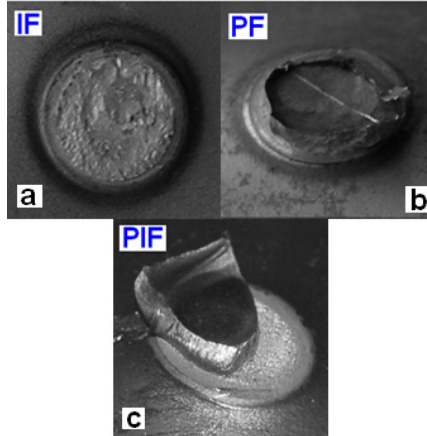


Figure 2. Typical observed failure mode during tensile-shear test: a) interfacial b) pullout and c) partial interfacial mode.

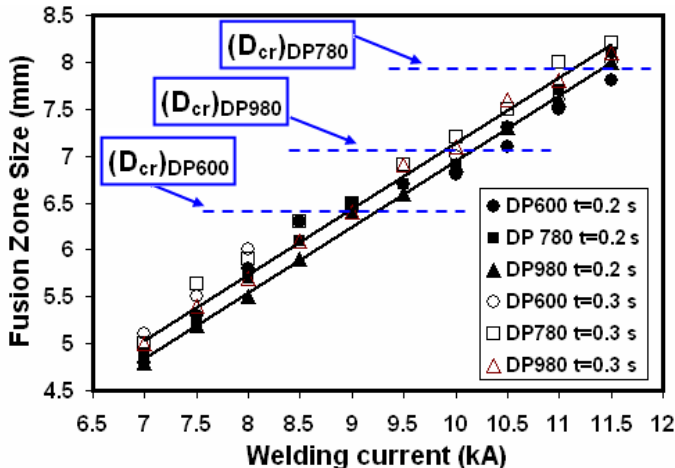


Figure 3 Effect of welding current and welding time ( $t$ ) on the FZ size and failure mode. Arrows show the critical fusion zone size for each grade below which the interfacial failure (or partial interfacial) mode was obtained and above that the pullout failure mode was observed.

It is well known that FZ size is the key physical weld attribute controlling the failure mode of RSWs. Fig. 3 shows the effect of the welding current and welding time on the FZ size. Increasing welding current and welding time, increase the FZ size. As can be seen, there is little effect of the steel grade on the FZ size. It is well documented that there is a critical FZ, above which, the pullout failure mode is guaranteed [1-4]. The critical FZ ( $D_{cr}$ ) to ensure pullout failure mode was determined by examination of the weld fracture surfaces. Maximum weld size leading to the IF mode and minimum weld size leading to the PF mode are given in Table 2. The critical FZ size is located between these two values. The critical FZ size increases from DP600 to DP980 and DP780. As can be seen, there is not a direct relationship between IF mode susceptibility and tensile strength of the (**base metal**) BM. This is in contrast to general expectations. Radakovic and Tumuluru [7] in their work on the prediction of spot welds failure mode, based on finite element modeling, concluded that higher tensile strength base metals require larger fusion zone size to avoid IF mode. However, as it is seen, critical FZ size of DP980 is smaller than that of DP780. Despite the fact that the tensile strength of DP980 is about 25% **higher** than DP970, its critical FZ size is approximately 12% **lower** than DP780's.

Table 2 Relation between hardness characteristics and failure mode of DP resistance spot welds

Material	Failure location	$H_{FZ}/H_{FL}$	Failure Mode	
			IF	PF
DP600	BM	2.1	$D < 6.4$ mm	$D > 6.4$ mm
DP780	BM/HAZ	1.68	$D < 7.7$ mm	$D > 8$ mm
DP980	Softened HAZ	1.9	$D < 6.9$ mm	$D > 7.1$ mm

### 3-2-Factors Controlling Failure Mode

Failure of spot welds in the tensile shear test is a competition between shear plastic deformation of FZ and necking in the BM or HAZ. Spot weld failure load in IF mode is controlled by the area of the FZ in the plane of sheet/sheet interface and the hardness of FZ. Spot weld failure load in PF mode is controlled by the area of the FZ in the plane perpendicular to the sheet surfaces and the hardness of the PF failure location. Based on a simple stress analysis, Pouranvari et al. [3] proposed a simple analytical model to predict the minimum FZ size ( $D_{cr}$ ) required to ensure PF mode of spot welds during the tensile-shear test:

$$D_{cr} = 8t \frac{H_{PFL}}{H_{FZ}} = 8 \frac{t}{K} \quad (1)$$

where  $t$ =sheet thickness;  $H_{FZ}$ = hardness of FZ;  $H_{PFL}$ = hardness of the failure location in PF mode;  $K$ = hardness ratio ( $H_{FZ}/H_{PFL}$ ).

Spot welds with  $D < D_{cr}$  tend to fail via interfacial mode, as opposed to welds with  $D > D_{cr}$  which tend to fail via the preferred pullout mode. However, the effect of voids on the failure mode should not be ignored. The presence of shrinkage voids in FZ has been recognized as one of the main reasons for the high susceptibility of AHSS steels to interfacial failure mode. It is shown that the presence of the voids in the weld centerline can increase the critical fusion zone size [6]. This is due to the fact that the presence of the voids in the FZ decreases the area of the load bearing surface in IF mode (i.e. sheet/sheet interface area). This leads to the development of much higher shear stress at the interface and consequently promote IF mode.

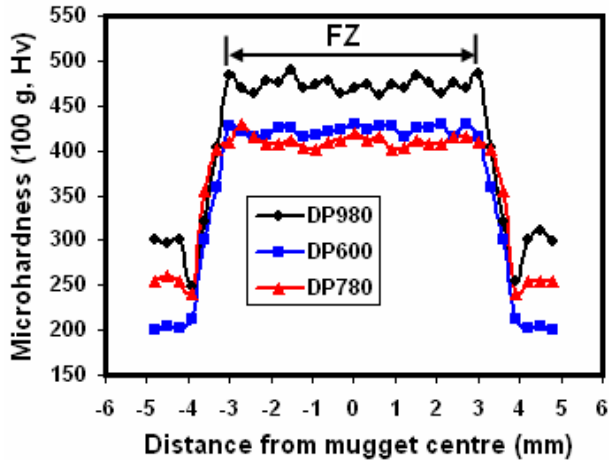


Figure 4. Horizontal hardness profile across the sheet/sheet interface

In the following sections, different failure mode of three different DP steel RSWs are discussed with regards to their hardness profiles and failure locations.

Fig. 4 shows a typical hardness profile of the spot welds. Hardness of FZ is higher than that of the BM. This can be attributed to the formation of martensite in FZ. Martensite formation in FZ of dual phase steel RSWs is well documented in literatures [2-4]. Hardness of FZ increases in order of DP780, DP600 and DP980. Hardness of martensite is primarily dictated by carbon content and alloying element. As can be seen there is a direct relationship between FZ hardness and IIW carbon equivalent (CE). A reduction in the hardness (softening) with respect to the BM was observed in the HAZ of DP780 and DP980 spot welds due to the tempering of the pre-existing martensite in the sub-critical areas of the HAZ.

In order to analyze the failure mode transition in these three different DP steel RSWs, the hardness ratio of FZ to pullout failure location was considered. Table 2 summarizes relationship between failure mode and hardness ratio. The highest critical FZ size of DP780 is attributed to low its HFZ/HPFL. Pronounced HAZ softening in DP980 explain its smaller  $D_{cr}$ . Softening in the HAZ would have promoted plastic strain to localize and fracture to follow outside the hard fusion zone. According to these results:

- (i) The effect of metallurgical factors on the  $D_{cr}$  is obvious (i.e. different  $D_{cr}$  for similar sheet thickness). Conventional weld size criteria are based

on the sheet thickness. Experimentally determined  $D_{cr}$  for the investigated steels are well above the conventional weld nugget size recommendation of  $4(t)^{0.5}$  (i.e. 4.9 mm) and  $5(t)^{0.5}$  (i.e. 6.1 mm). Therefore, there is a need to propose new weld quality criterion for resistance spot welded dual phase steels. Metallurgical characteristics of welds should be considered to predict and analyze the spot weld failure mode precisely.

- (ii)  $D_{cr}$  in the tensile-shear test is related to  $H_{FZ}/H_{PFL}$ , and not the tensile strength of the BM. As can be seen in Table 2, there is an inverse relation between  $D_{cr}$  and hardness ratio. Higher  $D_{cr}$  of the AHSS weld is related to both their low hardness ratio due to their higher BM hardness and their higher tendency to the shrinkage void formation.

## Conclusions

1. The conventional weld size recommendations of  $4(t)^{0.5}$  and  $5(t)^{0.5}$  are not sufficient to guarantee pullout failure mode for DP980 steel RSWs during tensile-shear test. It is required to search for new weld quality criterion for resistance spot welded dual phase steels.

2. There is not a direct relationship between tendency to fail in interfacial failure mode and ultimate tensile strength of the base metal.

3. Interfacial to pullout transition is controlled by the hardness ratio of fusion zone to pullout failure location not the tensile strength of the base metal. Interfacial mode susceptibility increased in the order of DP600, DP980 and DP780.

4. HAZ softening plays an important role in mechanical properties of DP steels, if any. HAZ softening improves interfacial to pullout failure transition. DP980 has lower tendency to interfacial failure in comparison with DP780, despite its higher BM and FZ strength.

## References

- [1] Goodarzi M., Marashi S.P.H., Pournavari M., J. Mat. Process. Tech, Vol.209,(2009),p 4379.
- [2] Sun X., Stephens E.V., Khaleel M.A., Engineering Failure Analysis, Vol.15 (2008)p:356.
- [3] Pournavari M., Asgari H. R., Mosavizadeh S. M., Marashi P. H, Goodarzi M., Sci.Technol. Weld. Joining, Vol.12, (2007),p.217.
- [4] Marya M., Wang K., Hector L. G., Gayden X., J.Manufact. Sci. Eng., 2006, p.287.
- [5] C. Ma, D.L. Chen, S.D. Bhole, G. Boudreau, A. Lee, E. Biro, Mater. Sci. Eng. A, Vol.485 (2008), p334.
- [6] M. Pournavari, P. Marashi, M. Goodarzi, H. Bahmanpour, " Metallurgical Factors Affecting Failure Mode of Resistance Spot Welds", Materials Science and Technology 2008, 5-9 October, Pittsburgh, Pennsylvania, USA, AcerS/AIST/ASM/TMS, p.2465.
- [7] D. J. Radakovic, M. D. Tumuluru, Weld. J., Vol. 87 (2008),p.96s

## **SIMULATING FORMATION OF CRACKS DURING COOLING ALUMINIUM ALLOY BILLETS IN A DIRECT CHILL ELECTROMAGNETIC CASTING PROCESS**

S. Markovic<sup>a</sup>, N. Korolija<sup>b</sup>, E. Romhanji<sup>a</sup>, S. Manasijevic<sup>c</sup>, M. Stakic<sup>d</sup>

<sup>a</sup> *Faculty of Technology and Metallurgy, University of Belgrade, Belgrade, Serbia.*

<sup>b</sup> *School of Electrical Engineering, University of Belgrade, Serbia,  
nenadko@etf.rs*

<sup>c</sup> *LOLA-Institute, Belgrade, Serbia.*

<sup>d</sup> *Eling, A.D., Loznica, Serbia.*

### **Abstract**

This paper gives theoretical background and suggests the use of chosen mathematical-physical model for simulating Al-alloy casting in a crystallizer of DCEC system. Non-uniform cooling of the material causes significant thermal stresses in the log during solidification, which sometimes exceeds the value of the material strength. Applying electromagnetic field during the production improves the material properties, due to more uniform material structure in the presence of Lorentz force. Simulating and comparing Al-alloy casting while varying the material uniformity is given in the paper. Results include simulated relevant parameters of all elementary cubes of the material, as well as calculated forces and stresses. According to these, pictures of cracks are generated in different stages, from which the animation is made. By varying various parameters of the simulator, the probability of crack formation is estimated. While the simulator is highly configurable and time-efficient, it can not simulate casting in irregularly shaped mold.

*Key words: simulating, cracks, aluminum alloy billets, direct chill electromagnetic casting (DCEC)*

### **Instruction**

Non-uniform cooling of the Al-alloy causes occurring of cracks in the log during the solidification process. Main reason for this is existence of significant thermal stresses during solidification. This chapter gives a theoretical background and describes mathematical and physical model used in this work for modeling and simulating cracks formation. One of the main goals was determining impact of electromagnetic field on the probability of cracks formation.

Aluminum cooling is done in the crystallizer continuously outputting a solid aluminum alloy. Walls of the mold are equipped with pipes for cooling water. Water flow is provided during whole process of casting in DCECT system. Due to the relatively rapid flow of aluminum through the crystallizer, considerable differences in temperature along the radius of the log occur. Volume is being cooled on the

surface of the mold, while the volume in the center of the mold is cooled indirectly and thus later. This way, volume in the center hardens later, causing significant thermal stresses in the log. The alloy solidifies first next to the walls. Hardened alloy forbids reducing the total volume of the mold. However, cooling the volume in the middle of the mold forces the volume to shrink. Therefore, stress on the outer part of the volume occurs. This stress sometimes exceeds the value of material strength. This can lead to cracks formation in the contact zone between the two layers. It has been empirically observed that the shape of cracks that occur at each point in mold is predominantly perpendicular to the radius of the cross-section passing through the observed point [1]. Examples of cross sections of aluminum are given in Figure 1.

The application of electromagnetic casting (EMC) technique for improving products quality has been studied in recent years, and considerable developments have been achieved. However, the traditional EMC always requires elaborate processing control and expensive devices [8]. It is proven that the applying electromagnetic fields during the casting process increases the uniformity of the structure and distribution of heat. The presented simulator is build to determine whether and to what extent the uniformity of the casting affects the appearance of cracks in the hardening process. Simulator calculates forces between each two adjacent elementary cubes of the material.

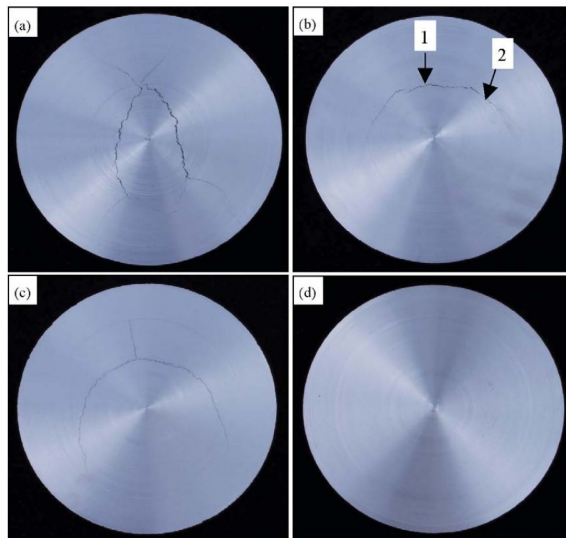


Figure 1. Influence of electro-magnetic field on the formation of cracks in the ingot: (a-c) DC process, (d) DCEC process

Technological parameters used for modeling casting are based on a number of known data. Figure 4 depicts scheme of DCEC process. Casting speed, or speed of moving the desk, is in the range of 5-10 cm/min. Pure aluminum starts hardening at 6600 °C, while above 5770 °C is almost whole alloy mold in the solid state (all phases and microconstituents) possibly with small puddles in doughy

(transition between solid and liquid) states [7]. We adopted the casting temperature between 680-7000 °C degrees Celsius. Reduction of the temperature gradient is achieved under the influence of the Lorentz force. Casting in the presence of electromagnetic field is shown on Figure 4. Induction coil is placed around the billet, creating Lorentz' force inside the crystallizer. Lorentz force also reduces the pressure on the walls of the crystallizer, resulting in the slower heat sinks, which further leads to slower cooling and smaller temperature differences.

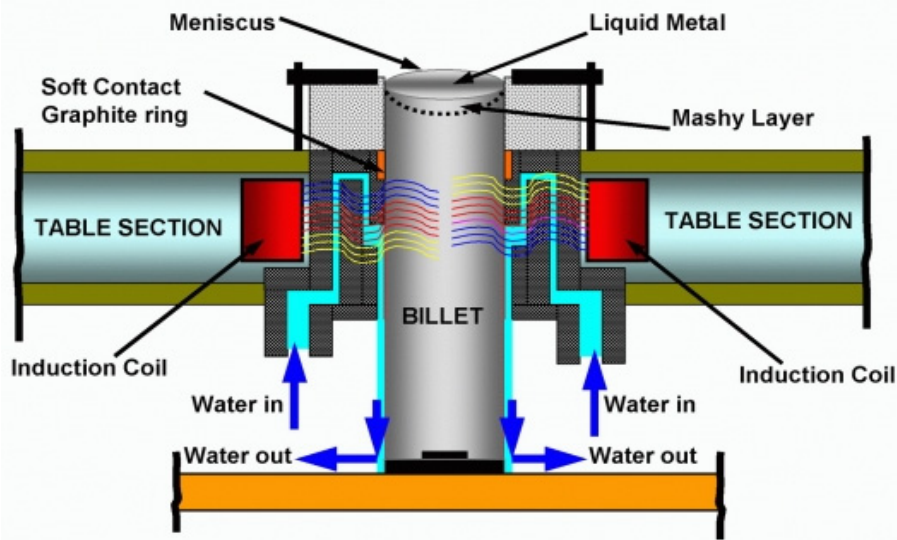


Figure 4. Casting plate with electromagnetic field

### Mathematical and physical model

Thin layer of aluminum molds will be considered as the sum of all the thin rings of which is formed. Each ring has diameter  $r$ , height  $h$ , and width  $dr$ . The temperatures within the ring will be considered uniform for all points. They will be noted as  $T(r)$ , where  $r$  is the radius of the observed thin ring.

The strength of the material is given as:

$$Rm(r) = f(T(r)) \quad (1)$$

The functional dependence of tensile strength on temperature alloy EN AW 6060 and alloy EN AW 7075 is modeled based on the data found in a literature [3, 4]

Each ring if formed from a large number of slices, called elementary cubes. Figure 2 depicts one elementary cube.

By pushing down disk through the crystallizer by a relatively small height  $h$ , the temperature of the disk will be reduced, resulting in the decrease of the volume of each elementary cube from  $V_0$  to  $V_1$ , where:

$$V_1 = V_0 [1 - \alpha_v (T_0 - T_1)] \quad (2)$$

where  $\alpha_v = 4.7\%$  for the aluminum alloy [5,6].

Shrinkage of aluminum during cooling is about  $\alpha_v$  percentages. For pure aluminum,  $\alpha_v = 8$ . For simulated alloys, it can be assumed that this factor is about 4.7% [5].

According to the formula (3), the difference in the volume of the elementary cube after and before cooling is:

$$\Delta V = V_0 [1 - \alpha_v (T_0 - T_1)] - V_0 = -\alpha_v (T_0 - T_1) V_0 \quad (3)$$

Shrinkage is defined as the product of empirically determined factors and the reduction in volume. Volume can reduce in any direction. Reducing the volume height is not of the importance of the work presented. Shrinkage that is of importance when simulating cracks formations inside the ring is given as a product of ring width and empirical constant  $k$ :

$$\sigma = k \times \Delta dr \quad (4)$$

where:

$k$  - is empirical constant,  $N/m^3$ ,

$\Delta dr$  - is the shrinkage in ring width, m.

Accordingly, the shrinking force  $F_s$  acting on an elementary cube is:

$$F_s = (\sigma / dr) \Delta V = -(\sigma / dr) V_0 \alpha_v (T_0 - T_1) = -(\sigma / dr) \frac{2\pi r h dr}{n} \alpha_v (T_0 - T_1) (=) N \quad (5)$$

where:

$A(\Delta V/h)$  – is area between two adjacent cubes with different radius,  $m^2$

$dr$  – is width of elementary cube of area  $A$ ,  $m^2$

For the purpose of simulation of cracks, it was necessary to calculate the shrinking force of disk with radius  $r_i$  acts on surrounding disk, where  $0 < r_i < R$ . For each value of radius  $r_i$ , the total shrinking force of disk with radius  $r_i$  acting on disk of outer radius  $R$  and inner radius  $r_i$ , is calculated as sum (integral) of acting of all rings with radius range from 0 to  $r_i$ , with width  $dr$ , where  $R$  is the radius of whole disk.

$$F_{stot} = - \int_0^{r_i} \frac{2\pi h}{n} k r \alpha_v (T_0 - T_1) dr = - \frac{2\pi h}{n} k \alpha_v \int_0^{r_i} r (T_0 - T_1) dr \quad (6)$$

It will be considered that the cracking will occur if for any internal disk radius of  $r_i$  is determined that:

$$F_{stot}(r_i) \geq F_m(r_i), \quad (7)$$

$$F_{stot}(r_i) \geq R m(r_i) 2\pi \eta h, \quad (8)$$

The separation of two adjacent elementary cubes, each of which belongs to one of two adjacent rings, inner and outer diameters  $r_i$ , will occur at the point of the tin ring for which is the ratio  $F_{stot}(r_i) / F_m(r)$  maximal.

### **Description of the simulator**

In order to determine whether the crack in the mold during the casting will occur, the simulator is built to calculate stresses between each of the elementary adjacent cubes of material. Aluminum passing through crystallizer is divided into imaginary discs. A disk corresponds to the cross section of the log. The disc will be composed of liquid aluminum at the entrance of the crystallizer to, while at the outlet, the mold will be in solid state. Each of these disks is divided into imaginary rings, and they are divided into rings, and further on elementary cubes.

At some point, due to the already hardened alloy at the outer part of the internal cooling, the force due to cooling shrinkage becomes greater than the strength between two adjacent elementary cubes, that is, the splitting of a material occurs. The simulated temperature at the outer edge of the disc changes from the top to the bottom of the crystallizer by function obtained on the basis of numerical data and graphics in Figures 8 and 10 from the paper [2]. The same is true for the temperature inside the mold. As reference points, the temperature values inside the mold are obtained using Procast simulation tools [2]. After the occurrence of the gap, the force that further separates cubes tend to be transferred to the two neighboring cubes, increasing the probabilities of crack expansion between them. Analogously, the force with which more separated cubes tend to further separate is transferred to separate adjacent cubes at each end of the crack. This phenomenon leads to the effect of spreading the crack. When the gap occurs at radius  $r_1$ , integrating forces that would lead to forming another cracking at radius  $r_2$  should be done from  $r_1$ , and not from zero, having in mind that disk of radius  $r_1$ , which is separated on the observed elementary cube from the rest of the disk of radius  $R$ , will not affect already separated part of the disk. Consequently, it reduces the probability of a crack occurring at the observed radius. This approximation is considered justified because of the available literature, describing empirically obtained cracks of the logs, that will almost never occur on the same radius.

### **The simulation results**

The simulator calculates values of temperatures, forces acting at elementary cubes, and strength in each of the observed elementary cubes. Crack is considered to occur at the point where the ratio of forces between elementary cubes and strength is maximal. Simulator further finds calculated values of forces and strengths at points near to the furthest two points of the cracks. According to these, it determines on which side the crack will advance, until the strength on both sides of the crack becomes high enough. It further produces crack photos from cross section of aluminum. From photos of cracks in different stages, simulator produces animation of crack formation. It also allows user to obtain information on whether the crack appeared. Each output of the simulator can be displayed or not by using appropriate options. Relevant parameters can be set to appropriate values.

Relations between force and strength are very small at small distances of elementary cubes from the vertical axis of the mold, due to relatively high temperatures, and thus the relatively low strengths. For large values of radius, it can be seen that the strength is disproportionately greater, due to the relatively low temperatures close to the crystallizer. It is obvious that the relation between strength and tension is largest in the range between 50% and 70% of the radius. Figure 5 depicts typical appearance of cracks obtained by simulating crack formations. Cracks usually appear on distances from center of the mold between 50% and 70% of the radius. By further improvements of the simulator, it became possible to adjust factor of influence of the whole crack on the points where crack spreads. This way, a simulated crack that is more similar to the one at the Figure 1, a) is obtained. The Figure also shows a snapshot of the simulation.

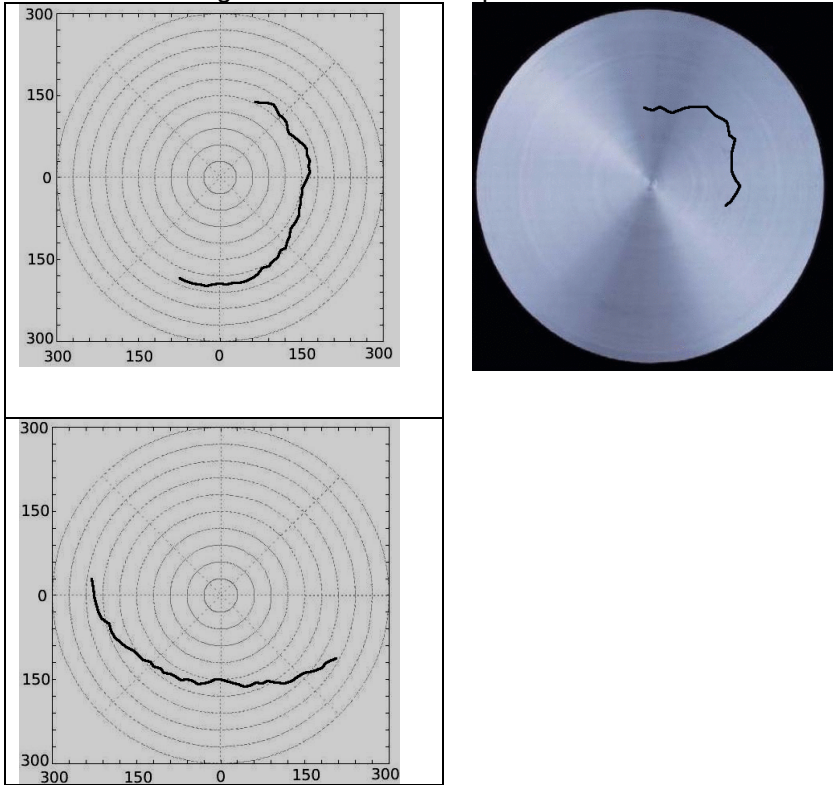


Figure 5. Typical appearance of cracks obtained from simulator

Table 1 shows the average probability of cracks obtained by calling the simulator 100 times for each of the given variations in  $\Omega$ . As can be seen, the probability of crack formation is very different for values of the variation between 8 and 11. At the same time, the number of elementary cubes is set to 10000, so that it is expected that for more than half of elementary cubes, there is a very low probability of occurrence of cracks. The reason for this are already described ratios

between forces and tensile strengths depending on the distance from the center of the disc.

Table 1: The influence of varying the strength on the elementary cubes cracking

Variation $\Omega$	7	8	9	10	11	12
Probability of crack formation	1%	2%	17%	64%	98%	100%

Variation changes between 8 and 11 affect the forces in areas where the ratio of tensile forces and strengths are highest, so that the probability of crack formation increases by over 95% for the variation changes from close to 10%. So the difference in forces of only a few percents can make huge differences in cracks appearance probability. Therefore, we can see that a relatively small variation in the uniformity of aluminum can greatly reduce the likelihood of cracking in the process of crystallization and cooling of aluminum.

As noted above, the calculated shrinkage force of each elementary cube is corrected for the random value forming corrected force that is from that point used as a shrinking force. In this way, non-uniform material is simulated. Random values were obtained using the so-called random number generator from library of programming language C. The obtained value is further passed to a function that returns a standard Gaussian distribution. Variation  $\Omega$  affects the density of distribution. It is well known that by applying Lorentz force, more uniform structure of aluminum is obtained, resulting in lower variation in strength between the elementary cubes. Simulation showed that a more uniform distribution reduces the likelihood of cracking in the aluminum. Some of the examples of the simulator results can be found on the web site representing results of this simulator [9].

## Conclusions

Presented simulator is relatively fast comparing to the existing simulation software. It is made to ease of simulator adaptation to new needs, and the possibility of doing calculations in parallel, on multi-core processors, as well as the clusters of computers. Disadvantage of the simulator compared to modern simulation software is that it can not simulate all phenomena. For example, it can not simulate cooling aluminum during casting in the mold of irregular shape.

In the case of tear, the location of the occurrence of relatively small cracks there is sufficient resistance to further crack propagation in this direction. Therefore, after the crack reaches for example. 30% of the width of the diameter of the cast, it is expected that the temperature will affect the collection of the materials separated, forming a relatively straight line gap. Future directions of research, in order to eliminate the differences between the shape of the relative long cracks obtained simulation and observing the cross-section castings could be the formation of cracks and the direction of increasing the likelihood of the spread just

by the way and simulating the impact of all points on the crack propagation capacity, not just those along the axis.

### **Acknowledgements**

The authors gratefully acknowledge the financial support of the Ministry of Education and Science of the Republic Serbia through the European project EUREKA 6735! ESPAL (<http://www.eurekanetwork.org/project/-/id/6735>) and the help and cooperation of the management and work teams of the Eling company, Loznica ([www.eling.rs](http://www.eling.rs)).

### **References**

- [1] Z.Yubo et all. *Materials Science and Engineering*, A 406(2005)286-292
- [2] H.Zang et all. *Materials Science and Engineering*, A 448(2007)189-203
- [3] L.F.Mandolfo, *Aluminum, Alloys, Structure&Properties*, London:Boston, Butterworths, 1796, p.705
- [4] *Metals Handbook*, 9th Edition, ASM (1979), Vol.2, p.856
- [5] J.R.Brown, *Fossecos Non-Ferrous Foundryman's Handbook*, 11th Edition, p.13
- [6] B.Kočovski, *Teorija Livarstva*, BIGZ, Beograd (1972), p.91-95, 215-218.
- [7] M.Tomović, *Livenje lakih i obojenih metala*, TMF, Beograd (1976) p.140
- [8] \*LI Jian-chao<sup>1</sup>, 2, CUI Jian-zhong<sup>1</sup>, WANG Bao-feng<sup>2</sup>, MA Yong-lin<sup>2</sup>, Effect of mould material on aluminum alloy ingot quality under low frequency electromagnetic casting, *China Foundry*, Vol.3, No4, Nov.2006, 288-292
- [9] Web site dedicated for the simulator:
- [10] <http://home.etf.rs/~nenadko/SrdjanMarkovic/index2.html>

## DEVELOPMENT OF A DATABASE OF ADVANCED MATERIAL PROPERTIES

Svetlana Pocajt<sup>1\*</sup>, Viktor Pocajt<sup>2</sup>, Karlo Raić<sup>2</sup>

<sup>1</sup> *Key to Metals AG, Zrenjaninski put 13p, Belgrade, Serbia, e-mail: s.pocajt@keytometals.com*

<sup>2</sup> *Faculty of Technology and Metallurgy, University of Belgrade, Karnegijeva 4, Belgrade, Serbia*

### Abstract

This paper describes a development of a large database of advanced material properties for metallic materials, and more recently polymers, ceramics and composites. This new database, which relies on a proprietary methodology that combines property acquisition and assessment, has a specific aim of serving the global engineering community with mechanical and physical properties needed for advanced CAE (Computer Aided Engineering) and FEA (Finite Element Analysis) calculations and simulations.

In the database, advanced material properties have been divided to (1) stress-strain curves, (2) formability curves, (3) cyclic properties, (4) fracture mechanics, and (5) creep properties. The biggest challenge in providing these properties for a large number of engineering materials and service conditions is a general scarceness of experimental data. Besides collecting and consolidating information for more than 100.000 datasets from more than 1.200 references, a specific set of algorithms has also been developed for streamlining and assessing/interpolating properties under various conditions (service temperature, heat treatment etc.).

*Keywords: material properties, metals, polymers, composites, stress-strain curves, cyclic properties*

### Introduction

The importance of accurate material properties information for engineering calculations and simulations can never be overstated. Even conventional mechanical properties such as yield strength, tensile strength, hardness, and ductility may vary more than tenfold for structural steels at room temperature, depending on the variations of alloying elements, heat treatment and fabrication. With a moderate change in working temperature, the subsequent property variation and associated changes can become even more profound and their approximations may lead to very serious errors. In fact, this lack of accurate information concerning material properties poses one of the highest risks in structural design, accounting for over 29% of structural failures [1].

The main mechanical properties such as yield and strength, hardness, ductility, and Young modulus are included within the standard dataset of Key to Metals database, together with international cross-reference tables, composition,

physical properties, and more. However, while these properties generally suffice for conventional calculations within the elastic range, they cannot fulfill the needs of advanced calculations that include plasticity, fatigue and fracture mechanics, needed for the most demanding CAE simulations [2].

Extended Range is a new part of the Key to Metals database, specifically designed to compile advanced mechanical properties information, which is typically very hard to find. Advanced mechanical properties have been divided into (a) stress-strain curves, (b) formability curves, (c) cyclic properties, (d) fracture mechanics, and (e) creep properties. The biggest challenge in providing these properties for a large number of materials and service conditions is a general scarceness of published experimental data. To overcome this problem, in the process of database development over 1,200 data resources have been acquired, ranging from relatively large data collections [3] to individual papers dating back from over 50 years ago [4] to more recent documents [5]. In addition, an innovative methodology has been developed for integrating raw data obtained from diversified experiments from all over the world, consisting of a specific set of algorithms for data selection, processing and assessment for each of the five advanced properties modules, Figure 1.

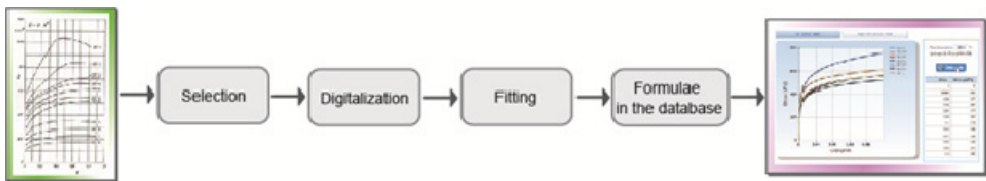


Fig. 1. The workflow for processing experimental results.

Since its introduction in 2011, the Extended Range database has gained significant popularity in the CAE community and in turn its application in various fields of CAE simulation has enabled dynamic further development. Besides an increase in the number of records and materials covered, a number of new features have been added, such as formability stress-strain curves, estimation of Wohler curves, statistical fatigue parameters and more [2]. Significant recent developments also include new methods for assessing advanced material properties, which will be briefly described in this paper.

### Stress-Strain Curves

Stress-strain curves are of particular importance for calculations that include plasticity either in static or in dynamic loading, e.g. for controlled plastic deformation, autofretage, forging, crash behavior and other areas of simulation. There are a relatively low number of materials for which experimental curves have been made, and even this information is hard to find. When found, the information is often in a form inconvenient for use, e.g. graphs on the paper. In addition to this, it is delicate to find and error-prone to assess properties under various conditions, such as working temperature, strain rate, and heat treatment.

Applying the methodology outlined in Figure 1, after digitizing using a strictly controlled process, a combination of Ramberg-Osgood and Ludwik equations is

applied on the set of obtained data points [6], together with a range of temperature-dependent physical properties like Young modulus. Using this methodology, equations that represent the best fit are obtained for various temperatures, strain rates and delivery conditions, depending on the available experimental data. The coefficients of the equations are embedded in the database, so the stress-strain curve can be created and displayed in real-time, or can be automatically recalculated for user defined working temperatures, Figure 2. As a result of this process, more than 25,000 stress-strain curves have been defined for about 3,000 materials; for many of them there is also a range of working temperatures and conditions available, which can account for over 100 curves for a single material.

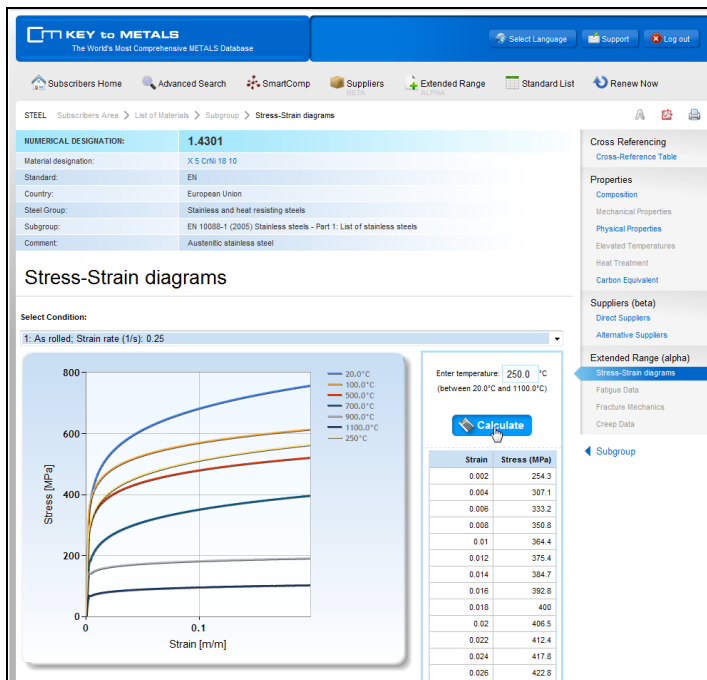
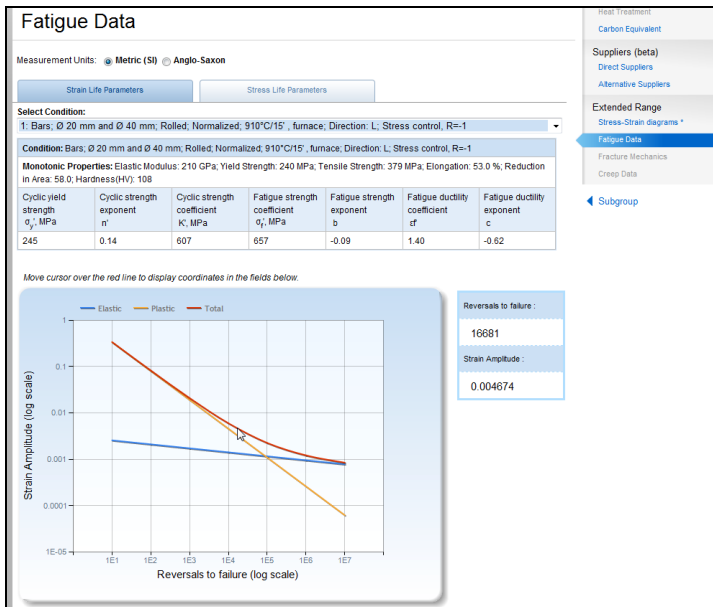


Fig. 2. An example of stress-strain curves, with a calculation of a curve for user-defined working temperature.

## Fatigue Data

Cyclic properties have also been processed using proprietary methodology, both for strain and stress life. In order to compile cyclic properties for a substantial number of materials, an extensive literature review project has been completed as an initial step. Although the scope of the project was large, available experimental data on cyclic properties is sparse. As with stress-strain data, the information is often presented in a format inconvenient for use and often created from a material that has been subjected to specific experimental conditions such as working temperature, strain rate or heat treatment leading to the potential for error in applying them for the concrete engineering structure or simulation.

Therefore, a workflow similar to that in Figure 1 was created which has resulted in fatigue data for more than 3.500 metallic alloys, again with multiple datasets where available, for different heat treatments and loading conditions. Statistical parameters have been provided where applicable, as well as graphical presentation of the data, Figure 3. The implemented graphs have been made interactive and the values of strain or stress amplitude versus number of cycles are displayed as the user moves the mouse cursor over the graph.



*Fig. 3. An example of strain-life fatigue data. Monotonic properties are provided for reference.*

### Advanced Material Properties Assessment

Due to a general scarcity of experimental data, even a database as large as Key to Metals Extended Range containing several thousand materials covers advanced properties information for only a relatively small part of all standardized and proprietary structural materials that are being used worldwide, the total number of which can be roughly estimated at more than 300.000.

As an alternative or supplementary method for properties assessment, the Key to Metals database provides the possibility to quickly and easily estimate unknown advanced properties of a material alloy using advanced properties of similar materials that are derived from the Key to Metals cross-reference tables. These tables of equivalent materials come from the recommendations of Standards Development Organizations (SDOs), literature and other sources. Since over 10 million cross-reference records are readily available within the Key to Metals database, the implementation of this approach is relatively straightforward and provides users with estimates of advanced properties for an additional 30.000 materials.

An example of such an estimate is given in Figure 4. The original material, in this case Japanese stainless steel SUS 304, does not have high temperature formability stress-strain curves available, but its European equivalent X 5 CrNi 18 10 does, so the stress-strain data of X 5 CrNi 18 10 can be used as an estimate for SUS 304. It should be noted that, regardless of the fact that the materials are declared equivalent, the user can check the similarity of the properties for the two materials by using a side-by-side comparison view and eventually decide whether the similarity between materials is sufficient for the particular application in mind.

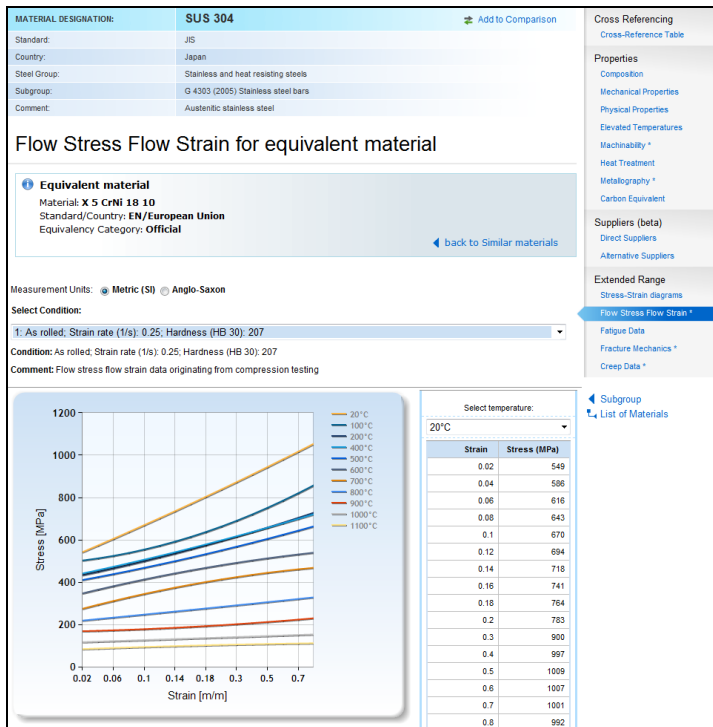


Fig. 4. An example of high temperature flow stress – flow strain (formability) curves of an equivalent material.

Of course, properties derived using similar materials cannot represent an ultimate solution or a replacement for experiments, but they can provide a useful starting point for further research and simulations. Initial benchmarking for delicate cyclic properties showed that using cross-reference tables to assess properties provides estimates that are at least comparable to those of other methods [8].

In addition, a new fuzzy-logic based module SmartCross<sup>2</sup> has been developed. Using a proven, patented algorithm for the identification and comparison of metals [9], SmartCross<sup>2</sup> is designed to find unknown equivalents by composition, mechanical properties, or any combination thereof autonomously, that is without user intervention. Once the list of “candidates” for similar materials is obtained, they can again be used to estimate advanced properties.

## **Conclusions**

As a consequence of a permanently increasing demand for accurate and reliable material properties data that can be used for sophisticated CAE analysis and simulations, the database of advanced material properties Extended Range has undergone very dynamic development that included an increased number of records and materials covered, and a number of new features added, such as formability stress-strain curves, estimation of Wohler curves, statistical fatigue parameters, new families of stress-strain curves, new methods for assessing advanced material properties, and integration possibilities with CAE software.

Besides further increase of data in the existing modules, on-going and future developments are focused to extending the data coverage for polymer, ceramic, composite and nano materials, including data needed for diversified material models such as orthotropic materials. Also, a completely new module for joints is being developed that can help CAE engineers to get a quick insight into properties of welded, soldered, glued and mechanical joints of metals and non-metals.

Future developments planned also include tighter integration with most popular CAE software packages, with an idea to use the complete data scope of the Key to Metals database from within the CAE tool, by the means of Web services that will be called by the CAE tool on an as-needed base.

## **References**

- [1] Radovic, A., Radovic, N., 2004. In: From Fracture Mechanics to Structural Integrity Assessment, Society for Structural Integrity and Life, Belgrade, pp. 83-90.
- [2] Pocajt, V., Baumann, N., 2012. Development of a Database of Material Properties for CAE. NAFEMS 2012 UK Conference, Lincolnshire 30th-31st May 2012.
- [3] Doege, E., Meyer-Nolkemper, H., Saeed. I., 1986. Fließkurvenatlas metallischer Werkstoffe: mit Fließkurven für 73 Werkstoffe und einer grundlegenden Einführung. ISBN: 3-446-14427-7. München: Hanser.
- [4] Hughes, P.J., Inge, J.E., Prosser S.B., 1955. Tensile and compressive stress-strain properties of some high-strength sheet alloys at elevated temperatures. NACA Technical Notes, No 3315.
- [5] Pla-Ferrando R., Sánchez-Caballero S., Selles, M.A., Martínez-Sanz A.V., 2011. TWIP/TRIP Steels. Future Trends in Automotive Industries. Annals of the Oradea University, Fascicle of Management and Technological Engineering, Volume X (XX), pp. 1.23-1.26.
- [6] Skrzypek, J. J., 1993. Plasticity and Creep. Theory, Examples, and Problems. ISBN 0-8493-9936-X. Boca Raton, FL: CRC Press.
- [7] Pocajt, V., Ogarevic, V., 2010. Estimation of mechanical properties of metals on the example of fatigue characteristics. In: 33 Convegno Nazionale AIM (in Italian), Brescia 10th-12th November 2010.
- [8] Pocajt, V., Sevarac, Z., Kovacevic, A., 2009. SmartMetals: A New Method for Metal Identification Based on Fuzzy Logic. Journal of Chemometrics, Volume 23 (11), pp. 555-561.

## NEW MODEL FOR COMPARISON AND CROSS-REFERENCING OF ENGINEERING METAL ALLOYS

Svetlana Pocajt<sup>1\*</sup>, Viktor Pocajt<sup>2</sup>, Karlo Raić<sup>2</sup>

<sup>1</sup> Key to Metals AG, Zrenjaninski put 13p, Belgrade, Serbia, e-mail: s.pocajt@keytometals.com

<sup>2</sup> Faculty of Technology and Metallurgy, University of Belgrade, Karnegijeva 4, Belgrade, Serbia

### Abstract

This paper presents an innovative model for the comparison and cross-referencing of metal alloys, in order to determine their interchangeability in engineering, manufacturing and material sourcing. The model uses a large alloy database and statistical approach to calculate alloy content and mechanical properties intervals. A classification of metals and fuzzy logic are then applied to compare metal alloys.

The model and its algorithm have been implemented and tested in real-life applications. In this paper, an application of the model in finding unknown equivalent metals by comparing their compositions in a very large metals database is described, with an example of its practical implementation.

*Keywords: metal alloys comparison, cross-referencing, equivalent metals, metal composition, metal properties*

### Introduction

Increasing international manufacturing, engineering, trade and global sourcing have led to a strongly increased need for international metals comparison, cross-referencing and interchanging, as a way to practically handle different international metals and specifications, and to select and use them effectively in the globalized manufacturing environment. However, there are many thousands of different metal alloys and consequently it is not easy to structure metal specifications in a uniformed way. Metal specifications are vital for classifying, evaluating, and specifying the chemical, mechanical, and metallurgical properties of different types of metal alloys that are used in nearly all manufacturing activities and hence of paramount importance for designers and manufacturing engineers [1].

Metal specifications are often defined by standards, which vary from country to country and can be based on different criteria. Since most of the metal specifications are complex documents, the comparison of metals, or cross-referencing, is also a challenging task. The main factors for estimating equivalency include composition, manufacturing method, finishing method, product shape, mechanical and physical properties. Additional factors such as hardenability, corrosion and heat resistance and other properties may also have significant influence on metal equivalency and potential interchangeability. Nevertheless,

equivalent metals from around the world are usually grouped on the basis of composition and, to some extent, mechanical properties [2], [3].

Cross-reference tables of equivalent metals often come from recommendations of Standards Development Organizations (SDOs). However, many SDOs do not issue these kinds of guidelines, which in turn creates great difficulties in international engineering due to hundreds of thousands of metal alloys and variations.

Unfortunately, besides being incompatible, specifications for metal alloys are often ambiguous and incomplete, with many missing values and intervals. For example, in specifications and standards for metal alloys, the content of alloying elements is given in the form of intervals, which sometimes define the minimum inclusion of an alloying element, e.g. chrome in stainless steel, or maximum, e.g. sulfur content in steel, and only sometimes both [4]. The base element, which forms the main metal matrix like iron in steel, is then assumed to comprise the rest of the balance [5]. The fact that the content of alloying elements and metal properties are defined with such incomplete intervals is often inconvenient and creates difficulties in various fields such as alloy identification, engineering calculations and notably in comparison and international cross-referencing of metals, creating again a source of possible costly errors in international engineering, material sourcing and manufacturing.

This paper presents a new model for the cross-referencing of metals, by using a statistical approach on a very large alloy database, consisting of over 180,000 alloys [6]. Similarly to the Classification And Regression Trees (CART) model which addresses the missing property data issue [7], this model applies classification and then fuzzy logic to calculate similarity of a metal with a given chemical composition with other metals and to discover “unknown” equivalents. Such “close matches” can provide engineers with a good starting point for further investigation of material equivalency and interchangeability in the process of material selection [2]. An evaluation of the model, which was done by applying it on a large database of metal alloys broadly used by engineering and manufacturing companies worldwide, will be presented as well.

### **The Model Description**

This model uses one version of SmartMetals, a general algorithm designed to search and identify similar metals from a database containing metal properties information [8]. The SmartMetals algorithm covers two main applications:

- (1) Finding unknown equivalent materials (cross-references) to a selected metal alloy, e.g. a metal alloy selected by user
- (2) Identifying an unknown metal when its chemical analysis is known, e.g. obtained by spectrometer.

For these applications, the model derived from SmartMetals applies the following logic sequence:

- (i) Starting from the composition of a selected metal (for the first application - cross-referencing) or a composition obtained by spectrometer (for material identification), the model classifies the composition using rule-based reasoning and pre-defined, built-in metal classification; depending

on the class of metal selected, applies weights and threshold parameters to distinguish the importance of alloying elements.

- (ii) Uses statistical methods to calculate missing minimums or maximums in chemical composition and mechanical properties.
- (iii) Applies fuzzy logic-based calculation to determine the level of similarity between the initial composition given and the composition of each of the metals in the database.

In this paper, the focus is on the application (1), that is cross-referencing. For the other two steps, the previously developed algorithms for material identification have been re-used [9] and modified where necessary.

In SmartMetals, similarity is defined as a degree of overlapping of material properties. In the material cross-referencing, the similarity applies to overlapping to the intervals of the alloying content (again e.g. carbon, manganese and chrome) in an alloy X and to the same intervals in an alloy Y. The intervals are defined by material specifications, issued in most cases by SDOs and sometimes coming from proprietary sources such as large metal producers and engineering companies.

The degree of composition overlapping can normally go from 0 (no overlapping) to 1 (the intervals of the alloying element content defined for the alloys X and Y are equal). There is also a fuzzy part, when there is a partial overlapping or when the intervals are not overlapping, but are relatively close to each other; consequently, the similarity level for the alloying element take a value between 0 and 1.

The total similarity factor between alloy Y and the reference alloy X is calculated as an average of similarities for all individual alloying elements, by applying weight factor for each alloying element according to the average weighted sum formula, which is very often used in fuzzy systems [10]:

$$S_t = \frac{\sum s_i w_i}{\sum w_i} \quad (1)$$

where

$S_t$  is the total similarity between the alloy given and the reference alloy  $s_i$  is the similarity factor for  $i$ -th alloying element  $w_i$  is the weight (impact) factor on total similarity for the  $i$ -th element

After determining the similarity factor with alloy Y, the same procedure is repeated with all relevant materials within the database. The number of alloys that can be used is practically unlimited; for example, in the KEY to METALS database the total number of alloys is over 180,000.

## **Model Verification and Applications**

The international cross-referencing of metals is one of the most important applications of KEY to METALS database; its "classic" cross-reference tables which have been made using the recommendations of SDOs have been used by the global engineering community for years. However, the recommendations of SDOs are intrinsically narrow and cover only a limited number of similar alloys

(usually several) of the total of 180,000 alloys, thus excluding many potential equivalents. Consequently, there was a substantial practical interest to apply this model in discovering “unknown” equivalents, which means similar materials which haven’t been included into the recommendations of SDOs.

After initial testing, the model has been applied to the complete KEY to METALS database. The total processing time to run all batch procedures was approximately 6 days, and the result was that the model discovered:

- 1) 49,676 alloys with the similarity of 100% with at least one other alloy; nearly 20% of them haven’t been declared by any SDO
- 2) 7,958 alloys with the similarity with at least one other alloy between 95% and 100%
- 3) 10,074 alloys with the similarity with at least one other alloy between 90% and 95%.

These results were proved as very good, since the similarity of 70% was already consider relevant, i.e. users could consider alloys with this level of similarity as potential candidates for equivalents, depending on the application of course.

An example of the implementation of the model is given in Fig. 1. The list of similar materials, which can be filtered and sorted in different ways, is given with the similarity factors. It should be noted that in this implementation it takes on average only 10 seconds to get the result list from the KEY to METALS database of over 180,000 alloys. An interesting feature is a link for side-by-side comparison, which shows the properties of the original and selected material side-by-side, thus providing the user with an opportunity to immediately check whether the differences in composition and mechanical properties are relevant for his/her particular application.

The screenshot shows the 'KEY to METALS' database interface. The main content area displays a 'Cross-Reference Table' for the material '00Cr17Ni14Mo2'. The table has columns for 'MATERIAL', 'COUNTRY / STANDARD', 'SUBGROUP', and 'SIMILARITY'. The results show several equivalent materials with similarity scores between 0.86 and 0.89. A 'SmartCross' button is visible at the bottom right of the table area.

MATERIAL	COUNTRY / STANDARD	SUBGROUP	SIMILARITY
RUS 316 LTB	Japan / JIS	G 3463	0.89
SUS 316 LBS	Japan / JIS	G 3447	0.89
SUS 316 LTP	Japan / JIS	G 3459	0.89
STS 316LTP	Korea / KS	D 3576	0.89
STS 316LTB	Korea / KS	D 3577	0.89
STS 316LTS	Korea / KS	D 3585	0.89
S31603	China / GB	GB/T 4356	0.89
WFS 316S11	United Kingdom / B.S.	BS 3605-1	0.86
CF8 316S11	United Kingdom / B.S.	BS 3605-1	0.86

Fig. 1. An example of the implementation of the model in the KEY to METALS in finding unknown equivalents for a Chinese steel.

A more recent application of the model implies extending it by adding mechanical properties to alloy comparison. The calculation of similarity is applied to the yield and tensile strength of alloys and thus mechanical similarity is obtained. This implementation also enables comparing alloys using a user-defined combination of mechanical and compositional similarity; the user can select the relative importance of mechanical vs. chemical similarity simply by moving the slider, Fig 2. The total similarity between two alloys is then calculated as a combination of chemical and mechanical similarity

$$S_t = S_c \left(1 - \frac{x}{100}\right) + S_m \frac{x}{100} \quad (2)$$

where

$S_t$  is the total similarity between the alloy given and the reference alloy  $S_c$  is the chemical similarity between the two alloys  $S_m$  is the mechanical similarity between the two alloys  $x$  is the relative importance of mechanical properties in %

Mechanical similarity can provide better comparison results in many cases where the similarity of mechanical properties is more important than the similarity of compositions, in the field such as structural calculations and Finite Element (FE) analysis.

The screenshot shows the 'KEY to METALS' website interface. The main content area displays the 'Cross-Reference Table' for material '00Cr17Ni14Mo2'. A slider allows users to adjust the similarity threshold between 'Chemical Composition (%)' (set at 0) and 'Mechanical Properties (%)' (set at 100). Below the slider, a table lists search results with columns for material designations, standards, and similarity scores.

Material Designation	Standard	Similarity Score	Action
04H18Ni10	Russia / GOST	GOST 7350	1.00 Compare
06Cr13Al	China / GB	GB/T 1220	1.00 Compare
06Cr18Ni9Cu3	China / GB	GB/T 1220	1.00 Compare
08H18Ni12B	Russia / GOST	GOST 9949	1.00 Compare
0C0117	China / GB	GB 4238	1.00 Compare
0C0134I	China / GB	GB 4238	1.00 Compare
0C018Ni10Mo5	China / GB	GB/T 4239	1.00 Compare
1.3953	Germany / DIN		1.00 Compare
1.4307	United Kingdom / B.S.	BS EN 10250-4	1.00 Compare
1.4307	Switzerland / SNV	SN EN 10250-4	1.00 Compare
1.4307	Sweden / SS	SS-EN 10250-4	1.00 Compare

Fig. 2. An extension of the model to mechanical similarity of alloys and its combination with chemical similarity.

## Conclusions

In this model, fuzzy-logic has been applied to a large alloy properties database to achieve successful comparison and cross-referencing of metals. Comparing to the standard approach in finding equivalent materials which involves

manual search by human experts or relies on the recommendations of SDOs, the model proved to be able to provide better and more diversified results, in a considerably more practical and faster way, especially when combined with a user-friendly software interface.

Future research will be oriented including more mechanical and physical properties into the model, which can open an opportunity to make a simultaneous multi-parameter comparison of different properties and define ad-hoc relative importance of the properties depending on the concrete application. A preliminary research has indicated that this kind of model could be applicable to other structural materials beyond metals, such as polymers, ceramics and composites.

Also, this kind of combined similarity can be used for predicting “non-standard” advanced material properties, such as fatigue, stress-strain curves and fracture mechanics parameters, which are becoming essential for the most demanding modern structural calculations, FE analysis and simulations, by using known properties of similar materials. An initial research [11] has shown that the model and especially the method for calculating missing property values are fully applicable to the mechanical properties of metals, and calculating some advanced properties such as fatigue based on this model was demonstrated to be at least comparable or better in comparison to the standard methods.

## References

- [1] Q. Wang, and A. Scott, Development of a metal selector system, *Int. J. Adv. Manuf. Technol.*, 2007, **32**, p 843–855
- [2] F. Cverna, *Worldwide Guide to Equivalent Irons and Steels*, ASM International, Cleveland, 2006
- [3] F. Cverna, *Worldwide Guide to Equivalent Nonferrous Metals and Alloys*, ASM International, Cleveland, 2007
- [4] P. Cunat, *Alloying Elements in Stainless Steel and Other Chromium-Containing Alloys*, Euro Inox, 2007, [http://www.euro-inox.org/pdf/map/AlloyingElements\\_EN.pdf](http://www.euro-inox.org/pdf/map/AlloyingElements_EN.pdf), accessed 6 February 2013
- [5] H. Chandler, *Metallurgy for Non-metallurgist*, ASM International, Cleveland, 1998
- [6] Key to Metals AG, *KEY to METALS Database*. <http://www.keytometals.com>, accessed March 2013
- [7] Y. Li, Predicting materials properties and behavior using classification and regression trees, *Mater. Sci. Eng. A*, 2006, **433**, p 261–268
- [8] V. Pocajt, *SmartMetals Method and System to Identify Metal Alloys*, United States Patent No US 2009/0076739 A1
- [9] V. Pocajt, Z. Ševarac, and A. Kovačević, SmartMetals: A New Method for Metal Identification Based on Fuzzy Logic, *J. Chemometrics*, 2009, **11**, p 555–561
- [10] H. Zimmermann, *Fuzzy Set Theory and Its Applications*, Springer Verlag, 2001
- [11] V. Pocajt, and V. Ogarević, *Determinazione di proprietà meccaniche di metalli in regime plastico con particolare riguardo al comportamento a fatica*, 33 Convegno Nazionale AIM, Brescia, 2010

## RECOVERY OF NICKEL FROM STAINLESS STEEL WASTE STREAMS

<sup>1</sup>Frank Rögner, <sup>2</sup>Carsten Dittrich

<sup>1</sup>VDEh-Betriebsforschungsinstitut (BFI), Sohnstr. 65, 40237 Duesseldorf, Germany,

E-Mail: frank.roegner@bfi.de

<sup>2</sup>MEAB Metallextraktion AB, Datavägen 51, 43632 Askim (Göteborg), Sweden,

E-Mail: carsten@meab-mx.com

### Abstract

The shortage of important alloying metals as well as the decreasing security of raw materials supply leads to rising stainless steel production costs. Thus, a significant increase in the efficiency of handling resources is essential in all production steps. Properties and quality of stainless steel are based on a defined surface finish. This is gained in pickling lines. However, pickling lines generate significant amounts of metal containing liquid or solid waste. Thus, valuable metals, such nickel, are irrecoverably lost: It is estimated that only in Europe more than 2.500 ton nickel per year is deposited.

*Key words: Nickel, recycling, leaching, solvent extraction, stainless steel*

### Introduction

Nickel can be recovered, either directly from spent pickling solutions or from solid sludge, generated during the neutralization of spent pickling liquors. The first option - referred to as "*The Waste Acid Route*" - requires the separation of not reacted acid to assure high process efficiency. The second option - referred to as "*The Neutralization Sludge Route*" - involves leaching of the sludge to dissolve nickel. This measure is also useful for nickel recovery from landfill ("landfill mining"). Both routes lead to solutions containing dissolved metals, which are the basis for metal recovery.

The two processing routes are investigated in laboratory tests and afterwards confirmed in field tests at locations of the stainless steel companies since each processing route has its own advantages concerning the economic efficiency and applicability. In order to guarantee the applicability at almost every location in Europe, the main pickling systems, HF/HNO<sub>3</sub> and HNO<sub>3</sub>-free pickling, are investigated since the waste acid and the neutralization sludge of the two pickling systems differ elementary in concentration and composition, respectively [1-4].

The engagement of **BFI** is mainly focused on the electrolysis of nickel and to prove its reliability for metal recovery from the actual solutions. In a first step, preliminary investigations with three different synthetic solutions were conducted using structural steel substrates. Solution 1 contained only nickel, solution 2 included nickel and chromium and solution 3 included iron, chromium and nickel. It

became obvious that the electro precipitation of elemental nickel was disturbed by the presence of iron. Instead of a thin metallic bright nickel layer, a relatively thick dark layer composed of metal hydroxides and oxides was formed. These results were also found with solutions gained by leaching industrial neutralization sludge.

The engagement of **MEAB** is focused on separation and purification processes by liquid-liquid extraction. The investigations involve the separation techniques of nickel, based on state-of-the-art solvent extraction technology. More precise, MEAB are responsible for design, adaption and operation of a solvent extraction pilot plant in order to demonstrate the nickel separation and purification. The pilot line will be set up at MEAB in Aachen, Germany and will include a nickel solvent extraction separation unit with mixer-settlers having a total processing flow capacity of 50 l/h.

### **Nickel containing Neutralization sludge**

The following chemical composition of neutralization sludge generated stainless steel production is shown in Table 1.

*Table 1: Composition of neutralization sludge from stainless steel production (average values of 1 month)*

<b>Element</b>	<b>Concentration</b>
Iron	10.0 ± 1.5 % dry matter
Chromium	2.7 ± 1.0 % dry matter
Nickel	1.1 ± 0.3 % dry matter
Manganese	0.2 ± 0.1 % dry matter
Calcium	28.7 ± 2.7 % dry matter
Fluoride	16.0 ± 1.9 % dry matter
Nitrate	2.3 ± 2.2 % dry matter
Sulphate	5.7 ± 2.0 % dry matter

### **Experimental Work in Leaching of Nickel using Sulphuric Acid**

Laboratory scale experiments carried out to remove nickel from the neutralization sludge as selective as possible, and/ or as much as possible. Based on former research work, sulphuric acid was identified as the most appropriate leaching solution as calcium leaching is suppressed to a large extend due to the formation of hardly soluble gypsum. The work describes the following hydrometallurgical test work:

- Investigation of leach solution concentration,
- Investigation of leach solution temperature and leaching time.

Figure depicts the visual results of neutralization sludge leaching at different pH values.

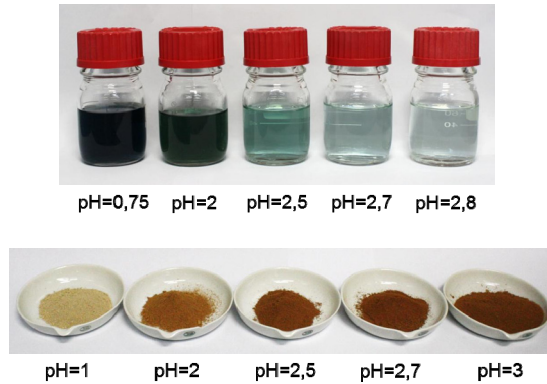


Figure 1: Visual results of neutralization sludge leaching with sulphuric acid

In Figure 2 the results of sulphuric acid leaching at different pH are summarized:

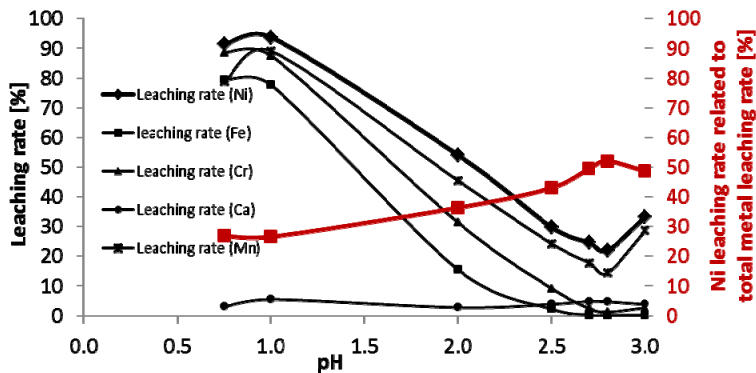


Figure 2: Leaching of nickel as a function of pH

(Leaching of neutralization sludge with  $H_2SO_4$  at room temperature,  $t=30$  min)

Accordingly, there are two options for the leaching process:

- Nearly selective nickel leaching with a maximum yield of about 30 % at  $pH=2.7$ , and
- Non selective nickel leaching with a maximum yield of about 90 % at  $pH=1$ .

### pH adjustment

The removal of chromium and iron from the leach solution carried out using lime milk. While at  $pH=3$  the precipitation of iron was already finished, total chromium precipitation takes place at  $pH=5$ . A small loss of nickel was detected; the amount of calcium and manganese remaining in the resulting filtrate.

## Experimental Work in Nickel Separation and Purification by Solvent Extraction

Laboratory-scale experiments have been carried out on nickel solutions emanating from leaching of neutralization sludge after pH adjustment.

The laboratory test programme comprises the separation and purification of nickel containing solutions with the aim to select a suitable reagent for nickel as well as to develop a preliminary process flow sheet. The work describes the following chemical and preliminary engineering work:

- Investigation of extractants (reagents), selective for nickel separation,
- Investigation of solvent extraction parameters (e.g. distribution coefficient, extraction rate, extraction selectivity),
- Determination of scrubbing and stripping liquors and conditions, and
- Equilibrium curves for extraction and stripping, including surface loading.

### Solvent Extraction of Nickel

The resulting aqueous feed solution from the neutralization tests are used to perform the solvent extraction experiments. As organic solution, 2-hydroxi-5-nonylacetophenone oxime (LIX 84-I), neo decanoic acid (Versatic 10) and 2-ethylhexyl phosphoric acid (D2EHPA) are used. All organic reagents are diluted in an aliphatic diluent (kerosene). No modifier was used in the experiments. The nickel extraction dependency of pH in sulphate media is shown in figure 3.

However, the very poor total selectivity of Versatic 10 compared to that of LIX 84-I, lead to our recommendation to use LIX 84-I as the most suitable extractant for further process development.

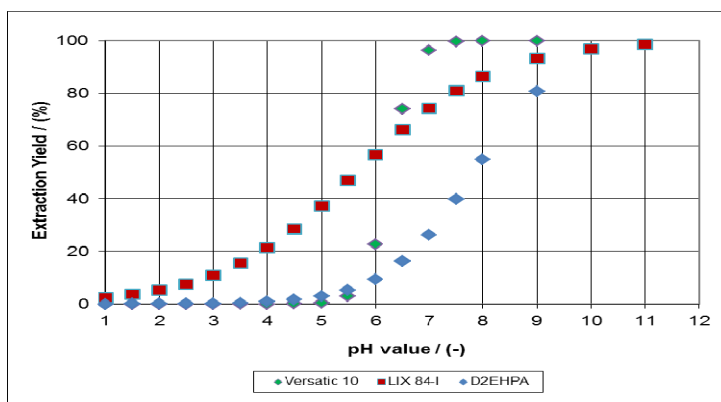


Figure 3: Extraction of nickel obtained from sulphate solution with LIX 84-I, D2EHPA and Versatic 10 in kerosene (D80). Aqueous solution (313 mg/l chromium, 124 mg/l iron, 790 mg/l manganese and 1540 mg/l nickel, initial pH 0)

For further nickel solvent extraction test work, a LIX<sup>®</sup> 84-I in a high flash point hydrocarbon diluent was prepared. The pH dependency of the extraction of nickel

was investigated and showed that the maximum loading of nickel in the organic solution achieved at pH 9 to 10. Co-extracted ammonia can be scrubbed from the loaded organic solution by using diluted sulphuric acid solution. The nickel-loaded reagent was then stripped with a strip solution, containing sulphuric acid and nickel sulphate.

Based on the laboratory test data, the nickel solvent extraction mixer-settler circuit shall comprise three extraction stages, two ammonia scrub stages and four strip stages (as shown at the Figure 4).



*Figure 4: The mixer-settler (MSU-2.5) set-up used in the experiments.*

## **Conclusion**

Our contribution with laboratory scale test work to the RECONI project was resulted in a better understanding of the removal of nickel from stainless steel neutralization sludge. We also have shown the application of the sulphuric acid leaching and solvent extraction procedure for the selective recovery of nickel with the aim to improve of the metal product quality.

## **Acknowledgements**

This work was carried out within the frame of RECONI (The European project contract RFSR-CT-2011-00039). The authors acknowledge the financial support given to this project by the European Commission (Research Fund for Coal and Steel). We also wish to thank our various partners in the project for providing us with real samples.

## **References**

- [1] Tels, M.; Lotens, J. P, Recovery of pure metal salts from mixed metal hydroxide sludges. Proceedings of the 9th National Waste Processing Conference (1980), pp. 109-119.
- [2] MAR – Hydrometallurgical Recovery Process (Recovery of copper and zinc from brass mill flue dust). Proceeding International Solvent Extraction

- Conference, Toronto 1977.
- [3] Mackenzie, J M, Virnig, J., M, Solvent Extraction Technology for the Extraction of Nickel using LIX<sup>®</sup> 84-I, International Laterite Nickel Symposium 2004.
- [4] Rydberg, J., Cox, M., Musikas, C., Choppin, G., Solvent Extraction Principles and Practice, Second Edition, New York, Marcel Dekker, Inc. 2004

## METHODS OF INVESTIGATION OF THE STRESS-INDUCED MARTENSITE IN ORTHODONTIC WIRE FROM THE SHAPE MEMORY ALLOY NiTi UNDER DIFFERENT STRESS STATES

Janko Ferčec<sup>1</sup>, Rebeka Rudolf<sup>1,2</sup>, Ivan Anžel<sup>1</sup>, Irena Pulko<sup>3</sup>, Evgenija Marković<sup>4</sup>, Dragoslav Stamenković<sup>4</sup>, Branislav Glišić<sup>4</sup>

<sup>1</sup> *University of Maribor, Faculty of Mechanical Engineering, Slovenia*

<sup>2</sup> *Zlatarna Celje d.d., Slovenia*

<sup>3</sup> *Polymer Technology College, Slovenia*

<sup>4</sup> *University of Belgrade, School of Dental Medicine, Serbia*

*E-mail: janko.fercec@um.si*

### Abstract

In commercially available orthodontic wire we measured the transformation temperatures and we performed tensile tests where we determined the stress at both the start and end of solid state transformation. Our experimental methods for instigation of stress-induced martensite in different stress state included measurements of electrical resistance and determination of the hardness. To achieve different stress states on orthodontic wire we used devices to simulate uniaxial and multi-axial stresses. With these devices we deformed orthodontic wire so that we created different stresses on the wire, such as tension, bending, torsion and combinations of these. The results of our investigation can be used to provide better understanding of the functional behaviour of NiTi wire in the oral environment.

*Key words: Ni-Ti alloy, phase transformation, orthodontic wire, electrical resistance, hardness*

### Introduction

In orthodontic treatment we achieve tooth movement by acting on it with a force. This force causes stresses in the periodontal ligament, which leads to the transformation of jaws and teeth to ensure movement to the correct position. The optimum force used in orthodontic treatment should be enough to produce tooth movement without tissue damage and with maximum comfort for the patient. In the initial level of the treatment of outstanding teeth in many cases wires from the Shape memory alloys (SMA) NiTi, NiTi SMA are used, which have been implemented in dentistry due their good biocompatibility and functional properties (superelasticity) [1,2].

Superelasticity is associated with the solid state transformation of austenite into martensite due to the applied stress (Figure 1). SMA shows this behaviour above  $A_f$  temperature and is associated with martensitic transformation from austenite into martensite due to the changes in stresses. This effect or behaviour can be seen on the curve stress-strain, where we have different areas of phase. In superelasticity SMA occurs in forward loading, first elastic deformation of austenite

and then transformation areas where there is a transformation from austenite to detwinned martensite [3,4].

Most investigations on SMA-s are performed under uniaxial loading and determination transformation temperature. The transition between phases in uniaxial loading can be determined by the uniaxial tensile test. However, the two-axle or three-axle stress state is harder, because the transitions between phases are under different loads [5,6].

The orthodontic wire in the mouth almost never loads with a uniaxial stress state, but by two-axle and mostly by three-axial stress states, so it is interesting to know at which deformation superelasticity in SMA comes into play. One of the most common methods for the detection of phase change in the materials is measurement of electrical resistivity [1,7]

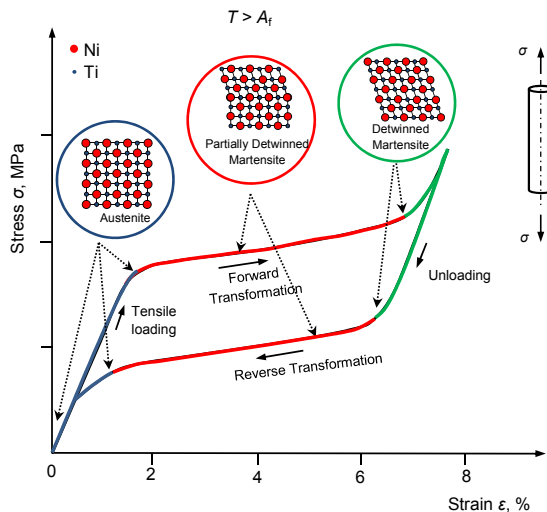


Figure 1: Stress strain curve for SMA NiTi under uniaxial loading

In our study we showed the methods of investigation of stress-induced martensite in SMA NiTi orthodontic wire. Tensile tests were performed on the wire where we set the stresses for the start and end of transformation. At different stress states (tension, bending, torsion and combination torsion bending), we performed measurements of electrical resistivity and measurements of hardness at different deformations.

### Materials and method

The investigation was carried out on the commercially available orthodontic wire SMA NiTi Truflex (Ortho Technology, USA). The cross-sectional area of the wire is an intersection of a round with a diameter of 0,014" (0,305 mm).

The DSC analyses were conducted on a STA 449 NETZSCH machine by using a liquid nitrogen cooling accessory. The specimen was heated to 100°C and then cooled to -100°C to obtain the cooling DSC curve. After that, the specimen

was heated from -100 °C back to 100°C to obtain the heating DSC curve. The cooling rate was 10°C/min as is usual in SMA NiTi.

The tensile tests were performed using a Zwick/Roell ZO 10 under the following conditions: Room temperature of 22°C, strain rates 0,025 sec<sup>-1</sup> (velocity of deformation  $v = 1,5$  mm/min) and pre-load of 5 N.

To achieve different deformation of orthodontic wire we used the deformation device for Simulation of Uni-Axial Stress (SUAS) (Figure 2a) and the deformation device for Simulation of Multi-Axial Stress (SMAS) (Figure 2b). Tensile deformation was achieved using the SUAS device, while with the SMAS device bending and torsion deformation was achieved, and a combination of these two.

A Micro-ohmmeter AOiP OM 21 was used to measure the electrical resistance between the two inner probes while a constant current was passed through the two outer probes using a constant current source. The electrical resistivity  $\rho$  of a wire of length  $l$  and cross-sectional area  $A$  is:

$$\rho = R \cdot \frac{A}{l},$$

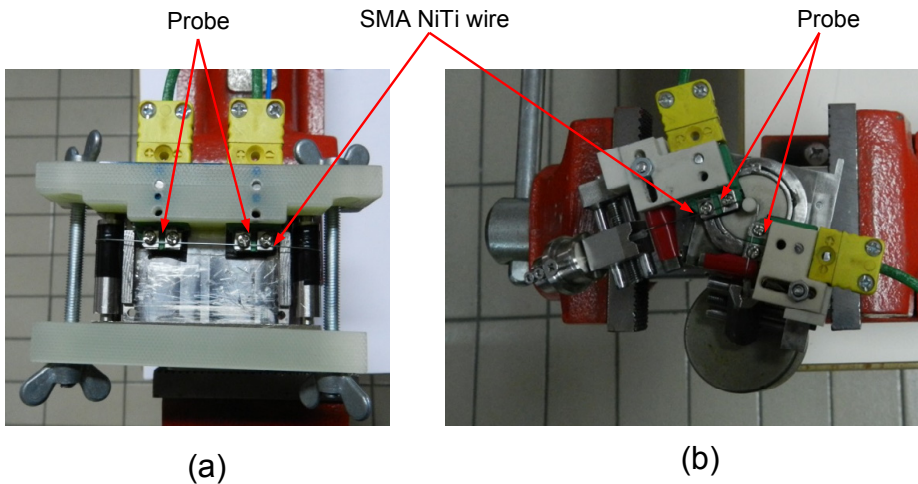


Figure 2: Measurement of electrical resistance: (a) SUAS device; (b) SMAS device

$R$  is the electrical resistance of the wire. The voltage drop across the two inner probes was measured. The distance  $l$  at the SUAS device was constant (20 mm), while at the SMAS device this distance  $l$  varied with the bending angle  $\alpha$ . For pure torsional load the distance was 13 mm.

A Vickers microhardness tester Zwick 3212 was used to measure micro hardness on the wire. The loading parameter was selected as HV 0,2. Samples were prepared using the SUAS and SMAS devices, where the samples were ground and polished on the longitudinal cross section. On the sample we chose the

points for measurements where the maximum stresses were. An average, we tested 6 points per sample.

## Results

The transformation temperatures (Figure 3a) of the martensite/austenite of orthodontic wire were found to be  $M_f = -14.58^\circ\text{C}$  (martensite start),  $M_s = 8.31^\circ\text{C}$  (martensite finish),  $A_s = 2.12^\circ\text{C}$  (austenite start) and  $A_f = 14.26^\circ\text{C}$  (austenite finish). The DSC analysis showed that, when the wire is inserted into the mouth, it is in the austenitic phase because the  $A_f$  temperature is lower than the body temperature ( $37^\circ\text{C}$ ).

The results of the tensile test are described in terms of stress deformation ( $\sigma$ - $\epsilon$ ) curve (Figure 3). The parameters considered as significant in describing the material behaviour of the curve are as follows: The elastic modulus of austenite is  $E_1 = 81300\text{ MPa}$ , the slope of the transformation phase or region (austenite to martensite) is  $E_2 = 4500\text{ MPa}$ . The elastic modulus of martensite is  $E_3 = 36300\text{ MPa}$ . The initial stress value for the start of the transformation is  $\sigma_{SM} = 451\text{ MPa}$ . The final stress value for the end of transformation is  $\sigma_{FM} = 649\text{ MPa}$ . The initial deformation value for the start of the transformation plateau is  $\epsilon_{SM} = 1,38\%$ . The final strain of the transformation plateau is  $\epsilon_{FM} = 8,4\%$ .

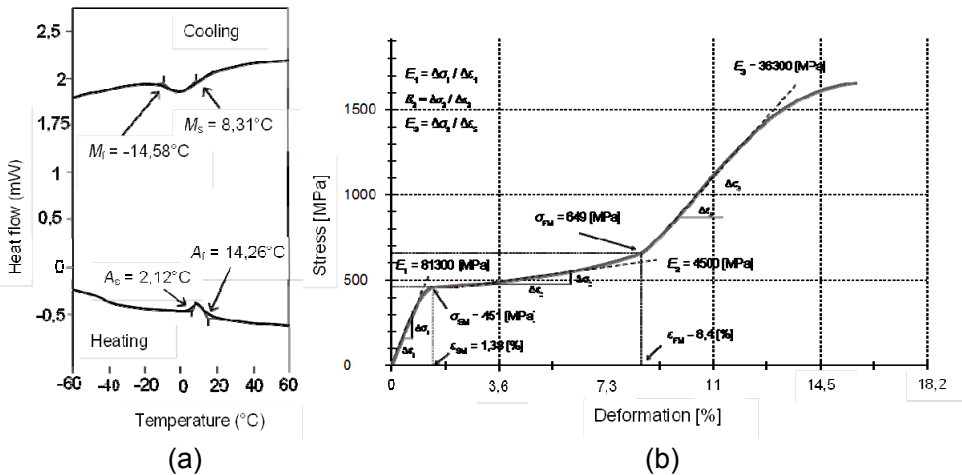


Figure 3: (a) DSC curves and phase transition temperature; (b) Stress-deformation curve for SMA NiTi wire

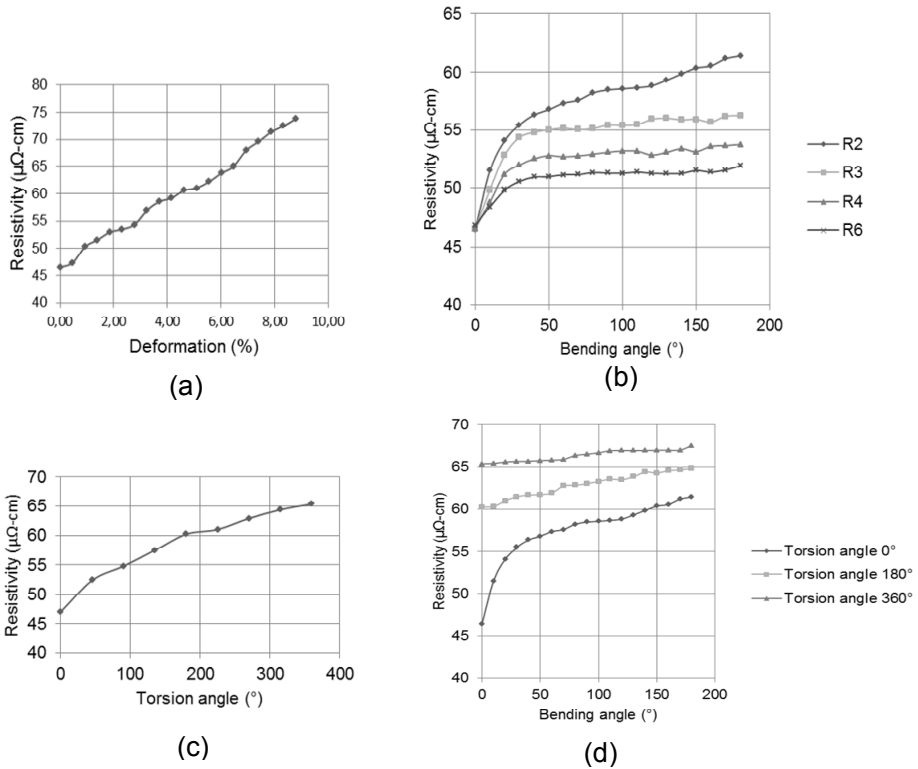


Figure 4: Deformation variation of the electrical resistivity of NiTi orthodontic wire: (a) Tension loading; (b) Bending loading; (c) Torsion loading; (d) Combination loading (torsion + bending)

Figure 4 shows the relationship between deformation and electrical resistivity. We can see that an increase of deformation caused a higher value of electrical resistivity. In Figure 4a, we can see the curve of electrical resistivity to the final value transformation plateau. Figure 4b shows the electrical resistivity at different bending angles for different bending radius R. A big change in electrical resistivity caused torsional load (Figure 4c). This can be seen also in the combination loads (bending and torsion), where the torsion had a big influence on the electrical resistivity.

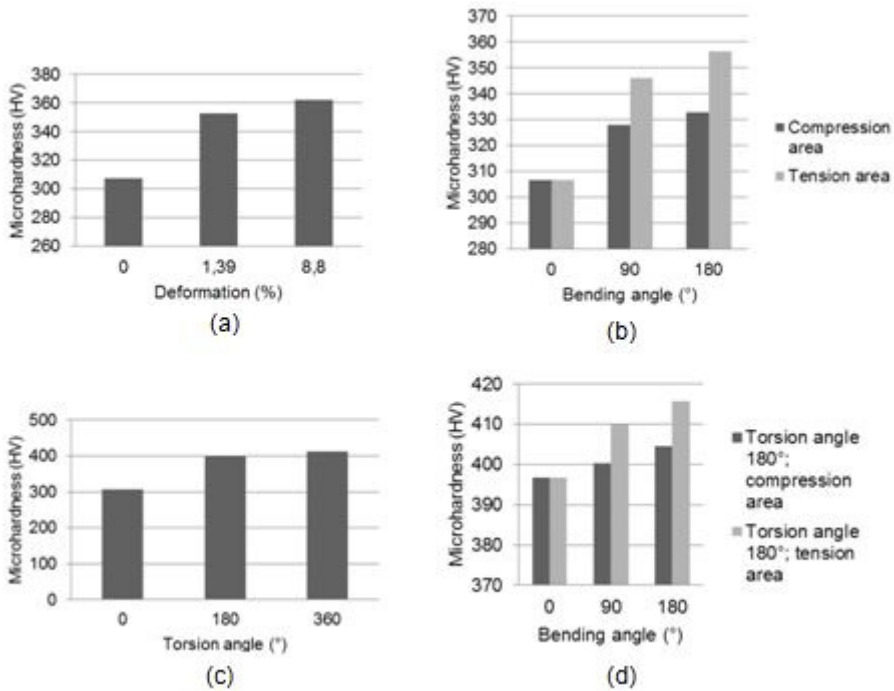


Figure 5: Deformation variation of hardness of NiTi orthodontic wire in the longitudinal cross section: (a) Tension loading; (b) Bending loading; (c) Torsion loading; (d) Combination loading (Torsion + Bending)

Figure 5 shows that micro-hardness values increased with the increase of deformation. Wire in the unloading condition had a hardness of 306 HV. The highest hardness on the wire caused a torsional load, as hardness increased over 400 HV (Figure 5c). Tension and pure bending loads caused hardness of about 350 HV on the wire (Figure 5a and 5b). Combination loads caused a small increase of hardness due to bending by pure torsion.

## Discussion

Both electrical resistivity and measurements of hardness were found to be helpful in understanding the transformations plateau in SMA NiTi under different loading conditions. By taking measurements of electrical resistivity we were successfully sensitive to the phase transformation. We noticed that the difference in electrical resistivity averaged  $15 \mu\Omega\text{-cm}$ , allowing us to know that there had been a change in the phase of NiTi SMA due to stress state. By measuring hardness we observed the different values of hardness at different values of deformation. Due to the stress state hardness was altered by 100 HV (torsion and combination loading).

## **Conclusions**

With measurement of the electrical resistivity and hardness we were able to prove the existence of various phases in SMA very well. With these two methods we could detect the change in phase under different stress states. Using these measurements we can explain where deformation occurs for better use of the superelasticity plateau. This research will be helpful to better understanding of orthodontic treatment.

## **Acknowledgments**

This article has been supported by EUREKA Programme ORTO-NITI E!6788 within the framework of the Ministry of Higher Education, Science and Technology of the Republic of Slovenia and Programme for Young Researcher within the framework of the Slovenian Research Agency.

## **Reference**

- [1] Proffit WR. Contemporary Orthodontics. 4rd ed. St. Louis: Mosby, Elsevier; 2007.
- [2] Ferčec J, Glišić B, Ščepan I, Marković E, Stamenković D, Anžel I, Flašker J, Rudolf R. Determination of Stresses and Forces on the Orthodontic System by Using Numerical Simulation of the Finite Elements Method. *A Phys Polonica A* 2012; 122: 659-665.
- [3] Lagoudas DC. Shape Memory Alloy: Modelling and Engineering Applications. Texas (USA): Springer; 2008.
- [4] Fernandes JD, Peres RV, Mendes AM, Elias CN. Understanding the Shape-Memory Alloys Used in Orthodontics. *ISRN Dentistry* 2011; 2011: 6.
- [5] Kusy PR. A review of contemporary archwires: their properties and characteristics. *Angle Orthod* 1997; 67: 197-207.
- [6] Thompson SA. An overview of nickel-titanium alloys used in dentistry. *Inter End J* 2000; 33: 297-310.
- [7] Uchil J, Mahesh K. K, Kumara Ganesh K. Electrical resistivity and strain recovery studies on the effect of thermal cycling under constant stress on R-phase in NiTi shape memory alloy. *Physica B* 2002; 324: 419-428.

## ADHESION OF LOW TEMPERATURE TIN COATING GOVERNED BY INTERFACIAL LAYER THICKNESS AND SURFACE ROUGHNESS

P.Terek, L.Kovačević, A.Miletić, D.Kakaš, B.Škorić, D.Kukuruzović

*Faculty of Technical Sciences, University of Novi Sad, Serbia*

### Abstract

Ion Beam Assisted Deposition (IBAD) was conducted at low temperature (~50°C) in order to produce TiN coatings on carburized steel samples without their distortion and softening. Mechanical properties of produced coatings are comparable to those obtained at usually used high temperatures. The improvement of the coating adhesion was carried out by incorporation of a Ti interfacial layer between the coating and the substrate. Significant improvement in scratch test adhesion was found with increase in interfacial layer thickness. In order to determine its influence on the adhesion strength, the substrate roughness was systematically varied. It was observed that adhesion strength increases with the increase in the surface roughness. This trend is contrary to the findings reported by other authors which suggest the existence of two opposing mechanisms acting during the adhesion testing. Atomic force microscopy (AFM) revealed that except the surface roughness the samples displayed differences in the coating grain size.

*Key words: IBAD, Low temperature deposition, Interfacial layer, Hard coating, Roughness, Adhesion*

### Introduction

The application of hard coatings on carburized steels results with a composite structure characterized by high case hardness, excellent core toughness and high load bearing capacity [1]. Successful production of such duplex composite requires low process temperatures during the coating deposition [2]. However, the most important exploitation properties of wear resistance coatings can hardly be attained by low temperature deposition processes. This is due to a lack of energy in the growing film that causes little surface or adatom mobility and hence results with a poor coating density and a coarse grain structure. In order to impart additional energy into a growing film ion bombardment of substrates is applied during deposition process. Such a treatment causes reordering of the atoms being deposited thus leading to a denser microstructure, reduced intrinsic stresses and enhanced mechanical properties of coatings [3]. Ion Beam Assisted Deposition (IBAD) is a combined process of coating and ion bombardment. It has a clear advantage of being successfully utilized at relatively low temperatures [4]. IBAD process offers a great ability of controlling different deposition parameters that affect the properties of the growing coating [3, 5].

Adhesion strength is the other hardly attainable property of low temperature deposited wear resistant coatings [6]. Improving the adhesion strength is

commonly done by incorporation of a Ti interfacial layer between the TiN film and the substrate material [5]. A lower elastic modulus of Ti interfacial layer enhances the deflection of the crack-tip into the plain of TiN coating [4, 7] in this manner it acts as a barrier to crack propagation. Additionally coating adhesion can be improved by Ion Beam Mixing (IBM) process which occurs during ion bombardment. In this process the coating adhesion is enhanced as a result of ballistic collisions where film atoms are driven into the substrate and substrate atoms into the coating [4].

The aim of this research was a low temperature preparation of TiN coatings which adhesion strength and hardness are comparable to those obtained at usually used high temperatures. Additionally, study of the influence of the interfacial layer thickness and substrate roughness on the coating adhesion is presented.

## **Materials and Experiment**

TiN coatings were deposited in an IBAD chamber using 5kW e-beam evaporator and 5cm Kaufman ion source. Carburizing steel 20MnCr5 disks quenched to a surface hardness of 750 HV were used as substrate material. Prior to deposition the substrates were sputter-cleaned by an argon ion beam for 15 min. During the deposition process the growing film was bombarded by argon ion beam applying 1KeV ion energy and  $53\mu\text{A}/\text{cm}^2$  ion current density. In all stages of the process the temperature did not exceed  $58^\circ\text{C}$ . The coatings were produced on previously polished substrates with interfacial layers in three different thicknesses (15, 25 and 60 nm). The verification of nanointerlayer thickness was done by HRSEM (JEOL JSM-7001F) analyses carried out on polished cross sections of the samples. Coating adhesion was evaluated by the progressive loading "Revetest" scratch tester. Coating hardness was measured using the CSM nanohardness tester and the "Fischerscope HM2000 S" Microhardness Measurement System. A coating with 60nm thick interfacial layer is produced in three degrees of surface roughness: sample 1 – substrates ground using 400 grit SiC paper; sample 2 - substrates ground using 1500 grit SiC paper; sample 3 - substrates polished using  $1\mu\text{m}$  diamond paste. Surface morphology was characterized by the atomic force microscope VEECO diCP II. Scanning electron microscope (SEM JEOL JSM 6460 LV) was employed to investigate scratch test channels and microstructure of the coatings.

## **Results and discussion**

Adjusting the deposition regimes and incorporation of the interfacial layer resulted with three different coatings in terms of interface layer thickness. Dimensional variance of the interfacial layer was obtained by extending the time of Ti evaporation during the stage of the layer formation. HRSEM analysis, conducted on the polished cross sections of the samples, clearly distinguished and confirmed the interfacial layer uniform thickness of 15, 25 and 60 nm. During the interfacial analyses a columnar grain structure of TiN layer was detected.

The total thickness of all deposited coatings was measured to an almost constant value of  $1\mu\text{m}$  due to same deposition conditions that were applied during their preparation. Nanohardness of TiN coating was measured to an average value

of 1961 HV. This is relatively high value considering that the deposition process was carried out at low temperatures. Such a high hardness was measured only on smaller number of coatings prepared at low temperatures by pulsed laser and cathodic arc deposition [8].

In order to evaluate the coating to substrate adhesion, scratch tests were performed on all samples. In the present study three critical loads were identified:  $L_{C1}$  - is the normal load at which the first crack occurs,  $L_{C2}$  - is the normal load at which the substrate is exposed for the first time, and  $L_{C3}$  - is the normal load at which the complete removal of the film occurs. Scratch test results are shown in Fig. 1. It can be observed that increase in the thickness of the interfacial layer progressively improves adhesion strength. First adhesive failure, i.e. flaking of the coating with thick interfacial layer occurs at the same load at which coating with thinner interface is completely detached. The highest adhesion strength was acquired for the coating with a 60 nm thick interfacial layer, where the critical loads  $L_{C1}$  and  $L_{C3}$  were measured to a value of 22 N and 79 N, respectively. The investigation of the coating with a 60 nm interfacial layer was continued on rougher substrates.

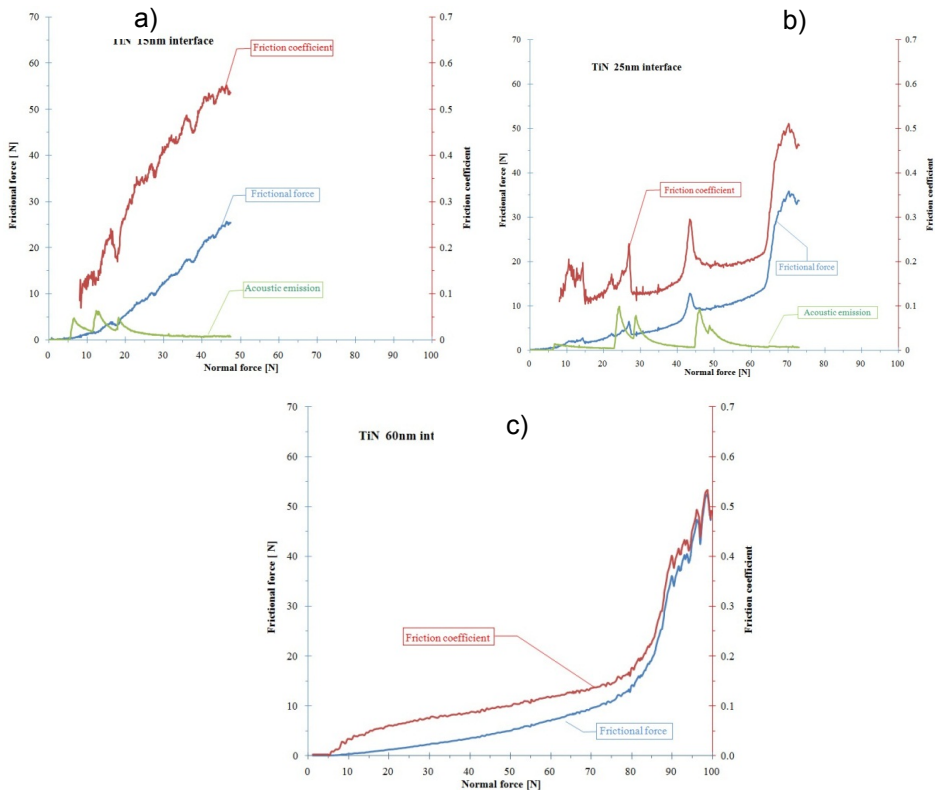
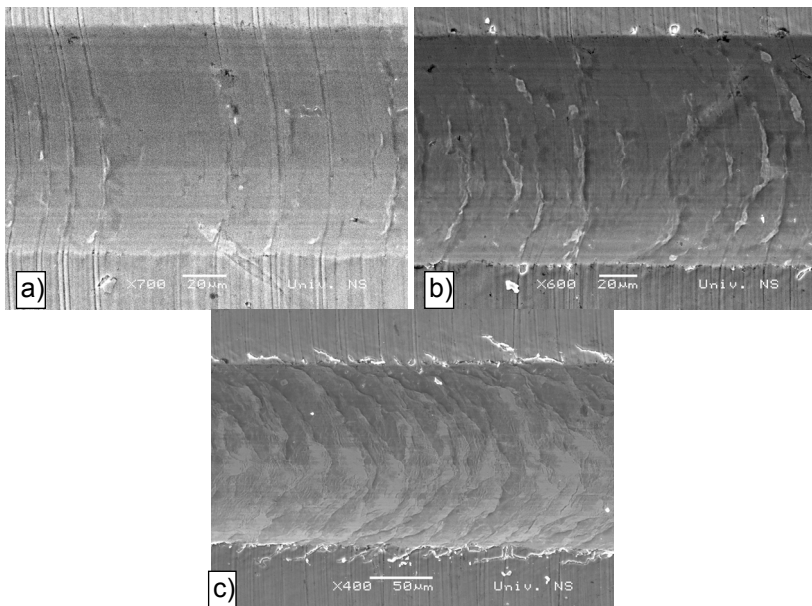


Figure 1. Scratch test graphs for coatings with: a) 15nm, b) 25nm and c) 60nm thick interfacial layer

The average surface roughness of the coated samples with 60nm interlayer was: sample 1  $Ra_1=53,03\text{nm}$ ; sample 2  $Ra_2=20,1\text{nm}$ ; sample 3  $Ra_3=3,54\text{nm}$ . The results of the scratch tests presented in the form of characteristic critical failure loads are summarized in Table 1. SEM micrographs of the scratch tracks formed on the roughest and on the smoothest sample are shown in Figs. 2 and 3, respectively. All samples show remarkable adhesion, with coating damage localized to the edge of the scratch track. Such behavior of TiN coatings is rarely found in published literature [9]. Buckling failure mode was observed for all samples. Buckling failures appear as a result of the compressive stress field in front of the moving slider, shown in Fig. 2c. Buckling was accompanied by chipping along the edge of the scratch track which occurs around the previously formed crack in the region of high tensile stress within the coating (Figs. 2b and 3b).



*Figure 2 SEM image of Scratch track of the sample 1 in its characteristic phases*

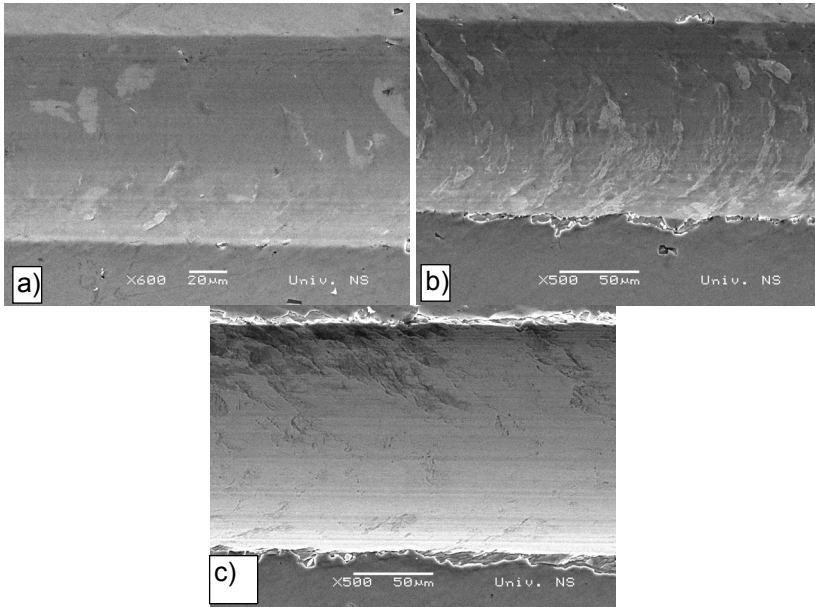


Figure 3 SEM image of scratch track of the sample 3 in its characteristic phases

The scratch resistance of TiN coatings deposited on the fine polished sample (sample 3) was found to be poorer than the scratch resistance of the same coating on the roughest sample (sample 1). First chipping formation on smooth sample occurs considerably earlier and the critical load of total coating detachment is approximately 10N lower than it is for sample 1 (see Table 1). In addition, chipping was present on a much larger scale on the polished sample (Fig 3c). The increase of the critical load with an increase of substrate roughness can be explained by different deformation modes of samples with different surface morphology. Rougher coating resists a greater amount of plastic deformation (Fig. 2a) before formation of the first chipping (Fig. 2b). As substrate roughness increases, the amount of energy required for plastic deformation of surface asperities increases as well.

Table 1 Critical load obtained during scratch tests, samples with 60nm interface

	Sample1 Ra <sub>1</sub> =53.0nm		Sample2 Ra <sub>2</sub> =20.1nm	Sample3 Ra <sub>3</sub> =3.5nm
	Parallel	Transverse	Transverse	Transverse
<b>Lc<sub>1</sub> (N)</b>	54	57	58	22
<b>Lc<sub>2</sub> (N)</b>	66	65	62	33
<b>Lc<sub>3</sub> (N)</b>	89	89	88	79

Presented results are contrary to the results reported by other authors who studied TiN coatings [10] and to the widespread belief that adhesion strength decreases with an increase in surface roughness. However, the authors cited did

not report the use of Ti interfacial layer, also the coating thickness was usually twice as large as the thickness of the considered coatings. Nevertheless, these differences are probably not sufficient to explain the opposite trends of adhesion variation with roughness. By comparing the absolute substrate roughness used in the articles cited with the one used in this research, it can be concluded that this research was conducted on generally smooth substrates. Thus, the results presented are only giving insight into a rarely studied area. It could be postulated that adhesion strength rises up to an optimum roughness, after which it starts to decline what can be explained by the existence of two groups of opposing mechanisms.

An increase of roughness induces growth of interface surface area resulting in lower shear stress values and an apparent increase in adhesion strength. Additionally, due to a higher coating hardness the load is transferred to the base material which starts to deform. On rough substrates, deformation work is used for ridge flattening, which prolongs the cracking of the coating. At the same time, peaks and valleys on the interface generate stress concentration that leads to easier crack formation and therefore, to a decrease in adhesion. This mechanism is dominant for rough surfaces characterized by high peaks and deep valleys. Considering this, an optimum coating roughness can be defined as the roughness where maximal adhesion strength can be achieved. The first group of mechanisms dominates adhesion behavior when surface roughness is below the optimum one while the second group of mechanisms dominates the region where the surface roughness is above the optimum one. In addition, for the sample with the highest adhesion (sample1) no significant difference in scratch resistance transversal and parallel to the ridges was found (see Table 1).

AFM examination of the surface morphology revealed cellular-like topography of the investigated coatings Fig.4. Regarding the columnar grain structure of tested TiN coating it is believed that the cellular cells are the curved tops of columnar grains. The different grain size and coating morphology were observed for coatings with different roughness. The roughest sample (sample 1) exhibited large grains Fig.4.a) while a coatings with intermediate and smallest surface roughness (sample 2 and sample 3) are characterized by the small grains and block cell structure where each block contains few sub cells, Fig.4.b) and c). The average grain sizes of the sample1, sample2 and sample3 are respectively: 100nm, 75nm and 80 nm. A denser coating comprised of smaller grains should require higher load for crack initiation and propagation to the substrate [11]. Accordingly, the coating life should be prolonged. It was expected that the samples with the small grains exhibit the highest adhesion strength, which is not true. Therefore, presented findings show that the adhesion failure is more governed by surface roughness mechanisms than by coating structural characteristics.

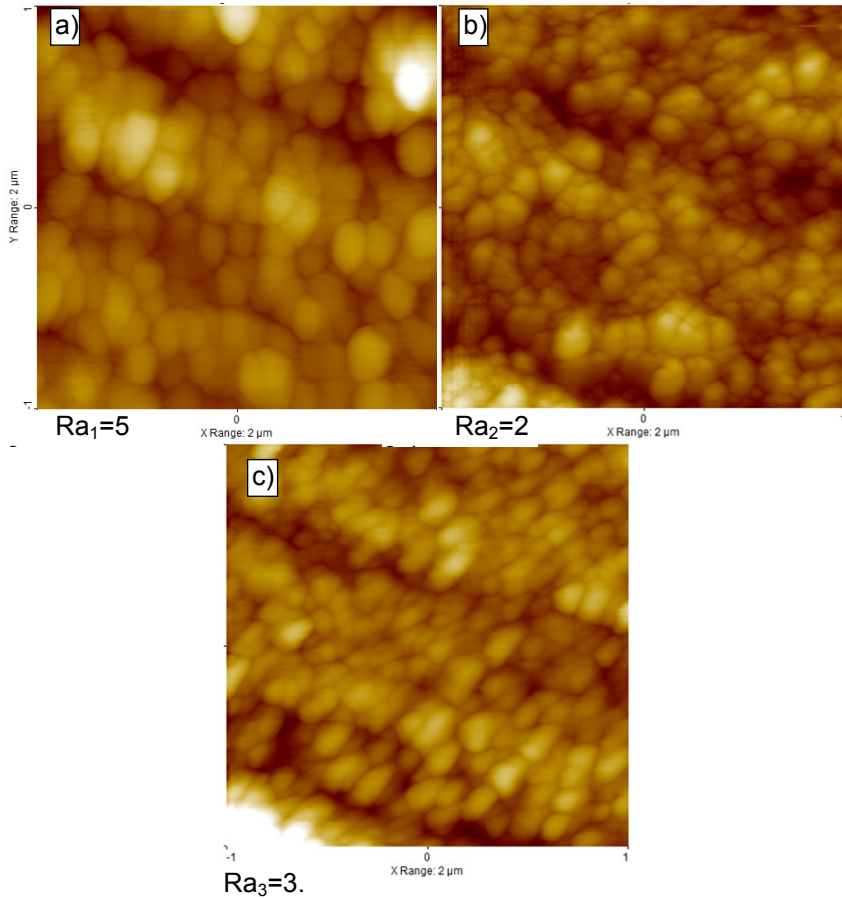


Figure 4 AFM images of coatings morphology: a)sample 1; b)sample 2; c)sample3

## Conclusions

TiN coatings produced by a low temperature IBAD exhibited mechanical properties comparable to those prepared at substantially higher temperatures. Improvement of adhesion was achieved by introducing an interfacial ion beam mixed layer between the TiN film and the substrate. An increase of interfacial layer thickness resulted in increased adhesion strength. Results of scratch tests revealed deterioration of adhesion with a decrease in substrate roughness. As these results were in contrast to the results reported by other authors, it was proposed that there exists an optimum surface finish after which adhesion starts to decline. Although the coating morphology showed dependence on the substrate roughness a correlation between the coating grain size and it's adhesion strength was not found.

## **Acknowledgement**

The authors gratefully acknowledge financial support provided by the Serbian Ministry of Education, Science and Technological Development grant III-45006.

## **References**

- [1] L.W. Ma, J.M. Cairney, M.J. Hoffman, P.R. Munroe., Effect of coating thickness on the deformation mechanisms in PVD TiN-coated steel, *Surface and coatings technology*, 2009, Vol. 204., pp. 1764
- [2] J. M. Lackner, Industrially-styled room-temperature pulsed laser deposition of titanium-based coatings. *Vacuum*, 2005, 2005, Vol. 78., pp.73
- [3] W.Ensinger., Ion bombardment effects during deposition of nitride and metal films, *Surface and coatings technology*, 1998, Vol. 99., pp.1
- [4] C. M. Cotell, J. K. Hirvonen. , Effect of ion energy on the mechanical properties of ion beam assisted deposition (IBAD) wear resistant coatings, *Surface and Coatings Technology*, 1996, Vol. 81., pp.118
- [5] J.H. Huang, C.H. Ma, H. Chen, Effect of Ti interlayer on the residual stress and texture development of TiN thin films, *Surface & Coatings Technology*, 2006, Vol. 200.
- [6] B. Navinšek, P. Panjan, A. Cvelbar., Characterisation of low temperature CrN and TiN (PVD) hard coatings, *Surface and coatings technology*, 1995, Vols. 74-75., pp.155
- [7] M.Y. He, F.E. Heredia, D.J. Wissuchek, M.C. Shaw, A.G. Evans., The mechanics of crack growth in layered materials, *Acta Metallurgica et Materialia*, 1993, Vol.41., pp.1223
- [8] B.K.Tay, X.Shi, H.S.Yang, H.S.Tan, D. Chua, S.Y.Teo., The effect of deposition conditions on the properties of TiN films prepared by filtered cathodic vacuum-arc technique, *Surface and coating technology*, 1999, Vol. 111., pp.229
- [9] J. Takadoum, H. Houmid Bennani., Influence of substrate roughness and coating thickness on adhesion, friction and wear of TiN films, *Surface and coatings technology*, 1997, Vol. 96., pp.272
- [10] F. Attar, T. Johannesson, Adhesion evaluation of thin ceramic coatings on tool steel using the scratch testing technique, 1996, Vol. 78., pp.87
- [11] D. Kakaš, B.Škorić, P. Terek, A. Miletić, L. Kovačević, M. Vilotić, Mechanical Properties of TiN Coatings Deposited at Different Temperatures by IBAD Process, *FME Transactions*, 2012, Vol.40, Broj 1., pp. 37

## "CAST IRON - A PREDICTABLE MATERIAL" NEW CAPABILITIES IN CASTING PROCESS SIMULATION TO ASSESS IRON CASTING PRODUCTION AND PROPERTIES

Jörg C. Sturm<sup>1</sup>, Janez Pristavec<sup>2</sup>, Guido Busch<sup>1</sup>

<sup>1</sup>MAGMA Gießereitechnologie GmbH, Aachen, Germany

<sup>2</sup>EXOTERM-IT d.o.o., Kranj, Slovenia

### Abstract

The classical casting material cast iron is experiencing a renaissance. High strength CGI or alloyed cast iron components are substituting previously used non-ferrous castings in automotive power train applications. The mechanical engineering industry has recognized the value in substituting forged or welded structures with stiff and light-weight cast iron castings. New products such as wind turbines have opened new markets, etc.

During the last 20 years, casting process simulation has developed from predicting hot spots and solidification to an integral assessment tool for foundries for the entire manufacturing route of castings. For cast iron foundries, the use of casting process simulation has become an important instrument to predict the robustness and reliability of their processes, especially since the influence of alloying elements, melting practice and metallurgy need to be considered to quantify the special shrinkage and solidification behavior of cast iron. This allows the prediction of local structures, phases and ultimately the local mechanical properties of cast irons.

### Introduction

The pace of change in today's marketplace is so rapid that time-to-market has to be the overriding priority. All too often metal casters feel forced to compromise on innovative ideas or approaches because it is believed there simply isn't enough time. With rapidly evolving CAE technologies including comprehensive casting process simulation, automatic casting process optimization, and new computer based component design tools it is possible for metal casters and designers to work together, concurrently, to optimize component design and casting process parameters. Through these engineering efforts metal casters can assure the sustainability and growth of their businesses while maintaining a sizable technical edge over competition [1-4].

For many cast iron foundries, casting process simulation has become a daily standard tool to assess gating and risering and predict feeding. It has become an instrument in quality systems and process optimization. State-of-the art simulation tools consider the special material behavior of cast irons with respect to its alloy composition, melting practice and metallurgy.

The current development efforts go far beyond the evaluation of casting and solidification. One focus is related to the prediction of complex defects resulting

from an interaction of metallurgy and process. A second development aspect is focused on the modeling and prediction of the entire manufacturing route. All that is required to get to the ultimate goal of casting process simulation: the prediction of local casting properties to assess the component's design, the entire technology and its economic impact on the profitability of cast iron castings.

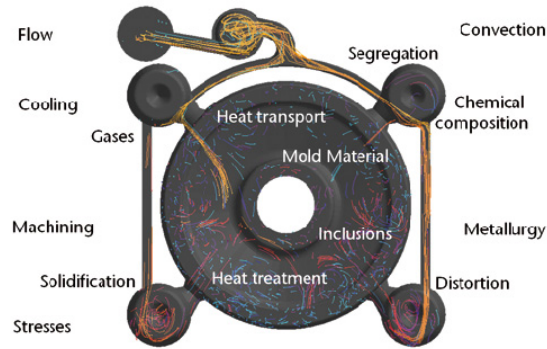


Figure 1: A challenging task: simulating the casting process to predict component properties. The biggest benefit of the casting process is its ability to perform many tasks at the same time. However, it is also its biggest draw-back, as many process parameters are linked to each other and have to be considered simultaneously.

### Pre-conditions for a successful use of casting process simulation for cast iron

The melting and metallurgical practice applied has a decisive impact on the casting integrity. This is especially true for cast iron components, in which the metallurgical processing is decisive for the ultimate casting structures and properties. Only if casting process simulation is capable of considering the impact of alloying and metallurgy can cast structures be predicted locally.

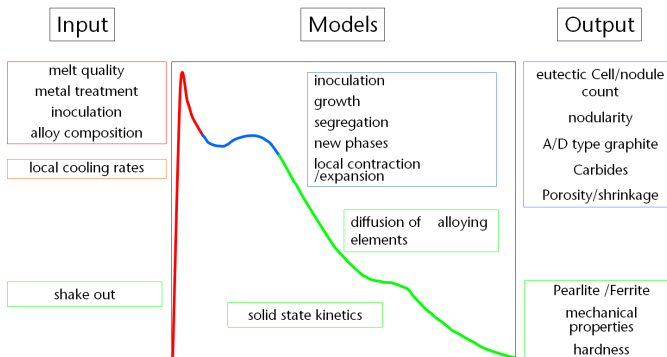


Figure 2: Modeling of the casting process for cast iron based on micro-models. Input information, applied models and results available if a microstructure model is applied for cast iron solidification simulation.

The support of the feeding related layout of the casting is still one of the most important duties for casting process simulation. Depending on the alloy poured, different feeding behaviors and self-feeding capabilities need to be considered to provide a defect free casting. Therefore, it is not enough to base the prediction of shrinkage defects solely on hot spots derived from temperature fields but also to be able to quantitatively predict them. Solidification simulation had to be combined with density and mass transport calculations in order to evaluate the impact of the solidification morphology onto the feeding behavior, as well as to consider alloy dependent feeding ranges.

The special feeding behavior of cast iron and its strong dependency of the solidification behavior on the metallurgy mean that a macroscopic hot spot prediction is not sufficient to assess the methoding of cast iron castings. In ductile iron, big hot spots mostly result in a perfect precipitation of the graphite and hence in a sound casting. On the other hand, small hot spots occurring early during solidification may lead to strong shrinkage due to austenite contraction and suppression of graphite.

To be able to predict the soundness of cast iron based on the real local shrinkage and expansion of the casting the program has to be capable of considering the kinetics of the phases being formed during the entire solidification path individually. For cast iron this means taking into account the effects of all alloying components and additionally the inoculation and melting practice and metallurgy applied.

Supercooling, recalescence and growth temperatures are dependent on local metallurgical and thermal conditions as a result of the simulations. In the same way that a real cooling curve is used as a measure for the melt quality, the „simulated cooling curve“ is a proof for the quality of the models used. Knowing the actual state of precipitating phases of graphite, austenite and cementite at any point, feeding and shrinkage can be predicted locally.

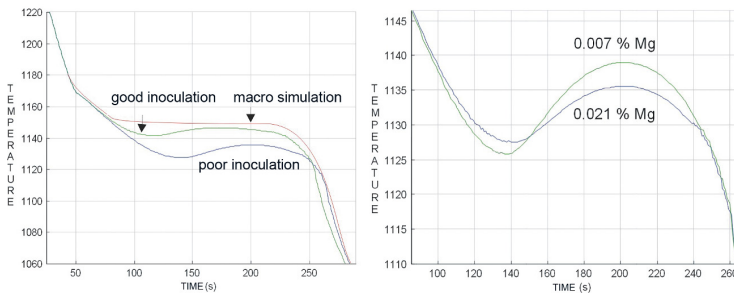


**Figure 3: Sensitivity of cast iron micromodels to the metal treatment applied. The figures show the differences between macroscopic and microscopic simulation (micromodeling) using simulated cooling curves. While the use of macroscopic heat transfer equations only modifies the shape of the cooling curve due to the released latent heat, micromodeling also considers the impact of different inoculation conditions (left). Even composition changes (i.e. change of effective Mg-content between 0.007% and 0.021%) modify the calculated undercooling, recalescence, and growth temperature (right).**

## Simulation supports methoding and robust process lay-out

The evaluation of a robust and efficient manufacturing route is still one of the main objectives to use casting process simulation in a foundry. Due to the tight interaction of metallurgy and material properties, the foundry specialist still has open questions with respect to filling and solidification of cast iron castings. This is the case for a reproducible generation of the expected graphite morphology as well as for the feeding performance, which is strongly related to the local graphite precipitation.

A first evaluation of how to make the casting can be done immediately after getting a casting design. Within minutes, the local thermal modulus, which is a good indicator for the casting lay-out, can be determined. Based on these findings, the software can propose locations and riser sizes taken from a database, **Figure 4**.

After designing the gating system and the pattern lay-out a first complete simulation of the entire process can be done. The basis for the simulation is the calculation of different phases and their amounts for the entire solidification of the casting. This allows the determination of the local sum of shrinkage as a function of the currently present contracting (liquid, austenite and cementite) and expanding (graphite) phases and its compensation through feeding from a riser.

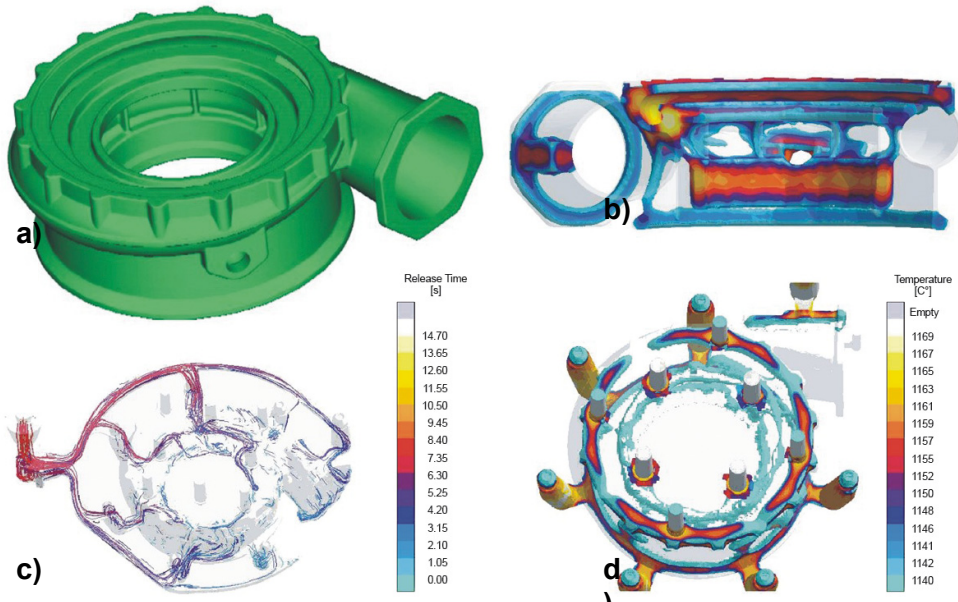


*Figure 4: Set-up of methoding for a ductile iron compressor housing. Based on the raw part CAD-model (a) a quick assessment of local thermal modulus was done (b) to determine the gating and risering lay-out (positions of chills and feeders). Subsequently the entire lay-out is simulated. Mold filling (c) and solidification (d) can be predicted quantitatively [5].*

Once isolated regions are formed which can no more be fed, the total feeding is a sum of remaining liquid and austenitic shrinkage and local graphite expansion. Additionally, mold stability and mold dilatation must be considered to take the self-feeding effects into account. Only this micromodeling approach enables the prediction of porosity in cast iron, **Figures 5, 6 and 7**.



*Figure 5: Predicting shrinkage in cast iron components. Secondary shrinkage below risers is shown for a ductile iron ring casting. This confirms that a simple heat flow calculation is not sufficient, as it only shows a ring shaped temperature distribution in the center of the casting. Only the combination of local shrinking and expansion behavior leads to a correct defect prediction.*

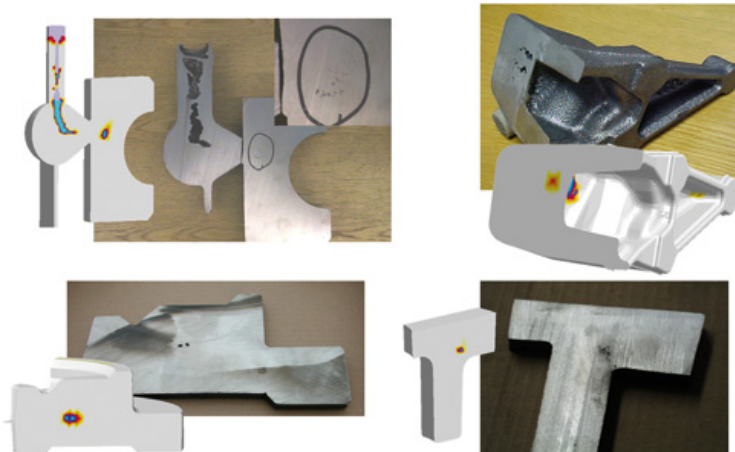


*Figure 6: Shrinkage prediction and reality. Examples displaying the accuracy of shrinkage prediction for different cast iron castings.*



Figure 7: Is a riser needed or not? The porosity prediction for an original riserless lay-out for a grey iron grade 250 casting shows problems near the top surface (left picture). The simulation clearly demonstrates the liquid shrinkage to be the root cause of the problem. Porosity prediction for a modified layout shows that a small riser completely compensates liquid shrinkage (right picture), (pictures with friendly courtesy of ITT Water and Wastewater AB (2008))

### Simulation predicts microstructures and mechanical properties in cast iron

The simulation of individual phases as a function of metallurgy, melting and inoculation practice also allows a prediction of microstructures after solidification (nodule count/number of eutectic cells, amount of grey/white solidification, amount of austenite/eutectic graphite. Through calculation of the further cooling and the local segregation down to the solid state reaction, the local phase distribution of the matrix (ferrite/pearlite distribution, coarseness of pearlite) can be assessed quantitatively. This is important information for the quality systems of foundries, **Figure 9** - a ductile iron hub (left), the accuracy of the simulation results (shown here by comparing the experimental findings and simulation results) helps to reduce continuous testing within the foundry at a customer site (right).

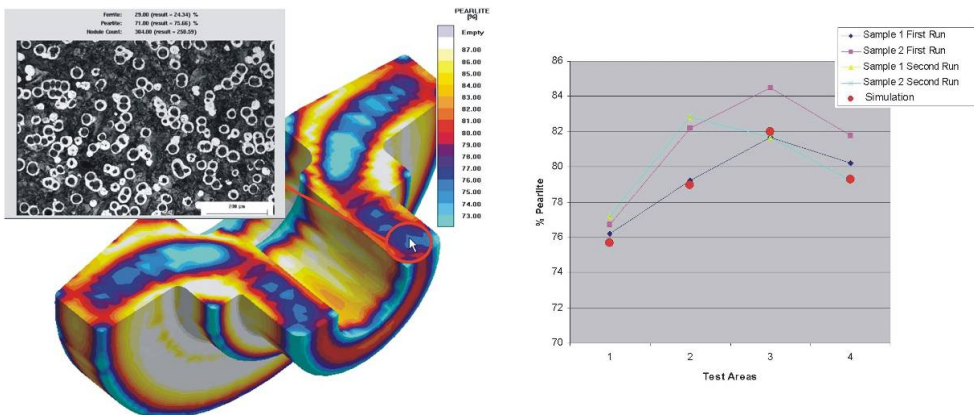


Figure 9: Assessment of microstructures and mechanical properties for ductile iron.

## **Summary**

The beauty of the casting process, realizing a complex component “in one pour” becomes a challenge if the complexity of the interactions between the different quality determining parameters are considered. A simulation tool has to meet this challenge, especially with respect to the complexity of cast iron solidification. Only if the degrees of freedom the foundry specialist has to manufacture sound castings are implemented in a simulation program, can the software become a tool for daily process and production optimization in a foundry.

On this background, the main goals of a foundry to use a casting process simulation tool - reproducible quality, increased profitability, adequate design for manufacture and entering into new markets - strengthen the competitiveness of the casting process as such. In this context “casting quality” means more than “soundness”, “cost reduction” means more than “improved yield”, and “casting properties” mean more than “meeting required standards”. The information provided by state-of-the-art casting process simulation tools supports the component’s designer in achieving a design which considers the material and process demands as well as supports the foundry specialist in setting up a robust manufacturing route.

## **References:**

- [1] P. N. Hansen, E. Flender and J. C. Sturm: “Casting Process Simulation – From the Idea 30 Years ago to Reality Today”, *International Foundry Research* 61 (2009) No. 4, pp. 12-29.
- [2] J.C. Sturm: „Die Prozess-Entwicklungs-Kette: Nutzung von Eigenschafts-Vorhersagen für Gusseisenwerkstoffe für innovative Bauteil-Konstruktionen“, *Giesserei* 90, No. 9, pp. 56-58.
- [3] Svensson, I.L., M. Wessén: "Foundry of Cast irons: Processing and Simulation ", *Numerical Simulation of Foundry Processes*, Sept. 2001, pp. 87-145.
- [4] C. Heisser, J. Sturm, “Casting Process Simulation of Compacted Graphite Iron”, (03-025), 107th Casting Congress Milwaukee, Wisconsin, 26-28 April, 2003, pp. 685-692.
- [5] J.C. Sturm: “Optimisation – Integration – Casting Property Prediction”, 66th World Foundry Congress, Istanbul, Turkey, 6-9 September 2004, pp. 171-168.

## INFLUENCE OF WALL THICKNESS ON PROPERTIES OF DUCTILE IRON FOR AUSTEMPERING

Gordana Gojsević Marić<sup>1</sup>, Damijan Žvegljić<sup>2</sup>, Branko Dikić<sup>2</sup>, Katarina Terzić<sup>3</sup>, Faruk Unkić<sup>3</sup>

<sup>1</sup> *Elkem AS Zagreb subsidiary, Radnička cesta 27, 10000 Zagreb, Croatia;* <sup>2</sup> *Kovis Livarna d.o.o., Železarska cesta 3, Štore, Slovenia;* <sup>3</sup> *Faculty of Metallurgy at University of Zagreb, Aleja narodnih heroja 3, 44103 Sisak, Croatia*

### Abstract

Investigation of wall thickness influence on production of nodular cast iron alloy intended for austempering was performed in industrial conditions. Chemical composition of the starting melt is as usual, for the production of ductile cast iron with 3.6 to 3.8% C, 1.8 to 2.2% Si, S 0.015% max, P 0.06% max, Mn 0.3% max. The melt is alloyed with Ni 18kg, FeMo 7.5 kg and 10 kg of 60-65% Cu. Those elements were added to increase hardenability of ductile cast iron for austempering or obtaining of ausferritic microstructure in samples with higher wall thickness. This low alloyed melt was treated with nodulariser FeSiMg 5,8%Mg by "Sandwich" process and inoculated in two steps; first with FeSiBa in the ladle and second in stream with FeSiRE. After melt treatment, Y-block samples were cast with 12.5-75mm wall thickness according to norm GJS 1564:2011. It was found that wall thickness significantly affects the microstructure and mechanical properties of low alloyed ductile cast iron for austempering.

*Key words: ductile cast iron, austempering microstructure, mechanical properties*

### Instruction

Commercial production of austempered ductile cast iron (ADI) started in 1972. An essential part of ADI production is high-quality nodular cast iron alloy with the adequate quantity of alloying elements.

According to definition [1], Ausferritic spheroidal graphite cast iron is: Iron based cast materials with the carbon being present mainly in the form of spheroidal graphite particles with an ausferritic matrix structure. In the English-speaking world, this material is most commonly referred to using the acronym ADI (Austempered Ductile Iron), which is produced via additional thermal processing, i.e. austempering from a normal nodular cast iron alloy with a ferrite and/or pearlite metal matrix. In Europe the material is referred to as austenite-ferrite, ausferrite or bainite nodular cast iron, wherein the first two are unambiguously connected to the microstructure of the matrix. [2].

Austempering heat treatment of spheroidal graphite cast iron is a process, consisting of heating the casting above the  $A_{C1}$  temperature and holding a sufficient time to allow transformation of the matrix to austenite (increase the carbon content of the austenite), followed by cooling at a rate sufficient to avoid the formation of

pearlite and transforming the matrix structure for a time and a temperature (above the martensite start temperature) sufficient to produce a matrix consisting of predominantly ferrite and austenite. This type of microstructure which consists predominantly of ferrite and austenite is called ausferrite and it is common to call the material austempered ductile iron. [1]

Austempered ductile cast iron (Ausferrite cast iron) strength ranges from 800 N/mm<sup>2</sup> to 1600 N/mm<sup>2</sup>, with elongation up to 10%, good toughness and high degree of dynamic strength. In comparison to various types of steel, their density is around 10% less, and with mass 2.6 times larger, their strength is three times larger than that of aluminium materials. In designs where stiffness is not a primary issue, the “specific strength” can be used to compare various materials for their suitability. **Figure 1** compares the specific strength (weight per unit of yield strength) of several engineering materials. [3]

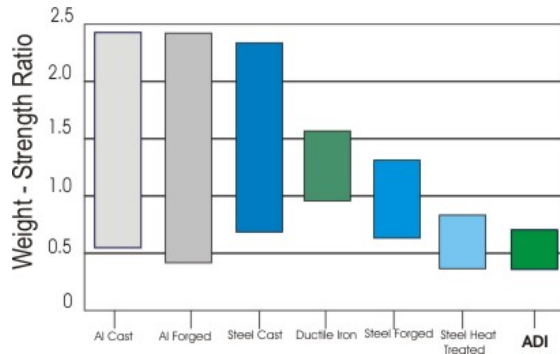


*Figure 1: Relative weight per unit of yield strength for various materials.[3]*

On the basis of their combination of properties, these materials are suitable for a variety of demanding and complex applications. Austempered ductile cast iron as a construction material is therefore used in a number of economic sectors.

**Figure 2 [4]**

The last several years have been marked by an increase in the production of austempered ductile cast iron in spite of the absence of coordinated standards and norms for its production. ASTM 897M-90 standard dating from 1990 was the first internationally recognized standard for austempered ductile cast iron. During the review of this standard EN 1564:1997 not only were the demands set in terms of differences in grade revised, but also in comparison to the previous version the name of the standard was changed to “Ausferritic spheroidal graphite cast irons“. Currently valid standard is the EN- GJS 1564:2011, according to which austempered ductile cast iron is classified according to grades listed in **Table 1** [1]

The most significant differences among EN-GJS 1564:2011 and SAE and ASTM standards are related to adding quality 800. Quality 800 of austempered ductile cast iron has the structure of a metal matrix comprising of pre-eutectoid ferrite and ausferrite. Therefore, Quality 800 is significantly more suitable for machine processing than other conventional qualities. This Quality 800 has not had

major success in the US, whereas in Europe it holds a vital role in production, where most components are processed mechanically only after austempering [ 5].

The influence of chemical composition and microstructure on the properties of ductile cast iron for austempering

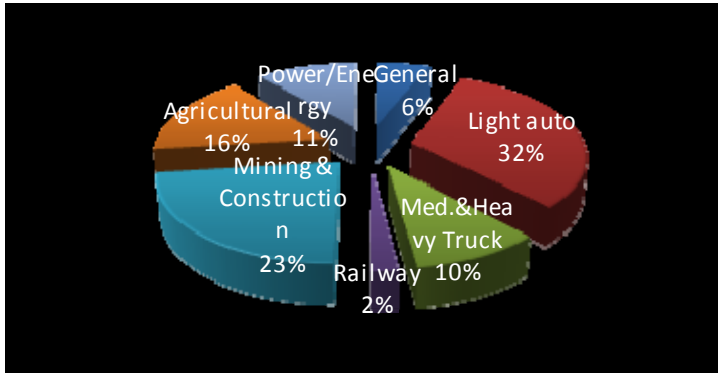


Figure 2. ADI production divided into different sectors. [4]  
Standardization of ausferrite ductile iron

A certain amount of alloying elements in ductile iron is necessary for hardenability or possibilities for ductile cast iron austempering. **Figure 3** shows the schematic illustration of austempering. In general, wall thickness higher than 19 mm requires the addition of alloying elements. A certain amount of alloying elements in ductile iron affects additionally the time period of austenitisation with the note that a material which is alloyed more requires a longer period of austenitisation. Alloying elements ensure the evasion of pearlite formation when cooling from the austenitisation temperature to austempering temperature. (C-D, **Figure 3**). **Table 2** presents recommendations for alloying ductile iron with the purpose of achieving the desired austempered ausferrite microstructure, while **Table 3** provides guidelines for carbon equivalent.[6]

Table 1. Mechanical properties measured on test pieces machined from cast samples.[1]

Material designation		Relevant wall thickness a t mm	0.2% proof strength Rp0,2 MPa min	Tensile strength Rm MPa min	Elongation A % min
Symbol	Number				
EN-GJS-800-10 EN-GJS-800-10-RT	5.3400 5.3401	t≤30 30<t≤60 60<t≤100	500	800	10 6 5
				750	
				720	
EN-GJS-900-8	5.3402	t≤30 30<t≤60 60<t≤100	600	900	8 5 4
				850	
				820	
EN-GJS-1050-6	5.3403	t≤30 30<t≤60 60<t≤100	700	1050	6 4 3
				1000	
				970	
EN-GJS-1200-3	5.3404	t≤30 30<t≤60 60<t≤100	850	1200	3 2 1
				1170	
				1140	
EN-GJS-1400-1	5.3405	t≤30 30<t≤60 60<t≤100	1100	1400	1
				To be agreed between the manufacturer and the purchaser.	
The relevant wall thickness does not affect the minimum 0.2% proof strength provided the heat treatment parameters and alloying are adjusted as a function of relevant wall thickness.					
As for relevant wall thickness of more than 100mm, the manufacturer and the purchaser shall agree on the type and size of the cast sample and the minimum values to be obtained.					

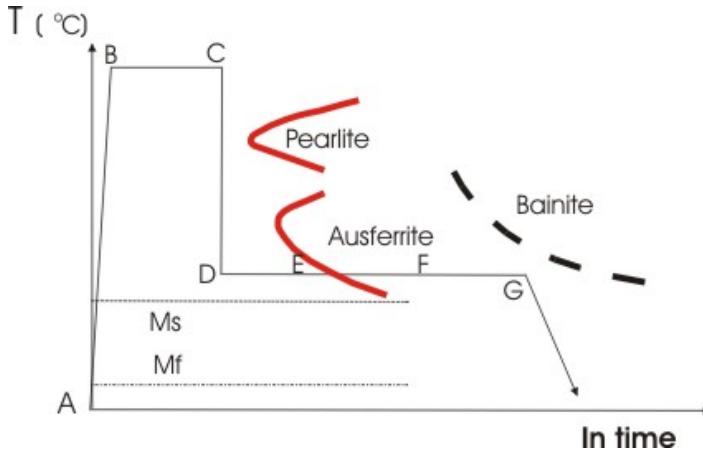


Figure 3. Schematic illustration of heat treatment schedule for realisation of ADI material. [6]

Table 2. Recommendations for Alloying ADI.[6]

Alloying elements	Recommended Limit (wt pct)	
	Manganese	Max section > 13mm
	Max section < 13mm	0.60 max
Copper	0.80 max-only as needed	
Nickel	2.00 max-only as needed	
Molybdenum	0.30 max-only as needed	

Table 3. Carbon Equivalent Guidelines for the Production of ADI [6]

Section Size (mm)	CE Range
0-13	4.4-4.6
13-51	4.3-4.6
Over 51	4.3-4.5

Most alloying elements in ductile cast iron have a significant influence on the maximum critical temperature/austenization temperature. The best mechanical properties are accomplished above austenization temperature, while temperatures higher or lower than optimal reduce strength properties. [7].

**Carbon:** by increasing carbon from 3 to 4% tensile strength is increased, but there is also a slight effect on elongation and hardness properties. Carbon should range from 3.6 to 3.8%.

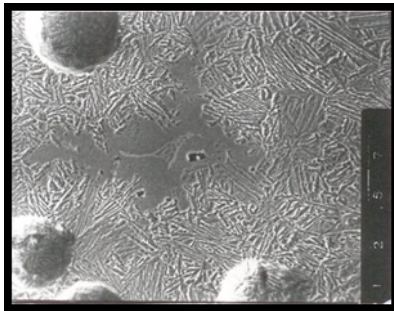
**Silicon:** has a significant influence on thermal processing cycle, it affects the increase in austenitization temperature and austempering, as well as acceleration of ferrite nucleation during austempering (D-E, **Figure 3**). In other words, it affects the speed of austempering reaction, reduces carbon solubility and accelerates carbon diffusion in austenite. By increasing silicon concentration, udarna žilavost of austempered ductile iron is enhanced, as well as the transient temperature from tough to brittle. Silicon should range from 2.4 to 2.8%. [7]

**Manganese:** lowers austenitization temperature and decelerates carbon diffusion in austenite, stabilizing the austenite and prolonging austempering reaction. Manganese also has a negative effect in terms of segregation by eutectic cell boundaries, due to which it should be added up to 0.3%. By using a special type of pig iron in the charge, Manganese level in base melt is reduced to the desired level of below 0.3%.

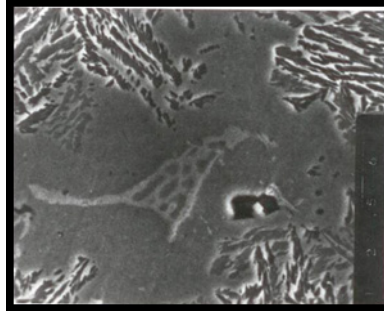
**Molybdenum:** is added to ductile cast iron intended for austempering as an alloying element that best increases the hardenability of the ductile cast iron and is vital to castings of higher wall thickness. During longer periods of solidification at higher wall thickness, u the last remains of melt there occur molybdenum carbides, which, among others, may have a harmful effect on mechanical properties and machine processing. Molybdenum carbides are clearly visible in the metal matrix when observing it with a scanning electron microscopy (SEM), **Figure 4** [8]. In castings of higher wall thickness, molybdenum should be limited to 0.2%. [7]

**Copper** is added to ductile cast iron for austempering as a more affordable substance for hardenability enhancement. It is less efficient than Mo, Mn and Ni. Copper creates a diffusion barrier to carbon at the metal-graphite border, slowing the carbon transfer between nodules and metal matrix. [9]. Austenite saturation with carbon is prolonged via a barrier (i.e. austenitization period may be significantly prolonged). Copper has a minimum or no effect on austenitization temperature, carbon solubility, carbon diffusion in austenite or austempering reaction time. However, it does have a significant impact on tensile properties and increases toughness if austempering temperature is below 350°C. It should be added up to 0.8%. [7]

**Nickel** has a very slight influence on thermal processing cycle. It only slightly reduces austenitization temperature and has no effect at all on carbon solubility and carbon diffusion in austenite. It effect on the prolongation of the beginning of isothermal and bainite reactions is minimum. Just as cooper, nickel is added in order to increase hardenability by adding up to 2 % of nickel. At austempering temperature of below 350°C, Nickel slightly reduces tensile properties, but increases impact and fracture toughness. [7]



a) SEI 500x



b) SEI1500x:



c) Mo-K $\alpha$  1500x

*SEI (secondary electron image) of Ni, Mo, Cu low alloyed ductile iron specimen, section size 25mm, austenitized 90 min. at 900°C and austempered 60 min. at 380°C. Intercellular Mo-carbide with a microvoid which appears to be formed due to shrinkage of last to freeze melt. [8].*

The castings should be free of non-metallic inclusions, carbides, shrink and dross. Proper purchasing, storage and use of charge materials will minimize the occurrence of carbides and gas defects. Proper moulding control will minimize surface defects and other sub-surface discontinuities. The castings should be properly gated and poured using consistent and effective treatment and inoculation techniques to yield shrink free castings. Any of the aforementioned non-conforming conditions will reduce the “toughness” of an ADI component (even if adequate for conventional ductile). [10]

Microstructure, i.e. nodularity degree, nodule count and the structure of the metal matrix influence significantly the selection of thermal processing parameters as well as the properties of austempered ductile cast iron [11]. The following should be met as minimum:

- Nodule Count: 100 / mm<sup>2</sup>
- Nodularity: 85%

## Experimental section

### Test material production process

The testing of wall thickness effect on the production of low-alloyed ductile cast iron intended for austempering has been conducted in industrial conditions at „Kovis Livarna d.o.o. foundry, Štore, Slovenia.

**Step 1:** Base melt produced in cupola furnace with metal charge;

- 40% special iron (Sorelmetal)
- 30% steel scrap / deep drawn steel tin
- 30% output material by EN-GJS-400-18

Upon melting in cupola furnace, the melt has been desulphurized by  $\text{CaC}_2$  in a ladle with constant stirring, after which slag has been removed and melt transferred to induction furnace.

*Table 4. Chemical composition of cupola furnace base melt after desulphurization with  $\text{CaC}_2$ .*

C	Si	Mn	P	S	Cr	Cu	Mg	Ni	Mo	CE
3.69	1.86	0.17	0.031	0.011	0.033	0.03	/	0.02	0.002	4.22

The chemical composition of base melt is within set limits for further melt treatment by pre-alloy FeSiMg and subsequent inoculation, which will increase Si level by approximately 0.75%.

**Step 2:** 2 tons of cupola furnace base melt is alloyed in medium-frequency induction furnace:

- 18kg Ni (pure)
- 7.5kg FeMo (65%)
- 10kg Cu (pure)

- Melt temperature in furnace 1439°C

The chemical composition of base melt for production of ductile cast iron intended for austempering, upon adding alloying elements is demonstrated in **Table 5**.

*Table 5. Chemical composition of the alloyed base melt.*

C	Si	Mn	P	S	Cr	Cu	Mg	Ni	Mo	CE
3.60	1.80	0.16	0.033	0.012	0.033	0.51	/	0.90	0.18	4.25

The chemical composition upon alloying is within desired limits. Quantities of elements prone to segregation, e.g. Mo and Mn are limited: Mo is 0.18 % and Mn 0.16 %.

**Step 3:** electric furnace alloyed melt is treated with FeSiMg. Processing is conducted in 1t ladle using a “Sandwich” process. Figure 5.

FeSiMg - treatment:

14 kg / t FeSiMg with ca 5.8 % Mg ( Elmag ® 5800 nodulariser ®, sizing 4-25mm, Elkem), covered with steel strips (deep drawn steel tin).



Figure 5. FeSiMg-treatment

Inoculation;  
3 kg/t FeSiBa 2-3%Ba (Barinoc® inoculant 2-6mm, Elkem) -into the ladle

1.5 kg/t FeSiRE 1.5-2%Ce (Reseed® inoculant 0.2-0.7mm, Elkem) –into the stream

Melt temperature of the first treated ton 1367°C

Melt temperature of the second ton 1343°C

The final chemical composition after FeSiMg-treatment and inoculation by FeSiBa (without FeSiRE, inoculation into the stream during casting) is presented in Table 6.

Table 6. Final chemical composition of the melt.

GSJ	C	Si	Mn	P	S	Cr	Cu	Mg	Ni	Mo
1/1	3.21	2.50	0.19	0.033	0.011	0.033	0.45	0.049	0.78	0.20
1/2	3.03	2.52	0.17	0.033	0.10	0.033	0.50	0.059	0.87	0.23

Melt quality review has been conducted using EPIC™ Thermal Analysis System. **Figure 6** presents thermal analyses sampling, and **Figure 7** the curve of thermal analyses.



Figure 6. Thermal analyses sampling.

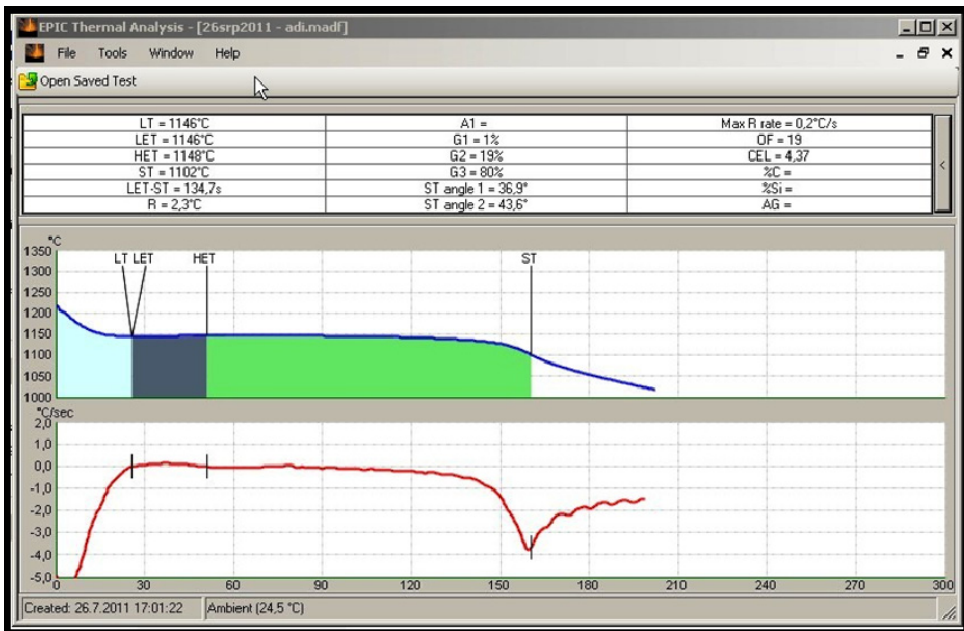


Figure 7. Thermal analyses of ductile iron melt treated with MgF<sub>2</sub>Si and inoculated with FeSiBa made by EPIC™ Thermal Analysis System, Elkem.

**Thermal Analyses parameters to look for when using EPIC™ Thermal Analysis System:**

**R** – Recalescence is a measure of carbide potential. A value between 2-7 °C is acceptable. A high R above 7°C indicates chill. A low value such as 1°C or lower can indicate over inoculation.

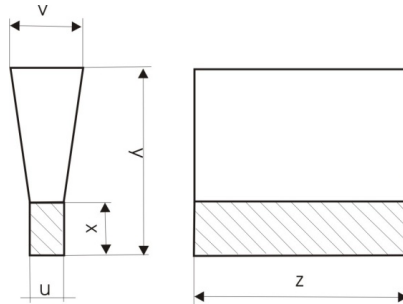
**LET** – is a measure of nucleation. In general the higher the LET value the better the iron quality.

**G1** – Is when austenite is being precipitated. In SG irons G1 should be 1% in the final treated and inoculated iron.

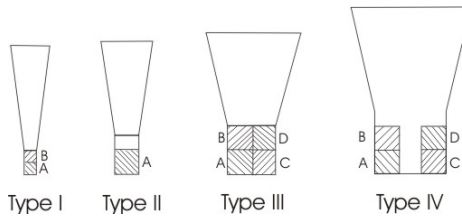
**G3** – Is a vitally important area. This is where pure graphite is being precipitated and in SG this is very important. A value of 70% of higher is required in the final treated and inoculated iron.

**LET** – ST (Graphitisation Time) – This value indicates the total time that graphite is being grown. Again this value should be as long as possible.

**ST** – This angle is the final stage of solidification and can give an indication of grain boundary activity. Generally speaking a tighter ST angle is desirable.



A) Y-shaped sample



B) Sectioning procedure for Y-shaped samples

Dimension (mm)	Type			
	I	II	III	IV
U	12,5	25	50	75
V	40	55	100	125
X	25	40	50	65
y <sup>a</sup>	135	140	150	175
z <sup>b</sup>	A function of the test piece length			

a for information only.

b z shall be chosen to allow a test piece of dimensions machined from the cast sample.

The thickness of the sand mould surrounding the samples shall be at least;

- 40 mm for type I and II;
- 80 mm for type III and IV.

Figure 8. Sectioning procedure for Y-shaped samples. [1]

Comparing the results of thermal analysis conducted on with ideal parameter values, it is apparent that the curve seen in Figure 7 presents ideal values for R with  $2.3^{\circ}\text{C}$ , LET  $1146^{\circ}\text{C}$ , i.e. it is equal to LT  $1146^{\circ}\text{C}$ , G1- 1%, G3  $80\%>70\%$ , LET-ST 134,7s /160s. ST-angle is  $36.9^{\circ}$ . According to these results, the obtained ductile cast iron quality is extremely high; however how well the thermal analysis results corresponds with the reality in the casting with a different wall thickness will be determined by metallographic testing.

**Step 4: Test sample casting**

With the purpose of testing wall thickness impact on the properties of low-alloyed ductile cast iron for austempering, samples of different wall thickness were cast (12.5 – 75 mm). Kovis Livarna d.o.o. foundry produced the models for test sample casting (Figure 9a) Figure 8 presents a schematic illustration of the principles of taking samples in accordance with BS EN-GJS 1564:2011 standard.[1]

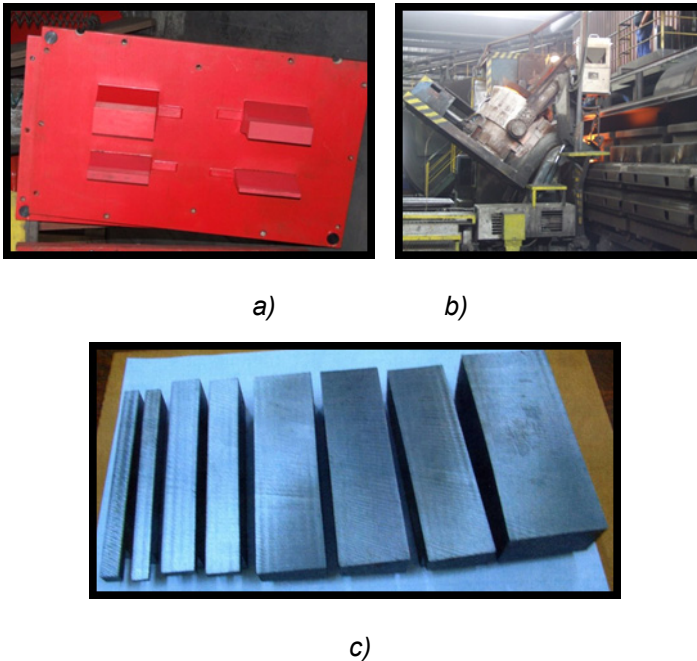


Figure 9. a) model plate for test sample casting; b) casting line c) samples relevant wall thickness ;12.5 mm, 25 mm, 50 mm and 75 mm; Y-shaped sample

**Test results**

Metallographic testing of samples taken from Y-shaped samples

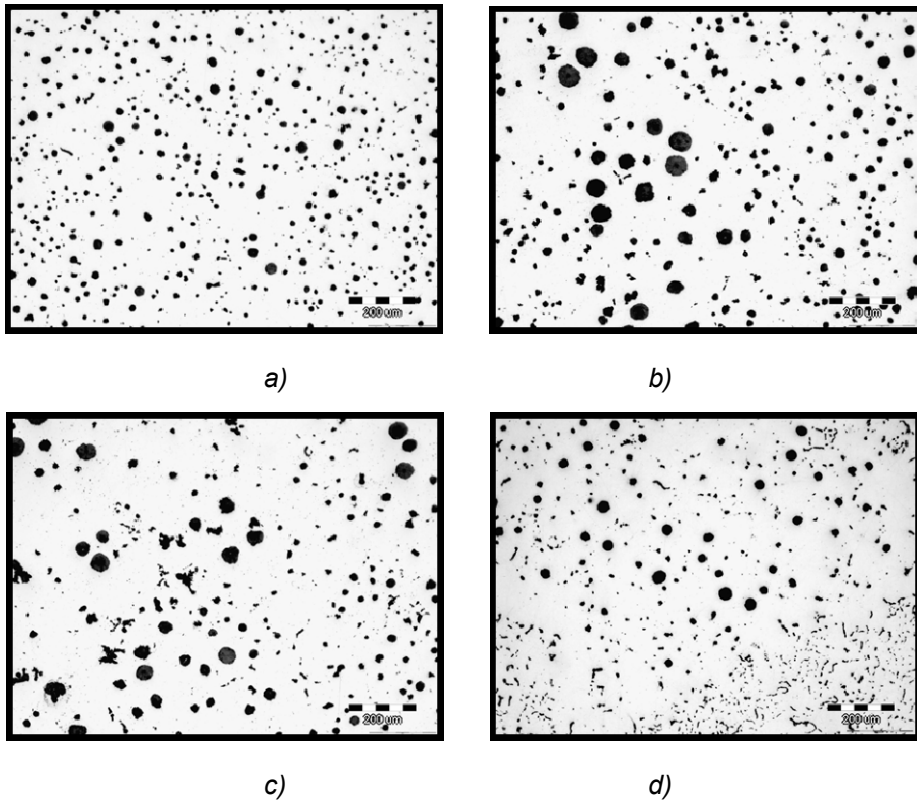


Figure 10. Graphite formation in samples relevant wall thickness:

a) 12,5 mm, b) 25 mm, c) 50 mm, d) 75 mm

Nodule count is the highest at 12.5 mm wall thickness (**Figure 10 and 13**),  $249/\text{mm}^2$ . Graphite form V+VI according to HRN EN ISO 945 standard is 95.09%, while the form III+IV is 4.59%. High nodule count and reduction of diffusion paths enable a larger share of ferrite, regardless of non-alloying elements such as Cu, Ni, as well as accelerated cooling.

With 25mm wall thickness, lower nodule count is observed with  $182/\text{mm}^2$ . Nodularity degree is approximately the same as at 12.5mm wall thickness (73%). Graphite form V+VI share is 2.21%, while the share of graphite form III+IV is increased to 6.80%. Reduction of nodule count influences the increase in pearlite share in metal matrix (almost 73%).

With 50mm wall thickness, nodularity is 10% lower, at nodule count of  $158/\text{mm}^2$ . The share of graphite form V+VI is only 77.06%, while the form III+IV is increased to 16.78%. Considering the noticed nodule degradation and appearance of “chunky” graphite, ferrite increase has been noted in comparison to wall thickness of 25 mm.

With 75mm wall thickness, graphite form V+VI share falls to only 62.27%, while graphite form III+IV share is increased to 5.49%. Nodularity degree also falls

to only 57% even though graphite particle count is  $171/\text{mm}^2$ , meaning that degradation of graphite nodules has occurred and that “chunky” graphite has appeared in the metal matrix. This graphite nodule degradation causes an increase in ferrite stage in the metal matrix (42%).

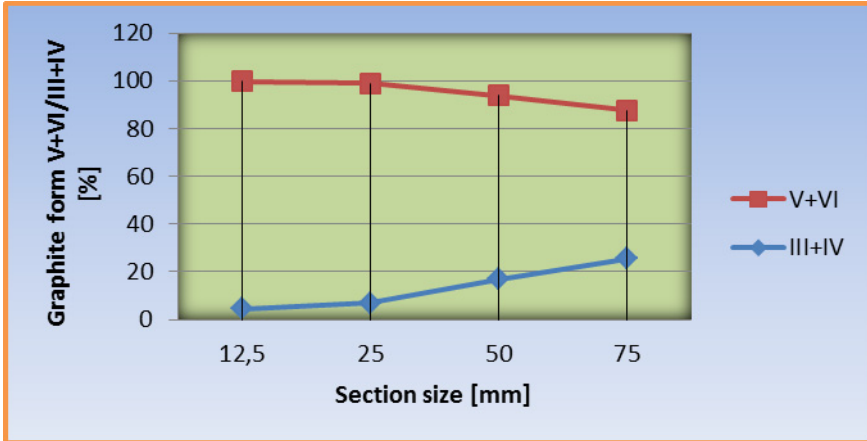


Figure 11. Graphite formation V+VI/III+IV by HRN EN ISO 945 standard in relation to the section size.

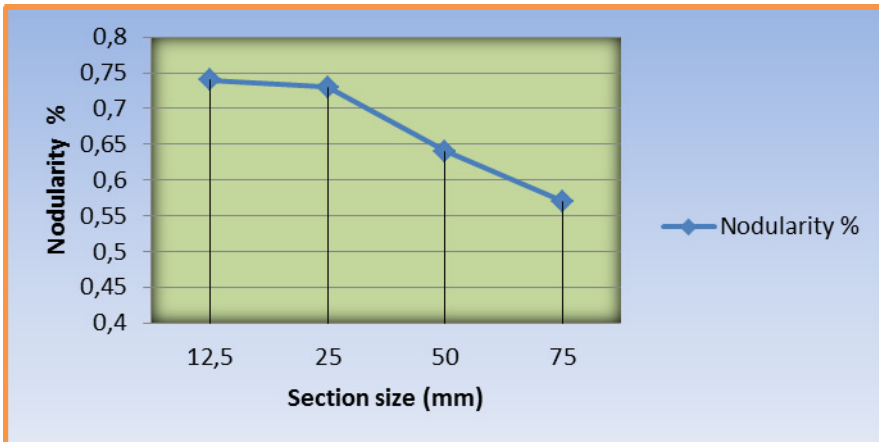


Figure 12. Decrease in nodularity, depending on wall thickness.

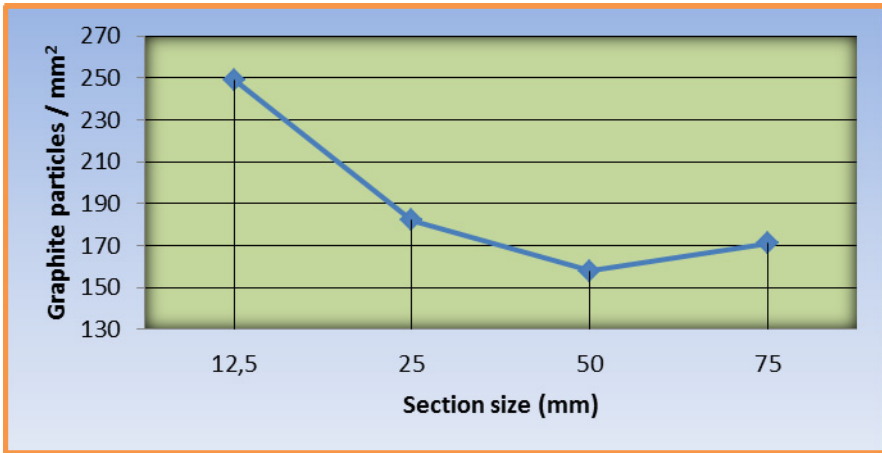
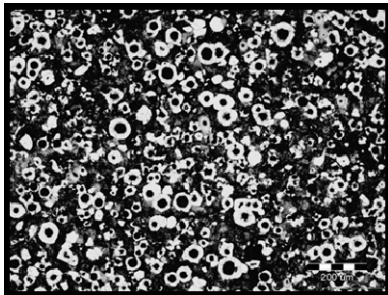


Figure 13. The diagram shows the dependence of graphite particles on wall thickness.

Nodularity degree is dependent on wall thickness, as visible in the **Figure 12** Its value decreases from 0.75% at 12.5 mm to 0.57% at 75 mm test sample wall thickness.

As wall thickness increases, nodule count in metal matrix decreases, as demonstrated in the diagram at **Figure 13** Graphite degeneration and the appearance of “chunky” graphite in the metal structure cause the increase in graphite particles by mm<sup>2</sup> at 75 mm wall thickness.

It should be noted that significant segregation of alloying elements and excretions of eutectic carbides at eutectic grain boundary has not occurred in test sample metal matrix.



a)



b)

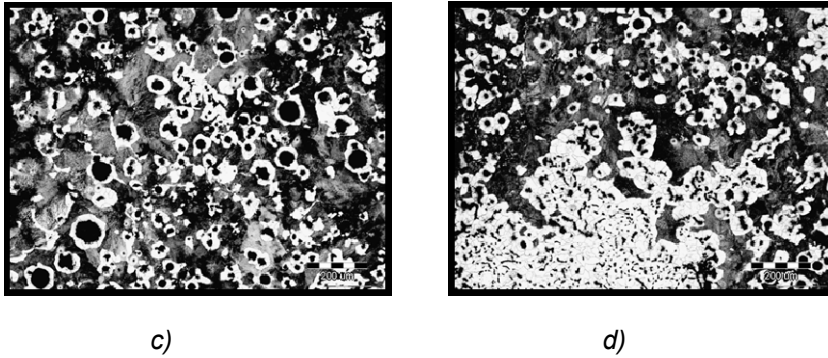


Figure 14. Microstructure of samples section size: a) 12.5mm, b) 25mm, c) 50mm, d) 75mm

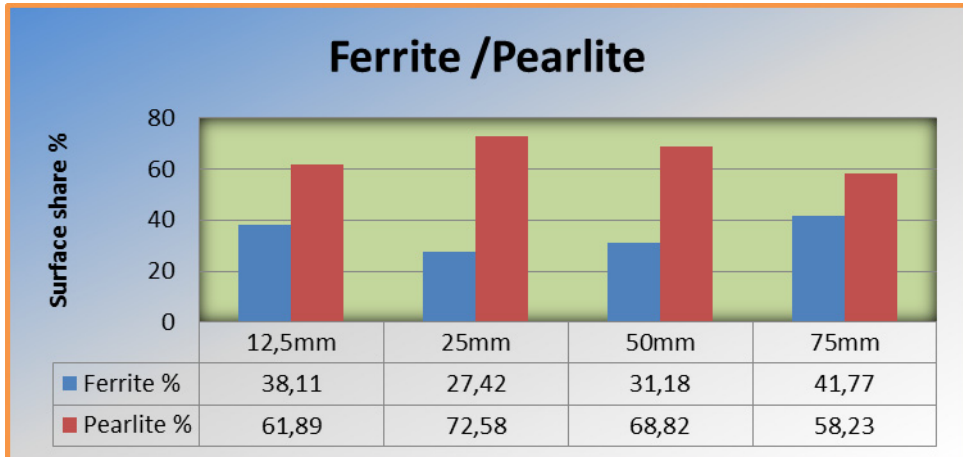


Figure 15. Graphical representation of ferrite / pearlite in metal matrix samples with different wall thickness.

The obtained results of micro structural testing confirm the significance of graphite form and distribution in terms of ferrite, i.e. pearlite share in metal matrix. Reduction of diffusion paths, whether in the form of nodule count increase or appearance of “chunky” graphite, causes the increase of ferrite in otherwise pearlite metal matrix.

The appearance of “chunky” graphite might be result of longer solidification period or increased quantity of RE in the composition, which should be determined in subsequent experiments.

#### Results of mechanical testing

The table presents the results of tensile properties of overflow samples on the tested ductile cast iron 20 mm in diameter.

Table 8. Results of mechanical properties overflow 20 mm samples.

Samples	Melt	$R_{p0,2}$	Rm	A (%)
1	GJS	444	718	7.2
2	GJS	445	709	7.8

Based on the results of mechanical properties of ductile cast iron as presented in **Table 8**, it is apparent that the sample in question is ductile iron EN GJS 700-2, even though the test sample elongation is almost triple the value in comparison to minimum according to EN 1563:2011 standard for EN GJS 700-2.

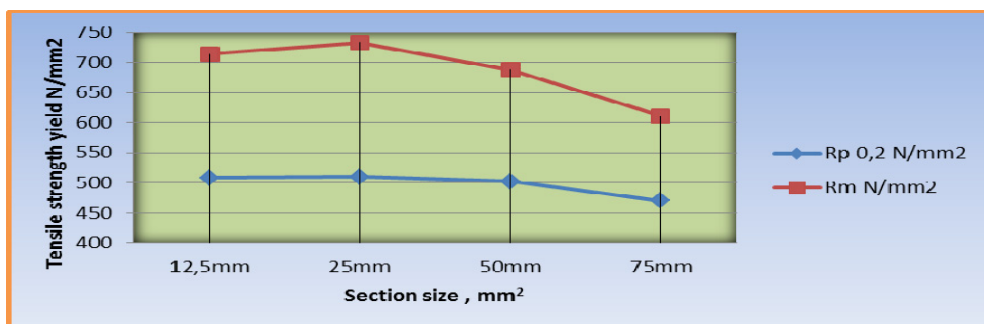


Figure 16. Graphical presentation of declining yield of the tensile strength with increasing section size.

**Figure 16** presents a graphical illustration of wall thickness influence on tensile strength and yield strength. The given diagram indicates that with the increase of wall thickness, there is a significant change in tensile strength, while a noticeable decrease in yield strength values is noted at 75 mm wall thickness. This significant reduction of strength may be the result of increased share of “chunky” graphite in the microstructure, as well as the related increase of ferrite share in metal matrix. On the other hand, tensile strength yield tensile strength maximum obtained at 25 mm wall thickness is connected to the highest share of pearlite in metal matrix of the tested ductile cast iron, which is the consequence of alloying and optimum graphite distribution in metal matrix.

## Conclusion

Based on the results of experimentally obtained values of wall thickness influence on the properties on ductile iron for austempering, it can be concluded that wall thickness influences ductile iron micro structural and mechanical properties quite significantly:

- By changing wall thickness, nodularity degree and nodule count is reduced noticeably.
- By changing wall thickness, there occurs a change in graphite form and the appearance of “chunky” graphite in the microstructure.

- Ferrite/pearlite ratio is changed depending on nodule count, i.e. the appearance of “chunky“ graphite in the microstructure.
- Mechanical properties also change depending on wall thickness, i.e. they follow the micro structural development (ferrite/pearlite ratio) directly.

The obtained micro structural properties dependent on wall thickness indicate that optimum properties of austempered ductile cast might be achieved at relevant 25 mm wall thickness, while maximum values of casting wall thickness could amount up to 50 mm. Parameters of thermal processing should be adjusted to the obtained values.

## **References**

- [1] European standard norm En 1564, June 2011, European Committee for standardization
- [2] M.Wohlfahrt, Dipl.Ing, P.Kainzinger, Dipl.Ing., W.Eichseder, Univ.-Prof.Dipl.-Ing: Austempered Ductile Iron –Steigerung der mechanischen Werkstoffeigenschaften und Einflüsse auf die Schwingfestigkeit, Giesserei-Rundschau 58 (2011), HEFT 11/12, s.261-267
- [3] John R.Keough, PEng, FASM: Austempered Ductile Iron (ADI)- A Green Alternative, Applied Process Inc. Technologies Div.-Livonia, Michigan, USA, April 2010.
- [4] Production data, 2004, <http://www.aditreatments.com>
- [5] Tim Dorn, Neenah Foundry-Neenah, Wisconsin, USA, John R. Keough, Applied Process Inc. Technologies Div.- Livonia, Michigan, USA, Tom Schroeder,Sintercast Inc.-Naperville, Illinois, USA,Tony Thoma,Wescast Industries-Brantford, Ontario, Canada: The Current State of Worldwide Standards for Ductile Iron, SAE Division 9 Iron & Steel Castings Standards Committee, 2003 Keith Millis Symposium on Ductile Cast Iron
- [6] Kathy L. Hayrynen: The production of Austempered Ductile Iron (ADI), 2002 World
- [7] B.Kovacs, Heat Treating of Austempered Ductile Iron, AFS-Transaction, Vol.99/1991/75, p.281-286
- [8] F.Unkić, FCajner, V.Novosel- Radović: A Study of the relationship between microstructure and impact toughness of low alloyed austempered ductile cast iron, ISSN 0543-5846, METABK 35(2) 73 (1996), UDK669.13:620.178.7:620.18-20
- [9] V. Goryany: Besonderheiten bei der Gefügeausbildung von ADI, Giesserei 92 (2005)09,
- [10] J. R. Keough: Suggested Foundry Requirements for Ductile Iron that is to be Austempered ADI, Updated April 2004
- [11] A. Sobota, G. Wolf, W. Stets: Einfluss von Gefügeabweichungen auf das Festigkeitsverhalten von ADI bei statischer, zyklischer und dyna, isher Beanspruchung; Düsseldorf , und Andreas Nissen, Elze Giesserei 99 04/2012 s.82-96

## **THE ROLE OF HYDROMETALLURGY IN THE PRODUCTION OF THE CRITICAL METALS**

*<sup>1</sup>Srečko Stopic, <sup>2</sup>Zeljko Kamberovic, <sup>3</sup>Efthymios Balomenos,  
<sup>3</sup>Dimitrios Panias, <sup>1</sup>Bernd Friedrich*

*1IME Process Metallurgy and Metal Recycling, RWTH Aachen University,  
Germany*

*2Faculty of Technology and Metallurgy, Belgrade University, Serbia*

*3 Laboratory of Metallurgy, National Technical University of Athens, Greece*

### **Abstract**

Critical materials (Platinum group, Rare earth elements, Ge, Ga, In,..) represent some metals having a big importance for the future of the economy in the European countries. It is very difficult to replace these critical metals by other metals. Because of the high application, the demands of these metals are increased, but the production can not follow its increased consumption in electronics, catalysis and medicine. The EU Raw materials Initiative in 2010 has reported a list of critical raw materials (totally 41) in European countries. The 14 elements as rare earth elements belong to critical materials. The future use of rare earth elements (lanthanum, yttrium, cerium,..) is expected to be increased in the European countries. The selective production of rare earth elements is the most important aim in the processing of raw materials. The hydrometallurgical treatment (dissolution of minerals under an atmospheric and high pressure, purification of solution through solvent extraction and fractional crystalization, filtration, precipitation and chemical reduction from solution) was mostly applied for the selective metal production from ores and secondary materials. The use of ionic liquids as solvent is the newest way in order to improve dissolution of critical metals. Hydrometallurgical treatment makes possible to limit the environmental impacts like residual waste producing, energetic expenditure and reagent consumption. Hydrometallurgy offers also an alternative to most used pyrometallurgical treatment. Although a pyrometallurgical treatment at higher temperatures is an efficient technique to recover some metals (copper, precious metals) from electronic waste, this treatment but does not allow the recovery of critical metals like gallium and rare earths that are lost during the process. The role of hydrometallurgy in the production of the critical metals shall be presented in this work.

### **Introduction**

Natural resources, including raw materials like minerals and metals, have a big importance for the European and global economy and inescapably govern the quality of modern life in each society. Taking into account global population increase and economic growth of developing and emerging countries, EU predicts that the pressures and risks on securing vital raw material resources for EU industries are increasing as a response to this, EU launched in 2009 the EU Raw

Materials Initiative which concluded already in ranking 41 mineral and metals as “critical” for EU based on their economic importance for the EU industry as well as their predicted supply risk (Antimony, beryllium, cobalt, fluorspar, gallium, germanium, graphite, indium, magnesium, niobium, platinum group metals, rare earths, tantalum, tungsten) [1]. Amongst these critical materials and with the highest score in supply risk, are listed the Rare Earth containing 14 elements (yttrium, scandium, and so called lanthanides: lanthanum, cerium, praseodymium, neodymium, promethium, samarium, europium, gadolinium, terbium, dysprosium, holmium, erbium, thulium, ytterbium and lutetium).

Table 1: List of critical raw material and selected emerging technologies [1]

Raw material	Emerging technologies (selected)
Antimony	Micro capacitors
Cobalt	Lithium-ion batteries, synthetic fuels
Gallium	Thin layer photovoltaics
Germanium	Fibre optic cable
Indium	Displays, thin layer photovoltaics
Platinum, palladium	Catalysts
Niobium	Microcapacitors, ferroalloys
Neodymium	Permanent magnets, laser technology
Tantalum	Micro capacitors, medical technology

Demand from emerging technologies and critical metals in 2030 is dramatically higher (as shown in Table 2)

Table 2: Global demand of the technologies/ raw materials of critical metals [1]

Raw material	Production in 2006 (t)	Demand from emerging technologies 2006 (t)	Demand from emerging technologies in 2030 (t)
Ga	152	28	603
In	581	234	1.911
Ge	100	28	220
Nd (REE)	16.800	4.000	27.900
Pt (PGM)	255	very small	345
Ta	1.384	551	1.410
Ag	19.051	5.342	15.823
Co	62.279	12.820	26.860
Pd (PGM)	267	23	77
Ti	7.211.000 2)	15.397	58.148
Cu	15.093.000	1.410.000	3.696.070

This category of raw materials, which the EU Raw Materials Initiative has labelled “critical” due to both their technological importance in the European industry and their high supply risk, as their primary production is based in a handful of countries, like China (antimony, fluorospar, gallium, germanium, graphite, indium, magnesium, rare earth, tungsten), Russia (PGM: platinum, palladium, iridium, rhodium, ruthenium, osmium), Republic of Congo (cobalt, tantalum) and Brazil (niobium und tantalum), rendering EU 100% import depended. Among these raw materials are the so called “Critical Metals (CM)”, small amounts or traces of which are used in numerous high-tech electronic, automotive and industrial applications [2]. With 8 to 9 million tons of electronic waste arising across the twenty seven members of the European Union in 2009, closing the loop for electronic and electrical devices would lead to the elimination of significant environmental problems and a create a sustainable source for critical metals in EU.



Figure 1: Average critical and precious metal concentration per high tech electronic device

Similarly to electronic waste, recycling spent automotive catalyst converters is valuable source of critical metals and namely of Platinum Group Metals (PGMs) and Rare Earth Elements (REEs). Environmentally processing 2 tons of the used auto catalytic converters can avoid mining 150 kg of ores and all the following stages which are necessary to obtain pure metal PGMs. Today it is estimated that almost 30 % of all PGM ever mined have been used for auto catalytic converters and more than 2,000 tons of these is still globally “on the road” [2]

### Rare Earth Elements (REE)

Rare Earth Elements (REE) is the collective name for the elements samarium, yttrium, lanthanum and the 14 elements following lanthanum in the periodic table (the so called lanthanides). They occur mainly in minerals like bastnaesite and monazite, and can only be mined collectively. Due their chemical similarities and high chemical activities REE extraction is very difficult to achieve

and requires intense processing conditions, while REE separation is practiced through multiple processing cycles. The REE and their compounds (oxides and chlorides) are used in numerous areas of industry for a wide range of purposes, including metallurgy, catalysts in the chemical industry, colouring of glass/ceramics, production of magnets, phosphors and batteries. Additionally they are vital elements in emerging technologies like Solid State Fuel Cells, Superconductors and high performance magnets.

Currently China controls one third of REE world reserves and has monopolized the global market of REE production as in 2009 it produced 97% of global consumption. In light of stockpiling practices and export taxes currently employed by China, REE prices have risen, while concerns for possible restrictions or even ban of Chinese REE exports exists. With numerous European industries heavily depended on REE raw materials, EU must secure a viable current and future supply of REE minerals as well as develop from the ground up the currently non-existent European REE extraction and processing industry.

### REE extraction and refining technologies

All existing REE extraction technologies while custom developed for processing specific ore concentrates, follow in general three steps: (i) **REE ore chemical treatment**, where REE are retrieved collectively from the ore concentrates, (ii) **REE separation** into separate industrial REE compounds (oxides, chlorides, etc) and **REE metal production**, in the cases where REE metals are required. The general outline of developed REE extraction processes is given in figure 2.

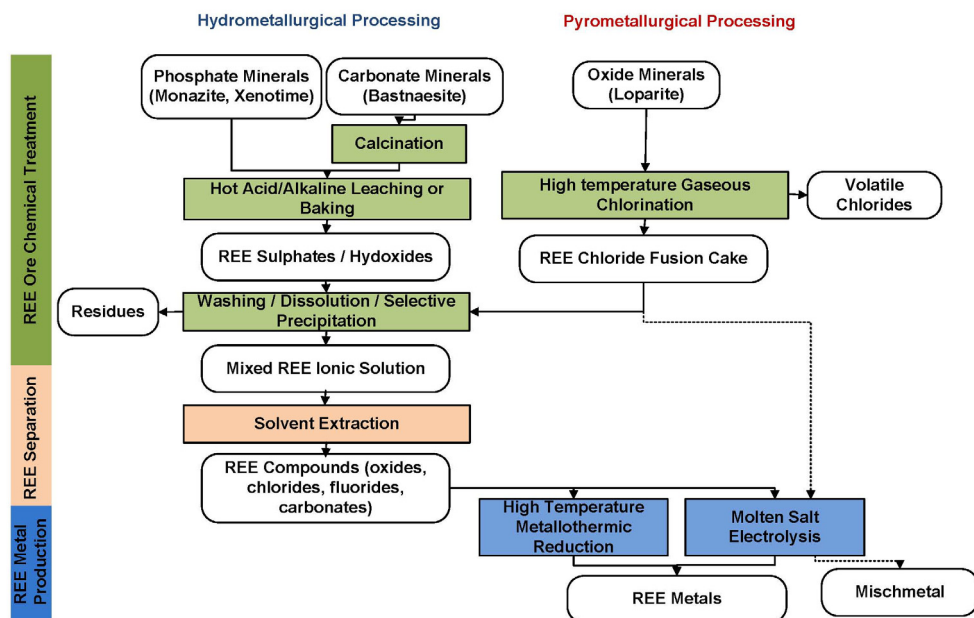


Figure 2: The most used technology for the winning of REE and their alloys

Developed **REE ore chemical treatment processes** differ significantly, depending on the type of ore processed. Phosphate and carbonate REE minerals follow hydrometallurgical processing, while oxide minerals follow pyrometallurgical processing.

**Hydrometallurgical processing** for phosphate minerals, like monazite ((Ln,Th)PO<sub>4</sub>) and xenotime (YPO<sub>4</sub>), begins with pressurized hot leaching with mineral acids or sodium hydroxide, in order to break the mineral's crystal lattice and convert REE in soluble compounds, like sulphates or hydroxides. Carbonate minerals, like bastnaesite (LnCO<sub>3</sub>F) are subjected first or in parallel in a heat treatment (calcination or baking with sulphuric acid), in order to assist decomposition of carbonates and fluorine gas removal [2]. The initial ore leaching stage is succeeded by a washing/dissolution/selective precipitation stage, whereby ore residues (including radioactive thorium oxides, where present) are removed and an ionic solution, containing only REE ions, is produced.

**Pyrometallurgical processing** is followed in the cases of oxide minerals like loparite ((Ln,Na,Ca)(Ti,Nb)O<sub>3</sub>), where gaseous chlorination at high temperature (1000- 1200°C) in the presence of reducing agents (carbon) is used [3]. The more volatile chlorides of titanium, niobium, and tantalum are separated from the less volatile chlorides of REEs and other elements, which remain as a fusion cake. This fusion cake of REE chlorides can be dissolved in sulphuric acid yielding an REE ionic solution or it can be treated directly by molten salt electrolysis to produce cerium mischmetal [4]

The **REE separation** from mixed ionic solutions poses one of the most difficult problems in inorganic chemistry [4], due to their chemical similarity. Fractional crystallization and ion-exchange techniques are used to separate them in small amounts but commercial separation generally is achieved using liquid-liquid solvent extraction [5]. This process consists of addition of a solvent composed of a mixture of organic compounds to the pregnant aqueous solution in a series of mixing/settling cells that allow repetitive fractionation during a more-or-less continuously flowing process. Following precipitation and drying, specific REE compounds (usually oxides) with purities in excess of 99.99% can be produced by such process.

The **REE metal production**, due to REE's highly electropositive character, is currently achieved through molten salt electrolysis of REE chloride and fluoride salts or through high temperature (1000-1300°C) metallothermic reduction of REE oxides or salts from alkali metals, alkaline earth metals or aluminium [4]. Thus, the current state-of-the-art processes for REE extraction follows complicated, energy and resource intensive technologies, such as pressurized leaching at elevated temperatures with large acids consumption (and therefore large acid waste water production) , as well as multi-staged solvent extraction. Some simplified hydrometallurgical scheme for the production of metal from some ore via prepared concentrate after beneficiation was presented at Figure 3:

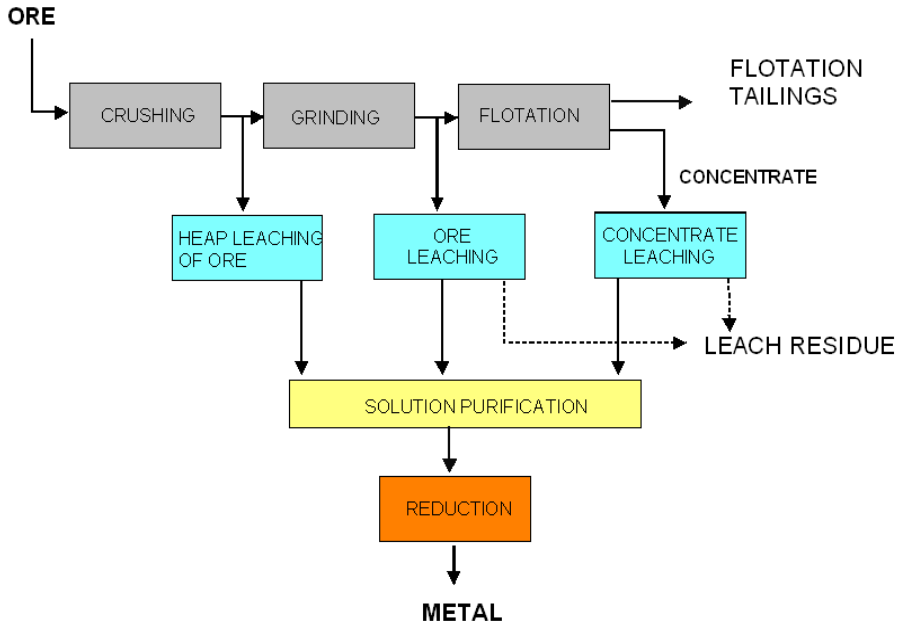


Figure 3: From ore to metal using hydrometallurgical process [6]

## Conclusion

The EU Raw materials Initiative was identified a list of 41 critical raw materials at the EU level in order to solve this problem in the future. Especially rare earth elements REE (14 elements) belong to critical materials for the economy of the European countries in the next twenty years. The future application of REEs is expected to be increased in the European countries. Regarding an environmental protection some selective winning of rare earth elements and their alloys via hydrometallurgical represents the most important aim in the processing of raw materials. Developed REE ore chemical treatment processes differ significantly, depending on the type of ore processed. Phosphate and carbonate REE minerals shall be treated by hydrometallurgical processing, while oxide minerals follow pyrometallurgical processing.

## Acknowledgment

“The research leading to these results has received funding from the European Community’s Seventh Framework Programme (FP7/2007-2013) under grant agreement n°309373. This publication reflects only the author’s view, exempting the Community from any liability”. Project web site: [www.eurare.eu](http://www.eurare.eu)”

## **References**

- [1] Critical raw materials for the EU, Report of the Ad-hoc Working Group on defining critical raw materials, EU-Commission, DG Enterprise and Industry, Brussels, 85 (**2010**)
- [2] I. MacGill, *Rare Earth Elements*, in Ullmann's Encyclopedia of Industrial Chemistry, Wiley-VCH & Co (**2005**)
- [3] Kogel et al (eds), *Industrial Minerals & Rocks*, 7th ed., Society for Mining, Metallurgy & Exploration, p. 769-792. (**2006**)
- [4] IAEA (INTERNATIONAL ATOMIC ENERGY AGENCY), VIENNA. , Technical Reports Series No. 402. (**2001**)
- [5] Dietz, M. L., *Separation Science and Technology*, 41, 2047-2063 (**2006**)
- [6] K. Knuutila, The Role of Hydrometallurgy in the winning of Non-Ferrous Metals, *World of Metallurgy-ERZMETALL* 62, 3, 142. (**2009**)

## EXFOLIATION AND PITTING CORROSION SUSCEPTIBILITY IN A MODIFIED 5083 TYPE ALUMINIUM ALLOY

Akram Halap<sup>1</sup>, Miljana Popović<sup>1</sup>, Veselin Vaščić<sup>2</sup>, Tamara Radetić<sup>1</sup>,  
Endre Romhanji<sup>1</sup>

<sup>1</sup>*Dept. Metall. Eng., Faculty of Technology and Metallurgy, University of  
Belgrade,*

Karnegijeva 4, 11120 Belgrade, Serbia

<sup>2</sup>Freelance Consultant

*e-mail: akrmhlp68@yahoo.com, endre@tmf.bg.ac.rs*

### Abstract

Exfoliation and pitting corrosion were tested in a 5083 type alloy sheet (modified with an addition of 0.5 wt.% Zn), after applying different thermo-mechanical treatments. Hot rolled 5083 plates were laboratory cold rolled to 15% - 54%, and subsequently annealed at 220°C and 280°C. The performed tests have shown that exfoliation corrosion developed after > 50% cold rolling deformation and low temperature annealing at 220°C and 230°C. The pitting corrosion was less aggressive and appeared to be active after higher cold rolling deformations (40% - 50%) and higher annealing temperatures (260°C and 280°C).

*Keywords: 5083 Aluminium Alloy, Thermo-mechanical Treatment, Exfoliation, Pitting*

### Introduction

Al-Mg alloys found a wide range of applications, especially in the constructions of transportation means due to the attractive strength to weight ratio, good weldability and formability as well as a high corrosion resistance [1-8]. However, Al-Mg alloys with more than 3% Mg, due to the limited room temperature solubility of Mg in Al matrix (1.9 wt.% Mg), can be sensitized and become susceptible to intergranular corrosion (IGC) [9-13]. One of the manifestations of IGC is a specific lamellar type of corrosion, with a blister surface appearance, known as exfoliation. It is a form of IGC that occurs on the surface of wrought aluminium alloys [14-16], with a highly flattened grain structure. Another, probably the most common corrosion type, also associated with a specific surface appearance, is a pitting corrosion. It is a form of extremely localized corrosion that leads to the creation of small holes or pits in the structure, usually covered by the corrosion products.

The objective of this work is a consideration of exfoliation and pitting corrosion appearance in a 5083 type alloy sheet, modified with Zn addition, after applying different thermo-mechanical treatments.

## Experimental

*Material.* The as received material was hot rolled 7.4 mm thick 5083 type alloy plate, supplied by Impol-Seval Aluminium Rolling Mill. The chemical composition of the tested alloy is given in Table 1. Commercial 5083 type alloy was modified with an addition of 0.5 wt.% Zn, which is approximately as double as the Zn level limit of 0.25 wt. % defined by the ASTM standard for 5083 type alloy (B 928/B 928M – 04a).

The as received hot rolled plates were laboratory cold rolled to 3.5 mm and inter-annealed at 350°C/3h. Such samples were further cold rolled by different deformations ranged from 15% to 54%, and then finally annealed in the temperature range of 220°C - 280°C for 1h, 2h and 3h and air cooled.

Table 1. Chemical composition of the tested alloy (wt.%)

Mg	Mn	Cu	Fe	Si	Zn	Cr	Ti	Sr
5.13	0.718	0.128	0.337	0.11	0.513	0.008	0.0254	0.003

*Corrosion Testing.* The susceptibility to exfoliation and pitting corrosion was determined by visual inspection using ASSET method (Method for Visual Assessment of Exfoliation Corrosion Susceptibility of AA5xxx Series Al alloys), described in ASTM G66 standard.

## Results

Exfoliation and pitting corrosion susceptibility was ranked by visual inspection, according to ASTM G66 standard, using the following letters to describe the degree of pitting corrosion: N - no appreciable attack or A, B and C level (A and B are acceptable, C is susceptible). In case of exfoliation corrosion (beside N) the ratings are as follows: A, B, C and D (A and B are acceptable, C and D are susceptible). Combination of two letters was used in many cases when the surface morphology could not be described by one letter due to mixed or boundary type surface appearance with respect to standard photographs given in ASTM G66 standard.

The ratings of different levels of exfoliation and pitting corrosion with respect to the applied cold rolling reductions and annealing temperatures are shown in Figs.1a-f and 2a-f. The results of previously determined general IGC susceptibility of the tested alloy, expressed as a mass loss per unit area [17], defined according to ASTM G67 standard, was also attached (square symbols in Figs.1 and 2).

The results shown in Fig.1 indicate that unacceptable C level of exfoliation appeared after 54% deformation and low temperature annealing at 220°C and 230°C, for all applied annealing times (Fig.1a and 1b).

It should be noted that annealing time did not bring any significant exfoliation or pitting susceptibility variations in the range of applied annealing temperatures and deformation degrees.

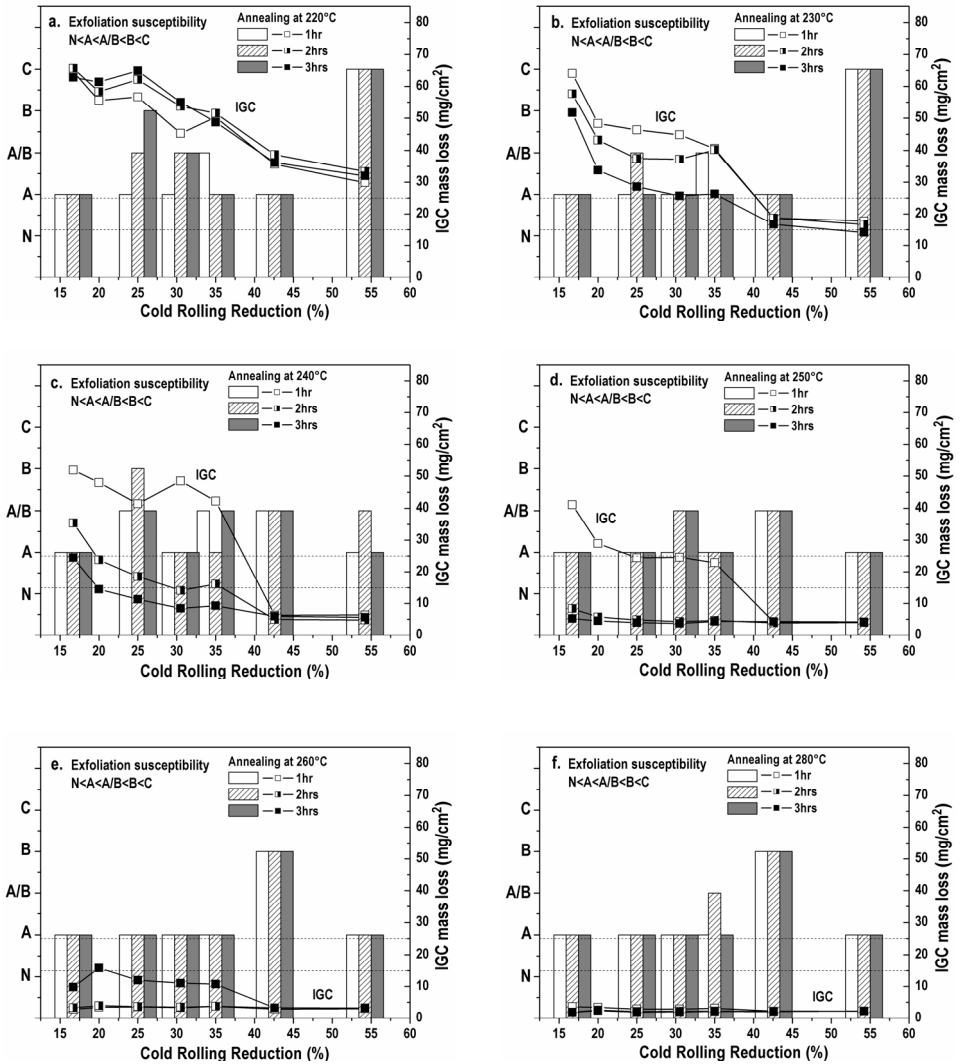
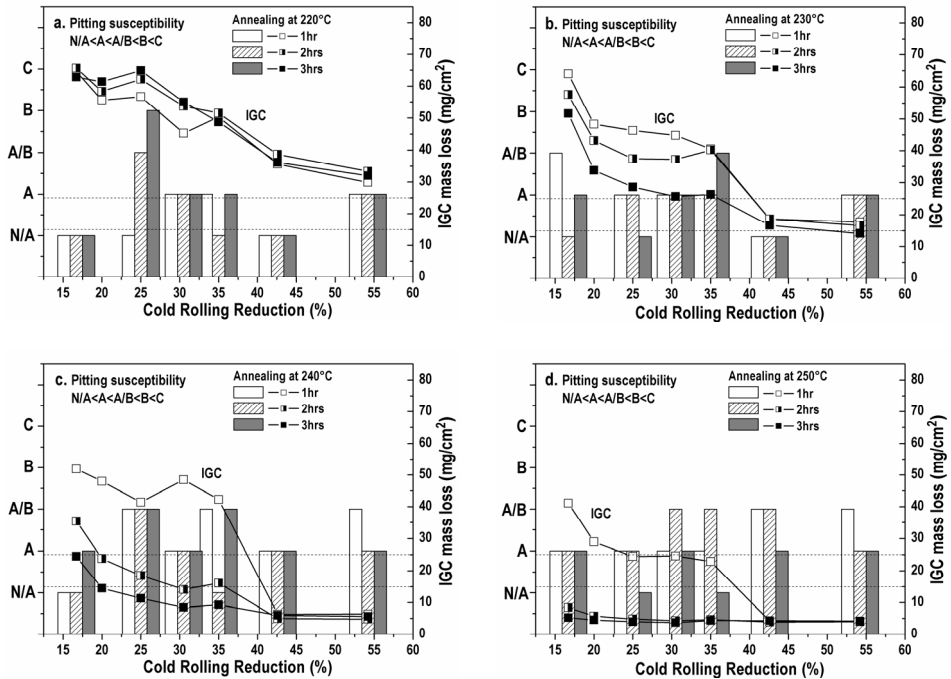


Figure 1(a-f). Ratings of different levels of exfoliation corrosion (according to ASTM G66 standard) for the samples cold rolled with different reductions (up to 55%) and subsequently annealed in the range of temperatures from 220 °C to 280 °C. The appropriate data for the IGC susceptibility were also shown (square symbols). Values below the lower line (IGC=15 mg/cm<sup>2</sup>) indicate IGC resistance, while above the upper line (IGC=25 mg/cm<sup>2</sup>) indicate IGC susceptibility.

The most detrimental pitting corrosion susceptibility, described as C type surface appearance, was not recognized at all (Fig.2). However, after higher degree of cold rolling reductions (42% and 54%) and higher final annealing temperatures (260°C and 280°C), B level of pitting susceptibility was identified (Figs.2e and 2f).

Illustrations of the surface appearances for the samples passed the ASSET test, and used for exfoliation and pitting assessment, are shown in Figs.3 and 4. Figure 3 shows that the surface appearances of the specimens cold rolled with low degree of deformation was without corroded surfaces and not affected by final annealing temperature. In the case of highly deformed samples (54%) subsequently annealed at low temperature (220°C or 230°C), severe C type of exfoliation appeared, as shown in Figs.4a and 4b. With increasing the annealing temperature and cold rolling reduction, the noticed exfoliation corrosion susceptibility vanished, but a B level pitting corrosion was recognized after annealing at 260°C or 280°, as shown in Fig.4e.



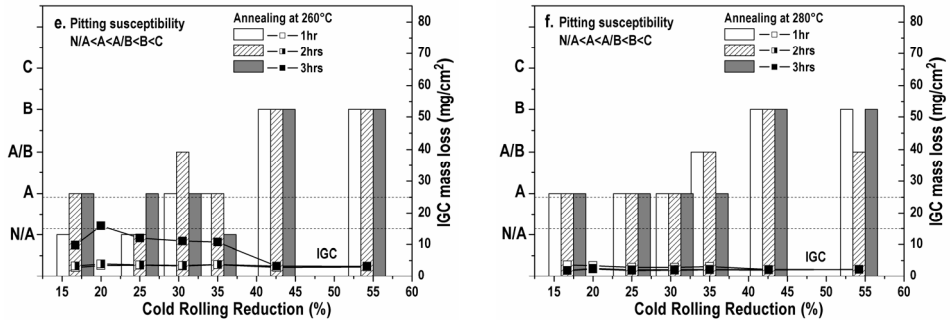
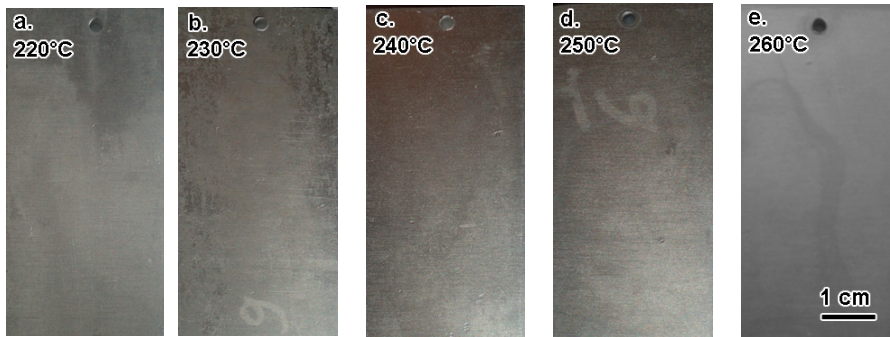
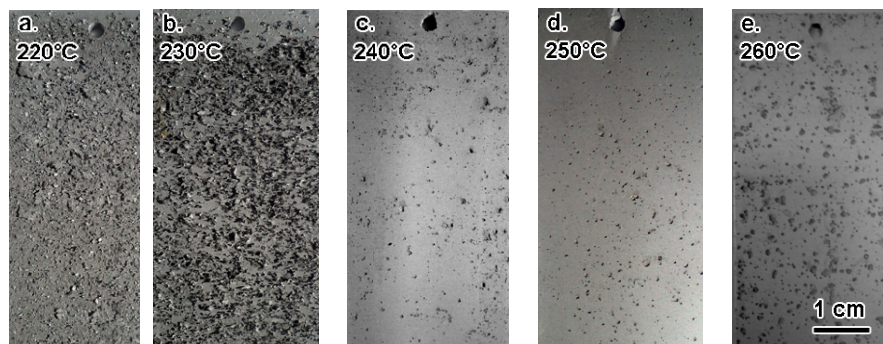


Figure 2 (a-f). The degree of pitting corrosion (according to ASTM G66 standard) identified at samples cold rolled with different reductions (up to 55%) and subsequently annealed in the range of temperatures from 220 °C to 280 °C. The appropriate data for the IGC susceptibility were also shown (square symbols). Values below the lower line (IGC=15 mg/cm<sup>2</sup>) indicate IGC resistance, while above the upper line (IGC=25 mg/cm<sup>2</sup>) indicate IGC susceptibility.



Exf.	N	N	N	N	N
Pitt.	N/A	N/A	N/A	A	N/A

Figure 3. Surface appearance for the samples deformed 16.7% and annealed at different temperatures for 2h.



Exf.	C	C	A/B	A	A
Pitt.	- (N)	- (N)	A	A	B

Figure 4. Surface appearance for the samples deformed 54.2% and annealed at different temperatures for 2h.

## Discussion

The given results rather support the earlier statement that the grain structure or grain shape introduced through different heat treatments can have an important role in developing the exfoliation corrosion [14-16]. The basic influence is related to the grain flatness or grain aspect ratio enabling a specific long – surface path IGC, and a formation of corrosion products in a few surface planes with a higher specific volume. On this way the expansion tendency developed compressive stress can lift the surface grains and form surface blisters. Therefore, the noticed appearance of exfoliation type corrosion in a highly deformed and low temperature annealed samples of the tested 5083 alloy (Fig.1.a,b and Fig.4.a,b) was assumed to be due to the highly flattened grain structure introduced by high degree of cold rolling deformation (54%) and a moderate recovery at low temperatures as 220°C or 230°C.

The exfoliation tendency was evident in a highly deformed and low temperature annealed samples, but after lower cold rolling deformations severe exfoliation was not recognized, independently on the annealing temperature or general IGC susceptibility (Fig.1a-e). Even after low temperature annealing (Fig.1a,b) when the IGC susceptibility was very pronounced, the exfoliation levels were graded as A-B. In other words, it seems that the grain flatness was a dominant parameter in developing exfoliation corrosion, which can not be correlated to IGC susceptibility. Such a behavior can be further considered in a light of the previous statement [14] that the IGC susceptibility preferably controls the penetration depth of exfoliation.

On the contrary, lowering the grain aspect ratio or having a structure with less elongated grains, the pitting type corrosion is thought to be the active process of intercrystalline corrosion [14,15]. In this experiment unacceptable C level pitting was not detected (Fig.2 and Fig.4). The appearance of a severe level of B pitting corrosion, observed after annealing at 260°C and 280°C and 40%-50% deformation (Figs.2e,f and Fig.4c,d), could be related to the recrystallization process and the development of less flattened grain structure, which enable the pitting by the progress of the intercrystalline corrosion over the shorter paths around the grains [14,15]. Using the results shown in Fig.2 it is difficult to correlate the degree of pitting susceptibility and a general intercrystalline corrosion (IGC) as the pitting was even stronger for the samples showing high IGC resistance (Fig.2e,f).

Obviously, the question of the relation of general IGC susceptibility, expressed as a mass loss, to the exfoliation or pitting appearance need some further examinations and improved understanding of the influence of basic thermo-mechanical treatment parameters and the appropriate structure features. In any case, the final relevance of exfoliation or pitting corrosion, in practice, should be considered in a limited range of structure states which are fully resistant to IGC.

## **Summary**

The exfoliation and pitting corrosion appearance was considered in a Zn modified 5083 type alloy sheet, after applying different thermo-mechanical treatments. The as received 5083 type hot rolled plates were laboratory processed by different cold rolling deformations (15% - 54%) and final heat treatments (220°C - 280°C for 1h, 2h and 3h). Exfoliation and pitting corrosion testing was performed according to ASTM G66 standard.

The results have shown that exfoliation or pitting type of corrosion can be significantly affected by applying different thermo-mechanical treatments. It was found that exfoliation corrosion developed after ~ 50% cold rolling deformation and low temperature annealing at 220°C and 230°C. Pitting corrosion was less aggressive and tend to be active after higher cold rolling deformations (40% - 50%) and higher annealing temperatures (260°C and 280°C) when the grain morphology is supposed to change, lowering the flatness in the recovery process.

The relationship between general intergranular corrosion susceptibility, defined by a mass loss, and the ratings of different levels of exfoliation and pitting corrosion should be established.

## **Acknowledgements**

The authors are grateful to the Ministry of Education, Science and Technological Development, Republic of Serbia, and Impol Seval Aluminium Mill, Sevojno, for supporting this research under contract TR 34018.

## **References**

- [1] Aluminum in Transport, Factsheet-European Aluminum Association, [www.aluminium.org](http://www.aluminium.org)
- [2] Transport and Aluminium, The Aluminium Association-IAI 2008.

- [3] Brown S, "Feasibility of Replacing Structural Steel with Aluminum Alloys in the Shipbuilding Industry", University of Wisconsin-Madison, April 29, 1999.
- [4] Raynaud GM, Gomiero Ph, "Aluminium Alloys for the Marine Market", Aluminium and its Alloys, No.79, June (1996) 73
- [5] Baumann K, Bertram M, Kistler P, In Conf. Proc.: "Light Metals in Transport Applications", Ed. by M. Pekguleryuz, Canadian Institute of Mining, Metallurgy and Petroleum, 2007, p.325-338
- [6] Summe T, "The Aluminum Advantage – Commercial Vehicle Applications", SAE, Automotive Aluminum - The Performance Advantage, [www.autoaluminum.org](http://www.autoaluminum.org)
- [7] Rail cars, Durability with High Pay Load, Internet presentation.
- [8] ATE TANKERS, Aluminium Road Tankers for fuel, chemical and water, [www.atetankers.com.au](http://www.atetankers.com.au)
- [9] Popović M, Romhanji E, Mater. Sci. Eng. A 492 (2008) 460–467
- [10] Popović M, Romhanji E, Minov B, Glišić D, In: J. Hirsch, B. Skrotski, G. Gottstein (eds.) Proc. of the ICAA11 - Aluminum Alloys: Their Physical and Mechanical Properties, vol. 2, pp. 2155–2162, 22–26 September 2008, Aachen, Germany
- [11] Davenport AL, et al, Mater Sci Forum, 519–521 (2006) 641
- [12] Chang JC, Chuang TH, Metall Mater Trans, 30A (1999) 3191
- [13] [Searles JL, Gouma PI, Buchheit RG, Mater Sci Forum, 396–402 (2002)1437
- [14] Robinson MJ, Corrosion Science, 22 (1982) 775–790
- [15] Robinson MJ, Jackson NC, Corrosion Science, 41 (1999) 1013–1028
- [16] Robinson MJ, Jackson NC, British Corrosion Journal, 34 (1999) 45–49
- [17] Halap A, et al, Unpublished work.

## NUCLEATION STAGES OF ISOTHERMAL TRANSFORMATION IN MEDIUM CARBON V-MICROALLOYED STEELS

Abdunnaser Fadel<sup>a</sup>, Dragomir Glišić<sup>a</sup>, Nenad Radović<sup>a</sup>, Djordje Drobňak<sup>a</sup>

<sup>a</sup> *University of Belgrade, Faculty of Technology and Metallurgy, Department of Metallurgical Engineering, Karnegijeva 4, 11120 Belgrade, Serbia,*  
naser.fadel@tmf.bg.ac.rs, gile@tmf.bg.ac.rs, nenrad@tmf.bg.ac.rs,  
drobnjak@tmf.bg.ac.rs

### Abstract

This work is focused on nucleation stages during isothermal austenite decomposition in two medium carbon V-microalloyed steels. Isothermal treatment was carried out in the temperature range from 350 to 600°C. Metallographic evaluation using optical and scanning electron microscopy (SEM) enabled determination of the nucleation curves of isothermally decomposed austenite. Three curves are found to be relevant to this initiation stage of transformation: the first curve is related to the grain boundary nucleated ferrite (GBF), the second curve is related to intragranularly nucleated ferrite (IGF) and the third to pearlite (P) curve. GBF and IGF curves are divided into the high and the low temperature segments as a consequence of either displacive or diffusion nature of transformation. Addition of Ti to V - microalloyed steel seems to be balanced by a slightly higher C and Mn content, leading to limited effect on nucleation stage of austenite decomposition.

*Key words: Microalloyed steel, Ferrite, Bainitic Sheaves, Acicular ferrite, Widmanstätten ferrite, Polygonal ferrite.*

### Introduction

Ferrite formation during austenite decomposition can result in two different morphologies: (i) diffusion controlled (allotriomorphic and idiomorphic), or (ii) displacive (Widmanstätten and intragranular plates) [1-5]. Allotriomorphic ferrite nucleates at the prior austenite grain boundaries and tends to grow along the austenite boundaries at a rate faster than in the perpendicular direction to the boundary plane. By contrast, idiomorphic ferrite nucleates at the inclusions/particles inside the austenite grains and can be identified in the microstructure by its equiaxed-polygonal morphology. Therefore, the balance between the number of intragranular nucleation sites and the number of sites at the austenite grain boundaries is a very important factor in the competitive process of allotriomorphic-idiomorphic ferrite formation. The prior austenite grain size exerts a significant influence on the decomposition of austenite [5,6]. An increase in austenite grain size leads to a reduction in the number of nucleation sites at the austenite grain boundaries indirectly favoring the intragranular nucleation of ferrite, i.e. the formation of idiomorphic ferrite, rather than allotriomorphic ferrite. In order to obtain bainite, the austenite grain size has to be small so that nucleation at grain

boundaries dominates, and subsequent growth then swamps the interior of the austenite grains. By contrast, acicular ferrite is nucleated intragranularly on inclusions within large austenite grains and then radiates in many different directions. The presence of a uniform layer of allotriomorphic ferrite along the austenite grain boundaries induces the transformation of austenite in acicular ferrite instead of bainite [1,3-6].

The acicular ferrite is in fact intragranularly nucleated bainite [4-6]. It is a much more disorganized microstructure with a larger ability to deflect cracks. Acicular ferrite is, therefore, widely recognized to be a desirable microstructure due to good mechanical properties [5].

Data related to nucleation phase of isothermal decomposition seems to be lacking; most of the published results deal with later steps (10s or longer), i.e. when the nucleation is well prolonged. Therefore, the aim of the present study is to clarify the influence of isothermal transformation temperature, time and titanium addition on the nucleation of ferrite and indirectly, on the development of the intragranular acicular ferrite in V-microalloyed forging steels.

## Experimental

Two commercial V- microalloyed medium-carbon forging steels with and without Ti addition have been studied. The chemical compositions of these steels are given in Table 1.

Table 1: Chemical composition of the experimental steels (wt%)

Steel	C	Si	Mn	P	S	Ti	V	N
V-Ti	0.309	0.485	1.531	0.0077	0.0101	0.011	0.123	0.0221
V	0.256	0.416	1.451	0.0113	0.0112	0.002	0.099	0.0235

Both steels were industrially ~~casted~~ cast and hot-rolled into 22mm (V-Ti steel) and 19mm (V steel) diameter bars. Bars were homogenized at 1250 °C for 4 hours, in argon as protective atmosphere and subsequently oil quenched. Specimens of 12mm height were cut and austenitized at 1100 °C for 10 min in an argon atmosphere. After austenitization, specimens were isothermally held at temperatures ranging from 350 °C to 600 °C for different holding times and subsequently water quenched to room temperature. The samples were prepared using standard metallographic techniques and etched in 2 % nital for their observation on optical and scanning electron microscope (SEM).

## Results and discussion

Fig. 1 shows the nucleation curves for both steels. In both steels, the nucleation is represented by two C curves, for low and high temperatures. In V-steel (Fig. 1a), apparently due to overlapping effects of diffusion and displacive transformations two curves are less differentiated in comparison to V-Ti steel (Fig. 1b).

The first phase to nucleate is the grain boundary ferrite (GBF) at both high (Fig. 2a) and low (Fig. 2b) test temperatures. While the GBF at high temperature is

definitely produced by diffusion, the low temperature GBF is assumed to be of Widmanstatten type [1,3,5]. High temperature behaviour is in very good agreement with results and model related to nucleation of GBF on temperatures higher than 600°C [6,7]. With increasing holding time, the intragranular ferrite (IGF) nucleation is initiated, what is represented by the IGF nucleation curve (Fig. 1). High temperature intragranular nucleation (600 – 500°C) is characterized by polygonal idiomorphic IGF ferrite. The amount of polygonal IGF ferrite increases with decreasing isothermal transformation temperature at the expense of GBF, Fig. 3a. The transformation at lower temperatures (450–350°C) is characterized by the acicular IGF ferrite, Fig. 3b. Again, there are two C curves to represent IGF nucleation due to transition from high temperature diffusion mechanism to low temperature displacive mechanism [4-6,8-10].

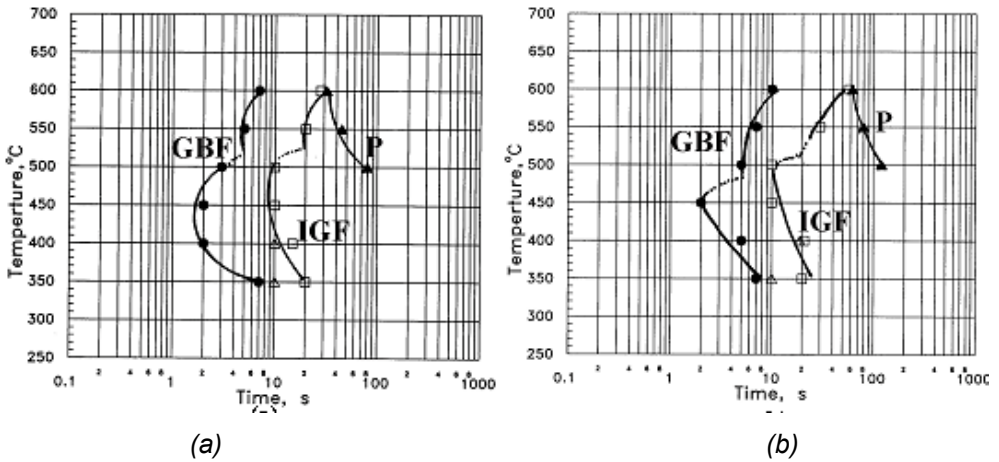


Figure 1. Initial stage of TTT diagram: (a) V- steel, (b) V – Ti steel; closed circles - grain boundary ferrite (GBF); open squares - intragranular ferrite (IGF), open triangles – bainitic sheaves (BS); closed triangles – pearlite (P).

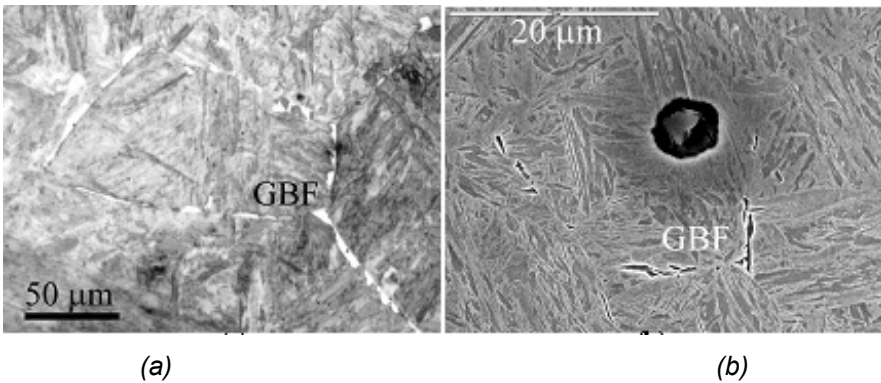


Figure 2. Grain boundary ferrite (GBF): (a) 600°C / 10 s, V-steel, optical image, (b) 350°C/10 s, V-Ti steel, SEM image.

Transition from high to low temperature takes place at about 500°C. With further increase of isothermal time, the nucleation of pearlite (P), Fig. 3a, is initiated what is represented by the P curve in Fig. 1. In the low temperature region in certain localized places bainitic sheaves (BS) and/or Widmanstätten ferrite (WSF) are formed on grain boundaries. The nucleation of these phases is indicated in Fig. 1 by open triangles. In regard to the effect of microalloying elements on the kinetics of isothermal transformation it has been shown that presence of vanadium delays the nucleation of ferrite, whereas Ti speeds it up [11-13]. In the V-Ti steel, a slightly higher carbon and manganese contents, which both delay transformation, seems to balance the influence of Ti addition. Therefore, the temperature at which the incubation time for ferrite nucleation is at the minimum (nose of the nucleation curves) is approximately the same for both steels (approx. 450 °C). In this sense Ti addition does not exert any influence on this temperature; neither the prior austenite grain size has any clear effect on the transformation as a whole.

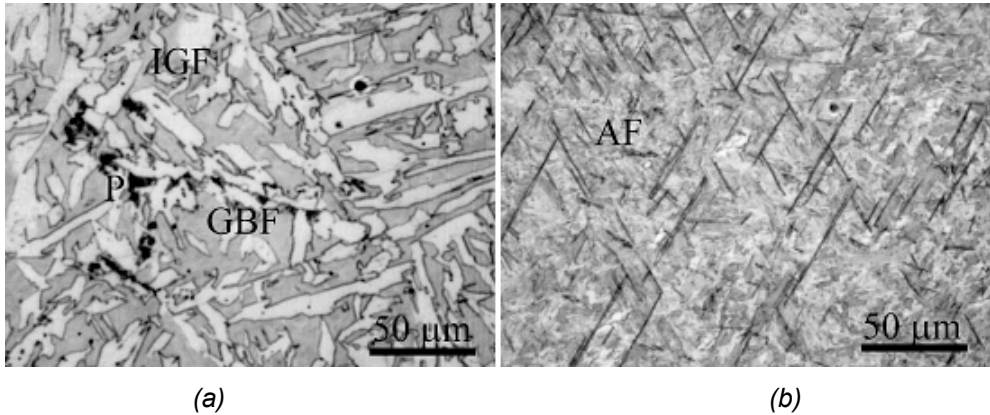


Figure 3. Intragranular ferrite (IGF): (a) 500°C/80s, V- steel, optical image of GBF, polygonal IGF and pearlite (P), (b) 350°C/20s, V-Ti steel, optical image of acicular ferrite (AF).

## Conclusion

The aim of the present study was to clarify the influence of isothermal transformation temperature, time and titanium addition on the nucleation of ferrite and indirectly, on the development of the intragranular acicular ferrite in V-microalloyed forging steels. Metallographic studies enabled determination of the nucleation curves of isothermally transformed ferrite in two medium carbon microalloyed steels. Three curves are found to be relevant to nucleation stage of transformation. First, GBF curves which extends over the entire temperature range studied (350-600°C), second, IGF curve which is divided into the high temperature polygonal and the low temperature acicular ferrite curve, and the third the pearlite (P) curve. Addition of Ti to V-microalloyed steel in this work seems to be balanced by a slightly higher C and Mn content.

## Acknowledgement

The authors are indebted to Ministry of Education and Science of Serbia for financial support (Project OI 174004) and Serbian Oil Company for supplying experimental materials. AF is thankful to Libyan Ministry of Education for providing PhD scholarship.

## References

- [1] H.K.D.H.Bhadeshia, *Bainite in Steels*. 2<sup>nd</sup> ed. London: The Institute of Metals; 2001
- [2] R.W.K.Honeycombe, H.K.D.H.Bhadeshia, *Steels: Microstructure and Properties*. 3<sup>rd</sup> ed. Oxford, Butterworth-Heinemann. 2006
- [3] C.Capdevila, F.G.Caballero, C.Garcia De Andres, *Metall.Mater.Trans.A*, **2001**, 32A, 1591
- [4] C.Garcia-Mateo, C.Capdevila, F.G.Caballero, C.Garcia De Andres, *ISIJ Int.* **2008**, 48, 1270
- [5] M.Díaz-Fuentes, I.Gutiérrez, *Mat.Sci.Eng.A* **2003**, 363, 316
- [6] C.Capdevila, F.G.Caballero, C.Garcia de Andres, *Scripta Mater.*, **2001**, 44, 593
- [7] C. Capdevila, C. Garcia de Andres and F. G. Caballero, *Scripta Mater.* **2001**, 44, 129
- [8] C.Capdevila, J.P.Ferrer, C.García-Mateo, F.G.Caballero, V.López, C.García de Andrés, *ISIJ Int.* **2006**, 46, 1093
- [9] F.G. Caballero, M.K. Miller, C. Garcia-Mateo, J. Cornidea and M.J. Santofimia, *Scripta Mater.* **2012**, 67, 846
- [10] G. Sidhu, S.D.Bhole, D.L.Chen and E. Essadiqi, *Scripta Mater.* **2011**, 64, 73
- [11] C.Garcia De Andres, C.Capdevila, D.San Martin, F.G.Caballero, *J. Mat. Sci.* **2001**, 20, 1135
- [12] A. Fadel, D.Glišić, N.Radović, Dj.Drobnjak, *J. Mater. Sci. Technol.*, **2012**, 28, 1053
- [13] A. Fadel, D.Glišić, N.Radović, Dj.Drobnjak, *J. Min. Metall. Sect. B-Metallurgy*, DOI:10.2298/JMMB120820001F, accepted for publishing, **2013**

## WELDABILITY OF PLASTICIZED POLYLACTID ACID FILMS

N. Stöhr<sup>1</sup>, B. Baudrit<sup>1</sup>, P. Heidemeyer<sup>1</sup> and M. Bastian<sup>1</sup>  
M. Nase<sup>2</sup>

<sup>1</sup> SKZ, German Plastics Center, Research and Development  
Friedrich-Bergius-Ring 22, 97076 Wuerzburg, Germany

<sup>2</sup> ORBITA-FILM GmbH, Koethener Straße 11,  
06369 Weissandt-Goelzau, Germany

### Abstract

The objective of the present work was investigations of systematically modified recipes based on polylactid acid (PLA) with polyethylene glycol (PEG) (4,000 g/mol) as one of the plasticizers frequently used in film application, in order to improve the weldability of PLA. Samples of plasticized PLA films were heated and ultrasonically welded with various processing parameters. These investigations show that plasticized PLA films can effectively be welded with heat as well as ultrasound. The obtained weld strength is strongly dependent on the amount of PEG and on the selected welding process and parameters.

*Keywords: PLA, biopolymers, films, weldability, heat welding, ultrasonic welding,*

### Introduction

PLA is a linear aliphatic thermoplastic polyester, produced from renewable resources. This biomaterial is a brittle and stiff polymer with low elongation at break. An interesting possibility is to modify the mechanical properties of PLA by adding compatible plasticizer systems [1]. When plasticized, PLA becomes increasingly flexible, so that a variety of products can be prepared in order to mimic polyvinyl chloride polyethylene, polypropylene and polystyrene, and thus meets most requirements for packaging applications [2].

For the production of packages it is essential that the package can be tightly sealed and that the sealing is sufficiently strong to withstand handling during distribution. Therefore, the weldability of bioplastics, especially PLA, is an important property regarding packaging materials [3].

Heat welding and ultrasonic welding are often used in packaging industry to join polymer films.

By heat welding, two films are pressed together in the die between heated plates to attain fusion at the interface between the films. In order to obtain a sufficient amount of molten material, films must be exposed to elevated temperatures, which may be particularly challenging in case of biomaterials.

Beside heat welding, ultrasonic welding is often used in packaging industry. When joining parts with ultrasonic welding, the required energy is applied by mechanical vibrations. The generated heat depends, among other parameters, on applied frequency, amplitude, time and pressure. As the amplitude increases, the power required to maintain the increased velocity of vibration also increases.

Subsequently, **short** time is required to deliver the same amount of energy because of the increased power. To avoid undesirable degradation of the biopolymer during ultrasonic welding, the welding parameters must be particularly defined.

The objective of the present work was investigation of systematically modified recipes based on PLA with PEG (4,000 g/mol) as one of the plasticizers frequently used in film application [Error! Reference source not found.] in order to improve the weldability of PLA.

### **Materials and sample preparation**

PLA was provided by NatureWorks under the reference 4032D. The used plasticizer was PEG 4000 supplied by IMPAG Import GmbH. Irganox 1010 and Irgafos 168 were provided by BASF SE and used as stabilizers. The polymer, plasticizer, and stabilizers were used as received.

First of all, melt-blends containing 5.3, 7.9, and 10.6 phr plasticizer (PEG 4000) were prepared using a Leistritz co-rotating twin-screw Extruder (L/D=45). To maintain the stability of the melt-blends Irganox 1010 and Irgafos 168 were added. Accordingly, a Dr. Collin single-screw extruder with a diameter of 30 mm and L/D ratio of 30 was used for the production of cast films. The thickness of the polymer films was set to be 0.05 mm.

### **Heat welding (sealing)**

All joints were made using a HSG/ETK laboratory heat sealer from Brugger. The used heat plates were flat and 2.0 mm in width. The weldability of the material as a function of welding process variables, die temperature, die pressure, and dwell time was investigated. The ranges of die temperature, die pressure, and dwell time were 85-130 °C, 1.0-3.5MPa, and 0.05-0.9s, respectively. All joints were made by welding two identical films between two plates set to the same temperature. After welding at appropriate conditions, the joint **was** cooled to room temperature at ambient conditions.

### **Ultrasonic welding (sealing)**

An ultrasonic welding system 2000 X from Branson, operating at a frequency of 20 kHz, was used for the trials. The settings of amplitude, pressure and time were determined in order to investigate their effects on the weldability of each material. The ranges of amplitude, pressure, and time were 13-31µm, 0.4-1.0 MPa, and 0.1-0.5 s, respectively. The holding time was kept constantly at 1.0 s and the holding pressure at 1.0 MPa. An anvil with a diameter of 4.0 mm was used.

### **Tensile testing**

The tensile tests of the films and the sealed samples were conducted on a tensile testing **Zwick machine**. The shape of the samples was rectangular with a width of 15 mm. The gauge length was 50 mm and the crosshead speed was 100 mm/min. The tensile tests were carried out in accordance with ISO 527. Values for maximum stress, maximum strain, and tensile weld strength were

evaluated from the trials. Reported values are the average of five or more measurements.

## Results and Discussion

### Heat welding

The tensile strength as function of dwell time, die temperature, and die pressure for the film blended with 10.6 phr PEG is shown in Figures 1, 2, and 3. The first appearance of measurable weld strength was observed at 1.0 MPa, 85 °C and 0.05 s. Increasing the dwell time from 0.05 to 0.5 s at 85 °C die temperature improved the weld strength. The weld strength remains rather constant, while increasing the dwell time from 0.5 to 0.9 s at 85 °C. At 100 °C die temperature the weld strength remains nearly unchanged, while dwell time increased. Increasing the dwell time from 0.05 to 0.5 s at 110 °C die temperature weld strength decreased. Further dwell time increase at 110 °C leads to weld strength increase.

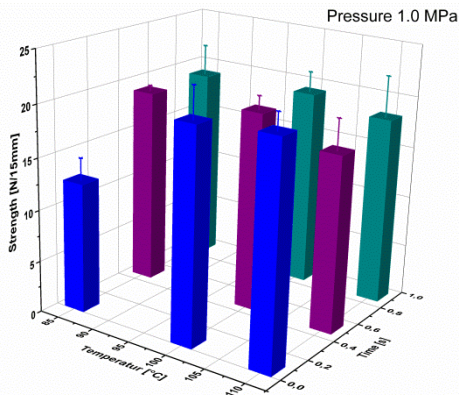


Figure 1: Tensile strength at 1.0 MPa die pressure, different die temperatures, and dwell times from welded film blended with 10.6 phr PEG

At medium (1.5 MPa) die pressure, dwell time and die temperature have strong influence on the strength in comparison with low (1.0 MPa) die pressure and thus lead to a narrow process window leading a good weld quality. As seen in Figure 2 the increasing the dwell time from 0.05 to 0.5 s at 85 °C die temperature weld strength remains constant. Further dwell time increase from 0.5 to 0.9 s at 85 °C leads to weld strength increase. At constant die temperature (100 °C) increasing the dwell time leads to a lower weld strength. Increasing the dwell time from 0.05 to 0.5 s at 110 °C die temperature resulted in a weld strength decrease. Further dwell time increase from 0.5 to 0.9 s at 110 °C leads to weld strength increase.

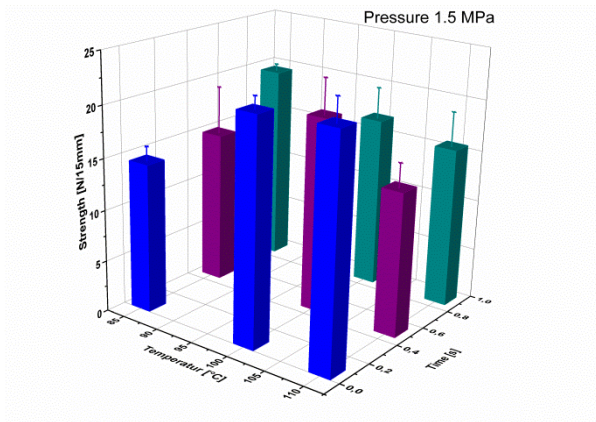


Figure 2: Tensile strength at 1.5 MPa die pressure, different die temperatures, and dwell times from welded film blended with 10.6 phr PEG

According to Figure 3 dwell time and die temperature have strong influences on the weld strength at high (3.5 MPa) die pressure too.

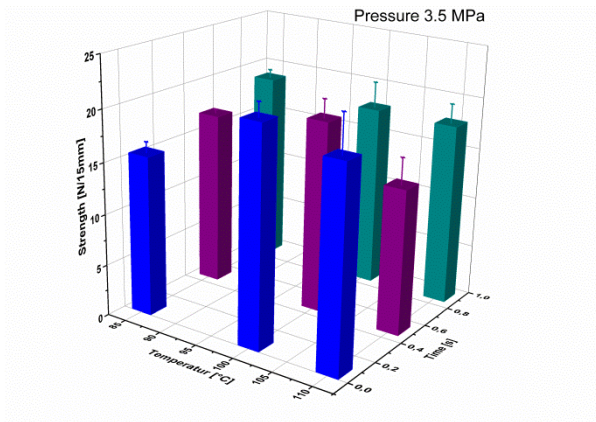


Figure 3: Tensile strength at 3.5 MPa die pressure, different die temperatures, and dwell times from welded film blended with 10.6 phr PEG

In order to determine the influence of a PEG addition of the weldability of films, all weld parameters were taken into account and the best weld strength was chosen as representative result (see Figure 4).

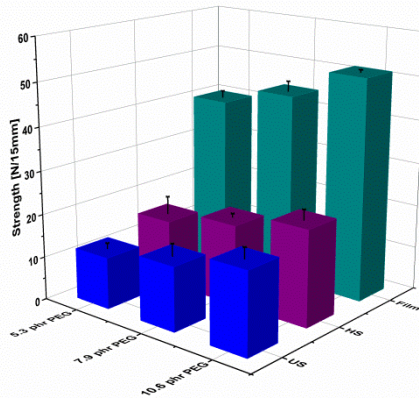


Figure 4: Best tensile strength of heat (HS) and ultrasonic (US) welded and base material

According to Figure 4 it was found that a higher amount of PEG leads to an increase in the strength of the welded samples as well as the non-welded films. Furthermore, these investigations showed that a higher amount of PEG also leads to a decrease in the applied die temperature. Thus, the minimum die temperatures were 100, 90 and 85 °C for the films with 5.3, 7.9, 10.6 phr PEG, respectively.

#### Ultrasonic welding

According to Figure 5, ultrasonic welding parameters amplitude and time have a significant influence on the resulting weld strength. At low welding pressure (0.4 MPa) and constant amplitude (12.6  $\mu\text{m}$ ) increasing the weld time leads to a weld strength increase. Increasing the weld time from 0.1 to 0.3 s at 18.9  $\mu\text{m}$  amplitude improves the weld strength. Further weld time increase from 0.3 to 0.5 s at 18.9  $\mu\text{m}$  leads to a lower weld strength. The effect of weld time at constant amplitude (31.6  $\mu\text{m}$ ) indicates that the weld strength is a strong function of weld time. Increasing the weld time from 0.1 to 0.3 s at constant amplitude (31.6  $\mu\text{m}$ ) leads to a weld strength decrease. Further weld time increase at 31.6  $\mu\text{m}$  amplitude leads to a weld strength increase.

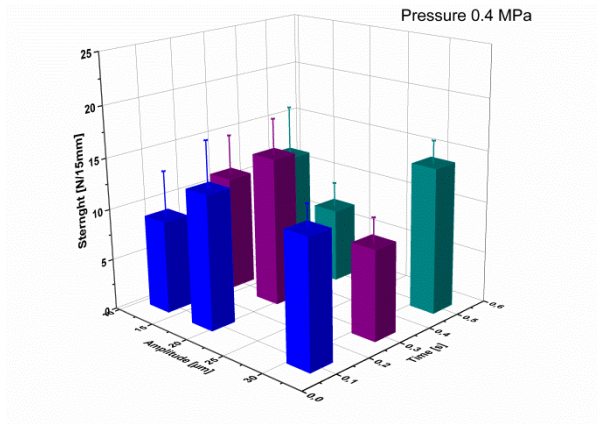


Figure 5: Tensile strength at 0.4 MPa weld pressure, different weld amplitudes, and times from welded film blended with 10.6 phr PEG

The effect of amplitude and time on weld strength at medium (0.75 MPa) and high (1.0 MPa) pressure is graphically illustrated in Figure 6 and 7.

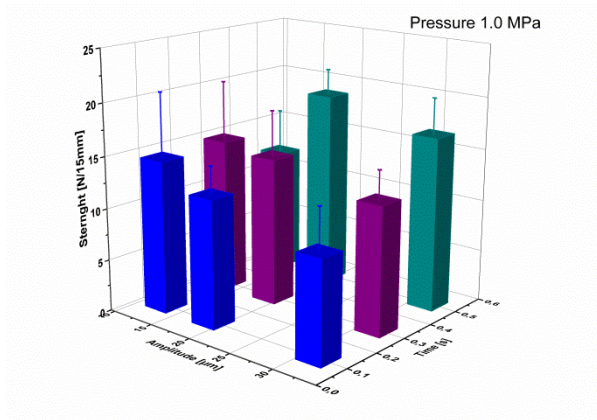


Figure 6: Tensile strength at 0.75 MPa weld pressure and different weld amplitudes and times of welded film blended with 10.6 phr PEG

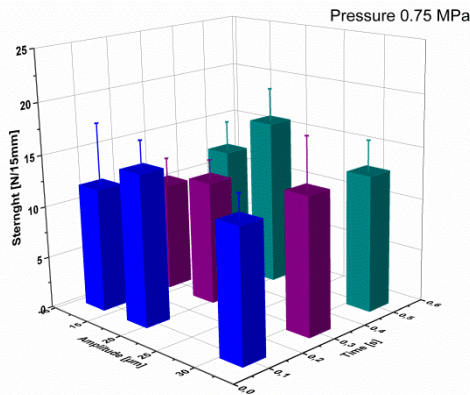


Figure 7: Tensile strength at 1.0 MPa weld pressure and different weld amplitudes and times of welded film blended with 10.6 phr PEG

According to Figures 6 and 7 time and amplitude have strong influences on the weld strength at medium (0.75 MPa) and high (1.0 MPa) weld pressure. As seen in Figure 4, a higher amount of PEG leads to increasing weld strength for ultrasonic welding as well.

## Conclusions

These investigations show that plasticized PLA films could effectively be welded by heat as well as by ultrasonic welding. The obtained weld strength is strongly dependent on the PEG amount, the selected welding process, and the welding parameters.

During heat welding, time during which die must be closed on the films to reach the desired weld strength, as well as die temperature are of primary importance. Die pressure has a relatively small influence on weld strength. A slight improvement in weld strength with increasing die pressure was found only with films plasticized with 10.6 phr PEG.

Regarding ultrasonic welding, it was expected that weld properties primarily depend on amplitude and time, but these investigations showed that the weld pressure as well affected the weld strength.

In order to determine the influence of a PEG addition on the weldability of films, all weld parameters were taken into account and the best weld strength was chosen as representative result (see Figure 4). These weld strength values were compared to the base material strength. Hence, it could be determined, if increasing PEG content only leads to an improvement in mechanical properties of the films or in weldability as well (see Figure 8). According to Figure 8 it was found that higher amount of PEG leads to improvement of weldability.

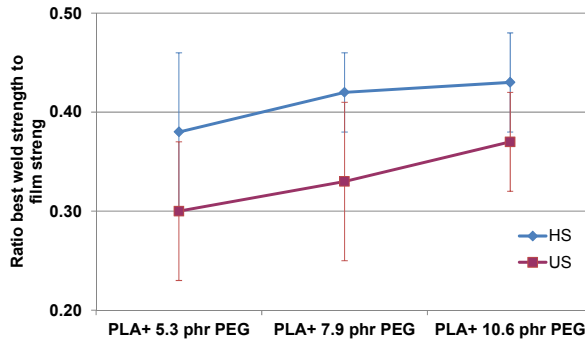


Figure 8: Ratio best weld strength to maximal film strength for different PLA/PEG blends

## References

- [1] S. Jacobsen, H. G. Fritz, *Polymer Engineering and Science*, 1999, Vol. 39, No. 7, 1303-1310
- [2] R.G. Sinclair, *Journal of Macromolecular Science, Part A Pure and Applied Chemistry*, 1996, A33 (5), 585-597
- [3] N. Ljungberg, *Plasticized Poly (lactic acid) Films- Preparation and Properties* - Ph.D. Thesis, Department of Polymer Science & Engineering, Lund Institute of Technology, Lund University, 2003
- [4] G. Wypych, *Handbook of Plasticizers*, ChemTec Publishing, Toronto, 2004, Chapter 11, pp-312

## **LIME AND LIME-BASED SOLUTIONS FOR ENVIRONMENTAL IMPACTS OF NON-FERROUS MINING AND METAL PROCESSING**

Pavel HANZL<sup>1</sup>, Siniša SRDIĆ<sup>2</sup>

*Carmeuse Europe, Mokra 356, 664 04 Mokra, Czech Republic,*

*pavel.hanzl@carmeuse.cz*

*Fabrika kreča Carmeuse Integral a.d., Ševarlije bb, 74000 Dobož, RS, BiH,*

*sinisa.srdic@carmeuse.ba*

### **Abstract**

Non-ferrous mining and processing by nature has a myriad of impacts on the environment. Non-ferrous metal producers prevent or mitigate these impacts, using a wide array of processes. Lime and lime-based products provide cost-effective options for many of them. Lime products can purify flue gases from thermal processes, treat process waters and wastewater from metal extraction and refining as well as neutralise acid drainage from underground ore mines. Lime-based binders can solidify sludge rejects in open-pit mines, improve grouts to fill underground mines and stabilise sludge in tailing ponds. Application cases in Europe and U.S. are presented.

### **Introduction**

Non-ferrous metallurgy belongs to leading industrial branches in South-eastern Europe, including former Yugoslavian states of Serbia, Bosnia and Montenegro. Despite the economic recession, the non-ferrous branch is under continuous development and the global production volumes grow constantly. This trend fully concerns Balkan countries. Intensification projects are in progress at existing deposits and plants while prospection works are running at new deposits of precious metals, zinc, lead and lithium ores.

Non-ferrous industry is a very complex branch comprising a wide array of different processes as mining, rock processing, metals extraction and refining by mechanical, thermal, other physical and chemical processes. However, each of these processes uses natural resources and has numerous impacts on environment – air, water, soil and landscape. In order to eliminate or reduce these impacts and to comply with more and more stringent European environmental legislation, the industry adopts state-of-art technical measures to control air, water and soil pollution both at existing plants and as an integrated part of new projects. Many of the mentioned adverse environmental impacts can be effectively controlled with the use of lime and lime-based solutions.

### **European environmental legislation**

The EU environmental legislation has developed over several decades from a series of branch rules and regulations to a complex system with the integrated

pollution prevention and control (IPPC) concept in the centre. Besides many others, two important legal principles - "Polluter pays" and "National limits equal or stricter than the EU-prescribed" - complete the basic concept.

The IPPC concept is codified in the IPPC Directive 96/61/EC, which defines the Best Available Techniques (BAT) as the most efficient processes with least adverse environmental effects. The BAT processes are listed in Best Available Techniques Reference Documents (BREF). If a BREF exists for a given industry, only BAT processes are permitted in new and/or refurbishment projects there.

A dedicated BREF has been issued for non-ferrous industries. It covers the production and refining steps while the ore mining and treatment are covered with another BREF on management of tailings and waste rock in mining. Both BREFs include comprehensive data on emission limits for each process listed.

The most relevant European segment directives concerning the non-ferrous industry are 2006/21/EC (mining waste), 2008/105/EC (surface water) and 2004/35/EC (Soil framework Directive, still in a proposal status). Numerous directives and regulations concern further interactions of this industry with environment as e.g. drinking water sources, hazardous waste management, listed toxins etc.

The national legislation in Balkan countries does not set any air pollution specific limits for in the non-ferrous industry. For the surface water- and soil pollution in general, the limits differ significantly state by state while the Bosnian regulation on water pollution is fully compatible with the 2008/105/EC Directive.

### **Lime – the most versatile chemical**

The history of lime production and usage is probably as old as the history of non-ferrous metallurgy. Lime has been used literally over millenniums as construction material but also as the most common chemical. Modern iron- and steelmaking processes invented in the 19<sup>th</sup> century, using limestone and lime as main slagging agents, turned lime production in a large industrialised branch.

Nowadays, the lime industry globally produces approx. 200 million tons per year; the European lime manufacturers produce 28 million tons and employ 11 000 people in total.

The lime industry is globally associated in the International lime association (ILA) while the European lime industry has formed the European lime association (EuLA), integrated in the Industrial minerals association (IMA). The authors are employees of Carmeuse Group, the leading global lime and limestone producer and a member of EuLA.

Main application branches of lime at ILA members are shown in Fig.1

Like in many other industrial branches, lime and lime-based products are used in the non-ferrous industry basically in two ways. Direct applications in the primary production comprise pH control at ore flotation, chemical extraction (e.g. aluminium, gold or lithium) or refining. The other family of applications include the environmental impacts control where lime can be used for almost every pollution stream.

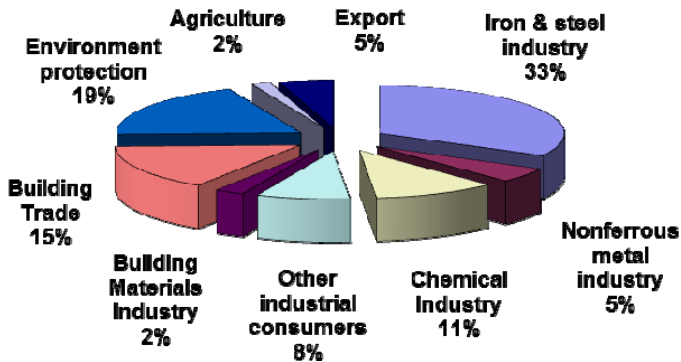


Fig. 1 Lime application branches worldwide – ILA members

## Lime-based processes to control environmental impacts

### Principles of lime action

The lime chemistry is basically very simple and there are just a few specific chemical or physical actions of lime used in the environmental technology:

- Alkali pH

The pH value of saturated  $\text{Ca}(\text{OH})_2$  solution is 12,6. This is high enough to neutralise effectively all acids in the liquid/liquid system but also to react with acidic fumes in gas/liquid or gas/solid systems.

Many metal salts precipitate at high alkali pH as hydroxides; this effect is used for coagulation /flocculation processes in wastewater treatment but also to insolubilize heavy metals and prevent their leaching from sludge and contaminated soils – see Fig. 2 - 3

- Calcium ions

Calcium ions react with reactive Si and Al oxides by so-called pozzolanic reaction, which results in complex Ca-Si- or Ca-Al-hydrated oxides. Active silica and alumina can occur in contaminated soils or can be added to lime as artificial reagents. Regardless their origin, the resulting complex compounds form impermeable matrix, which can block many contaminants from leaching.

- Reaction heat

The reaction heat released by exothermic hydration of CaO (slaking), can be used to dry and solidify industrial sludges. Both the reaction speed and temperature are adjustable with new generations of lime products.

Although the chemical principles described are very simple, each individual application requires special know-how. This is always based on physical properties of given lime products, their possible adjustment, combining and customising to specific processes. These processes and lime products' requirements are described further in details.



Fig. 2 Solubility of individual metals vs. pH

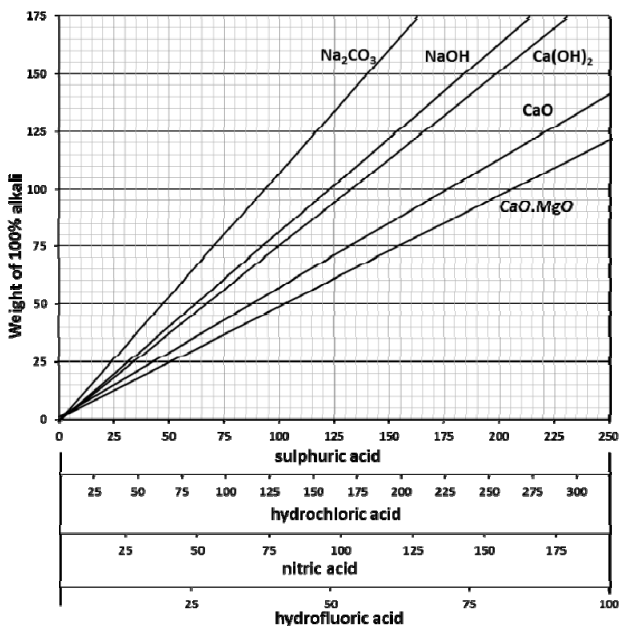


Fig. 3 Neutralisation curves for main alkalis

### Flue gas treatment (FGT)

Flue gases from thermal industrial processes always contain three main pollutant groups: Inorganic acids in a gas form, evaporated or dispersed heavy metals and toxic organics with dioxins and furans (PCDD, PCDF) as the most toxic compounds. The flue gas composition in non-ferrous industry is very specific to a given plant or process but almost every time it is a combination of all above.

As there are no specific EU emission limits for non-ferrous industry, European producers always shall comply with those prescribed by local authorities within the IPPC permission. These limits usually comprise all three pollutant groups listed.

Lime relevant FGT processes for industrial flue gases include wet sorption, semi-dry and dry sorption systems. As no special BAT exist for the non-ferrous FGT processes relevant ones for power generating or waste-to-energy plants are practically used here.

Dry FGT systems can operate both at lower temperatures 150°C till 400°C or high temperatures (above 800°C) as so-called hot-side injection. In some cases, such process could not reach the minimal efficiency requested by BAT if relevant. Nevertheless, those processes are widely used as a primary FGT option or a polishing (additional FGT) step. A typical dry FGT process scheme is shown in Fig.4

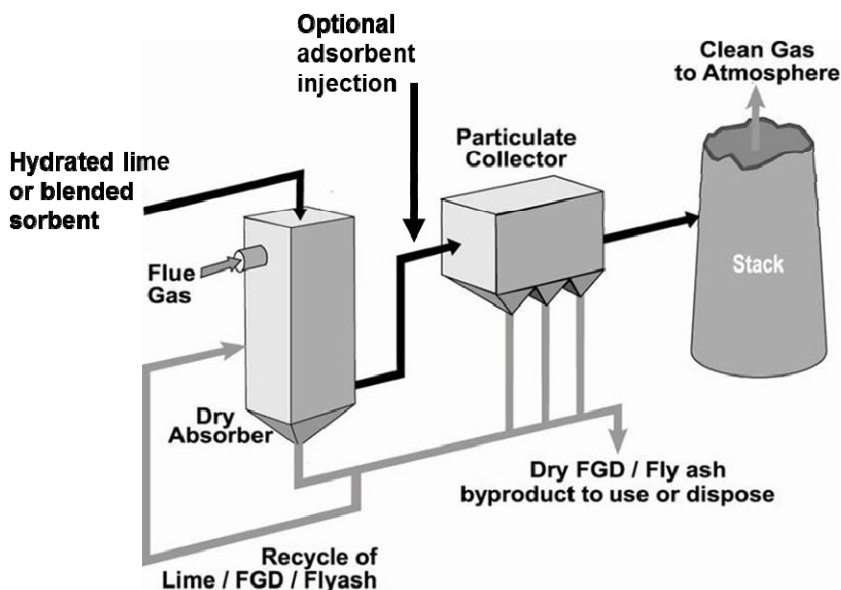


Fig.4 Dry low-temperature FGT process – basic scheme with optional sorbent injection points

Lime is used for the mentioned processes in the following forms:

Quicklime (Ca-oxide) can be slaked in water to a slurry called milk-of-lime (MOL), which is used as sorbent in wet or semi-wet processes. MOL can be also prepared by dispersing lime hydrate (Ca-hydroxide delivered as a dry powder) in water without slaking.

Lime hydrate is exclusively used for dry sorption in several quality grades from standard to advanced types, tailor-made to the unit. Advanced lime hydrates differ by special physical properties (specific surface area, internal pore volume and distribution); this combination is adjustable to capture a leading inorganic pollutant.

Lime hydrate can be blended with inorganic (mineral) or organic (active carbon and similar) adsorbents for so-called multi-pollutant treatment. These blends can capture most of the complex pollution by dosing in one injection point in a flue gas stream.

As an example of a lime-based FGT unit, the Hammerer Co. installation in Arad, RO, can be mentioned. The dry FGT system treats fumes with SO<sub>2</sub> as the main pollutant with additional micro-pollutants as heavy metals and organics. Lime-based sorbent containing activated carbon is injected to this installation.

### *Water treatment*

While no environmental restrictions are applied on process water quality in non-ferrous industry, this is not a case for its wastewater streams. In EU states, wastewater discharged in watercourses shall comply with the pollution limits prescribed in the 2008/105/EC Directive. Limit concentrations for dissolved cadmium, lead, mercury and nickel are the most relevant for the non-ferrous industry. These limits can be subject to further local restrictions.

A range of water pollutants from non-ferrous processes is very wide and always specific to the branch; metal salts are the main pollution source. Some extraction processes generate highly acidic wastewater. Organics (flocculants, surfactants, frothers) from ore enrichment steps can be another group of pollutants.

The range of wastewater treatment installations is also very wide - from simple compact neutralisation units to large multi-step plants with an integrated alkalisating part.

A MOL form is a traditional and almost exclusive way of lime application in these systems. As mentioned above, MOL can be prepared by quicklime slaking or by dispersing hydrated lime in water. MOL of an initial concentration of 25% dry solids is usually prepared at a wastewater unit operated within the non-ferrous plant.

The lime industry also offers advanced solutions:

For MOL processes, it can be satellite MOL units, built and operated by the lime supplier at the non-ferrous plant, or ready-made MOL distributed in containers. The ready-made MOL can be delivered in a range of concentrations; the most advanced products can reach up to 50% dry solids with high fluidity and extremely low settling in storage tanks.

Another advanced product option is delayed reactivity quicklime, which can be mixed directly with wastewater. It reacts with water in an adjusted time; ideally in the precipitate, during or after its dewatering. The exothermic reaction supports the precipitate (sludge) dewatering and drying.

Two examples of uranium mining and processing water treatment plants are shown in Fig. 5-6. A large installation, operated by DIAMO Co., CZ, treats highly acidic water from underground ore leaching.

A medium-size compact unit operated by Mecsek Oko Co., HU, treats drainage from uranium mine tailings. Lime is applied to support the desalination process.

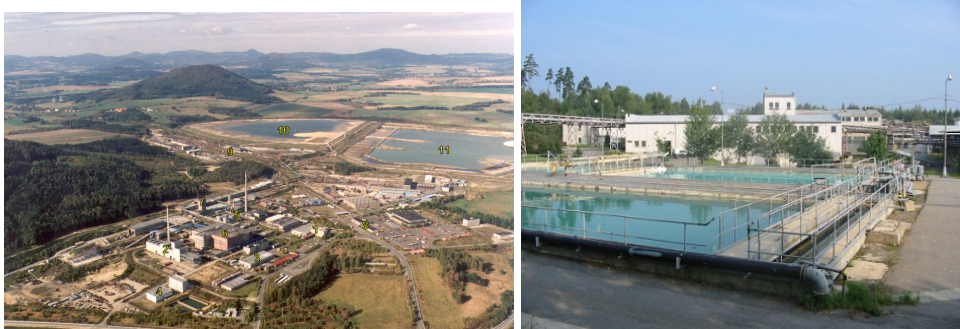


*Fig. 5 Wastewater treatment plant in DIAMO (Straz pod Ralskem, Czech Rep) – general view of the extraction plant with tailing ponds; neutralisation basin*



*Fig.6 Wastewater treatment unit Mecsek (Pecs, Hungary) – general view, post-precipitation basin*

### *Acid mine drainage control*

Acid drainage, a result of reactions among sulphides and underground water at the presence of air, is a typical environmental impact of ore mining. Free sulphuric acid and metal sulphites / sulphates are the most important pollutants here. Pollution limits and BAT for acid mine drainage are identical as for industrial wastewater.

Generally speaking, there are two basic ways to control the acid drainage – mitigation and prevention.

Acid pollution is mitigated by two basic techniques: passive (e.g. anoxic limestone drains) or active - various types of neutralisation plants. In many cases, the neutralisation systems require special design to operate in distant locations or on a seasonal basis.

Lime solutions for these systems are similar as for conventional acidic wastewater treatment. The standard product range used includes quicklime or hydrated lime for MOL preparation. Ready-made MOL with prolonged stability is an efficient solution for small units in distant locations. Delayed reactivity quicklime can be used in compact units to reduce the water content and hence total volumes of resulting sludge.

Fig.7 shows an example of a distant neutralisation unit in a U.S. mine at Snow Fork, Ohio, U.S. This has been designed to work seasonally and independently on electric power supply. In that case, lime dosage is powered by the water stream itself.



*Fig.7 Acid mine drainage unit Snow Fork: General view, lime dosing powered by a water wheel*

Acid mine drainage can be prevented by mine grouting, i.e. backfilling with inert or reactive material. Grouting is largely used to control underground mine subsidence and self-ignition in coal mines. When used for drainage control, the grout in a form of slurry fills the hollow spaces and prevents the residual ores from reacting with water and air.

A cost effective option for the grout design is a mix of fly ash, possibly with further flue gas treatment products and lime as an additional binder. This solution also provides double positive environmental effect by using by-products, which otherwise would be stored at deposits as waste.

Depending on the project size and grout preparation unit design, lime can be used either in a form of ready-made MOL mixed with dry products or dry quicklime / hydrated lime mixed with the slurry. Delayed reactivity quicklime in combination with further additives could be a special solution addressing special needs of grout fluidity, underground settling, dewatering and final setting and hardening.

Fig. 8 shows examples of closed-circuit mine grout preparation units. An open-air grout preparation unit in Hungary (Matraszentimre mine) operated by Mecsek Oko Co. is shown at Fig. 9. The grout consists of fly ash, wet FGD gypsum and quicklime.



Fig. 8 Closed-circuit grout units by Surchiste (Forbach region, France) and HBZS (Ostrava, Czech Rep.)



Fig. 9 Open-air lime/ash grout preparation by Mecsek Oko (Matraszentimre, Hungary)

#### *Tailings' reclamation and remediation works*

Ore tailings, as a residue of ore enrichment processes, are collected in ponds and heaps. Tailings always contain residual metals, which, when drained, can cause similar harmful effects as the acid mine drainage.

Modern tailing ponds' design always includes waterproof insulation, leachate draining, collection and treatment to prevent the mentioned environmental impacts. However, there are many tailings' deposits around Europe with limited technical lifetime where reclamation works are necessary.

BAT for tailing ponds closure and aftercare focus on physical and chemical stability and with special attention to water management.

No specific BAT exist for tailing ponds or heaps remediation; in practice, a wide range of processes is used here. Among them, the solidification / stabilisation techniques are a proven and easily applicable option in many cases. Contaminants are usually controlled by combined chemical action – neutralisation - and

insolubilizing and physico-chemical action – encapsulation by treated base soil or binders.

3 basic solidification/stabilisation techniques are used in remediation works:

In the ex-situ process, the contaminated material is removed from the site and mixed in a centralised unit.

In the on-site process, this excavation and treatment are performed directly on the site and the treated material is stored back at its original place. The in-situ process, where the treated material is mixed with binders without removal, is the least demanding option and is always preferred.

Depending on the site conditions, static, semi-mobile or mobile (deep mixing) machinery is used.

Lime for tailings solidification/stabilisation can be used as such in a form of quicklime in various reactivity grades, hydrated lime and possibly MOL injected in voids.

The complex nature of the processes often requires treatment with more than 1 chemical or binder. This can be solved by multi-step treatment where liming is the first step or, more advantageously, by using tailor-made blended binders, prepared as a ready mix in the lime plant.

A good example of a complex tailing remediation project is the Montenegrin site of Mojkovac, supplied by the Vodni Zdroje Co., CZ and financed by the UNDP and bilateral funding of the Dutch Government. Fig. 10 shows the deep soil mixing machinery and the remediated site.



*Fig. 10 Tailing pond remediation in Mojkovac, Montenegro: Deep mixing with mobile machinery, general view of the treated site*

### **Environmental challenges for new non-ferrous projects in Balkan**

As we could see in the recent years there is a big development potential for non-ferrous industry in Balkan area.

In Serbia there are two major projects: one in RTB Bor where new smelter construction is undergoing and another one in Jadar where we have Rio Tinto's project on exploitation of lithium and borates. Two projects are indicated in Bosnia and Herzegovina: one in Čelebići where the concession right was awarded to Western Mining for research of lead, zinc and copper deposits, the second one in

Lopare were Lithium Balkal has concession rights for research of lithium and borates deposits. All the projects listed are being designed to comply with EU environmental limits in their operation.

Apart from these new projects in Balkan area there are several running non-ferrous mines, processing and refining plants that have been designed and are operated in accordance with existing local environmental legislation. It is obvious that these plants will require further investments in the upcoming years to match the stricter EU environmental standards.

Extensive remediation works, supported by European and international funding, are also expected at so-called environmental hot spots - polluted areas resulting from the existing mining and processing activities – to reach their compatible environmental status.

## **Conclusions**

The non-ferrous industry is a complex process that includes mining, rock processing, mechanical, thermal and chemical extraction of metals and their refining. All these operation have significant environmental footprint in air, water, soil and landscape pollution. A vast array of processes in environmental technology is used to prevent or mitigate these negative effects and comply with pollution limits stated in the European and local legislation.

Lime, as the most versatile chemical, can be used in cost-effective process solutions to control most of the listed environmental impacts. Special lime hydrates and blended sorbents are used to capture multiple pollutants in flue gas streams from thermal industrial processes. Milk-of-lime is commonly used to neutralise acid wastewater and mine drainage as well as to control pH in complex chemical wastewater treatment plants. Ash- lime slurries are widely applied as underground mine grouts used as an alternative way to control the acid mine drainage. Quicklime and quicklime-based binders are the best product solution to solidify and stabilise sludge in tailing ponds and similar remediation works linked to non-ferrous mining. Thanks to the large application know-how and extensive product development, leading companies in the lime industry can provide efficient tailor-made products for each of these applications.

Non-ferrous metallurgy is one of the leading industrial branches in Balkan countries. Besides the existing plants undergoing development projects, new mines are being surveyed and prepared in operation. Both for the existing plants and those in preparation, implementing the demanding environmental measures will be a big challenge here. The European lime industry is ready to support these efforts with product and process solutions.

## **References**

- [1] Reference document on best available techniques for Management of tailings and waste- rock in mining activities, European Commission, 2009
- [2] Reference document on best available techniques for Management of tailings and waste rock in the non-ferrous metal industries, European Commission, 2001

- [3] HANZL, P. et al: Remediation and reclamation of a hazardous waste deposit at a former lead and zinc ore tailing pond in Mojkovac, Montenegro *Proceedings of Rudarstvo 2012, Zlatibor*
- [4] GOMBKOTO, I. et al: Using fly ash - lime slurry for underground mine backfilling in Gyöngyösoroszi, Hungary *Proceedings of Sustainable development in power plant and mining, Palic, 2012*
- [5] Boynton, R.S.: Chemistry and technology of lime and limestone, second edition, John Wiley & Sons,

# Poster session



## ANALYSIS OF AIR POLLUTION DISPERSION FROM THE STEEL PLANT IN THE REGION OF SMEDEREVO FORTRESS BY NUMERICAL SIMULATION (CFD)

Mirko Kozic<sup>1</sup>, Suzana Polic-Radovanovic<sup>2</sup>, Slavica Ristic<sup>3</sup>,

<sup>1</sup>VTI, Ratka Resanovića 1, Belgrade, Serbia, mkozic@open.telecom.rs

<sup>2</sup>CIK, Terazije, Belgrade, Serbia

<sup>3</sup>Institute Goša, Milana Rakića 35, Belgrade, Serbia

### Abstract

This paper presents the results obtained by numerical simulation of air pollution dispersion from the stacks of Smederevo steel plant in the direction of Smederevo fortress. Trajectories and concentrations of pollutants were determined by commercial software ANSYS FLUENT. The relief of the terrain was included in the geometry of the numerical domain (10x4x1km). An unstructured mesh composed of more than three million cells was generated. Southeast wind speed was 2.9 m/s blowing in the direction parallel to the longest side of the domain. Atmospheric conditions correspond to convection, i.e. increase in temperature with height. The sources of pollution included in the simulation are central agglomeration stack, blast furnaces stack and central stack of steel-making. Computed concentration of carbon monoxide in the vicinity of the fortress is about 1 ppm. Obtained results represent the first step in a complex, multidisciplinary research of the industrial zones impact on cultural heritage objects.

### 1.Introduction

Air quality management is a significant segment of the environment protection and it is based on a number of conventions, laws and regulations [1,2]. Determination of trajectories and concentrations of gaseous pollutants is of great importance in protection of human health, ecosystems, industrial or urban areas, historical and cultural heritage [3]. There are many methods dealing with the identification and monitoring of air pollution [4-7].

The last twenty years, one of the methods, which is more and more used to examine air pollution is a numerical simulation. This method takes into account the different parameters depending on the terrain, weather conditions and technical characteristics of the pollution emitter. Software for computation fluid dynamics (CFD) is characterized by high reliability and resolution. Besides, other applications CFD methods are used in ecology to examine the spread of pollutants originating from various sources such as industrial plants, transportation, etc. [7].

One of the Source of pollution, which has a direct impact on the Smederevo fortress is a steel plant. In spite of implementation of environmental protection measures, which have been conducted over the years, and are being carried out today [8], monitoring shows that there were significantly higher emissions of harmful gases and particulate matters, which is very common in the work of such facilities [2,8,10,11].

Smederevo Fortress is a monument of exceptional national importance [9]. Due to its complexity it remains today an object of scientific and archaeological interest. The fortress is one of the most monumental architectural buildings from medieval Serbia. Today the Fortress is in a state of slow, but constant decay, due to many natural and man-made factors (nearby a river port, marina and part of the urban centre of Smederevo, industrial zones, etc). The Smederevo steel plant until recently, U.S. Steel) and several district heating plants, emit CO<sub>2</sub>, CO, NO, NO<sub>2</sub>, particulate matter, soot, etc. Automatic monitoring of air pollution was started in 2007. This paper presents the results of CO dispersion numerical simulation, emitted from the steel plant stacks. Figure 1 shows the Google terrain map with numerical domain for the simulation of pollution and wind rose in 36 directions; Smederevo1\_ Radinac, 2007. years.

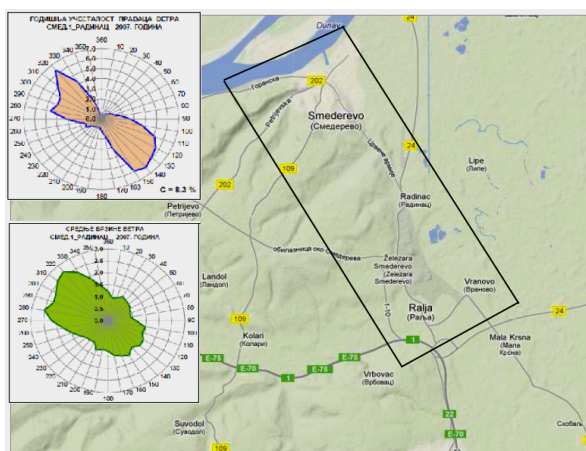


Figure 1 Google map, numerical domain and wind rose

## Numerical simulation of pollutant dispersion

Numerical simulation was performed solving the averaged Navier-Stokes equations of ANSYS FLUENT software package where species transport without chemical reactions was modelled. This model solves conservation equations for chemical species predicting the local mass fraction of each species through the solution of a convection-diffusion equation.

### Numerical domain and mesh

The numerical simulation was carried out in the domain that was 11400 m long, 3600 m wide and 1000 m high. The longest side was set at about 25° relative to the south-north direction. The geometry of the ground was generated using digitalized relief [12]. Three stacks of Smederevo steel plant were modelled in pollution dispersion, namely the central agglomeration stack, blast furnaces stack and central stack of steel-making. Height and diameter of the central agglomeration stack were 150 m and 8 m, respectively. The blast furnaces stack was 65 m high with diameter 3.6 m, while height and exit diameter of the central

stack of steel-making were 60 m and 3.6m respectively. In Fig.2 Smederevo fortress and the stacks can be seen. The fortress was at about 8000 m from the stacks. All the fortress towers were 25 m high, whereas height of all its walls was 10m.

An unstructured tetrahedral mesh composed of 3 397 961 volume elements was generated. The surface of the ground and fortress were discretized with 388 838 and 61 086 triangular elements. At the exit of central agglomeration stack there was 748 surface elements, while 394 elements were placed at the exits of blast furnaces stack and central stack of steel-making.

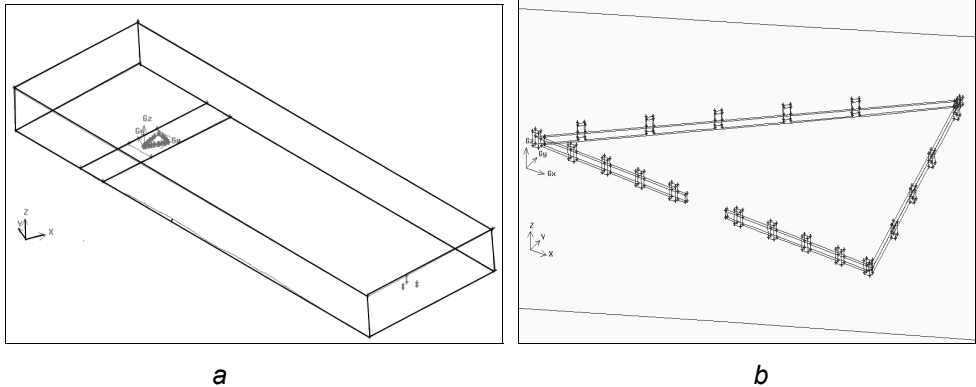


Figure 2. Geometry of the whole numerical domain and Smederevo fortress

The volume mesh in the numerical domain and volume elements in the horizontal plane through the fortress and stacks are shown in Fig.3. There was a large number of small elements near the fortress and stacks because large gradients of the flow field appear in these regions.

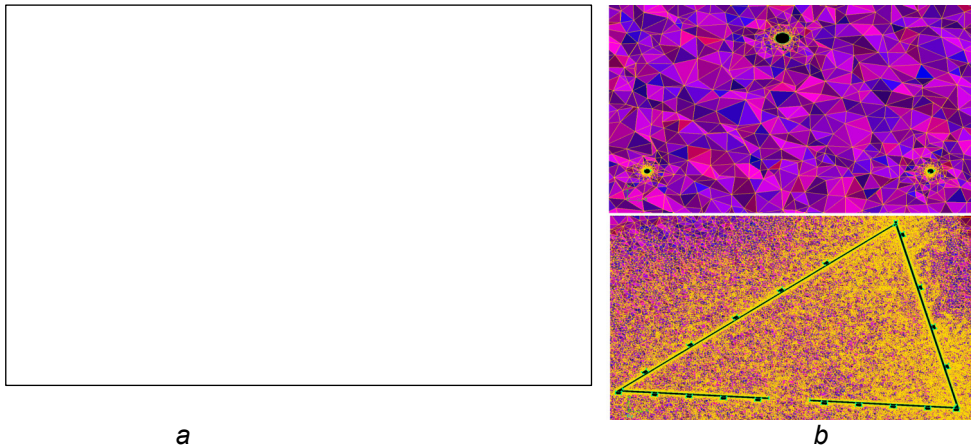


Figure 3. Volume mesh; a – in the whole numerical domain, b – near stacks and fortress

### *Numerical procedure*

Procedure consists of several steps that include modeling transport of multicomponent mixture and turbulence, selecting the solver formulation, specifying boundary conditions, specifying fluid properties, initializing the solution, monitoring solution convergence, postprocessing and examining the results.

Boundary conditions at the inlet of the numerical domain were defined with logarithmic profile of the wind velocity. In this way the influence of the ground boundary layer was included. The turbulence kinetic energy and its rate of dissipation at the inlet are not constant, but change as a function of height. Also, the temperature profile was prescribed along the inlet height. The mass fraction of predominant pollutants were specified at the exits of the considered stacks using data from references and measurements of authorized institution [8,11]. At the exit of the central agglomeration stack and central stack of steel-making the mass fraction of carbon monoxide was  $1.1 \cdot 10^{-3}$  and  $1.2 \cdot 10^{-4}$ , respectively.

The standard  $k$ - $\epsilon$  turbulence model was used that includes convection of hot gases and thermal diffusion. This is a semi-empirical model in which transport equations for the turbulence kinetic energy  $k$  and its dissipation rate  $\epsilon$  are solved. Widespread use of the model is provided by its robustness, economy, and reasonable accuracy for a wide range of fully turbulent flows and heat transfer simulations.

Initially, the first-order accurate numerical scheme was used for reason of the calculation stability. Later on, the calculation was shifted to the second-order accurate numerical scheme. Finally, obtained results were prepared in the form of figures and tables.

### **Analysis of numerical simulation results**

The dispersion of gaseous pollutants from the stacks is most affected by wind speed and temperature gradient. Numerical simulation was performed for a wind speed of 2.9m/s, and the temperature gradient 1.6°C/100m. These conditions correspond to a moderately stable atmosphere, and stability class F according to the classification given in [5]. Selected atmospheric conditions are in agreement with data for many years of measurements carried out in the AMSKV Radinac.

The research included simulation of CO<sub>2</sub>, CO, NO, NO<sub>2</sub>, particulate matter and soot diffusion, but this paper presents only the results of CO dispersion. Figure 4a shows the shape of a plume smoke from the chimney to the Smederevo fortress, as well as details of the pollution spreading in the vicinity of the fortress (sl.4b). The concentration of CO on the walls of the fortress is shown in fig 5. and it is between  $10^{-8}$  and  $10^{-7}$ .

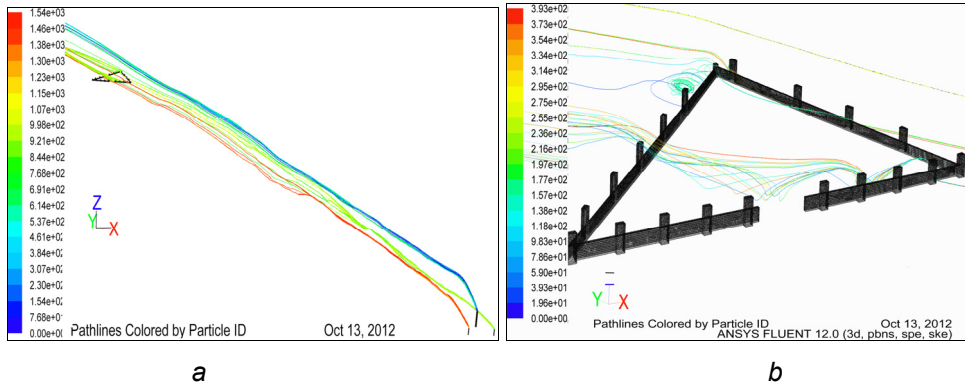


Figure 4. Trajectories of gaseous pollutants, a-in the whole numerical domain, b- details at the fortress

The results of numerical simulations show that the highest concentrations of pollutants is around point A (Fig. 2), which is parallel to the direction of the wind blowing. The minimum concentrations, with magnitude lower by an order are obtained around the point C (Fig. 5). Diagram (fig 5b) present the CO concentration versus distance in the direction of the wind.

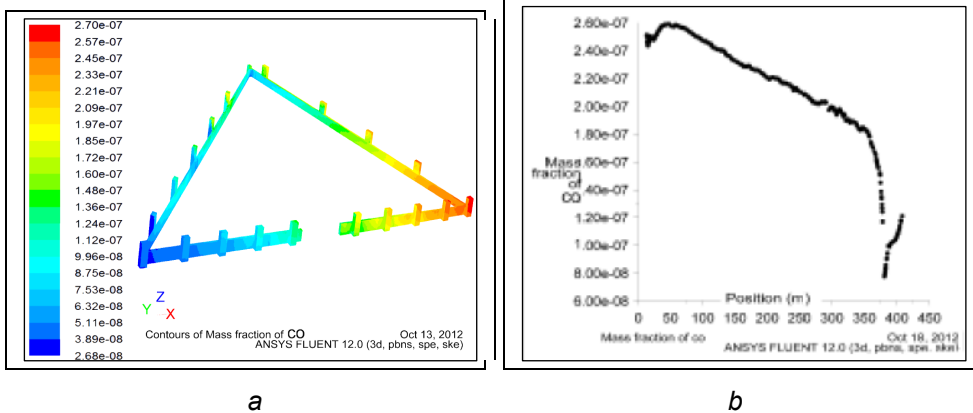


Figure 5 Concentrations of CO a-at the walls of the fortress, b- i CO concentration versus distance in the direction of the wind

In Figure 6, the concentrations of CO in the vertical planes, perpendicular to the direction of the wind blowing are presented. Three planes are set at 900 m, 3700 m and 7000 m from the steel plant stacks, and the last one at 200 m behind the forteress. It can be observed that The forteress is located between the last two planes fig 6a). It is clearly seen that the concentration decreases with distance from the stacks.

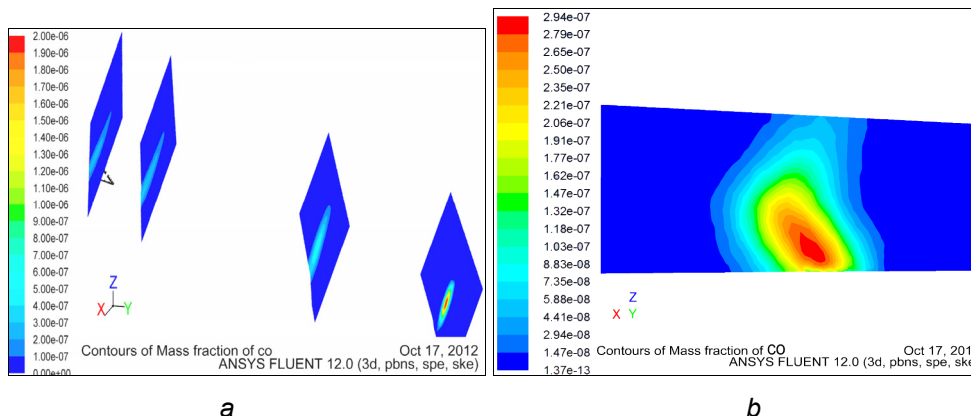


Figure 6, Concentrations of CO in a-the four vertical planes,b-in vertical plane on the 200m behind the fortress

## Conclusion

Research of pollution dispersion from the stacks of Smederevo power plant and its impact on Smederevo fortress represents the first step in a complex, multidisciplinary approach in analysis influence of industrial zones on cultural heritage objects. Calculation was performed using model of species transport in numerical simulation software.

The sources of pollution considered in the simulation were the central agglomeration stack, blast furnaces stack and central stack of steel-making. The temperature gradient corresponding to inversion was set in the boundary conditions as most unfavorably for level of pollution near the ground. The concentration of carbon monoxide in the vicinity of the fortress obtained by the calculation was about 1 ppm, primarily due to large distance from the stacks that is about 8 km.

The relief of the terrain was included in the model because its influence increases when stack height decreases. Local flow field and level of pollution around the fortress could be changed due to buildings in Smederevo that were not modelled because of limited computer resources.

For a comprehensive understanding of the problem, it is needed to perform identification of all sources of pollution and determine its parameters relevant to the impact on the environment, particularly the objects of cultural heritage. Of great importance are the data collected by the competent institutions in the monitoring process. These data are processed by the selected models and used in order to assess the damage and in preventive protection.

## Acknowledgments

This paper is the result of the research within the project TR 34028, which are financially supported by the Ministry of Education and Science of Serbia

## References

- [1] Zakona o zaštiti vazduha ("Sl. gl. RS" br.36/09)
- [2] Republika Srbija Ministarstvo energetike, razvoja i zaštite životne sredine, Agencija za zaštitu životne sredine Godišnji izveštaj o stanju kvaliteta vazduha u Republici Srbiji 2011. godine, Beograd, 2012. godine
- [3] Polic-Radovanovic S., Research unfavorable environmental Impact to the Cultural heritage in Light of International heritological Practice, International Scientific Conference on Environment and biodiversity, ECOLOGICA, Beograd, pp.161, 2010
- [4] Pasquill, F., Atmospheric Diffusion, 2nd ed., Halstead Press-Wiley, New York, 1974, 17
- [5] Trini Castelli, S., Anfossi, D. and Finardi, S. Int. J. Environment and Pollution, 40, 1/2/3, 10–25, 2010
- [6] D:L: Doushanov, Control of polution in the iron and steel industry, Pollution control technology, Vol. III,Encyclopedia of Life Support Systems (EOLSS), [http://www. Eolss.net/Eolss-sampleAllChapiter.aspx](http://www.Eolss.net/Eolss-sampleAllChapiter.aspx).
- [7] Z. P. Karamchandani, K. Lohman, C. Seigneu,Using a sub-grid scale modeling approach to simulate the transport and fate of toxic air pollutants, Environ Fluid Mech (2009) 9:59–71, DOI 10.1007/s10652-008-9097-0
- [8] Izveštaj o merenjima emisije štetnih materija iz dimnjaka čeličane u Smederevu, koje je izvršio Sektor za kontrolu i nadzor Ministarstva životne sredine, rudarstva i prostornog planiranja, u periodu od 2006. godine do 2010. godine
- [9] [www.tvrdjava.com/ sartid](http://www.tvrdjava.com/sartid)
- [10] <http://www.balkanphotocontest.com/index.php?menu=7&img=73743>
- [11] <http://www.ekologija.rs/povecana-zagadjenost-u-okruzenju-zelezare>
- [12] Rasterska karta 1 : 25000, Br. 430-4 (2,4), 2. Digitalni model terena – grid, za područje koje obuhvata Smederevsku tvrđavu i US Steel (površine oko 16 km<sup>2</sup>, dužine oko 8km, a širine 2km) u formatu DXF, Vojnogeografski institut VS, Beograd, 2012

## CHANGES OF Co-Cr BASED DENTAL ALLOY INDUCED BY MULTIPLE CASTING

V. M. Maksimović<sup>1</sup>, M. M. Stoiljković<sup>1</sup>, A. D. Čairović<sup>2</sup>,

<sup>1</sup>*Institute of Nuclear Sciences Vinča, University of Belgrade, PO Box 522,  
11001 Belgrade, Serbia*

<sup>2</sup>*Clinic for Dental Prosthetics, Faculty of Stomatology, University of  
Belgrade,  
Rankeova 4, 11000 Belgrade, Serbia*

### Abstract

Changes induced by multiple casting of commercially available Co-Cr based dental alloy were the object of this paper. Changes in the microstructure and ion release kinetic of once, four and eight times recast samples have been investigated. Each casting shows distinctive dendritic solidification microstructure with diverse chemical composition of dendrite and interdendritic regions. Such structure gradually disappears with the number of recasting. Ion release was measured *in vitro* in artificial saliva media over the period of twenty one weeks. Measurements show rapid ion release process of multiple recast samples in comparison to once recast where extremely slow ion release was evidenced. In all recast samples, Fe ion release was about 20 times faster than Co ion.

*Keywords: Co-Cr dental alloy, ion release, microstructure, artificial saliva*

### Introduction

Many different alloys have been used for fixed prosthodontic restorations [1-3]. Noble metal alloys have been found to be ideal for dental restorations, because of their corrosion resistance and biocompatibility. The rise in the price of gold led to widespread use of base metal alloys [4]. The base metal alloys Co-Cr and Ni-Cr generally have superior mechanical properties compared to noble or high-noble alloys including hardness, elastic modulus, etchability for resin bonding and high melting range. These alloys also have several negative characteristics such as markedly higher corrosion in an acidic environment, difficult finishing and polishing features, dark and thick oxides, risk of patient allergy and difficult soldering and casting [5]. Currently, the majority of commercial dental laboratories are reusing scrap alloy (used once or more times) either alone or in combination with the new alloy for fabricating the dental prosthesis. Taking into account only the cost of the material they disregard manufacturers' instructions changing the properties of material during numerous reuses [6]. In oral cavity, the salinity of saliva approaches the salinity of seawater and tends to be highly corrosive to most non-noble metals. Depending on the food intake, the pH of saliva may vary between 2 and 11 while the temperature in the oral cavity may be between 0 °C and 70 °C. Generally, an artificial solution of saliva is used for the laboratory studies since natural saliva composition cannot be generalized [7].

The aim of this study was to estimate the effects of repeated casting of Co-Cr base dental alloy on the microstructure, chemical composition and the metal ion release kinetic.

### **Experimental procedure**

In this study the commercially available Co-Cr based dental alloy was tested. The composition of the alloy as given by the manufacturer (wt. %) was: Co-61, Cr-30, Mo-5.5, Nb-1 and C, Si, Cu, Fe, Mn as other elements. The alloy was melted in the induction furnace at temperature 1450°C, and the test coins, diameter of 10 mm and thickness of 1 mm were cast in accordance with the manufacturer's instructions. For multiple casting, Co-Cr dental alloy was melted once, four times and eight times and cast.

Artificial saliva of pH 2.3 was prepared by weighting 7.69 g of  $K_2HPO_4$ , 2.46 g of  $KH_2PO_4$ , 5.3 g of NaCl, 9.3 g of KCl (Honeywell Riedel-de Haen), 16.6 ml of lactic acid (Fluka Chemica) and dissolved into 1 dm<sup>3</sup> of distilled water [8]. Coins were separately inserted into 250 ml of artificial saliva, heated to 37±1 °C and stirred permanently. Every seven days aliquots of 25 ml were sampled.

For the microstructural analysis the coins were wet grinded and polished on metallographic polishing table, cleaned with alcohol and distilled water and air dried. Samples were then etched in solution of 15 ml  $HNO_3$ , 15 ml  $CH_3COOH$ , 60 ml HCl and 15 ml  $H_2O$  [9]. No etching was performed on the samples used for ion release kinetic measurement.

Such prepared sample were examined by Carl Zeiss Axiovert 25 light microscope (LM) equipped with the digital Panasonic camera WV-CD50 and a FEI Quanta 200 scanning electron microscope (SEM) equipped with an Oxford Instruments INCA X-sight system energy dispersive spectrometer (EDS). Chemical composition of dendrite and interdendrite regions was determined by point and surface analysis.

Concentration of ions released into artificial saliva media was determined by using inductively coupled plasma optical emission spectroscopy (ICP-OES) Spectroflame P, 27.12 MHz and 2.5 kW.

### **Results and discussion**

Typical dendritic microstructures of the recast samples of Co-Cr based alloy are shown in Fig.1. It is well known that the dendrite structure exhibits compositional variations, with the dendritic arms containing less alloying and impurity elements than interdendritic regions. Because of such compositional changes the rate of etching of interdendritic regions differs from that at dendrite arms. There are noticeable changes in the microstructure with the number of castings. Also, EDS analysis confirms that the chemical compositions of the dendrite and interdendritic regions are different. There is the difference in amount of the base metal Co between dendrite and interdendritic regions, Fig.2. At once recast sample, interdendritic region contains about 20% less of Co in comparison to the bulk sample. No matter of number of casting, the base element Cr was always homogeneously spread in both regions.

To the contrary, the amount of Mo is much higher into interdendrite regions, Fig.2. In once recast sample interdendritic region contains about 2.5 times higher amount of Mo in comparison to the bulk sample. As the number of recasting increases the difference between dendritic and interdendritic regions is reduced and the chemical composition becomes more uniform, i.e. both ratios tend to unit. Obviously, after ninth or tenth recasting, the subsequent casting will not further affect changes of microstructure and uniformity of chemical composition, Fig. 2.

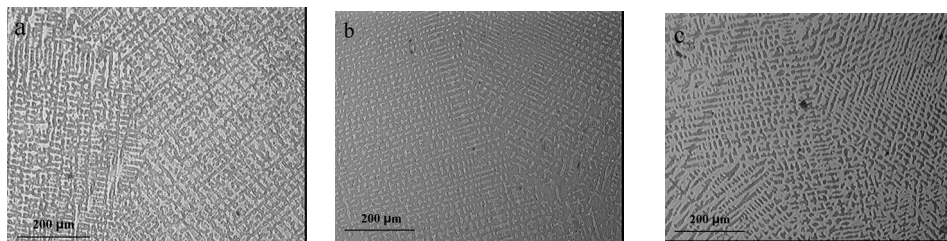


Fig.1 LM micrographs. Typical microstructure of Co-Cr dental alloy; (a) once recasting, (b) four times, and (c) eight times recasting.

Interdendritic regions contain less Co, but more Mo with respect to the bulk sample. With an increase the number of recastings, both ratios tend to unity which means homogenization in chemical composition.

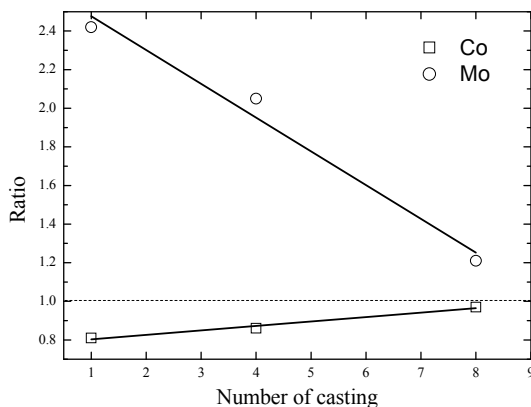


Fig. 2 Interdentritic regions-to-bulk samples ratios of Co and Mo as a function of the number of recasting.

Only Fe and Co ions were detected and could be measured *in vitro* in the artificial saliva. All other alloying elements were below the limit of quantification even in eight times recast sample. It was also found that in all recast samples, Fe ion release was about 20 times faster than Co ion. Concentration of Fe and Co in successively sampled volumes fits Weibull cumulative distribution function (CDF),

Fig. 3. Once the cast specimen gives values of Weibull shape parameter very close to unity indicating the ions release rate is close-to-constant over time. Precisely, scale parameters for Fe and Co were about 28 years and longer than 700 years, respectively. It means that once recast sample is the most durable. However, four times and eight times recast samples give values of Weibull shape parameters higher then unity indicating the ion release rate increase over time. Thus, the scale parameters for Fe and Co are 6 months and 10 years, respectively. In addition, there is no remarkable differences in scale parameters between four times and eight times recast samples (about 30% for both Fe and Co), Fig. 3.

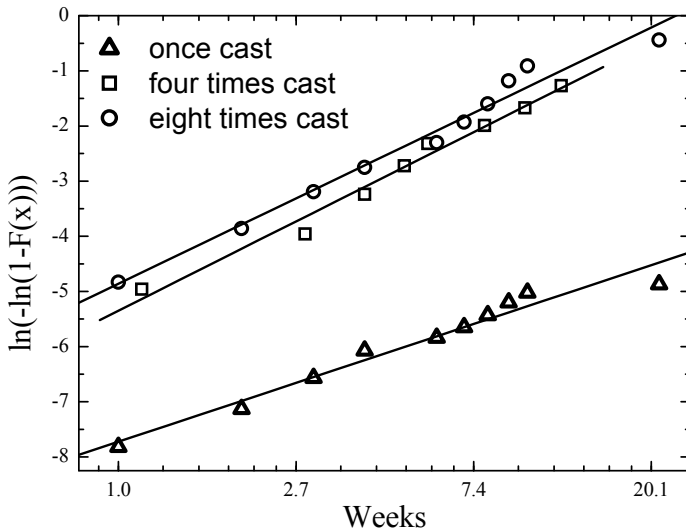


Fig. 3 Linearized Weibull cumulative distribution function (CDF) of Fe ion concentration released in artificial saliva by multiple recast coins.

## Conclusions

The main results are as follows:

1. Metallographic analysis shows that all samples have dendritic solidification microstructure, typical for commercial dental alloys.
2. EDS analysis confirms that the chemical compositions of the dendrite and interdendritic regions are different. As the number of recasting increases, the difference between dendritic and interdendritic regions is reduced.
3. Only Fe and Co ions were detected and could be measured in the artificial saliva. The once recast sample is the most durable. In the case of four and eight times recast samples, the ion release rate increases over time.

### Acknowledgements

This investigation was funded by the Serbian Ministry of Education and Science through research projects III 45012 and 172019.

### References

- [1] J.C.Wataha, *The Journal of Prosthetic Dentistry*, 83 (2) (2000) 223-234.
- [2] J.C.Wataha, R.L.Messer, *Dent. Clin. N. Am.*, 48 (2004) 499-512.
- [3] C.Manaranche, H.Hornberger, *Dental Materials*, 23 (2007) 1428-1437.
- [4] L.A.Dobrzanski, L.Reimann, *Journal of Achievements in Materials and Manufacturing Engineering*, 49 (2) 2011 193-199.
- [5] F. Nejatidanesh, O. Savabi, A. Yazdanparast, *Journal of Dentistry, Tehran University of Medical Sciences, Tehran, Iran*, 2 (4) (2005) 168-173.
- [6] T.S.Chandra, N.S.Kumar, B.K.Kumari, *Trends Biomater. Artif. Organs*, 25 (2) (2011) 51-59.
- [7] M. Sharma, A.V. R. Kumar, N. Singh, N.Adya,B.Saluja, *Journal of Materials Engineering and Performance*, 17 (5) (2008) 695–701.
- [8] L.Multi-Sagens, G. Ergun, E. Karabulut, *Dental Materials Journal*, 30(5) (2011) 598–610.
- [9] G. Petzow, *Metallographic Etching*, 2<sup>nd</sup> Edition, ASM International 1999.

## PRODUCTION OF HIGH GRADE PURE MAGNESIUM USING VACUUM DISTILLATION PROCESS

V. Matković<sup>1</sup>, V. Manojlović<sup>1</sup>, M. Sokić<sup>1</sup>, B. Marković<sup>1</sup>, Z. Gulišija<sup>1</sup>,  
Ž. Kamberović<sup>2</sup>

<sup>1</sup> Institute for Technology of Nuclear and other Mineral Raw Materials,  
Belgrade, Serbia

<sup>2</sup> Faculty of Technology and Metallurgy, University of Belgrade, Serbia

### Abstract

In this paper the procedure of obtaining of high purity magnesium by using the vacuum distillation process has been shown. Vacuum distillation process has been conducted under low and high vacuum at different operating temperatures and times. Also, the condenser structure in vacuum equipment is set up in such a way to get the optimal conditions for obtaining of high purity magnesium. Based on experimental results, optimal process parameters were determined which justify the economy and technology of the process.

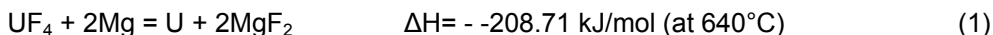
*Keywords: distillation, magnesium, vacuum, high purity*

### Introduction

Demand for high purity magnesium (Mg) has been notable in many research fields such as metallurgy, solid state physics, atomic energy, organic chemistry, biology, nanomaterial's, etc. A variety of methods for preparing organomagnesium compounds utilize elemental magnesium, and for many of them the purity and form of the metal is important or even critical. Magnesium is readily available in a purity of 99.8%, and this grade is satisfactory for many routine purposes [1].

Magnesium alloys are currently of great interest, as their extraordinary low density, high specific strength, and easy-recycling ability are very attractive for further applications in aeronautics, electronics and other consumer goods [2–4]. In investigation of these alloys, for instance investigation on the microstructure and mechanical properties, high purity magnesium has been used for alloying with other elements [5, 6]. Also, high purity magnesium has been used as an anode material in seawater activated batteries because he offers several advantages such as a high electrode potential of  $-2.73$  V vs. normal hydrogen electrode, a high faradic capacity, appropriate corrosion rate and low density [7, 8].

The reduction of uranium tetra-fluoride ( $UF_4$ ) by magnesium with the magnesiothermic reduction is one of the main industrial methods for producing commercial pure uranium ingot. The magnesiothermic reaction is given by [9, 10]:



Magnesium used for this purpose has to be exempted from elements with a large neutron cross section such as Boron (B), Cadmium (Cd), Cobalt (Co) etc. These elements gave long-living high activity isotopes (eg.  $Co^{60}$ ). The content of

impurities in high pure magnesium used for this purpose must not exceed the following values [10]:

Fe	25 ppm
Mn	50 ppm
Al	30 ppm
Si	125 ppm
C	100 ppm
Zn	300 ppm
Cl	25 ppm
Co	10 ppm
Ni	10 ppm
Cd	0.5 ppm
B	0.3 ppm

In this paper we will show a method for refining of technical magnesium (in different shapes and with different chemical compositions) in order to obtain high purity magnesium which satisfy the limitations mentioned below. The most common method for obtaining of high purity magnesium is vacuum distillation process [12, 13].

### Materials and methods

Refining experiments were conducted in steel crucible which is schematically shown in figure 1. This crucible should satisfy the long term service on high temperatures (up to 800 °C) and high vacuum (up to  $1 \cdot 10^{-3}$  Pa) in evaporator, with achieving of required drop temperature in condenser zone. Evaporator, length of 53 cm, is made of heat resistant Böhler steel, while condenser is made of common carbon steel [11]. Sealing of crucible on the closure was made with a rubber sealant. Crucible is heated in muffle furnace to a target temperature. In evaporator, vessel of heat resistant steel was loaded with crude magnesium. Condenser is cooled with water and placed outside of the furnace in order to obtain low temperatures, corresponding to the condensation of magnesium vapours.

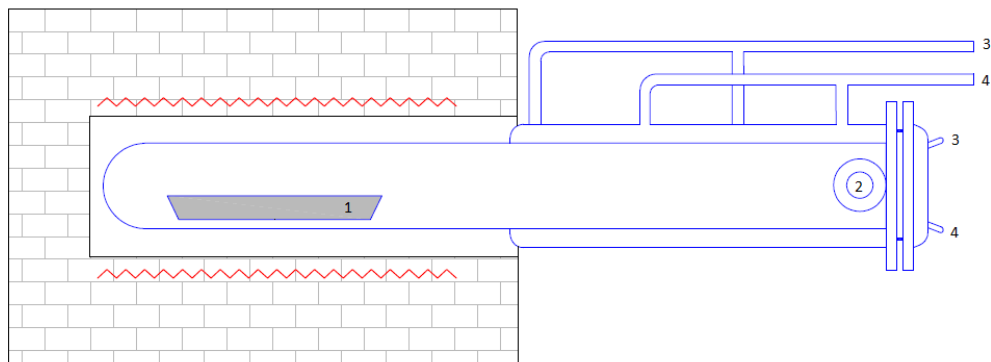


Figure 1 Horizontal steel crucible for vacuum distillation process: 1-vessel for crude magnesium; 2-connection for vacuum system; 3-water inlet; 4-water outlet

In order to obtain fractional distillation of magnesium and its impurities on different temperatures, multi zone system was installed into condenser by setting of the partition plates of stainless steel. First zone was marked as one immediate to evaporator from the first partition plate. Size and number of zones are variable and can be simply moved and placed in condenser as desired.

Temperature was measured by pyrometer placed inside of stainless steel pipe in such a way to manage temperatures measurement along the entire length of crucible. Vacuum system was connected with crucible via inlet on the condenser. Distillation experiments were performed on the pressures of the low and high vacuum and temperatures from 550-800 °C at different times.

Crude magnesium used as starting material for testing is divided in three different groups by shapes: chippings, strips and scraps. In experiment, ten samples of each variation of parameter were taken for distillation process, and then mean value was calculated and entered in the table. The mean chemical compositions of these groups are noticeably different and shown in Table 1.

Table 1 Analyses of impurities in crude magnesium, mean values

Group	Chemical composition of impurities, in ppm								
	Fe	Mn	Ni	B	Si	Zn	Cd	Al	C
1 (chippings)	57	400	5	0.86	107	300	0.4	10	5
2 (strips)	86	850	5	0.86	500	1000	0.4	100	5
3 (scraps)	250	162	5	0.2	500	2000	2.01	-	-

Variable parameters in this experimental work are: temperature, vacuum pressure and time of distillation process. The aim of this work is to determine optimal condition of process in aspect of pureness of final product in economic and environmental friendly manner.

## Results and discussion

Experiments for distillation process, with two zone system, were performed on 60 samples (10 for each variation of parameters) of approximately the same amount (from 50 to 110 grams) and temperatures of 550-800 °C under vacuum pressure of  $1.3 \cdot 10^{-3}$  to 11 Pa (high and low vacuum). The mean values were calculated and represented in table 2 and 3.

Table 2 Parameters of distillation process of crude magnesium, two zone system, mean values

No. of group	Crude Mg, gr	T <sub>sub</sub> , °C	T <sub>con</sub> , per zones, °C		Time, min	Vacuum, Pa	% Mg per zones	
			I	II			I	II
1	50	610	485	-	90	11	84.5	-
2	60	745	570	465	105	9	35.8	64.2
3	90	800	-	588	45	11	-	100
4	110	550			60	1.3-2.7·10 <sup>-3</sup>	42	58
5	100	600			60	4-6.7·10 <sup>-3</sup>	59	41
6	100	600			40	4-6.7·10 <sup>-3</sup>	100	

Table 3 Chemical composition of impurities in magnesium obtained by distillation process, two zone system, in ppm

No. of group, zone	Fe	Mn	Al	Si	Ni	Co	Cd	B	Zn	Cl	C	
1, I	5	9	10	55	5	-	0.4	0.20	50	-	-	
2	I	38	200	10	25	5	-	0.4	0.20	50	-	-
	II	5	65	-	25	5	-	0.4	0.20	435	-	-
3, II	9.2	9.2	10	25	5	5	0.4	0.20	14	-	-	
4	I	10	20	10	500	5	5	0.4	0.30	-	-	-
	II	10	14	10	210	5	5	0.4	0.20	2000	-	-
5	I	10	20	12	50	5	5	0.4	0.84	-	-	-
	II	250	154	20	77	5	5	0.4	0.20	2000	-	-
6, I and II	10	20	10	500	-	0.5	0.4	0.2	-	-	-	

According to the results, represented above, lower temperatures of distillation of about 600 – 650 °C and lower vacuum pressures gives advanced purification of impurities. Also, we can note that the boron content decrease to 0.2 ppm and concentration of Cd remains on 0.4 ppm. Higher concentration of Zn is expected due to the higher vapour pressure of Zn compared to the Mg, but it is possible to depart Zn from Mg by placing of two zone system. Time of complete distillation of magnesium is 40 min on lower vacuum pressure and temperature of 600 °C, so there is no need for longer times of distillation process.

Processes of distillation with multy-zone system were conducted on high vacuum (with argon working atmosphere) and different temperatures and times along with fraction condensation (Groups: 7-10, Table 4-5). Also, multiple distillation process was conducted under three stages, on temperature of 700 °C, and vacuum of 1.3-2.7·10<sup>-3</sup> Pa (Groups: 11', 11'' and 11''' Table 4-5).

Table 4 Parameters of distillation process of crude magnesium, multy-zone system, mean values

No.	In. Mg, gr	T <sub>dis.</sub> , °C	T <sub>con.</sub> per zones, °C					Time min	Vac., Pa ·10 <sup>-3</sup>	% Mg per zones, Residue				
			I	II	III	IV	Res.			I	II	III	IV	Res.
7	270	590	515	485	-	-	590	30	3.7	20.2	10	-	-	69.8
8	160	660	525	430	-	-	660	40	4.3	19	66	-	-	18
9	300	700	625	588	470	400	700	50	7.3	26.1	34.3	31.9	2.7	5
10	70	800	-	610	550	510	-	60	2.7	-	42	40	18	-
11'	110	700	620	590	480	400	700	60	1.3	30	29.5	25	9.5	6
11''	75	700	620	590	480	400	700	60	1.3	35.3	30.2	24.3	4.2	6
11'''	54	700	630	600	480	405	700	60	2.7	38	33.2	21.1	3.5	4.2

According to the results, represented in tables 4 and 5, it is observed that with increasing of temperature, during the fractional distillation process, the number of zones rises. Impurities in the condensate do not vary greatly, both in multy zone system whit one stage and with two and three stages.

Table 5 Chemical composition of impurities in magnesium obtained by distillation process, multy-zone system, in ppm

No. of group, zone	Fe	Mn	Al	Si	Ni	Co	Cd	B	Zn	Cl	C	
7	I	5	10	10	25	5	5	0.4	0.2	76	-	-
	II	10	10	10	25	5	5	0.5	0.2	125		
8	I	9	20	10	96	5	3	0.4	0.2	50	-	-
	II	5	10	10	25	5	5	0.4	0.2	125		
9	I	5	8	10	25	5	5	0.4	0.2	30	-	-
	II	5	10	10	25	5	5	0.4	0.2	59	-	-
	II	5	10	10	10	5	5	0.4	0.2	50	-	-
	IV	5	10	10	20	5	5	0.5	0.2	96	-	-
10	II	115	30	50	100	5	0.5	0.4	0.2	34	-	-
	III	39	25	50	80	5	0.5	0.4	0.3	81		
	IV	20	25	50	60	5	0.5	0.5	0.3	200	-	-
11'	mean	10	20	10	50	-	5	0.5	0.3	150	-	-
11''	mean	10	20	10	50	-	5	0.4	0.3	90	-	-
11'''	mean	10	20	10	50	-	5	0.4	0.3	50	-	-

## Conclusion

Based on the presented experiments of vacuum distillation process for producing of high purity magnesium, we can conclude the following:

- The optimum conditions for distillation of crude magnesium are: temperatures of 600-660 °C, vacuum pressure of  $1.3-4.3 \cdot 10^{-3}$  Pa and time of 40 min, with two zone system.
- For removing of Zn and Cd, higher temperatures of distillation are required, from 700-750 °C in order to capture high concentration of Zn and Cd in last, fourth zone, which can be removed.
- Multiple distillation process is reasonable only for removal of volatile impurities such as Zn, Cd and alkaline metals.

This method is simple and efficient in technological, environmental and economic point of view. The main disadvantage of this method is high initial investment in the equipment, which can be offset with price of high grade pure magnesium.

## Acknowledgement

The authors wish to acknowledge the financial support from the Ministry of Education and Science of the Republic of Serbia through the projects TR34002 and TR34033.

## Reference

- [1] Wakefield, B.J. (1995) Organomagnesium Methods in Organic Synthesis. Preparation of Organomagnesium Compounds, pp. 21-71. ISBN: 978-0-12-730945-3, Elsevier Ltd.
- [2] Kim, B., Park, K., Park, Y., Park, I. (2011) Effect of Pd on microstructures and tensile properties of as-cast Mg–6Al–1Zn alloys. *Materials Letters*, 65, pp. 122-125.
- [3] Zheng, J., Wang, Q., Jin, Z., Peng, T. (2010) Effect of Sm on the microstructure, mechanical properties and creep behavior of Mg–0.5Zn–0.4Zr based alloys. *Materials Science and Engineering: A*, 527, pp. 1677-1685.
- [4] Yang, M., Pan, F. (2010) Effects of Sn addition on as-cast microstructure, mechanical properties and casting fluidity of ZA84 magnesium alloy. *Materials & Design*, 31, pp. 68-75.
- [5] Jo, S.M., Kyung, C.P., Kim, B.H., Kimura, H., Park, S.K., Park, Y.H. (2011) Investigation on the Microstructures and Mechanical Properties of Mg-Al-Yb Alloys. *Materials Transactions*, 52, pp. 1088-1095.
- [6] Shao, X.H., Yang, Z.Q., You, J.H., Qiu, K.Q., Ma, X.L. (2011) Microstructure and microhardness evolution of a  $Mg_{83}Ni_6Zn_5Y_6$  alloy upon annealing. *Journal of Alloys and Compounds*, 509, pp. 7221-7228.
- [7] Odhayan, R., Muniyondi, N., Mathur, P.B. (1992) Studies on magnesium and its alloys in battery electrolytes. *British Corrosion Journal*, 27, pp.68.
- [8] Zhao, Y., Yu, K., Hu, Y., Li, Sh., Tan, X., Chen, F., Yu, Z. (2011) Discharge behaviour of Mg-4wt%Ga-2wt%Hg alloy as anode for seawater activated

- battery. *Electrochimica Acta*, 56, pp. 8224-8231.
- [9] Saliba-Silva, A.M., Aguiar, B., Carvalho, E.U., Da Silva, D.G., Riella, H.G., Durazzo, M. (2011) Analysis of slag formation during  $UF_6$  Magnessothermic Reduction. RERTR 2011 – 33<sup>rd</sup> International Meeting on Reduced Enrichment for Research and Test Reactors, October 23-27, Santiago, Chile, CD-Proceedings.
- [10] Gupta, C.K., Singh H. (1999) Uranium Resource Processing: Secondary Resources. Developments in uranium resources, production, demand and the environment: Proceedings of a technical committee meeting held in Vienna, 15–18 June, pp. 73-80.
- [11] Böhler Bleche, GmbH & Co KG, Austria, [http://www.boehler-bleche.com/english/heat\\_res\\_steel.php](http://www.boehler-bleche.com/english/heat_res_steel.php) (February 20, 2013).
- [12] Sabirov, Kh.Kh., Topalova, G.N. (2000) Development of Effective Technology for Deep Refining of Magnesium. *Russian Journal of Non-Ferrous Metals*, 41, pp. 72-75.
- [13] Gao, F., Nie, Z., Wang, Z., Gong, X., Zuo, T. (2008) Assessing environmental impact of magnesium production using Pidgeon process in China. *Transactions of Nonferrous Metals Society of China*, 18, pp. 749-754.

## PHASE EQUILIBRIA INVESTIGATION AND CHARACTERIZATION OF THE ALLOYS IN THE Bi-Cu<sub>0.75</sub>Ni<sub>0.25</sub> SECTION OF THE Bi-Cu-Ni SYSTEM

Branislav R. Marković<sup>1\*</sup>, Dragana T. Živković<sup>2</sup>, Dragan M. Manasijević<sup>2</sup>,  
Nadežda M. Talijan<sup>3</sup>, Miroslav D. Sokić<sup>1</sup>

1. Institute for Technology of Nuclear and Other Mineral Raw Materials,  
86 Franchet d'Esperey Street, Belgrade 11000, Serbia

2. Technical Faculty, University of Belgrade, 12 VJ Street, Bor 19210,  
Serbia

3. Institute of Chemistry, Technology and Metallurgy, 12 Njegoseva Street,  
11000 Belgrade, Serbia

\*Corresponding author: b.markovic@itnms.ac.rs

### Abstract

The Bi-Cu-Ni ternary system represents one among the systems interesting as potential advanced lead-free solder materials for high temperature application. The results of phase equilibria investigation and characterization of the alloys selected in the Bi-Cu<sub>0.75</sub>Ni<sub>0.25</sub> section from bismuth corner with molar ratio Cu:Ni = 3:1, are presented in this paper. Thermodynamic calculation was done according to the CALPHAD method using PANDAT software, while chosen alloys in the selected section were experimentally investigated using different experimental methods – DTA, DSC, SEM-EDS, hardness and electrical conductivity measurements.

*Keywords: Bi-Cu-Ni alloys, lead-free solders, phase equilibria, characterization*

### Introduction

Alloys of Pb-Sn system are most commonly used solder materials in electrical and electronics industry because of low cost and unique combination of physical, chemical and mechanical properties as well as their reliability. Due to recent EU legislation DIRECTIVE WEEE (Waste from Electrical and Electronic Equipment) and DIRECTIVE 2002/95/EC, Restriction of the use of certain Hazardous Substances (RoHS) in electrical and electronic equipment) which prohibit use of lead containing solders in many industries from July 1st, 2006, a great effort has been placed on the development of new Pb-free soldering and brazing materials [1-6]. The phase diagram provides basic information to design new Pb-free soldering materials. Various authors developed a thermodynamic databases for phase diagrams using the calculation of phase diagrams (CALPHAD) method, which provides an extremely useful tool for the design of materials because it significantly decreases the amount of required experimental work. On the basis of thermodynamic calculation, information on the melting temperature range for solder, the solidification path, and the susceptibility to intermetallic formation with various substrates is available.

One of the potential Cu-Ni-based lead-free systems for high temperature application is the Bi-Cu-Ni system. This system represents environmental friendly alternatives to Sn-based solders which has been examined recently in the frame of COST MP0602 "HISOLD" project [7] and has been described in two recent references [8,9]. Gao et al. [8] investigated phase equilibria of the Bi-Cu-Ni system at 300, 400, and 500 °C using metallography and electron probe microanalysis on equilibrated alloys and diffusion couples, while Marković et al. [9] performed thermodynamic modeling of the Bi-Cu-Ni system using CALPHAD method.

Having in mind the importance of knowledge of the Bi-Cu-Ni alloys for the understanding of the processes occurring during soldering and during operation of the soldered devices, the results of phase equilibria and characterization of the alloys in the CuNi-Bi section of the Bi-Cu-Ni system are presented in this paper. The investigations were performed using different experimental methods – thermal analysis, SEM-EDS analysis, hardness and electrical conductivity measurements.

## Experimental

Investigated samples were chosen in the Bi-Cu<sub>0.75</sub>Ni<sub>0.25</sub> section of the Bi-Cu-Ni system. The samples were prepared by induction melting of pure metals (purity higher than 99.99%) under argon atmosphere. The alloy samples were homogenized at 800 °C for several hours under argon atmosphere and then furnace cooled to room temperature. The total mass losses of the prepared ingots were less than 1 mass%. The composition and masses of chosen samples are given in Table 1. These samples were experimentally investigated using DTA/DSC, SEM-EDS, hardness and electrical conductivity measurements.

Table 1. Composition and masses (in g) of the investigated samples

Sample	$x_{Bi}$	$x_{Cu}$	$x_{Ni}$	$m_{Bi}$	$m_{Cu}$	$m_{Ni}$
A2	0,1	0,675	0,225	1,62844	3,3424	1,02917
B2	0,2	0,6	0,2	2,73583	2,49571	0,76846
C2	0,3	0,525	0,175	3,53776	1,88257	0,57967
D2	0,4	0,45	0,15	4,14531	1,41805	0,43664
E2	0,5	0,375	0,125	4,6215	1,05397	0,32453
F2	0,6	0,3	0,1	5,00478	0,76092	0,2343
G2	0,7	0,225	0,075	5,31993	0,51996	0,1601
H2	0,8	0,15	0,05	5,58363	0,31835	0,09802
J2	0,9	0,075	0,025	5,80753	0,14716	0,04531

The DTA/DSC measurements were performed on a SDT Q600 (TA Instruments) device. Alumina crucibles were used and measurements were performed under flowing argon atmosphere. Samples weighing about 50 mg were investigated using the heating rate 5 °C/min. In order to test reproducibility of the results every measurement was repeated, but no significant temperature deviation was found between the first and repeated series of DTA/DSC measurements.

SEM analysis was done using JEOL JSM 6460 apparatus with energy dispersive spectrometry, EDS (Oxford Instruments).

Electrical conductivity of the investigated samples was measured using the standard apparatus – SIGMATEST 2.069 (Foerster) eddy current instrument for measurements of electrical conductivity of non-ferromagnetic metals, based on complex impedance of the measuring probe with diameter of 8mm.

Hardness measurements were done using standard procedure according to Vickers.

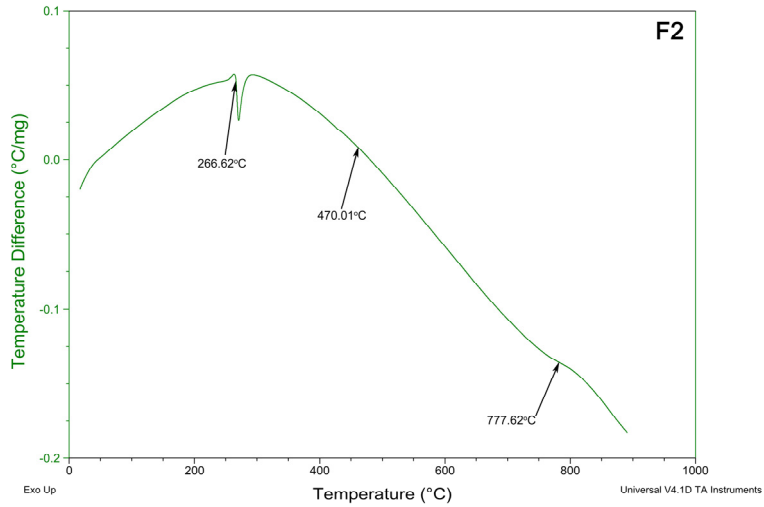
The samples were prepared without using of etching agents for structure development.

## Results and discussion

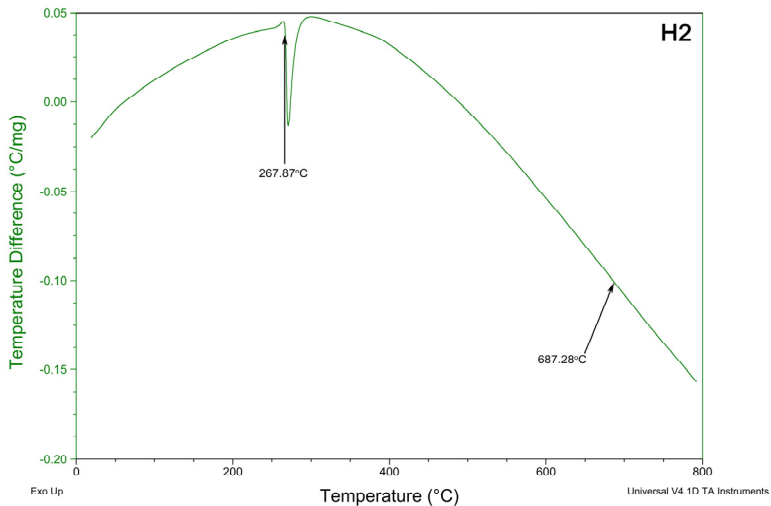
The results of the DTA/DSC heating measurements of the chosen samples in the Bi-Cu<sub>0.75</sub>Ni<sub>0.25</sub> section of the Bi-Cu-Ni system, including liquidus temperatures and other phase transition temperatures are presented in Table 2 and Figure 1 for the samples F2 and H2.

Table 2. DTA/DSC results for the investigated alloys in the Bi-Cu<sub>0.75</sub>Ni<sub>0.25</sub> section (taken from [9])

Sample	Sample composition (at.%)	Temperature (°C)	
		Phase transitions	Liquidus
F2	Bi <sub>60</sub> Cu <sub>30</sub> Ni <sub>10</sub>	266, 470	777
G2	Bi <sub>70</sub> Cu <sub>22.5</sub> Ni <sub>7.5</sub>	267	722
H2	Bi <sub>80</sub> Cu <sub>15</sub> Ni <sub>5</sub>	267	687
J2	Bi <sub>90</sub> Cu <sub>7.5</sub> Ni <sub>2.5</sub>	267	-



(a)



(b)

Figure 1. Characteristic DTA curves for the samples F2 (a) and H2 (b)

The phase diagram of the investigated Bi-Cu<sub>0.75</sub>Ni<sub>0.25</sub> section has been calculated using PANDAT software Vs. 8.0 [10, 11] and is presented in Figure 2, together with experimentally determined DTA/DSC points.

It could be noticed that calculated phase diagram is in good agreement with DTA/DSC experiments.

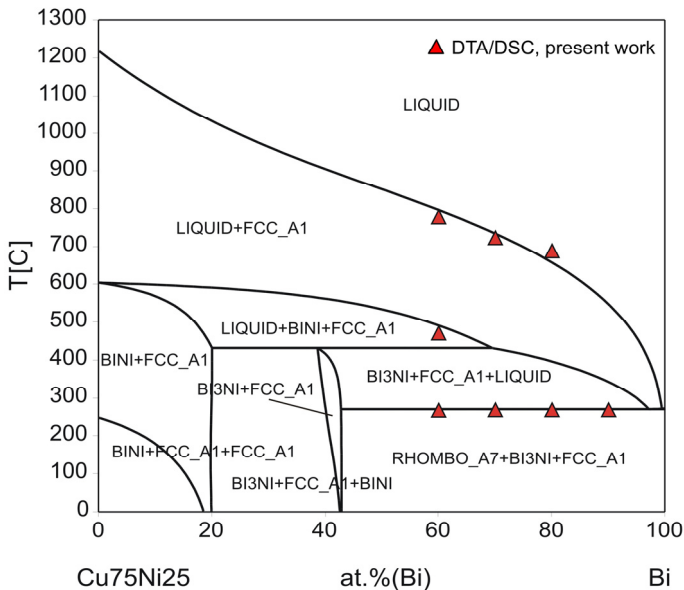


Figure 2. Calculated phase diagram of the Bi-Cu<sub>0.75</sub>Ni<sub>0.25</sub> section compared with thermal analysis results from the present study (taken from [9])

Further characterization of the investigated alloys in the Bi-Cu-Ni system, have been done using SEM-EDS analysis and hardness and electrical conductivity measurements.

Structural analysis done using SEM-EDS method confirmed that the Bi-Cu-Ni system consists of five phases (liquid, RHOMBO\_A7 (Bi), FCC\_A1 (Cu,Ni), BiNi and Bi<sub>3</sub>Ni), which is in accordance with its crystallographic data, given in [12].

The results of hardness measurements are shown in Table 3. As can be seen, the hardness decreases rapidly with bismuth concentration increase for selected alloys in the investigated section. Noticed behaviour can be explained as the consequence of dominant phases present in the alloys structure, mostly Bi-based phases - BiNi, Bi<sub>3</sub>Ni and RHOMBO\_A7, due to the fact that bismuth poses the lowest hardness value among the three constitutive metals in ternary system Bi-Cu-Ni.

The results of electrical conductivity measurements are given in Table 4 (three measuring series), where the electrical conductivity dependence on the composition is showed. It can be noticed that increase of bismuth content influences the decrease in electrical conductivity for all samples in the investigated section, which is in accordance with the electrical conductivity of pure bismuth ( $\approx 0.867$  MS/m [13,14]). The electrical conductivity decrease with bismuth content increase is the consequence of prevailing phases presence in the structure, i.e. the bismuth based phases BiNi, Bi<sub>3</sub>Ni and RHOMBO\_A7 influencing the electrical conductivity decrease.

Table 3. The results of hardness measurements

Sample	HV5
A2	99
B2	70,4
C2	43,3
D2	40,9
E2	30,8
F2	28,6
G2	23,4
H2	15,5
J2	13,7

Table 4. The results of electrical conductivity measurements

Sample	Electrical conductivity (MS/m)		
A2	2,826	2,824	2,830
B2	1,907	1,904	1,905
C2	1,5231	1,5196	1,5216
D2	1,4126	1,4139	1,4150
E2	1,2641	1,2616	1,2583
F2	1,169	1,166	1,168
G2	1,1301	1,1297	1,1289
H2	1,005	1,006	1,006
J2	0,8969	0,8953	0,8952

## Conclusion

The Bi-Cu-Ni alloys, from the Bi-Cu<sub>0.75</sub>Ni<sub>0.25</sub> section, have been characterized using different experimental methods, such as thermal analysis, SEM-EDS, hardness and electrical conductivity measurements. The phase diagram of this section has been calculated by thermodynamic modeling using Pandat software, and confirmed by DTA/DSC and SEM-EDS results. Measured values of hardness and electrical conductivity decreases with bismuth concentration increase in all investigated alloys.

Obtained results represent a contribution to the better knowledge of thermal, structural mechanical and electrical properties of Bi-Cu-Ni alloys as a new potential lead-free solder material for high temperature application.

## Acknowledgment

This work is part of realization of projects N<sup>o</sup>172037 and N<sup>o</sup> 34023 that are supported by the Ministry of Education, Science and Technological Development of the Republic of Serbia.

## References

- [1] Y. Li and C.P. Wong: Recent advances of conductive adhesives as a lead-free alternative in electronic packaging: Materials, processing, reliability and applications. *Mater. Sci. Eng.*, R 51 (2006) 1.
- [2] T. Laurila, V. Vuorinen, and J.K. Kivilahti: Interfacial reactions between lead-free solders and common base materials. *Mater. Sci. Eng.*, R 49 (2005) 1.
- [3] Y. Takaku, I. Ohnuma, R. Kainuma, Y. Yamada, Y. Yagi, Y. Nishibe, and K. Ishida: Development of Bi-base hightemperature Pb-free solders with second-phase dispersion: Thermodynamic calculation microstructure, and interfacial reaction. *J. Electron. Mater.* 35 (2006) 1926.
- [4] J.N. Lalena, N.F. Dean, and M.W. Weiser: Experimental investigation of Ge-doped Bi-11Ag as a new Pb-free solder alloy for power die attachment. *J. Electron. Mater.* 31 (2002) 1244.
- [5] M. Rettenmayr, P. Lambracht, B. Kempf, and M. Graff: High melting Pb-free solder alloys for die-attach applications. *Adv. Eng. Mater.* 7 (2005) 965.
- [6] A.T. Dinsdale, A. Kroupa, J. Vizdal, J. Vrestal, A. Watson, A. Zemanova, COST 531 Database for Lead-free Solders, Ver. 2.0 (2006) unpublished research, COST531 homepage: <http://www.univie.ac.at/cost531/>.
- [7] <http://cost602.ipm.cz/>
- [8] F. Gao, X. Liu, Y. Takaku, I. Ohnuma, K. Ishida, *J. Mater. Res.*, 24 (2009) 2644-3652
- [9] B. Marković, D. Živković, J. Vřešťál, D. Manasijević, D. Minić, J. Stajić-Trošić, R. Todorović, *Calphad*, 2010, 34(3) 294-300
- [10] <http://www.computherm.com>
- [11] W. Cao, S.-L. Chen, F. Zhang, K. Wu, Y. Yang, Y.A. Chang, R. Schmid-Fetzer, W.A. Oates: *CALPHAD*, 33 (2) (2009) 328-342.
- [12] Dinsdale, A., Watson, A., Kroupa, A., Vrestal, J., Zemanova, A., Vizdal, J. *COST Action 531 - Atlas of Lead free soldering*: COST office, Brussels, 2008, pp. 124.
- [13] [www.chemicool.com](http://www.chemicool.com)
- [14] [www.webelements.com](http://www.webelements.com)

## **PHYSICAL AND CHEMICAL CHANGES DURING HYDROMETALLURGICAL TREATMENT OF NON-STANDARD COPPER CONCENTRATE**

Miroslav M. Sokić<sup>1</sup>, Aleksandra M. Mitovski<sup>2</sup>, Nada D. Štrbac<sup>2</sup>,  
Ivan N. Mihajlović<sup>2</sup>, Jovica N. Stojanović<sup>1</sup>, Velibor Đ. Andrić<sup>3</sup>

<sup>1</sup>*Institute for Technology of Nuclear and Other Mineral Raw Materials, Belgrade,  
Serbia*

<sup>2</sup>*University of Belgrade, Technical Faculty, Bor, Serbia*

<sup>3</sup>*Institute of Nuclear Sciences Vinca, Beograd, Srbija  
e-mail: amitovski@tf.bor.ac.rs*

### **Abstract**

Non-standard concentrates will represent the basic raw materials for the primary metal production in the future, having in mind the continuous impoverishment of the ore reserves rich on valuable metals. Enargite-based non-standard copper concentrate was investigated in this paper. The samples were subjected to hydrometallurgical treatment (leaching in NaClO media), varying several parameters by the predefined experiment design. Physical and chemical changes during treatment were observed, and the results of the chemical analysis, XRD and EDXRF are presented in the paper.

*Keywords:* non-standard copper concentrate, enargite, leaching, hypochlorite

### **Instruction**

Progressive decrease in the amount of rich copper-based ore, brought a necessary option to impose ore exploitation with lower copper content, but, unfortunately, with higher concentrations of toxic elements (eg. As, Ni, Cd). Due to that, researchers' important goal in the near future should be finding the most optimal technological solution to reduce the concentration of unwanted elements in ores or concentrates, so they could still be processed by conventional metallurgical processes - pyrometallurgical and hydrometallurgical, in accordance to the current rigorous law and environmental regulations on the allowable contents of pollutants in poorer non-standard copper concentrates.

Control of toxic elements, especially arsenic, because of its harmful effects on human health, during extractive metallurgy operations requires its removal, subsequent safe disposal and the avoidance of emissions either in gaseous or aqueous phases [1,2].

Removing and storing arsenic in the form of stable disposable solid compound or as a saleable/ marketable product is a challenging task[3]. Numerous attempts are made to reduce the arsenic content in ores by roasting in order to remove arsenic and produce a clean feed for copper smelters [4-11].

Upon reductive or neutral roasting or smelting enargite concentrates, arsenic-bearing gases are released (mostly As<sub>2</sub>S<sub>3</sub>), which need to be captured,

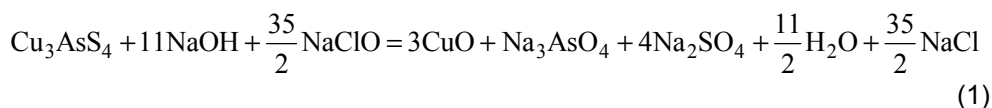
separated, oxidized, and stabilized. This imposes further gas/dust collection and separation facilities that make such processing quite expensive. Furthermore, pressure on smelters to reduce the quantities of SO<sub>2</sub> and toxic metals in fugitive gases is increasing. These features make it difficult to consider a pyrometallurgical process for the treatment of enargite rich concentrates. Presently, the maximum allowable arsenic content in copper concentrates for smelting is set at 0.5%. This figure is expected to be lowered in the future with an arsenic level of 0.3% being under consideration [12].

The leaching of refractory complex concentrates such as enargite represent a major metallurgical challenge and several hydrometallurgical options have been shown to be unsuccessful for the leaching of enargite concentrates.

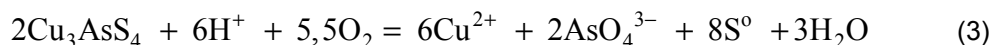
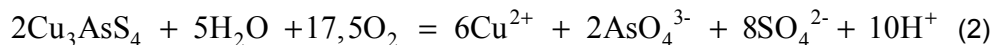
Recently, the effect of different media on the leaching degree of arsenic and its removal from

copper ores and concentrates has been investigated: NaHS [13], alkali Na<sub>2</sub>S solution [14], and others. The application of sodium sulfide alkaline solutions favors the selective leaching of arsenic, while copper, which remains as part of the solid residue, is suitable for further pyrometallurgical treatment. Experiments have shown that more than 90% of arsenic can be separated by extraction from alkaline enargite leaching at 90 °C and under atmospheric conditions [15].

Selective oxidation of alkali-oxidative enargite leaching with hypochlorite solution can be used to remove arsenic from copper concentrates. The reaction of arsenic leaching with hypochlorite can be described with following reaction:



In the presence of oxygen, two reactions are possible, where it was shown that reaction (3) is dominant under ambient conditions:



These results agree with literature data [16,17] in terms of forming tenorite (CuO) as the enargite oxidation product in the described conditions. Following, arsenic from the solution can be stabilized by precipitation with Ca(OH)<sub>2</sub>.

## Experimental

A sample of non-standard enargite based copper concentrate was used for the experimental investigation. In order to determine chemical composition of the initial concentrate, chemical analysis was performed.

The hydrometallurgical treatment included following procedure: finely powdered sample was subjected to leaching in the NaClO aqueous solution, with 5g/dm<sup>3</sup> NaOH, for the pH regulation (pH was approximately 12), the solution volume was 0.8 dm<sup>3</sup>. The aim was to decrease the arsenic amount in the leaching

residue and prove the leaching selectivity of the NaClO media, so the concentrate can be applicable as a part of the smelter feed.

Experiments were carried out by varying following parameters:

- NaClO concentration (0.18; 0.3 and 0.42) mol dm<sup>-3</sup>,
- temperature of NaClO solution (25; 40 and 60) °C,
- sample mass (0.3; 0.5 and 0.7) g,
- stirring speed (100; 300 and 600) min<sup>-1</sup> and
- leaching time (20; 60 and 120) min.

In order to determine mineralogical composition of the raw concentrate sample and physical and chemical changes that occurred after the selective leaching with hypochlorite, XRD (*X-Ray Diffraction*) and EDXRF (*Energy Dispersive X-Ray Fluorescence*) analysis were done on the initial sample and on the solid residue after leaching. The leaching was done under the following conditions:

- *minimum parameter values* (according to predefined experiment design): NaClO concentration 0.18 moldm<sup>-3</sup>; NaClO solution temperature 25 °C; sample mass 0.3 g; stirring speed 100 min<sup>-1</sup> and leaching time 20 min.

- *medium parameters values* (according to predefined experiment design): NaClO concentration 0.3 moldm<sup>-3</sup>; NaClO solution temperature 40 °C; sample mass 0.5 g; stirring speed 100 min<sup>-1</sup> and leaching time 60 min.

- *maximum parameters values* (according to predefined experiment design): NaClO concentration 0.42 moldm<sup>-3</sup>; NaClO solution temperature 60 °C; sample mass 0.7 g; stirring speed 600 min<sup>-1</sup> and leaching time 120 min.

The arsenic content in the liquid phase after leaching was obtained using ICP-AES (*Inductively Coupled Plasma-Atomic Emission Spectrometer*), and then the arsenic leaching rate was calculated.

## Results and discussion

Chemical analysis results of investigated concentrate are shown in Table 1.

Table 1. Chemical composition of the non-standard copper concentrate sample

Element	Cu	Fe	S	As	Zn	Sb	Pb	Ni	Cd
Content [%mass]	9.52	10.07	11.00	3.44	0.18	0.15	0.006	0.0005	0.0009

Results of the XRD analysis for the initial sample is shown in Figure 1, while the EDXRF results of the solid residues are shown in Figure 2.

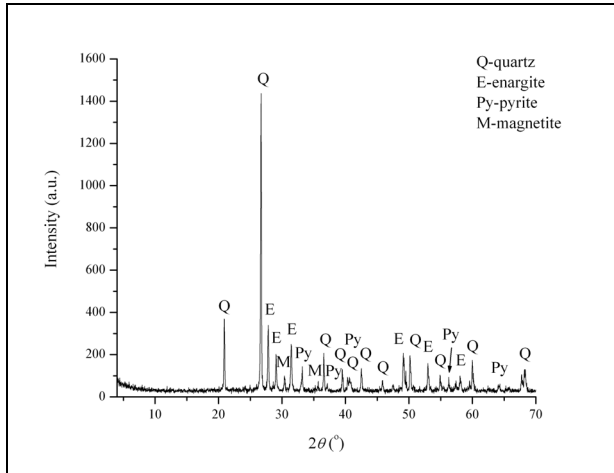


Figure 1. XRD analysis of the investigated non-standard concentrate sample

Chemical composition results indicate that investigated concentrate was polymetallic, while XRD results showed that metals are found in the form of sulfides: copper and arsenic are found in the enargite mineral form, sulfur is distributed in enargite and pyrite, while metal iron occurs as magnetite.

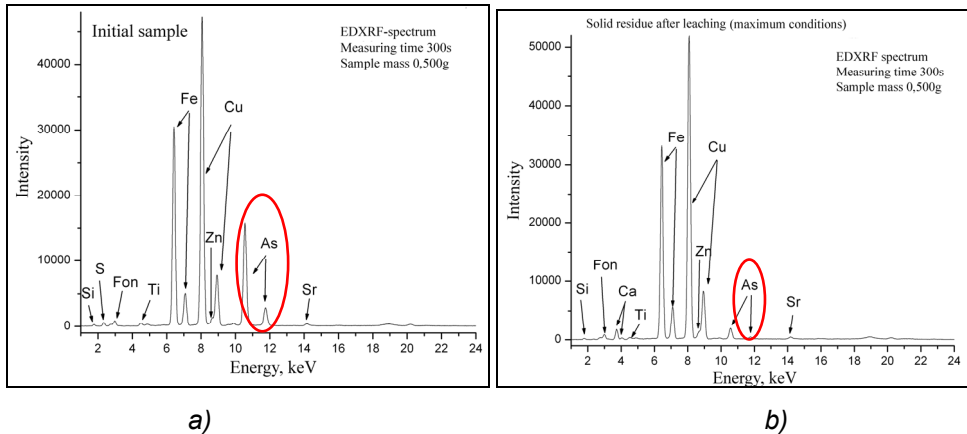


Figure 2. EDXRF results (a-initial sample, b-solid residue under max. leaching parameters)

The EDXRF results show significant decrease in the arsenic quantity after hydrometallurgical treatment in NaClO media. The arsenic occurrence intensity (the first As - peak) decreases about eight times under maximum leaching parameters (Fig. 2), which is proportional to the amount of arsenic in the solid residue. The EDXRF results show that the leaching rate of arsenic is about 90%, which is in a good accordance with the ICP-AES result (95.51% for the maximum leaching parameters values).

The leaching rate of arsenic for various experimental conditions is presented in Table 2:

Table 2. Amount of arsenic in the leach residue

Parameter	Minimum	Medium	Maximum
M(NaClO), mol dm <sup>-3</sup>	0.18	0.3	0.42
Temperature, °C	25	40	60
Sample mass, g	0.3	0.5	0.7
Stirring speed, min <sup>-1</sup>	100	100	600
Leaching time, min	20	60	120
% As	29.07	75.58	95.51

The leaching results show progressive increase of the arsenic content in the liquid leaching residue, i.e. the As amount decrease in the solid residue, with the increase of the experimental parameters. Compared to the EDXRF results, the other components (Cu, Fe, Zn, Si) left in the solid residue with slight or no losses, which proved the possibility for the selective arsenic leaching from enargite in NaClO media.

## Conclusion

Non-standard copper concentrate was investigated in this paper, from the aspect of its potential future usage in existing copper production.

Based on chemical analysis results, the investigated concentrate is rich on Cu, Fe and S. Also, the amount of As is significant-3.44%, which is highly above the legislative upper limit. Nevertheless, this concentrate, based on copper content, can be used in metallurgical processing, but it must be pretreated in order to decrease arsenic level under 0.5%.

Chemical analysis of liquid phase after hydrometallurgical experimental pretreatment in hypochlorite media showed that in all performed experiments arsenic was leached into liquid phase.

Results of XRD analysis show that the initial sample consists mostly of sulfide copper minerals with iron and arsenic: enargite (Cu<sub>3</sub>AsS<sub>4</sub>) and magnetite (Fe<sub>3</sub>O<sub>4</sub>). The rest is pyrite (FeS<sub>2</sub>) and silicon based oxide mineral quartz (SiO<sub>2</sub>).

EDXRF results confirmed XRD results and showed that the amount of arsenic is significantly decreased comparing to the initial sample and solid leaching residue after leaching under maximum experimental conditions. On the contrary, the negligible amount of copper decreased after leaching, which proofs that selective extraction of arsenic present in the nonstandard copper concentrates with NaClO is possible and feasible.

## Acknowledgement

Authors are grateful to the Ministry of Education, Science and Technological Development, Republic of Serbia, for financial support in this research as a part of the Project TR 34023.

## References

- [1] Terry, B.S., Sánchez, M., 1995. Environmentally friendly processing of copper minerals bearing arsenic and/or sulfur by pyrometallurgical route. In: Casali, A., Dobby, G.S., Molina, C., Thoburn, W.J. (Eds.), *Proceedings of Copper 95 International Conference*, vol. II, pp. 337–345. Santiago, Chile.
- [2] Terry, B.S., Sánchez, M.A., Ulloa, A.G., 1994. Calcium oxide as a reagent for the capture of arsenic emissions during the roasting of enargite. In: Hager, J.P., Hansen, B.J., Imrie, W.P., Pusateri, J.F., Ramachandran, V. (Eds.), *Proceedings of Extraction and Processing for the Treatment and Minimization of Wastes 1994*. The Minerals, Metals and Materials Society, Warrendale, PA, pp. 201–215.
- [3] Riveros, P.A., Dutrizac, J.E., Spencer, P., 2001. Arsenic disposal practices in the metallurgical industry. *Can. Metall. Q.* 40, 395–420.
- [4] Acuna, C.M., Berg, G., Lindquist, B., 2005. Roasting of high arsenic concentrate flue dust mixtures. *Proceedings of the European Metallurgical Conference (EMC)*, vol. 2, GDMB Medienverlag, Clausthal-Zellerfeld, Germany, pp. 695–706.
- [5] Padilla, R., Fan, Y., Sanchez, M., Wilkomirsky, I., 1997. Arsenic volatilization from enargite concentrate. In: Mishra, B. (Ed.), *Proceedings of EPD Congress 1997*. The Minerals, Metals and Materials Society, Warrendale, PA, pp. 73–83.
- [6] Padilla, R., Fan, Y., Sánchez, M., Wilkomirsky, I., 1998. Processing high arsenic copper concentrates. In: Sánchez, M.A., Vergara, F., Castro, S.H. (Eds.), *Proceedings of Environment & Innovation in the Mining and Mineral Technology, IV Conference on Clean Technologies for the Mining Industry*, vol. 2, pp. 603–612. Santiago, Chile.
- [7] Padilla, R., Fan, Y., Wilkomirsky, I., 1999. Thermal decomposition of enargite. In: Mishra, B. (Ed.), *Proceedings of EPD Congress 1999*. The Minerals, Metals and Materials Society, Warrendale, PA, pp. 341–351.
- [8] Padilla, R., Aracena, A., Ruiz, M.C., 2010b. Decomposition/volatilization of enargite in nitrogen-oxygen atmosphere. In: Vidal, E.E. (Ed.), *Proceedings of Materials Processing and Properties*, held during TMS 2010 Annual Meeting & Exhibition, vol. 1, pp.497–504. Seattle, WA.
- [9] Padilla, R., Aracena, A., Ruiz, M.C., 2010c. Oxidation-volatilization of enargite and stibnite at roasting/smelting temperatures. *Proceedings of Copper 2010*, Hamburg, Germany, vol. 6, pp. 2443–2452.
- [10] Welham, N.J., 2001. Atmospheric temperature oxidation of enargite (Cu<sub>3</sub>AsS<sub>4</sub>). *AusIMM, Proc.* 306 (1), 79–81.
- [11] Kusik, C.L., Nadkarni, R.M., 1988. Pyrometallurgical removal of arsenic from copper concentrates. In: Reddy, R.G., Hendrix, J.L., Queneau, P.B. (Eds.), *Proceedings of Arsenic Metallurgy: Fundamentals and Applications*. The Metallurgical Society, Warrendale, PA, pp. 337–349.
- [12] Baxter, K., Scriba, H., Vega, I., 2010. Treatment of high-arsenic copper-gold concentrates – An options review. *Proceedings of Copper 2010*, Hamburg, Germany, vol. 5, pp.1783–1802..
- [13] W. Tongamp, Y. Takasaki, A. Shibayama, Arsenic removal from copper ores

- and concentrates through alkaline leaching in NaHS media, *Hydrometallurgy*, 98 p. 213-218, 2009.
- [14] L. Curreli, C. Garbarino, M. Ghiani, G. Orrù, Arsenic leaching from a gold bearing enargite flotation concentrate, *Hydrometallurgy* 96 258–263, 2009.
- [15] Balaz P., Achimovicova M., Sanchez M., Kammel R., Attrition grinding and leaching of enargite concentrate, *Metall*, 53 , 1-2, p. 53-56, 1999.
- [16] J. Gersten, V. Fainberg, G. Hetsroni, Y. Shindler, *Fuel*, 79, p. 1679-1686, 2000.
- [17] J. Vinals, A. Roca, M. C. Hernandez, O. Venevente, *Hydrometallurgy*, 68, p.183-193, 2003.

## CHARACTERISTICS OF MATERIALS USED FOR CORROSION PROTECTION OF METAL AND CONCRETE STRUCTURES IN AGGRESSIVE ENVIRONMENT

<sup>1</sup>Zoran Avramovic, <sup>2</sup>Milan Antonijevic, <sup>3</sup>Milos Avramovic,

<sup>1</sup>*Copper Smelter and Electrolysis Plant Bor LTD, TiR, D.Vajfert 22, 19210 Bor, Serbia, e-mail: avramovictir@open.telekom.rs*

<sup>2</sup>*University in Belgrade, Technical Faculty Bor, VJ 12, 19210 Bor, Serbia*

<sup>3</sup>*University in Belgrade, Faculty of Organizations Sciences, 11000 Belgrade, Serbia*

### Abstract

Aggressive environment present in the plants production of copper, gold and sulfuric acid, it requires quality materials to protect metallic and concrete structures. Each of the plants specifically acts on structural materials, and therefore it is necessary to application of appropriate protection systems. The copper smelter plant there are high temperatures and large amounts of different gases; the copper and gold refinery plants, there is a wide variety of acid solution in the copper(II)-sulphate as a by-products; in the plant for the production of sulfuric acid present, almost all of her concentration, which adversely influence of both the metal and the concrete. In order to prevent the negative consequences of harmful effects and aggressive materials, shall be continued protection of metal and concrete structures.

In this paper there are different systems of protection, based on epoxides, polyurethanes, polyesters, and restraints inhibitors. We will give an overview of materials resistant to the effects of an aggressive environment, and the manner of their application.

*Keywords: corrosion, concrete, sulphate, protection*

### Introduction

Refinery Plant of copper, gold and silver is particularly aggressive environments with conditions of work and production. Aggressiveness of the environment is reflected in the destructive effects of electrolyte-acid solution of copper (II)-sulphate, both the concrete and the steel structure. Example aggressiveness may best be seen on the effect of electrolytes on the steel structure of commercial tanks made of high quality steel CrNi18-8, where the chloride ion causes a marked "pitting" corrosion [1,2].

Corrosion under the influence of sulphate compounds with cations such as  $\text{Cu}^{2+}$ ,  $\text{Zn}^{2+}$ ,  $\text{Fe}^{2+}$ ,  $\text{Mg}^{2+}$ ,  $\text{Al}^{3+}$ , is the dangerous form of corrosion of concrete, for the range pH 0-14. In the treating of sulfate, sulfate ions, react with calcium hydroaluminat, building a new compound calcium hydrosulphoaluminat. If sulfate is not in the form of gypsum, but in the form of sodium sulphate, magnesium

sulphate, copper sulphate or other salts, a process generally flows first to the forming of gypsum and gypsum by creating towards calcium hydrosulfoaluminat (ettringite), which can be represented by the equation:



The damaging concrete significantly depends on the solubility products of the reactions that occur in acid and concrete components, with the increased solubility of reaction products increases the destruction of concrete.

Armature in armature concrete subject to corrosion, depending on the concentration of corrosive agents present in the concrete or the surrounding environment. Corrosion of steel armature in concrete is an electrochemical process and depends both on the properties of steel armature, and the structure and properties of concrete, and also the character of the surrounding environment in which the structure.

Under the effect of an electric current, DC and AC, subject to electrocorrosion all components of reinforced concrete: cement stone, fillers and reinforcement steel. Electrocorrosion primarily caused by wandering currents which are the sources of various electrical devices, whereby an electric current moving through the least resistance. Then the parts of the armature steel related with the negative pole of the direct current source, acting as the cathode, and parts armature positively related with pole source of direct current, as the anode. In this case anodically polarized armature parts subject to dissolution due course of the anodic reaction and the cathodic polarized parts of the armature reduction takes place, usually  $\text{H}^+$ -ions to  $\text{H}_2$ .

Protect the armature concrete approach in cases where aggressive environments could cause corrosion of concrete and metal in it.

Basic methods of protecting concrete from corrosion based are: application of prophylactic measures (installation of ventilation equipment, installation of drainage grooves for aggressive liquids ...) modify the structure of concrete (density, impermeability and chemical resistance can be adjusted to the conditions of exploitation of concrete), the application of protective and insulating coatings and coverings; application of electrochemical protection.

Coatings are widely used to protect concrete surfaces. Depending on the degree of aggressiveness of the environment is done and the system of choice.

In areas such as plants for electrolysis copper and gold applied three-component epoxy protection systems, in which structure compile: filler (quartz), hardener and resin. Previously, the concrete surface must priming, usually epoxy primer. This system can be in our conditions proved to be effective and of good quality, with a lifespan exceeding 20 years. The part of the plant electrolysis of gold, protection system consisting of epoxy resin and acid-resistant tiles sizes 100x100mm, with a useful life exceeding 30 years.

Armature protection is achieved with used various corrosion inhibitors, such as nitrite-dicklohexilamine, HMTA, hexamethylene, inhibitors based on sodium nitrate and contact inhibitors. Also, a very effective way of protecting the armature is electrochemical protection. In this sense, the use of magnesium alloys, zinc and aluminum. The most commonly used magnesium alloys to be used as a protector,

has the following composition: 7.5-9.3% Al, 0.2-0.8% Zn, 0.15-0.5% Mn and Mg 89.4-92.15%.

### Corrosion in operating conditions

The Refinery plant of copper and gold, the main corrosive agent is an acidic solution of copper (II)-sulphate. The concentration of sulfuric acid is about 20%, copper (II)-ions  $45\text{g/dm}^3$  and chloride ions  $35\text{mg/dm}^3$ . Temperature of  $59^\circ\text{C}$  is a solution, a pH-value of less than 2. Acidic solutions readily reacts with the concrete at a pH value of about 12 due to the presence of calcium hydroxide formed during hydration and minerals alit and belit.

Concrete floors they were placed where the electrolytic copper, consist of a buffer zone (smelting slag, quartz sand), unreinforced concrete slabs, "sandwich" films (two PE sheets, among which is a PVC sheet) and reinforced concrete slabs. Concrete surfaces are protected acid resistant, thickness 25-30mm, placed in acid-proof resin, based on epoxy, polyester resin or furan. Channels, aggregate pits, supporting pillars of electrolytic bath, also protected by acid-proof materials, with the reinforcement of protection and waterproofing, the aggregate pit he built and lead. During an earlier recovery, an attempt was made to overlay channels plastic materials, which did not give good results (Figures 1 and 2).

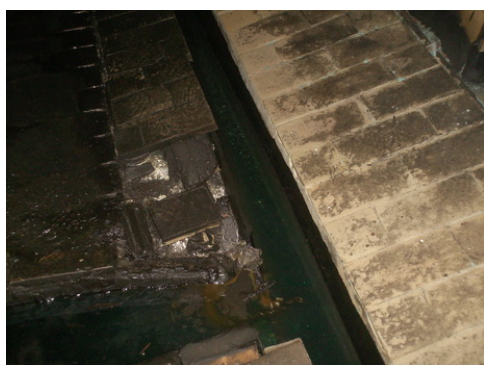


Figure 1. Channel to drain electrolyte



Figure 2. The effect of electrolyte on the floor

At the plastics and concrete, there was a breakthrough acidic solution of copper (II)-sulphate on concrete and mutual chemical reactions create compounds with ettringite. This process follows the increasing volume of solid mass of up to 55%, which leads to the generation of very strong internal stresses in the cement stone and crack formation [3,4]. Also, in places, due to the deterioration of the protective material breach occurred aggregate pits, followed by the effect of electrolyte on the concrete structure, the crystallization of copper sulphate, the creation of concrete and acid compounds and "raise" the concrete foundation, concrete ties without compromising protection (Figures 3,4). Acid resistant protection, shown in figures (1-4), consists of the following: the dry and prepared concrete surface is applied a layer of epoxy primer, after drying for 2-3 hours,

applied acid-proof three component weight epoxy resin (polyurethane, furan) in which "shall" acid resistant tiles, thickness 25-30mm.



Figure 3. Connection plates and ground with concrete



Figure 4. Raising the concrete foundation

In Figure (5) shows the appearance of the damaged bearing pole where electrolysis plant. Restoration of such a supporting pillar shall be acid-proof ground-based tar-epoxy and quartz. At a height of two feet, the protection is performed acid-proof epoxy compound and acid resistant.



Figure 5. Supporting pillar electrolysis plant



Figure 6. The appearance of the floor and fittings in the electrolysis plant

Figure (6) shows the appearance of the floor and armature concrete in electrolysis plant of copper. When you create the necessary conditions for armature-steel in concrete reacts with the environment to form compounds such as oxides, sulfides and chlorides and then loses its initial physical and chemical properties. If the steel is surrounded by concrete in whose pore is an aqueous solution of high pH, it was pulled  $Fe_2O_3$  oxide layer that protects it from further corrosion, i.e. passivity him.

Corrosion of armature usually belongs to the type of electrochemical corrosion that occurs in electrically conductive (wet) environments. When the steel comes into contact with a substance chemically more active, he'll lose two electrons and becomes positively charged:



In a system in which the positively charged steel is surrounded by wet conditions for the separation of hydroxyl ions to react with steel exceeding the chemically stable compound,  $\text{Fe}(\text{OH})_3$ , known as "rust". This compound, with still insufficiently clear indicators, reacts with chloride and steel becomes depassivation, expressed prone to destruction. Reliable protection of armature steel is inhibiting corrosion inhibitors or by applying a thin coating. Particularly effective form of protection is cathodic protection.

### **Conclusion**

Processes corrosion in operating conditions requires maximum involvement of experts from different fields. The complexity of regular construction works, and works on anticorrosion protection of concrete and steel armature, is best reflected in the plants and installations with multiple activities of various corrosive agents. When makes works to protect concrete surfaces, it is necessary to avoid the "combination" of different materials, but do protect uniform procedure. Also, the quality and selection of appropriate materials is of great importance, because only high quality materials, with quality installation, can guarantee a long service life, and the undisturbed production process.

### **References**

- [1] S.Mladenović, M.Pavlović, D.Stanojević, *Korozija i zaštita betona i armiranog betona*, SISZAM Beograd, 2008.
- [2] M.A.Shalimo, *Zashchita betonnikh konstruksii i zhelezobetonnykh konstruksii ot korozzii*, Izd. „Visheishaya shkola”, Minsk, 1986.
- [3] V.I.Babushkin, *Fizichko-khemicheskie procesy korozii betona i zhelezobetona*, Izdatelstvo literaturyu po stroitelstvu, Moskva, 1968.
- [4] Z.Gulišija, Č.Lačnjevac, *Korozija i zaštita materijala-monografija*, ITNMS, IDK, Beograd, 2012.

## NANOCOMPOSITE Ag-SnO<sub>2</sub> ELECTRICAL CONTACTS PREPARED BY TEMPLATE METHOD

V. Ćosović<sup>1</sup>, A. Ćosović<sup>2</sup>, M. Pavlović<sup>1</sup>, A. Kostov<sup>3</sup>, D. Živković<sup>4</sup>,  
N. Talijan<sup>1</sup>

<sup>1</sup> *Institute of Chemistry, Technology and Metallurgy, University of Belgrade,  
Njegoševa 12, 11000 Belgrade*

<sup>2</sup> *Institute for Technology of Nuclear and Other Mineral Raw Materials,  
Franseska ulica 86, 11000 Belgrade*

<sup>3</sup> *Institute for Mining and Metallurgy Bor, Zelene bulevar 35, 19210 Bor*

<sup>4</sup> *Technical Faculty in Bor, University of Belgrade, Vojske Jugoslavije 12,  
19210 Bor*

### Abstract

Template method was applied for introduction of SnO<sub>2</sub> nanoparticles and preparation of Ag-SnO<sub>2</sub> composite powders, whereas the final (92:8) contacts were produced via conventional powder metallurgy (PM) route. Soluble starch and ashless filter paper were investigated and compared as possible template materials in terms of their influence on microstructure and physical properties such as density, porosity, hardness and electrical conductivity of Ag-SnO<sub>2</sub> electrical contact materials. Structure and properties of the obtained materials were discussed and compared to each other and to their microparticle counterpart prepared by conventional powder mixing. Despite noticeable differences in microstructure, both nanocomposites were found to have very low porosity and high density. The highest increase in hardness of about 30%, compared to conventional microparticle PM material, was observed for the sample produced using soluble starch as a template. The measured values of electrical conductivity were found to be comparable with conductivities of electrical contact materials of this type.

*Keywords: Ag-SnO<sub>2</sub> electrical contacts, template method, SnO<sub>2</sub> nanoparticles, microstructure, Vickers hardness, electrical conductivity*

### Introduction

Important functional properties of Ag-SnO<sub>2</sub> electrical contact materials such as anti-welding behavior, conductivity and wear resistance are strongly related to their microstructure. The Ag-SnO<sub>2</sub> contacts produced by common commercial routes e.g. powder metallurgy and internal oxidation of silver-tin alloys [1] are characterized by rather poor over-temperature behaviour and poor workability [2]. Considering their wide application in different low voltage switchgear devices [3] and especially since they are considered as a potential environmentally-friendly substitute for hazardous Ag-CdO, different methods have been developed and numerous attempts have been made to improve their performance and applicability. It is generally accepted that the performance of Ag-SnO<sub>2</sub> contact

materials can be enhanced by an increase in the composite's dispersion [4], which is usually achieved by use or synthesis of finer metal oxide particles. Furthermore, it is generally accepted that smaller metal oxide particles promote formation of anti welding characteristics and under certain conditions decrease erosion rate [4].

In order to obtain homogenous microstructure and very fine metal oxide dispersion within the silver matrix alternative methods have to be used as the conventional mixing techniques either wet or dry reach their technical limit for the powder particle sizes about 1-2 micron, due to more or less pronounced agglomerate formation [5]. For that purpose different electroless chemical methods based on chemical precipitation [4-6] were investigated. In addition, modern polymer assisted inorganic nanocomposite formation [7] and bio-casting methods [8] that utilize different organic templates offer a lot of new possibilities for preparation of very uniform nanocomposite structures.

In view of that, an attempt has been made to increase dispersion of Ag-SnO<sub>2</sub> contact materials by introduction of SnO<sub>2</sub> nanoparticles in silver matrix and preparation of composite powders using template method. Microstructure and physical properties such as density, porosity, hardness and electrical conductivity of the obtained Ag-SnO<sub>2</sub> electrical contact materials were studied. Properties of the obtained silver-nanoparticle metal oxide composites are discussed and presented in comparison to each other as well as to their micro particle metal oxide counterpart.

## **Experimental**

Commercial SnO<sub>2</sub> nanoparticles (40-100 nm) and commercial AgNO<sub>3</sub> powder were used as precursors for the template method of synthesis of Ag-SnO<sub>2</sub> composite powders. The applied synthesis method is based on a simple principle that AgNO<sub>3</sub>, unlike most metal nitrates, when heated thermally decomposes to elemental Ag instead of respective oxide. Final (92:8) Ag-SnO<sub>2</sub> contact materials were prepared via conventional powder metallurgy route.

Sample 1 was produced by a modified method developed by Wang et al. [9] which uses commercial ashless quantitative filter paper (Whatman Inc., burning ash < 0.005%) as the template. The SnO<sub>2</sub> nanoparticles were firstly suspended in a weak ethanol/water solution and then mixed with 1M AgNO<sub>3</sub> solution, in quantities necessary to achieve desired Ag to SnO<sub>2</sub> ratio in final composite. Filter paper sheets were immersed in the obtained mixture solution and then dried in chamber dryer. Dried sheets were then burned and put into a muffle furnace preheated at 500°C, where they were calcinated for 2h. During the combustion and subsequent calcination silver nitrate was transformed to elemental Ag with embedded SnO<sub>2</sub> nanoparticles and the template was removed.

In case of sample 2, soluble starch was used as a template. In the first step soluble starch was added into distilled water, preheated at 40-50°C under continuous stirring. Solution was further heated up to boiling point (~100°C), where it was kept for 15 min, and then cooled down to 50-70°C. Previously prepared SnO<sub>2</sub> nanoparticle suspension was slowly added to solution during vigorous mixing. After few minutes AgNO<sub>3</sub> water solution was slowly added. Both AgNO<sub>3</sub> and SnO<sub>2</sub> were added in quantities necessary to achieve desired Ag:SnO<sub>2</sub> weight

ratio in final material. The prepared mixture was dried at 80°C in chamber dryer until water was evaporated and solid composite was obtained. The solid composite was subsequently burned and put into a muffle furnace pre-heated at 650°C, where it was calcinated for 4h. During the combustion and later calcination, silver nitrate was transformed to elemental Ag with embedded SnO<sub>2</sub> nanoparticles and the starch template was removed.

Sample 3 was produced by mixing of pure Ag powder, produced by chemical precipitation synthesis route, and very fine commercial (SnO<sub>2</sub> - 99.9%) micro particle powder. Comprehensive characterization of the starting powders is given in [10]. Both wet and dry homogenizations of the powder mixtures were carried out.

The final Ag-SnO<sub>2</sub> electrical contacts were produced by cold pressing of the obtained composite powders and powder mixtures into blocks with dimensions 25.4×11×3 mm, by applying pressure of 360 MPa. The obtained green compacts were sintered for 3h at 820°C in the air atmosphere and subsequently forged at 800°C with the low degree of reduction. The obtained samples were then annealed at 750°C for 30 min and quenched in water.

Microstructures of the prepared contact materials were studied on polished cross-section surfaces using JEOL JSM 6610LV scanning electron microscope (SEM). Density of the obtained samples was determined by standard methods. By applying the procedure given in more detail in [10] porosity of the samples was calculated. Hardness measurements were carried out on polished samples at room temperature using a Vickers hardness tester applying load of 5 kp. The reported hardness values are an average of five readings. Electrical conductivity of the investigated materials was measured using Foerster SIGMATEST 2.069 eddy current instrument with the 8 mm diameter probe.

## **Results and Discussion**

SEM images of polished cross-sections of the studied electrical contact materials after sintering, mechanical treatment and subsequent annealing are presented in Fig. 1.

Generally speaking, from the presented metallographic images (Fig.1) it is obvious that high uniformity of the Ag-SnO<sub>2</sub> contact materials was obtained. Nevertheless, visible differences in homogeneity between individual samples can be observed. Both materials produced by template method (Fig.1a, b) exhibit significant reduction of agglomerates compared to the sample produced by conventional mixing of powders (Fig.1c). The sample 1 (Fig. 1a) prepared using filter paper as a template displays nearly lamellar structure which can be associated with the used template material. Due to the “coffee stain” effect, the uneven radial distribution of SnO<sub>2</sub> nanoparticles on the filter paper was obtained. Hence, the prepared Ag-SnO<sub>2</sub> leaf like composite is characterized by enriched pure silver zones and zones with high concentration of SnO<sub>2</sub> nanoparticles. Such structure of the obtained composites is responsible for the formation of the observed lamellar structure after subsequent processing stages. Consequently, this could have impact on the structure dependant properties of the final electrical contact material. In contrast, particularly significant improvement of SnO<sub>2</sub>

dispersion in the silver matrix was obtained for the sample 2 (Fig. 1b) produced using starch as a template.

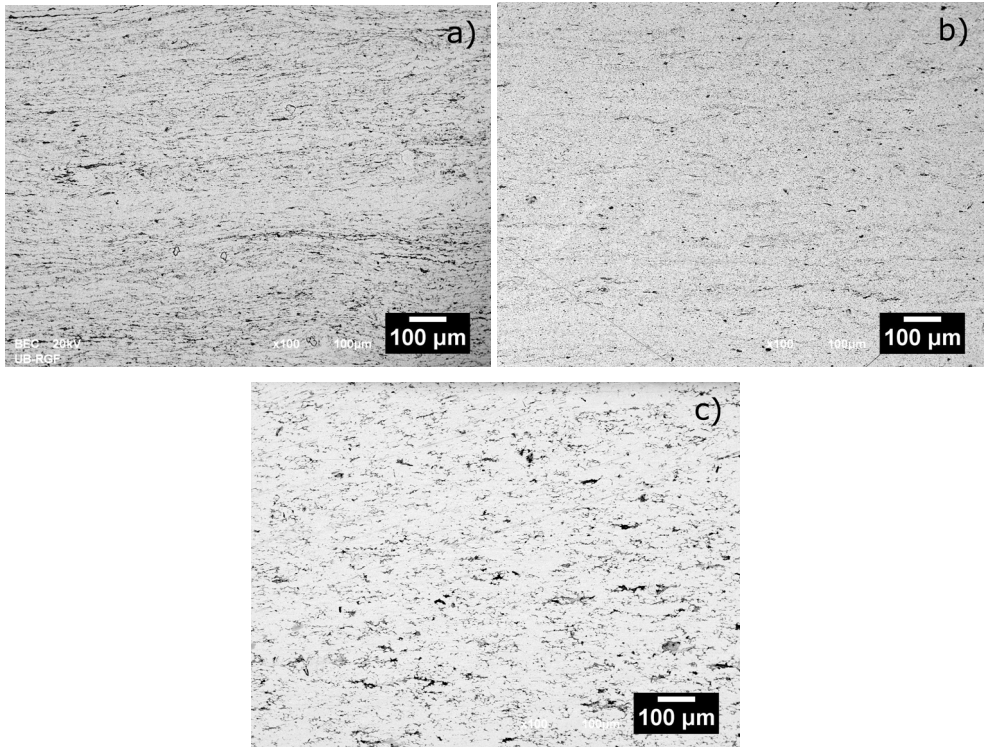


Fig. 1. Microstructures of the obtained Ag-SnO<sub>2</sub> electrical contact materials prepared: a),b) using template composite powders and c) from starting micropowders

Given that the high density and low porosity are prerequisites for good electrical contact materials, density and porosity of the samples were closely monitored. The determined values of density and porosity of green compacts and materials in the final stage after sintering and forging are presented in Table 1.

Table 1. Density and porosity of the prepared Ag-SnO<sub>2</sub> materials

Sample No.	Green compacts		Final	
	Density [g/cm <sup>3</sup> ]	Porosity [%]	Density [g/cm <sup>3</sup> ]	Porosity [%]
1	7.20	23.13	9.83	2.47
2	6.77	27.74	9.86	2.18
3	7.99	14.70	9.53	5.45

Although initially sample 3 had higher density and lower porosity (Table 1.), in the final stage after sintering and forging, template materials (samples 1 and 2) exhibited significant increase of density and decrease of porosity.

Hardness of the investigated Ag-SnO<sub>2</sub> electrical contact materials in soft and hard state is presented in Fig. 2. The obtained values (Fig. 2) clearly illustrate influence of the introduction of nanoparticulates and method of their introduction into a silver matrix on mechanical properties of the investigated materials. As expected, with the increase of density and more uniform distribution of SnO<sub>2</sub> nanoparticles, higher values of hardness were obtained. It is evident that the introduction of nanoparticles has provided higher values of hardness, considering that all investigated materials containing SnO<sub>2</sub> nanoparticles (samples 1 and 2) possess significantly higher hardness than their micro particle counterpart (sample 3). Comparing the values of hardness for sample 2 and sample 3 prepared by template method using starch and conventional powder mixing, respectively, enhancement of hardness of almost 30 % can be observed. This enhancement can be attributed to greater dispersion hardening of otherwise soft silver matrix.

In contrast, the results of electrical conductivity measurements given in Fig. 3 follow different trend.

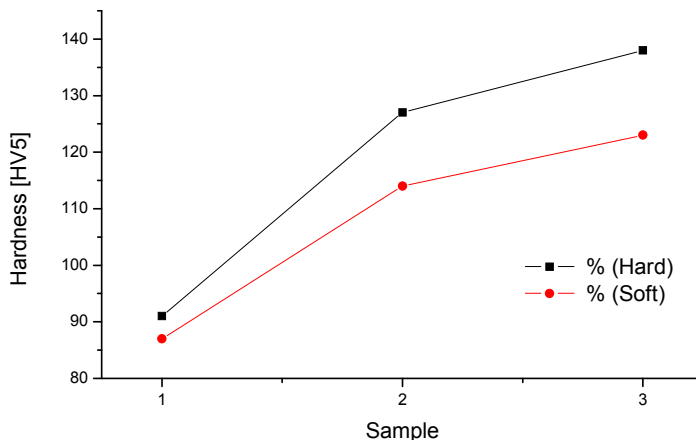


Fig. 2 - Hardness of the investigated Ag-SnO<sub>2</sub> electrical contact materials

The sample 3 containing micro particle tin oxide was found to have the highest value of electrical conductivity despite the porosity of about 5%. This is can be ascribed to the presence of the oxide free zones in microstructure, that can be observed on (Fig. 1c), resulting in better connectivity of individual silver grains. Lower values of electrical conductivity observed for samples 1 and 2 can be generally associated with presence of pores [2], straining of silver lattice [1] and particle spacing [4,5,11] which all influence mean free path of conduction electrons and thus electrical conductivity. Somewhat higher electrical conductivity of the sample 1 can be attributed to its almost lamellar structure with oxide-free zones which give raise to the electrical conductivity.

The greater SnO<sub>2</sub> dispersion of the sample 2 as well as high density, hardness and lower porosity are all prerequisites for better wear resistance and

longer exploitation life. It is evident that such fine oxide dispersion cannot be achieved by conventional metallurgical powder mixing. Hence, the benefit of application of the soluble starch template method of preparation is illustrated by enhancement of structure dependent properties.

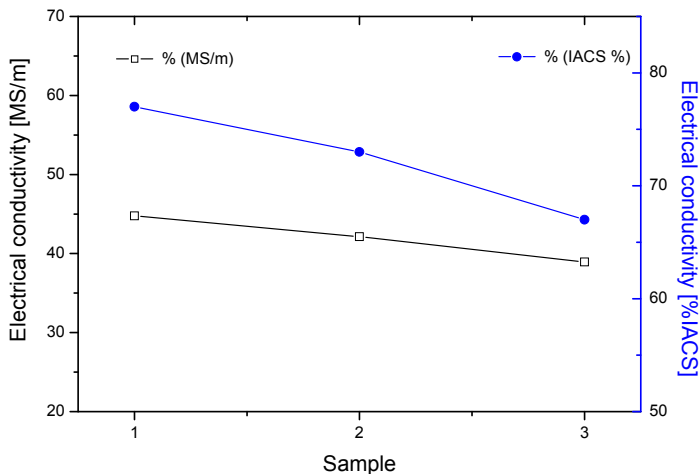


Fig. 3. - Electrical conductivity of the investigated Ag-SnO<sub>2</sub> electrical contact materials

## Conclusion

Template method was applied for introduction of SnO<sub>2</sub> nanoparticles and preparation of composite powders, as a way to improve dispersion of metal oxide in Ag-SnO<sub>2</sub> (92:8) contact materials. Soluble starch and ashless filter paper were investigated and compared as possible template materials in terms of their influence on microstructure and physical properties such as density, porosity, hardness and electrical conductivity of the prepared electrical contact materials. Both materials produced by template method were found to exhibit high density and low porosity and significant reduction of agglomerates i.e. such fine oxide dispersion which cannot be achieved by conventional metallurgical powder mixing. Observed greater SnO<sub>2</sub> dispersion, high density and lower porosity of the sample prepared using soluble starch are responsible for enhancement of hardness of almost 30% compared to the sample produced by conventional mixing of powders. The benefit of use of the soluble starch as a template material is illustrated by enhancement of structure dependent properties. Moreover, in terms of practicality, it is much more convenient to use starch as template than filter paper given that the process is more time demanding and it suffers from so called coffee stain effect. The measured values of electrical conductivity of the both template samples were found to be within the required range for this type of electrical contact materials.

## **Acknowledgement**

This work has been supported by the Ministry of Education, Science and Technological Development of the Republic of Serbia (Projects OI 172037 and TR 34023). The presented study is realized in the frame of COST Action MP0903.

## **References**

- [1] .A. Pandey, P.Verma, O.P. Pandey, Indian J. Eng. Mater. Sci. 15 (2008) 236.
- [2] Ji Zheng, LI Songlin, DOU Fyqi, LI Tonghui, Rare Metals, 28(1) (2009) 19.
- [3] M. Braunović, N.K. Myshkin, V.V. Konchits, Electrical contacts – Fundamentals, Applications and Technology, CRC Press, Taylor and Francis Group, Boca Raton, 2007.
- [4] F. Heringhaus, P. Braumann, D. Ruhlicke, E. Susnik, R. Wolmer, On the Improvement of Dispersion in Ag-SnO<sub>2</sub> based Contact Materials, Proc. 20th Int. Conf. on Electr. Contact Phenom. Stockholm 2000, 199-204.
- [5] R. Wolmer, M. Mueller, D. Ruehlicke, D. Goia, US patent Pub. No.: US 2001/0051102 A1
- [6] E. Romhanji, M. Filipović, Ž. Kamberović, Met. Mater. Int., 18(1) (2012) 171.
- [7] B.A. Rozenberg, R. Tenne, Prog. Polym. Sci. 33 (2008) 40.
- [8] C.K. Sia, Y. Sasaki, N. Adachi, T. Ota, J. Ceram. Soc. Jpn. 117 (9) (2009) 958.
- [9] P. Raveendran, J. Fu, S.L. Wallen, J. Am. Chem. Soc. 125 (2003) 13940.
- [10] V. Čosović, N. Talijan, D. Živković, D. Minić, Ž. Živković, J. Min. Metall. Sect. B-Metall. 48 (1) B (2012) 131.
- [11] S. Link, M.A. El-Sayed, J. Phys. Chem. B 103 (1999) 8410.

## DEVELOPMENT OF MODERN TECHNOLOGIES OF COPPER ALLOYS CASTING

Zagorka Aćimović-Pavlović<sup>1</sup>, Ljubiša Andrić<sup>2</sup>, Anja Terzić<sup>3</sup>  
Gavrilo Šekularac<sup>1</sup>, Marko Pavlović<sup>1</sup>

<sup>1</sup>*Faculty of Technology and Metallurgy, University of Belgrade, Karnegy st. 4, Belgrade, Serbia*

<sup>2</sup>*Institute for Technology of Nuclear and Other Raw Mineral Materials, Franchet d'Esperay st.86, Belgrade, Serbia*

<sup>3</sup>*Institute for Materials Testing, Vojvode Mišića Boulevard 43, Belgrade, Serbia*

### Abstract

In this paper, results of investigation of casting technology of complex thin-wall copper alloy castings with accent on Lost Foam casting procedure are given. Phases of casting procedure were investigated, along with important process parameters and their influence on structure and properties of obtained castings. This technology enabled obtaining of the castings with complex construction and thin walls, and significant savings in casting procedure: expensive operations such as cleaning and machine processing of castings are minimized, while exploitation of metal is increased. Critical parameters of the process were investigated: casting temperature, types of refractory coatings, types of polymer models and their influence on formation of the structure. Results showed that new technology can be applied for obtaining of quality copper alloy castings which can be widely used in mechanical industry.

*Key words: copper castings; Lost foam process; quality of castings; savings.*

### Introduction

Evaporative patterns casting (Lost foam casting process) is patented by H.F. Shroyer in 1958. Since then, up to today, development and practical application goes on with changeable success. Mainly, the problems of the development of this process are lack of appropriate materials for making evaporative patterns and refractory pattern coatings. Unlike casting in the sand moulds, the process uses patterns and pouring systems, which remain in the mould after its making until pouring of metal. This justifies the title "full mould casting", Fig. 1. In the contact with liquid metal, the pattern is split in a relatively short time. At the same time, the castings crystallization takes place. As the consequence of the pattern splitting, a great quantity of gaseous and liquid products is produced. If the conditions of their elimination from the mould are not fulfilled, many defects will appear on the castings, which are considered characteristic for this process. [1-5]

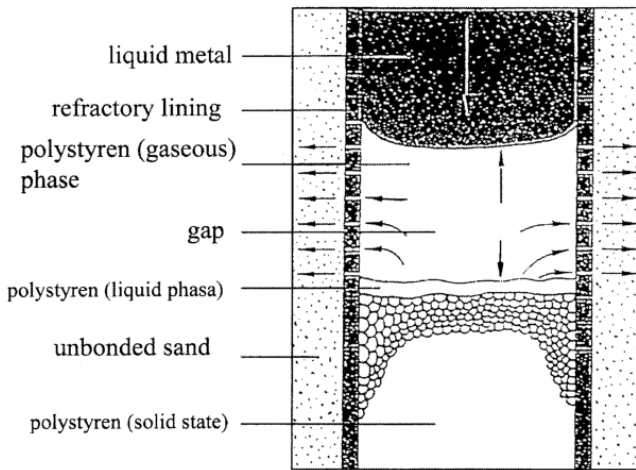


Fig. 1. System balance: liquid metal-refractory lining-pattern-sand

Important factors on pattern's decomposition and evaporation process, besides temperature and pattern's density, are also the type and refractory coat layer's thickness which the evaporable pattern is been covered with, type and size of sand grain for modeling, respectively permeability of sand for modeling, castings and gating of moulds' construction. The pattern's density and permeability of refractory coat and sandy cast determine polymers evaporation velocity. The velocity of liquid metal coming into the cast and its contact with the pattern is regulated by proper defining the gating of moulds. [6-9]

In order to obtain castings of a priori desired quality, critical process parameters should be determined for each particular polymer pattern, as well as the type of alloy for casting. That requires long-lasting researches with a goal to achieve optimization of Lost foam casting process and obtain the castings of a priori specified properties. In order to understand correctly the Lost foam process optimization it is necessary to know that various types of castings' structure determine their different properties. Besides this dependency for obtaining the castings of a priori specified properties there also should be determined the fundamental structure dependency on technology, which implies critical process parameters' control and control of useful castings' properties, and a special consideration in this paper was given to that matter. [10, 11]

## Experiment

A two series of experiments were done with the goal of analyzing the possibilities for appliance of refractory coats based on talc (series mark: T) and cordierite (series mark: C) in Lost foam casting process. The coats' compositions were defined (table 1) and the coats components' preparation methods were determined. Grinding and fine grinding of refractory loaders of talc and cordierite was done in mill with balls of Cr-Ni steel, capacity 20 kg/h, with mill load of 70% and grinding time 45-60 minutes.

Table 1. Compositions of used refractory coats on talc, (T), and cordierite (C) base

<p><b>Composition of refractory coat type T:</b> -refractory filler: talc with grain size of 40<math>\mu</math>m, 93 -95 % -binding agent: bentonite 1.5-2.5%; bindal H, 0.5-1%, -suspension maintenance agent: Na<sub>3</sub>P<sub>3</sub>O<sub>3</sub> 1-3%, carboxymethylcellulose (CMC), 0.5-1% -solvent: water</p>
<p><b>Composition of refractory coat type C:</b> -refractory filler: cordierite with grain size of 40<math>\mu</math>m, 92 -94 % -binding agent: bentonite 1.5-2.5%; bindal H, 0.5-1%, -suspension maintenance agent: Na<sub>3</sub>P<sub>3</sub>O<sub>3</sub> 1-3%, carboxymethylcellulose (CMC), 0.5-1% -solvent: water</p>

At applying refractory coat on polymer pattern by techniques of immersion into the tank with coat, overflowing and coating with brush, a special attention was given to coat's quality control, Fig. 2. The basic criteria for quality evaluation of this type of refractory products were-pertinence for applying, drying behavior, resistance to attrition, sedimentation and penetration.

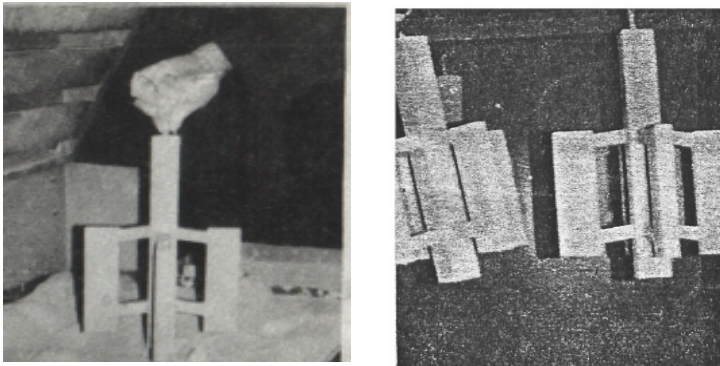


Fig. 2. Coatings and drying

The process parameters for production of refractory coats series T and C, methods of coat applying on patterns and drying, when optimal results of testing the structure and properties of obtained aluminum alloy castings were:

- Coat densities: 2g/cm<sup>3</sup>
- Coat temperature: 25°C
- The way of coat's excess remove from the pattern after pulling out from the tank for lining: patterns are been seeped, in vertical position, 5-10 s, and then set 5 s under 45° angle in order to coat layers on pattern's surface get equally even
- Slowly coat mixing in tank during the coat applying on pattern: velocity 1 revolutions/min

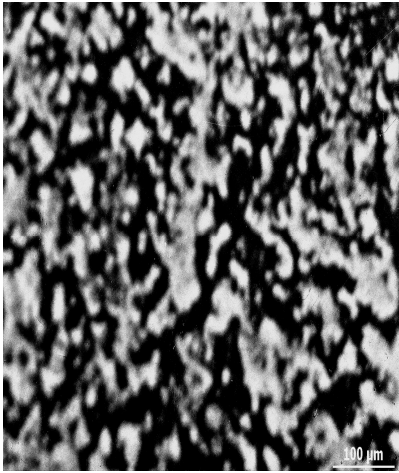
- Methods of coat applying on pattern: "cluster" immersion into tank with coat; overflowing; coating with brush
- Drying: first layer 2 hours; final layer 24 hours
- Coat layer's thickness on the pattern after drying: 0,5-1,5 mm.

The experimental parameters of Lost foam casting process regarding which were done the selection of composition and preparation of refractory coats series: T and C were:

- Tested alloy: copper alloy (chem. composition (%): Cu 86,0; Sn 13,9; P 0,1)
- Preparation methods of liquid die: refinement by  $\text{Cu}_3\text{P}$
- Casting temperature: 1150 °C
- Evaporable polystyrene pattern: density 20-25 kg/m<sup>3</sup>; pattern construction: plate (200x50x20)mm; polystyrene grain size 1-1,5 mm
- Mounting pattern for casting: "cluster" with four patterns-plates set on central runner gate
- Gating of moulds: central runner gate (40x40x400) mm; ingates (20x20x10) mm, 2 pieces.
- Dry quartz sand for cast production: grain size: 0,17 mm; 0,26 mm; 0,35 mm.

## **Results and discussion**

By controlling the critical process parameters for refractory coats' production and controlling the coat's properties it was determined that the coats of all series comply with conditions for appliance in Lost foam casting process. It was determined that coats were easy to apply on polymer patterns, being equally lining at overflowing and immersion, were easy to be coated with brush, without any mark of brush, leakage, drops and clots' formation. After drying, the coat surface was smooth; coat's layers were of equal thickness everywhere on pattern's surface, without any bubbles, crazing, peelings or attrition. The coat quality and refractory loader's homogeneity in the coat depends on coat preparation. In order to achieve even coat layers' thickness on pattern's surface it is necessary to slowly constantly mix the coat during its applying on patterns, to maintain defined density (2g/cm<sup>3</sup>) and temperature (25°C) of coat. On the contrary, the coat composition's inhomogeneity appears, Fig.3.



a) homogenous composition coats



b) non-homogenous composition coats

*Fig.3. Refractory coats*

In order to observe the effects of casting process, evaluation of certain operation phases and analysis of applied refractory coats' influence, a visual control of the obtained castings was done, testing their structural and mechanical properties. After pulling out the founded "clusters" from the cast, their surface is covered with coat layer which is easy to be broken and removed from it, so the cleaning is not necessary, which significantly reduces the production costs. The refractory coats of all series have demonstrated positive effects on the surface quality – shiny and smooth castings' surfaces were obtained. The castings are true copy of the patterns (dimensionally are precise) which indicates that the decomposition and evaporation of polystyrene pattern was in totality, and that the gating of moulds' solution was satisfactory. It was noted that the lower castings' parts of all series have flat and sharp edges, clean and shiny surface. At some castings from the series with coat layers of higher thickness (above 1,5 mm) the upper castings' surfaces are a bit uneven and folded, and also on certain castings' parts a surface roughness appears, and more often at the castings from the series with patterns' density above  $20 \text{ kg/m}^3$ .

The study results of castings' structural and mechanical characteristics were within the limits predicted by the standards for this type of alloys. That would be the castings from series with used polystyrene patterns up to  $20 \text{ kg/m}^3$ , refractory coats of less thickness layers, below 1 mm, applied quartz sand for modeling with its grain size above 0,26 mm, casting temperature within the limits of  $1180^\circ\text{C}$  and casting velocity which enabled even decomposition and evaporation of polystyrene, with complete elimination of gassy products from patterns' evaporation, without any cast falling in and liquid metal penetration into sand.

On the other hand, castings from the series with applied patterns of densities above  $20 \text{ kg/m}^3$  and coat thickness above 1,5 mm have expressed subsurface and volumetric porosity too, Fig.4.

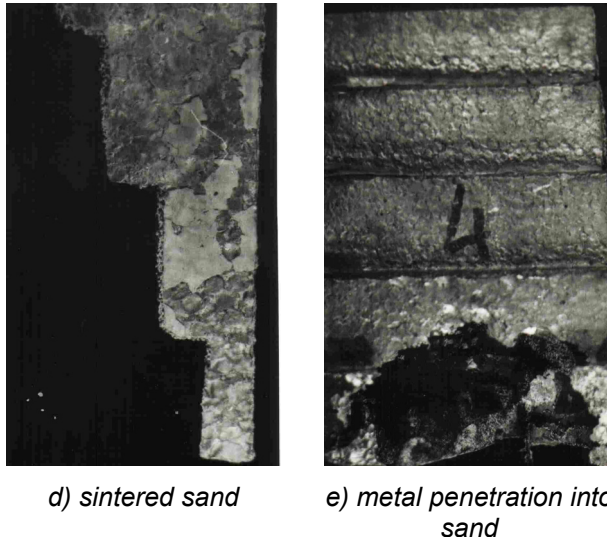


*Fig. 4. Errors on castings*

This indicates that the reasons for these type of errors are primarily the polystyrene pattern, and next the refractory coat and high casting velocity.

## **Conclusion**

In order to attain a quality and cost-effective castings production by the Lost foam casting process, it is necessary to attain the balance in the following system: evaporable polymeric pattern- liquid metal-refractory coating – sand mold during metal inflow, polymeric pattern decomposition and evaporation, castings formation and solidification. All this points to complexity of the castings solidification conditions by the Lost foam casting process, as well as to the necessity to determine the correlation between the casting parameters, structure and properties of castings.

## **Acknowledgement**

This investigation was supported by Serbian Ministry of Science and Education, Republic of Serbia and it was conducted under following projects: 33007 and 172013.

## **References**

- [1] M.M.Ristić: Principles of materials science, Monographs. Vol. DCXVII, No 36, Serbian Academy of Sciences and Arts, Belgrade (1995).
- [2] R. Monroe: Expandable Pattern Casting, AFS Inc. (1994), SAD

- [3] S. Shivukumar, L. Wang, B. Steenhof: Physico-Chemical aspect of the Full mould casting of aluminium alloys, part I: The Degradation of Polystyrene, AFS Trans. 87-84, p. 791, (1989).
- [4] Z.Aćimović-Pavlović, Ljubiša Andrić, Vladan Milošević, Sonja Milićević: Refractory coating based on cordierite for application in new evaporate pattern casting process, Ceramic International, 37 (2011) 99-104.
- [5] R. Ballman: Assembly and coating of polystyrene foam patterns for the Evaporate Pattern Casting Process, 92nd Casting Congress, Hartford, Connecticut, USA, Proceedings, p. 250. (1988).
- [6] Lj. Trumbulovic, Z. Acimovic-Pavlovic, Z. Gulisija, Lj. Andric: Correlation of technological parameters and quality of castings obtained by the EPC method, Materials Letters 56 (2004) 1726-1731.
- [7] Z.Aćimović, Lj.Pavlović, Lj.Trumbulović, Lj.Andrić, M. Stamatović: Synthesis and characteriyation of the cordierite ceramics from nonstandard raw materials for application in foundry, Materials Letters, 57 (2003) 2651-2656.
- [8] Nam Don Cho: Effect of coating materials on fluidity and temperature loss of molten metals in full mould, 56th World Foundry Congress, Dusseldorf GIFA, p. 7.1.7.10 (1989).
- [9] R.S. Yang, H.C. Hsiao: Trans. JPN. Foundry Eng, Soc. 14 (1995) 10-17.
- [10] A. Prstić, Z. Acimović-Pavlović, Z. Gulišija, Z. Janjušević: Development of EPC process for manufacturing parts in automotive industry, 10th DEMI 2011, Banja Luka (2011), Proceedings, pp.315-320.
- [11] A. Prstić, Z.Aćimović-Pavlović, A. Terzić, Lj. Pavlović, S. Grujić: Development of new cordierite –based refractory coatings for casting application, International Journal of Applied Ceramic Technology, 1-11 (2012) , IJAC-12010, DOI:10.1111/ijac.12010.

## **COPPER ECONOMIC PROJECTION FROM OSTRELJ WASTE DUMPS AND OLD FLOTATION TAILING DUMP LOCATION BOR, SERBIA**

Gordana Slavkovic<sup>1</sup>, Radmila Markovic<sup>2</sup>, Mile Bugarin<sup>3</sup>

*(Mining and Metallurgy Institute Bor, Bor, Serbia)*

### **Abstract**

The last decade is characterized by the trend of higher prices of non ferrous and precious metals on world markets. Copper, gold and silver are centuries old known products of mining in Bor. By long years of copper production and processing have been created flotation tailing dumps. Tailing dumps contain a significant share of metals and can be exploited to evaluate the useful materials. Economic projections are based on projection the annual evaluation of copper Ostrelj waste dumps and the old flotation tailing dumps for the next ten years in consideration of cost-effectiveness framework to the total production capacity of about 3040 t of cathode copper on the basis of technical and technological research. Preliminary economic consideration showed highly positive results of the success and profitability through profit or loss account, economic cash flow, cost price and so on. Economic analysis and possibility of investment return basis on data for technical possibility to production annual sum of 3040 tone copper cathode. Cumulative evaluation of economic analysis shows: period of project: 10 years, investments in fixed assets 13.495.000USD, average net profit 4.000.000 USD, average product price 2884,2 USD per tone copper cathode, Payable of Investments: Internal rate of return 53,7%, Pay back period 2 years, Net present value (10%) 24.670.000 USD. Specify data according to technical elements, shows that starting economic analysis gives very good results.

*Key words: copper, analysis, flotation tailing dumps,*

### **Introduction**

Expert analyzes show that the exploitation of flotation tailings, or obtaining metals from the waste raw material, far cheaper than the standard procedure of mining that involves blasting, excavating, drilling them in this case no. If the flotation tailings does not contain a significant share of copper and precious metals reclamation process is carried out. Trend increase in metal prices has intensified further geological studies as well as professional and scientific advanced training technologies of production and processing of copper.

On the basis of technical-technological parameters for copper valorization from Ostrelj waste dumps and the old flotation tailings initial parameters are:

1. Financial parameters are in US Dollars
2. Selling prices for copper cathode 4200 USD/t
3. Calculations of material and other costs are from technical part and planing prices.

4. Costs of maintenance are: 15% on value of investments for equipment and 5% on value of other investments, and insurance are 2 % on value of investments.
5. Amortization of fixed assets has been determined according to the current regulations for new investments in Serbia.
6. Employers salaries have been calculated at the level of USD 1000 per month and per one worker over the entire period.
7. Other costs are compute according revenue.
8. Profit tax is determined according to the current regulations at the rate in Serbia.
9. Current assets are compute about ¼ average revenue.
10. Evaluation period is 10 years .

Total investments for fixed assets are:

13.495.000 USD

- Total loan is 12.500.000 USD

Repayment period 8 years,

Interest rate is 10% ,equal annual instalments.

### Calculate of revenue

Revenue calculated on basis copper cathode quantity and selling prices .

Table 2. Calculate of revenue

u 000

Product	price	revenue	revenue
<b>* year : 1-10</b>			
1 Cu	1500.0000	4.2000	6,300.00
1 Cu	1540.0000	4.2000	6,468.00
<b>** years revenue</b>		<b>12,768.00</b>	<b>12,768.00</b>
<b>* total revenue</b>		<b>127,680.00</b>	<b>127,680.00</b>

### Product price

#### TOTAL PRODUCT PRICE 3040T COPPER CATHODE PER YEAR

Table 3. \*Total product price

000

Years	1	2	3	4	5	6
1. Raw & material .	2620	2620	2620	2620	2620	2620
2. Energy	182	182	182	182	182	182
3. Maintenance	1271	1271	1271	1271	1271	1270
4. Amortization	1501	1501	1501	1501	1501	1496
5. Other mat. Costs	1000	1000	1000	1000	1000	1000
6. Non mater.costs	800	800	800	800	800	800
7. Salaries	420	420	420	420	420	420
8. Interests	1250	1137	1012	876	725	559
9. Insurance	270	270	270	270	270	269
<b>I. TOTAL</b>	<b>9313</b>	<b>9200</b>	<b>9076</b>	<b>8939</b>	<b>8788</b>	<b>8616</b>
10. Taxes	345	357	369	383	398	415

Years	7	8	9	10	TOTAL	AVERAGE
1. Raw &material	2620	2620	2620	2620	26200	2620
2. Energy	182	182	182	182	1815	182
3. Maintenance	1270	1270	375	375	10914	1091
4. Amortization	1496	1496	751	751	13495	1350
5. Other mat.costs	1000	1000	1000	1000	10000	1000
6. Non mater.costs	800	800	800	800	8000	800
7. Salaries	420	420	420	420	4200	420
8. Interests	390	204			6154	615
9. Insurance	269	269	150	150	2458	246
I. TOTAL	8447	8261	6298	6298	83236	8324
10. Taxes	432	451	647	647	4444	444
II.Full product price	8879	8712	6945	6945	87681	8768

Average product price is 2884,2 USD/T cathode

## PROFIT & LOSS ACCOUNT

Table 4. Profit&Loss Account

000

Years	1	2	3	4	5	6
A. Revenue	12768	12768	12768	12768	12768	12768
B. Costs	9313	9200	9076	8939	8788	8616
1. Operating costs	8063	8063	8063	8063	8063	8057
-Raw &material	2620	2620	2620	2620	2620	2620
-Energy	182	182	182	182	182	182
-Maintenance	1271	1271	1271	1271	1271	1270
-Insurance	270	270	270	270	270	269
-Amortization	1501	1501	1501	1501	1501	1496
-Serv.other mat.	1000	1000	1000	1000	1000	1000
-Non.mater.costs	800	800	800	800	800	800
-Salaries	420	420	420	420	420	420
2. Financial costs	1250	1137	1012	876	725	559
-Interests	1250	1137	1012	876	725	559
C. Gross profit	3455	3568	3692	3829	3980	4152
-Taxes	345	357	369	383	398	415
E. Net profit	3109	3211	3323	3446	3582	3737

-years	7	8	9	10	total	average
A. Revenue	12768	12768	12768	12768	127680	12768
B. Costs	8447	8261	6298	6298	83236	8324
1. Operating costs	8057	8057	m 6298	6298	77082	7708
- Raw &material	2620	2620	2620	2620	26200	2620
- Energy	182	182	182	182	1815	182
- Maintenance	1270	1270	375	375	10914	1091
- Insurance	269	269	150	150	2458	246
- Amortization	1496	1496	751	751	13495	1350
- Serv.other mat.	1000	1000	1000	1000	10000	1000
- Non.mater.costs	800	800	800	800	8000	800
- Salaries	420	420	420	420	4200	420
2. .Financial costs	390	204			6154	615
- Interests	390	204			6154	615
C. Gross profit	4321	4507	6470	6470	44444	4444
- Taxes	432	451	647	647	4444	444
E. Net profit	3889	4056	5823	5823	39999	4000

**ECONOMIC CASH FLOW AND DINAMICAL EVALUATION**

Table5 .Economic Cash Flow

000

Years	1	2	3	4	5	6
<b>I. CASH INFLOW</b>						
1. CASH FROM SALES	12768	12768	12768	12768	12768	12768
<b>2. Residual</b>						
-Fixed assets						
-Current assets						
<b>TOTAL</b>	12768	12768	12768	12768	12768	12768
<b>II. CASH OUTFLOWS</b>						
4. Investments	16695					
6. Operational costs	6142	6142	6142	6142	6142	6141
7. Salaries	420	420	420	420	420	420
8. Taxes	345	357	369	383	398	415
<b>TOTAL</b>	23603	6919	6931	6945	6960	6976
<b>Net cash flow</b>	-10835	5849	5837	5823	5808	5792
<b>Cumulative</b>	-10835	-4986	851	6674	12481	18274
<b>DISCOUNTED VALUE</b>						
- 8.00 %	-10835	5416	5004	4622	4269	3942
-10.00 %	-10835	5317	4824	4375	3967	3597
-12.00 %	-10835	5222	4653	4145	3691	3287
-53.17 % (IRR)	-10835	3819	2488	1620	1055	687

-YEAR	7	8	9	10	TOTAL	AVERAGE
<b>I. . CACH INFLOW</b>						
1. CASH FROM SALES	12768	12768	12768	12768	127680	12768
<b>2. Residual</b>						
- Fixed assets						
- Current assets				3200		
<b>TOTAL</b>	12768	12768	12768	15968	130880	13088
<b>II. CASH OUTFLOWS</b>						
4. Investments					16695	
1670						
6. Operational costs	6141	6141	5127	5127	59387	5939
7. Salaries	420	420	420	420	4200	420
8. Taxes	432	451	647	647	4444	444
<b>TOTAL</b>	6993	7011	6194	6194	84726	8473
<b>Net cash flow</b>	5775	5757	6574	9774	46154	4615
<b>Cumulative</b>	24049	29806	36380	46154		
<b>DISCOUNTED VALUE</b>						
-8.00 %	3639	3359	3552	4889	27858	2786
-10.00 %	3260	2954	3067	4145	24670	2467
-12.00 %	2926	2604	2655	3525	21872	2187
-53.17 % (IRR)	447	291	217	211	0	

**Dynamical evaluation is very good by all methods:**

- Internal rate of return is 53,17%
- Payback period is 2 year
- Net present value ( 10%) is: 24.670.000 USD

### STATICAL EVALUATION IN 5. YEAR

**1. Koefficient of economic:**

Revenue/total costs=12.768.000/8.788.000=**1,45**

**2. Rate of accumulation:**

Gross profit/total investments=3.980.000/16.695.000=**23,8%**

**3. Simple rate of return:** Net profit/total investments=  
3.582.000/16.695.000=**21,46%**

**4. Reproduction:** Net profit+Amortization/ total investments  
=5.083.000/16.695.000= **30,44%**

**5. Rate of profit:** Gross profit/revenue=3.980.000/12.768.000=**31%**

### STATICAL SENSIBILITY ANALYSIS

Total fixed costs **5.704.000**  
**BREAK EVEN POINT(BEP) = -----\*100= ----- \*100=**  
 Total revenue-Total variable costs **12.768.000-2.620.000**  
**= 56,2% - 1708 t total Cu cathode.**

On that point revenues are equivalent to costs. Above that point is profit and under is loss.

### DINAMICAL SENSIBILITY ANALYSIS

*TABLE OF SENSIBILITY*

*Table 9. Table of sensibility with changes*

%chang.	-30%	-25%	-20%	-15%	-10%	- 5%	IRR%	+ 5%	+10%	+15%	+20%	+25%
<b>+30%</b>												
<b>REVENUE</b>												
-E :	12	18	24	31	38	45	53	62	72	83	95	> 100
-F :	5	10	16	21	27	33	40	47	55	64	73	84
-D :	12	19	26	33	41	49	59	69	81	95		> 100
<b>COSTS</b>												
-E :	85	79	73	68	63	58	53	49	45	41	37	33
-F :	65	61	56	52	48	44	40	36	33	30	27	24
-S :	98	90	83	76	70	64	59	54	49	44	40	36
<b>INVESTMENTS</b>												
-E :	0	88	78	70	63	58	53	49	46	43	40	37
-F :	69	62	56	51	47	43	40	37	35	33	31	29
-S :	0	98	87	78	70	64	59	54	50	47	44	41
<b>SALARIES</b>												
-E :	55	55	54	54	54	53	53	53	53	52	52	52
-F :	41	41	41	41	40	40	40	40	40	39	39	39
-D :	61	60	60	60	59	59	59	58	58	58	57	57
<b>TAXES</b>												
-E :	55	55	54	54	54	53	53	53	53	52	52	52
-F :	41	41	41	41	40	40	40	40	40	39	39	39
-D :	59	59	59	59	59	59	59	59	59	59	59	59
<b>Legend: E = Economic IRR</b>												
<b>F = Financial IRR.</b>												
<b>S = Social IRR</b>												

From present table follows that project is very sensitive on revenue changing. If revenue falls 30% - IRR is 12% and that is equivalent to interest rate.

Sensitivity analysis with raise investments, through softer „REMIP“ computers, economic model of investments planning, shows:

<b>+60%</b>	<b>+50%</b>
IRR-19,7%	IRR-23,77%
NPV(12%) -6.633.000 USD	NPV(12%)-9.490.000 USD
Pay back period -5years	Pay back period -4 years

### TOTAL EVALUATION

DESCRIPTION	VALUE	U.M.
<b>1. Period of project</b>	<b>10</b>	<b>year</b>
<b>2.Total investments:</b>	<b>16.695.000</b>	<b>USD</b>
Fixed assets	13.495.000	
Current assets	3.200.000	
<b>3. REVENUE</b>		
- Total revenue	127.680.000	USD
- Average revenue	12.768.000	USD
<b>4. COSTS</b>		
- Total costs	83.236.000	USD
- Average costs	8.324.000	USD
<b>5. Profit</b>		
-Total gross profit	44.444.000	USD
-Average gross profit	4.444.000	USD
-Total net profit	39.999.000	USD
-Average net profit	4.000.000	USD
<b>6. Average product cathode price per tone</b>	<b>2884,2</b>	<b>USD</b>
<b>7. Total rate of profit</b>	<b>34,8</b>	<b>%</b>
<b>8.BEP</b>	<b>56,2</b>	<b>%</b>
<b>9.PAYABLE OF INVESTMENTS:</b>		
IRR - Internal rate of return	53,17	%
PP - Pay back period	2	YEAR
NPV – Net present value (10%)	24.670.000	USD

According to technical elements economic analysis shows very good results.

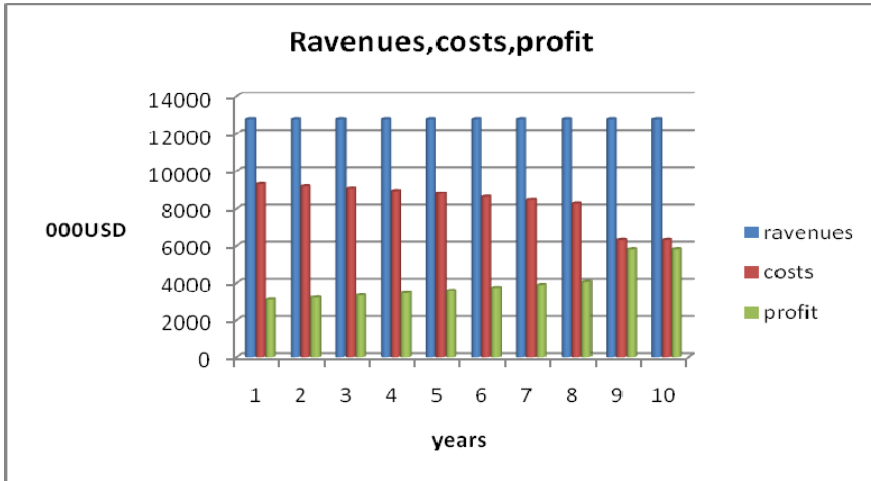


Figure 1. Revenues, costs, profit

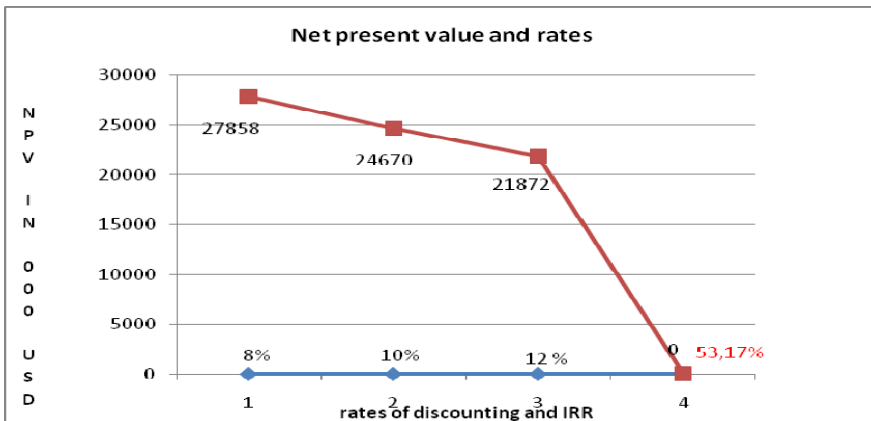


Figure 2. Net present value according to rates

### Conclusion

Economic analysis and possibility of investment return basis on data for technical possibility to production annual sum of 3040 tone copper cathode. Cumulative evaluation of economic analysis shows: period of project: 10 years, investments in fixed assets 13.495.000USD, revenue: Total revenue 127.680.000 USD, Average revenue 12.768.000 USD, costs: Total costs 83.236.000 USD, Average costs 8.324.000 USD, profit: Total gross profit 44.444.000 USD, Average gross profit 4.444.000 USD, Total net profit 39.999.000 USD, Average net profit 4.000.000 USD; Average product price 2884,2 USD per tone copper cathode, Total rate of profit 34,8%, Break even point 56,2%; payable of investments: Internal rate of return 53,7%, Pay back period 2 years, Net present value (10%) 24.670.000 USD. Specify data according to technical elements, shows that prime analysis gives very good results.

## **References**

- [1] B. Cavender, Mineral Production Costs - Analysis and Management, SME, (1999).
- [2] N. Dondur, Economic analysis of projects, Mechanical Engineering, Belgrade (2002).
- [3] G.Mankju, Principles of Economics, Faculty of Economics, Belgrade, (2005).
- [4] M.Bugarin, G.Slavkovic "Techno-economic evaluation" Copper Institute, Bor (2006).
- [5] T. Kuronen: Capital Budgeting In A Capital-Intensive Industry, Helsinki University of Technology, 2108 Mat-Independent Research projects in applied mathematics, (2007).

This paper is result of Project No. 37001, „The impact of mining waste from RTB Bor on the pollution of surrounding water systems with the proposal of measures and procedures for reduction the harmful effects on environment“, funded by the Ministry of Education, Science and Technological Development the Republic of Serbia.

**\*Table are from softver REMIP\*-own software Computational model of economic investment planning of Mining and Metallurgy Institute Bor**

## **INVESTIGATION OF HARDENING OF THE NIOBIUM MODIFIED HEAT RESISTANT STAINLESS STEEL GX40CrNiSi25-20 DURING SINTERING PROCESS**

Dr.sc Samir Butković<sup>1</sup>; Dr.sc Mirsada Oruč<sup>2</sup>; Dr.sc Emir Šarić<sup>1</sup>;  
Dr.sc Muhamed Mehmedović<sup>1</sup>; Dr.sc Sulejman Muhamedagić<sup>2</sup>

*1 University of Tuzla, Faculty of Mechanical Engineering, Univerzitetska 4,  
Tuzla, BiH*

*2 University of Zenica, Faculty of Metallurgy and Materials, Travnicka cesta  
1. 72000 Zenica, BiH*

### **Abstract**

Hardening of niobium modified heat resistant stainless steel GX40CrNiSi25-20 during sintering process, as a final stage of metal injection molding technology, was investigated in this paper. Debinding of injection molded parts was performed by catalytic debinding method, while removing of residual binder was done by thermal debinding process.

Correlation between the sintering parameters and the hardening degree of steel was established using hardness testing results, chemical and metallographic analysis of sintered parts. Hardening of steel was described by comparing the hardness testing results, achieved by sintering in atmospheres of hydrogen, nitrogen and argon at different temperatures and sintering times, taking into account variations in chemical composition of the parts after sintering (carbon, nitrogen). Also, hardness distribution over cross section for some specific samples was investigated.

*Key words: Sintering, heat resistant stainless steel, sintering atmospheres, hardening*

### **Introduction**

Metal injection molding is a very suitable technology for high-volume production of small and complex parts. MIM technology starts with preparation of feedstock, where metal powder is mixed with a proper binder to form feedstock. Next, prepared feedstock is injected into the tool cavity using injection molding machine, to form green part (Fig. 1). The most of the binder is then removed from the parts by solvent/chemical debinding. Small quantity of the binder remains in parts after debinding to hold the shape of the parts, and is debound during early stage of sintering process. Sintering process, as a final stage of MIM technology, has the great importance for successful processing of stainless steel [1,2]. It encompasses many elements from furnace type and atmosphere selection to process parameters choices (temperature, time, heating and cooling rate, atmosphere partial pressure) [1,2].

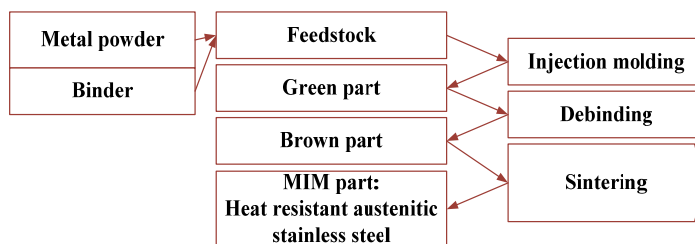


Figure 1 Metal injection molding technology

Mechanical properties and corrosion resistance of heat resistant stainless steel are highly dependent on the nature of interactions with the sintering atmosphere.

Absorption and desorption of some elements during sintering can significantly effect properties of sintered materials. Typical sintering atmospheres for stainless steels include hydrogen, hydrogen-nitrogen mixtures, dissociated ammonia, and vacuum [1,2,3]. Interaction between atmosphere and material varies during sintering process and is mostly dependent on sintering temperature profile. Sintering PM austenitic stainless steels in hydrogen atmosphere is usually done to avoid chromium nitrides precipitation, which are responsible for reduced corrosion resistance [1,2]. Sintering in nitrogen containing sintering atmosphere leads to reduced corrosion resistance, but superior mechanical properties of austenitic stainless steel, which is still acceptable in many applications. Sintering temperature controls diffusion processes during sintering [4] causing faster or slower pore closing and participates in atmosphere/material interactions. Also, temperature determines maximal solubility of nitrogen in steel [5,6]. In this regard, hardening of niobium modified heat resistant stainless steel GX40CrNiSi25-20\* during sintering process, is presented in this paper. Effect of sintering temperature and atmosphere on hardness of the sintered parts was investigated, where contribution of individual parameters and their interactions were analyzed using ANOVA method. Also, hardness distribution over cross section of parts, as function of sintering atmosphere and temperature was investigated.

## Experimental work

Experimental investigation was performed using ready-to-mold granules for the production of Nb-modified heat resistant stainless steel with a chemical composition of metal powder corresponding to equivalent standard GX40 CrNiSi 25-20\*, (Table.1). Injection molding of prepared feedstock was done using machine ALLROUNDER 320 C 600-100. Feedstock, based on polyacetal, has ability to be decomposed using nitric acid [7]. Thus, debinding process was performed using catalytic debinding method applying nitric acid dispersed by nitrogen gas. Debinding was done using temperature of 120 °C, in a time period of 4 h. This temperature converts the polymer into gas without melting, where parts stay stiff during debinding, avoiding any plastic deformation and giving better tolerances [7].

Table 1 Typical chemical composition after sintering- **GX40CrNiSi25-20<sup>1</sup>** niobium modified

C (%)	Cr (%)	Ni (%)	Si (%)	Nb (%)	Mn (%)	Rest (%)	Fe
0,2-0,5	24-26	19-22	0,75-1,3	1,2-1,5	<1,5	<2	Balance

After catalytic debinding, there is a residual amount (usually 10 weight %) of an acid resistant binder which provides certain strength for handling to the pre-shaped powder [7]. Debinding of residual binder was performed using thermal debinding method. Thermal debinding was done at the temperature of 600 °C, in a period of 2 h. After thermal debinding, parts were heated to the sintering temperature. Sintering experiments were performed using atmospheres: hydrogen, nitrogen, argon, 50%H<sub>2</sub>+50%N<sub>2</sub>, at the temperatures of 1200 °C and 1310 °C. The most of experiments were performed using the sintering time of 3 h. However, in order to see effect of sintering time on hardening of steel for some specific samples, sintering time was prolonged to 6 h. Hardness distribution over cross section of parts was performed after sintering process. Also, metallographic examination, as well as nitrogen and carbon content analysis was done to investigate hardening of steel during sintering.

## Results and discussion

Effect of sintering atmosphere and temperature on hardness of investigated material was analyzed using full factorial experiment. Analysis of variance (ANOVA) was used to demonstrate the significance of the variables, as well as the effects (contribution) of the sintering variables on hardness of the sintered parts. Influential factors, their levels and average hardness for selected set of parameters are presented in the table 2.

Table 2 Hardness examination results

Atmosphere	Temperature [°C]	Time [h]	Partial Pressure [mbar]	Average Hardness [HV 1]	St.Dev
H <sub>2</sub>	1200	3	400	132,8	2,68
H <sub>2</sub>	1310	3	400	150,6	2,60
N <sub>2</sub>	1200	3	400	180,6	2,07
N <sub>2</sub>	1310	3	400	230,2	5,97
Ar	1200	3	400	144,6	6,84
Ar	1310	3	400	165,8	2,16
N <sub>2</sub>	1310	3	600	255,8	3,19
Ar	1310	6	400	161	4,69
50%H <sub>2</sub> - 50%N <sub>2</sub>	1310	3	400	228	9,41

N <sub>2</sub>	1200	3	800	185,7	3,5
H <sub>2</sub>	1200	6	400	137	3,6
Ar	1200	6	400	152	5,87
Ar	1310	6	400	160,7	3,90

From ANOVA (Tab. 3) we can see that both, the temperature and the time have significant influence on hardness of the sintered parts. The most influential factor is atmosphere contributing with 72 %, followed by temperature with 21 %. Also, interaction between temperature and atmosphere has significant effect on achieved hardness. It is noticeable that hardness of sintered parts increases with sintering temperature (Fig. 2). Increasing of temperature for parts sintered in hydrogen atmosphere resulted in increased hardness for about 15 % (Fig. 2). Higher resistance to penetration of the indenter caused by decreased residual porosity (Fig. 3) and increased density [8] resulted in higher achieved hardness of the sintered parts (Tab. 2).

Table 3 Analysis of variance for hardness

Factor	Type	Levels	Values					
Atmosphere	fixed	Ar H <sub>2</sub> N <sub>2</sub>						
3		1200 1310						
Temperature	fixed			<b>Adj SS</b>	<b>Adj MS</b>	<b>P</b>	<b>F</b>	<b>Contr%</b>
2				22533,3	11266,6	0,000	640,76	<b>72,637</b>
Source		<b>DF</b>	<b>Seq SS</b>	6541,6	6541,6	0,000	372,04	<b>21,087</b>
Atmosfer		2	22533,3	1524,5	762,2	0,000	43,35	<b>4,91</b>
Temperat		1	6541,6	422,0	17,6			
Atmosfer*Temperat		2	1524,5					
Error		24	422,0					
Total		29	31021,4					

However, parts sintered in argon atmosphere showed higher sintered hardness compared to the parts sintered in hydrogen atmospheres. Change in sintering atmosphere from hydrogen to argon (vacuum) resulted in increasing of average hardness from 141 HV1 to 152 HV1. In this case, lower carbon concentration for parts sintered in hydrogen atmosphere (Fig. 4) caused significant hardness reduction. Reduction of residual porosity and increasing of density [8] by higher sintering temperatures for parts sintered in argon atmosphere had the same effect on hardening as noted for hydrogen atmosphere.

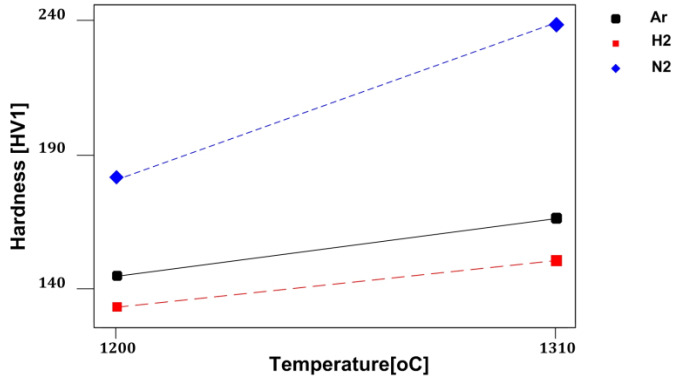


Figure 2 Hardness as function of temperature and atmosphere

The highest hardness was observed on parts sintered in nitrogen atmosphere. In addition to highest carbon content (Fig. 4), the parts sintered in nitrogen atmosphere experienced nitrogen absorption during sintering (Fig. 4). Nitrogen atmosphere and temperature 1310 °C generated 0,53 % of absorbed nitrogen during sintering for 3 h. Absorbed nitrogen participates in solid solution strengthening of steel and nitrides forming, leading to hardness increasing [1].

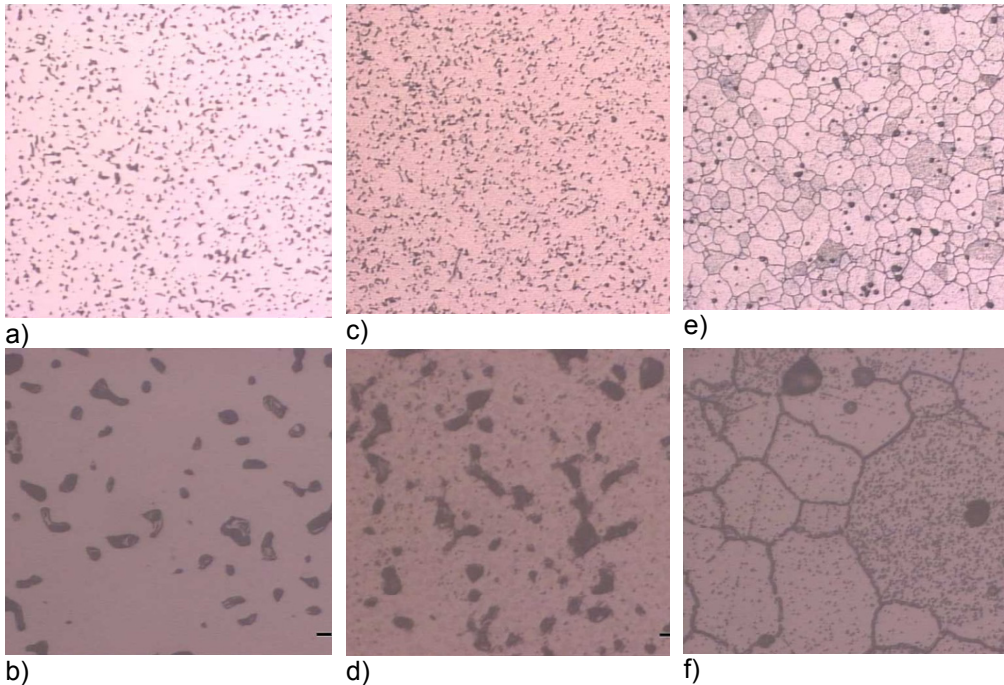


Figure 3 Microstructure of parts sintered at: a, b)  $H_2$ , 1200 °C, 400 mbar c, d)  $N_2$ , 1200 °C, 400 mbar; e, f) 50% $H_2$ -50% $N_2$ , 1310 °C, 400 mbar

Lines representing hydrogen and argon atmospheres, in interaction chart (Fig. 2), are almost parallel which indicates that increasing of density and reduction of porosity mainly controls hardening of steel, for these atmospheres. However, parts sintered in nitrogen atmosphere showed significantly higher percent of residual porosity (Fig.3 c, d) compared to parts sintered in hydrogen atmosphere (Fig. 3 a,b), for the same sintering temperature (1200 °C). Hardness, in this case was not influenced by residual porosity. Average hardness for the part sintered in nitrogen atmosphere was 185 HV1, while sintering in hydrogen produces hardness of 132,8 HV1. This implies that hardening by absorbed nitrogen is dominant compared to hardening due to increased density and reduction of residual porosity.

Also, increasing of hardness to 28%, for parts sintered in nitrogen atmospheres, was observed as the sintering temperature raises from 1200 °C to 1310 °C. All mentioned suggest that two sources that contribute to hardening of steel exist during sintering in nitrogen atmosphere: porosity reduction (Fig.3) and hardening by absorbed nitrogen. Also, it should bear in mind that larger concentrations of nitrogen in steel can cause chromium nitrides formation, causing deterioration ductility, impact energy and corrosion resistance [1].

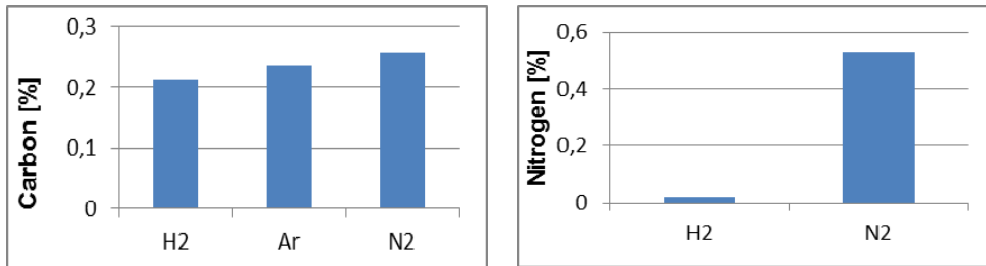


Figure 4 Carbon and nitrogen concentration after sintering

Sintering in 50%H<sub>2</sub> and 50%N<sub>2</sub> at 400 mbar partial pressure produces the parts with hardness almost equal to parts sintered in fully nitrogen atmosphere (Fig. 3 e,f). Hardening of steel induced by absorbed nitrogen is evident in this case too. Thus, it can be concluded that addition of hydrogen to nitrogen sintering atmosphere will not significantly deteriorate hardening effect of nitrogen. However, addition of hydrogen to sintering atmosphere can intensify densification of steel, and thus reduce sintering time [8].

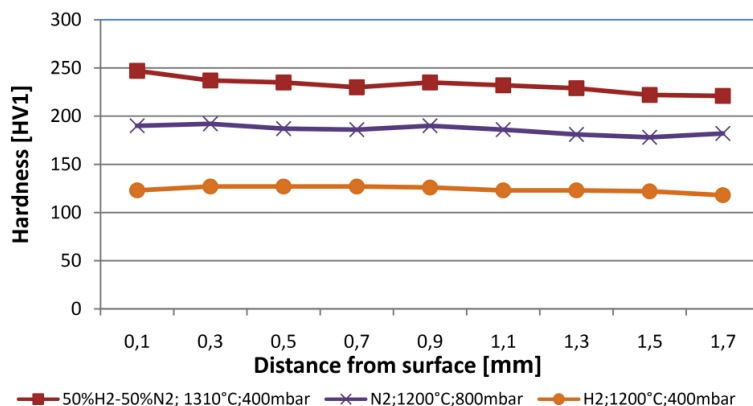


Figure 5 Hardness distributions through cross section of the sintered parts

Significant effect of time was observed on parts sintered at lower temperatures where prolongation of time more importantly affects density and reduction of porosity.

Increasing of time for parts sintered in argon and hydrogen atmospheres at temperature 1200 °C resulted in increased hardness for about 5,5 % and 3,4%, respectively. However, prolongation of time for parts sintered at 1310 °C, in argon atmosphere, caused slight reduction of hardness. In this case, prolonged sintering time can not significantly increase density [8], but may cause carbon percent reduction, which leads to reduced hardness.

Distribution of hardness for the parts sintered in nitrogen containing atmosphere with different sintering temperatures is presented in figure 5. Higher temperatures cause faster pore closing resulting in nitrogen absorption through the outer surface of the parts. As a result, slight increased hardness can be noted near the surface. As for the parts sintered at lower temperatures, where open porosity exist longer time, hardness is distributed more evenly.

## Conclusion

Hardening of Nb-modified heat resistant stainless steel GX40CrNiSi25-20\* during sintering is highly dependent on sintering parameters. Sintering temperature and atmosphere are the most influential factors. Ability to increase hardness using argon and hydrogen atmospheres mainly depends on residual porosity, density and carbon concentration in steel. Sintering in hydrogen atmosphere leads to slight carbon concentration reduction compared to argon and nitrogen atmospheres, giving the lowest achieved hardness of steel. Nitrogen containing sintering atmosphere causes absorption of nitrogen which significantly increases hardness of steel. In addition to nitrogen absorption, parts sintered in nitrogen atmospheres showed maximal carbon concentration, causing the most emphasized hardening of steel. Hardening of steel using nitrogen atmosphere is a function of nitrogen partial pressure and temperature. Increased partial pressure of nitrogen atmosphere causes more intensive hardening of steel. Also, experiments showed that

prolongation of sintering time has more important effect on hardness of parts sintered at lower temperatures.

Hardness distribution investigation showed that lower temperatures, where open porosity exist longer time, gives hardness distribution more evenly. Absorption of nitrogen through the outer surface of the parts sintered at the higher temperatures produces unevenly distributed hardness with a maximal values near the surface of the parts.

## **References**

- [1] Erhard Klark, Prasan Samal, Powder metallurgy stainless steel, processing, microstructure and properties, ASM International, Ohio 2007.
- [2] ASM Handbook, Powder Metal Technologies and Applications, Volume 7, 1998.
- [3] Josef R. Davis, Stainless Steels, ASM speciality handbook, Materials Park, 1994.
- [4] Randall M. German, Sintering theory and practice, New York, 1996.
- [5] Richard P. Reed, "Nitrogen in Austenitic Stainless Steels, JOM, Vol. 41, Issue 3, 1989, pp.16-21.
- [6] Andre Paulo Tschiptschin, Powder metallurgy aspects of high nitrogen steels, High nitrogen steels and stainless steels, Alpha Science International Ltd, 2004.
- [7] Catamold Feedstock for Metal Injection Molding: Processing – Properties, Applications, Technical Information, BASF AG, May 2003.
- [8] Dr.Samir Butković, Dr.Mirsada Oruč, Dr.Emir Šarić, Dr.Muhamed Mehmedović: Effect of sintering parameters on density, microstructure and mechanical properties of niobium modified heat resistant stainless steel GX40CrNiSi25-20 produced by MIM technology: *Materiali in tehnologije / Materials and technology*, Volume 46 (2012) 2, pp.185–190.

## **SURFACE ROUGHNESS CHANGES AROUND TIG WELDS OF AlMg<sub>5</sub> SHEETS**

Z. Karastojković<sup>1</sup>, R. Perić<sup>2</sup>, Z. Janjušević<sup>3</sup>, N. Bajić<sup>4</sup>, A. Sedmak<sup>5</sup>

*1- Technical Colege, 11070 Novi Beograd, blvd. Dr Zorana Đinđića 152a,  
Serbia*

*2- Perić&Perić, d.o.o., 12000 Požarevac, Dunavska 114, R. Serbia*

*3- Institute of Nuclear and Other Mineral Raw Materials, 11000 Beograd,  
Franché d'Esperey 86,  
Serbia*

*4- IHIS-Tehnoekspert, 11080 Beograd-Zemun, Srbija, Batajnički put 23,  
Serbia*

*5- Mechanical engineering faculty, 11000 Beograd, kraljice Marije 16,  
Serbia*

*e-mail: zoran.karastojkovic@gmail.com*

### **Abstract**

Aluminium as a metal (or metalloid) has shown some difficulties in the welding processes, so that many welding methods are not available. For aluminium and its alloys TIG welding is widely accepted method of joining. The sheet from AlMg<sub>5</sub> alloy is one of commonly used semiproduct in practice. TIG or plasma welding represents successful methods for joining of such or similar aluminium alloys, satisfying the mechanical properties of the weld.

The TIG welding technique itself requires the high level of skills about the welder. In every case, the welding of aluminium must be provided in a pretty short time cycle, for preventing an oxidizing of the welding pool. The welding of AlMg<sub>5</sub> alloy still is a problem from mentioned or another reasons. The problem arises in increasing the surface roughness just around the TIG weld area. It is evident the changing of the aesthetic appearance at surface near welding zone, even when the smooth (cold rolled) sheet is used for welding. The changes near the zone of welding usually are described as the technological property (good, bad, appropriate, etc.), rather than measured. Here are provided some measurements of the surface roughness by the using a profilometer.

*Key words: TIG welding, AlMg<sub>5</sub> sheet, surface roughness, weld zone*

### **Introduction**

Aluminium alloys are widely used for producing the variety of profiles or castings, which further serve in different structures. Here used aluminium alloy AlMg<sub>5</sub> (from 5XXX series of alloys) belongs to a group of wrought alloys, commonly produced in the form of sheet, and is available for welding. One successful technique for welding of such alloy is TIG and/or plasma method [1]. It is considered that principles about TIG/plasma welding are well known, so the

used welding method will not be, anymore, explained in details. For better understanding the welding behavior, it is worthy to mention that 5XXX series of alloys principally have very poor laser welding characteristics.

The used alloy contains relatively small amount of alloying element: the content of magnesium is on the level of 5% (4,8-5,8%), with small amounts of manganese (0,10%) and chromium(0,10%) or more, dependently from the national standards [2,3]. According to Al-Mg constitutional diagram, the solubility of magnesium gradually is decreased with decreasing the temperature, to less than 2% with decreasing the temperature, so that theoretically these alloys could be strengthened by precipitation hardening. But, in practice the effect of such strengthening is pretty low. The chosen alloy belongs to a group of nonheat-treatable alloys, and its properties are not changed appreciably in resistance to corrosion after welding [1,4,5]. Small additions of manganese and chromium have led to improving the distribution of precipitates or refining the grain size. So, this alloy is widely used in general engineering, even at marine atmospheres, etc.

For welding of 5mm thick AlMg5 sheet will be applied the square type of butt joint, i.e. without any preparing of edges after cutting is done. Other types of groove also are available, mainly for minimizing the distorsion etc, but here is the matter of monitoring just a surface roughness around the weld line.

The roughness profilometry is a technique rather used for measuring the surface roughness in cutting machining operations (as like turning, milling, grinding, etc.) than in welding technologies [6]. The precisiuous measuring of the surface roughness of course offers an advantage in comparison to only descriptive explanation, and this will be the matter of here provided experiment. The changing of surface roughness does not influenced on lowering the measures/dimensions of welded components or the mechanical properties, but rather on aesthetic appearance.

## **Experoment**

For TIG welding here is chosen the cold rolled AlMg5 sheet,  $\approx$  5mm thick, cutted from a larger table in strips, 50mm wide and about 120mm long each. Cold rolled table from this alloy ordinary possesses a shine surface. Welding is performed manually, although this process sometimes could be automated [1]. Welding is performed at next technological parameters: direct current 14V, A, voltage 240V, argon consumption 5lit/min. For welding is chosen the butt welding position, either another (more complicated) types of position may be used for this type of material [7]. The edges of the strips to be welded are not specially prepared, it means they remained quadratic, Fig. 1a).

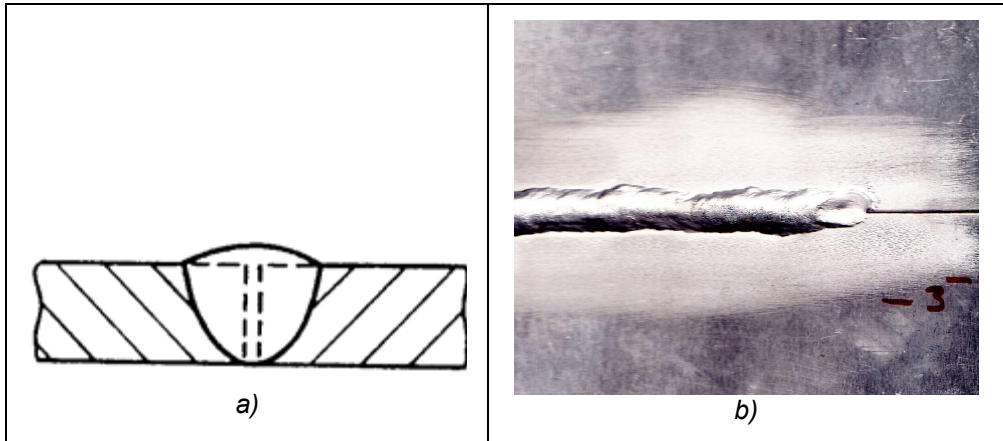


*Fig. 1. Butt position of strips for welding a) and the end of TIG welded AlMg5 strips b)*

The end of such weld at those strips with surrounding area is shown in Fig. 1b). Welding is done by using an appropriate filler rod material, here it means from the same alloy AlMg5, in the diameter of 5mm. At the end of the weld, see right part in Fig. 1b), strips still are not welded. In this position the welding is interrupted, but either of this in front of TIG nozzle the surface also is roughened. This is due to the temperature distribution around the TIG nozzle. Manual welding cannot produce a straight welding line as in automated procedure, but this is not a problem in this investigation.

## Results and discussion

Both metals, magnesium and aluminium, are light metals which possess relatively low melting temperatures [5,8,9], and they are not suitable for welding as other industrial metals are. From the Al-Mg system many alloys have found their applications, one of those is AlMg5 alloy, which is suitable for deforming and welding. Many structures were built up from the mentioned alloy.

The difference of the surface states, before and after welding, was clearly distinguished by the naked eye. The cold rolled strip away (over 20mm) from the welding line still remains smooth and highly shined, while near the welding line the surface was rough and matted, as clearly can be seen from Fig. 2. at larger magnification. The matting, i.e. the roughening, was at least 15mm from the each side of the welding line. But, monitoring of roughness by the naked eye does not represent a kind of scientific nor an accurate measuring, so the more precise diagnostics, it means measuring, of surface state should be provided.

The surface roughness is measured by using a profilometer at the cold rolled zone (as referent state) and at three different positions along the welding line (direction), as sketched in Fig. 2. At position (1) is measured the initial (cold rolled) state about 30mm from the visible change in roughness, i.e. matted surface. Another measuring position (2) is situated about 3mm inside the matted surface or

about 12mm from the welding line. Finally, the measuring position (3) was far about 5mm from the end of weld, as illustrated in Fig. 2.



*Fig. 2. Enlarged view near welding line and positions (1÷3) for measuring of surface roughness around TIG welds of AlMg5 strips, x 5*

The measurements of surface roughness were provided on the sampling length of 10mm, as usually is provided in surface roughness monitoring. Such obtained profilograms from those positions are shown in Fig. 3÷5. On those diagrams the every graduation valids  $2\mu\text{m}$

The initial roughness, it means on cold rolled state, is shown in Fig. 3. Next measurement, pos. 2, gives the roughness profile as shown in Fig. 4. Only small increasing in surface roughness is visible, when diagrams from figs. 3 and 4. are compared.

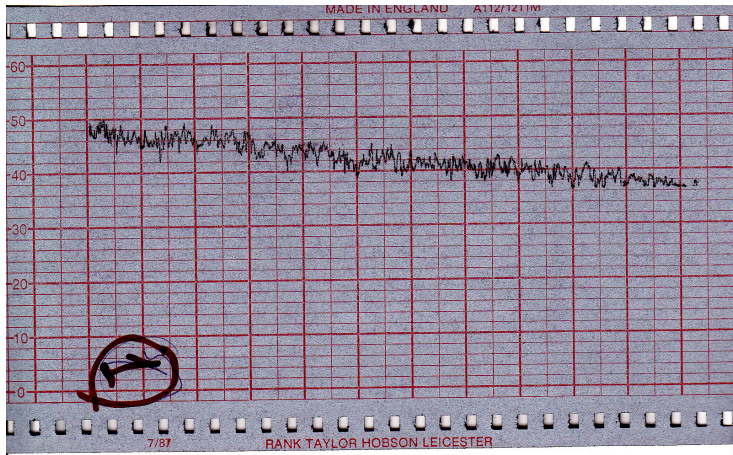


Fig. 3. Profilogram of cold rolled plate of AlMg5 sheet, pos. 1. from Fig. 2.

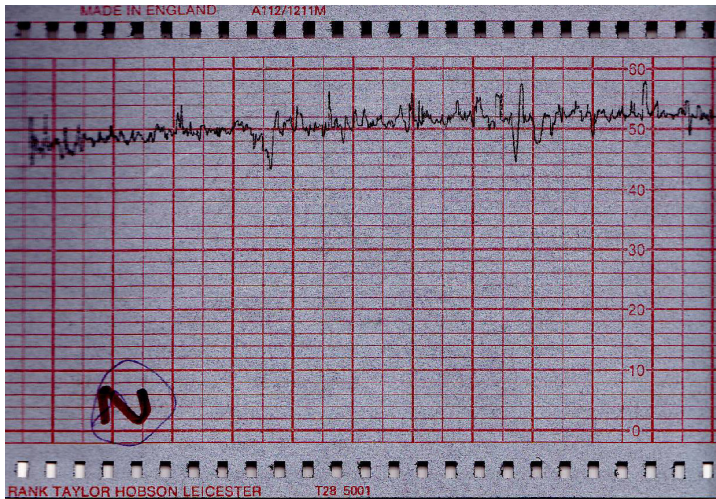


Fig. 4. Profilogram at pos. 2. from Fig. 2.

The highest roughness is measured near welding line, as can be seen from Fig. 5.

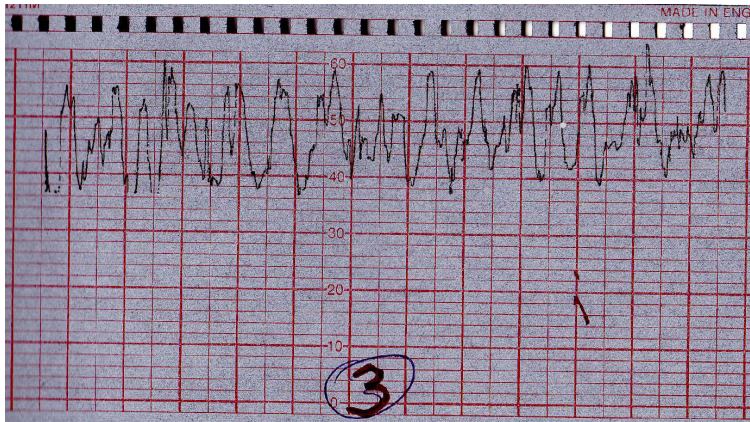


Fig. 5. Profilogram obtained a about 5mm from welding line of AlMg5 sheet, pos. 3. from Fig. 2.

More precise data about surface roughness, it means by applying an arithmetical average roughness ( $R_a$ ) are given in Table 1.

Table 1. Characteristic arithmetical average roughness ( $R_a$ ) values for measured profiles

State	$R_a$ , $\mu\text{m}$
cold rolled surface - pos. 1.	0,55
position 2.	1,1
position 3.	4,6

The boiling point of magnesium is  $1110^{\circ}\text{C}$ , and this temperature is pretty lower than evaporation of aluminium,  $2060^{\circ}\text{C}$  [5,8,9], and that could be the main reason for roughness increasing after TIG welding. From registered data is evident an increasing the arithmetical average roughness ( $R_a$ ) also is increasing closer to the welding line. The obtained results are not surprising but rather expected, because any kind of surface protection as sprays etc., were not applied here.

## Conclusion

The roughness measurements were provided after TIG welding on cold rolled AlMg5 sheet,  $\neq 5 \times 50 \times 120 \text{mm}$ . Such cold rolled sheet from this alloy ordinary possesses a shine surface. Here TIG welding is performed manually. The difference of the surface states, before and after welding, was clearly distinguished by naked eye. Over 15mm from the welding line, the surface of cold rolled strip still remained smooth and high shined, while near the welding line the surface was rough and mat, as it was shown on Fig. 2. The mat surface also is roughened.

The surface roughness is measured by using a profilometer. The initial roughness of cold rolled sheet  $R_a = 0,55 \mu\text{m}$  was changed. At position (2), about 10mm from the welding line and about 3mm inside the matted surface, is obtained an average surface roughness of  $1,1 \mu\text{m}$ . At the position (3) was far about 5mm from the end of weld, is obtained an average surface roughness of  $4,6 \mu\text{m}$ .

Such obtained data suggest the using any kind of protection of surface (sprays, etc.), before starting the TIG welding process on aluminium alloys, when magnesium is an alloying element.

### **Acknowledgement**

Here represented results are provided in companies „Lovčević“ Sremčica-Beograd, Serbia, and „Industrija pricezne mehanike“, Beograd, Serbia, and we are grateful to them.

### **References**

- [1] Welding Alcoa Aluminum, Aluminum Company of America, Pittsburgh 1972, USA, pp.29-40.
- [2] E.C. Rollason: Metallurgy for engineers, London 1973, Arnold, pp. 327-347.
- [3] Yu. Lakhtin: Engineering Physical Metallurgy and Heat-treatment, Moscow 1979, MIR Publishers, pp. 372-391.
- [4] V. Sedlaček: Non-ferrous metals and alloys, Amsterdam 1986, Elsevier, pp. 200-207.
- [5] H. Šuman: Metalografija, in Serbian, Beograd 1968, Zavod za izdavanje udžbenika Srbije, pp. 518-544.
- [6] B. Vasiljević, B. Nedić: Modifikovanje površina, Kragujevac 2003, Mašinski fakultet u Kragujevcu, pp. 5-17.
- [7] D. Smith: Veštine i tehnologija zavarivanja, Paraćin 1995, Vuk Karadžić, pp. 313-345.
- [8] [F.D. Gelin: Metaličeskie materialy, in Russian, Minsk 1987, Vešejšaja škola, pp. 321-338.
- [9] R.E. Reed-Hill: Physical Metallurgy Principles, New York 1973, van Nostrand, pp. 38-59.

## ELLIPSOMETRIC MEASUREMENTS OF $\tan(\psi)$ AND $\cos(\Delta)$ AT ANNEALED AND COLD ROLLED STRIPS MADE FROM GOLD ALLOY 585

Z. Karastojković<sup>1</sup>, R. Perić<sup>2</sup>, M. Jovanović<sup>3</sup>, M. Srećković<sup>4</sup>, Z. Janjušević<sup>5</sup>,  
G. Radoš<sup>3</sup>

1- Technical College, 11070 Novi Beograd, Blvd. Dr Zorana Đinđića 152a,  
Serbia

2- Perić&Perić, d.o.o., 12000 Požarevac, Dunavska 114, R. Srbija

3- Institute for Physics, University at Belgrade, 11080 Zemun, Pregrevica  
118, Serbia

4- Electrotechnical Faculty, 11000 Beograd, Blvd. kralja Aleksandra 73,  
Serbia

5- Institute of Nuclear and Other Mineral Raw Materials, 11000 Beograd,  
Franché d'Esperey 86, Serbia  
e-mail: zoran.karastojkovic@gmail.com

### Abstract

The shining (optical) properties principally depend upon the material structure and the kind of technological processing. Chosen golden alloy, finess of 585, is one of the common used alloy for jewel making. Optical properties from the system Au-Ag-Cu generally are known for almost jewelers, but rather on the descriptive manner (good, poor, satisfied, etc.) than on the exactly measured optical (elliptical) parameters. Here will be represented some ellipsometric measurements of  $\tan(\psi)$  and  $\cos(\Delta)$ , at annealed and cold rolled strips.

The used alloy was melted in a vacuum induction heated furnace from refined (99,99%) metals and casted in a protective atmosphere, containing the nitrogen gas. Cold rolling of golden strips is provided by height reduction of 10, 20 and 30%. The small reductions, as here applied, are just needed when such treated metal further is undergoing to shaping, for obtaining the desired jewel product(s).

The measurements of  $\tan(\psi)$  and  $\cos(\Delta)$ , as parameters of elliptical polarized light, will be done in the range of 300-800nm of electromagnetic spectrum.

*Key words: 585 golden alloy, ellipsometry,  $\tan(\Psi)$  and  $\cos(\Delta)$  values*

### Introduction

The optical properties of noble metals are of an extremely importance, when those metals will be used in jewelry production. For almost pure noble metals (Au, Ag, Cu, Pd, Pd, etc.) the optical properties were fully examined [1] but not for their alloys. Ellipsometry is a non-destructive characterization technique used for determination the principal optical constants, ( $n$ ) and ( $k$ ) indices, as real and imaginary components of refractive index, further for determination the ratio of

amplitude diminutions ( $\Psi$ ) and phase difference induced by the reflection ( $\Delta$ ). Those parameters usually are determined at a surface, even at an interface. Changes in refractive indices can be further used in industrial processing technology, especially in coating technology, for measuring the porosity, also in other fields such as biology and/or medicine, etc.

In the schedule of golden jewel production many different technological operations should be used, main of those are: melting, alloying, casting, rolling, deep-drawing, welding, brazing and/or polishing (2÷4). After alloying many properties of an alloy become quite different in accordance to the initial properties of pure metals, what is excellent known to metallurgists. The golden alloy used here is composed from min. 58,5%Au. This alloy (14kt) is one of the most popular in jewelry. This is one ternary alloy, but some time also is added the zinc, for strengthening the alloy and, of course, from economic reason. The optical properties, in the sense of different visible colors of this ternary system, are given in Fig. 1.

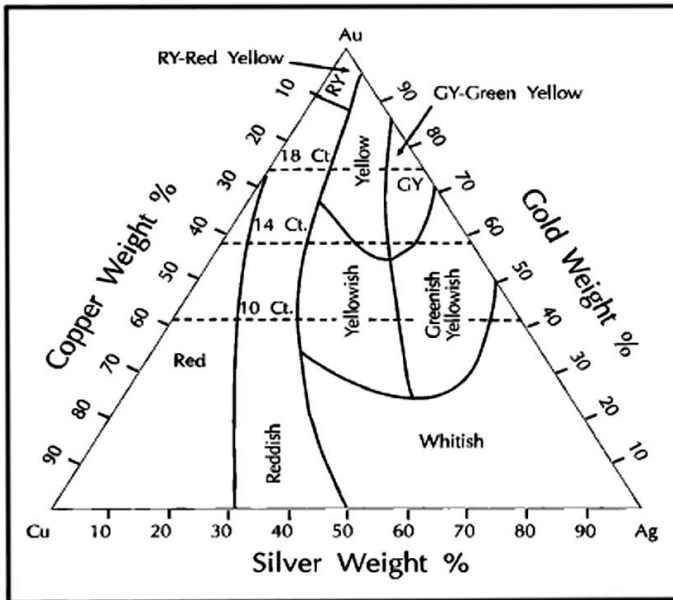


Fig. 1. Colors of pure metals and their alloys throw entire ternary Au-Ag-Cu system

The jewels, especially those made from noble metals, should possess a high level of brilliance. The shining properties frequently are judged individually on a descriptive manner as: good, proper, poor, well, etc. Those criteria, indeed, are not based on scientific measurings.

### Ellipsometry in metal studying

The measuring of optical properties in metals does not represent a target in physical metallurgy, in the studying of diffraction behavior at a surface to be

analyzed [5], it is rather a matter of studying in other fields of physics, for example in solid state physics or similar [6,7]. Ellipsometry became one usual technique for measuring the optical properties [8,9], in which is monitoring the interaction of incident light with material. In an appropriate literature could be found many applications of ellipsometry for thickness determination, crystallography, anisotropy, roughness, etc. The principal positions of needed equipments for providing the ellipsometric measurements are shown in Fig. 2a). The ellipsometric measuring is based on using the linearly polarized light, as an incident beam [10,11]. The reflected light beam is elliptically polarized in the s- and p-planes, see Fig. 2b).

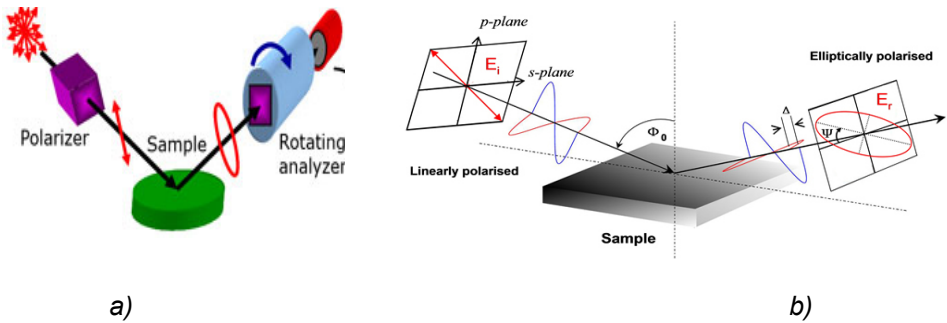


Fig. 2. From known input of linearly polarized beam a) and details about  $\psi$  and  $\Delta$  for measuring of reflected output b)

The measure for elliptical polarization are parameters  $\psi$  and  $\Delta$ , as could be seen from Fig.2b). The reflectance of pure noble metals (gold and silver) as a function of wavelength in the visible spectra of the light is shown in Fig. 3a), according to literature data (internet + Poole).

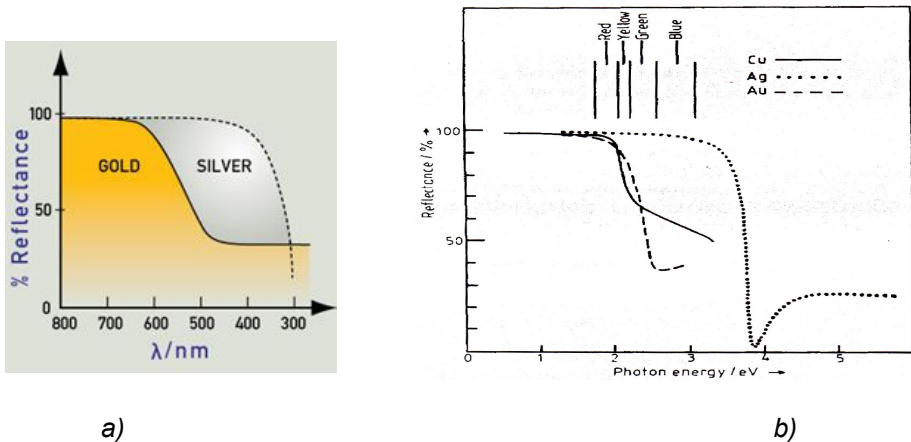


Fig. 3. Trajectories of reflectance vs wavelength for gold and silver a) and reflectance vs photon energy of gold, silver and copper b) [10]

It could be said that reflectance represents “a kind of reflecting power” of investigated metal [6,11]. Reflectance and absorptivity for metals in the sum are equal to 1, because they are not transparent. It means that when the reflectance is high then the absorptivity must be low. It is an explanation for different colors of metals, Fig. 3b). The shape of reflecting power curve for gold, silver and copper is shifted according to the photon energy, and producing the variety in colors for every metal, as can be seen from Fig. 3b).

### Preparing of 585 gold alloy strips

Melting, alloying, casting and rolling were provided in jewelry shop “Perić&Perić”Co, Požarevac, Serbia. The melting was done in a vacuum furnace by using pure metals (99,99% of finess), after that is obtained next chemical composition, Table 1.

Table 1. Chemical composition of used 585 gold alloy

<b>Au</b>	<b>Ag</b>	<b>Cu</b>	<b>Zn</b>
58,5	8,3	25,7	7,5

Casting is provided in the presence of nitrogen gas as a protective atmosphere. Cold rolling of strips always is done to the final thickness of 0,5mm. For such ellipsometric measuring of this alloy, strips are prepared in dimensions 0,5x10x10mm. One sample (1) is annealed at 680°C, while other specimens (2-4) are cold rolled with low degree of deformation: 10, 20 and 30%, respectively. As frequently is practice in metallurgy, on the same specimens is measured also the microhardness, and those results are presented at Table 2.

Table 2. Assignment of samples and their hardness values ( $HV_{0,25}$ )

<b>N° specimen - %def.</b>	1 - 0%	2 - 10%	3 - 20%	4 - 30%
<b>microhardness</b>	117,20	139,36	157,66	172,55

As could be seen from Table 2, the values of microhardness always are increasing with increasing the cold deformation percents.

### Results discussion of $\tan(\psi)$ and $\cos(\Delta)$ measurements

The ellipsometric measurements were performed by using spectroscopic ellipsometer SOPRA GES5E IR, with the incident angle of 70°, in the range of 300-800nm. The obtained curves of  $\tan(\psi)$  and  $\cos(\Delta)$  in the visible range of light are represented in Figs. 4-7.

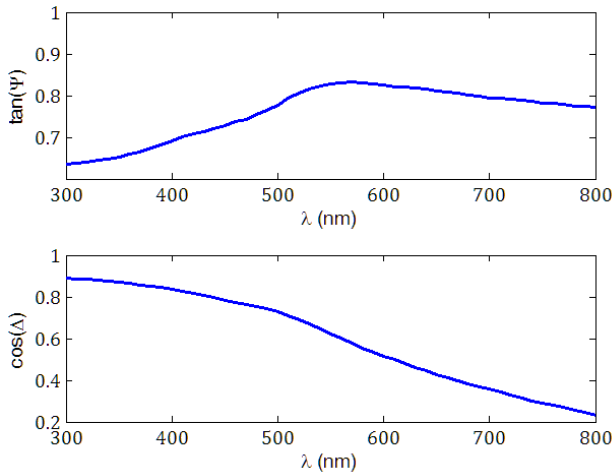


Fig. 4. Trajectories of  $\tan(\psi)$  and  $\cos(\Delta)$  for gold 585 strip, annealed, specimen (1)

The value of  $\tan(\psi)$  for specimen 1 is 0,63 at wavelength of 300nm, the maximum of 0,83 is reached at 560nm, and at 800nm the value of  $\tan(\psi)$  is 0,78, see Fig. 4a). Another value,  $\cos(\Delta)$ , continuously is decreased from 0,9 to 0,0,22 on the manner as shown in Fig. 4b). After applying the cold deformation of 10%, specimen 2, the maximum value becomes lower and reaches the value of 0,757, Fig. 5a). Changes in values of  $\cos(\Delta)$ , Fig. 5b), are minor to previous, Fig. 4b).

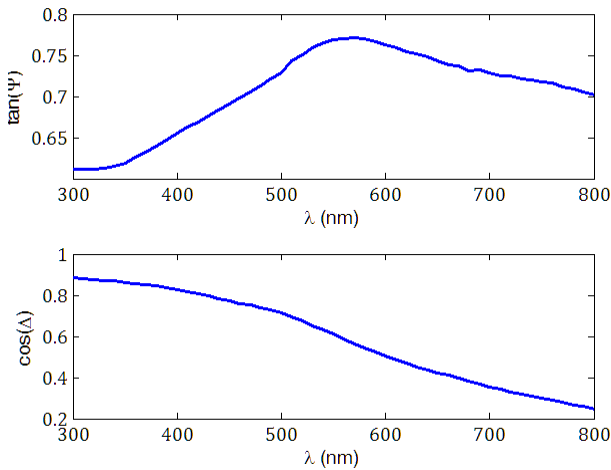


Fig. 5. Trajectories of  $\tan(\psi)$  and  $\cos(\Delta)$  for gold 585 strip, 10% deformation, specimen (2)

Trajectories for samle 3, deformed with 20%, are similar to previous, but the maximum further is lowered, the value of  $\tan(\psi)$  is about 0,757. All values for  $\tan(\psi)$  are lowered, see Fig. 6a).

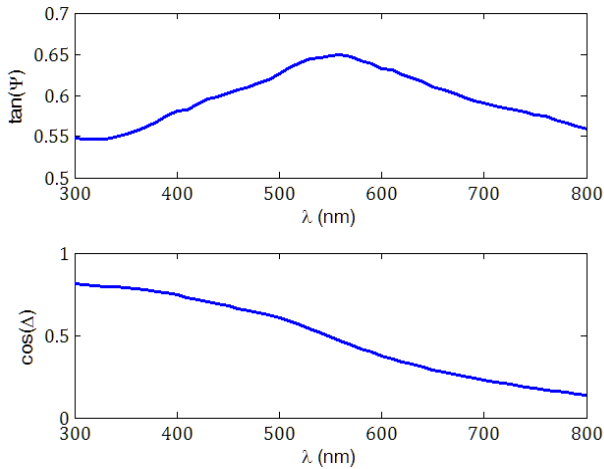


Fig. 6. Trajectories of  $\tan(\psi)$  and  $\cos(\Delta)$  for gold 585 strip, 20% deformation, specimen (3)

Values for  $\cos(\Delta)$ , are decreased as previously described.

The highest applied deformation, here 30%, has produced similar behaviour for  $\tan(\psi)$ , Fig. 7a), as in earlier cases, but,  $\cos(\Delta)$  value in the same range of wavelengths now reaches the minimum value of zero, Fig. 7b).

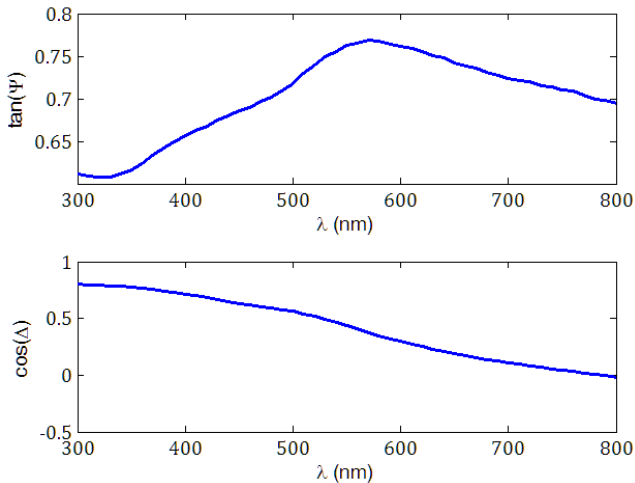


Fig. 7. Trajectories of  $\tan(\psi)$  and  $\cos(\Delta)$  for gold 585 strip, 30% deformation, specimen (4)

Maximum values of  $\tan(\psi)$  in all cases were reached at 560nm, as could be seen from figs. 4-7. Their inflection points for all curves  $\cos(\Delta)$  vs wavelength were the same for all values of wavelength, here for 585 gold alloy at 560nm.

Principally,  $\Delta$  ranges from zero to 3600 (or -180 to 1800), but here  $\cos(\Delta)$  vary from 0,9 (Fig. 4b) to 0 (Fig. 7b).

Other demands for definition of a gold jewel quality are widely defined [12,13].

## **Conclusion**

The optical properties of pure noble metals are pretty well examined, but not their alloys. Here is investigated 14kt gold, which consists min. 58,5%Au, further 8,3%Ag, 25,7%Cu and 7,5%Zn. Melting is provided in an induction furnace and casting in nitrogen protective atmosphere, for obtaining the clear surface. The strips were cold rolled by applying small deformations (10-30%), while one sample is annealed.

Those specimens were investigated at ellipsometer by using the incident angle of 700C, in the range of 300 to 800nm. The obtained results of amplitude diminution are shown in relation  $\tan(\psi)$  vs wavelength. The maximum value of  $\tan(\psi)$  was reached to be 0,83 at 560nm - for annealed specimen, while the minimum value was 0,55 at 300nm- for cold rolled specimen with reduction of 20%. The inflection points for all curves  $\cos(\Delta)$  vs wavelength were the same for all values of wavelength, here for 585 gold alloy at 560nm. The values of  $\cos(\Delta)$  varied from 0,9 (Fig. 4b) to 0 (Fig. 7b).

## **Acknowledgement**

Represented results were done by kindly supporting of Laboratory for solid state physics and optics, Institute for Physics, Beograd-Zemun, Serbia, and specimens were fabricated in "Perić&Perić"Co, Požarevac, Serbia, and we are grateful to them.

## **References**

- [1] Sokolov, A.V. Optical Properties of Metals, in Russian, Moscow 1961, pp. 75-92; 142-152.
- [2] Mališev. V.M. Mališev, D.V. Rumjancev: Zoloto, in Russian, Moskva 1979, Metallurgija, pp. 212-221.
- [3] P. Gertik: Plemeniti metali, in Serbian, Autor's edition, Beograd 1997, pp. 131-167.
- [4] S. Marković, V. Radovanović, Ž. Kamberović: Umetničko livenje, Beograd 2005, Klasa, pp. 11- 64.
- [5] R.E. Reed-Hill: Physical Metallurgy Principles, New York 1973, van Nostrand, pp. 38-59.
- [6] R. J. Weiss: Solid state physics for metallurgists, Oxford 1963, Pergamon Press, pp. 222-227.
- [7] G. Schulze: Metallphysik, Russian translation, Moskva 1971, MIR, pp. 366-371.
- [8] M.A. Ordal, L.L. Long, et all, Applied optics, 22/1983/No 7, pp. 1099-1119.

- [9] H. G. Tompkins, A Users's Guide to Ellipsometry, Academic Press Inc, London (1993), pp. 24-48.
- [10] R.T. Poole: The colour of the noble metals, Phys. Educ. 18/1983, pp. 279-284.
- [11] V. Sedlaček: Non-ferrous metals and alloys, Amsterdam 1986, Elsevier, pp. 306-7, 388-391.
- [12] R. Perić, Z. Karastojković, G. Đorđević: Prilog raspravi o kvalitetu šupljeg nakita od legure zlata 585, Kvalitet 8/2008/3-4, str. 65-67.
- [13] Karastojković, Z., Perić, R., Srećković, M., Janjušević, Z., Jakovljević, S., Kovačević, Z.: Metallurgy of gas and laser welding of thin parts made from 585 gold alloy, 10<sup>th</sup> National Conference of Metallurgy with International Participation, Varna – Bulgaria 2007, A 27.
- [14] R. Perić<sup>1</sup>, Z. Karastojković<sup>2</sup>, M. Jovanović<sup>3</sup>, M. Srećković<sup>4</sup>, Z. Janjušević<sup>5</sup>, G. Radoš<sup>3</sup>: Ellipsometric measuring of mplitude dimunitions at annealed and cold rolled strips with low deformations of gold alloy 5885, III Kongres .. Jahorina 2013, CD pp. ?????????

## DETERMINATION OF METAL-MOLD HEAT TRANSFER COEFFICIENT DURING CO<sub>2</sub> SAND CASTING

L. Kovačević, P. Terek, D. Kakaš, A. Miletić, D. Kukuruzović

*Faculty of Technical Sciences, Trg Dositeja Obradovića 6, 21000 Novi Sad, Serbia*

### Abstract

The accuracy of every numerical simulation is dependent on the accuracy of input parameters. One of the important input parameters required for modeling of casting solidification is interfacial heat transfer coefficient (IHTC). This paper presents a method for determination of IHTC during CO<sub>2</sub> sand casting. A specific experimental setup has been developed for the study of heat transfer across the metal-mold interface. The experimental setup and various influential parameters are thoroughly explained. Thermal history obtained from the experiment was used to solve an inverse heat conduction problem (IHCP) and estimate transient IHTC values. The used numerical algorithm is based upon fully implicit finite difference method and Beck's sequential function specification method. Preliminary results are presented and comparison is made with IHTC results taken from the literature. The results show that the developed experimental setup is more adequate for usually simulated thin wall castings than previously employed setups.

*Keywords: IHTC, inverse heat conduction, solidification, aluminum*

### Introduction

Increasing demand for highly competitive products in foundry manufacturing has led to development of computer aided engineering methods which reduce cycle time and costs for producing high-quality castings. The goal is to predict and/or optimize shape, microstructure, mechanical properties and durability of cast components [1,2]. However, result of every numerical simulation is dependent on the accuracy of input parameters. Material properties such as thermal conductivity, density, viscosity and specific heat are usually readily available and independent from the shape of a casting. Contrarily, interfacial heat transfer coefficient (IHTC) depends greatly on the casting shape and process parameters [1,3,4]. Therefore, it should be estimated for every casting process individually.

The most common method of determining transient IHTC is by ensuring one-dimensional heat transfer and solving an inverse heat conduction problem (IHCP). The one-dimensional nature of the heat transfer is usually achieved by the use of cylindrical [5] or similarly shaped castings where one dimension is significantly larger than the other two, Fig. 1. The lateral sides of the casting are heavily insulated and IHTC is measured at the base which is in contact with the mold material. Large thickness of the casting wall is necessary in order to prolong solidification time and acquire reasonably stable and accurate results from the IHCP algorithm. Unfortunately, the casting thickness changes the process

dynamics and consequently transient IHTC values. Therefore, the usually employed method is probably not suitable for thinner wall castings, which make large part of the average foundry portfolio.

The work reported in this paper presents new experimental setup developed to determine transient IHTC values for thin walled sand castings.

### Development of experimental methodology

To avoid usually used extremely thick casting walls and at the same time provide one-dimensional heat transfer, casting geometry is selected to be as shown in Fig. 1b. The molds used to determine IHTC in the present study were prepared by a CO<sub>2</sub> process. Sodium silicate of 8% by weight was mixed with silica sand. The molds were prepared by regular hand molding technique and then hardened by using CO<sub>2</sub> gas. They were kept at the room temperature prior to pouring of molten metal.

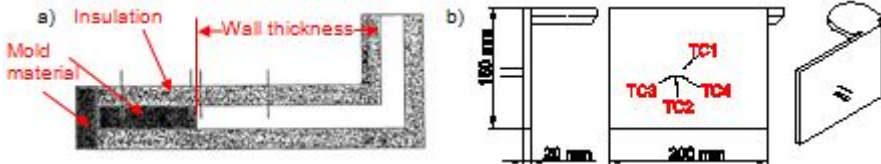


Figure 1 Model of the experimental apparatus used to determine IHTC: a) typical experimental setup [5]; b) proposed experimental setup.

Considering that solution of an inverse heat conduction problem (IHCP) is highly sensitive to the temperature measurements, special attention should be given to selection and fixing of thermocouples.

Heat transfer from the mold to the casting is a transient phenomenon and thermocouple time constant has considerable influence on accuracy of temperature measurement. As thermocouple has some finite dimensions, certain time is required to equilibrate temperatures of thermocouple hot spot and environment. This causes time lag in temperature measurements. The lag is proportional to the thermocouple size and thermal conductivity. In order to obtain accurate IHTC estimation, smallest commercially available thermocouple wires should be used. Wire used in presented experiment had a minute diameter of 0.0799 mm (Omega TT-K-40-SLE). For such a minute thermocouples the manufacturer gives extremely rapid hot water response time of 15ms. Sand mold response time was calculated to a value of 0.2s which is 2.5 times faster than the rate of temperature measurement of 2Hz. Therefore, thermocouple response time should not introduce significant measurable error.

Presence of thermocouples inside the mold causes perturbation of the thermal field and results in erroneous IHTC estimation [6,7]. In order to reduce this effect, heat loss through thermocouple leads should be minimized. This is usually accomplished by placing thermocouples parallel to the isotherms [7]. However, in sand molds this requirement is difficult to achieve. Since the thermocouples have to be positioned near the mold cavity their presence severely undermines the strength of the surrounding sand. As a consequence flash occurrence is very

probable and thermocouple measurements are corrupted. Images of thermocouple placement during one experiment with parallel thermocouple positioning are shown in Fig. 2.

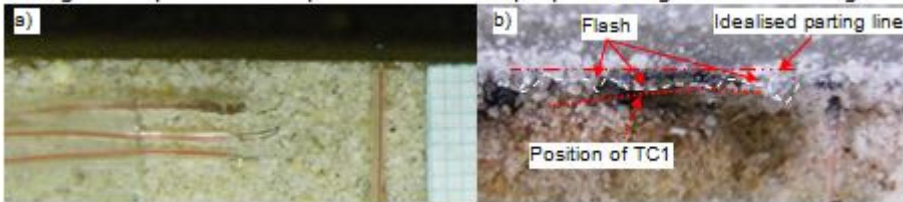


*Figure 2 Appearance of thermocouples positioned parallel to the interface: a) before pouring; b) after pouring.*

Therefore, in order to avoid flash formation, thermocouple leads need be placed perpendicular to the interface. Heat conduction through the leads can be minimized by carefully selecting the thermocouple tip geometry in a form of a flattened and elongated hoop, as shown in Fig. 3. With such an arrangement, the strength of surrounding mold is not compromised and possibility of flash occurrence is substantially reduced. On the other hand, error of temperature measurement can be controlled by adequate length of flattened portion of the hoop. This length can be calculated following thermocouple immersion depth recommendations for fluid temperature measurements given by Nicholas and White [8]. They propose immersion length of approx. 7 thermocouple diameters for temperature measurement error of 0.1%. For selected thermocouples this corresponds to a value of 0.56mm. However, this value is adequate for thermocouple immersion in stirred liquid. For measurements in still air Nicholas and White recommend multiplying this value by a factor of 10. By assuming that the multiplication coefficient corresponding to measurements in sand mold is 4, calculated minimum length of flattened portion of the hoop is 2.2mm.



*Figure 3 Appearance of thermocouples positioned perpendicular to the interface, and their relative distance from the casting.*

Considering that the experimental setup provided one-dimensional heat transfer between the mold and the casting, following equation can be used to describe the process:

$$\frac{\partial}{\partial x} \left( \lambda \frac{\partial T}{\partial x} \right) = \rho c_p \frac{\partial T}{\partial \tau} \quad (1)$$

where  $x$  is Cartesian coordinate defining distance from the metal-mold interface,  $\lambda$  is thermal conductivity,  $T$  is temperature,  $\rho$  is density of the sand,  $c_p$  is specific heat capacity of the sand, and  $\tau$  is time. The initial and boundary conditions are described by following equations:

$$T(x, 0) = T_i(x) \quad (2)$$

$$\lambda(T) \frac{\partial T}{\partial x} \Big|_{x=0} = q(0, \tau) \quad (3)$$

$$T(x_4, \tau) = Y_4(\tau) \quad (4)$$

where  $T_i$  is initial temperature of the mold,  $q$  is heat flux at the metal-mold interface,  $x_4$  is distance of the fourth thermocouple (the furthest one from the interface) and  $Y_4$  is temperature measured by that thermocouple. The above equations were discretized using the fully implicit finite volume method. Given that the thermocouple positions were determined after mounting, control volume size was variable. The numerical model was solved using the iterative algorithm based on Beck's sequential function specification method, Fig. 4. More details on the numerical model can be found elsewhere [4]. Stopping criteria used in this investigation were as follows:

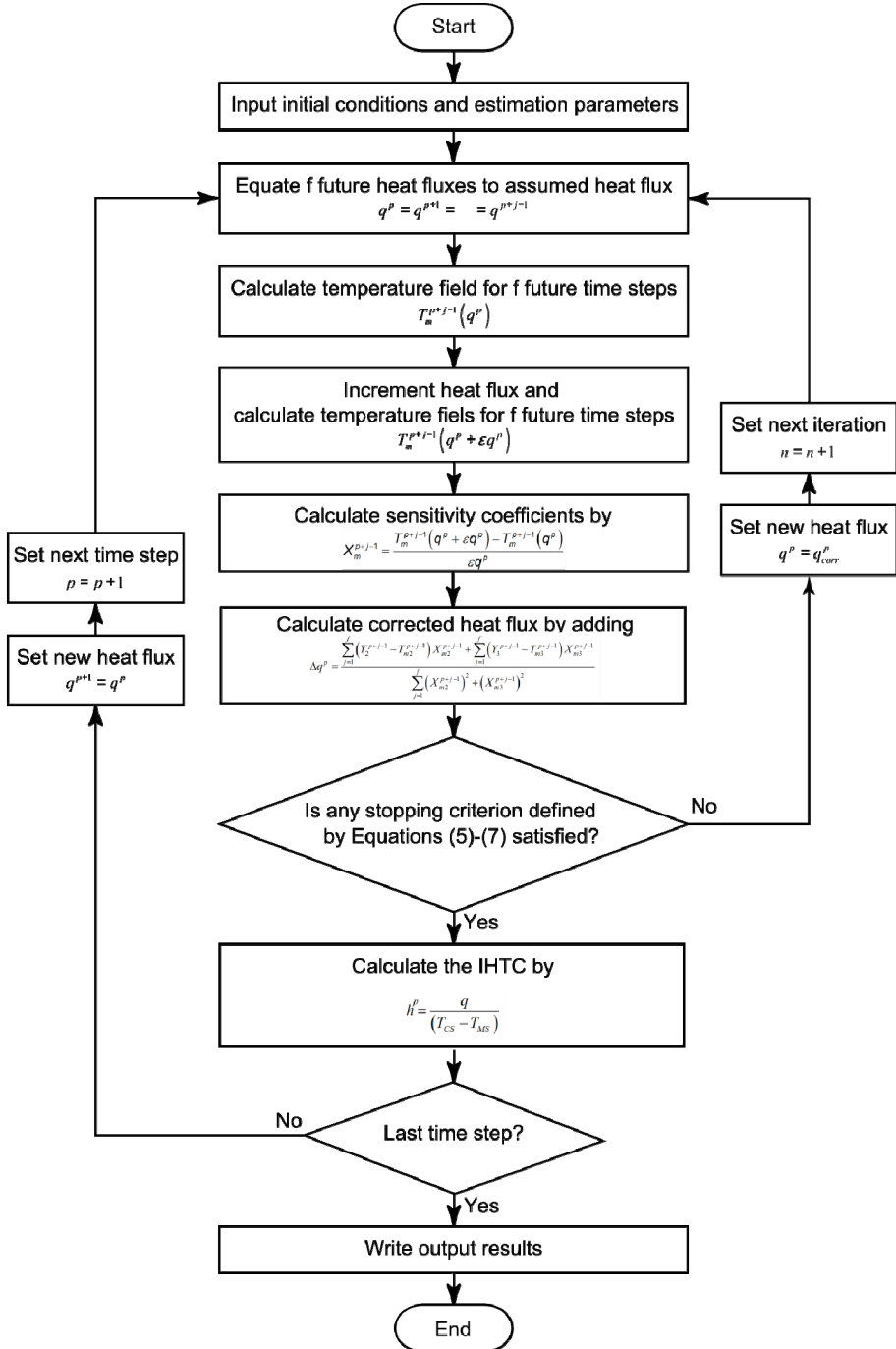


Figure 4 Flowchart of the solution procedure used for estimation of IHTC

$$\left| q^p + \Delta q^p \right| > 2 \frac{W}{m^2} \quad (5)$$

$$\frac{\Delta q^p}{q^p} < 0.0005 \quad (6)$$

$$n < n_{\max} \quad (7)$$

## Results and Discussion

The IHTC values plotted against the casting surface temperature estimated by proposed experimental methodology are shown in Fig. 5a. IHTC has almost constant values at temperatures up to about 550°C. Then, with a rise in temperature to a liquidus value, the IHTC increases following “S” shape curve to a value of 620 W/m<sup>2</sup>K. Between T<sub>liq</sub> and 640°C the IHTC values are again constant before sudden drop with further rise in the casting surface temperature. This drop is probably a consequence of the underestimation of heat flux values during the first 12 seconds and therefore does not represent the physics at the metal-mold interface [4]. Obtained shape of the IHTC curve is nearly theoretical and can be explained as follows. At high temperatures molten metal has high fluidity and conforms more easily to rough mold surface. This leads to a better contact and consequently to high IHTC values. As superheat is lost and solidification starts contact area diminishes, gas pockets in the roughness profile valleys get bigger and IHTC values gradually decrease. When the casting skin develops enough rigidity to offset the effect of surface tension and hydrostatic pressure gas gap starts to develop and IHTC values start to drop significantly. After the size of gas gap reaches critical value (depending on mold surface roughness), further increase in gap does not cause significant change in IHTC values and the lower plateau is reached.

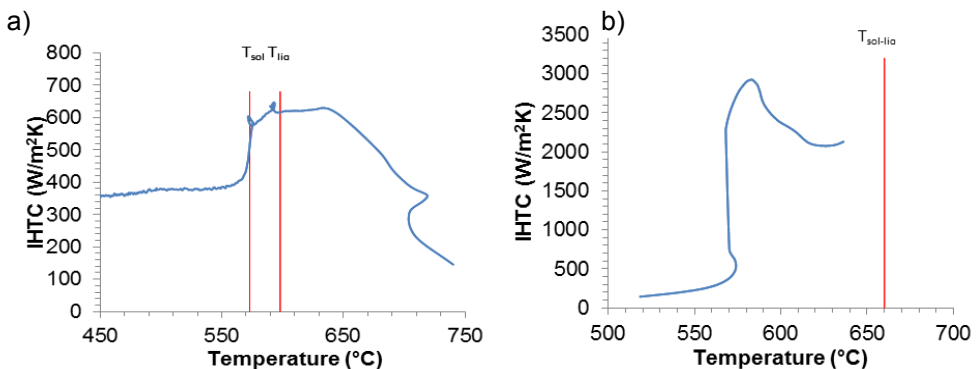


Figure 5 IHTC in function of casting surface temperature: a) obtained for Al-9 wt.% Si alloy cast in sand mold by proposed experimental methodology [4]; b) obtained for pure Al cast in steel mold by classical method [1]

Due to experimental difficulties, transient IHTC values for sand casting are not easily found in the literature. Therefore, qualitative comparison is made with the results for Al–steel mold experimental combination taken from the reference [1]. Results were digitized and, in contrast to original work, given as a function of casting surface temperature, Fig 5b. Two main differences can be observed: maximum plateau is missing and decrease influenced by air gap formation is observed at lower temperature. Although the absence of the maximum plateau might be a consequence of the large thermocouple time constant and their large distance from the interface [1,4], due to slow cooling rates of the large casting this is probably not the dominant cause. Probable explanation for both differences can be found in the fact that large casting dissipates substantially more heat and therefore the mold expansion dominates the first stages of solidification. Therefore, increase in interfacial pressure caused by mold expansion is probable cause of the rise in IHTC during cooling in liquid region. The same mechanism causes the delay in air gap formation and the IHTC–temperature curve is shifted toward lower temperatures. This effect is absent in thin wall castings and in IHTC curve estimated by a proposed experimental methodology thus making it more suitable for the practical application.

## **Conclusions**

The novel methodology for determining transient values of IHTC for sand mold castings has been developed and thoroughly explained. The test experimental casting and qualitative comparison has been made with IHTC results taken from the literature. It has been shown that the IHTC values for thin wall castings can be more accurately estimated by using proposed experimental techniques since the influence of the mold thermal expansion is more realistically taken into account.

## **Acknowledgements**

The authors gratefully acknowledge financial support provided by the Serbian Ministry of Education, Science and Technological Development.

## **References**

- [1] Coates B L 2004 Heat transfer at the casting metal-mold interface during solidification (PhD thesis: University of Toronto)
- [2] Kim Y, Kang C, Cho J, Jeong C and Choi S 2008 Die Casting Mold Design of the Thin-walled Aluminum Case by Computational Solidification Simulation *Journal of Materials Science & Technology* **24** 383–8
- [3] Kumar T S P and Kamath H C 2004 Estimation of multiple heat-flux components at the metal/mold interface in bar and plate aluminum alloy castings *Metallurgical and Materials Transactions B* **35** 575–85
- [4] Kovačević L, Terek P, Kakaš D and Miletić A 2012 A correlation to describe interfacial heat transfer coefficient during solidification of Al–Si alloy casting *Journal of Materials Processing Technology* **212** 1856–61
- [5] Griffiths W D 1999 The heat-transfer coefficient during the unidirectional solidification of an Al-Si alloy casting *Metallurgical and Materials*

- Transactions B **30** 473–82
- [6] Sheehy C, Bouchard D and Charette A Process Parameters and Modeling Features Affecting Interfacial Heat Transfer Coefficients in the Casting of a Semi-Solid 357 Aluminum Alloy 2011 Die Casting Congress & Tabletop (NADCA) (Columbus, OH, USA)
- [7] Li D I and Wells M A 2005 Effect of subsurface thermocouple installation on the discrepancy of the measured thermal history and predicted surface heat flux during a quench operation Metallurgical and Materials Transactions B **36** 343–54
- [8] Nicholas J V and White D R 2001 Traceable Temperatures, An Introduction to Temperature Measurement and Calibration (Chichester,,: John Wiley & Sons Ltd)

## THE INFLUENCE OF SYNTHESIS PARAMETERS ON STRUCTURAL AND MECHANICAL PROPERTIES OF Cu-ZrB<sub>2</sub> ALLOY

J. Ružić<sup>1</sup>, D. Božić<sup>1</sup>, J. Stašić<sup>1</sup>, V. Rajković<sup>1</sup>, K. Raić<sup>2</sup>

<sup>1</sup>Materials Department, Institute of Nuclear Sciences "Vinča", University of Belgrade,  
Belgrade,

Mike Petrovića Alasa 12-14, Belgrade, Serbia

<sup>2</sup>Faculty of Technology and Metallurgy, University of Belgrade, Karnegijeva  
4, Belgrade, Serbia  
e-mail: jrusic@vinca.rs

### Abstract

The aim of this paper was to determine the conditions for obtaining Cu-ZrB<sub>2</sub> alloy by powder metallurgy techniques and to analyze the microstructural and mechanical properties of obtained materials. The powder mixture with composition: 94,78 wt.% copper, 4,1 wt.% zirconium and 1,12 wt.% boron were used as starting materials. Mechanical alloying of powder was performed in order to obtain the proper distribution of Zr and B particles in the structure of Cu matrix as well as mechanical activation of Zr and B particles for easier the *in situ* formation of ZrB<sub>2</sub> by the hot pressing process. The structural changes occurring in the samples after milling and during hot pressing process were studied with the use of X-ray diffraction. Scanning electron microscopy (SEM) was applied to examine the morphology of the hot-pressed samples as a function of milling times. Also, hardness of the Cu-ZrB<sub>2</sub> alloy were investigated, and the results showed that hardness of the samples has increased as the milling time increased.

*Key words: mechanical alloying, hot pressing process, Cu-ZrB<sub>2</sub> alloy, hardness.*

### Introduction

Copper-zirconium alloys have high values of electrical and thermal conductivity and tensile strength which enable widespread use of these alloys. In recent years, great attention has been given to the study of Cu-Zr alloys containing various alloying elements (chromium, cobalt, titanium, boron, and hafnium) in order to obtain copper alloys with low content of alloying elements [1]. These kinds of alloys are provided the highest possible thermal conductivity with good mechanical properties sufficient to resist static and cyclic loads [2].

Copper reinforced with Zr and B additions (ZrB<sub>2</sub> particles are *in situ* formed in proper conditions) shows excellent thermal conductivity, wear resistance and sparking, and retains the high strength at specified operating temperatures [3]. Metal borides are favored due to their high melting point, low solubility in copper and a slight influence on the thermal conductivity of the base metal. In previous studies [4, 5] it has been shown that Cu-ZrB<sub>2</sub> reinforced alloys retain respectable strengths at predicted operating temperatures, but problem were inhomogeneous

microstructure which were resulting from the frequent presence of  $ZrB_2$  agglomerates that were several microns in size.

The aim of this work was to establish the better microstructural homogeneity in copper matrix and to obtain material with better mechanical properties through the process of synthesis Cu-7% $ZrB_2$  alloys by powder metallurgy techniques.

## **Experimental**

Starting powders copper (99.5% purity, 30  $\mu\text{m}$ ), zirconium (99.5% purity, 3  $\mu\text{m}$ ) and amorphous boron (97% purity, 12  $\mu\text{m}$ ) were homogenized for 1 hour. Then, homogenized mixtures were mechanically alloyed in Netzsch attritor mill in protective atmosphere (argon) for 5, 10, 15 and 20 hours, with steel balls (diameter 6mm) and with stirring speed of 330 rpm. Mechanically alloyed powders (for times 5, 10, 15 and 20 hours) were hot pressed in a graphite mold (10 mm diameter) at temperature of 950°C and pressure of 35 MPa with retention time of 2.5 hours. Determination of density compacts was carried out by hydrostatic method in water. The powder mixtures and corresponding compacts were characterized by X-ray diffraction (XRD) analysis which was performed using an X-ray powder diffractometer with  $\text{CuK}_\alpha$  Ni filtered radiation. The micro hardness of powders was examined under the load of 100g (Buehler MicroMet Vickers Microindentation Hardness Tester). Macro hardness of compacts was determined under the load of 1kg after hot pressing. Microstructural analysis of powders and compacts was studied by scanning electron microscope (SEM – Philips XL20).

## **Results and discussion**

Scanning electron photomicrographs of mechanical alloyed powders is shown on Figures 1 a-b. It is noted that most of the particles has an irregular shape, and as the time of mechanical alloying is increased the particle size is decreased, and the shape is more rounded. On Figure 2 the characteristic shape and size of particles is shown. On these photomicrographs can be noticed layers formed by mechanical alloying, as a result of cold welding. At higher magnification lamellar structure it can be seen, which is characteristic for mechanically alloyed powders. Occurrence of the lamellar structure is closely associated with the changes of the powder particles incurred during milling. Due processes of deformation and cold welding, which is carried at the same time as the process of milling, the lamellae become parts of new particles [6].

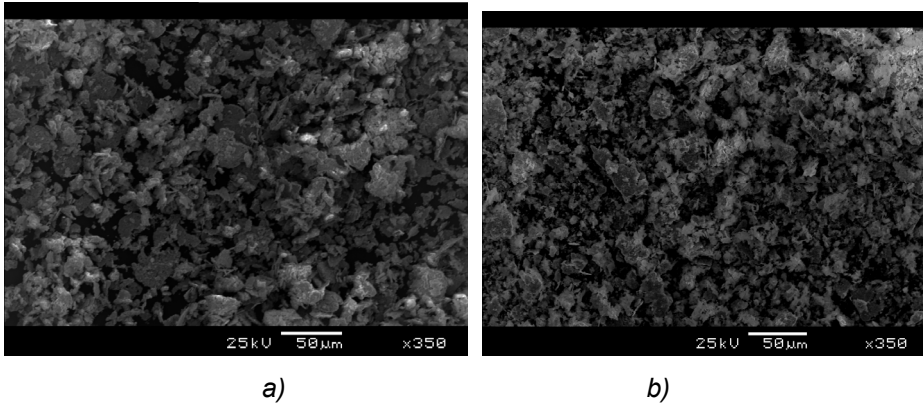


Figure 1. The shape and size of mechanically alloyed powders for a) 5 hours; b) 20 hours.

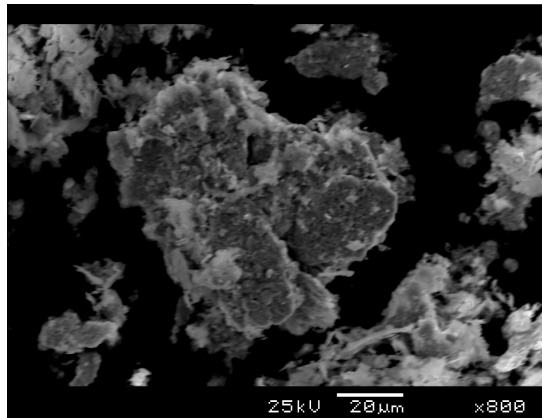


Figure 2. The characteristic shape of mechanically alloyed particles.

The micro hardness of powders was determined at a load of 100g. The obtained values indicate that with increasing mechanical alloying time the micro hardness is also increasing. The values of micro hardness are shown in Figure 3. Increase of micro hardness is due to the presence of fine-grained structure which is characteristic of all powders treated by mechanical alloying, as well as more evenly distributed particles in copper matrix. The highest values of micro hardness have particles of powder mechanically alloyed for 20 hours.

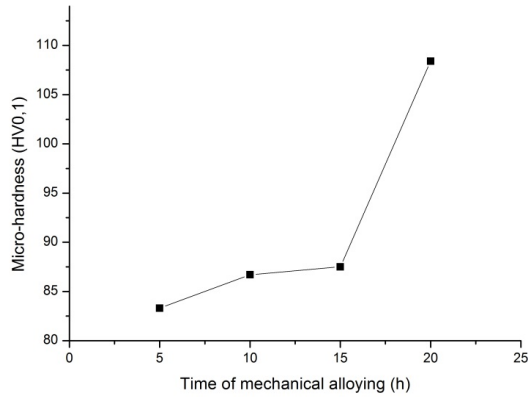


Figure 3. Micro hardness of mechanical alloyed powders.

The analysis of data obtained by X-ray powder diffraction, it was found that there was no *in situ* forming of  $ZrB_2$  in after mechanical alloying (Figure 4), but for compacts it can be identified peaks of  $ZrB_2$  (*in situ* formed). X-ray analysis of mechanically alloyed powders and compacts of CuZrB alloy are showed that forming of  $ZrB_2$  particles is always after hot pressing process regardless of the length time of mechanical alloying.

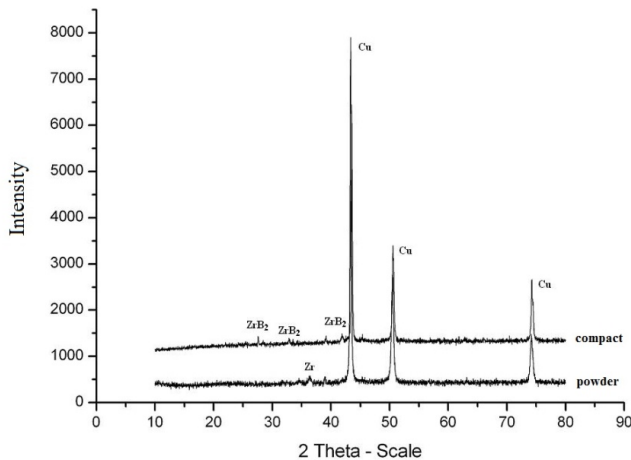


Figure 4. X-ray diffraction patterns of mechanically alloyed powder and compacts.

Obtained values of macro hardness of hot pressed compacts CuZrB alloys were analyzed and results show that the highest values of macro hardness have compacts obtained from mechanically alloyed powders for 20h. Macro hardness is

increased as a consequence of more evenly distribution of formed  $ZrB_2$  particles [7]. Results of macro hardness are shown in Figure 5. All hot pressed samples have density above 95% of its theoretical density.

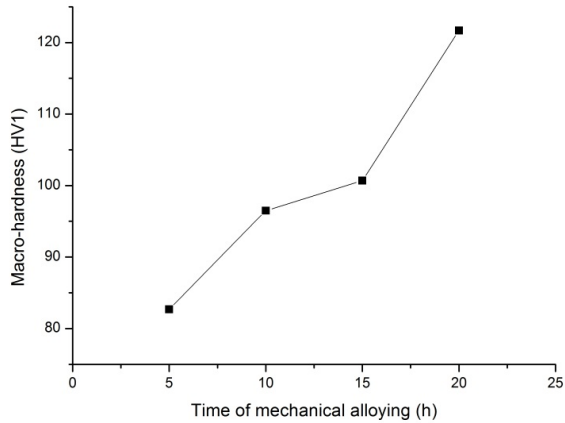


Figure 5. Macro-hardness of CuZrB alloy compacts.

Microstructure of hot-pressed samples mechanically alloyed 5 and 20 h are shown in Figure 6. XRD analysis has already confirmed the presence of  $ZrB_2$  particles which can be seen in the structure of the copper matrix as an individual or as agglomerates. The expectation that the agglomerates of  $ZrB_2$  particles would disappear during the hot pressing was not realized. However, with an extension of mechanically alloying time is reached more homogeneous particle distribution of reinforcements, in this case  $ZrB_2$  particles, and lower diameter size of agglomerates.

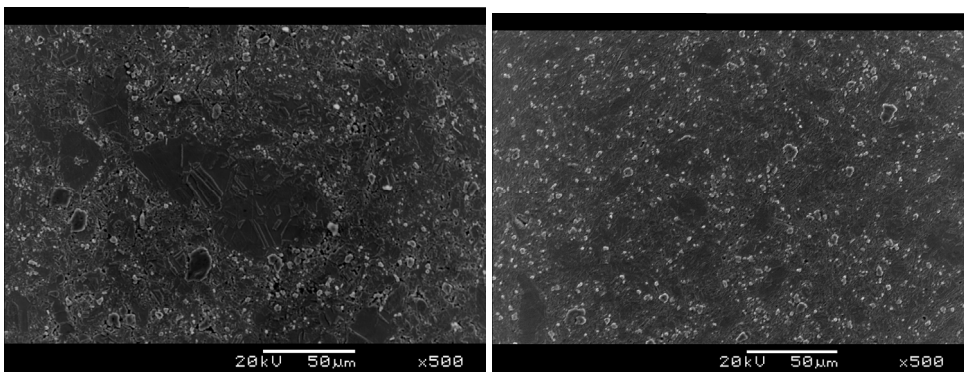


Figure 6. Microstructure of hot-pressed samples of powders mechanically alloyed for: a) 5 hours, b) 20 hours.

## **Conclusions**

1. Copper alloy reinforced with in situ formed ZrB<sub>2</sub> particles has been produced by powder metallurgy techniques up to near theoretical density.
2. Morphology and microstructure of mechanically alloyed powders are being changed during milling time as a consequence of deformation and cold welding.
3. With increasing the time of mechanical alloying shows an enhancement in micro and macro hardness.
4. Distribution of ZrB<sub>2</sub> particles and agglomerates in the copper matrix depends on the time of mechanical alloying.

## **Acknowledgement**

This work was financially supported by the Ministry of Education and Science of the Republic of Serbia through the Project No 172005.

## **References**

- [1] M. J. Saarivita, High Conductivity Copper-Rich Cu-Zr Alloys, Transaction of the metallurgical society of aims, Vol. (218), 1960
- [2] S. Z. Zhu, D. L. Gong, Z. Fang, Q. Xu, Preparation and Properties of ZrB<sub>2</sub>-Cu Composites by Spark Plasma Sintering, Key Engineering Materials, (Volume 512-515), p.739-743, 2012
- [3] J. S. Shelley, R. LeClaire, J. Nichols, Metal-Matrix Composite for Liquid Engines, JOM, Vol. 53, No.4 pp. 18-21, 2001
- [4] J.S. Andrus and R. G. Bordeau, Thrust Chamber Material Technology Program,, NASA Contract Report 187207, Cleveland, OH,1989
- [5] K. S. Kumar, Development of Dispersion – Strengthened XD<sup>TM</sup> Cu Alloys for High Heat-Flux Applications, NASA Contractor Report 191124, Baltimore, Maryland, 1993
- [6] C. Suryanarayana, Mechanical alloying and milling, Progress in Materials Science 46, USA,2001
- [7] T. R. Chen, P.Y. Lee, Formation of amorphous Cu-Zr alloy powder by mechanical alloying, Journal of Marine Science and Technology, Vol. 1, No. 1, pp. 59-64, 1993

## MICROSTRUCTURE OF ALUMINUM PISTON ALLOYS

Srecko Manasijevic<sup>1</sup>, Srdjan Markovic<sup>2</sup>, Radomir Radisa<sup>1</sup>

<sup>1</sup> LOLA-Institute, Kneza Visoslava 70a, Belgrade, Serbia,  
srecko.manasijevic@li.rs

<sup>2</sup> Faculty of Technology and Metallurgy, University of Belgrade, Karnegijeva  
4, Belgrade, Serbia

### Abstract

This paper presents the results of testing the microstructure of aluminum piston alloys. Piston alloy microstructure can be very different. It is not accidental, but rather caused by the strictly defined rules. The microstructure is caused, on the one hand, by the chemical composition of the alloy and solidification method and, on the other hand, by heat treatment. The results show dependence between the combination of alloying elements, casting conditions and heat treatment given to different microstructures. In the piston alloys there are at least six elements (Al, Si, Cu, Ni, Mg and Fe), which have a significant impact on the solidification path of these alloys. Interactions among them create different phases and intermetallics, the shape and distribution of which in the as-cast and heat-treated alloys depend on the corresponding process parameters.

**Keywords:** *piston, piston alloy, microstructure*

### Introduction

Piston alloys are a special group of industrial aluminum alloys that have good mechanical properties at elevated temperatures (approximately up to 350 °C) [1–3], and are resistant to sudden temperature changes [1–8]. During exploitation, these alloys are exposed to the aggressiveness of the environment in which they are used [1,5,8]. Typical aluminum piston alloys are very complex with respect to their chemical composition and the obtained structures. Different piston alloys have various contents of major and minor alloying elements [1,4,5]. The usual ranges for some of the alloying elements used by the well-known manufacturers of pistons KS Kolbenschmidt GmbH and MAHLE GmbH from Germany and the local Concern PDM Mladenovac, Serbia are: 11–23 wt.% Si; 0.5–3 wt.% Ni; 0.5–5.5 wt.% Cu; 0.6–1.3 wt.% Mg; up to 1.0 wt.% Fe and up to 1 wt.% Mn [1,8].

Al-Si piston alloys have different structure depending on the content of silicon and other alloying elements. However, their basis in both hypoeutectic and hypereutectic alloys is eutectic mixture and solid solution ( $\alpha$ Al). For example, in the microstructure of the AlSi13Cu4Ni2Mg piston alloy, the presence of the following phases was observed: Mg<sub>2</sub>Si, Al<sub>3</sub>Ni, Al<sub>6</sub>NiCu<sub>2</sub> and a multicomponent phase with Al, Mg, Si, Fe, Ni etc [1–8]. The structural composition of material has a direct impact on the physical and mechanical properties of the casting.

Based on the data from the literature, the microhardness of silicon crystals is 1320 HV. However, in the microstructure of an Al-Si piston alloy there are also other phases (Al<sub>2</sub>Ni<sub>3</sub>→770 HV, Mg<sub>2</sub>Si→450 HV, AlCuFe→608 HV,

Al<sub>3</sub>(Cu<sub>2</sub>Ni)→1120 HV, Al<sub>6</sub>Cu<sub>3</sub>Ni→1000 HV) [8]. Based on these microhardness values, it may be concluded that silicon has the role of a phase that reinforces the piston alloy. However, the shape and distribution or dispersion of silicon crystals in the alloy greatly affect the mechanical properties of piston alloys. The conditions of making and modification of these alloys have a great impact on the change in the shape and distribution of crystals [7,8].

The shape, distribution and dispersion of microconstituents in the microstructure is not the same in all sections of the piston casting and piston casting manufacturers strive to create the necessary conditions for forming the needed microstructure in the desired section that provides optimal properties.

Taking into account that the piston casting microstructure, i.e., properties depend on its chemical composition, solidification conditions and heat treatment, this paper gives an analysis of the microstructure in two critical spots of castings made of 4 alloys of different chemical composition with two different solidification times and the same heat treatment. The aim of the paper is to show the impact of the above factors on the microstructure, i.e., mechanical properties of piston castings.

### **Experimental procedure**

The tests were performed on an Ø89 mm piston used for OM604 diesel engine with turbocharger. A CAD model of the cast piston is shown in Fig. 1.

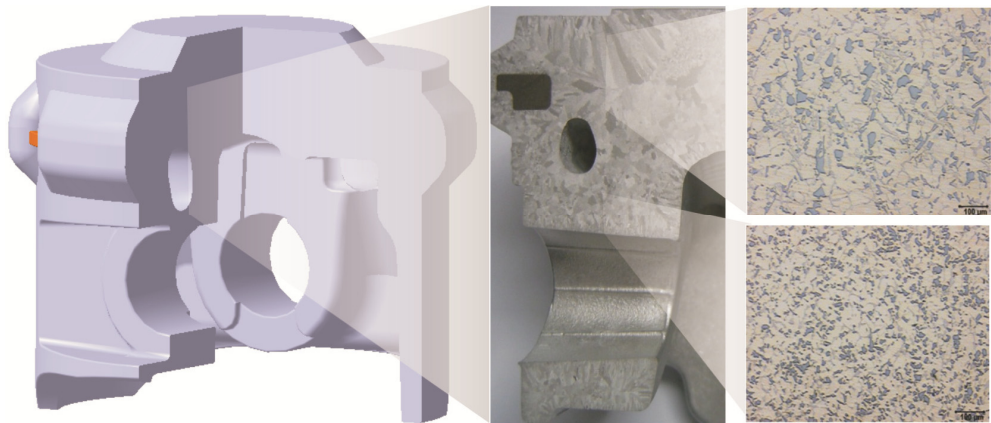


*Figure 1 CAD model of cast piston*

Four different piston alloys (Table 1) of approximately eutectic composition were used to analyze the influence of heat treatment on microstructure. The content of the alloying elements varied between: 10.51–13.05 wt.% Si, 1.13–7.45 wt.% Cu, 1.04–3.90 wt.% Ni, 0.38–1.35 wt.% Mg and 0.43–0.55 wt.% Fe, to ensure separation of the dominant phase in each of the test structures.

In the case that real changes occur, the medium concentrations of the alloying elements due to redistribution into rich or depleted melt alloying elements could lead to significantly higher or lower changes in mean concentrations than the nominal value thereby creating conditions for the formation of new phases. Any

change during the entire curing process (primary, secondary and tertiary) of piston alloys has a significant impact on the concentration profiles of the alloying elements in the solid phase [19]. Therefore, several alloys with different ratios of the main alloy elements were investigated.

*Table 1 Nominal chemical composition of the experimental alloy*

Alloys	Chemical composition (wt.%)										
	Si	Cu	Ni	Mg	Fe	Mn	Cr	Ti	Zr	V	Al
L <sub>1</sub>	12.71	1.13	1.04	1.35	0.47						
L <sub>2</sub>	13.05	3.80	2.01	0.90	0.52	0.02	0.09	0.07	≈0.03	≈0.01	residue
L <sub>3</sub>	11.43	5.62	1.71	0.38	0.43						
L <sub>4</sub>	10.51	7.45	3.90	0.51	0.55						

Melting of alloy for piston cast was performed in a RIO 750 80 kW tub-like electro-resistant inclined furnace with the capacity of 120 kg/h. Preparation of Al-alloy was performed in a RIO 250 85 kW electro-resistant muffler-like furnace with black lead muffler. In order to improve its mechanical properties, the piston cast was exposed to some treatments (refining, modification and degasification processes) during preparation. All three operations were performed at a temperature of 725±5 °C. The temperature of liquid cast was measured by using a Ni-Cr-Ni digital pyrometer.

The investigated pistons were cast in the semi-automatic machines under industrial conditions in Concern PDM, Serbia. The casting was done in a metal mold within defined internal procedures of the piston manufacturer.

In this case, all piston castings with the chemical composition given in Table 1 were treated under the same heat treatment mode. Homogenization was performed at a temperature of 510 °C for 4 h. The homogenization was followed by quenching in water at 20 °C. Then the castings were heat-treated at 180 °C for 6 h in an aging process. All castings were marked for the purpose of monitoring the change in the results.

Samples of cast pistons were solution heat treated in a furnace chamber with electric heating, type "KPA 16/32 CER Cacak", with fans for hot air recirculation. The capacity of this furnace is 500 kg/h and its consumption is 212 kWh. The piston castings were automatically quenched by pulling the furnace floor out and lowering the metal basket with pistons directly from the furnace into a water tank. For the aging and stabilization, a CER Cacak EPC 200/300 furnace with the capacity of 3000 kg/h and the consumption of 180 kWh was employed. The temperature in the furnace was maintained in the prescribed narrow limits (±5 °C), with good atmosphere control.

An optical microscope (Leica DMI type 5000M) was employed for visualization of the microstructure formed with the aim of collecting data for determining the internal construction, i.e., the structure of the material. Further characterization of the structure was performed by reflection electron microscope (REM) with up to 1000 x zoom.

## Results and discussion

Figures 2 and 3 show the microstructure of piston castings in their most critical section (the edge of the fire zone), which were cast of different piston alloys from Table 1. Two solidification conditions were analyzed (solidification time of 110 and 140 sec) for all of the piston alloys. Heat treatment modes are the same in both cases.

Figures 4 and 5 show the microstructure of piston castings in their most critical section (top surface of the pin hole), which were cast of different piston alloys from Table 1. Also, two solidification conditions were analyzed (solidification time of 110 and 140 sec) for all of the piston alloys.

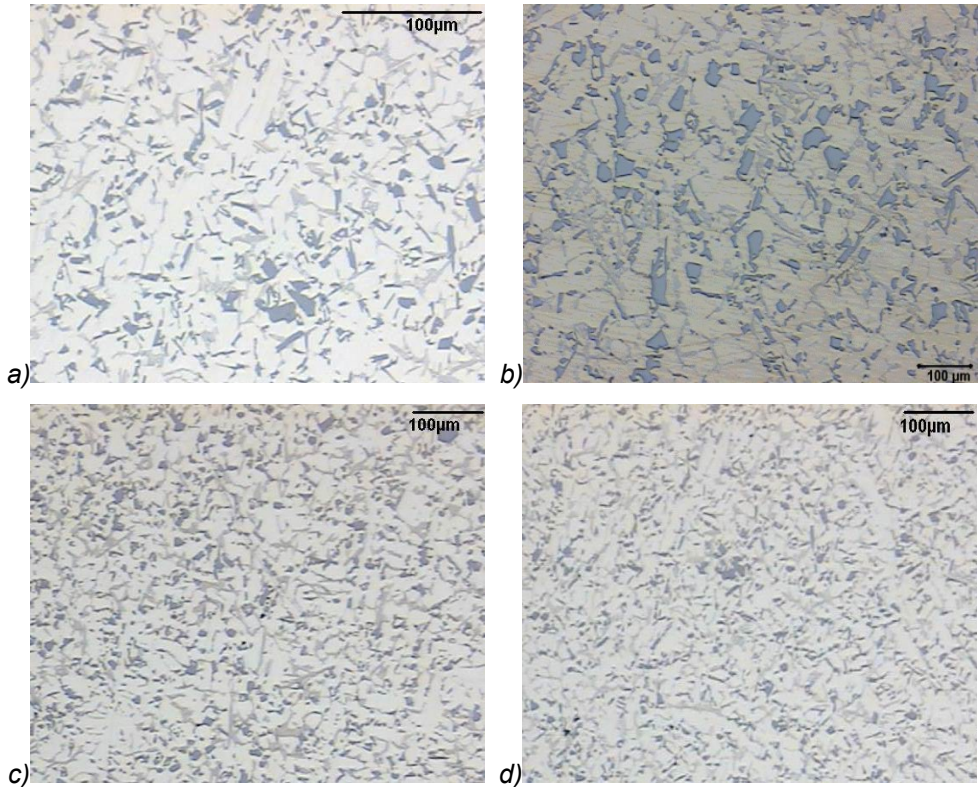


Figure 2 Comparative view of microstructure, solidification time 110 sec, a) alloy L<sub>1</sub>, b) alloy L<sub>2</sub>, c) alloy L<sub>3</sub>, d) alloy L<sub>4</sub>

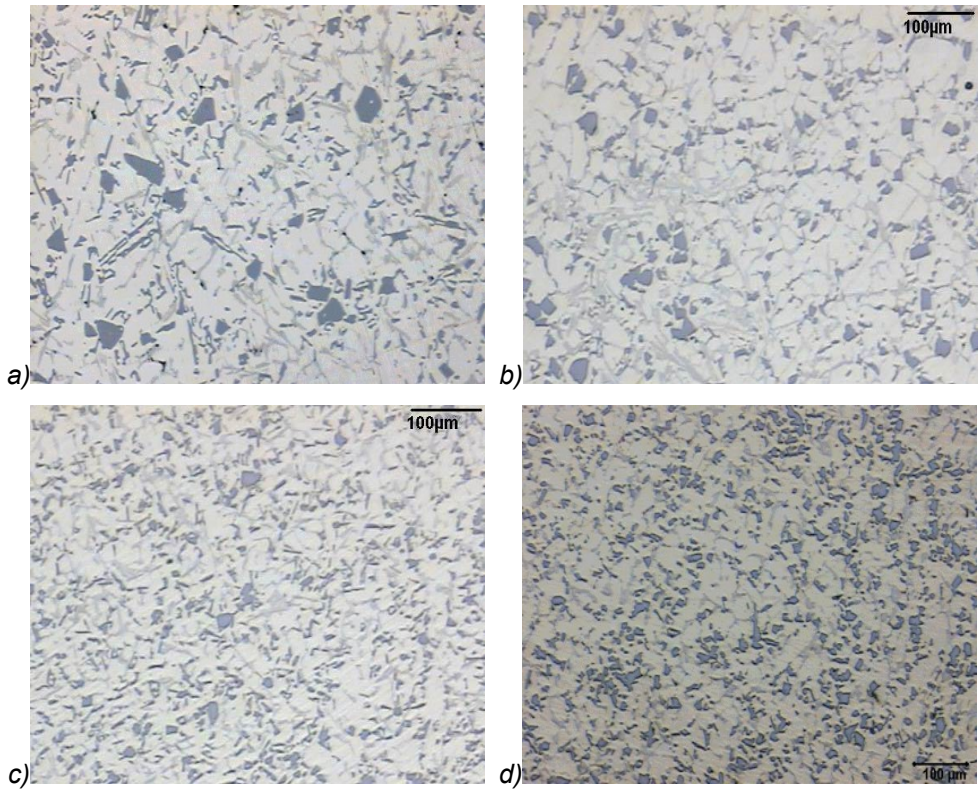


Figure 3 Comparative view of microstructure, solidification time 140 sec, a) alloy L<sub>1</sub>, b) alloy L<sub>2</sub>, c) alloy L<sub>3</sub>, d) alloy L<sub>4</sub>

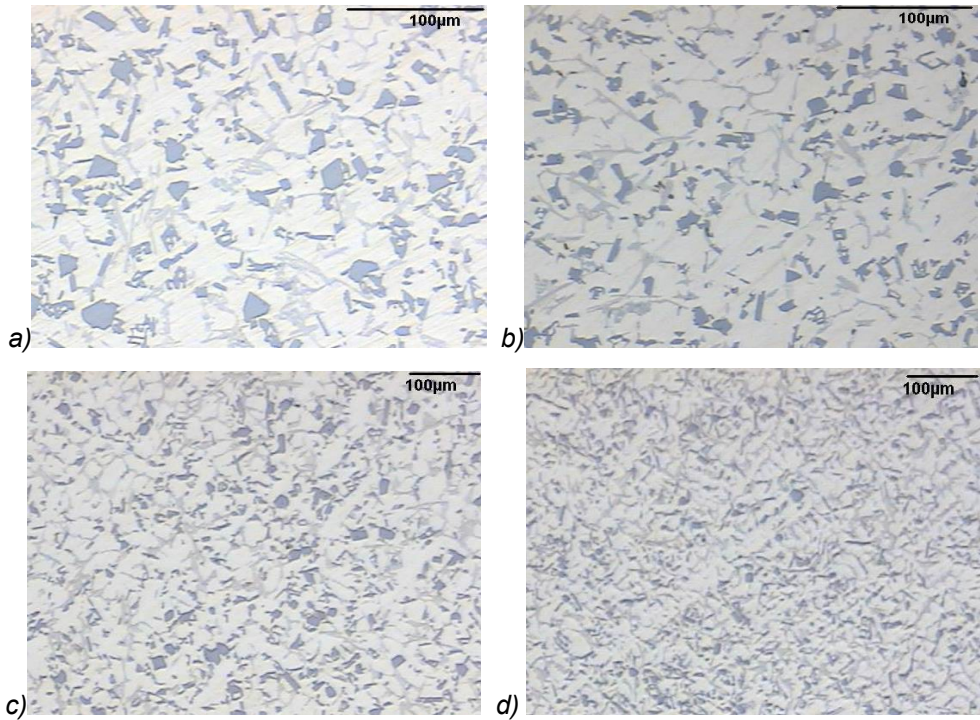


Figure 4 Comparative view of microstructure, solidification time 110 sec, a) alloy L<sub>1</sub>, b) alloy L<sub>2</sub>, c) alloy L<sub>3</sub>, d) alloy L<sub>4</sub>

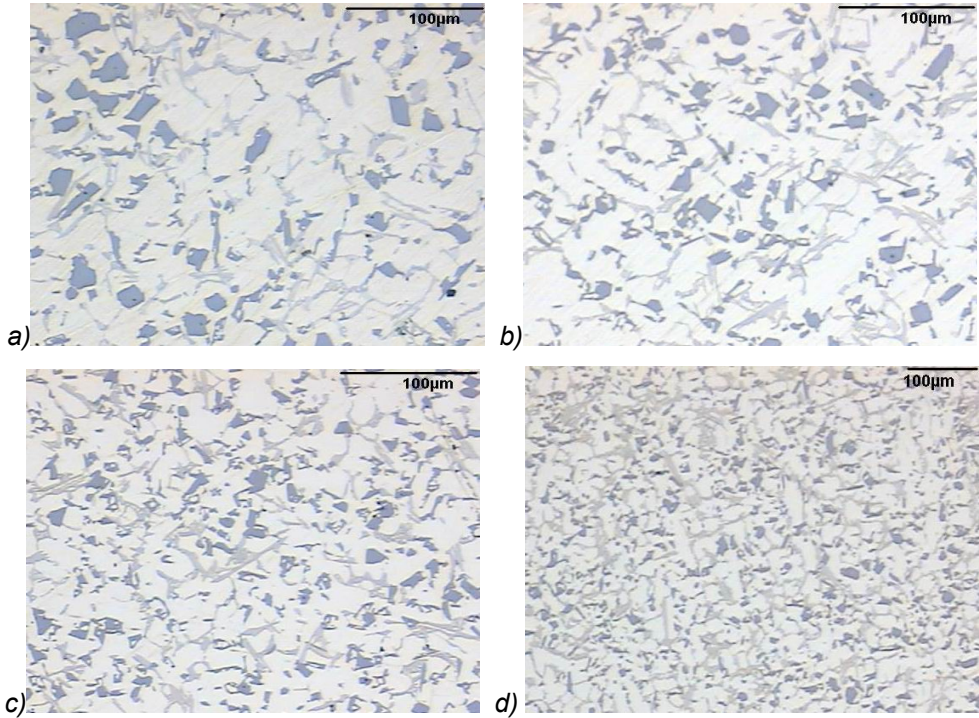


Figure 5 Comparative view of microstructure, solidification time 140 sec, a) alloy L<sub>1</sub>, b) alloy L<sub>2</sub>, c) alloy L<sub>3</sub>, d) alloy L<sub>4</sub>

Figure 6 shows the microstructures in the most critical sections of the piston made of piston alloy A (Table 1). There are the same microconstituents in the compared zones of piston castings and only their size, shape and distribution differ due to different conditions of cooling, i.e., solidification. The average size of primary crystals in the pin hole zone is around 25÷29 µm, while the average size of primary crystals in the critical zone of gas chamber is around 50 µm.

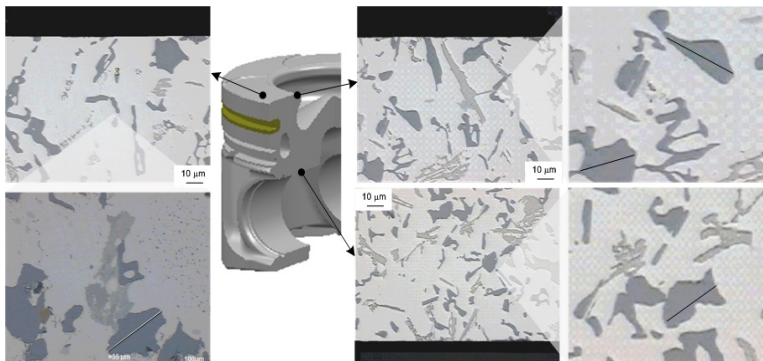


Figure 6 The shape of created microstructure in critical zones

## **Conclusion**

Based on the analysis of the results of experimental tests presented in this paper, it could be concluded:

- that the shape, size, proportion and distribution of primary crystals and other microconstituents is the function of chemical composition, solidification conditions and heat treatment and
- that an appropriate microstructure may be obtained in each segment of the piston casting by providing the necessary solidification conditions.

## **Acknowledgements**

The research presented in this paper was funded by the Ministry of Education and Science of the Republic of Serbia

## **References**

- [1] S. Manasijevic, R. Radisa, S. Markovic, Z. Acimovic–Pavlovic, K. Raic, Thermal analysis and microscopic characterization of the piston alloy AlSi13Cu4Ni2Mg, *Intermetallics*, 19 (2011) 486–492.
- [2] E. R. Wang, X. D. Hui, G. L. Chen, Eutectic Al–Si–Cu–Fe–Mn alloys with enhanced mechanical properties at room and elevated temperature, *Materials and Design*, 32 (2011) 4333–4340.
- [3] R. Gholizadeh, S. G. Shabestar, Investigation of the effects of Ni, Fe, and Mn on the formation of complex intermetallic compounds in Al–Si–Cu–Mg–Ni alloys, *Metallurgical and Materials Transactions A*, 42 (2011) 3447–3458.
- [4] N. Belov, D. Eskin, N. Avxenieva, Constituent phase diagrams of the Al–Cu–Fe–Mg–Ni–Si system and their application to the analysis of aluminum piston alloys, *Acta Materialica*, 58 (2005) 4709–4722.
- [5] S. Manasijevic, Z. Acimovic–Pavlovic, K. Raic, R. Radisa, V. Kvirgic, Optimization of cast pistons made of Al–Si piston alloy, *International Journal of Cast Metals Research*, [doi:10.1179/1743133612Y.0000000007](https://doi.org/10.1179/1743133612Y.0000000007), in press 2013.
- [6] R. C. Hernández, J. H. Sokolowski, Thermal analysis and microscopical characterization of Al–Si hypereutectic alloys, *J. Alloys Compd.*, 419 (2006) 180–190.
- [7] Z. Qian, X. Liu, D. Zhao, G. Zhang, Effects of trace Mn additional on the elevated temperature tensile strength and microstructure of a low-iron Al–Si piston alloy, *Materials Letters*, 62 (2008) 2146–2149.
- [8] S. Manasijevic, *Pistons for IC engines*, Monograph ISBN 978-86-912177-0-9, print: Bureau for Graphic Engineering of the Faculty of Technology and Metallurgy, University of Belgrade, published by LOLA Institute Belgrade, (2009).

## CURRENT DENSITY AND TEMPERATURE EFFECTS ON MICROHARDNESS OF DECORATIVE GOLD COATINGS OBTAINED FROM THE AURI-MERCAPTOTRIAZOLE-COMPARISON WITH CYANIDE

Silvana B. Dimitrijević<sup>1</sup>, Mirjana M. Rajčić-Vujasinović<sup>2</sup>, Radmila M. Jančić-Hajneman<sup>3</sup>, Vlastimir K. Trujić<sup>1</sup>, Dejan D. Trifunović<sup>3</sup>

<sup>1</sup> Mining and Metallurgy Institute Bor, Zeleni bulevar 35, 19210 Bor, Serbia

<sup>2</sup> Technical faculty Bor, VJ 12, 19210 Bor, Serbia, University of Belgrade

<sup>3</sup> TMF Belgrade, Karnegijeva 4, 11000 Belgrade, Serbia, University of Belgrade

*silvana.dimitrijevic@irmbor.co.rs*

### Abstract

The aim of this work is to investigate the effects of current density and temperature on the microhardness of electrochemically deposited gold decorative coating, obtained from conventional cyanide electrolyte and organic electrolyte based on mercaptotriazole. Mechanically and chemically prepared brass samples are first nicked from acidic electrolyte. Nickel was substrate deposit and then decorative gold coatings were deposited from two types of electrolytes at different current densities and temperatures. Microhardness of gold coating was measured using the Knoop method. The highest values of microhardness were obtained at current density of  $1\text{A/dm}^2$  at room temperature for both electrolytes. Microhardness of gold coatings from cyanide electrolytes was  $\text{HK}=740\text{MPa}$ , and coatings obtained from auri-mercaptoptriazole  $\text{HK}=660\text{MPa}$ . The difference is not relevant for decorative purposes.

*Keywords: electroplating, decorative coating of gold, microhardness, Knoop method*

### Introduction

Electroplating of gold is important in many areas including rapidly growing fields of micro- and optoelectronics, where the gold acts as a conducting material [1].

In modern technologies the electroplating processes are still used widely for fabrication of interconnectors. The gilding, used in the electronic industry, can be broadly classified into hard gold and soft gold [2].

Hard gold is used as a contact material for electrical connectors and printed circuit boards (PCBs), relays and switches, which should be resistant to the mechanical wear, whilst having a low electrical contact resistance [2-4]. Soft gold, on the other hand, is used for electronic packaging, such as fabrication of interconnects in the integrated circuits (ICs), or forming connections to external devices, using tape automated bumping (TAB) or chip-on-glass (COG) and chip-onflex (COF) techniques [2-5].

The physical properties of significance for the gold deposits are appearance, wear resistance, hardness, brittleness, residual stress, porosity, thickness, density, and deposit uniformity. The chemical properties of importance include the chemical composition of the deposits and solutions, segregation of impurities, and inertness to oxidation. Each of the physical and chemical properties can be tested [6].

Deposit hardness can be determined by mechanical deformation of test specimens. Commercial instrumentation and scales of hardness exist [7]. Two of the most common instruments use the pyramidal diamond indenters with equal (Vickers) or unequal (Knoop) diagonals. Hardness is usually determined using the cross sections of suitable thickness. Indenting normal to the surface often leads to the erroneous results because the surface roughness can lead to nonuniform loads and thin samples give hardness representative of the base substrate and not the plated gold [6]. Gold films used in the electronics industry for protection or electrical conduction should be both hard and ductile, in order to minimize wear-out. In electrodeposited gold films, the required levels of hardness are met at the expense of ductility by incorporating hardening agents which co-deposit together with large amounts of foreign atoms [8].

Electroplated hard gold, the most commonly used contact material for high reliability electrical connectors, electromechanical relays, and printed circuit boards [9], is a polycrystalline in microstructure with its grain size in the range of 20–30nm, and its hardness is as high as 17–20kg/mm<sup>2</sup> in the Knoop hardness, compared to 50–80 kg/mm<sup>2</sup> for pure, soft gold [4].

## **Experimental**

In the order to study the effect of current density and temperature on the Knoop microhardness of decorative gold coatings, obtained by electrochemical deposition from conventional cyanide electrolyte (commercial product AUROCIN DPB produced by the Metal Salts and Metal Products Plant-Bor), and from electrolyte, based on mercaptotriazole (Au-MT), the microhardness testing was performed.

Before insertion into the electrochemical cell, the samples have to be smoothed, degreased and coated without a layer of invisible oxides. Consequently, the plates are prepared before the gold plating process. The preparation consists of mechanical preparation, chemical degreasing of metal, chemical polishing and nickel plating. Mechanically and chemically prepared brass samples are first nicked from acidic electrolyte. Nickel is a substrate deposit and then the decorative gold coatings were deposited from two types of electrolytes at different temperatures.

Operation conditions in research the influence of current density and temperature on microhardness of decorative gold coatings, are given in Table 1 for conventional cyanide electrolyte (AUROCIN DPB), and in Table 2 for electrolyte, based on mercaptotriazole.

Table 1. Operational conditions in research the influence of current density and temperature on microhardness of decorative gold coatings, obtained in electrochemical cell for cyanide electrolyte AUROCIN DPB

Bath composition	Research the influence of current density	Research the influence of temperature
Gold concentration (g/dm <sup>3</sup> )	1.5	1.5
Concentration of free cyanide (g/dm <sup>3</sup> )	6	6
AUROCIN DPB additive (g/dm <sup>3</sup> )	20	20
AUROCIN DPB additive (ml/dm <sup>3</sup> )	4	4
pH	9	9
Temperature (°C)	22	20; 30; 40
Time (s)	35; 40; 160	35
Cathode current density (A/dm <sup>2</sup> )	0.1; 0.4; 1	1
Current intensity (A)	0.012; 0.05; 0.12	0.12

Table 2. Operational conditions in investigations of the influence of current density and temperature on microhardness of decorative gold coatings obtained in electrochemical cell for gold complex based on mercaptotriazole

Bath composition	Research the influence of current density	Research the influence of temperature
Gold concentration (g/dm <sup>3</sup> )	2.5	2.5
pH	9	9
Temperature (°C)	22	20; 40; 60
Cathode current density (A/dm <sup>2</sup> )	0.1; 0.5; 0.83; 1; 1.7	1
Current intensity (A)	0.012; 0.06; 0.1; 0.12; 0.2	0.12
Time (s)	120; 60; 40; 35; 25	105

Microhardness of gold coating, obtained from both electrolytes, was measured using the apparatus type Kleinhärter prüfen für Vickers, Knoop, und Ritzhärte produced by LEITZ 2 using the Knoop method (HK) under 25N loading. All hardness values were reported in the Knoop (HK) scale.

## Results and discussion

Each sample was subjected to hardness measurements at three different locations (left and right edges of the sample and intersection of diagonals) and the average value of three measurements is shown for each sample.

Macrophoto of gold plate with the locations of measured microhardness is shown in Figure 1.

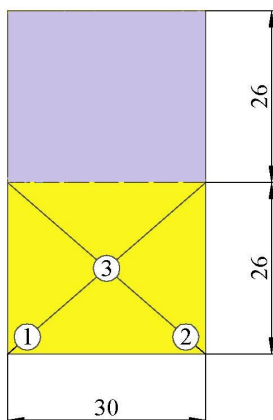


Figure 1. Decorative gold plate with the locations of the measured microhardness

In Figure 2, microhardness of gold deposit, obtained from cyanide electrolyte at three different current densities, was compared to the samples plated from gold complex based on mercaptotriazole at five values of current densities. Microhardness of gold, deposited from the both electrolytes at three different temperatures, is shown in Figure 3.

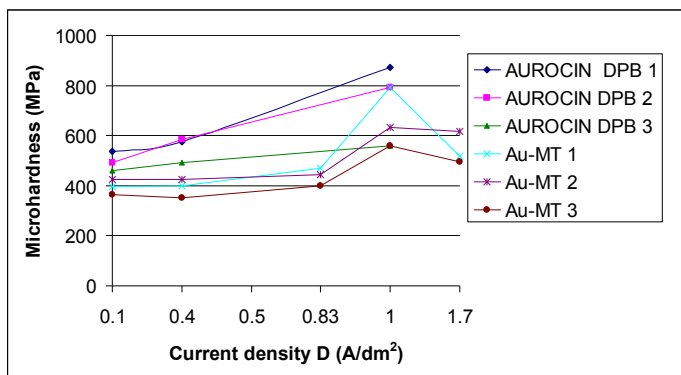


Figure 2. Microhardness of decorative gold coating at different current densities from conventional cyanide electrolyte AUROCIN DPB, obtained at:  $C_{Au}=1.5 \text{ g/dm}^3$ ,  $t=25 \text{ }^\circ\text{C}$ ,  $\tau=35 \text{ s}$  and gold coating from electrolyte based on mercaptotriazole, obtained at:  $C_{Au}=2.5 \text{ g/dm}^3$ ,  $t=25 \text{ }^\circ\text{C}$ ,  $\tau=105 \text{ s}$

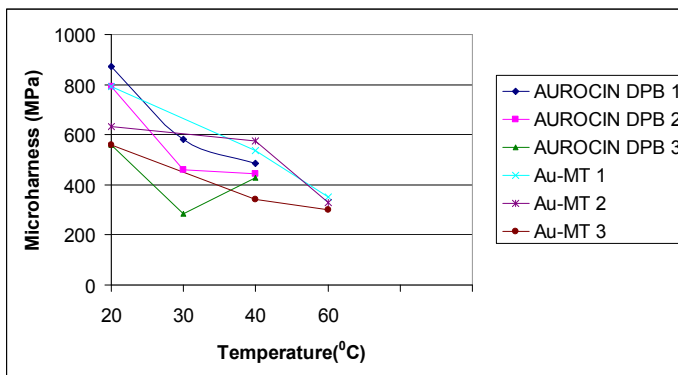


Figure 3. Microhardness of decorative gold coating at different temperatures from conventional cyanide electrolyte AUROCIN DPB, obtained at:  $C_{Au}=1.5 \text{ g/dm}^3$ ,  $t=25 \text{ }^\circ\text{C}$ ,  $\tau = 35 \text{ s}$  and gold coating from electrolyte based on mercaptotriazole, obtained at:  $C_{Au}=2.5 \text{ g/dm}^3$ ,  $D=1 \text{ A/dm}^2$ ,  $\tau=105 \text{ s}$

From the dependence of microhardness of decorative gold coatings on current density, shown in Figure 2, it can be seen that for cyanide electrolyte microhardness,  $HK_{sr}$ , ranges between 496 and 740MPa, while for the organic gold complex values between 394 and 660MPa were measured. Microhardness of the coating obtained from the cyanide electrolyte increases with the increase in current density (for  $D=0.1\text{A/dm}^2$ , the mean value for all three measuring points is  $HK_{sr}=496\text{MPa}$ , for  $D=0.5\text{A/dm}^2$  is  $HK_{sr}=552\text{MPa}$  and for  $D=1\text{A/dm}^2$  is  $HK_{sr}=740 \text{ MPa}$ ). The increasing in current density leads to the increase of crystalline nuclei number formed in the unit time as a consequence of higher cathodic overvoltage and a fine-grained deposit is formed as a result. Fine-grained deposit, on the other hand, leads to increased microhardness of coating. With increasing current density in organic complex of gold, the coating microhardness increases to the current density of  $D=1\text{A/dm}^2$ , and then decreases (for  $D=0.1\text{A/dm}^2$ , the mean value for all three measuring points is  $HK_{sr}=394\text{MPa}$ , for  $D=0.4\text{A/dm}^2$  is  $HK_{sr}=392\text{MPa}$ , for  $D=0.83\text{A/dm}^2$  is  $HK_{sr}=438 \text{ MPa}$ , for  $D=1\text{A/dm}^2$  is  $HK_{sr}=660\text{MPa}$  and for  $D=1.7\text{A/dm}^2$  is  $HK_{sr}=543\text{MPa}$ ). The increase in microhardness with increasing current density (up to the current density of  $D=1\text{A/dm}^2$ ) can be explained, as in case of cyanide electrolytes, with obtaining the fine-grained precipitate. Decrease in microhardness with increasing current density above  $D=1\text{A/dm}^2$  is a consequence of gold powder appearance. With increasing current density above the certain limit (in this case  $1\text{A/dm}^2$ ) at constant concentration of gold ions in electrolyte results in parallel deposition of gold and evolution of hydrogen, and in this case, the rough and spongy deposits are obtained. At high current densities, there is a significant influence of higher cation concentration on crystallite micro peaks, due to higher diffusion and surface roughness increases [10]. When the limiting current density is reached, the sponged and powdered deposits are usually formed (this is also reported in testing the impact of current density on coating thickness) [11]. In the case of limiting current density, the concentration of cations on electrode surface is close to zero, and there are large fluctuations in periodic

concentration of cations. As the result of this phenomenon, there is a great discrepancy in the growth of crystals, formation of separate groups of crystals, which grow and form micro dendrites. The current is practically concentrated on them, which leads to a disturbance of crystallization and formation of metal powder. The measured values of microhardness at measuring points 1 and 2 (left and right edges of plates) are greater than the microhardness values, measured at measuring points 3 (intersection of plate diagonals) in both types of electrolyte. At the same current densities, higher values of microhardness were measured in coatings obtained from cyanide electrolytes. The measured microhardness values of coatings, obtained from organic complex of gold, are close to the values obtained from other non-cyanide electrolytes [1].

In Figure 3, showing the dependence of microhardness of decorative gold coatings on temperature, it can be seen that the microhardness is in the range  $HK_{sr}=453-740\text{MPa}$  for cyanide electrolyte and in the range of  $HK_{sr} = 327-660\text{MPa}$  for electrolyte based on mercaptotriazole. With temperature increase in cyanide electrolyte, the microhardness of coating decreases (for  $t=20^{\circ}\text{C}$ , the mean value for all three measuring points is  $HK_{sr}=740\text{MPa}$ , for  $t=30^{\circ}\text{C}$  is  $HK_{sr}=442\text{MPa}$  and for  $t=40^{\circ}\text{C}$  is  $HK_{sr}=453\text{MPa}$ ). Increasing the temperature also increases the rate of electrochemical reactions, what can be explained by decrease of overpotential and appearance coarse crystalline deposit. Increase in temperature also leads to an increase in diffusion or increase in concentration of cations on cathode and occurrence of coarse crystalline deposit.

With increasing temperature in the organic complex of gold, the coating microhardness also decreases (for  $t=20^{\circ}\text{C}$ , the mean value for all three measuring points is  $HK_{sr}=660\text{MPa}$ , for  $t=40^{\circ}\text{C}$  is  $HK_{sr}=484\text{MPa}$  and for  $t=60^{\circ}\text{C}$  is  $HK_{sr}=327\text{MPa}$ ). Decrease of microhardness with increasing temperature can be explained, as in cyanide electrolytes by obtaining the coarse crystalline deposit. The measured values of microhardness at measuring points 1 and 2 (left and right edges of plates) are higher than the measured microhardness values at measuring point 3 (intersection of plate diagonals) in both types of electrolytes. At the same values of temperature, higher values of microhardness were measured in coatings obtained from cyanide electrolyte.

## **Conclusion**

Testing the effect of current density on microhardness of decorative gold coatings, obtained from classic cyanide electrolyte and gold complex, based on mercaptotriazole has shown that the microhardness value is in the range  $HK_{sr}=496-740\text{MPa}$  for cyanide electrolyte and in the range  $HK_{sr}=394-660\text{MPa}$  for organic complex of gold. At temperatures of 20 to  $40^{\circ}\text{C}$ , the microhardness values are in the range  $HK_{sr}=453-740\text{MPa}$  for cyanide electrolyte and in the range of  $HK_{sr}=327-660\text{MPa}$  for organic complex of gold with the highest obtained values of microhardness at  $20^{\circ}\text{C}$  for both electrolytes, and the lowest value at  $40^{\circ}\text{C}$  for cyanide electrolyte and at  $60^{\circ}\text{C}$  for organic complex of gold. The highest value of microhardness of decorative gold coatings from cyanide electrolyte is  $HK=740\text{MPa}$ . Maximum value of microhardness for deposits obtained from organic complex of gold, based on mercaptotriazole amounted to  $HK=660\text{MPa}$ . In both

electrolytes, maximum value of hardness was obtained at the current density of  $1\text{A}/\text{dm}^2$  and at temperature of  $20^\circ\text{C}$ .

### **Acknowledgment**

This work has resulted from the Project funded by the Ministry of Education and Science of the Republic of Serbia, No. 34024 "Development of Technologies for Recycling of Precious, Rare and Associated Metals from Solid Waste in Serbia to High Purity Products" for which the authors would like to thank on this occasion.

### **References**

- [1] M. J. Liew, S. Roy and K. Scott, Development of a non-toxic electrolyte for soft gold electrodeposition: an overview of work at University of Newcastle upon Tyne Green Chemistry, 5, (2003), pp. 376-381
- [2] Y. Okinaka, M. Hoshino, Some Recent Topics in Gold Plating for Electronics Applications, Gold Bulletin 31(1), (1998), pp. 3-13
- [3] I. R. Christie and B. P. Cameron, Gold Electrodeposition Within the Electronics Industry, Gold Bulletin, 27(1), (1994), pp. 12-17
- [4] Y. Okinaka, Significance of Inclusions in Electroplated Gold Films for Electronics Applications. Gold Bulletin, 33(4), (2000), pp. 117-127
- [5] H. Watanabe, S. Hayashi and H. Honma, Microbump Formation by Noncyanide Gold Electroplating, J. Electrochem. Soc., 146(2),(1999), pp. 574-579
- [6] Paul A. Kohl, Modern Elektroplating, Chapter 4, Joan Wiley&Sons Hoboken, Ontario, Canada (2010), pp. 115-130
- [7] R. W. Beattie, G. Forshow, and E. N. Loney, Proc. IEE (London), B-109 (suppl. 21), (1962), pp. 109-113
- [8] J.A. Augis, C.C. Lo and M.R. Pinnel, The Hardness and Ductility of Sputtered Gold Films, Fourth International Congress on Thin Films, Loughborough, Gt. Britain, September 11–15, (1978), Paper 4J11
- [9] Y. Okinaka, M. Datta, T. Osaka, J.W. Schultze (Eds.), Microelectronic Packaging, CRC Press, Boca Raton, FL, (2005), p. 421
- [10] S. Dimitrijevic, M.Rajcic-Vujasinovic, R. Jancic-Hajneman, J. Bajat, V. Trujic, D. Trifunovic, Temperature Effect on Surface Roughness of Decorative Gold Coatings, 43<sup>th</sup> International October Conference on Mining and Metallurgy, (2011), pp. 440-443
- [11] S. Dimitrijevic, M.Rajcic-Vujasinovic, R. Jancic-Hajneman, J. Bajat, V. Trujic, D. Trifunovic, Current Density Effect on the Surface Roughness of Decorative Gold Coatings, XXII Congress of Chemists and Technologists of Macedonia, (2012), EL-18.

## **ECONOMIC ASPECTS OF ENERGENTS CONSUMPTION IN COPPER MELTING AND REFINING PLANTS**

Gordana KOKEZA, Karlo T. RAIĆ

*Faculty of Technology and Metallurgy, University of Belgrade, Karnegijeva  
4, 11120 Belgrade, Serbia*

### **Abstract**

Copper production is an energy intensive industry. Traditional energy saving methods employed have been single-equipment-orientated. Based on the reduction to conditional fuel, this paper presents the method that analyzes the effects of unit process fuel consumption on overall fuel consumption of copper. Therefore, the authors suggest the employment of the energy equivalent (conditional fuel) of the process and products in the production of copper and process materials in the melting and refining plants as a criterion for energy efficiency rating. By application of this methodology, a comparative analysis of economic aspects of energy consumption in different production procedures is presented.

*Key words: copper metallurgy, energents consumption economics, conditional fuel*

### **Introduction**

Mass exploitation of ore deposits leads to drastic reduction in their metal content, which is certainly disturbing in relation to the consumption of fossil fuels. Fossil fuels can be replaced by other appropriate energy sources while metal substitution is not always possible since the energy consumption for the production of metals increases in absolute terms as the metal content in the ore decreases. Considering that metal demand will also increase in the future, the consumption of energy will exponentially increase.

According to current data, 5 to 6% of the total world fossil fuel consumption is used for the production and processing of metals, such as copper, iron and aluminium [1].

Technological procedures for copper production differ in the manner and location of their execution. They are divided into pyrometallurgical and hydrometallurgical procedures. Pyrometallurgical procedures for copper production (Fig.1.) can be classified as autogenous (Flash Smelting and Bath Smelting) and "standard" procedures (Melting in a Reverberatory Furnace, Electric Furnace or Blast Furnace) and they participate in more than 80 % of the world's production of copper, Table 1. [2]. Percentual share of autogenous technologies processing primary raw material in 2000 is given in Table 2.

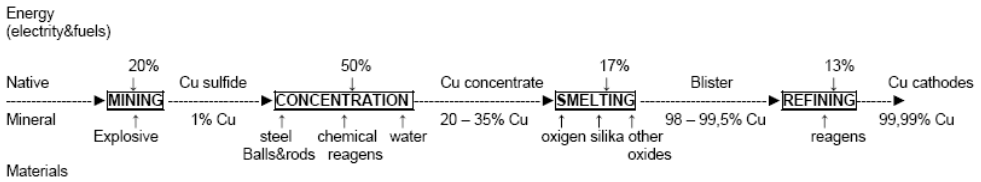


Fig. 1. The main external inputs in the pyrometallurgical route in copper production.

The energy is given as percentage of the total Specific Energy Consumption (SEC)

Table 1. Percentual share of the basic technologies processing concentrate and primary raw material in 2000

Technologies	Share in copper concentrate processing (%)	Share in primary raw material processing (%)
Autogenous processes	75.1	68.5
Reverberatory furnaces	13.5	18.6
Electric furnaces	5.6	5.0
Other technologies	5.8	7.9
<b>Total</b>	<b>100.0</b>	<b>100.0</b>

Table 2: Percentual share of autogenous technologies processing primary raw material in 2000

Technologies	Number of active copper smelters in 2000	Annual capacity of copper production from primary raw material in thousands of tons	Share percentage
Outokumpu Oy (present Outotec)	26	4671	51.4
EI Teniente converter	8	1634	18.0
ISA Smelt	6	763	8.4
Mitsubishi	4	804	8.8
Noranda	3	400	4.4
Inco	3	536	5.9
Vanjukov	2	285	3.1
<b>Total</b>	<b>52</b>	<b>9093</b>	<b>100.0</b>

### Autogenous technologies

Autogenosity in pyrometallurgical copper production has been known for more than a century in sulphide concentrate roasting, pyrite ore smelting and copper matte conversion. A characteristic of the classical procedure for sulphide copper concentrate is that it includes a roasting stage in which a large amount of heat is released and lost irreversibly, while the following smelting stage requires the consumption of a large amount of extra, expensive heat in the form of heavy oil, coal or natural gas. There were some more unfavourable circumstances, such as a sharp rise in energy prices and strict environmental laws that, in the middle of the last century, led to imperative requirements for the development and implementation of modern and rational technological solutions based on the

principles of smelting autogenosity, *i.e.*, the use of the chemical energy of sulphur from the sulphide copper concentrate.

The main part of the energy required to enable autogenous smelting of copper concentrate is obtained by exothermic oxidation reactions of sulphide minerals from the concentrate, primarily from iron and copper sulphides: pyrite ( $\text{FeS}_2$ ) and chalcopyrite ( $\text{CuFeS}_2$ ) [3–5]. Accordingly, the content of the sulphide component in a copper concentrate defines the parameters of the oxidation agent: the degree of air enrichment (oxygen content in the air), the temperature of the enriched air and the quantity of supplementary fuel [5]. Sulphides contain high chemical energy that should be maximally used in the smelting process of the copper concentrate. Such a procedure reduces the costs of additional energy in the form of coal or gas and improves the economy of the whole technological process [6].

Based on the autogenous properties of the smelting process, modern development of extractive copper metallurgy contributes to the development of totally new pyrometallurgical processes, starting from the requirement for the consolidation of the individual processing stages (roasting, smelting, conversion), *i.e.*, their primary aims are:

- Better utilization of the chemical energy of the concentrate and reduction of specific fuel consumption,
- Maximum environmental protection and the production of gas with a high content of  $\text{SO}_2$ .
- High recovery of copper and precious metals.

Starting from these basic principles, many world companies developed their own technologically and operationally different autogenous processes for copper concentrate smelting. Technologically, the processes differ in method of sulphide combustion and smelting [7]. Nowadays, there are two dominant ways of fine-grained copper concentrate combustion and smelting: flash smelting (in a flame) and bath smelting.

#### *Modern Flash Technologies vs Standard Smelting in a Reverberatory Furnace [8-16]*

Generally, all autogenous smelting procedures are better than the standard smelting treatments in reverberatory furnaces, having a lower energy consumption per ton of anode copper and higher recoveries of copper and sulphur. In addition, the following requirements are mandatory:

- processing of copper concentrate with an average copper content of 19-21% and a sulphur content of 32%,
- minimal energy consumption per anode copper ton,
- maximum recovery of copper, precious metals and sulphur,
- usage of oxygen for the technological smelting process,
- gas quality of 9-10%  $\text{SO}_2$  for the production of sulphuric acid,

- continuity of the complete technological process of anode copper production,
- required percentage of copper in the copper matte and in the slag after the smelting process,
- chemical composition and physical properties of the smelting energents,
- chemical composition of the flux and fraction size (limestone and quartz),
- ecological aspects of anode copper production and its impact on the environment,
- qualified labour.

The technologies Inco and Noranda, in relation to other flash smelting technologies, provide lower recovery of copper and sulphur (Table 3). The Inco technology provides the lowest energy consumption per anode copper ton (Table 3) but it has the disadvantage of complex and expensive charge preparation. The Noranda technology, on the other hand, has some restrictions (degree of air enrichment and short life expectancy of aggregates); hence, this technology is no longer applied.

The Mitsubishi Technology presents a continual melting process of copper concentrate to anode copper with high recovery of copper (97%) and sulphur (99.5%) (Table 3). However, the aggregates are placed in the form of cascades with a height distance of 1.5m, inter-connected with channels, which is sometimes not possible under the given conditions.

The Vanukov process is a good process with respect to energy consumption and copper recovery (98-98.5%) but the sulphur recovery is significantly lower (90%) than in other smelting procedures (Table 3). Considering the fact that the ecological standards are becoming increasingly more strict for the SO<sub>2</sub> concentration in the atmosphere, this technology would not completely satisfy the standard conditions.

Two technologies that could fulfill the standard conditions have provoked different discussions. They are the Australian Isasmelt and the Finnish Outotec technologies for copper concentrate smelting. Both technologies provide high copper and sulphur recovery (Table 3), as well as lower energy consumption per anode copper ton, in the range 35-45 %, compared with the standard smelting procedure in reverberatory furnaces.

The Outotec process has undergone a very successful development during the last fifty years and, nowadays, it is the most widespread process in copper metallurgy, and technically and instrumentally the most perfect autogenous procedure for the smelting of sulphide copper concentrates. The following facts illustrate this: in 2000, 26 smelter plants worldwide utilized this melting technology and realized an annual production of 4,671,000 tons, which was amounted to 51.4% of total production resulting from the application of modern autogenous smelting procedures (Table 2).

Table 3. Technical and economic indicators of autogenous procedures for smelting copper sulphide concentrate

Indicator		Outokumpu (present Outotec)	Procedures of melting				Reverberatory furnace	Vanjukov
			INCO	Noranda	Mitsubishi	Isasmelt		
Specific capacity	t/m <sup>2</sup> day	10–12	10–12	10	20–24	86–90	4.2–4.7	70–75
Concentrate	% Cu	24–30	25–30	35	34.2	27–29	19–30	19–23
Copper matte	% Cu	65–70	55–60	73	67–72	55–60	36–45	40–55
Slag	% Cu	0.5–0.65	0.8–1.65–6		0.6–0.9	0.5	0.5–0.6	0.5–0.7
O <sub>2</sub> content in the air	% O <sub>2</sub>	45–70	95–98	35–36	45–49	42–50	21–25	50–70
SO <sub>2</sub> content in the gas	% SO <sub>2</sub>	33–45	75–80	6	29.0	7.5–11	1.5–2.5	20–35
Copper matte temperature	°C	1250	1170	1250	1210	1165	1150	1210
Slag temperature	°C	1300	1250	1300	1250	1175	1200	1250
Copper recovery	% Cu	98	97.5	95	97	97–98	93	98–98.5
Sulphur recovery	% S	94–99	93.6	86	99.5	97–98	50	90

## Methodology

All forms of expended energy are reduced to primary energy or to the same energy form, *i.e.*, to the energy equivalent of process (EEP), raw material and process material, and also, energy equivalent of process and waste products (water vapour, thermal energy and similar) are balanced [17,18].

Therefore, the authors suggest the employment of the energy equivalent of the process and products in the production of copper and process materials in the Melting and Refining Plants as a criterion for energy efficiency rating, besides the level of energy recovery, taking into account the extended energy for production, transport and exploitation of energy generating products, process materials and raw materials. To complete the consumption of the energy generating products in copper production, they are reduced to conditional fuel [8] (coal equivalent=29.3 MJ/kg).

By application of the methodology of reducing the energy generating products to the energy equivalent of the process (EEP) and conditional fuel in anodic copper production, a comparative analysis of energy consumption in production stage was realised and the “standard” smelting procedure in reverberatory furnaces was compared with modern autogenous procedures, Table 4 [18].

Table 4: Comparative review of energy equivalents in anode copper production for selected procedures [18]

Pyrometallurgical procedure of anode copper production	Drying	Roasting g	Smelting g	Conversion	Fire refining g	Sulphuric acid production	Other products	Secondary energy (-) Ev	Energy equivalent, EEP, MJ/t of anode copper
<b>a) Concentrate processing with copper grade of 29.5%</b>									
1.Reverberatory furnace, raw charge			14800	1876	1564	2646	588	3454	<b>21474</b>
2.Reverberatory furnace, roasted charge		398	11045	1390	1564	3144	588	6485	<b>18129</b>
3.Electric furnace	1708		18748	1876	1564	3764	588	3454	<b>28248</b>
4.Flash furnace Outotec (air temperature 250°C)	1917		7175	1302	1564	3282	588	3877	<b>15828</b>
5.Flash furnace, INCO (air temperature 250°C)	1834		2843	1784	1564	2952	588	1801	<b>11565</b>
6.Process Mitsubishi	2148		8562		1564	3366	588	4614	<b>16228</b>
7.Process Noranda (without oxygen)			17296		1564	5150	588	8029	<b>24598</b>
8.Process Noranda (with oxygen)			8466	607	1564	3056	588	3133	<b>14281</b>
<b>b) Concentrate processing with copper grade of 19%</b>									
9.Vanjukov, melting in dried charge melt									<b>13300</b>
10.Vanjukov, melting in raw charge melt									<b>10900</b>

- 1) Raw concentrate treatment 940 t/day, copper matte 35% Cu, air heated to 220°C, 2.287 t H<sub>2</sub>SO<sub>4</sub>/t anode, 3.440 t concentrate/t anode.
- 2) Raw concentrate treatment 940 t/day, copper matte 43.5% Cu, air heated to 220°C, 2.835t H<sub>2</sub>SO<sub>4</sub>/t anode, 3.440 t concentrate/t anode.
- 3) Raw concentrate treatment 1360 t/day, copper matte 35% Cu, 3.112t H<sub>2</sub>SO<sub>4</sub>/t anode, 3.440t concentrate/t anode.
- 4) Raw concentrate treatment 880 t/day, copper matte 61.4% Cu, 3.179t H<sub>2</sub>SO<sub>4</sub>/t anode, 3.425t concentrate/t anode.
- 5) Raw concentrate treatment 1350 t/day, copper matte 54.3% Cu, 3.165t H<sub>2</sub>SO<sub>4</sub>/t anode, 3.442t concentrate/t anode.
- 6) Raw concentrate treatment 610 t/day, copper matte 65.5% Cu, 3.174t H<sub>2</sub>SO<sub>4</sub>/t anode, 3.444t concentrate/t anode.
- 7) Raw concentrate treatment 770 t/day, 3.139t H<sub>2</sub>SO<sub>4</sub>/t anode, 3.440t concentrate/t anode.
- 8) Raw concentrate treatment 1870 t/day, copper matte 75% Cu, 3.175t H<sub>2</sub>SO<sub>4</sub> /t anode, 3.439t concentrate/t anode.

## **Conclusion**

In the countries with economy in the process of transition, with constant changing of input parameters, makes it impossible to predict the future economic effect of copper production. Therefore, it is perhaps the only reliable possibility for estimation of fuel consumption in copper production the using of method of reduction to conditional fuel.

So, the basic aim of any technological process must be to improve the efficiency of mining and metallurgical processes, which is expressed in cost reduction per production unit. It should be a continuous process as the resource quality (low copper content in the ore) is becoming poorer and poorer. Comparative analysis of the energy consumption clearly indicates that the “standard” procedure is uneconomic. A great amount of energy is released and irreversibly lost, while the following melting stage requires the consumption of a large amount of additional expensive energy in the form of coal. Process of the modernization of copper production can improve economic efficiency and to increase competition of the economic subject in that area.

## **References**

- [1] Valero AI and Valero A. A prediction of the energy loss of the world's mineral reserves in the 21st century. *Energy* 2011, p.1848–1854.
- [2] Davenport W, King M, Schlesinger M. and Biswas A. *Extractive metallurgy of copper*. Elsevier: Oxford; 2002.
- [3] Moreno A. (editor). *World copper data book*. Metal Bulletin Books. UK: Survey; 1999.
- [4] Charles, Pitt H, and Milton E. Wadsworth. *Current Energy Requirements in the Copper Producing Industries*. IM June 1981.
- [5] Kellogg HH. *Sizing up the Energy Requirements for producing primary materials*. E/MJ April 1977;
- [6] [6] Alicia V, Antonio V, Immaculada A. Evolution of the decrease in mineral energy throughout the 20<sup>th</sup> century. The case of copper in the US. *Energy* 2008, p.107–115.
- [7] Kellogg HH, and Henderson JM. *Energy use in sulfide smelting of copper*. New York: 1976.
- [8] Diaz C et al. *Pyrometallurgy of copper*. Volume IV. New York: Pergamon Press; 1991.
- [9] Anderson B, Hanniaba P and Harkki S. Use of Oxygen in the Outokumpu Flash Smelting Process. *CIM Bulletin*, September 1992;172–177.
- [10] Shilasaaki T, Kanamori K and Hayashi M. Construction of new Mitsubishi furnaces for modernization of Naoshima smelter and refinery. In: *Inter. Symp. Pyrometallurgy of Copper*, Ottawa: August 1991, p. 3–13.
- [11] Themalis NJ and Kerrow Mc GC. *Production of Copper by the Noranda process*. *Advances in extractive metallurgy and refining*. London: IMM;1972.
- [12] Vanjukov AV. *Plavka v žitkoj vanie*. Moskva: Metallurgiya; 1988.
- [13] *Copper raw materials*. Monthly publications. Commodities Research (CRU). London: 2004.
- [14] Fountain CR, Tuppurainen JM. et al. *New development for the Copper*

- Isasmelt Process. In: Extractive Metallurgy of Copper, Nickel and Copper, Copper and Nickel operation, TMS Annual Meeting, Pennsylvania, February 1993; p. 1461–1473.
- [15] Chapman PF and Roberts F. Metal resources and energy. London: Butterworth; 1983.
- [16] Brook Hunt Mining & Metal Industry Consultants. 2004.
- [17] Najdenov I, Raić K and Kokeza G. Economic insight into energents consumption in copper melting and refining plants of Serbia using the method of reduction to conditional fuel (coal equivalent). *Metalurgia International* 2011; 16, No. 10.
- [18] Najdenov I, Raić K and Kokeza G. Aspects of energy reduction by autogenous copper production in the copper smelting plant Bor (2012) *Energy*, 43 (1), pp. 376-384.

## CHARACTERIZATION OF HYDROXYAPATITE–COATED Ti SURFACE MICROSTRUCTURE PREPARED BY PLASMA SPRAYING

Rebeka Rudolf<sup>a</sup>, Karlo T. Raić<sup>b</sup>, Zoran Aleksić<sup>c</sup>, Vojkan Lazić<sup>c</sup>, Aleksandar Todorović<sup>c</sup>, Dragoslav Stamenković<sup>c</sup>, Vukoman Jokanović<sup>d</sup>

<sup>a</sup>University of Maribor, Faculty of Mechanical Engineering, Maribor, Slovenia,

<sup>b</sup>University of Belgrade, Faculty of Technology and Metallurgy, Belgrade, Serbia,

<sup>c</sup>University of Belgrade, School of Dentistry, Belgrade, Serbia,

<sup>d</sup>University of Belgrade, VINCA Institute of Nuclear Sciences, Belgrade, Serbia

email: rebeka.rudolf@um.si

### Abstract

The thin hydroxide apatite (HA) films were coated on the cp-Ti samples by the plasma spraying process. The specific plasma installation was used for the plasma spray process to obtain an appropriate modified outer implant surface. Microstructural observation of the modified implant surface was done by use of SEM imaging as well as AES spectroscopy with the aim of detecting the elements contained in the new surface of the samples.

*Key words: cp-Ti implants, hydroxide apatite (HA), plasma spray coating*

### Introduction

Titanium and titanium alloys have been used widely as biomedical materials in dental surgeries due to their high mechanical properties, corrosion resistance, no cell toxicity and very poor inflammatory response in peri-implant tissue, which is proving a high biocompatibility. Their favorable biological performance is attributed to a thin native oxide film, which forms spontaneously on the titanium surface [1-3].

Surface texture of dental cp-Ti implants is very important in Osseo integration and bone response. Implant surface topography at the micro and nano levels has been regarded as the most influential factor for successful implant implementation.

The titanium surface can be modified chemically and/or physically in order to improve biomaterial–tissue integration. Different treatments are used to modify the titanium surface: hydroxyapatite coatings, preceded or not by acid etching, are used to create a rough, potentially bioactive surface [4-6]. Oxide blasting treatments, either with or without chemical etching [7-9], are used to develop rough surfaces, and thick oxide films obtained by anodic [10,11] or thermal oxidation [12] have been used currently to accelerate the Osseo integration process.

It is well known that surface roughness plays an important role in the implant Osseo integration process. Accordingly, some authors have indicated the existence of an optimal range of surface roughness [7]. However, other characteristics such as oxide thickness, oxide crystallinity and ions present in the external layer may also influence bone bonding [13].

Therefore, how to prepare the ideal microtopography of the surface is still unknown, because it is very difficult to associate surface properties with clinical results [14]. Although more accurate knowledge is required, typical cp-Ti surfaces have been treated by different high-voltage plasma process parameters.

Many new plasma processes are finding their way from the research lab to the manufacturing plants. These require high voltage (HV) pulse power equipment, which must be optimized for application, system efficiency, and reliability. Although no single HV pulse technology is suitable for all plasma processes, various classes of high voltage pulsers may offer a greater versatility and economy to the manufacturer. Here, the experimental presentation of coating thin hydroxide apatite (HA) on the cp-Ti samples by specific plasma installation [15] is performed. The aim of this work was, namely, producing the problematic HA coating with new methods in order to get a more stable structure which could be usable for further clinical applications. Moreover, the comparative analysis was done by the use of the classical preparation method: chemical etching in order to get information for new plasma technology.

## **Materials and methods**

The plasma installation PJ-100 (Plasma Jet, Serbia) was used for the plasma spray process. The basic parameters of the installation used for the coating deposition are presented in ref [15,16]. We used two commercially available HA powders: HA powder, XPT-D-703 (Sulzer Metco, USA) and HA powder Captal 90 (Plasma Biotol, UK). Data on the granulation of the powders used were obtained from the manufacturer's specifications.

The samples were made from cp-Ti Grade 2 - ASTM F 67-100 (C = 0.08% max, N = 0.030% max, O = 0.25% max, Fe = 0.30% max, H = 0.015% max) in dimension  $\phi = 10$  mm and thickness 2 mm. The properties of cp-Ti Grade 2 are: Melting point 1668°C, Hardness, Vickers 180 HV, 0.2% yield strength 275-450 MPa, Tensile strength >350 MPa, Elongation >20%, Density 4.5 g/cm<sup>3</sup>, Coefficient of thermal expansion 25 - 400°C  $9.4 \times 10^{-6}$ /K, Elasticity modulus 110 GPa.

Commercially pure (cp), titanium is unalloyed, undergoes an allotropic transformation from the hexagonal close-packed alpha phase to the body-centered cubic beta phase at a temperature of 882.5°C. At service temperature it consists of a 100% hcp alpha phase. As a single-phase material its properties are controlled by chemistry (iron and interstitial impurity elements) and grain size. Cp-Ti is classified into Grades 1 through 4, depending on the yield strength and allowable levels of the elements iron, carbon, nitrogen, and oxygen. Cp-Ti Grade 2 has a minimum yield strength of 275 MPa, and relatively low levels of impurity elements, which places it between Grades 1 and 3 in terms of strength. Grade 2 is widely used because it combines excellent formability and moderate strength with superior corrosion resistance. This combination of properties makes Cp-Ti Grade 2

titanium a candidate for a large variety of chemical and marine, as well as aerospace and medical applications.

A standard procedure of sand blasting with corundum particles of 2mm preceded the deposition. After that, additional treatment of the cp-Ti Grade 2 surface was performed as follows:

(SAMPLE 1) - Treatment with high-voltage: 500 eV – 1 h, 700°C

(SAMPLE 2) - Treatment with high-voltage: 500 eV – 2 h, 700°C

(SAMPLE 3) - Treatment with high-voltage: 500 eV – 1 h, 800°C

(SAMPLE 4) - Chemical treatment with NaOH - 5 h .

After that, the complete plasma coating process was performed by PJ-100 (Plasma Jet, Serbia) in two to three short intervals from 7 to 10 s each, with a break rate of a few minutes between the cycles.

For microstructural observation of the modified implant surface SEM imaging, as well as AES spectroscopy with particular element's depth profiling, were used on the surface of the samples. This was performed by using a VG-Scientific (now Thermo Scientific) Microlab 310 F SEM/AES. AES spectra were acquired using Avantage 3.41v data acquisition, and the data processing software was supplied by Thermo Scientific.

The parameters of analysis were: Primary electron beam kinetic energy: 10 keV; primary electron beam current: Approximately 10 nA, resolution: Diameter of electron beam approximately 10 nm. For Auger analysis the sample was sputtered with Ar<sup>+</sup> 3 keV for 5 min, after which we performed AES analysis. For depth profiling the sample was sputtered with Ar<sup>+</sup> 3 keV sputter rate about 0,8 nm/min. Analysis was performed before the first sputtering and after each sputter cycle.

## Results and discussion

The surface of the base material was analyzed after the samples were cut out using the wire erosion process and polishing of each disk. AES analysis showed at the surface, there are supposed to be Ti, O and C due to the environment contamination—see Fig. 1.

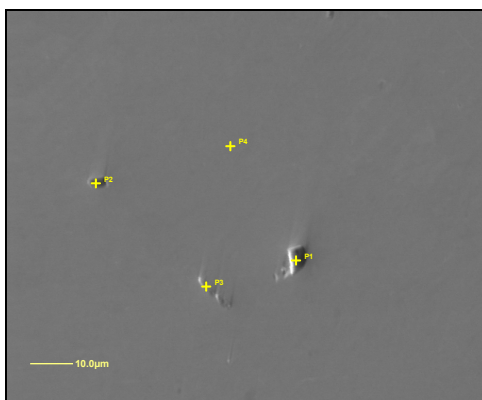


*Figure 1: Surface of base material with AES spectra in presented points*

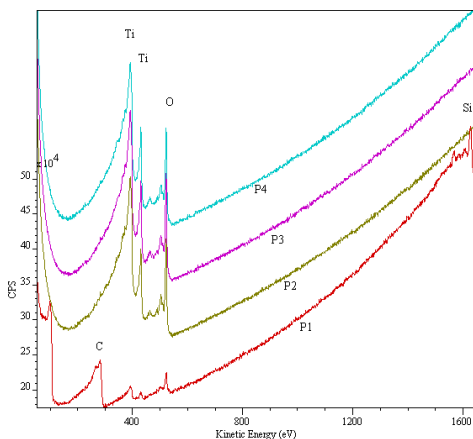


Figure 2 show the typical ground plan of all samples. The detailed analysis of the upper microstructure of samples indicates roughness, which is obtained by different preparation or by development of an HA structure during the different plasma spraying. It could be concluded that the surface is changing according to the parameters of plasma spraying: If the temperature is higher - the roughness is greater. Contrary to this, the chemical etching causes the higher level of roughness compared to the plasma process.

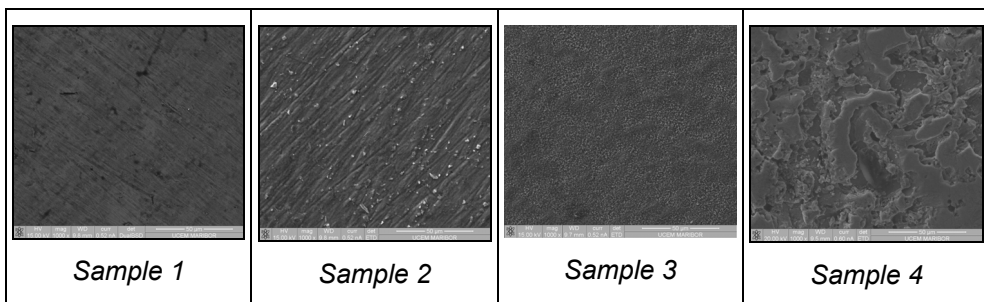


Figure 2: SEM micrographs of upper surface for all samples

AES spectroscopy observations of the morphology of the obtained HA structures on the titanium substrate surfaces and chemically treated surfaces are presented in Figure 3. It could be seen that the thickness of the obtained HA layer is dependent on the technological parameters: Temperature and time of exposure. The situation is almost the same as with the formation of surfaces` morphology (see Fig.2). The HA layer is visible as a white layer. On this base of observation it was concluded that the direction of formatted HA layers in non-homogenous and in precedence directions is where there are surface hollows. On the other hand, the chemically etched surface is completely different to the plasma obtained layers. Moreover, this chemical layer is also wavier, which could be the reason for a lower level of biocompatibility.

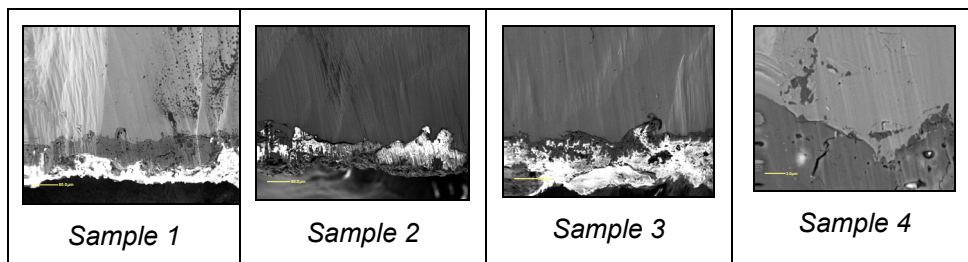


Figure 3: AES spectroscopy

Moreover, on Figure 4 there are Auger spectra of the obtained HA layer and they were at least in 4 points.

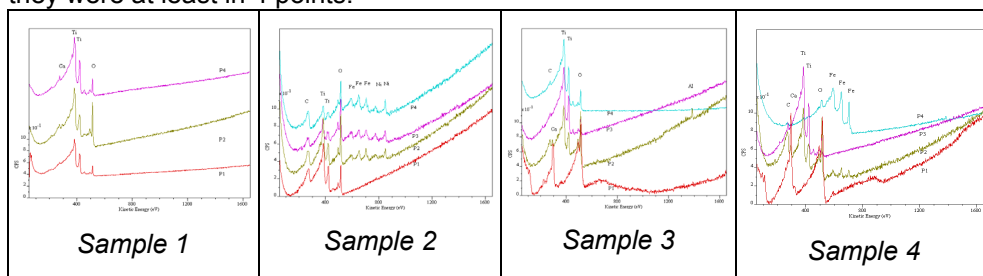


Figure 4: The AES spectra and elements depth profiles of elements in the layer

By analyzing the obtained spectra it became clear that the surfaces are covered by Ti-oxide with combination with different phases. This is the most important fact which was obtained by this research. Further investigation must reveal which HA or chemically etched coating enables the use of this material in bio-applications.

## Conclusions

Our investigations show that HA coatings on cp-Ti Grade 2 surfaces could improve morphological and physical properties, while the biological properties are still unknown. We expect that such implant morphology could increase Osseointegration after HA particles` incorporation.

It is supposed that the use of the plasma installation PJ-100 (Plasma Jet, Serbia) enables the formation of the high quality coating.

## Acknowledgements

This paper is part of Eureka Project E! 5831 Cell-Ti. The authors acknowledge gratefully the Ministry of Higher Education, Science and Technology of the Republic of Slovenia and the Ministry of Science and Technological Development of the Republic of Serbia.

## References

- [1] Lausmaa, J. (1996) *Journal of Electron Spectroscopy and Related Phenomena* 81: 343–361.
- [2] Eisenbarth, E., Velten, D., Schenk-Meuser, K., Linez, P., Biehl, V., Duschner, H., Breme, J. & Hildebrand, H. (2002) *Biomolecular Engineering* 19: 243–249.
- [3] Sul, Y.T. (2003) *Biomaterials* 24: 3893–3907.
- [4] de Groot, K., Wolke, J.G. & Jansen, J.A. (1998) *Proceedings of The Institution of Mechanical Engineers* 212: 137–147.
- [5] Barrere, F., Van Blitterswijk, C.A., de Groot, K. & Layrolle, P. (2002) *Biomaterials* 23: 2211–2220.
- [6] Sena, L.A., Andrade, M.C., Rossi, A.M. & Soares, G.A. (2002) *Journal of Biomedical Materials Research* 60: 1–7.
- [7] Wennerberg, A. (1998) *International Journal of Machine Tools and Manufacturing* 38: 657–662.
- [8] Yerokhin, A.L., Nie, X., Leyland, A. & Mathews, A. (2000). *Surface and Coating Technology* 130: 195–206.
- [9] Diniz, M.G., Soares, G.A., Coelho, M.J. & Fernandes, M.H. (2002) *Journal Materials Science: Materials in Medicine* 13: 421–432.
- [10] Sul, Y.T., Johansson, C.B., Jeong, Y. & Albrektsson, T. (2001) *Medical Engineering and Physics* 23: 329–346.
- [11] Sena, L.A., Rocha, N.C.C., Andrade, M.C. & Soares, G.A. (2003) *Surface and Coatings Technology* 166: 254–258.
- [12] Velten, D., Biehl, V., Aubertin, F., Valeske, B., Possart, W. & Breme, J. (2002) *Journal of Biomedical Materials Research* 59: 18–28.
- [13] Jones, F.H. (2001) *Surface Science Reports* 42: 75–205.
- [14] Milinković, I., Rudolf, R., Raić, K.T., Aleksić, Z., Lazić, V., Todorović, A., Stamenković D. A. (2012) *Materiali in Tehnologije*, 46 (3), pp. 251-256.
- [15] M. Vilotijević, Dc plasma arc generator with increasing volt-ampere characteristic, *RS Patent No 49, 7062007*
- [16] J. Ružic, M. Vilotijevic, D. Božic, K. Raic, *Metallurgical & Materials Engineering*, 2012, Vol 18 No 4 273

## DETERMINATION OF MICROSTRUCTURAL CHANGES BY SEVERELY PLASTICALLY DEFORMED OXIDE DISPERSION STRENGTHENED COPPER ALLOY

Matija Kos<sup>1</sup>, Ivan Anžel<sup>1</sup>, Rebeka Rudolf<sup>1,2</sup>, Matina Gilič<sup>3</sup>, Maja Romčević<sup>3</sup>, Milica Petrović Damjanović<sup>3</sup>, Uroš Ralević<sup>3</sup>, Branka Hadžić<sup>3</sup>, Miodrag Mitrić<sup>4</sup>, Nebojša Romčević<sup>3</sup>

<sup>1</sup>University of Maribor, Faculty of Mechanical Engineering, Slovenia

<sup>2</sup>Zlatarna Celje d.d., Slovenia

<sup>3</sup>Institute of Physics, University of Belgrade, 11080 Belgrade, Serbia

<sup>4</sup>Vinča Institut, University of Belgrade, Serbia

### Abstract:

Presented research work deals with the problem of producing a complex metal-ceramic nanostructural composite using processes of internal oxidation and severe plastic deformation. For this purpose, Cu-Al alloy with 0.4 wt.% of Al was used. The internal oxidation (IO) of the sample serves in the first step of the processing as a means for attaining a fine dispersion of nano-sized oxide particles in the metal matrix. The production technology continues with repeated application of severe plastic deformation (SPD) of the resulting metal-matrix composite to produce the bulk nano-scaled structural material. SPD was carried out with equal channel angular pressing (ECAP), which allowed that the material could be subjected to an intense plastic strain through simple shear. The microstructural evolution of one phase and multiphase material was studied on internally oxidized Cu-0.4%wt. Al sample composed of one phase copper-aluminum solid solution in the core and fine dispersed oxide particles in the same matrix in the mantle region. Our purpose is to identify the microstructural features resulting in the microstructure after the ECAP process. In this manner X-ray diffraction was used. The results reflect structural changes completely. Local structures in plastically deformed samples registered with X-ray diffraction reflect the presence of Cu, Cu<sub>2</sub>O, Cu<sub>4</sub>O<sub>3</sub> or Al<sub>2</sub>O<sub>3</sub> structural characteristics, depending on the type of sample.

*Key words: Cu-Al alloy, microstructure, ECAP process, X-ray diffraction*

### Introduction

Internal oxidation (IO) is a diffusion-controlled process involving selective reactions of a less noble solute or second phase particles with oxygen (also nitrogen or carbon) diffusing in from the surface. The phenomenon is well understood for single phase solid solutions and can be interpreted according to the known theoretical models. From a technological standpoint the process can be used for oxide dispersion strengthening of alloys (ODS alloy) which retain improved mechanical properties at high temperatures [1]. Tensile strength of ODS alloys can be improved additionally by grain refinement, which can be achieved with equal channel angular pressing (ECAP) [2]. The ECAP process (Figure 1) is a

novel technique for producing ultra-fine grain structures on the submicron level by introducing a large amount of shear strain into the materials without changing the billet shape or dimensions [3]. Previous research on grain refinement and microstructural evolution during the ECAP process are based mainly on one phase materials such as Cu and Al [4-6].

The combination of the IO and ECAP process on the microstructural evolution has not yet been studied and therefore only little information is available concerning the deformation mechanism of severely plastically deformed ODS alloys.

This paper describes the influence of the ECAP process on the microstructural evolution of one phase and multiphase materials. The comparison of evolution of microstructure in one phase and multiphase material was studied on partially internally oxidized Cu-0.4%wt. Al sample composed of one phase copper-aluminum solid solution in the core and fine dispersed oxide particles in the same matrix in the mantle region.

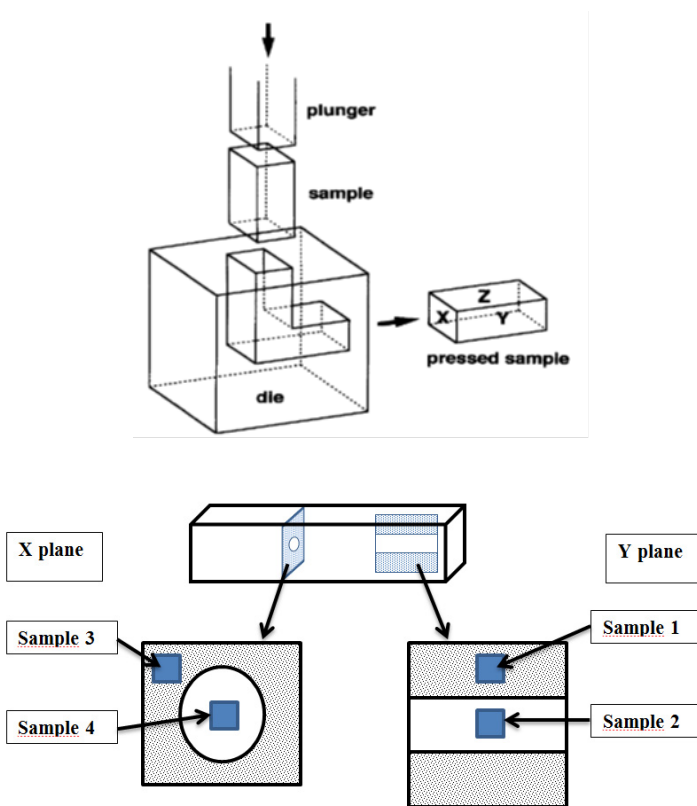


Figure1. Schematic illustration of equal channel angular pressing (ECAP) [4] and samples which were observed in our experiment.

## **Experimental details**

Internal oxidation of the samples was used in the first step of the processing to attain a fine dispersion of nano-sized oxide particles in the metal matrix. Furthermore, the second step, the repeated application of severe plastic deformation of the resulting metal-ceramic composites is applied as an effective technique for producing bulk nano-scaled structures [7].

The experiments have been performed using a sample of internally oxidized Cu-0.4% Al alloy. Billet cross-sections of 10 x10 mm and 50 mm in length were made by vacuum melting, mold casting and calibration rolling. Billets were then homogenized for 1 hour at 1173K. The internal oxidation procedure was performed in a mixture of equal parts of copper oxide and copper metal powders enclosed in a glass ampule and held at 1173K for 72 hours in a tube furnace. This procedure allowed a partial pressure of oxygen equal to the decomposition pressure of copper oxide and maintained the saturation concentration of oxygen in the surface of the billet.

Within our research we have designed our own ECAP tool. Many parameters had to be taken into consideration regarding billet shape, size and maximum work load. We decided to use a 90° die with a square section of 10 x 10 mm<sup>2</sup> cross - section and billet length of 50 mm. The outer radius of curvature was 1mm. The die that consisted of two blocks which were bolted together to give a single internal channel and the piston were made from UTOP Mo1 tool steel, hardened to approximately 61 HRc. A simple standard press with 60 metric tons capacity was used. The ECAP pressings were carried out at room temperature using route B<sub>a</sub> where the billet is rotated by 90° in alternate directions. The billet was pressed four times through the ECAP die. The samples were taken transversely (x plane) and longitudinally (y plane) to the pressing direction as shown in Figure 2. From each plane two samples were taken, one from the mantle region and one from the core.

Microstructural characterization was carried out by optical microscopy, scanning electron microscopy and X-ray diffractions. The samples for optical microscopy were prepared with standard metallographic preparation methods using mechanical polishing with alumina 0.05 µm and etched with FeCl<sub>3</sub>+HCl. The observed samples were those from Figure2 (samples 1, 2, 3 and 4).

## **Results and discussion**

After internal oxidation we obtained a one phase copper-aluminum solid solution in the core and finely dispersed oxide particles (oxidation zone) in the same matrix in the mantle region as shown in Figure 2. The mean width of the oxidation zone was 2.6 mm.

In the oxidation zone nano-scale Al<sub>2</sub>O<sub>3</sub> particles are distributed homogeneously in the interior of the grain and on the grain boundaries. The grains were smaller (100-200 µm) than in the core region because the sample was recrystallized during internal oxidation and the nano-sized Al<sub>2</sub>O<sub>3</sub> particles slowed down the growth of the grains.

It can be seen that the oxidation front is straight, which means that there was no preferential diffusion on the grain boundaries. The growth of the oxidation zone was held by the volume diffusion of oxygen (Figure 2).

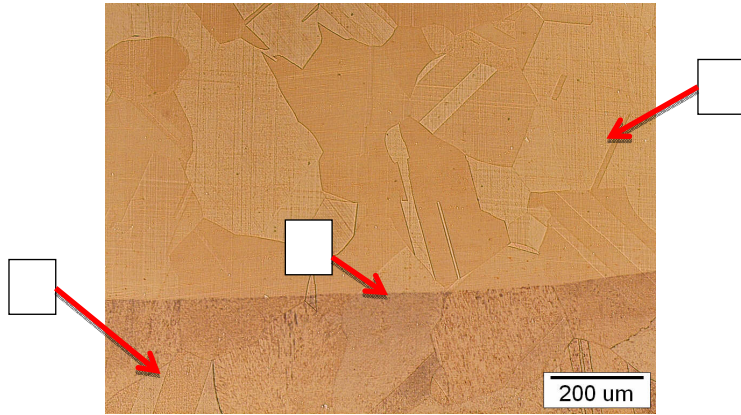


*Figure 2: Optical microscopy image of internally oxidized Cu-0.4% Al sample. Arrow 1 shows the area of the oxidation zone  $\text{Cu-Al}_2\text{O}_3$ , arrow 2 shows the area of the Cu-0.4% Al alloy and arrow 3 shows the oxidation front.*

Figure 3 shows the optical microscope image after the ECAP process transverse to the pressing direction using mechanical polishing with alumina as a preparation method. In the core region we can see flow bands of the material as a consequence of severe plastic deformation.

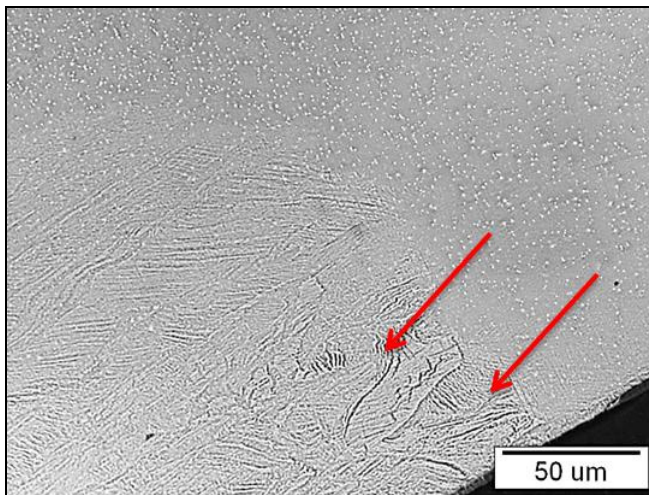


*Figure 3: Optical microscope image after the ECAP process. The arrows indicate the flow bands of the material.*

ECAP samples were examined with SEM transversely (x plane) and longitudinally (y plane) to the pressing direction as shown in Figures 4 and 5. From each plane two samples were taken, one from the mantle region and one from the

core. Oxide particles could be seen in the oxidation zone in Figure 4. In Figure 4 the deformed grains in the core region (sample 4) are well defined too.

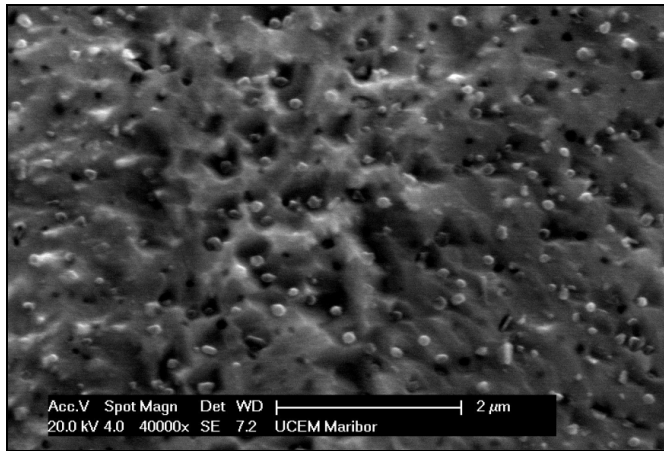


Figure 4: SEM image of the oxidation zone transverse to the pressing direction- sample 3

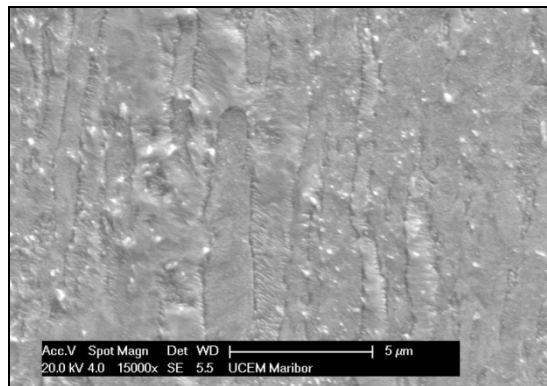


Figure 5: SEM image of the core region transverse to the pressing direction- sample 4

Micro-hardness of the sample before and after four passes through the ECAP die in the Cu-0.4%wt. Al alloy (samples 2 and 4) and in the oxidation zone (samples 1, 3) was measured. The results are shown in Table 1.

Table 1: Micro hardness of the core and oxidation zone

Core: Cu-0.4%wt.Al		Oxidation zone: Cu-Al <sub>2</sub> O <sub>3</sub>	
Before ECAP	After ECAP	Before ECAP	After ECAP
41,7 HV5	146,4 HV5	64,1 HV5	156,5 HV5
$\Delta$ HV=104,7		$\Delta$ HV=92,4	

It would be expected that, because of interaction between the  $\text{Al}_2\text{O}_3$  particles and sliding dislocations after four passes through the die,  $\Delta\text{HV}$  would be larger in the oxidation zone. As shown in Table 1,  $\Delta\text{HV}$  in the oxidation zone is lower than in the primary alloy. On this basis it can be concluded that, because of the presence of oxide particles ( $\text{Al}_2\text{O}_3$ ) in the volume of the grain, the sliding of dislocations is disabled, which means that the sliding was preferable along the grain boundaries. That is the reason why the rate of hardening is lower in the oxidation zone than in the core Cu-0,4%wt.Al.

X-ray diffraction: The formation of phase and crystal structure of our samples after ECAP longitudinally ( $y$  plane) to the pressing direction, were approved using the X-ray diffractometer, Model Philips PW 1050 diffractometer equipped with a PW 1730 generator, 40kV x 20mA, using Ni filtered  $\text{CoK}_\alpha$  radiation of 1.778897 Å at room temperature. Measurements were done in the  $2\theta$  range of 10-100° with a scanning step of 0.05° and 10s scanning time per step.

Obtained diffraction patterns (Figure 6) clearly shows the diffraction maxima crystalline phases that crystallized in the cubic structure in the 225th space group Fm-3m in the Cu-structural type. In addition to these diffraction maxima, weak diffraction maxima can be observed that can be joined at two (in the case of core Cu-0.4%wt. Al) or three (in case of the oxidation zone of the Cu-0.4%wt. Al sample) phases. These are the phases  $\text{Cu}_4\text{O}_3$ ,  $\text{Cu}_2\text{O}$ ,  $\text{Al}_2\text{O}_3$  (diffraction maxima are indicated on diffraction). The presence of these phases in the sample is significant in the oxidation zone of our sample.

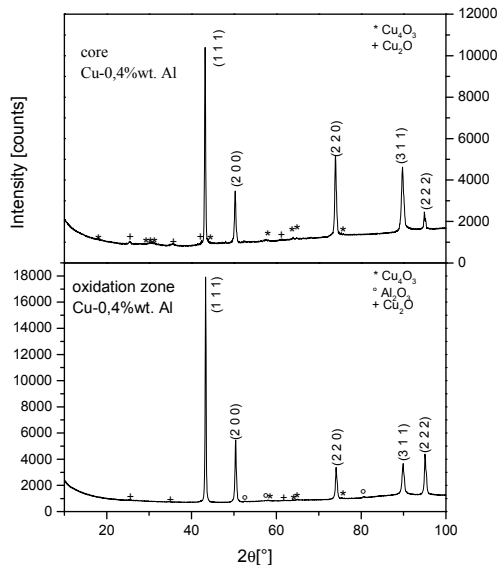


Figure 6: X-ray diffraction pattern of the of Cu-0,4%wt Al samples after ECAP in a longitudinal ( $y$  plane) to the pressing direction.

## **Conclusions**

In our research we investigated the microstructural evolution of multiphase material based on internally oxidized Cu-0.4%wt Al. From the obtained results several conclusions and their analysis have been made:

- With high temperature internal oxidation we obtained homogeneously distributed Al<sub>2</sub>O<sub>3</sub> particles in the coat region of the billet;
- In the core region plastic flow is carried out with sliding of the dislocations;
- In the coat region plastic flow is probably composed of dislocation sliding and gliding along grain boundaries.

## **Acknowledgments**

This article has been supported by EUREKA Programme ORTO-NITI E!6788 within the framework of the Ministry of Higher Education, Science and Technology of the Republic of Slovenia and by the European Union, European Social Fund for young researchers (SPIRIT Agency).

## **References**

- [1] I. Anžel, L. Kosec, A. C. Kneissl; The Creation of Desired Microstructures by Internal Oxidation, *Microsc. Microanal.*, 2005.
- [2] R. K. Islamgaliev, W. Buchgraber, Y. R. Kolobov, N. M. Amirkhanov, A. V. Sergueeva, K. V. Ivanov, G. P. Grabovetskaya, Deformation behavior of Cu-based nanocomposite
- [3] V.M. Segal, V.I. Reznikov, A.E. Drobyshevskiy, V.I. Kopylov, *Metally* 1, 1981, 115
- [4] P.B. Prangnell, A. Gholinia, V.M. Markushev, in: T.C. Lowe, R.Z. Valiev (Eds.), *Investigations and Applications of Severe Plastic Deformation*, Kluwer Academic Pub., Dordrecht, 2000, pp. 65–71.
- [5] Y. Iwahashi, Z. Horita, M. Nemoto, T.G. Langdon, *Acta Mater.* 46 (1998) 3317.
- [6] Y. Iwahashi, Z. Horita, M. Nemoto, T.G. Langdon, *Acta Mater.* 45 (1997) 4733.
- [7] K. Nakashima, Z. Horita, M. Nemoto, and T.G. Langdon; *Mater.Sci. Eng. A*, 2000, A281, 82-87

## An Atomic-Scale Wetting Model of the Liquid Metal/Ceramic Interface

M. Mihailović<sup>1</sup>, A. Patarić<sup>1</sup>, T. Volkov-Husović<sup>2</sup>, K. Raić<sup>2</sup>

<sup>1</sup>*Institute for Technology of Nuclear and other Mineral Raw Materials, Belgrade, Serbia*

<sup>2</sup>*Faculty of Technology and Metallurgy, University of Belgrade, Serbia  
m.mihailovic@itnms.ac.rs*

### Abstract

Wetting of ceramic by liquid metal is the essential step during metal /ceramic joining process. The macroscopic measured contact angle,  $\theta$ , can be interpreted as the bonding quality of the metal/ceramic interface. The wetting properties of the liquid metal/ceramic interface can be strongly affected by composition of the solid and liquid components, surface pattern of the ceramic substrate, and aside of the reactive or non-reactive wetting, by the mechanisms occurring at micro and atomic (nano) level. These have been to some extent investigated using modern experimental techniques, but there is still the need for further investigations and modeling of the wetting at liquid metal/ceramic interface.

The wetting here will be discussed on both, the grain boundary scale and the atomic-scale. The atomic-scale wetting model will be proposed and tested on results published in literature.

*Key words: wetting, metal/ceramic, atomic scale model*

### Introduction

Wetting as an initial stage of the liquid metal to ceramic brazing have been investigated both, experimentally and theoretically for almost two decades [1-5]. There are several theories used to describe interface bonding in the two adjacent components: liquid metal and solid ceramic, materials different due to the different types of atomic bonding [5]. Although such different materials in terms of heat and electric conductivity, as well as hardness, ductility, wear or corrosion resistance, they brought out the advantages of their difference in many contemporary applications when operating together.

Despite the modern experimental techniques, the investigation on the metal/ceramic wetting mechanisms acting on micro- and nano-level is still demanding, both for experiments and theory [5,6 ]. These mechanisms are important for understanding of metal/ceramics interfacial bonding and further process development [3]. The trend in several science fields today is miniaturization, and even the developing towards the nano-scale, both for the sake of sensitive processes and for lowering the costs; whereas for metal/ceramic systems the challenge is the miniaturization of electronic devices [7]. Alongside with new technical development, the new theoretical concepts are also needed.

This consideration starts from the assumption that no chemical reaction occurs at the interface, and all the energy changes in the system are due to the new phase formation.

### Micro-Scale Wetting Mechanism

The well-known fact is that the wetting properties of the liquid metal/ceramic interface are strongly affected by surface structure of the ceramic substrate, such as roughness and other irregularities on the macro level, or grain boundary grooves and lattice pits at micro-scale [6, 8, 9].

When considering the wetting of the real ceramic surface at micro-scale as a wetting process at the grain boundary grooves, the growth of reaction layer can be observed as a two-step process: an initial rapid thickening rate and the second parabolic rate, assumed to be diffusion controlled [6, 10]. The initial rapid layer growth can be related to the substrate surface roughness, while the slower growth may be governed by capillarity. The capillary mass transport reveals by developing a grain boundary groove (GBG) on the surface of a polycrystalline material, wherever a boundary intersects an interface between a solid and another phase.

Mass transport can involve several mechanisms: interfacial diffusion, volume diffusion on each side of the interface, and interfacial reaction. Depending on the physical characteristics of the system and the groove size, one of these mechanisms will control the rate, resulting in characteristic groove shapes and growth kinetics [11-13].

The rate of reaction for the solid ceramic substrate/liquid metal may depend on:

- surface kinetics, which may change with developing of the grain boundary grooves;
- grain boundary groove (GBG) resistance, which sets up internal concentration gradients;
- temperature gradient at the liquid metal/solid ceramics interface, which is caused by heat changes during reaction; and,
- concentration gradients across the liquid metal film (film diffusion resistance).

Surface kinetics and GBG diffusion cannot be treated as steps in series, they influence the rate equation together. When treating interaction of heat and mass transfer resistances, the rate for surface kinetics will be expressed using the first order of reaction:  $-r_A''' = k'''C_{As}\varepsilon$ .

The effectiveness factor  $\varepsilon$ , which value varies between 0 and 1, accounts for the GBG diffusion resistance. Effectiveness factor is equal to 1 for the case of no diffusion resistance, while  $k$  and  $C$  have their usual meaning in kinetics equation. This factor takes into account the Thiele modulus (including an effective diffusivity) and the ratio of ideally flat and nano-structured surface [6].

### Nano-Scale Wetting Mechanism – An Atomistic View

The nano-scale wetting properties have the important influence on the macroscopic wetting behavior of liquids on solid surfaces [4]. Investigations have

been aimed to overcome the various technological problems of metal/ceramic contacts [11, 14]. The nano-scale wetting approach has been studied theoretically [4, 8], looking for the models which could encompass the understanding these phenomena over the several scale ranges. Recently, there are new experimental studies concerning the phenomena on the nano-scale [4].

In evaluating the complete wetting model, an original atomistic view will be considered here. There are difficulties in comprehension the interface bonding of different materials such as metal and ceramic, due to different types of atomic bonding in the two components adjacent to the interface. Metallic bonding bordering the covalent or ionic bonding in ceramics makes indistinct determination which type of bonding exists through the interface. Besides the fact that ordinarily metal and ceramic surfaces are not flat prior to mutual bonding, what causes the interface irregularities, there is a variety of influencing parameters, such as chemical reactions and chemical gradients, steps and facets, dislocation and their networks, that must be considered to understand the nature of interface bonding.

The extensive investigations on the atomistic structure of specific interfaces were carried out using HREM, TEM, AFM, x-ray techniques, ellipsometry and interference scattering from a substrate to determine the wetting behavior. Extensive researches indicated that the crystallographic orientations of the substrate could modify the electronic and atomic structures of the interfaces. The fracture energy of the interface varies upon crystallographic orientation, so for predicting optimal interface strength, the atomic arrangement should be controlled [11]. The well known structures, considered to be the reference, {0001} Al<sub>2</sub>O<sub>3</sub>, {10 $\bar{1}$ 0} Al<sub>2</sub>O<sub>3</sub> and the same metal with its two the characteristic planes: {112} Cu, {123} Cu, will be the frame in evaluation the mathematical model for contact angle calculation in this paper.

Starting from the well known Young-Dupré Equation, the balance of interfacial energies, for the case when liquid metal spreads over the solid ceramic surface, can be expressed with the apparent contact angle  $\phi$ :

$$\cos\phi = (\gamma_{SA} - \gamma_{LS}) / \gamma_{LA} \quad (1)$$

where:  $\gamma_{SA}$ ,  $\gamma_{LS}$  and  $\gamma_{LA}$  are solid-air (i.e. the corresponding atmosphere), liquid-solid and liquid-air interfacial energies, respectively.

This consideration starts from the assumption that no chemical reaction occurs at the interface, and the energy changes in the system are due to the new phase presence. To analyze the net energy,  $E_N$ , of the system liquid metal/solid ceramic surface, the total area of solid-liquid interface ( $f_1$ ) and the total area of liquid-air interface ( $f_2$ ) are considered. When the liquid metal spreads over the unit area of the ceramic substrate, a solid-air interface is destroyed, while the solid-liquid interface forms over the same area ( $f_1$ ). Then, the net energy  $E_N$  of the system (per unit geometrical area) will be:

$$E_N = f_2\gamma_{LA} - f_1\gamma_{LA}\cos\alpha = \gamma_{LA}(f_2 - f_1\cos\alpha) \quad (2)$$

The  $(\gamma_{LS} - \gamma_{SA})$  is the energy,  $E$ , required to form unit area of the solid-liquid interface, which could also be expressed as the energy to form the unit area of the metallic atom/ceramic atom contact. Using this energy expression, the cosine of the apparent contact angle,  $\varphi$ , for the porous surface can be expressed as:

$$\cos\varphi = -E_N / \gamma_{LA} = f_1 \cos\alpha - f_2 \quad (3)$$

Reflecting this analysis onto atomistic approach, while the liquid-solid-air phase relations remain the same, the new dimensions of  $f_1$  and  $f_2$  can be introduced. Areas  $f_1$  and  $f_2$  can be derived from the value  $\alpha$  and the atom packing density in the plane of the crystal lattice along which the contact with liquid metal is established. The atomistic arrangement of atoms in a liquid metal is not entirely random. During melting the crystal structures are being break down, and the average packing density becomes smaller than in solid state. The interatomic forces keep trying to establish original arrangement, at the same time being disturbed by the thermal motion of the atoms. So, the melt is much more alike to the crystal than to the the completely random state of a gas. If the reciprocal atom packing density is denoted with  $s$ , and expressed through atom radius in the plane along which the wetting process occurs in monocrystal, than the total plane area,  $P$ , will be:

$$P = s \cdot \pi r^2 \quad (4)$$

$P_1$  is the ceramic atom surface area in contact with metal atoms:

$$P_1 = 2\pi r^2 \cdot [1 - \sin(\alpha - 90^\circ)] \quad (5)$$

while  $P_2$  is the area of the liquid metal at the metal/ceramic interface, which is not in contact to the crystal lattice atoms:

$$P_2 = P - \pi r_1^2 \quad (6)$$

The contact point of liquid metal atoms in contact with solid substrate atoms is at the distance  $r_1$ , shown in Figure 1.

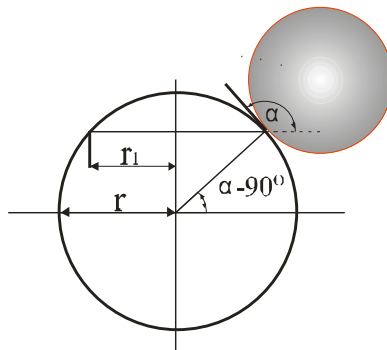


Figure 1 Angles describing the position of liquid metal atoms in contact with ceramic substrate atoms.

According to Fig. 1, it can be written:

$$r_1 = r \cdot \cos(\alpha - 90^\circ) \quad (7)$$

and hence the  $f_1$  and  $f_2$  are:

$$f_1 = \frac{P_1}{P} = \frac{2 \cdot [1 - \sin(\alpha - 90^\circ)]}{s} \quad (8)$$

$$f_2 = \frac{P_2}{P} = \frac{s - \cos^2(\alpha - 90^\circ)}{s} = 1 - \frac{1}{s} \cos^2(\alpha - 90^\circ) \quad (9)$$

Based on this mathematical model, the results of contact angle,  $\varphi$ , calculation, for the characteristic apparent contact angles,  $\alpha$ , of  $90^\circ$ ,  $120^\circ$  and  $150^\circ$ , are:

- for plane {112}Cu, where  $s=2.77$ , the values for calculated contact angle  $\varphi$  are as follows:  $85.2^\circ$ ,  $155.4^\circ$  and  $173.7^\circ$ , respectively;

- for {123}Cu, here  $s=3.29$ , the values for calculated contact angle  $\varphi$  is as follows:  $95.04^\circ$ ,  $157.5^\circ$  and  $173.8^\circ$ , respectively.

The calculated the contact angle  $\varphi$  values indicate the influence of atomic interactions, i.e. the influence of crystallographic orientation on the wetting mechanism at the interface liquid metal atoms/solid ceramic atoms.

The results from this calculation and other theoretical studies [1,2,9] can help in predicting the wetting modification on nano-scale depending on the metal/substrate atomic interactions, i.e. the substrate crystallographic orientation. Moreover, even if nanopatterning of surfaces may result in strong changes of their wettability, some theoretical studies have discovered symmetries, so-called covariances, which bring into correlation the local adsorption/wetting properties of different substrate geometries [9]. This is the direction in which the theoretical models can be developed.

## Conclusion

The wetting phenomena at metal/ceramic interface here is analysed on both, micro- and the atomic-scale. The micro-scale discussion took into account the phenomena in the vicinity of grain boundary grooves.

The atomic-scale wetting model is proposed and tested according to obtained results of apparent contact angles. The wetting effect depends on the structure of crystal lattice and planes orientation.

The results from this combination of approaches should contribute the better understanding of the complex interface wetting behavior and should help in predicting the wetting modification on both, micro- and nano-scale.

## Acknowledgement

The authors wish to acknowledge the financial support from the Ministry of Education, Science and Technological Development of the Republic of Serbia through the projects TR 34002 and P-172005.

## References

- [1] B. Drevet, K. Landry, P. Vikner, N. Eustathopoulos, *Influence of substrate orientation on wetting kinetics in reactive metal/ceramic systems*, Scripta Materialia, Vol.35, No11 (1996) p. 1265-1270
- [2] P. Wynblatt, The effects of interfacial segregation on wetting in solid metal-on-metal and metal-on-ceramic systems, Acta mater. 48 (2000), p. 4439-4447
- [3] G.W.Liu, M.L. Muolo, F. Valenza, A. Passerone, *Survey on wetting of SiC by molten metals*, Ceramics International 36 (2010) p.1177-1188
- [4] T. Hofmann, M. Tasinkevych, A. Checco, E. Dobisz, S. Dietrich, B. M. Ocko, Wetting of Nanopatterned Grooved Surfaces, PHYSICAL REVIEW LETTERS, PRL 104, 106102 (2010) 1-4
- [5] M. W. Finnis, *The theory of metal-ceramic interfaces*, J. Phys: Cond. Mat. 8, (1996) p. 5811-5836.
- [6] K.T. Raic: Ceramics International, Vol. 26 (2000) p.19
- [7] S Dietrich, M.N. Popescu, M Rauscher, Wetting on structured substrates, J. Phys.: Condens. Matter 17 (2005) S577–S593
- [8] Marija Mihailović, Tatjana Volkov-Husović, Karlo Raić, *Micro- and Nano-Scale Wetting of Reactive Metal at Metal/Ceramic Interface*, Advances in Science and Technology, Vol.45 (2006) p.1526-1531
- [9] M Tasinkevych, S Dietrich, *Complete wetting of pits and grooves*, Eur. Phys. J. E 23, (2007) p. 117–128
- [10] K.T.Raic, *Unsteady or starting phenomena at liquid metal/ceramic interfaces*, Advances in Science and Technology, 32, (2003) p. 725-733
- [11] Katusaki Sukanuma, ISIJ Int. Vol 30 (1990), No.12, pp.1046-1058
- [12] E. Saiz, R.M. Cannon and A.P.Tomsia: Acta mater. Vol.47 (1999)p. 4209
- [13] J. Schöllhammer et al.: Z.Metallkd. 90 (1999) 9, p.687
- [14] M. Mihailovic, S. Mesarovic, K. Raic, T. Volkov-Husovic, *Multiscale modelling of wetting during metal-ceramic joining*, Proceedings: 10th International Conference and Exhibition of the European Ceramic Society ECERS, ed. J.G.Heinrich and C. Aneziris, Goeller Verlag, Baden-Baden, (2007), June 17-21, 2007, Berlin, Germany, p. 101-105

## THE THERMIC HARDENING OF Au-Ag-Cu ALLOYS IN JEWELRY PRODUCTION – AGE-HARDENING

R. Perić<sup>1</sup>, Z. Karastojković<sup>2</sup>, Z. Kovačević<sup>3</sup>, D. Gusković<sup>4</sup>

<sup>1</sup> „PERIĆ&PERIĆ“&Co.d.o.o., Serbia, Požarevac, Dunavska 116,  
pericradisa@gmail.com;

<sup>2</sup> Technical College, 11070 Novi Beograd, Serbia, bul. Dr Z. Đinđića, 152 a,  
karastojkovic@visokatehnicka.edu.rs;

<sup>3</sup> Institute for Testing of Materials, 11000 Beograd, Serbia, bul. Vojvode  
Mišića, 43, zorica.kovacevic@institutims.rs;

<sup>4</sup> University of Belgrade, Technical Faculty Bor, 19210 Bor, Serbia, Vojske  
Jugoslavije 12, dguskovic@tf.bor.ac.rc.

### Abstract

Thermic treatment at temperatures below the recrystallization temperature i.e. age-hardening has significant and increasing role in jewelry production. Owing to the ternary Au-Ag-Cu state diagram, alloys used in manufacturing of golden and silver jewelry, can be more easily studied. However, there are still uninvestigated areas in the ternary Au-Ag-Cu alloys state diagram, areas that need to be treated in the proper way. The goal of this paper is to study some of possibilities of getting both semi and final product with desired mechanical properties, by controlling phase transformations by proper thermic treatment. The attempt is to reduce costs this way and also to improve the quality of finished products, especially considering the high price of precious metals.

*Keywords:* 585 gold alloys, 925 silver alloys, age-hardening, hardness, state diagram;

### Introduction

The gold alloys with properties of hardening by thermic treatment i.e. age-hardening, have the important role in production of dental alloys. The phenomena of age-hardening is known for a long time and, it can be said that it has been investigated and used in dental alloys during the whole 20<sup>th</sup> century [1].

In the last few years, there is a constant increase in need for production of alloys for jewelry manufacturing with property or ability to be brought in the state of higher hardness, by proper thermic treatment. This need is in constant increase, especially taking into consideration the increase in value of precious metals in the past decade, which is the highest so far, [2]. Increase in hardness by annealing, in this case, brings material into the state of lower energetic state, where the effect of better polishing is achieved, and also better corrosion stability during the exploitation, [3].

Considering that the amount of gold and silver in alloys for jewelry production is defined by law, [4], the investigation is pointed on alloys with 58.5% of gold, and with 92.5% of silver, that are in fact the matrix for alloy production. The alloying is

conducted for different reasons: the color of gold, hardness, workability, ability of alloy to withstand different types of plastic deformation, ability on soldering and welding, etc. However, the base, that is the matrix of the alloy, is defined by law and projected mass of precious metal should be always kept in mind [5].

It is known that, cold deformation causes strengthening of material, because a part of mechanical energy is accumulated in metal as the energy of different defects in lattice generated during the deformation. This way, the material becomes thermo-dynamically unstable, with constant long for returning into the undeformed state, closer to equilibrium state. However, for turning into the state with lower free energy, activation energy is required for taking place of different necessary processes, such as diffusion, transversal skidding, creeping of dislocations, etc. [6].

The goal of this paper is to present some basic principles while studying the alloys of gold and silver for jewelry production, and also to point to all that should be taken into consideration during the production as well as the influence of different temperatures of annealing on the quality of the final products.

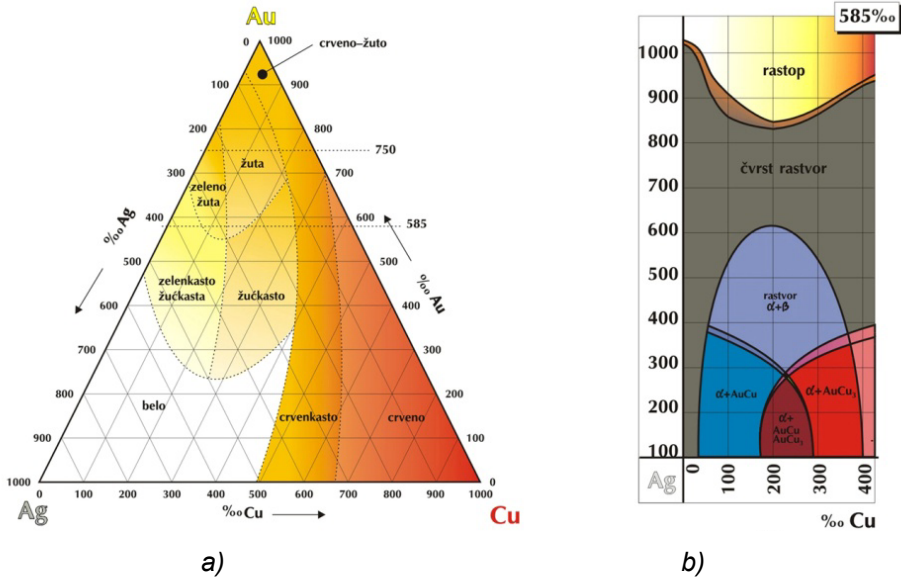
### **Age-Hardening**

Bringing of energy, that is warming of cold deformed metal, brings to change in structure and properties that change gradual, depend on temperature and time of keeping on that temperature. These processes are called *recovery* and *recrystallization*, [7]. Annealing of gold and silver alloys, most often alloyed with metals that crystallize with f.c.c. lattice, on temperatures below the temperature of recrystallization, brings to changes in material, both in macro and micro structure, and this way of thermic treatment is also known as ageing, [8]. By this thermic treatment mechanical properties are changed, strength and hardness are increased, elastic properties are improved, and partly the value of plasticity is decreased.

### **Alloys with gold matrix (58.5% Au)**

Alloys with amount of gold that is defined by law are necessary for the production of jewelry [4], and that is 58.5% of Au, while for the other characteristics of alloy knowledge of influence of other alloying elements is required [9]. For basic quality, the color of jewelry is very important, that is the color of alloy, the color that is considered and accepted in one specific environment (ethnic group, nation, a part of a country, etc.)

In Fig.1 Ternary diagram of Au-Ag-Cu state (a) is represented, along with quasi-binary diagram of state, with "matrix" of 58.5% Au, and with possibility of change in Ag and Cu, as well as with possibility of replacing them with some other elements. Today the most used alloys are Au-Ag-Cu alloys, with addition of other elements, precious and not. Beside Ag and Cu, during the alloying the most often used elements are Zn, Pd, In, Pt and Rh. Also used as micro alloying elements, with mass of alloying element lower than 1,0% are B, Ti, Zr, Fe, etc [9].



a) b)  
 Fig.1.- Ternary diagram of Au-Ag-Cu a) and quasi-binary diagram at 58.5 wt% Au b)

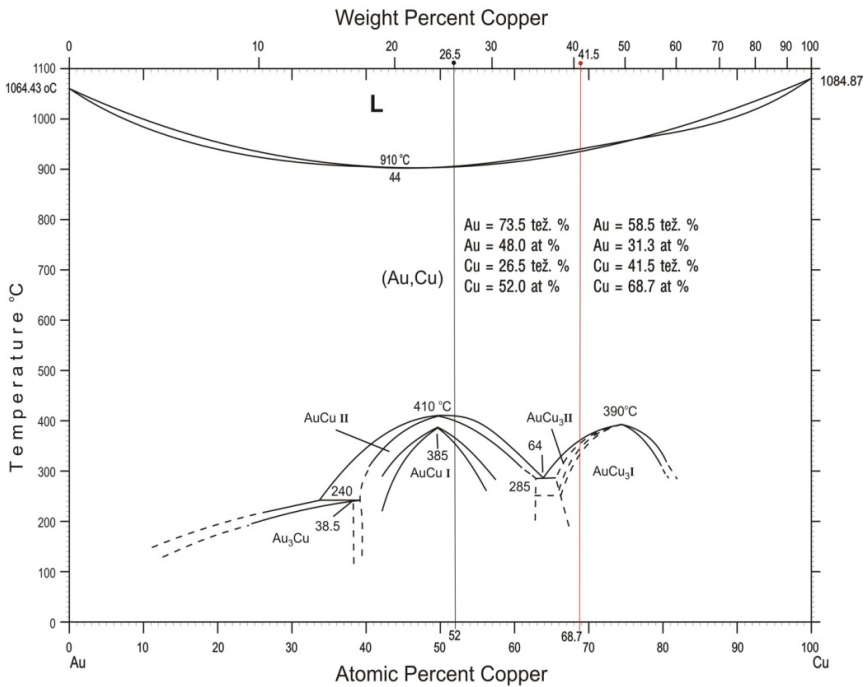


Fig.2.- Phase diagram of the Au-Cu system [10]

In Fig.2 state diagram of Au-Cu is shown, with characteristic property, including the alloy with "matrix" of 58.5% Au, of forming ordered solid solutions: AuCu, Au<sub>3</sub>Cu, and AuCu<sub>3</sub>. Complete discussion on these diagrams would take too much time, so the basic orientation would be on hardening of alloy by annealing on temperatures below the recrystallization temperature that is age-hardening.

### Generating of superlattice in Au-Cu alloys (AuCuI and AuCuII)

In alloys, when single alloying elements crystallize with f.c.c - face centered cubic, lattice, the case in alloys for jewelry production, the effect of hardening of alloy occurs, by annealing on temperature below the recrystallization temperature of single alloys. In metallurgy, this procedure is called *age-hardening* [1,6,8]. The effect of hardening is applied more and more in jewelry production, especially during the production of important elements and parts (covers, different rings, chain production, final annealing of hollow jewelry, earrings, etc.) Researches of other authors, and also my own researches, have shown that this effect occurs only at products treated by plastic deformation (rolling, drawing, bending, deep drawing, etc.).

In Au-Cu alloys, as shown in Fig.2, there is complete solubility in solid state. Both metals have f.c.c lattice, and solid solution is stable up to 684K (410°C), Fig 3a.

At lower temperatures two crystallographic structures occur (AuCuI and AuCuII), [1]. Below 658K (385 °C), ordered phase at f.c.t. - face centered tetragonal lattice AuCuI is stable, where alternately on (002) plane are occupied by even gold or copper atoms, as shown in Fig3b. Because of difference in atom diameter of these two micro constituents, contortion of crystal lattice from f.c.c to f.c.t. occurs, that brings to bigger tension inside material and with that to increase in hardness.

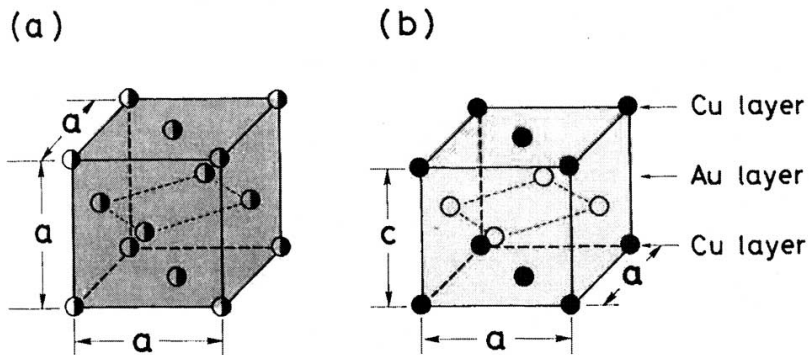


Fig.3 - Schematic view of AuCu I superlattice a) Disordered state with f.c.c lattice b)

In Fig.4 superlattice generated between temperatures of 658K (385°C) and 683K (410°C) is shown - AuCuII, [1,9], and it is of orthorhombic structure.



Most often the effect of twinning can be seen in microstructure as multiple strips, that pass from one side of grain to another, and with straight and parallel boundaries,[6,11]. This phenomena occurs in most of metals with f.c.c. lattice and that is shown in Fig.6,[6].

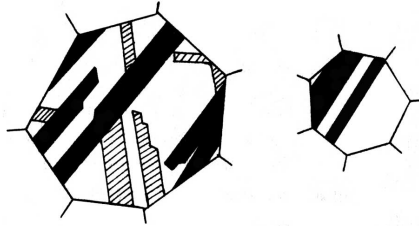


Fig.6.- Strips of annealing twinning in the grain of f.c.c. metal after the annealing [6]

The influence of the effect of alloying of certain elements on generating of super structure, as well as antiphase domain, and therefore twinning was reported in [9,11].

### The alloys with silver matrix (92.5% Ag)

The amount of silver in silver alloys for jewelry production is regulated by law [4], as well. In Serbia, the "matrix" in the manufacturing is 92.5% Ag, while the rest of 7.5% is variable for other different elements, most commonly Cu. For the other characteristics of alloys, knowledge of influence of other alloying elements, and proper treatments is required [12,13].

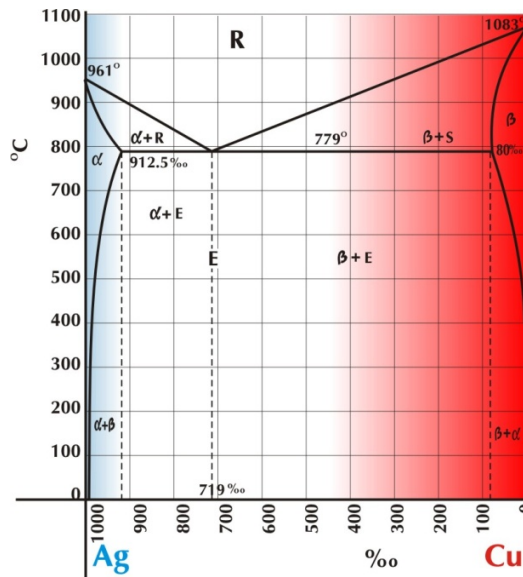


Fig.7.- Diagram of state of Ag-Cu [13]

Different from Au-Cu state diagram on Fig.2, where solubility in solid state is complete, Ag-Cu state diagram represent a simple eutectic system with limited solubility in solid state, shown in Fig.7. Hardening of alloys with silver matrix of 92.5% Ag is by different mechanism of that of Au-Ag-Cu alloys, no matter similarity of Ib group of elements where Au, Ag and Cu belong, [12].

Mechanism of increase of hardness and strength, in 92,5% Ag – 7.5% Cu alloys is achieved by following mechanisms [12]: increase in number of dislocations by cold deformation, increase in number of grain boundaries, generating of solid solutions, generating of phase transformations, through texture creation, creation of composites: by particles and by fiber armoring and by age-hardening [13].

First five mechanisms, hardening and increase in hardness are achieved by direct aggravation of dislocation motion that comes from their compression, often as a result of cold deformation. Hardening by mechanism of creation of composites by particles and fiber armoring, marked as sixth mechanism, that beside generating of dislocations of loops and accumulating of dislocation during cold plastic treatment, also allows hardening of composite because of difference in hardness of single fibers (steel, and so) directly into the matrix.

The special review in this paper is on increasement of hardness by mechanism of thermic treatment of ageing that is annealing on temperatures below the recrystallization temperature, shown in Fig.6. Namely, it is known that in alloys with constituent elements with f.c.c.- lattice, especially with elements of Ib group of periodic system of elements, mechanism of increase in hardness by annealing on temperatures below the recrystallization temperature occurs [6], the case presented here.

### **The Results of Research - Age-Hardening**

Considering the theoretical assumptions given in this paper, the results of researches on four-component alloy Au585Ag90Cu264Zn61, as well as on two-component alloy Ag925Cu75 are presented. Research is conducted by hardness measurement, by Vickers method, with loading of 250gr, HV0.25.

Phenomena that in certain alloys, most often with phase changes in solid state, and that by heating on temperatures below the recrystallization temperature, that is on recover temperature, there is a change of increase in certain mechanical properties (strength, hardness, etc.), is called *age-hardening* [8]. This effect occurs in cold deformed materials, especially in alloys with elements that crystallize with f.c.c.- lattice. By this thermic treatment mechanical properties are changed, strength and hardness increase, corrosion resistance is improved, while plastibility is partly decreased.

### **585/1000 gold alloys**

The results of research on four-component Au585Ag90Cu264Zn61 alloy are shown In Fig.8 and Fig.9. It is visible that the matrix Au 58.5%, is in the alloy. It should be noticed that Zn is used as alloying element in this alloy, and it crystallizes with h.c.p.- lattice, and it is used for the reasons of color, and grain refinement, but also speeding of the process of dispersion hardening. Zn packs in

(002) plane in crystal f.c.c.- lattice [3], so based on this, Zn enters in the AuCuI lattice, especially in case when the ratio of Zn atoms is nearly equal to the ratio of Cu atoms.

Dependence of hardness on annealing temperature is presented in Fig.8. The initial state of samples are cold rolled products with deformation degree:  $\epsilon=66.66\%$  (Group I). Annealing times are 15, 30 and 60 minutes that are actual annealing times applied in the production.

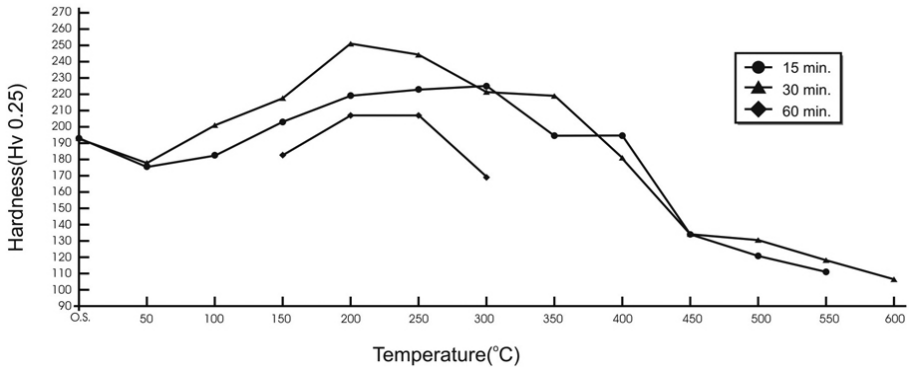


Fig. 8 – Group 1: Changes in hardness with annealing temperature of age-hardening (Representation of the diagram in the plane – two dimensions)

In Fig.9, there is the diagram of the samples, Group II, that were first cold rolled with deformation degree of  $\epsilon=66.66\%$ , and then tempered from  $680^{\circ}\text{C}$ , cooling in  $\text{HCl}:\text{H}_2\text{O}=1:1$ . Then they were annealed on ageing temperatures with different timings of 15, 30 and 60 minutes.

From Fig.8 and 9 it is visible that there is increase in hardness in the part of the diagram with temperature from  $150^{\circ}\text{C}$  to  $300^{\circ}\text{C}$ . These changes in hardness increase are visible on different annealing temperatures. Fig.10, represents a part of the diagram from Fig.7 in "3D", on ageing temperatures from  $150^{\circ}\text{C}$  to  $300^{\circ}\text{C}$ , while in Fig.11, there is a part of the diagram from Fig.8, with the same temperature interval,[3].

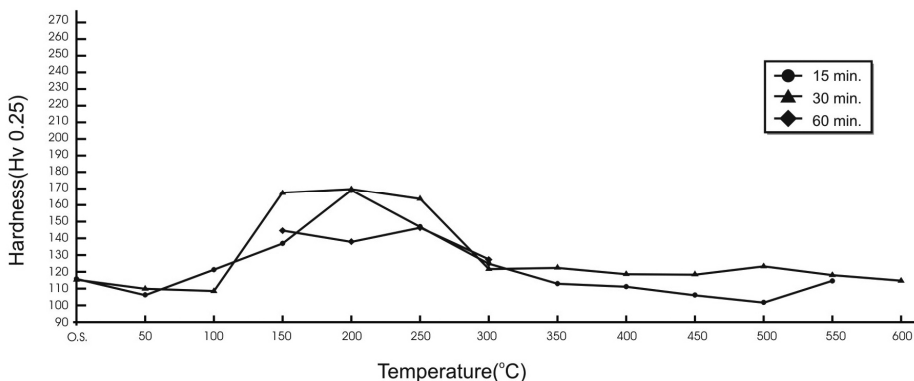


Fig. 9 – Group 2: Changes in hardness with annealing temperature of age-hardening (Representation of the diagram in the plane – two dimensions)

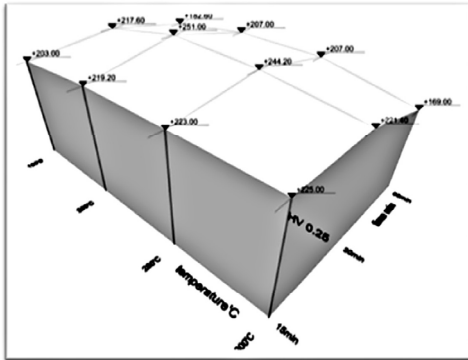


Fig.10. Group 1: Change in hardness depending on annealing temperature age-hardening; Representation of a part of the diagram in „3D“ (three dimensions);

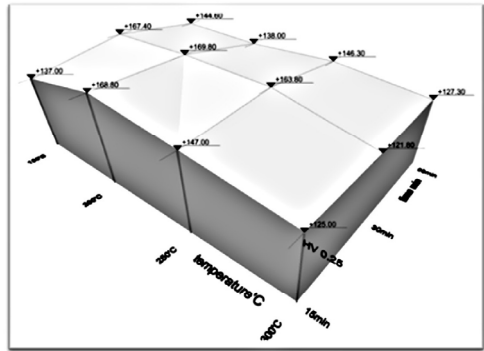
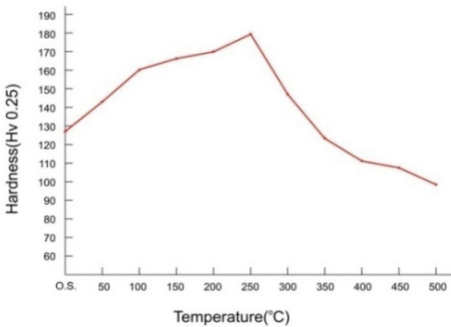


Fig.11. Group 2: Change in hardness depending on annealing temperature age-hardening; Representation of a part of the diagram in „3D“ (three dimensions);

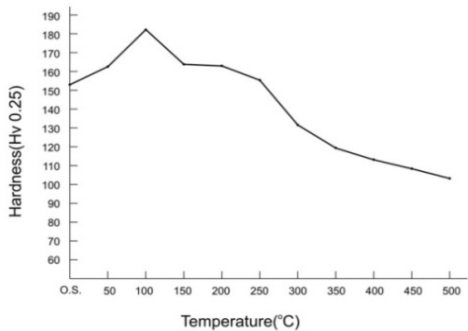
### 925/1000 silver alloys

Changes in hardness generated by thermic hardening - age-hardening, in silver alloys, with matrix of 92.5% Ag, mark 925/1000, are shown in Fig.12.

It is visible that on annealing on ageing temperature, that is on temperature below recrystallization temperature, it comes to increase in hardness and in temperature interval from 100 to 300 °C, and with different previous thermic treatment. It has to be said that in Fig.12,a), tempering is performed from monophase alpha area, and then annealing on ageing temperatures.



a)



b)

Fig.12.- Changes of hardness with annealing temperature in Ag925Cu75 [5]: a) cold deformed samples with deformation degree of  $e=66.66\%$ , subsequently tempered from  $680\text{ }^{\circ}\text{C}$  and b) cold deformed samples with deformation degree of  $e=66.66\%$

## Discussion of Results

Thermic hardening, in alloys of Au-Ag-Cu system for jewelry production, so called age-hardening, is in accordance with theoretical assumptions and literature papers [1,6,8]. In the theoretical part of the paper possible models of hardening of gold alloys with matrix of 58.5% Au, and silver alloys with matrix of 92.5% Ag are presented.

In Fig.8 and Fig.9 on Temperature diagram (C) - Hardness (HV0.25), there are changes in hardness depending on ageing temperature, for Au585Ag90Cu264Zn61 alloy. Fig.8, shows change in hardness in products that first were cold deformed, by cold rolling, with deformation degree of  $\epsilon=66.66(\%)$ . As it can be seen from the diagram, the optimal change in hardness generate in temperature interval from 150 to 300°C. After this temperature value hardness starts to decrease, so that it would, on 600°C, entered in the value of recrystallization hardness [3]. Maximum hardness, achieved in temperature range 150 to 300°C, as shown in "3D" diagram, in Fig.10, for different annealing timings, is 251.96HV0.25, that is, regarding to initial hardness of 191.00HV0.25 increased by 31.9%. Parameters where maximum hardness is achieved are: timing 30 minutes, and temperature 200°C. In Fig.9 and Fig.11, there is change in hardness in products that, after cold deformation of  $\epsilon=66.66(\%)$ , were tempered/quenched from 680°C, and with initial hardness of 115.00HV0.25. By annealing, on low temperatures, in temperature range from 150°C to 300°C, increase in hardness occurred, up to max. 169.8HV0.25, with parameters: timing 30 minutes, and temperature 200°C. During this treatment increase in hardness of 54.8HV0.25, in absolute amount, or for 47.6%, occurred. By further increase of temperature decrease in hardness occurred, to the value of initial hardness, that is to the recrystallization hardness. The effect of hardness increasement can be interpreted by changes generated, and explained, in Fig.1, to Fig.6. In both cases, besides twining, [1,3,6], there is the effect of ordering and generating of AuCu phase, [1,3], during heating and cooling.

Fig.12a) and Fig12b), show diagram of Temperature (°C) - Hardness(HV0.25), for Ag925Cu75 alloy, with the same treatment of product, as explained for the gold alloy. In Fig12b) the results for cold rolled products are shown, while In Fig.12a) there are the results for cold rolled and then tempered products, from monophase alpha-area, Fig.7. As it can be seen from the diagram, increase in hardness is in temperature range from 50 to 300°C. In Fig12a) there is shown that from 127.00HV0.25 in initial tempered state to 179,4HV0.25, on annealing temperature of 250°C and annealing timing of 30 minutes, there is increase in hardness of 52.4HV0.25, or 41,0%. Fig.12b) shows the formed difference in hardness, in cold rolled samples, from 153,00Hv0.25 in initial state, to 182.20HV0.25, on annealing on temperature of 100°C, and annealing timing of 30minutes. This way, increase of 29.20Hv0.25, or 19.00% is achieved, [14]. The effect of increase in hardness, in alloy with Ag925 matrix, that is Ag925Cu75, can be achieved with occurrence of annealing twinings, [6,13,14]. The Ag-Cu state diagram is a simple eutectic diagram, without known phase changes in solid state [12].

## Conclusion

Based on everything written, and also on results of practical researches, the next conclusions can be made:

- The phenomena of thermic hardening by annealing, on temperatures below the recrystallization temperature, are evident and it exists in alloys of Au-Ag-Cu system for jewelry production. That is shown, both by the citation from the theoretic papers, and by the hardness measurements, and achieved results for alloys used in jewelry production.

- Alloys used for this research are Au585, and Ag925, predicted by law for jewelry production in Serbia. Alloys with different matrix are foreseen, but their use is minor.

- Mechanism of increase in hardness in Au585 and Ag925 alloys, beside the difference in structure because of ordering of crystal lattice in Au-Cu system, there is similarity in occurrence of annealing twinings, considering that all the components of the Au-Ag-Cu system, crystallize by f.c.c.- lattice. Zn lattice is h.c.p., but there is a possibility that, in alloys with most components with f.c.c.- lattice, Zn distributes by plane (002) of f.c.c.- lattice, so it has no influence on order degree of the structure: AuCu, Au<sub>3</sub>Cu, AuCu<sub>3</sub>.

- Application of the thermic hardening in the process of jewelry production is varied, starting with improvement of surface quality for more quality polishing and more quality appearance of product, through production of elements of technical support (covers, rings, special effects, etc.) that are loaded more in finished products, to improvement of jewelry parts, where during the process of production there are soldering and welding applied. It can be said that soldering and welding, as technological operation during the jewelry production, are used in about 99.0% of products.

## References

- [1] K.Yasuda, Age Hardening and Related Phase Transformations in Dental Gold Alloys, Gold Bulletin, 1987, 20(4), p.p. 90-103;
- [2] www.kitco.com;
- [3] R.Perić, Z.Karastojković, Z.Kovačević, D.Gusković, Age-Hardening Effect of Au585Ag90 Cu264Zn61 and Application in the Manufacture of Jewelry, Metalurgia International (2013), SP-4, p.p. 352-361;
- [4] R.Srbija, Zakon o kontroli predmeta od dragocenih metala, Sl.glasnik R.S., br.36/ 2011;
- [5] R.Perić, Z.Karastojković, Z.Kovačević, D.Gusković, Starenje legura zlata za proizvodnju nakita, Zbornik radova, D-HTM, Požarevac, (2012), p.p. 86-94;
- [6] B.Perović, Fizička Metalurgija, NIO, „Univerzitetska riječ“, Univerzitet „Veljko Vlahović“ u Titogradu, Podgorica, (1984), p.p.396-417;
- [7] H.Šuman, Metalografija, Udžbenik, (1965);
- [8] P.Gertik, Plemeniti Metali, Beograd, (1997), p.p. 167-227;
- [9] R.Süss, E.v.d.Lingen and L.Glaner, 18 Carat Yellow Gold Alloy With Increased Hardness Physical Metallurgy Division, Mintek, Priv.Bag x 3015, Randburg 2125, South Africa, Gold Bulletin, (2004), 3713-4, p.p. 196-207;
- [10] H.Okamoto, D.J.Chacrabarti, D.E.Janghlin & Massalski, The Au-Cu System,

- Bulletin of Alloy Phase Diagrams, Vol.8, No. 5, (1987), p.p.454-473;
- [11] R.Perić, Z.Karastojković, Z.Kovačević, D.gusković, The Age-Hardening Mechanism of Au585Ag90Cu264Zn61 Gold Alloy for Jewelry Production, III Int.Kongres, Jahorina, R.Srpska, Proceedings;
- [12] V.M.Mališev, D.V.Rumjancev, Srebro, Moskva, „Metalurgija“, (1987) p.p.75-97;
- [13] R.Perić, Z.Karastojković, Z.Kovačević, D.Gusković, Changes of Mechanical properties of Ag925Cu75 in Ageing Process, D-HTM, Proceedings, (2011), p.p.74-81;
- [14] R.Perić, Z.Karastojković, Z.Kovačević, D.Gusković, Hardness Changes in Ag925Cu75 Jewel Alloy After Tempering of As-Casted, Rolled and Queched States, 43<sup>rd</sup> IOC on Mining and Metallurgy, Proceedings, Kladovo (2011), p.p. 171-174.

## OPTIMIZATION OF THE MINERAL RESOURCES VALORIZATION IN NON-FEROUS METALLURGY OF THE REPUBLIC OF MACEDONIA

A. Efremov

*e-mail: antonie.efremov@gmail.com*

### **Abstract**

Non-ferrous metallurgy is a strategic industrial branch in the Republic of Macedonia. The country possesses significant competitive advantages for achieving farther intense development of non-ferrous metallurgy. Macedonia disposes mineral resources of all significant heavy non-ferrous metals, existing mine facilities for ore exploitation and the smelting facilities for production of zinc, lead and ferroalloys of the non-ferrous metals.

Despite their competitive advantages, serious problems exist resulting from the unharmonized relationships between the installed mining and smelting capacities for production of lead and copper and temporarily shut down the ISP smelter in Veles since 2003. The subject paper presents the basic data related to the domestic mineral resources, the concept for revitalization of existing smelter and building the new metallurgical complex for processing of the surplus of domestic lead and copper concentrates. In addition, the economics for integrated zinc, lead and copper smelting complex is evaluated.

*Keywords: ISP, smeltings, mine, raw materials, coke*

### **Ore reserves and mine production of lead, zinc and copper in Macedonia**

According to the size and quality, the deposits of lead-zinc ores, which are mostly located in the exploitable fields of the three existing mines in northern-eastern Macedonia, is of biggest importance. At the end of the last decade, the reserves of lead-zinc ores amounted to 39,2 million tons of ore with an average content of 1508200 tons of lead, 975100 tons of zinc and 1200 tons of silver<sup>1</sup> [1]. Last year market value of this ore reserves was 5,5 billion US Dollar. According the last report of Euromines for world mining production, in 2010 Republic of Macedonia is second lead producer and fifth producer of zinc in Europe<sup>2</sup>. The Macedonian mines Zletovo, Sasa and Toranica were built with the total annually capacities for ore treatment of two million tons. Taking into account the existing economic condition in the Republic of Macedonia and the efforts for strict carrying out of sustainable development, a regime of exploitation of the domestic mines

---

<sup>1</sup> Exploitive ore at the input of concentrator plant

<sup>2</sup> Annual mining production of 41300 tons of lead with a share of 17,8% in Europe and 0,3% in World, i.e 32900 tons of zinc with a share of 3,8% in Europe and 0,3% in World.

which corresponds to utilization of 77% of the installed capacities is proposed for the future development of the non-ferrous metallurgy. In such conditions, the domestic mines should realize annual production up to 74500 tons lead concentrates and 65800 tons zinc concentrates with a total content of 54100 tons of lead, 33000 tons of zinc and 34 tons of silver. The available resource potential is sufficient for continuous operation of the domestic mines in the next 26 years. The lead mine production will be treated in a new lead smelter. Domestic mines can also provide for 57% share of total need of zinc concentrates for this Smelter.

Bucim Copper Mine is in operation since mid 1979. The mining and process facilities are designed for maximal ore treatment capacity of 7,2 million tons per year. Actually exploitation of the mine is at an annually rate of 4,5 million tons, i.e. 35 to 38 thousand tons production of copper concentrat. In June 2008 EurOmax Resources Limited from Canada has announced the results received from exploration of the Ilovitza copper-gold deposit in Macedonia. The first results conclude that the deposit contains an inferred resource of 303 million tones grading 0,23% copper, 0,31 grams per tone gold and 0,005% molybdenum, or 0,51 copper Eq%. This is an excellent first step for investigation of the deposit, and it is assessed as one of the largest undeveloped copper-gold resources in Europe [2]. Recent publicated data on available ore reserve is 375 million tons with a content of 790000 tons of copper and 95 tons of gold. Last year market value of the Macedonian copper ore reserves was 9,2 billion US Dollars.

### **Metallurgical production of zinc and lead in the Republic of Macedonia**

The smelting production of zinc and lead in the period 1973-2003 was realized within the smelter of MHK Zletovo, located in Veles. The smelter is designed to produce market grades of zinc, lead, cadmium and silver. The installed annual capacity is 105000 tons of slab zinc and lead bullion, and 145000 tons of acid sulfuric. The slab zinc and lead bullion are treated in two refining plants, that are also provided with the sections for production of alloys and chemical products. The installed annually capacity of Chemical Complex is 50000 tons of phosphoric acid, which is finalized into 150000 tons of mineral fertilizers. MHK Zletovo use the Imperial Smelting Process. Author of this paper has carried out cumulative mass balance for the heavy metals and sulfur for the period 1973-1995. This calculation shows that the unallocated losses were 5,5% at zinc, 10% at lead, and 18% at cadmium of their quantity in the used concentrates. The investigations have also shown that the main pollution problem is the use of one-step agglomeration roasting of concentrates, due to the high dust generation in the process. Aerosols and aero sediments are the biggest transmitters of heavy metals to the environment. The way of transmission is mostly by uncontrolled, i.e. fugitive emission.

There are two concepts for revitalization and improvement of environmental protection of the existing smelting complex, the both were evaluated in the period 1996-1997. The first concept that based mainly on installing the new filters does not fulfill the needed goal for resolving environmental problems. The reason is that at the dust generation rate of 200 tons per day, cleaning efficiency of 99,5% and

achieved dust content in de-dusted gases of 10 mg per m<sup>3</sup>, achieving environmental protection can be provided by operation with a total volume of 4,17x10<sup>6</sup> m<sup>3</sup> of gasses per hour, or 5 times more than actual situation. This regime of operation has no reason, neither from technical, nor from economical point of view [3].

The concept for revitalization of the existing smelting complex proposed by the author of this paper is based on application of several innovative solutions for reduction of the dust generation through impact in the pollution sources, i.e. by implementing preventive environmental protection. The proposed concept is mainly based on ecological unburdening of the city of Veles with transformation of used Imperial Smelting Process into wasteless technology, dislocation of toxic by-products processing of the existing smelter on the location of Chemical Complex, and so on [4].

The Imperial Smelting Process for producing zinc and lead in a blast furnace has been in commercial operation in 13 countries since 1959. In the period 2002-2003 the economics of the Process became extremely difficult as they became squeezed between low metal prices and continually increasing operating costs. This resulted in the closure of the ISP smelters in United Kingdom, Australia, France, Macedonia and Italy. The Smelter in Macedonia had been affected for years by the political turmoil in the Balkans. These had affected its markets and transportation of raw materials and left the smelter in a fragile economic state. The cessation of the production of domestic concentrates and the falls of the zinc price led to a decision to shut down temporarily.

A major advantage of the ISP was its ability to consume bulk concentrates and secondary materials due to their low costs. The ISP has a disadvantage compared to the electrolytic process, in that smelter outputs are much smaller than many of the modern electrolytic smelters. Disadvantages are also scheduled shutdowns and long duration maintenance on the Sinter plant and the need for condenser cleanouts every three weeks. The dependence of the ISP on metallurgical coke and its continuing high price represents a serious threat to the future of the ISP. Because of their access to indigenous raw materials and their low labour costs the main future of the ISP will lie in India and China [5].

### **New Lead and Copper Smelter**

The problem of environmental pollution by toxic emissions from metallurgical plants is urgent for all countries, producing non-ferrous metals. It is undoubtedly that solving of this problem is impossible without modernization of metallurgical production and implementation of environmentally save technologies. The most used conventional technology for world lead production, i.e. "Roasting and agglomeration of raw materials and blast smelting of agglomerate" does not meet requirements of international ecological standards. Advantages of modern direct lead smelting processes are not only ecologically cleaner, but also more effective energetically in comparison with conventional technology. They require less energy consumption and do not need using of expensive blast-furnace coke. Direct smelting of lead-bearing materials is carried out in more smaller, compact and sealed units at minimum heat losses through the walls and minimum harmful gases

and fumes leakage into atmosphere. Using oxygen or rich oxygen-air mixture provides minimal flows of high sulfurous smelting gases, facilitating their cleaning from dust and utilization of sulfur dioxide. Technologies of direct smelting are also in possibility to reduce power consumption by using waste heat generated from burning of sulfide concentrates. At present, five processes for direct smelting of raw materials in industrial exploitation are used in world for lead production. Method of direct "bubbling smelting" using different ways of air-oxygen blast injection into liquid bath is implemented at QSL, TSL and SKS process. Method of direct "flash smelting" of powdered raw materials, fed through burners with oxygen-bearing gas flow is implemented at KIVCET and Outokumpu (process for direct smelting of copper concentrates). Kaldo TBRC process use top nonsubmerged lance feeding of raw materials, coal and oxygen.

Integrated metallurgical complex for lead, zinc and copper should advisably be oriented on "flash smelting" processes, because only they provide effective and stable smelting to produce lead bullion and blister copper from raw materials of different grade. KIVCET process has no comparable analogues among existing lead smelting technologies<sup>3</sup>.

Other temporary technologies for direct smelting operate with high grade raw material (more then 44% lead content in charge) and limitations on content of iron, zinc and copper in raw material due to the presence of intensively agitated bath of rich lead slag and high volatility of lead compounds. The KIVCET process is continuous and provides comparably highs speeds of oxidizing and reducing smelting stages combined in one smelting shaft. It provides minimum residence time of volatile lead compounds in high temperature melts and low degree of lead distribution into smelting dusts. Advantage of KIVCET process is also unit campaign of 2 to 3 years [6].

### **Concept for building of lead and copper smelters**

To support the Macedonian lead-zinc and copper mines economy, there is a need to use existing and build two new smelters. The Imperial Smelting Process, despite its weaknesses, is planned for further usage in the treatment of bulk concentrates and secondary zinc bearing materials. The investment projects that should make possible processing of the surplus of domestic lead and copper mining production was intensively worked out in the period 1980-1990. The development activities resulted in proposals for building of two new metallurgical capacities for autogenously flash smelting of concentrates by technologies that provide optimal environmental protection [7, 8]. The construction of the new smelting capacities is anticipated in the frameworks of the fertilizers production complex located 12 km southeast from the city of Veles, to which the most risky process plants from the existing smelter should be dislocated [9].

Basic data related to the needed raw materials for realization of metallurgical production are given in the Table 1.

---

<sup>3</sup> Cominco Kivcet Lead Smelter has been processing all residues from Trail Zinc Smelter in Canada for production 120 thousand tons of lead bullion per year, having the average level of content in charge 33% at lead (minimum 20%), 10,4% at zinc, 15,6% at iron, etc.

Table 1: Annually input of metals in smelters (in thousand tons, gold and silver in tons)

Raw materials	Zinc/Lead Smelter			Lead Smelter		Copper Smelter		
	zinc	lead	silver	lead	silver	copper	gold	silver
Total input	76,9	27,9	51,2	103,3	76,8	64,1	4,937	34,1
Domestic origin	41,8	4,3	4,4	58,8	29,7	36,9	2,630	18,9
Shear (%)	54	15	9	57	39	58	53	55

Based on a treatment of the above presented raw materials, Zletovo Smelter will produce 71200 tons of SHG zinc, 21350 tons of refined lead, 46 tons silver, 270 tons cadmium, 16 tons indium, 2500 tons copper matte and 92600 tons of acid sulphuric. In the same time, the new Lead Smelter will produce 100000 tons of refined lead, 75 tons silver, 20 tons bismuth, 3300 tons copper matte and 90500 tons of acid sulphuric. By treating the above presented raw materials, the new Copper Smelter will produce 62950 tons of cathode copper, 4694 kg gold, 32 tons silver, and 148900 tons of acid sulphuric. The total production of acid sulfuric will achieve up to 332000 tons, which is more then two times of the available capacity of MHK Zletovo Chemical Complex.

### Evaluating the economics of the smelting processes

The assessment of the economics of smelting processes is performed on the base of 5 years average LME settlement price for a period 2008-2012 as follows (in US\$- 2012): 2033 \$/t of zinc, 2151 \$/t lead, 7509 \$/t copper, 3612 \$/t cadmium, 21878 \$/t bismut, 41650 \$/kg gold, 766 \$/kg silver, 580 \$/kg of indium.

The annual interest rate of 7,5 percent for a ten years period of loans return (at the copper smelter for 25 years), as well as the share of foreign capital expenditures of 51 percent are taken into account for the economics evaluation of the projects. The estimated capital costs<sup>4</sup> are prepared by factoring and escalating of the costs presented in the suitable proposal and in a published paper. The operating cost estimate is evaluated, using unit costs applicable to the Republic of Macedonia. In this conceptual stage, where the feasibility of general reconstruction of Zletovo ISP Smelter and building of new lead and copper smelter is being analyzed, it is intended to present only a general indication of their rate of return. Smelter's revenues related to 100 percent of installed capacities are estimated on the base of a previous prepared investment and other documentation, published data related to the treatment charge and suitable analyzes prepared by the author of this paper. Relevant figures are presented below.

<sup>4</sup> 160, 190 and 255 million US dollars-2012 for zinc/lead, lead an copper smelter, respectively.

Table 2: Estimated rate of return on investment (in million US\$ -2012 per year)

Item	Zinc/Lead ISP Smelter	Lead Smelter	Copper Smelter
Smelter revenue	117,7	114,3	114,5
Operating cost (with depreciation)	78,8	30,5	38,1
Operating profit	38,8	83,7	76,4
Estimated rate of return, %	24,3	44,0	30

*Comment:* The estimated rate of return (ERR) is very good for all three smelters.

The most important economic highlights of the smelters obtained from the financial analysis are presented in the table below.

Table 3: Economic highlights of the smelters (in million US\$-2012 per year)

Item	ISP Smelter	Lead Smelter	Copper Smelter
Gross metal sales	278,3	324,6	717,0
Net cash flow before tax	18,5	32,5	24,6
Pre-tax IRR, %	10,4	17,8	14,6
Pre-tax NPV (7,5%), million US\$	21,8	98,5	174,3
Net hard currency income	103,3	162,8	424,5

*Comment:* All above presented figures related to the pre-tax internal rate of return of the investment (IRR) and pre-tax Net Present Value (NPV) are acceptable. Total annual gross metal sales achieves 1,32 billion of US dollars. The total annual net hard currency income of 690 millions dollars is very high and it can cover important part of estimated country deficit in the export/import of goods and services.

In Table 4 the data of the sensitivity analysis that indicates approximate effect on the ERR and IRR are given below. For the ISP and Lead smelter the operating rate has most sensitive impact upon the profit (+/-39%; +/-24%), while for the copper smelter it is the price change of metals (+/-42,5%).

Table 4: Sensitivity analysis at the 100% use of installed capacities (effect are given in %)

Variation +/-10%	Zinc/Lead Smelter		Lead Smelter		Copper Smelter	
	ERR	IRR	ERR	IRR	ERR	IRR
Base metal price	10,3/-10,3	39,8/-43,1	7/-7	20,6/-15,0	12,0/-11,7	29,9/-31,8
Treatment charge	11,5/-11,5	36,9/-39,8	4,2/-4,2	20,2/-15,4	8,3/-8,0	17,8/-18,5
Energy cost	-15,4/15,8	-54,7/49,5	-1,4/1,4	-4,5/4,4	-1,0/1,3	-2,5/2,5
Capital cost	-11,4/14	-41,4/46,6	-10,6/13	-26,8/30,7	-11,0/13,7	-17,4/20,5
Operating rate	18,6/-18,5	58,3/-65,8	12,7/-12,7	28,3/-30,3	11,3/-12	21,3/-22,6

Comment: Variations in operating rate has most sensitive impact upon ERR and IRR for the ISP and Lead smelter, while for the copper smelter it is the price change of metals. Variations in the energy costs is of significant importance only for the Zinc/Lead Smelter.

## **Conclusion**

There are real possibilities to establish very important integrated production complexes in the national non-ferrous metallurgy. The mineral resource base is sufficient for future development of industrial capacities, especially for lead, copper, phosphoric acid and mineral fertilizers production. The proposed technological solution will assure acceptable environmental protection. The integrated production complexes will assure annual 690 millions dollars net hard currency income and 1,32 billions of US dollars gross metal sales. The future development of Macedonian non-ferrous metallurgy should be assured by introducing of a suitable national policy in the exploitation and metallurgical treatment of mineral resources.

## **References**

- [1] Extended summary of "Elaborates for geological ore reserves in the deposits of Zletovo, Sasa and Toranica mines", Ministry of Economy, Skopje, 2002
- [2] "Preliminary Economic Assessment on the Ilovica project", [www.euromaxresources.com](http://www.euromaxresources.com), December 5, 2012
- [3] "Ecological Study of Technological Solutions for Pollution Protection the city of Veles from Zletovo Smelter", ATREZ Ltd- Skopje, 1997, pg. 49 table 3-4, pg. 50 table 3-6
- [4] A. Efremov, "Revitalization and new technologies in non-ferrous metallurgy of Republic of Macedonia", Second International Scientific Conference on Metallurgy of Non-Ferrous & Rare Metals, Krasnoyarsk- Russian Federation, September 9-12, 2003 (Paper published in Tsvetnye Metally No 3/2004)
- [5] R. W. Lee, "Whither the Imperial Smelting Process?", Lead & Zinc '05 Conference, Kyoto, Japan, October 17-19, 2005
- [6] V.A. Shumskiy, "Role of the raw material grade at the lead smelting process selecting", SA "VNII tsvetmet", Ust-Kamenogorsk, Kazakhstan Republic
- [7] "Feasibility Study for Construction of a Lead Smelter", Mining Institute-Metallurgy and Inorganic Technology Department - Skopje, February 1989
- [8] A. Efremov, "Report on autogenously smelting of copper and nickel concentrates", Specialization in Outokumpu Copper&Nickel Smelter, Hariavalta, Finland, November 1979
- [9] "Study of Economic Development of Veles Municipality", Agency ATREZ Ltd, Skopje Republic of Macedonia, September 2001, pg. 45 and 46

## **MATERIAL CHARACTERIZATION OF 1Cr0.25Mo0.25V POWER PLANT STEEL AFTER PROLONGED SERVICE**

G.Bakić<sup>1</sup>, V. Šijački-Žeravčić<sup>1</sup>, M. Đukić<sup>1</sup>, V. Maksimović<sup>2</sup>, B. Rajičić<sup>1</sup>

<sup>1</sup>*Faculty of Mechanical Engineering, University of Belgrade, Kraljice Marije 16, 11035 Belgrade, Serbia*

<sup>2</sup>*Institute of Nuclear Sciences Vinca, University of Belgrade, PO Box 522, 11001 Belgrade, Serbia gbakic@mas.bg.ac.rs*

### **Abstract**

Changes of mechanical properties and microstructure of specimens, which were taken from pipelines, made of heat resistant steel 1Cr0.25Mo0.25V after approximately 200000 hours of service at temperature of 540°C and stress 70MPa are considered in this paper. Also, the initial specimens, made of same steel that had not been at service were investigated. Results obtained by different experimental technique show that microstructural degradation had been dominant process during prolonged service in creep conditions, which lead to the changes of mechanical properties. Microstructural degradation and damages, like creep cavities and oxidation on internal surface of pipe, were observed. The changes of mechanical properties and significant decrease of hardness and micro hardness during service are explained by different processes that take place during microstructural degradation.

*Key words: heat-resistant steel, microstructural degradation, creep damages*

### **Introduction**

In materials subjected to creep mechanical strength and deformation properties were mutually correlated, and for a given geometry, they depends exclusively on current state of material and dynamics of the processes which occurring in it. Apart from service conditions (stress and temperatures) microstructural degradation, as a long-term diffusive process, always take place under conditions that are usual for power plants and it causes a changes in mechanical and fracture behavior of material. Taking these facts in consideration, it is obvious that the evaluation of deterioration of commercial low-carbon, low-alloy CrMoV steels after long-term service can provide the new data for residual life estimation. Microstructural degradation during prolonged service of 1Cr0,25Mo0,25V steel at real service condition ( $T=540^{\circ}\text{C}$ ,  $\sigma=70\text{MPa}$ ) are considered in this paper. For this purpose several specimens were taken from the main steam pipelines after service of ~200000 hours. Also, the initial specimens, made of same steel that had not been in service were investigated.

### **Material and experimental technique**

Specimens were taken from investigated main steam pipelines made of 1Cr0.25Mo0.25V (12H1MF, GOST) low-alloy heat-resistant steel, designed for

long-term service in the 540-580°C temperature range. Typical heat treatment of this steel consists of normalization (960-980°C) and tempering (740-760°C) [1,2] which provide ferritic-pearlitic-bainitic microstructure with carbide precipitations. This paper presents an analysis of the results obtained by extensive testing of specimens cut from the high-pressure main steam pipelines after service of ~200000h (specimen B) and the specimens in the initial state (specimen A). The main objective of this study was microstructural characterization of material after long-term service and comparison with initial state. Analysis of chemical composition was performed by mass spectroscopy, while for the hardness measurement stable Vickers hardness device, type TP-7R-1, was used. Grain microhardness was measured by the optical microscope type Leitz, Jena with application of 5gr load. Specimens for scanning electron microscopy (SEM) examination of the microstructure were prepared in the standard way, by cutting, grinding, polishing, etching and vapor deposition of gold. A metallographic examination was carried out on scanning electron microscope, type JEOL JSM-6460LV at different magnifications. In order to identify the chemical content of alloying elements Energy-dispersive X-ray spectroscopy (EDS) analysis of ferrite matrix and characteristic phases were performed. SEM micrographs at low magnification (500x 200) were used for linear analysis in order to determine the proportion of perlitic-bainitic phase, as well as the average grain size according to ASTM. Quantitative analysis, using SEM micrographs with dimensions of 1024 x 900 pixels and software program KVI POPOVAC, provided determination of the grain size on the basis of linear analysis results. As a benchmark for determining the grain size GOST 5639-82 standard was used.

### Results and analysis

The results of chemical composition analysis of specimen of the initial material and specimen after long-time service (~200000 hours), as well as the standard recommended values for 12H1MF steel, are given in Table 1. Content of analyzed alloying elements in specimens do not differ essentially, and hence they passed a similar heat treatment, they can be considered to be fully comparable.

Table 1: Chemical composition analysis of specimens by mass spectroscopy

Spec.	C	Si	S	P	Mn	Ni	Cr	Mo	V	Cu
A	0.123	0.280	0.020	0.003	0.624	0.131	1.100	0.271	0.210	0.013
B	0.122	0.284	0.022	0.004	0.588	0.215	1.130	0.278	0.167	0.028
TU 14-3-460-03 12H1MF	0.08-0.15	0.17-0.37	≤ 0.025	≤ 0.025	0.4-0.7	≤ 0.25	0.9-1.2	0.25-0.35	0.15-0.3	≤0.2

The results of hardness and microhardness, Table 2, show that the hardness and microhardness of ferrite grains during long-term operation decreased significantly. This data is an important indicator of the impact of long-term service on the material microstructural changes and development of microstructural degradation, particularly due to the depletion of the solid solution due to the transfer of alloying elements in the carbide phase [1-4].

Table 2: Hardness and microhardness of specimens

Specimen	Microhardness of ferrite grains, HV <sub>0,05</sub>	Hardness, HV <sub>30</sub>
A	155-168	168-173
B	120-128	121-130
TU 14-3-460-03 for 12H1MF	-	137-199

Typical microstructure of the specimen in initial state (specimen A) is shown in figure 1. Microstructural examination revealed that the material in the initial state is characterized by a typical homogeneous ferritic-pearlitic-bainitic microstructure with 13-15% of perlite-bainite microconstituent and grain size No. 7-8 (ASTM). In addition to these phases, also carbides with different morphologies, primarily spherical and rod-shaped, segregated in grain and along grain boundaries are present, as a result of tempering. Different types of non-metallic inclusions were present, mainly sulfide and oxide type. In their initial state, it was characterized by a continuous inclusion-matrix interface.

Specimen B (200000h service time), basic microstructural phases are ferrite and carbides of different morphologies, figures 2 and 3. Figure 3 shows the details of the main microstructural features: the shape and size of carbides at grain boundaries and spherical and tapered shaped pores. Carbides are rod-spherical and irregular shape with a high proportion of large particles, but the largest particles are mostly carbide phase segregated along the grain boundaries and along the boundaries of the new recovered grains. Fine carbide particles are segregated mainly within grains. Carbide size indicates on the late stage of coarsening, with the coalescence of carbide phase (joining of several different carbides that are in close proximity). Chains of precipitates (carbides) on ferrite grain boundaries indicate on grain boundary migration during the creep process.

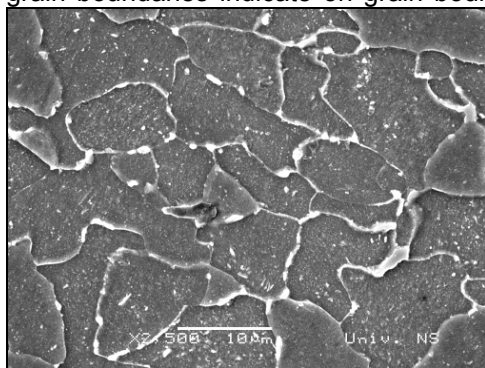


Figure 1: Microstructure of specimen A (initial state). Ferritic and pearlitic-bainitic microstructure.

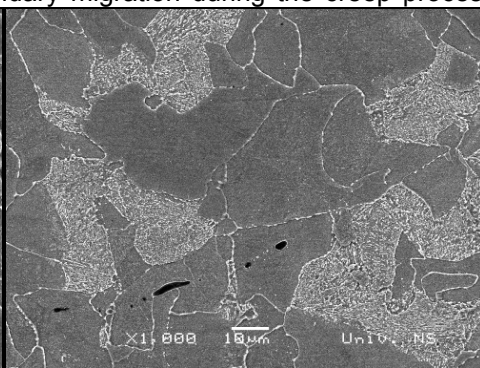
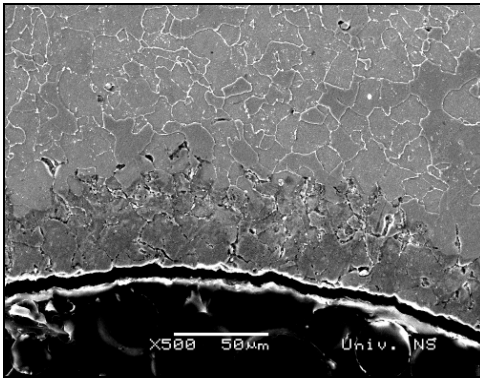
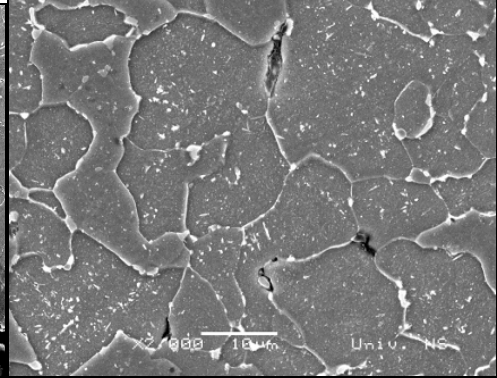


Figure 2: Microstructure of specimen B (200000h service). Ferrite and carbides. Coarse carbides along grain boundary.



*Figure 3: Microstructure of specimen B. Ferrite and carbides. Spherical and wedge shaped pores. Partial decohesion of inclusions.*



*Figure 4: Microstructure of specimen B. Internal oxidation.*

As a result of long-term service, complete separation of oxide inclusions from the matrix is observed. MnS inclusions behaviour depends on their position in the microstructure. In microstructure there are no traces of the initial perlitic-bainitic microconstituent, hence microstructure of specimen B is characterized by a high degradation and also the high degree of spheroidization which is close to the class F and grain size No. 6-8. The number of small grains due to process of grain polygonization and recovery of larger grains is significantly higher compared to their number in initial state material.

Material degradation through the structural changes is manifested by the presence of the pores along the grain boundaries, double and triple grain boundaries, carbide-grain boundaries and inclusion-matrix interfaces.

On specimen B internal oxidation is observed, as a result of long-term service and water vapor in contact with material. This type of damage is characterized by the separation along the grain boundaries due to segregation of oxides, their expansion and further progress along the grain boundaries, as the energy most favorable path, Figure 4. Internal oxidation is general and not localized and has approximately constant depth of ~60 μm.

Changes in the microstructure of materials are directly related to development of carbide precipitation processes, changes in the type and morphology of the carbide phases, chemical composition of particular carbide phase and the redistribution of alloying elements between the solid solution and carbide phase. According to the literature [5], alloying elements are included in the carbide phase during the initial period of service, and then, during prolonged service, tend to be redistributed among the different types of carbide striving to increase M/C ratio.

In all low-alloy creep resistance CrMoV steels the presence of MC and  $M_{23}C_6$  carbides were observed after a long-time service, which indicates that these carbides are very stable and are partially segregated during heat treatment. Cementite-type  $M_3C$  carbide is present in large quantities only after shorter times of

service, while the dispersive  $M_2C$  phase is formed only in steels with high molybdenum content.  $M_6C$  carbide is formed only in steel containing a high content of Mo (about 1%) and is present only in steel with  $M_2C$  carbides in the initial state. The amount of  $M_{23}C_6$  carbides is growing during service and becoming the dominant phase in 12H1MF steel after service of 100000 h.

EDS analysis shows that in all ferrite grains of specimen B the presence of chromium and vanadium is detected (solid solution and fine carbides of chromium and vanadium, and probably some of them contain a certain amount of manganese), while the amount of molybdenum is less than the detection limit of EDS unit. The results of EDS analysis of ferrite matrix of both specimen A and B, pearlite-bainitic microconstituents of specimen A and carbide phase of specimen B are given in Table 3.

Table 3: EDS analysis of chemical composition of phases – specimen A and B

Specimen	Phase	Chemical elements, wt%								
		Cr K	Mo K	V K	Mn K	Si K	Ni	Cu	Fe K	$\Sigma$
A (0h)	F	1.28	0.46	0.26	0.55	0.29	0.00	0.30	96.87	100
	P+B	1.30	0.50	0.26	0.50	0.31	0.00	0.00	97.13	100
B (~200000h)	F	0.84	0	0.2	0.4	0.38	0	0	98.18	100
	C	10.87	6.5	0.4	4.27	0	0.35	0	77.61	100

\* F- ferrite; P- pearlite; B- bainite; C- carbides

In material in initial state the presence of chromium, molybdenum, vanadium and manganese are detected in the ferrite grains. In pearlite, in addition to chromium and vanadium, also Mo was detected in significant amounts (Mo is mostly present in carbide phase, therefore it is sporadically detected in ferrite, and there's a greater amount of them in pearlite).

Carbides whose composition is checked for specimen B are precipitated at the grain boundaries, at the boundaries of the former grain (subgrain) or at the non-metallic inclusions. According to the chemical composition analysis they were mainly alloy carbides  $(Cr, Fe, V, Mn)_x C_y$ , and to a lesser extent  $(Cr, Fe, Mo, V, Mn)_x C_y$ , Table 3. It is interesting to note that the content of molybdenum at all carbide are substantial. Fundamental changes in the content of alloying elements in ferrite matrix and carbide phase during long-term service of investigated 1Cr0.25Mo0.25V steel, demonstrate that dynamic processes taking place in the material, which leads to a redistribution of alloying elements between the ferrite matrix and carbides and between carbides. Redistribution of alloying elements in ferrite matrix is essentially characterized by the solid solution matrix impoverishment due to the coagulation, coalescence and growth of carbides inside ferrite grains or at the grain boundaries.

Experimental results showed that molybdenum content, after service time of 150000 h, remains in very small amounts in the solid solution (below the limit of detection in the present study) [6]. Change of chromium content in the ferrite matrix and carbides is consistent, with the reduction of Cr content in matrix it increases in carbide phase. Chromium content change is not monotonic and has peak value after long-time service, which could be explained by dissolution of smaller carbide,

and increase of chromium content in the matrix again from which chromium is transported by diffusion to the larger carbides. The change of vanadium content in ferrite matrix is very little, while practically negligible in carbide phase, which is consistent with the data published by other researchers. Change of manganese content shows a similar trend as chromium but with less intensity, as can be expected given its low content in the investigated steel.

Grain size analysis was performed in order to estimate the number of favorable location for the occurrence of damage. Since the grain boundaries present the location for vacancy annihilation and also favorable location for formation of creep pores and their coalescence, the formation of microcracks and their spread along the grain boundaries, leading to a creep-rupture, the determination of the grain size is mandatory. The results of linear analysis of grain size are shown in table 4. Investigated values: number of analyzed grains, grain size maximum and minimum measured values, as well as the average grain size value and standard deviation, were determined according to GOST 5639-82 standard.

Table 4: Grain size analysis for 12H1MF steel specimens

Specimen	Number of analyzed grains	Grain size min./max. (µm)	Average grain size d, (µm)	Grain size (GOST 5639-82)	Standard deviation
A	60 (52+8)	0.91/47.68	13.54	10	sd ± 9.58
B	156 (148+8)	0.4/45.58	10.35	10-11	sd ± 8.01

Changes in microstructure that occur during long-term service at elevated temperature have influence of the grain size, lead to grain fragmentation that corresponds to the process of polygonization which precedes the recrystallization processes. With the increase of service time, the number of favorable sites for the development of damage due to creep, also increase.

## Conclusions

High-temperature pressurized pipes of thermal power plant, like thick-walled main steam pipelines are during service dominantly exposed to creep regime. The processes of damage and deformation accumulation during creep are significantly controlled by microstructural degradation of metal that includes several processes in commercial steels for elevated temperatures like: spheroidisation of perlite/bainite microconstituent, changes in type of precipitated carbides, coagulation of carbides, decrease of alloying elements in solid solution, etc. Long term exposure of the 1Cr0.25Mo0.25V steel pipeline components at the elevated temperatures and high level of internal pressure causes significant changes as a result of creep followed by microstructural degradation, sequential carbide phase transformation, appearance of micro- and macro-damage and internal oxidation. Results obtained by different experimental technique show that microstructural degradation had been dominant process during prolonged service in creep

conditions, which lead to the changes of mechanical properties. Microstructural degradation and damages, like creep cavities and oxidation on internal surface of pipe, were observed. The changes of mechanical properties and significant decrease of hardness and micro hardness during service are explained by different processes that take place during microstructural degradation.

## **References**

- [1] Бугай Н.В., Березина Т.Г., Трунин И.И., Работоспособность и долговечность металла энергетического оборудования, Энергоатомиздат, Москва, 1994., с. 120
- [2] Е. И. Крутасова, Надежность металла энергетического оборудования, Москва энергоиздат, 1981.
- [3] Gordana Bakić: Model procene preostalog radnog veka komponenti termoenergetskih postrojenja, Doktorska disertacija, Mašinski fakultet Univerziteta u Beogradu, Beograd, 2011.
- [4] Radović M., Šijački Žeravčić V., Voldemarov V.A., Kovačević K., Bakić G.: The Influence of Microstructural Degradation of 1Cr0.25Mo0.25V Steel on Mechanical Properties and Fracture Mechanisms After Long-term Service at High Temperature, Association for Engineering Mechanics, Brno, Czech Republic, Vol.5, No3, 1998, pp 175-180
- [5] G. D. Pigrova, Y. M. Sedov and Y. I. Archakov, Carbide transformations in Cr – Mo steels during long – term ageing and service, Materials Ageing and Component Life Extension, Vol I, 1995.
- [6] G. D. Pigrova, Effecty of long-term operation on carbide phases in Cr – Mo – V steels, Metal Science and Heat Treatment Vol. 45, Nos. 3 – 4, 2003, 2 – 4

## CAVITATION EROSION RESISTANCE OF HYPOEUTECTIC ALUMINUM ALLOY

V.M.Maksimović<sup>1</sup>, A.M.Došen<sup>1</sup>, I.Bobić<sup>1</sup>, T.Volkov-Husović<sup>2</sup>

<sup>1</sup>*Institute of Nuclear Sciences, "Vinča", University of Belgrade, 11001  
Belgrade, P. O. Box 522, Serbia*

<sup>2</sup>*Faculty of Technology and Metallurgy, University of Belgrade, 11000  
Belgrade, Serbia*

### Abstract

The fluid dynamic system experimental methodology is used in this project to produce ultrasonic erosive wear. In the present study, hypoeutectic A356 aluminum alloy (hereafter referred as A356) was used. Scanning electron microscopy and light microscopy were used for microstructure analysis. Mass loss and level of degradation were measured before and during the experiment. Level of surface erosion of the samples was monitored using Image Pro Plus program for image analysis. Obtained results pointed out that the sample exhibited very good erosion resistance.

*Keywords: aluminum alloy, cavitation resistance, surface erosion, image analysis*

### Introduction

Hypoeutectic A356 aluminum alloy is a casting alloy consisting of aluminum, silicon and magnesium. It has good mechanical characteristics and high ductility, as well as excellent casting characteristics and high corrosion resistance. The alloy has been widely applied in the machinery, aircraft and defense industries and particularly in the automotive industry as a replacement for the steel components [1].

Cavitation erosion, due to its mechanical and economical impact has been studied for a very long time by many authors [2-5]. The characteristic feature of cavitation is the cyclic formation and the collapse of bubbles on a solid surface in contact with a fluid. Upon the collapse of the bubble large contact forces are imparted on the material's surface. Transient pressures have been measured as high as 1.5 GPa [2-5]. Accumulated work-hardening and crack formation are the results of the repeated bubble collapse. Most of the engineering materials are sensitive to fatigue damage but the extent of the damage is highly dependent on the mechanical properties of the material. Main mechanical properties particularly hardness, toughness and work hardening rate are parameters which have to be taken into account when the cavitation erosion is discussed. A soft metal will tend to form deep craters, whereas a ceramic material tends to fail by cracking and spallation [5-8].

The aim of the present study was to investigate the water droplet erosion resistance of the hypoeutectic aluminum alloy A356 in as-cast condition as an

indicator of cavitation-erosion resistance and to confirm the ability of this material to be used in conditions where the cavitation resistance is expected.

## Experimental

In the present study, hypoeutectic A356 aluminum alloy was used. The chemical composition (wt.%) of A356 aluminum alloy was: Si-7.20; Cu-0.02; Mg-0.29; Fe- 0.18; Zn-0.01; Ni-0.02; Ti-0.11; and Al balance. The samples of A356 alloy were produced by gravity squeeze casting techniques. Polished samples were observed under a light microscope equipped with a digital camera and with a scanning electron microscope. The fluid dynamic system for the cavitation erosion testing was used [5,6]. Cavitation erosion testing was accomplished by utilizing the recommended standard values: frequency of vibration:  $20 \pm 0.2$  kHz, amplitude of vibrations at the top of the transformer  $50 \pm 2$   $\mu\text{m}$ , gap between the test specimen and the transformer 1.0 mm, temperature of water in the bath:  $25 \pm 1$   $^{\circ}\text{C}$ .

## Results and discussion

The cavitation erosion testing was conducted for 150 minutes. Results for the mass loss are given in the Fig.1. Mass loss after 150 minutes of testing sample was 0,0012 g. Further investigation of the behavior of the samples was to monitor the level of destruction during testing. Samples were photographed before and during testing, and the results for the level of destruction obtained by image analysis are given in the Fig.2.

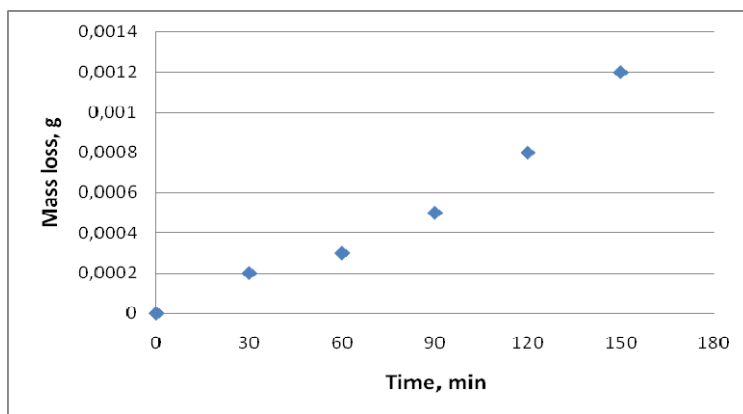
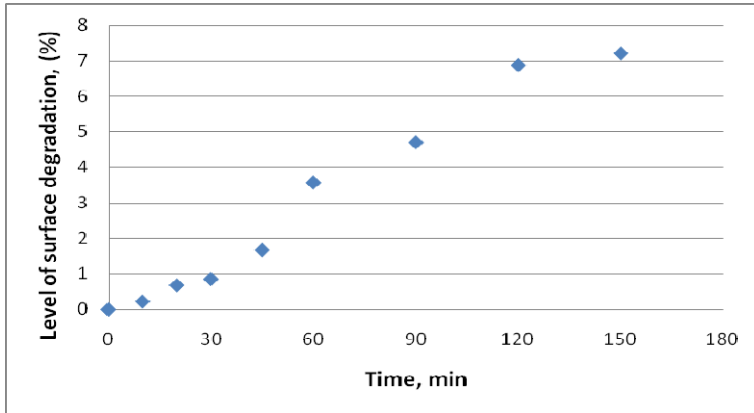


Fig.1. Mass loss of the samples subjected to the cavitation erosion.



*Fig.2. Surface degradation during the cavitation testing.*

Level of the degradation during the cavitation erosion testing was increasing during the experiment as shown in the Fig.2. Level of degradation was measured up to 7.2 % of the original surface area of the sample.

The microstructure of A356 aluminum alloy in as-cast condition is shown in the Fig. 3. It exhibits a typical dendritic structure of the A356 alloy which consists of fully dendritic primary  $\alpha$ -Al phase and a eutectic in interdendritic area.

In the Fig. 4 microstructure (LM) of the sample after 150 minutes of testing was given.

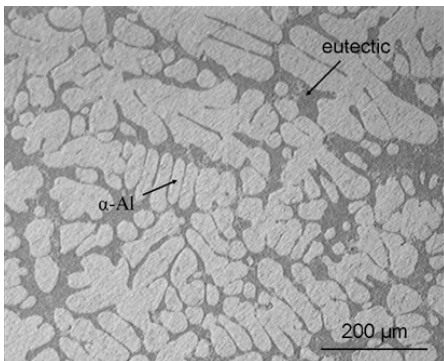


*Fig.3. The microstructure (LM) of as-cast A356 alloy*

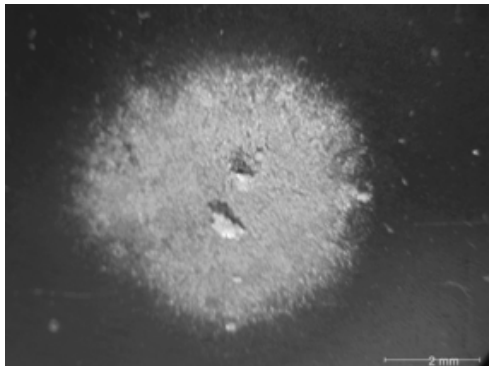


*Fig.4. The microstructure (LM) of as-cast A356 alloy after 150 minutes of the cavitation erosion testing in water. The eroded surface is shown.*

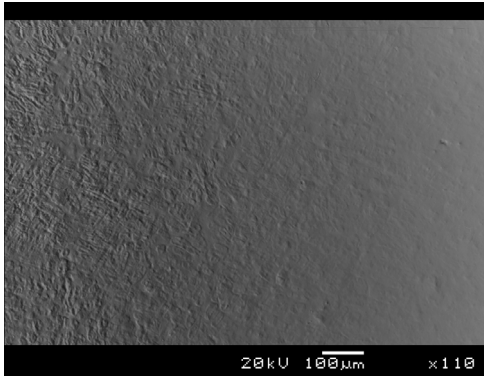


*Fig.5. The microstructure (SEM-BSE) of the as-cast A356 alloy , after 150 minutes, transition zone.*

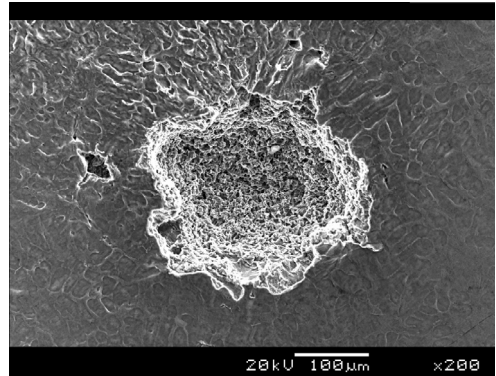


*Fig.6. The microstructure of the typical pit (SEM-SE) of the as-cast A356 alloy after 150 minutes.*

The transition zone shown in the Fig.5. indicates the difference between the damaged and the non damaged structure. Image of the typical spherical pit is given in the Fig. 6 and the damage was observed both in the eutectic region, and in the dendritic areas. Further investigation will be focused on the mechanism of damage, as well as the influence of the different phases on the cavitation erosion. So far, from obtained results, and photographs of the microstructure after 150 minutes of testing, we conclude that the damage is limited to the eutectic region.

## Conclusions

Hypoeutectic A356 aluminum alloy was used in the present investigation. Testing of the cavitation resistance of the A356 was the goal of this paper. Cavitation erosion resistance was monitored by:

- Mass loss,
- Monitoring the level of degradation of the sample during the erosion testing.

Obtained results showed that the mass loss was increasing up to 0.0012g after 150 minutes of testing and the level of damage was 7.2 %.

Based on the obtained results it can be concluded that the investigated A356 alloy can be used in the conditions where the erosion resistance is expected, as a reliable material.

## Acknowledgement

This investigation was funded by the Serbian Ministry of Education and Science through research projects 37021 and 45012

## References

- [1] A. Venci, I. Bobić, M.T. Jovanović, M. Babić, S. Mitrović, *Tribol. Lett.* 32 (2008) 159–170.
- [2] G.W. Stachowiak, A.W. Batchelor, *Engineering Tribology*, second ed., Elsevier, Oxford, UK, 2001.
- [3] A. Karimi, F. Avellan, *Wear* 113 (1986) 305–322.
- [4] K.R. Trethewey, T.J. Haley, C.C. Clark, *Br. J. Corros.*, 23 (1988) 55–60.
- [5] D.M. Garcia-Garcia, J. Garcia-Anton, A. Igual-Munoz, E. Blasco-Tamarit, *Corros. Sci.*, 48 (9) (2006) 2380–2405.
- [6] G. Garcia-Atance Fatjo, M. Hadfield, K. Tabeshfar, *Ceramics International* 37 (2011) 1919–1927.
- [7] M. Dojčinović, V. Đorđević, *MJoM, Metalurgija – Journal of Metallurgy* 14, (3) 2008, 217-228.
- [8] S. Martinović, M. Dojčinović, J. Majstorović, A. Devečerski, B. Matović, T. Volkov Husović, *J. Eur. Ceram. Soc.*, 30 (2010) 3303–3309.

## OPTICAL POLYMER NANOCOMPOSITES PMMA – NANOPHOSPHORS

Ivana Radovic<sup>a</sup>, Vesna Radojević<sup>a\*</sup>, Dejan Trifunovic<sup>a</sup>, Petar S. Uskoković<sup>a</sup>,  
Dušica Stojanović<sup>a</sup>, Miroslav Dramićanin<sup>b</sup>, Radoslav Aleksić<sup>a</sup>

<sup>a</sup> Faculty of Technology and Metallurgy, University of Belgrade, Karnegijeva  
4, 11 000 Belgrade, Serbia

<sup>b</sup> Institute of Nuclear Sciences "Vinča", P.O. Box 522, 11 000 Belgrade,  
Serbia

Corresponding author: Tel.: +381 11 3303 616

E-mail address: iradovic@tmf.bg.ac.rs

### Abstract

In this study, processing and characterization of optical polymer nanocomposites PMMA–Gd<sub>2</sub>O<sub>3</sub> (Eu<sup>3+</sup>) and PMMA–Y<sub>2</sub>O<sub>3</sub> (Eu<sup>3+</sup>) were studied. The nanophosphor powder was dispersed in the PMMA host matrix and nanocomposites were produced using a mixing compounder device. Two series of the composite samples were fabricated with Gd<sub>2</sub>O<sub>3</sub> (Eu<sup>3+</sup>) and Y<sub>2</sub>O<sub>3</sub> (Eu<sup>3+</sup>) nanopowders and different contents of nanoparticles. The influence of particle content on the optical and dynamic-mechanical properties of the nanocomposites was investigated. The performance of these composites was analyzed in terms of the photoluminescence, infrared spectroscopy and dynamic-mechanical properties of the nanocomposites, which are shown to be with the optimal values for 1.0 wt % of particle loading.

*Keywords: Polymer nanocomposites, Photoluminescence, Dynamic-mechanical analysis;*

### Introduction

Contemporary devices for optoelectronic applications such as light-guides, sensors and data communication utilizes nanotechnology procedures as well as nanostructured materials. Nanocomposites with polymer matrix are very often used in these areas with the special care taken for tailoring the desired properties through the selection of nanofiller composition, content and morphology, chemistry of the polymer matrix and the composite processing routes. [1–3].

Nanocomposites are emerging as promising materials for polymer optical fibers (POF), which have, due to their high signal attenuation in the visible spectra, a variety of use as short-distance optical communication medium, signal links in medical devices, illuminating systems, fiber optic sensors and amplifiers [4, 5]. Materials doped with the rare earth ions such as Tb, Eu, Yb and Er have attracted considerable interest due to energy transfer, up-conversion effects and broad application possibilities. Among the inorganic oxides, Gd<sub>2</sub>O<sub>3</sub> [6–8] and Y<sub>2</sub>O<sub>3</sub> [9-12] were widely employed as ideal host materials because of their low-phonon

energy, high chemical- and photo stability, and efficient sensitization (host-to- RE energy transfer).

Thermoplastic polymer matrix nanocomposites have wide range applications in photonic devices and polymer optical fibers. Despite the fact that the research related to nanophosphors is widely published, the application of such nanoparticles in composites was seldom reported [6, 13-18]. Optical properties and thermal stability of composites with PMMA matrix filled with  $Gd_2O_3$  ( $Eu^{3+}$ ) were investigated by Antic et al. [19, 20]. Our previous work, reports the modest influence of  $Y_2O_3$  ( $Eu^{3+}$ ) on the optical and mechanical properties of PMMA nanocomposite [21]. Selected nanophosphors satisfy the prerequisites for presented hypothesis in that the size of particles in optical composites should be less than the wavelength of light because of light scattering and the appropriate deagglomeration of nanoparticles in composite preparation could lead to the increase of mechanical properties. The aim of this study is to produce composite with PMMA matrix reinforced with nanophosphor powder with enhanced mechanical and optical properties utilizing the quasi-industrial melt-mixing technique

## Experimental

The polymer component of composite was PMMA granule for extrusion (Chi Mei). The  $Gd_2O_3$  and  $Y_2O_3$  doped with 3 at. %  $Eu^{3+}$  nanopowder was synthesized performed using the combustion reaction based on polyethylene glycol (PEG) fuel [26]. The nanopowders were obtained with average particle size in the range of 20–50 nm [19, 20]. The nanocomposites were fabricated by laboratory molder [21, 22]. The FTIR spectra were recorded by Hartmann & Braun, MB-series between 4000 and 400  $cm^{-1}$  with a resolution of 4  $cm^{-1}$ . An insight of dispersion and deagglomeration of nanoparticles was performed using FESEM (TESCAN MIRA 3) with fracture surfaces sputtered with gold. A dynamic mechanical analyzer (DMA, TA Instruments Q800) was used to determine the dynamic mechanical properties of the samples. The experiments were performed in the single-cantilever mode over a temperature range from 25 °C to 160 °C at a fixed frequency of 1 Hz. The emission spectra were analyzed using a HR250 monochromator (Jobin-Yvon) and then detected by an ICCD camera (Princeton Instrument). The index of refraction of composites was measured using a spectroscopic ellipsometer GES-5E (SOPRA) in the wavelength range from 400 nm to 800 nm [22].

## Results and discussion

### *Characterization of starting materials and composites*

The FTIR spectra of the powders, PMMA and the composites are illustrated in Fig. 1. The peaks at 2946  $cm^{-1}$  and 1735  $cm^{-1}$  are assigned to C–H stretching and C=O stretching vibrations, respectively. The absorption peaks of PMMA (1439, 840, 750 and 440  $cm^{-1}$ ), and the vibration bands of the PMMA (3458, 1385, 1133 and 974  $cm^{-1}$ ) were observed in the spectrogram. In the spectrum of  $Gd_2O_3$  ( $Eu^{3+}$ ), the transmission band centered at 543  $cm^{-1}$  is attributed to Gd–O lattice vibrations. This peak appeared in all spectra of the composites with different powder content. No chemical shift has been observed which indicates the absence

of any chemical attachment of the polymer chain at the particle–polymer interface. Thus, the transmission properties of the polymer and the emission spectra of the particles should be undisturbed.

Fig. 2 shows SEM photos of the composite fracture surfaces. Fig. 2a reveals  $Gd_2O_3:(Eu^{3+})$  particles deagglomerated in the PMMA matrix with the inset showing primary particles with dimensions about 200-300 nm. Fig. 2b shows deagglomeration of  $Y_2O_3:(Eu^{3+})$  particles in the inset, while the large photo presents the backscattering mode which resembles in completion the standard SEM photo raising the confidence that particles are spotted in standard SEM photos. Composites reinforced with  $Y_2O_3:(Eu^{3+})$  particles **show** fair dispersion with several primary particles (about 50 nm) in the agglomerate, as shown in Fig 2c. SEM analysis reveals that the dispersion of nanoparticles is achieved despite the fact that there was no functionalization of particles and that the quasi industrial method of melt-mixing processing is utilized. This feature, however, is valid up to 1 wt %, for higher particle content it is expected that the agglomeration will take place which should be reflected in the mechanical properties of composites.

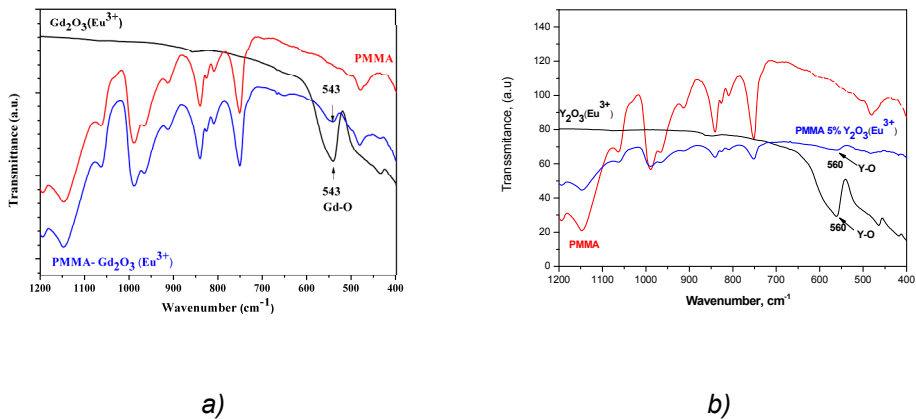


Fig.1. The FTIR spectrum of PMMA,  $Gd_2O_3 (Eu^{3+})$ ,  $Y_2O_3 (Eu^{3+})$  powders and the composites

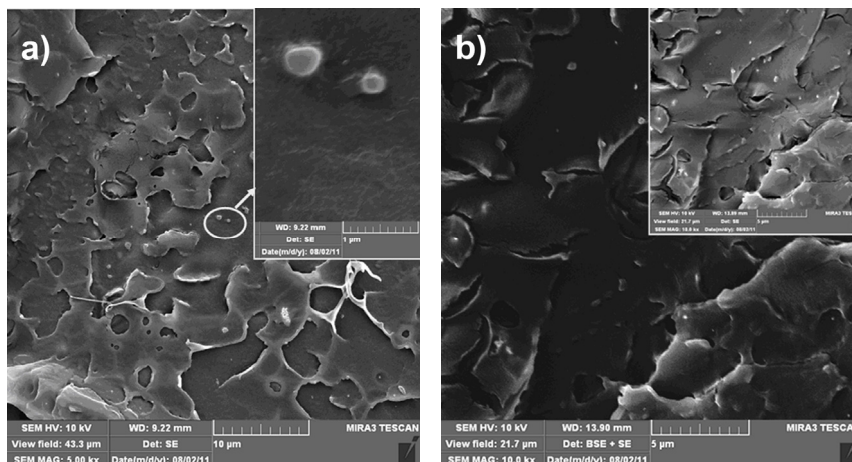


Fig. 2. FESEM of composites: a) FESEM of PMMA-  $Gd_2O_3$ : ( $Eu^{3+}$ ) 1.5 wt %  
b) FESEM of PMMA- $Y_2O_3$ : ( $Eu^{3+}$ ) 1.0 wt %

### Mechanical properties

The DMA results (Fig. 3) revealed that the values of the storage modulus of the composites were higher than for pure PMMA at 30 °C. A nanopowders content of 1 wt % raised the storage modulus of the composite by 30.1 % related to pure PMMA for  $Gd_2O_3$ : ( $Eu^{3+}$ ) and for  $Y_2O_3$ : ( $Eu^{3+}$ ) storage modulus was raised by 15.5 % [26]. It is obvious that even in the absence of specific interactions with the polymer, the particles behaved as highly functional physical crosslink and hence reducing the overall mobility of the polymer chains, as was already reported [2, 23, 24]. Normally, the glass transition temperature ( $T_g$ ) of a polymer increases after the addition of inorganic fillers. The results also suggested that the nanoparticles were not individually dispersed but **they** formed aggregates; however, the notable increments in the glass transition temperature were in the order of 2 to 8 K.

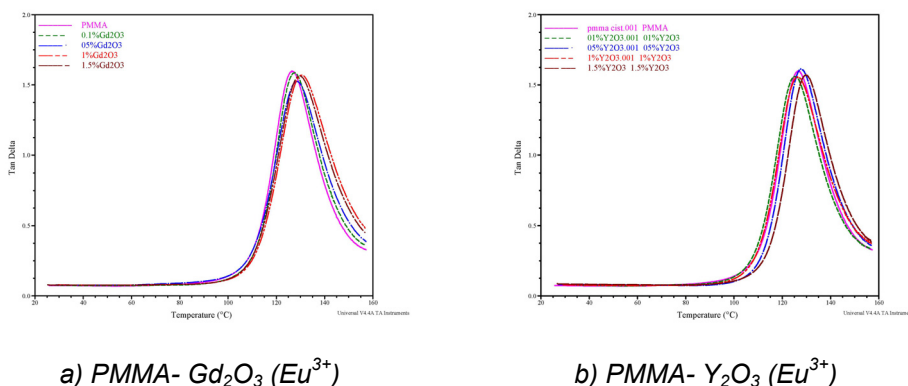
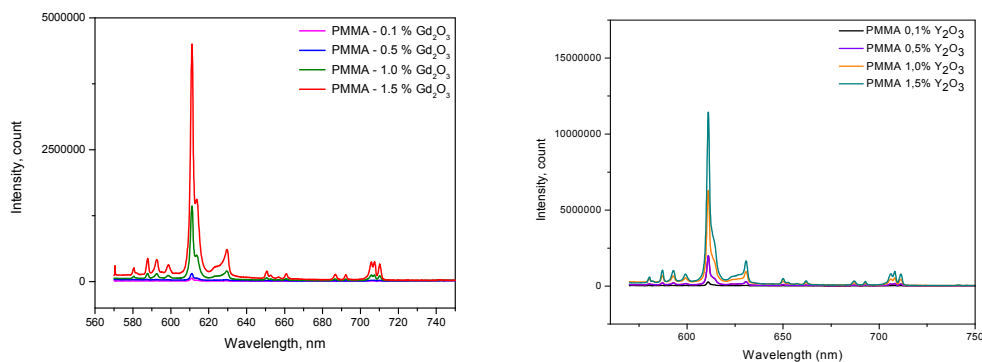


Fig. 3. DMA - Temperature dependence of the tan Delta for pure PMMA and composites with different compositions

### Optical properties

The emission spectra of the nanocomposites are presented in Fig. 5. The spectra exhibit five groups of distinctive emission peaks in the 550–720 nm range. These emission peaks can be related to each one of the  ${}^5D_0 \rightarrow {}^7F_J$  ( $J=0,1,2,3,4$ ) transitions of  $\text{Eu}^{3+}$ , which are characteristic of the  $\text{Eu}^{3+}$  ion within a crystallized cubic phase. The strongest emission peak at 611 nm is caused by the electron dipole transition of  $\text{Eu}^{3+}$  ( ${}^5D_0 \rightarrow {}^7F_2$ ), corresponding to red luminescence. The splitting of ( ${}^5D_0 \rightarrow {}^7F_1$ ), ( ${}^5D_0 \rightarrow {}^7F_3$ ), and ( ${}^5D_0 \rightarrow {}^7F_4$ ) transitions, due to the crystal field effect, confirms the actual incorporation of  $\text{Eu}^{3+}$  ions in the host gadolinium oxide structure.



a) PMMA –  $\text{Gd}_2\text{O}_3$  ( $\text{Eu}^{3+}$ )

b) PMMA –  $\text{Y}_2\text{O}_3$  ( $\text{Eu}^{3+}$ )

Fig. 5. Emission spectra of the nanocomposites at room temperature.

The intensity of the emission increased as the powder content in composite raise. The maximum luminescence was obtained in the range of maximum signal attenuation of PMMA, as expected [42].

### Conclusions

The addition of nanophosphor particles into PMMA matrix, using a feasible quasi-industrial method, and the particle influence on the nanocomposites optical and mechanical properties was studied. In order to preserve the optical properties, the particles were not treated, which led to the agglomeration with the encapsulation of several primary particles. The results of DMA revealed that the storage modulus of the composites was higher than that of pure PMMA and increased with nanophosphor content. The highest modulus was achieved with 1.0%  $\text{Gd}_2\text{O}_3:(\text{Eu}^{3+})$  particle content. Further increase of particle content leads to the decrease of the modulus as a consequence of the particle agglomeration. The luminescence intensity of the composites increased with increasing particle content. The use of melt mixing method for preparation of composites with

luminescent properties leads to well-dispersed Gd<sub>2</sub>O<sub>3</sub>: (Eu<sup>3+</sup>) nanoparticles even with the particles used without surface treatment in order to avoid deagglomeration.

### **Acknowledgement**

This work was supported by the Ministry of Education and Science of the Republic of Serbia, Projects No. TR 34011 and III 45019

### **References**

- [9] Paul D R, Robeson L M. Polymer nanotechnology: Nanocomposites. *Polymer*, 2008, 49:3187.
- [10] Misra R K D, Nerikar P, Bertrand K, Murphy D. Some aspects of surface deformation and fracture of 5–20% calcium carbonate-reinforced polyethylene composites. *Mater Sci Eng, A* 2004, 384: 284.
- [11] Unal H, Mimaroglu A, Alkan M. Mechanical properties and morphology of nylon-6 hybrid composites. *Polym Int*, 2004, 53: 56.
- [12] Anh T K, Benalloul P, Barthou C, Giang L K, Vu N, Le Quoc Minh. Luminescence, energy transfer, and upconversion mechanisms of Y<sub>2</sub>O<sub>3</sub> nanomaterials doped with Eu<sup>3+</sup>, Tb<sup>3+</sup>, Tm<sup>3+</sup>, Er<sup>3+</sup>, and Yb<sup>3+</sup> ions. *J. Nanomaterials*, 2007, 1.
- [13] Osada Y, DeRossi D E. *Polymers for Optical Fiber Sensors. Polymer Sensors and Actuators*. Edited by Y. Osada and D E DeRossi, Berlin Heidelberg. Germany: Springer-Verlag: 2000.
- [14] Goldys E M, Drozdowicz-Tomsia K, Jinjun S, Dosev D, Kennedy I M, Yatsunenko S, Godlewski M. Optical characterization of Eu-doped and undoped Gd<sub>2</sub>O<sub>3</sub> nanoparticles synthesized by the hydrogen flame pyrolysis method. *J. Am. Chem. Soc.*, 2006, 128:14498.
- [15] Xia G, Wang S, Zhou S, Xu J, Selective phase synthesis of a high luminescence Gd<sub>2</sub>O<sub>3</sub>:Eu nanocrystal phosphor through direct solution combustion. *Nanotechnology*, 2010, 21: 345601.
- [16] Bazzi R, Flores M A, Louis C, Lebbou K, Zhang W, Dujardin C, Roux S, Mercier B, Ledoux G, Bernstein E, Perriat P, Tillement O. Synthesis and properties of europium-based phosphors on the nanometer scale: Eu<sub>2</sub>O<sub>3</sub>, Gd<sub>2</sub>O<sub>3</sub>:Eu and Y<sub>2</sub>O<sub>3</sub>:Eu. *J. Colloid. Interface Sci.*, 2004, 273: 191.
- [17] Ritzhaupt-Kleissl E, Boehm J, Hausselt J, Hanemann T. Thermoplastic polymer nanocomposites for applications in optical devices. *Mater. Sci. Eng., C* 2006, 26: 1067.
- [18] Xinyu Y, Wengui G, Libin X, Huaping N, Weidong Z A modified solution combustion method to superfine Gd<sub>2</sub>O<sub>3</sub>:Eu<sup>3+</sup> phosphor: preparation, phase transformation and optical properties. *Journal of rare earths*, 2010, 28 (3): 345.
- [19] Phan T L, Phan M H, Vu N, Anh T K, Yu S C, Luminescent properties of Eu-doped Y<sub>2</sub>O<sub>3</sub> nanophosphors. *Phys Status Solidi A*, 2004, 201: 2170.
- [20] Vu N, Anh T K, Yi G C, Streck W. Photoluminescence and cathodoluminescence properties of Y<sub>2</sub>O<sub>3</sub>: Eu nanophosphors prepared by combustion synthesis. *J Lumin*, 2007, 122–123 : 776.

- [21] Anh T K, Vu N, Nam M H, Minh L Q. Preparation, Optical Properties and Energy Transfer of Y<sub>2</sub>O<sub>3</sub>: Rare Earth (RE: Tb, Eu, Er, Yb) Nanophosphors. *Adv. Nat. Sci*, 2006, 7: 63.
- [22] Dhiraj K S, Chandra S, Gruber J B, Gorski W, Zhang M, Shim J H. Preparation and spectroscopic characterization of Nd<sup>3+</sup>:Y<sub>2</sub>O<sub>3</sub> nanocrystals suspended in polymethyl methacrylate. *J Appl Phys*, 2009, 105: 093105.
- [23] Peng L, Luo Y, Dan Y, Zhang L, Zhang Q, Xia S, Zhang X. The study of preparation and luminescence of polymethyl methacrylate/rare earth composite luminescent materials. *Colloid & Polymer Science*, 2006, 285: 153-60.
- [24] Bian L, Qian X, Yin J, Zhu Z, Lu Q. Preparation and luminescence properties of the PMMA/SiO<sub>2</sub>/EuL<sub>3</sub>•2H<sub>2</sub>O hybrids by a sol–gel method. *Mater. Sci. Eng. B.*, 2003; 100: 53-8.
- [25] Chandra S, Gruber J B, Burdick G W, Sardar D. Fabrication and absorption intensity analyses of Er<sub>2</sub>O<sub>3</sub> nanoparticles suspended in polymethyl methacrylate. *Jour. Appl. Pol. Sci.*, 2011, 122: 289.
- [26] Yu Y Y, Chien W C, Chen S Y, Preparation and optical properties of organic/inorganic nanocomposite materials by UV curing process. *Materials and Design*, 2010, 31: 2061.
- [27] Antic Z, Krsmanovic R, Marinovic-Cincovic M, Dramicanin M D. Gd<sub>2</sub>O<sub>3</sub>: Eu<sup>3+</sup>/PMMA Composite: Thermal and Luminescence Properties. *Acta Phys. Pol A*, 2010, 117: 831.
- [28] Antic Z, Synthesis and characterization of luminescent nanopowders doped with Eu. PhD Thesis. University of Belgrade Faculty of Technology and Metallurgy, 2010.
- [29] Musbah S S, Radojević V, Borna N, Stojanović D, Dramićanin M, Marinković A, Aleksić R. PMMA-Y<sub>2</sub>O<sub>3</sub> (Eu<sup>3+</sup>) nanocomposites: Optical and mechanical properties. *J. Serb. Chem. Soc.*, 2011, 76 (8): 1153.
- [30] Radović I, Radojević V, Stojanović D, Zrilić M, Uskoković P, Aleksić R. Funkcionalni kompozitni materijali: optička i mehanička svojstva nanokompozita na bazi PMMA. *Zbornik radova sa Savetovanja Napredni materijali i njihova primena, Požarevac*, 2011.
- [31] Vacatello M. Monte Carlo Simulations of Polymer Melts Filled with Solid Nanoparticles. *Macromolecules* 2001, 34:1946.
- [32] Fu S Y, Feng X Q, Lauke B, Mai Y W. Effects of particle size, particle/matrix interface adhesion and particle loading on mechanical properties of particulate-polymer composite. *Composites: Part B*, 2008, 39933

## DYNAMIC MECHANICAL PROPERTIES OF ARAMID FABRICS IMPREGNATED WITH CARBON NANOTUBE/POLY (VINYL BUTYRAL)/ETHANOL SOLUTION

V. Obradović, D. Stojanović, M. Grković, I. Živković, V. Radojević,  
P. Uskoković, R. Aleksić

*Faculty of Technology and Metallurgy, University of Belgrade,  
Karnegijeva 4, 11120 Belgrade, Serbia*

### Abstract

In this study six samples of polyurethane/*p*-aramid multiaxial fabric forms (Colon fabrics) were coated with 10 wt.% poly (vinyl butyral) (PVB)/ethanol solution with the addition of multiwalled carbon nanotubes (MWCNT). The solution was impregnated on both sides of each of the fabrics. All composite samples consisted of four pieces of the impregnated fabrics. The MWCNT/PVB content was 0, 0.1 and 1 wt.%. The three samples of the fabrics with different MWCNT/PVB content were coated with  $\gamma$ -aminopropyltriethoxysilane (AMEO silane)/ethanol solution due to the surface modification. The mechanical properties of the prepared composite samples were studied by dynamic mechanical analysis (DMA). The pristine multiwalled carbon nanotubes (MWCNT) were introduced in order to enhance additionally the mechanical properties of the materials for ballistic protection.

*Keywords: p-aramid fabrics, multiwalled carbon nanotubes, AMEO silane, dynamic mechanical analysis*

### Introduction

Carbon nanotubes (CNT) represent cylindrical carbon molecules constituted of carbon atoms linked in hexagonal shapes (Figure 1) [1]. Their dimensions are nanometer in diameter and several millimeters in length. Carbon nanotubes have different structures, varying in length, thickness, type of helicity and number of layers [2]. In multi walled carbon nanotubes (MWCNT), multiple rolled graphitic layers make up concentric tubes [1].

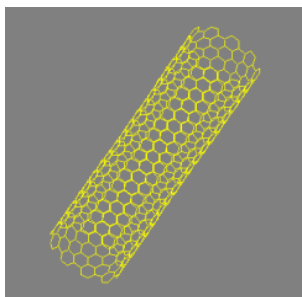


Figure 1- Carbon nanotube structure

The carbon-carbon bond in graphite is one of the strongest compositions, making CNTs great candidates for the stiffest construction ever synthesized. It is impressive that the tubes are flexible and do not crack in bending while testing under a transmission electron microscope (TEM) [3].

Carbon nanotubes exhibit extraordinary mechanical, electronic and magnetic properties. CNTs are probably the strongest composition with a tensile strength greater than steel, but only with one sixth of the weight of steel [4]. The graphene layer (in-plane) is as stiff as diamond at low strain [2].

A common purpose for adding fillers into polymers is to increase their modulus or stiffness. Various filler parameters are taken into consideration for their good fulfillment in the composite. They include the size of particles, their geometry, orientation, stiffness, dispersion, aspect ratio (high ratio is eligible), and the strength of filler-matrix connections [5, 6]. The interactions between the filler and the polymer matrix are important to enhance the filler dispersion and the adhesion of the polymer matrix to the filler surface, which increases the effective filler volume and creates the load transfer from the matrix to the filler when the material is exposed to mechanical distortion [6]. If the adhesion between the matrix and the CNTs is not strong enough to sustain high loads, the reinforcement with the high tensile strength of CNTs is lost. Surface treatments are always used to improve interfacial bonding if the adhesion between the matrix and the CNTs is not strong enough. The two main ways of improving adhesion and shear strength are increasing the surface roughness or the surface reactivity of the outer surface of CNTs [7]. Compatibility with the polymer matrix can be maintained by chemical modification of MWCNTs [8].

CNTs are an excellent choice as fillers in polymer composites because of their high aspect ratio (length/diameter ratio, which can be up to 132000000/1), high strength and stiffness, small size, small mass, low density and high conductivity. When a conducting polymer is used as a matrix, the nanotube fillers improve electrical transfer greatly at low nanotube concentrations [3, 6, 9].

MWCNTs have broad applications, from electronics and space industry to medicine and building industry. They can be used for sensors, lithium ion batteries, fuel cells, atomic force microscope (AFM) tips, technical textiles, drug delivery, etc [2, 8].

In the study, the pristine multiwalled carbon nanotubes (MWCNT) were introduced in order to additionally enhance mechanical properties of materials for ballistic protection. The six samples of polyurethane/*p*-aramid multiaxial fabric forms (Colon fabrics) were coated with MWCNT/poly (vinyl butyral) (PVB) ethanol solution. The surfaces of three samples were coated with  $\gamma$ -aminopropyltriethoxysilane (AMEO silane)/ethanol solution. The mechanical properties of prepared fabrics were analyzed by the dynamic mechanical analysis (DMA).

## **Materials**

A polymer powder poly (vinyl butyral) (Mowital B60H, Kuraray Specialities Europe) and absolute ethanol (Zorka Pharma, Šabac) were taken for preparing the PVB solution. The multiwalled carbon nanotubes (Cheap Tubes Inc, USA) were

added into the PVB solution. The nanotubes lengths were from 3  $\mu\text{m}$  to 30  $\mu\text{m}$  with their outer diameters from 13 nm to 18 nm. Multiaxial aramid fabrics (Martin Ballistic Mat, Ultratex, Serbia) were used with polyurethane/*p*-aramid fiber type Colon (Heracron, Kolon Industries, Inc, Korea) impregnated with polyurethane (Desmopan, Bayer) [10]. The fabric sample dimensions were 15 cm  $\times$  15 cm.

### Experimental part

The experiments were carried out with the PVB solution in concentration of 10 wt.% where ethanol was used as the solvent. At first, the MWCNTs were added into ethanol with concentration of 0, 0.1 and 1.0 wt.% and ultrasonicated for 30 minutes separately in order to provide good dispersion of the carbon nanotubes. After the dispersion process, the ethanol-MWCNT mixture was put into the 20 wt.% PVB solution in order to achieve 10 wt.% solution. The solution was then mixed on a magnetic stirrer overnight. The stability of this solution is long term. Figure 2 displays the difference between the PVB solution with MWCNT and the ethanol-MWCNT mixture where after a while the MWCNT formed residue.



Figure 2- MWCNT/PVB/ethanol solution (left) and MWCNT-ethanol mixture with the same content of MWCNT (right)

There were six samples of composites which consisted of four pieces of fabrics. The three of them with different MWCNT/PVB content were firstly coated with  $\gamma$ -aminopropyltriethoxysilane (AMEO silane)/ethanol solution due to the surface modification of the fabrics. The modification of these composites was managed by impregnation with 2 wt.% AMEO silane/ethanol solution where 2 g of AMEO silane dissolved in 98 g of 96 wt.% ethanol solution for each sample. The solution was stirred for ten minutes on a magnetic stirrer for the hydrolysis of AMEO silane. After the impregnation, the fabrics were left to stay for 24 hours.

The numbers of the samples represent the following:

1- The sample impregnated with PVB solution (8 g of PVB was dissolved in 72 g of ethanol, and the same content of this solution was used for the next seven samples); 2- The sample impregnated with PVB and AMEO silane solutions;

3- The sample impregnated with 0.1 wt. % MWCNT/PVB solution (8 mg of MWCNT was added into the PVB/ethanol solution);

4- The sample impregnated with 0.1 wt. % MWCNT/PVB and AMEO silane solutions;

5- The sample impregnated with 1 wt. % MWCNT/PVB solution (80 mg of MWCNT was added into the PVB/ethanol solution);

6- The sample impregnated with 1 wt. % MWCNT/PVB and AMEO silane solutions.

The samples were obtained by impregnation of both sides of the fabric with the appropriate solutions, after which they were left to stand for 24 hours for ethanol evaporation. They were processed in the compress machine (N 840 D Hix Digital Press) at a temperature of 170 °C and under a pressure of 3 bar for 30 minutes. The produced *p*-aramid composites with different content of MWCNT are depicted in Figure 3.

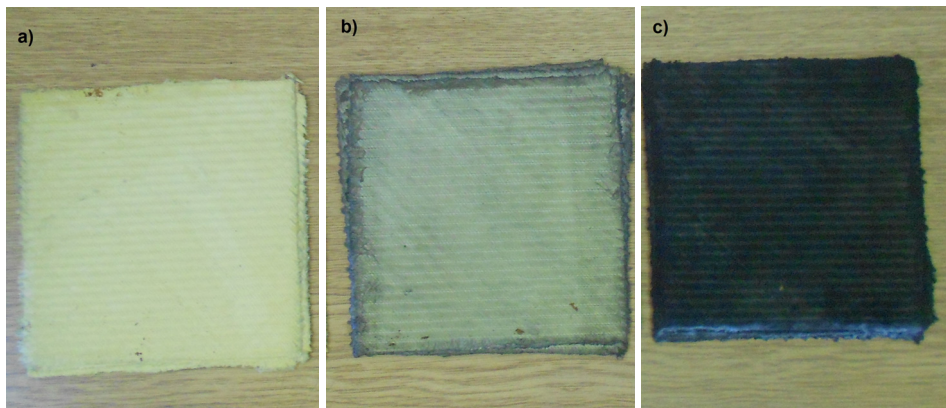


Figure 3- Colon fabrics impregnated with: a) 0, b) 0.1 and c) 1.0 wt.% MWCNT/PVB/ethanol solution

Dynamic mechanical thermal analysis (DMA, Q800 TA Instruments, USA) for the *p*-aramid fabrics was carried out in a dual cantilever mode at a frequency of 1 Hz where the temperature ranged from 40°C to 170 °C with a heating rate of 3 °C/min for the estimation of the storage modulus ( $E'$ ) and damping factor (Tan Delta,  $\tan \delta$ ).

## Results and discussion

The plot depicted in Figure 4 shows that the modulus of Colon/PVB samples increased with the addition of pure multiwalled carbon nanotubes. The storage modulus at the temperature of 40°C for the Colon/PVB and Colon/PVB/1 wt.% MWCNT composites was 1377 MPa and 1669 MPa, respectively (Figure 4, Table 1).

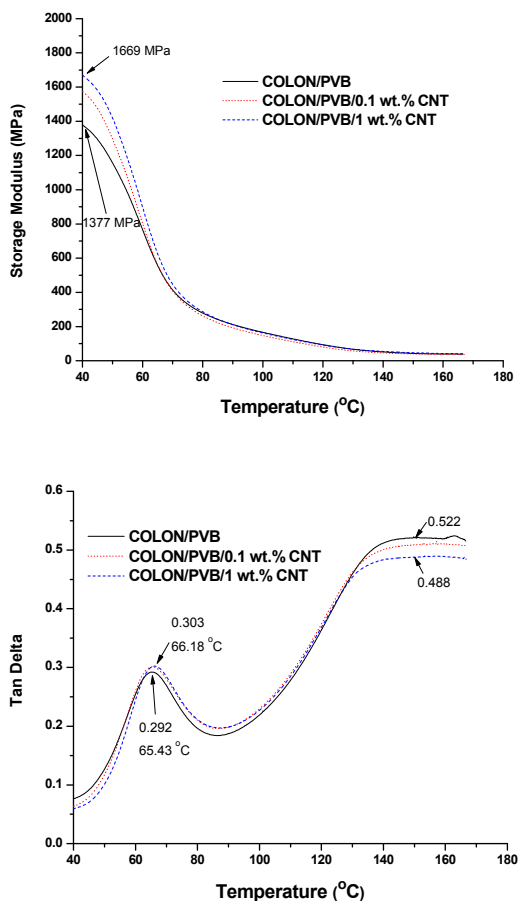


Figure 4- Storage modulus and Tan Delta of Colon/PVB fabrics with various content of MWCNT

The high value of Tan Delta of these fabrics indicated to the steady motion of polymer macromolecules. The first peak showed the glass transition temperature,  $T_{g1}$ , of PVB and the second one,  $T_{g2}$ , the glass transition temperature of hard segment of polyurethane in the impregnated Colon fabrics (which was  $\sim 150$  °C). The  $T_{g1}$  value for the Colon/PVB sample was 65.43 °C, and the values for all other samples with various content of MWCNT were very similar to this one (Figure 4, Table 1). It is obvious that there was no increase in thermal stability with the addition of MWCNT. Tan Delta of these fabrics showed that the strongest bond between PVB and fabrics was with the Colon/PVB composite (0.292, Figure 4). Contrary to that fact,  $\tan \delta_2$  for the same composite had the highest value at the temperature of about 150 °C (0.522, Table 1) which indicated that the bonds were the weakest (Table 1).

Table 1 - DMA results of Colon/PVB fabrics with various content of MWCNT

Composite	E' (MPa, 40°C)	T <sub>g1</sub> (°C)	tan δ <sub>1</sub> (T <sub>g1</sub> )	tan δ <sub>2</sub> (150 °C)
Colon/PVB	1377	65.43	0.292	0.522
Colon/PVB/ 0.1 wt% MWCNT	1576	65.51	0.301	0.509
Colon/PVB/ 1 wt% MWCNT	1669	66.18	0.303	0.488

Impregnation of Colon fabrics with AMEO silane maximized the storage modulus for all the samples due to stronger bonds between CNT and AMEO modified Colon/PVB surface (Figure 5). The storage modulus value for the Colon/AMEO/PVB and Colon/AMEO/PVB/1.0 wt.% MWCNT composites were 2204 MPa and 1936 MPa, respectively, while they had the same value for the modulus - 812 MPa at the glass transition temperature of PVB (Figure 5, Table 2). The glass transition temperature of all the AMEO modified composites was increased compared to the unmodified ones, which provided thermal stability in all cases (Figure 5, Table 2). For example, the T<sub>g1</sub> value for Colon/PVB/0.1 wt% MWCNT composite was 65.51 °C while the same value for AMEO modified counterpart composite was 69.92 °C.

With the glass transition temperature of polyurethane (~ 150 °C), all the AMEO modified composites had the decreased values of the damping factor (Figure 5, Table 2).

Table 2 - DMA results of Colon/AMEO/PVB fabrics with various content of MWCNT

Composite	E' (MPa, 40°C)	T <sub>g1</sub> (°C)	tan δ <sub>1</sub> (T <sub>g1</sub> )	tan δ <sub>2</sub> (150 °C)
Colon/AMEO/PVB	1936	69.16	0.286	0.267
Colon/AMEO/PVB/ 0.1 wt% MWCNT	1818	69.92	0.304	0.249
Colon/AMEO/PVB/ 1 wt% MWCNT	2204	68.85	0.299	0.261

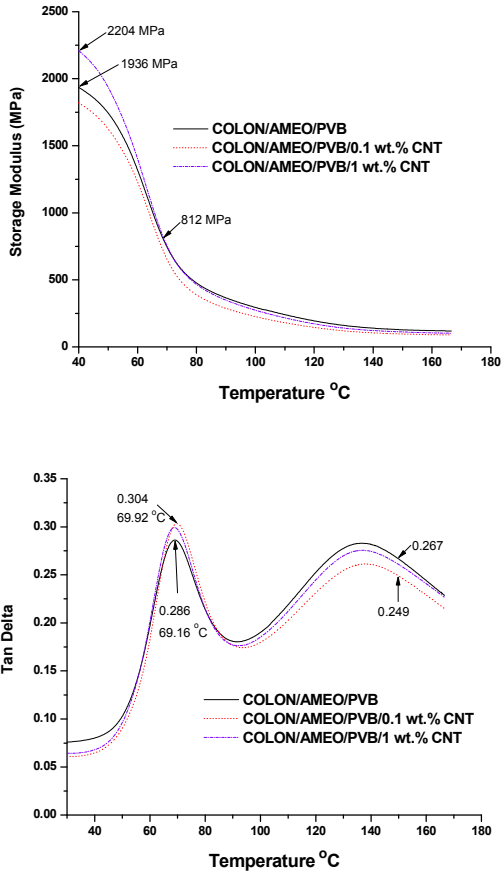


Figure 5 - Storage modulus and Tan Delta of Colon/AMEO/PVB fabrics with various content of MWCNT

## Conclusion

The mechanical properties of the prepared composites were studied by DMA. The increase of storage modulus was achieved by addition of MWCNT and impregnation of aramid fabrics with AMEO silane. In that way, the chemical modification of aramid fabrics was accomplished and stronger bonds between CNT and AMEO modified Colon/PVB surface of fabrics enhanced the mechanical properties of the composites as well as the higher content of MWCNT.

## **Acknowledgements**

This research was financially supported through the Projects No. III 45019 and TR 34011, Ministry of Science and Education – Republic of Serbia.

## **References**

- [1] Peter J. F. Harris, Carbon nanotube and related structures, Cambridge University Press, 1999.
- [2] Ch. Prabhakar, K. Bala Krishna, A review on carbon nanotubes, Research Journal of Pharmaceutical, Biological and Chemical Sciences, 2 (2011), 850-854.
- [3] M. Terrones, Science and technology of the twenty-first century: Synthesis, Properties and Applications of Carbon Nanotubes, Annual Review of Materials Research, 33 (2003), 419–501.
- [4] A. Fakhru'l-Razi, M.A. Atieh, N. Girun, T.G. Chuah, M. El-Sadig, D.R.A. Biak, Effect of multi-wall carbon nanotubes on the mechanical properties of natural rubber, Composite Structures, 75 (2006), 496–500.
- [5] L. Bokobza, Multiwall carbon nanotube-filled natural rubber: Electrical and mechanical properties, eXPRESS Polymer Letters, 6 (2012), 213–223.
- [6] L. D. Perez, M. A. Zuluaga, T. Kyu, J. E. Mark, B. L. Lopez, Preparation, Characterization, and Physical Properties of Multiwall Carbon Nanotube/Elastomer Composites, Polymer Engineering and Science, (2009), 866-874.
- [7] J.-P. Salvetat, J.-M. Bonard, N.H. Thomson, A.J. Kulik, L. Forró, W. Benoit, L. Zuppiroli, Mechanical properties of carbon nanotubes, Applied Physics A: Materials Science & Processing, 69 (1999), 255-260.
- [8] M. M. Tomishko, O. V. Demicheva, A. M. Alekseev, A. G. Tomishko, L. L. Klinova, O. E. Fetisova, Multiwall carbon nanotubes and their applications, Russian Journal of General Chemistry, 79 (2009), 1982–1986.
- [9] <http://www.cambridgecnt.org/2010/08/carbon-nanotubes-overview>.
- [10] A. M. Torki, D. B. Stojanović, I. D. Živković, A. Marinković, S. D. Škapin, P. S. Uskoković, R. R. Aleksić, The viscoelastic properties of modified thermoplastic impregnated multiaxial aramid fabrics, Polymer Composites, 33 (2012), 158-168.

## **SYNTHESIS OF CATALYTIC MATERIALS BASED ON SYSTEM Ni/ $\alpha$ -Al<sub>2</sub>O<sub>3</sub> Supported On Monolith Ceramic Foams**

Vesna Nikolić<sup>1,\*</sup>, Željko Kamberović<sup>2</sup>, Zoran Anđić<sup>3</sup>, Marija Korać<sup>2</sup>, Miroslav Sokić<sup>4</sup> and Jovica Stojanović<sup>4</sup>

<sup>1</sup> *Innovation Centre of the Faculty of Technology and Metallurgy, University of Belgrade, Karnegijeva 4, Belgrade, Serbia;*

<sup>2</sup> *Faculty of Technology and Metallurgy, University of Belgrade, Karnegijeva 4, Belgrade, Serbia;*

<sup>3</sup> *Innovation Centre of the Faculty of Chemistry, University of Belgrade, Studentski trg 12-16, Belgrade, Serbia;*

<sup>4</sup> *Institute for Technology of Nuclear and other Raw Materials, Franše d' Eperea 86, Belgrade, Serbia;*

\* Corresponding author; e-mail: vnikolic@tmf.bg.ac.rs; Tel.: +381-62-515-592; Fax: +381-11-3370-400

### **Abstract**

In the present investigation, nanostructured Ni/Al<sub>2</sub>O<sub>3</sub> catalyst supported on reticulated alumina-mullite foam was synthesized by aerosol assisted coating. The synthesis process was optimized from the technological and economic aspect. Ultrasonically generated NiCl<sub>2</sub> water solutions were applied to  $\alpha$ -Al<sub>2</sub>O<sub>3</sub>-mullite foam in a tubular quartz reactor. The first procedure involved calcination at 773 K for 1 h in order to obtain NiO/Al<sub>2</sub>O<sub>3</sub> precursor. The second procedure involved drying at 473 K for 1 h without oxidation. The activation step involved hydrogen reduction at 633 K. The effectiveness of the low-temperature hydrogen reduction was compared for those systems. It was determined that the samples were reduced in a high degree at 633 K for 90 minutes and the hydrogen flow rate of 20L/h. However, SEM of calcined sample shows presence of agglomerates. The samples reduced from NiCl<sub>2</sub> had no agglomerates and the metallic phase was homogeneously dispersed compared to the samples obtained by NiO reduction. The most probable reason for the effective low-temperature reduction was the formation of thin coatings consisted of oxide and chloride precursors for the catalytically active components. XRD analyse of the samples after the reduction at 633 K for 90 minutes showed only metallic nickel, alumina and mullite phases. Residual phases of NiO and NiCl<sub>2</sub>, as well as NiAl<sub>2</sub>O<sub>4</sub>, were not detected. The production process can be simplified and economically more favourable by avoiding the calcination step.

*Keywords: Nickel; Alumina; Reticulated foam; Catalyst; Aerosol assisted coating*

### **Introduction**

Reticulated ceramic foams are used in many industrial processes involving fluid transport. High pore volumes, low pressure drops during fluid flow, good heat conductivity and mass transfer make them suitable for the application of

heterogeneous catalysis and filtration.<sup>1-4</sup> Examples include Pt<sup>1</sup> and Rh<sup>5</sup> based catalysts supported on cordierite and alumina foams, respectively. Alumina is low cost material with good mechanical properties and good resistance at rigorous process conditions, such as steam reforming.<sup>6</sup>

Nickel based catalysts supported on ceramics are applied in a variety of catalytic processes, e.g. ethanol steam reforming for the production of H<sub>2</sub> or H<sub>2</sub>/CO mixture (synthesis gas) and carbon nanotubes synthesis. Ni is effective substitute for high cost noble metals and it is recommended for industrial application. It has good selectivity towards hydrogen production.<sup>7, 8</sup> Nowadays, conventional routes for synthesis of catalysts include mixing and neutralization of precursor salts solutions or contacting the ceramic support with the impregnating solution. Precursor salts are transferred into suitable mixture of oxides by calcination. The catalyst is activated by hydrogen reduction, where only active component is transferred to metallic state.<sup>9</sup> Novel methods involve calcination of ultrasonically generated aerosols consisted of precursor salts solutions. They enable formation of fine spherical catalyst particles, precise stoichiometry control and high purity of products.<sup>10, 11</sup> There is a possibility of energy consumption savings and economic benefits if the calcination step is avoided during the production.

The aim of the present research was the optimization of the synthesis process of nanostructured Ni based catalyst supported on reticulated alumina-mullite foam, assisted by ultrasonic generated aerosol coating. The aerosol of NiCl<sub>2</sub> water solution was applied to alumina-mullite foam at elevated temperatures. The low-temperature reducibility of dried samples with chloride precursor and of calcined samples with oxide precursor was compared. It was determined that nickel compounds in all samples were reduced with high degree. The procedure resulted in homogeneous dispersion of Ni on the  $\alpha$ -Al<sub>2</sub>O<sub>3</sub>-mullite surface. In the proposed synthesis route the calcination step was avoided, which contributed to the economic and technological efficiency of the catalysts production. Ni particles were mainly sintered during the reduction process. Therefore, a lower sintering temperature is to be investigated further.

## **Experimental section**

In order to economically enhance the synthesis of nanostructured Ni/Al<sub>2</sub>O<sub>3</sub> catalyst supported on reticulated ceramic foam assisted by aerosol coating, two experimental procedures were conducted and the synthesis process was optimized. Oxide precursor for the production of catalysts was obtained by calcination of Al<sub>2</sub>O<sub>3</sub> foam coated by NiCl<sub>2</sub> at 773 K for 1 h and the chloride precursor was obtained by drying Al<sub>2</sub>O<sub>3</sub> foam coated by NiCl<sub>2</sub> at 473 K for 1 h. Thin layers of NiO and NiCl<sub>2</sub> particles were deposited on alumina-mullite foam. Afterwards, the effectiveness of the hydrogen reduction on a low temperature was investigated.

Ultrasonic nebulizer (Profi Sonic, Prizma) with 1.7 MHz resonator frequency was attached to a tubular quartz reactor set in an electro resistant furnace (Fig. 1). A predetermined amount of NiCl<sub>2</sub>·6H<sub>2</sub>O was dissolved in distilled water to achieve Ni to alumina-mullite ratio of 20 mas.%. The Ni<sup>2+</sup> ion concentration was 0.15 mol/L. The first experimental procedure involved the calcination of  $\alpha$ -Al<sub>2</sub>O<sub>3</sub>-mullite foam

(Sivex A40, Pyrotek) coated with  $\text{NiCl}_2$  by using ultrasonically generated aerosol of the solution at 773 K for 1 h.  $\text{NiCl}_2$  was transferred to  $\text{NiO}$ . The second procedure involved the drying of  $\alpha\text{-Al}_2\text{O}_3$ -mullite foam coated with  $\text{NiCl}_2$  at 473 K for 1 h. The latter procedure enabled the drying of samples without oxidation. Obtained samples were reduced by hydrogen at 633 K for 90 minutes, with the hydrogen flow rate of 20 L/h.

The microstructure of oxide precursors and samples obtained by the reduction of both oxide and chloride precursors was investigated using a JEOL SEM JSM 5800 scanning electron microscope (SEM). Microstructure represents correlation between the production technology and properties. The chemical composition of the reduced samples was investigated by XRD.

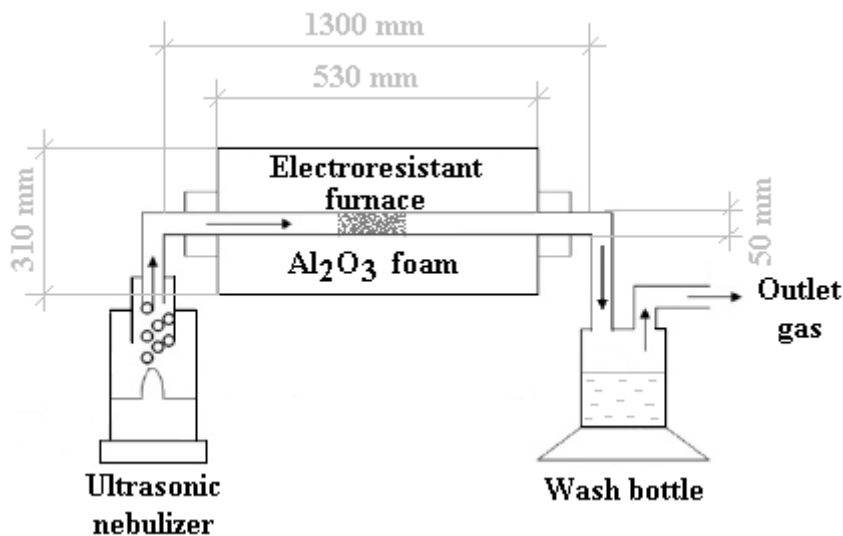


Figure 9. Set-up of aerosol assisted coating experiment

## Results and discussion

The aerosol assisted coating process was successful in all experiments. Alumina-mullite foam was uniformly covered with nickel coating after the reduction. Photographs of un-coated alumina-mullite foam and the nickel-coated foam are presented in Fig. 2.

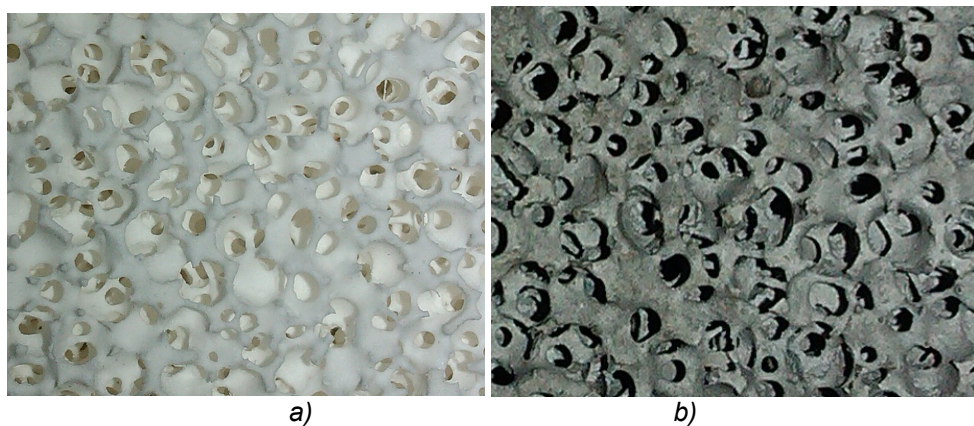


Figure 10. Photographs of a) alumina-mullite foam, b) Ni-coated alumina-mullite foam

SEM analysis of the strut surface of the calcined sample clearly indicates presence of NiO sponge-like agglomerates consisted of particles between 100 and 200 nm in diameter on the  $\alpha$ -Al<sub>2</sub>O<sub>3</sub>-mullite surface (Fig. 3). The agglomerates were about 1  $\mu$ m in diameter. The faceted surface of  $\alpha$ -Al<sub>2</sub>O<sub>3</sub>-mullite is also clearly visible.

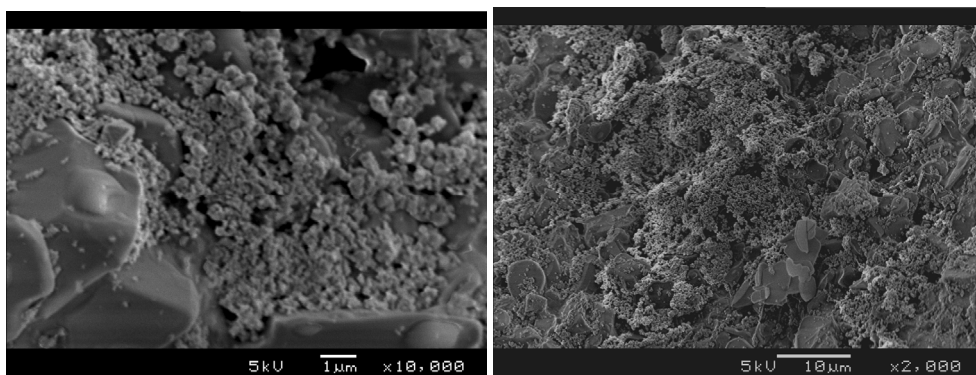


Figure 11. SEM of NiO supported on alumina-mullite foam, obtained by calcination at 773 K for 1 h

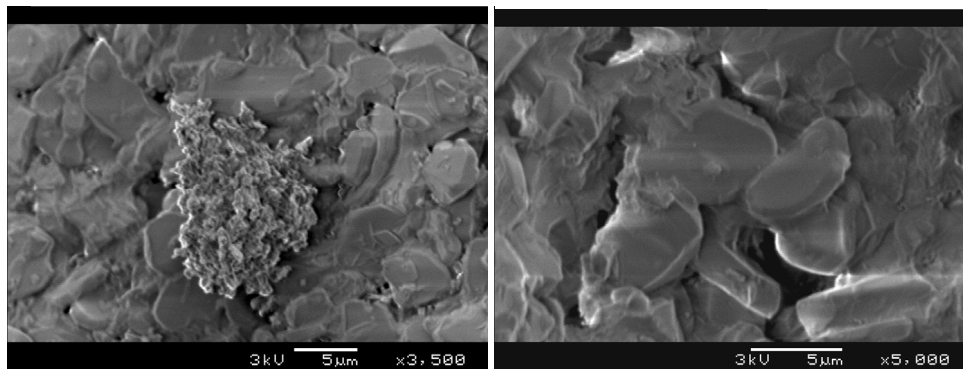


Figure 12. SEM of Ni supported on alumina-mullite foam, obtained by reduction of a) NiO calcined at 773 K and b) dried NiCl<sub>2</sub>, reduced at 633 K for 90 minutes

SEM of samples reduced at 633 K, obtained from oxide and chloride precursor, is presented in Fig. 4. Solid-state reactions between the catalytically active component and the carrier, i.e. ion adsorption reactions of the active component on the support that occurred during the reduction process at 633 K ensured the formation of the final structure of the catalyst (Fig. 4.b). Sponge-like agglomerates were present on the sample obtained by the reduction of NiO, Fig. 4.a. The presence of agglomerates is undesirable because it impairs the catalytic activity and leads to abrasion of the coating in a gas stream. Compared to that, the samples obtained by NiCl<sub>2</sub> reduction had smoother surface, with homogeneously dispersed active component, without detected agglomerates.

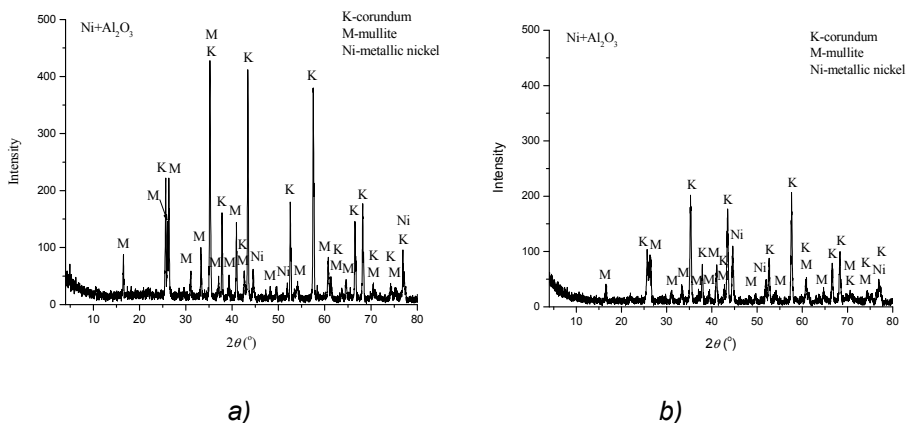


Figure 13. XRD of Ni supported on alumina-mullite foam after a) NiCl<sub>2</sub> and b) NiO reduction at 633 K for 90 minutes

XRD analyses clearly indicate that the residual NiO and NiCl<sub>2</sub> phases, as well as NiAl<sub>2</sub>O<sub>4</sub>, were not detected after the reduction (Fig. 5). In all samples, alumina, mullite and metallic nickel phases were detected, which indicates that the transferring of inactive form of the catalyst to its active form was complete. Intensity

of peaks, corresponding to metallic nickel, was higher in the sample obtained from chloride precursor. The most probable reason for the high degree of low-temperature reduction was the formation of thin film containing of nickel precursors. SEM of NiO supported on  $\alpha$ -Al<sub>2</sub>O<sub>3</sub>-mullite foam shows that nanoscale NiO particles were not uniformly distributed on the ceramic surface. Compared to mentioned, Ni particles obtained by reduction of NiCl<sub>2</sub> were more homogeneously dispersed and formed smoother metallic coating on the surface of ceramic foam. Based on the obtained results, it can be concluded that the catalysts can be synthesized by the direct reduction of NiCl<sub>2</sub> coated alumina-mullite foam, where the calcination step is avoided. The proposed process is more favourable from the technological and economic aspect. Considering that the the reduction was most probably complete at 633 K, a lower reduction temperature is proposed for further investigations.

## **Conclusions**

In the present research, the synthesis process of Ni/Al<sub>2</sub>O<sub>3</sub> catalyst by aerosol assisted coating was optimized. The low-temperature hydrogen reduction of NiO and NiCl<sub>2</sub> supported on reticulated  $\alpha$ -Al<sub>2</sub>O<sub>3</sub>-mullite foam was investigated. Based on the XRD and SEM analyses, it was concluded that the Ni/Al<sub>2</sub>O<sub>3</sub> catalysts were successfully synthesized from chloride precursor and the catalytically active component was homogeneously dispersed on the surface of  $\alpha$ -Al<sub>2</sub>O<sub>3</sub>-mullite foam. SEM analysis of calcined samples showed the presence of sponge-like agglomerates, which are undesirable because they impair the catalytic activity. Obtain results indicate that the calcination step can be avoided, that is, the direct reduction of chloride precursor after the ceramic foam impregnation with NiCl<sub>2</sub> aerosol and drying is sufficient for the synthesis of the catalysts. Proposed method can significantly contribute to the economic efficiency of the catalyst production process, as well as the production efficiency. Further research will be focused on the study of solid-state reactions between the catalytically active component and the carrier, i.e. ion adsorption reactions of the active components on the carrier, which enable the formation of the final homogeneous catalyst's structure at lower temperatures, in order to obtain the catalysts with service properties.

## **Acknowledgements**

This paper was done with financial support for projects No 34033 'Innovative synergy of by-products, waste minimization and clean technologies in metallurgy' and No 34023 'Developing technological processes for nonstandard copper concentrates processing with the aim to decrease pollutants emission', by Ministry of Education, Science and Technological development of the Republic of Serbia.

## **References**

- [1] F. Ribeiro, J. M. Silva, E. Silva, M. Fatima Vaz and F. A. C. Oliveira, *Catal. Today*, 176 (2011) 93.
- [2] J. Grosse, B. Dietrich, G. Incera Garrido, P. Habisreuther, N. Zarzalis, H. Martin, M. Kind and B. Kraushaar-Czarnetzki, *Ind. Eng. Chem. Res.*, 48 (2009) 10395.

- [3] M. V. Twigg and J. T. Richardson, *Chem. Eng. Res. Des.*, 80 (2002) 183.
- [4] P. Ciambelli, V. Palma and E. Palo, *Catal. Today*, 155 (2010) 92.
- [5] A. Donazzi, B. C. Michael and L. D. Schmidt, *J. Catal.*, 260 (2008) 270.
- [6] R. Faure, F. Rossignol, T. Chartier, C. Bonhomme, A. Maitre, G. Etchegoyen, P. Del Gallo and D. Gary, *J. Eur. Ceram. Soc.*, 31 (2011) 303.
- [7] C. B. Alcock, *Thermochemical Processes: Principles and Models*, Elsevier Butterworth-Heinemann, Oxford, 2001.
- [8] Y. Zhang, Y.H. Tang, E.L. Zhang, L.W. Lin, L.Z. Pei, *Materials Science-Poland*, (2010), 805.
- [9] A. J. Akande, R. O. Idem, A. K. Dalai, *Appl. Catal. A*, 287 (2005) 159.
- [10] M. Watanabe, H. Yamashita, X. Chen, J. Yamanaka, M. Kotobuki, H. Suzuki, H. Uchida, *Appl. Catal., B*, 71 (2007) 237.
- [11] X. Wei, P. Hug, R. Figi, M. Trottman, A. Weidenkaff, D. Ferri, *Appl. Catal., B*, 94 (2010) 27.

## CARBIDE PHASES IN Fe<sub>19</sub>Cr<sub>2.9</sub>C<sub>3.3</sub>V ALLOY IN AS-CAST CONDITION

M. Filipović, Z. Kamberović and M. Korać

*Department of Metallurgical Engineering, Faculty of Technology and Metallurgy, University of Belgrade, Karnegijeva 4, 11120 Belgrade, Serbia.  
E-mail: mirjanaf@tmf.bg.ac.rs*

### Abstract

The microstructure of tested Fe<sub>19</sub>Cr<sub>2.9</sub>C<sub>3.3</sub>V alloy consists of M<sub>7</sub>C<sub>3</sub> and vanadium rich M<sub>6</sub>C<sub>5</sub> carbides in austenite-martensitic matrix. Eutectic colonies are mainly composed of a very fine rod-like M<sub>7</sub>C<sub>3</sub> carbides at the center and become coarser rod-like or blade-like with increased distance from the center. The volume fraction, size and distribution of rod-like and blade-like carbides in the eutectic colonies are changing with vanadium addition to the alloy. The formation of the eutectic colonies of different morphology is the consequence of the segregation of alloying elements in the alloy melt, which was confirmed by EDS analysis of the chemical composition of carbides. Three different compositions of M<sub>7</sub>C<sub>3</sub> carbides were found in tested alloys. The main difference between them is in the amount of chromium and iron and in the degree of their replacement by vanadium. Due to different melt composition in particular zones, the constitutional undercooling, and subsequently the growth rate, will be different, which will induce the formation of eutectic colonies of different morphologies. The precipitation kinetic of carbides in austenite was found dependent on the vanadium content. TEM analysis revealed that secondary carbides were square shaped, 40-100 μm in size, and precipitate along preferred crystallographic planes. The transformation of austenite into martensite in the Fe-C-Cr-V alloy is closely related to the precipitation of secondary carbides.

*Key words: Fe<sub>19</sub>Cr<sub>2.9</sub>C<sub>3.3</sub>V alloy, M<sub>7</sub>C<sub>3</sub> carbides, M<sub>6</sub>C<sub>5</sub> carbides, secondary M<sub>23</sub>C<sub>6</sub> carbides, constitutional undercooling; growth rate*

### Introduction

White cast irons have been widely used for abrasion resisting applications, so the primary characteristic of this alloy is a good abrasion resistance, and a modest resistance to brittle fracture. Most improvements in abrasion resistance are accompanied by lower toughness caused by higher content of eutectic carbide [1]. Studies concerning the effect of eutectic carbides on the abrasive wear resistance of high chromium white cast irons have been focused primarily on the volume fraction of carbides, or their sizes, as it was estimated that fine carbides were more beneficial to the wear resistance than coarse ones [1-3]. There is a significant amount of work regarding the improving impact of carbiding elements such as tungsten, niobium, vanadium, titanium, and boron on the properties of high chromium white iron [1,2,4-7]. Vanadium appeared to be of special interest, due to

its double effects, on both the matrix structure and stereological characteristics of carbides.

Dependent upon the chemical composition of the melt, solidification of high chromium white cast irons begins with the formation of primary phase (i.e. austenite in hypoeutectic alloys, or  $M_7C_3$  in hypereutectic alloys), and ends with the formation of the eutectic phase. Alloy with eutectic composition solidifies with eutectic cellular structure ( $\gamma + M_7C_3$ ) [1,3]. The hexagonal  $(Cr,Fe)_7C_3$  carbides grow as rods and blades, with the fastest [0001] growth direction, and form a continuous network within each eutectic colony [2,5]. In the casting these eutectic colonies are oriented perpendicular to the mold surface in the columnar region, but have a random orientation in the equiaxed zone [3].

In this work, influence of vanadium addition on the type, volume fraction and morphology of carbide phases present in the as-cast microstructure of high chromium white iron was examined.

### Experimental procedure

The chemical composition of tested alloys is listed in Table 1. The melting of various alloys has been conducted in induction furnace. Test samples for structural analysis have been cut from the cast bars (200 mm long and 30 mm in diameter) cast in the sand molds.

Table 1. Chemical composition of tested Fe-Cr-C-V alloys.

Alloy	Chemical composition of tested alloys (mass%)									
	C	P	S	Si	Mn	Mo	Cu	Ni	Cr	V
1	2.89	0.025	0.061	0.85	0.71	0.48	0.99	0.100	19.03	0.0012
2	2.91	0.027	0.061	0.84	0.73	0.44	1.00	0.096	19.05	3.28

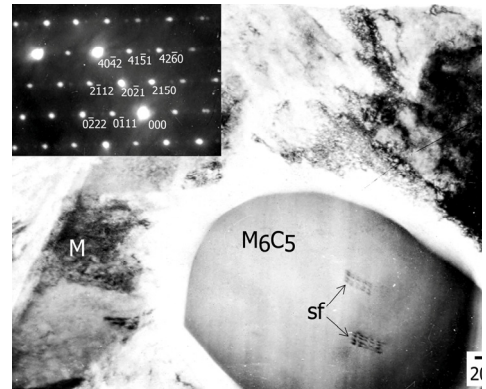
The morphology of  $M_7C_3$  eutectic carbides was examined by a scanning electron microscope, JEOL 733-FCXA, using an accelerating voltage of 25 kV. For this examination, the polished samples were deep etched in a 10% HCl solution in methanol for 24 h then cleaned in an ultrasonic bath. The chemical composition of the eutectic carbides was determined using energy dispersive X-ray spectroscopy (EDS). Discs for TEM examinations were prepared by using a twin-jet electropolisher. These samples were examined at 200 kV in a JEOL-2000FX transmission electron microscope.

### Results

The as-cast microstructure of tested hypoeutectic Fe-Cr-C-(V) type alloys consists of primary austenite dendrites and eutectic colonies composed of  $M_7C_3$  carbides and austenite [5]. Using by the image analyzing technique it was found that the volume fraction of eutectic carbides increased from 31% in alloy with no vanadium to 34.3% in alloy containing 3.28% V. Fig. 1 shows a part of the eutectic  $M_7C_3$  carbide containing many twins. Also, vanadium rich carbides are found in alloy containing 3.28% V (Fig. 2). TEM observation reveals that vanadium carbide is being of  $M_6C_5$  type. Stacking fault is clearly visible within the carbide (Fig.2).

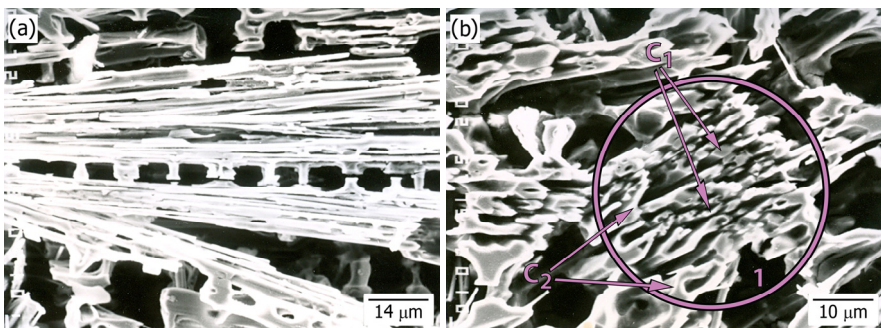


*Fig. 1. TEM micrographs of Fe19Cr2.9C3.3V alloy showing hexagonal  $M_7C_3$  eutectic carbide and selected-area diffraction pattern (in the corner) from the region in this micrograph.*



*Fig. 2 TEM micrograph of Fe19Cr2.9C3.3V alloy showing vanadium carbide and selected-area diffraction pattern (in the corner) from the region in this micrograph.*

The SEM micrographs of deep etched sample revealed that single  $M_7C_3$  carbides in Fe-Cr-C alloy with no vanadium addition, were rod or blade shaped (Fig. 3), where the blades are basically consist of multiple rods (Fig. 3d). A larger number of long carbide rods within the eutectic colonies usually grow along their longitudinal axes (Fig. 3a). When viewed perpendicular to their fastest growth direction, the  $M_7C_3$  carbides within the eutectic colonies are very fine rod-like at the center, but become coarser rod-like (Fig. 3b) or blade-like (Fig. 3c) with increasing distance from the center. In addition, eutectic colonies in which blades spread radially from the center are observed in the columnar zone of this alloy (Fig. 3d).



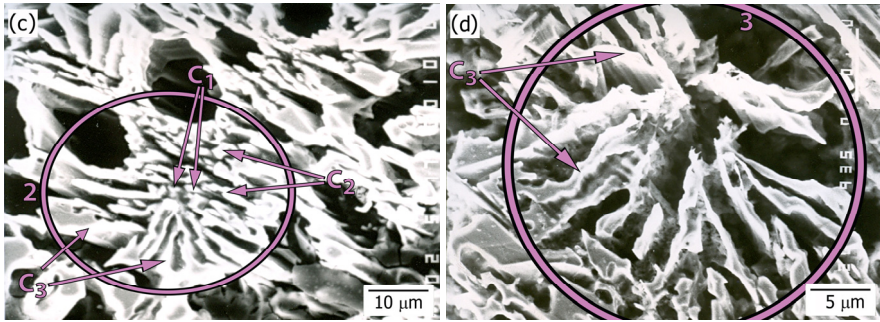


Fig. 3. SEM micrographs of deep etched sample showing morphology of  $M_7C_3$  carbides in Fe-Cr-C alloy with no vanadium addition

Alloying high chromium white iron with vanadium resulted in increased number of carbide rods within the eutectic colonies, and, the rod or blade-like  $M_7C_3$  carbides were finer (Fig. 4). It should be emphasized that in alloy with 3.28% V, eutectic colonies with radially spreading blade shaped carbides were not observed (Fig. 4).

Results obtained by EDS analysis of the eutectic  $M_7C_3$  carbides in the tested alloys are given in Table 2. The carbon content was calculated by balancing with the other elements. As shown in Table 2, three different compositions of  $M_7C_3$  carbides were found in the tested alloys. The main difference between them has been recognized in various chromium and iron content. In alloy containing 3.28% V, chromium and iron atoms have been substituted by vanadium in all three different compositions of eutectic carbides. In cases of  $C_1$  and  $C_2$  carbides greater number of chromium atoms were substituted by vanadium, while in carbides  $C_3$  greater number of iron atoms have been substituted.

The eutectic colony consists of carbides of different compositions in examined alloys (Figs. 3 and 4). Blade-like carbides predominantly show  $C_3$  composition.

Table 2. Chemical composition of  $M_7C_3$  eutectic carbide in tested alloys.

Alloy	$M_7C_3$	Chemical composition of $M_7C_3$ (mass%)						Formula
		C	Mn	Mo	Cr	Fe	V	
1	$C_1$	8.17	0.673	0.557	53.36	38.07	-	$Cr_{4.2}Fe_{2.8}C_3$
	$C_2$	8.55	0.548	0.674	45.44	44.68	-	$Cr_{3.6}Fe_{3.3}C_3$
	$C_3$	8.43	0.659	0.494	39.77	50.11	-	$Cr_{3.2}Fe_{3.8}C_3$
2	$C_1$	8.56	0.461	0.451	45.46	34.54	10.62	$Cr_{3.6}Fe_{2.6}V_{0.8}C_3$
	$C_2$	8.62	0.676	0.564	38.33	43.92	7.74	$Cr_{3.1}Fe_{3.2}V_{0.6}C_3$
	$C_3$	8.28	0.427	0.448	35.52	46.01	8.35	$Cr_{2.8}Fe_{3.4}V_{0.7}C_3$

The values are based on an average of thirty different measurements per each of three different chemical compositions of  $M_7C_3$  eutectic carbide in all tested alloys

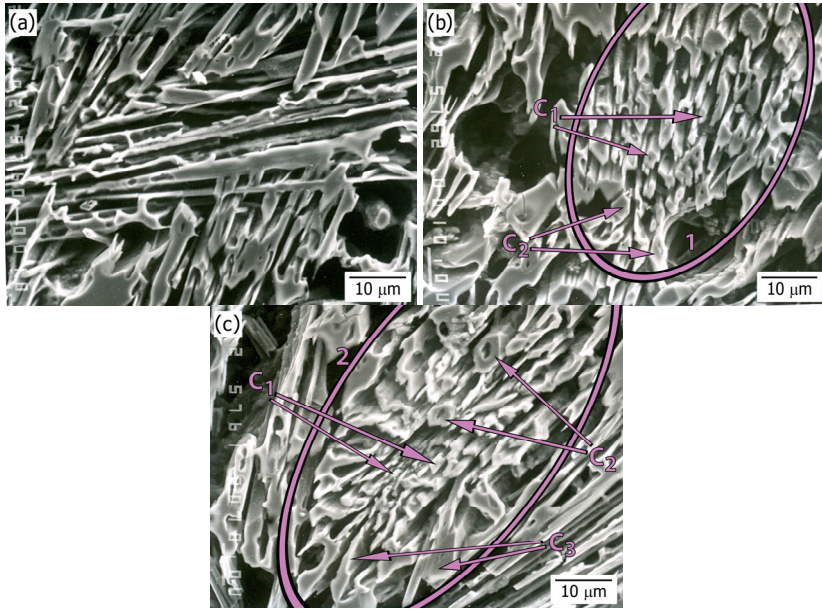


Fig. 4. SEM micrographs of deep etched sample showing morphology of  $M_7C_3$  in Fe19Cr2.9C3.3V alloy.

TEM observation revealed that the secondary carbides were present in the matrix in tested Fe-Cr-C-V alloy (Fig. 5). The particles precipitated in the matrix were identified to be carbides of  $M_{23}C_6$  type. The secondary carbides appear to have a square shape, approximately 40-100 nm in size, and precipitate along preferred crystallographic planes (Fig. 5a). The martensite is noted around the carbide particles (Fig. 5b).

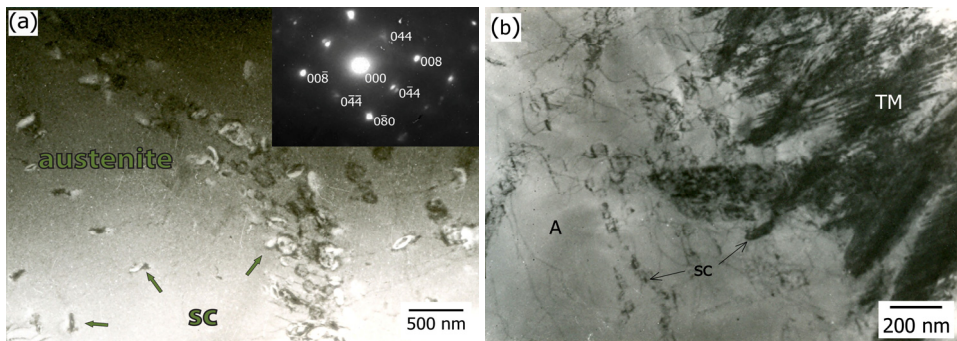


Fig. 5. TEM micrographs of Fe19Cr2.9C3.3V alloy showing: (a) secondary  $M_{23}C_6$  carbides and selected-area diffraction pattern (in the corner) from the region shown in (a) showing a  $[100]$  zone axis, (b) secondary carbides and martensite.

## Discussion

In the tested Fe-Cr-C-(V) type alloys the solidification starts with the formation of austenite dendrites. In the course of primary  $\gamma$ -phase growth, the composition of the remained liquid was changing. Due to limited solubility of carbon, chromium and vanadium in the austenite, these elements accumulated in front of the progressing solid-liquid interface. At temperature lower than liquidus temperature during the eutectic reaction that takes place, in local areas enriched in vanadium, eutectic composed of vanadium rich  $M_6C_5$  carbide and austenite was developed. This effect was considered previously in detail [5]. As the temperature falls and solidification progresses, primary austenite dendrites reject solute (mainly carbon, chromium and vanadium) in to the remaining liquid until the eutectic composition is reached and the monovariant eutectic reaction ( $L \rightarrow \gamma + M_7C_3$ ) takes place. From the melt remained in interdendritic regions the coupled  $M_7C_3/\gamma$  (faceted-nonfaceted) eutectic was forming.

Irregular eutectic structures are developed when a nonfaceted phase is coupled with a faceted phase. In such eutectics, local morphological adjustment of interphase spacing is severely encumbered by the limited branching ability of the highly anisotropic faceted phase containing planar defects. Thus, the spatially non-uniform or irregular structure that evolves during faceted-nonfaceted eutectic solidification is inherently three-dimensional, where the relationship between the growth mechanisms of the faceted phase and the complex non-isothermal interface structure gives rise to a more diverse range of solidification microstructures than that exhibited by regular eutectics [7-9]. It has been reported [9] that solute elements, even in trace amounts, may have a strong influence on eutectic growth morphology.

In the columnar zone of as-cast structures, the eutectic carbides are usually aligned so that the long axis of the carbide rods is parallel with the direction of heat flow, forming a highly anisotropic morphology. The formation of eutectic colonies of different morphologies is assumed to be related to the segregation of alloying elements in the melt. That is confirmed by EDS analysis which indicates different  $M_7C_3$  carbide compositions (Table 2). During solidification, solute segregation will influence nucleation and growth kinetics through its influence on constitutional undercooling (the constitutional undercooling of a particular phase is dependent on the liquidus and/or eutectic temperature which, in turn, is dependent on the local liquid composition). Due to different melt composition in particular regions, the constitutional undercooling and also the growth rate are different and the formation of eutectic colonies with different morphologies will be induced (Figs. 3 and 4). According to solidification theory [8], for a hypoeutectic alloy composition, the alloy liquidus is much higher than the eutectic temperature. Thus the corresponding primary phase is highly constitutionally undercooled, due to the long-range boundary layer built up ahead of the solid-liquid interface in this case, and tends to grow faster than the eutectic. Consequently, primary phase will destabilize the solid-liquid interface. At the time when eutectic nucleation and growth occur, the conditions in the melt will in part be imposed by the characteristics of the previous reaction. Since it can be assumed that thermal conditions, such as thermal gradient and cooling rate, are the same, the morphology of the eutectic growth

front will depend on melt composition in particular zones. In the regions with a smaller content of alloying elements, the rosette-like eutectic colonies in which carbides are located radially from the center will be formed (Fig. 3d), whereas in regions of enriched melt, the formation of eutectic colonies consisting of a larger number of long  $M_7C_3$  carbide rods will be favored (Figs. 3a and 4a).

In examined alloys, the morphology of the eutectic carbides vary from the center to the edge of eutectic colonies marked 1 and 2 in Figs. 3 and 4. The rod shaped carbides are finer at the center of the eutectic colony and become coarser rod-like or blade-like with increased distance from the center (Figs. 3 and 4), as indicates that eutectic solidification begins at the center with a certain undercooling and proceeds radially outward. As solidification progresses, the constitutional undercooling decreases, and thus the rod-like or blade-like carbides that form during the later stages of solidification are coarser. This can be explained by the fact that, during  $M_7C_3/\gamma$  eutectic growth, the solute atoms (as carbon, chromium and vanadium), which are rejected by one phase, are usually needed for the growth of the other. Therefore, lateral diffusion along the solid-liquid interface perpendicular to the growth direction, will become dominant and effectively decreases the solute build-up ( $\Delta C$ ) ahead of both phases. This lateral diffusion causes the interphase spacing  $\lambda$  in the eutectic structure to be decreased. However, as  $\lambda$  decreases, an opposing force (capillary effect), which arises from the increased energy associated with the increased curvature of the solid/liquid interface, comes into effect. As shown in Fig. 6, the diffusion effect can be expressed in terms of a constitutional undercooling ( $\Delta T_c$ ) while the latter can be expressed in terms of a curvature undercooling ( $\Delta T_r$ ) [8,10]. The sum of the solute ( $\Delta T_c$ ) and curvature ( $\Delta T_r$ ) undercoolings must therefore equal the interface undercooling,  $\Delta T$ . Both undercoolings vary with  $\lambda$  in opposite ways:  $\Delta T_c$ , which is proportional to  $\Delta C$  (the driving force for solute diffusion) increases with  $\lambda$ , while  $\Delta T_r$  decreases. The interphase spacing in the eutectic structure is eventually established by the equilibrium between an attractive force arising from the diffusion effect and a repulsive force arising from the curvature effect. Decrease in growth rates will shift  $\Delta T_c$  to  $\Delta T_{c1}$  without changing the  $\Delta T_r$  curve, leading to a higher spacing value,  $\lambda_1$ . It is also evident from Fig. 6 that for small values of  $\lambda$ , eutectic growth is controlled by capillary effects ( $\Delta T_r > \Delta T_c$ ), while diffusion is the limiting process at large spacing values. With increasing  $\lambda$  values the size of  $M_7C_3$  carbides increases.

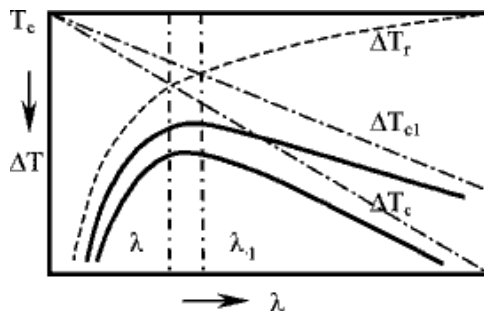


Fig. 6. Adjustment of interphase spacing during eutectic growth [8,10].

Changes in conditions of solidification, as a result of adding vanadium to Fe-Cr-C white iron, influence the change in composition of austenite. At temperatures below solidus, in the course of further cooling after solidification,  $M_{23}C_6$  carbides precipitate in austenite in tested alloy containing vanadium (Fig. 5). The transformation of austenite into martensite in this alloy is closely related to the precipitation of secondary carbides. Precipitation of  $M_{23}C_6$  carbides minimizes the carbon and chromium content in the matrix, and increases the  $M_s$  temperature. This effect was considered previously in detail [6].

## **Conclusions**

The microstructure of tested Fe19Cr2.9C3.3V alloy consists of  $M_7C_3$  and vanadium rich  $M_6C_5$  carbides in austenite-martensitic matrix.

Eutectic colonies are mainly composed of very fine rode-like  $M_7C_3$  carbides in the center of the colonies, becoming coarser rod-like or blade-like with increased distance from the centre. The volume fraction, size and distribution of rod-like and blade-like carbides in the eutectic colonies are changing with vanadium addition in high chromium white iron.

The formation of eutectic colonies of different morphologies is the consequence of the segregation of alloying elements in the alloy melt. Due to different melt composition in particular zones, the constitutional undercooling, and subsequently the growth rate, are different, which will induce the formation of eutectic colonies of different morphologies.

At temperatures below solidus, in the course of further cooling after solidification,  $M_{23}C_6$  carbides precipitate in austenite in tested alloy containing vanadium. Precipitation of  $M_{23}C_6$  carbides minimizes the carbon and chromium content in matrix, and increases the  $M_s$  temperature.

## **References**

- [1] C. P. Tabrett, I. R. Sare and M. R. Ghomashchi, *Int. Mater. Rev.*, 41 (1996), 59-82.
- [2] A. Wiengmoon, T. Chairuangsi, A. Brown, R.J.T.H. Pearce, *Acta Mater.*, 53 (2005), 4143-4154.
- [3] G. Laird II and Ö. N. Doğan, *Int. J. Cast Metals Res.*, 9 (1996), 83-102.
- [4] A. Bedolla-Jacuinde, *Int. J. Cast Metals Res.*, 13 (2001), 343-361.
- [5] M. Filipovic, Z. Kamberovic and M. Korac, *Mater. Trans.*, 52 (2011), 386-390.
- [6] M. Filipovic, E. Romhanji, Z. Kamberovic and M. Korac, *Mater. Trans.*, 50 (2009), 2488-2492.
- [7] M. Filipovic, E. Romhanji and Z. Kamberovic, *ISIJ Int.*, 52 (2012), 2200-2204.
- [8] W. Kurz and D.J. Fisher, *Fundamentals of Solidification*, Trans Tech Publication, Switzerland, 1984.
- [9] M. Asta, C. Beckermann, A. Karma, W. Kurz, R. Napolitano, M. Plapp, G. Purdy, M. Rappaz, R. Trivedi, *Acta Mater.*, 57 (2009), 941-971.
- [10] L. Lu, H. Soda and A. McLean, *Mater. Sci. Eng. A*, 347 (2003), 214-222.

Book of abstract



## **DEVELOPMENT OF HIGH-STRENGTH Al-Alloys Reinforced With Quasicrystals**

1B. Markoli, 2K. Delijić, 1I. Naglič, 1N. Štrekelj, 3T. Bončina, 3F. Zupanič

*1University of Ljubljana, Faculty of Natural Sciences and Engineering,  
Ljubljana, Slovenia*

*2University of Montenegro, Faculty of Metallurgy and Technology,  
Podgorica, Montenegro*

*3University of Maribor, Faculty of Mechanical Engineering, Maribor,  
Slovenia*

*bostjan.markoli@omm.ntf.uni-lj.si*

Reducing the weight of vehicles, such as cars and trucks, is one of the motives of modern automotive industry. In this respect, research and development is conducted to provide new light-weight and high-strength alloys that will allow further reductions in fuel consumption while increasing power and reduce harmful emissions. The aim of developing new alloys in automotive and aerospace industries is to achieve the best possible ratio of strength versus specific density while the synthesis of such alloys should be as simple as possible. Aluminum-based alloys are very suitable in this sense because they allow for strengthening via various mechanisms, such as precipitation hardening, grain size reduction, increasing the concentration of dislocations and the like. Recently, as the possibility of strengthening through the synthesis of aluminum-based alloys, hardening occurs by precipitation of primary and secondary particles of quasicrystals, *i.e.* via production of natural in-situ composite. Namely, quasicrystals can be deformed along with aluminum-based matrix, during the mechanical processing. Since quasicrystals are generally harder than the parent aluminum matrix they will harden **the matrix**. In this respect we have designed a series of new Al-Mn-Cu-(X) alloys containing quasicrystals and have submitted them to characterization (using DSC, LOM, SEM, XRD, TEM/HRTEM, in-situ mechanical testing on nano-scale, nanoindentation) and mechanical testing gaining very interesting results.

## **THE INFLUENCE OF THE VISCOSITY VALUE AND THE METHOD OF ITS IMPLEMENTATION IN THE NUMERICAL MODEL OF THE STEEL CONTINUOUS CASTING PROCESS ON THE DISTRIBUTION OF THE SOLIDIFYING STRAND TEMPERATURE.**

Katarzyna Miłkowska-Piszczek M. Sc., Marta Korolczuk-Hejnak M. Sc.

*E-mail: kamilko@agh.edu.pl, mkorolcz@agh.edu.pl*

Based on the chemical composition of the steel grade examined and the algorithms implemented in the thermodynamic data bases, it is possible to determine a number of material properties i.e. enthalpy, thermal conductivity, density, viscosity, solidus and liquidus temperatures. The paper presents the influence of viscosity values on the temperature distribution calculated with the numerical model of the steel continuous casting process. The viscosity values were determined on the basis of experimental research and with the thermodynamic data bases CompuTherm LLC supplied along with the *ProCAST* software.

As part of the project rheological tests were performed with modern equipment -a high-temperature rheometer FRS1600 -equipped with a furnace that enables temperatures above 1500 C to be obtained in the sample. The aforementioned measurements were carried out for the S235 steel in the liquid and in the semi-solid states to examine the influence of temperature on the viscosity value changes obtained. A system of Searle-type coaxial cylinders was used for the measurements.

A 3D model was developed on the basis of the process parameters of an actual continuous steel casting process. The temperature distribution in a solidifying strand, with dimensions of 220 x 1100mm, was analysed for the S235 steel.

The calculated temperature distribution of the solidifying CC strand was verified with the database that was created during measurements which were conducted in the industrial conditions and enabled the temperature to be checked in the inspection points. The thickness of the shell leaving the mould and the metallurgical length measured from the liquid steel meniscus to the total solidification of the cast strand will be subjected to a detailed analysis.

*Keywords: continuous steel casting, numerical modelling, viscosity, rheology, ProCAST*

## **WELDING OF 5083 ALUMINUM ALLOYS WITH FSW METHOD**

Specialist M. Sc. Kaan OZEL<sup>1</sup>, Asst. Prof. Dr. Cem S. CETINARSLAN<sup>2</sup>,  
Prof. Dr. Mumin SAHIN<sup>3</sup>

*1, 2, 3 Faculty of Engineering & Architecture, Department of Mechanical  
Engineering, Trakya University, 22180 – Edirne / TURKEY  
E-mail: 1kaanozel@trakya.edu.tr*

### **Abstract:**

Friction Stir Welding (FSW) is a solid state welding method whereby the metal is not melted and takes place in non-traditional welding techniques. FSW is used for industrial applications where the original metal characteristics must remain unchanged. Parts in various geometries can be welded by not using additional materials with this method. This welding method has some advantages according to traditional methods and brings material and energy saving.

In this study, welding properties of 5083 Aluminum Alloys, joined with FSW, were investigated.

*Keywords: Friction Stir Welding, 5083 Aluminum Alloys, Welding Properties*

## ANALYSIS OF COPPER LOSSES THROUGHOUT WEAK ACID EFFLUENT FLOWS GENERATED DURING OFF-GAS TREATMENT IN THE NEW COPPER SMELTER RTB BOR

Dragana Ivšić-Bajčeta<sup>a</sup>, Željko Kamberović<sup>b</sup>, Jelena Rogan<sup>b</sup>,  
Milorad Ćirković<sup>c</sup>, Toplica Pavlović<sup>d</sup>

<sup>a</sup> *Innovation Center of the Faculty of Technology and Metallurgy in Belgrade, University of Belgrade, Karnegijeva 4, 11120 Belgrade, Serbia, divsic@tmf.bg.ac.rs*

<sup>b</sup> *Faculty of Technology and Metallurgy, University of Belgrade, Karnegijeva 4, 11120 Belgrade, Serbia*

<sup>c</sup> *Mining and Metallurgy Institute Bor, Zelene bulevar 35, 19210 Bor, Serbia*

<sup>d</sup> *Megatrend University in Belgrade, Goce Delceva 8, 11070 Novi Beograd, Serbia*

### Abstract

The previous inadequate treatment of off-gas in RTB Bor in Serbia has resulted in serious pollution of the environment and the possibly high losses of copper through the effluent flows. The project of New Copper Smelter RTB Bor, besides the new flash smelting furnaces (FSF) and the reconstruction of Pierce-Smith converter (PSC), includes more effective effluent treatment. Paper presents an analysis of the new FSF and PSC off-gas treatment, determination of copper losses throughout generated wastewaters and discussion of its possible valorization. Assumptions about the solubility of metals phases present in the FSF and PSC off-gas, obtained by the treatment process simulation, were compared to the leaching results of flue dusts. Determined wastewaters characteristics indicate that the PSC flow is significantly richer in copper, mostly present in insoluble metallic/sulfide form, while the FSF flow has low concentration of copper in the form of completely soluble oxide/sulfate. The possible scenario for the copper valorization, considering arsenic and lead as limiting factors, is the separation of the FSF and PSC flows, return of the metallic/sulfide solid phase to the smelting process and recovery from the sulfate/oxide liquid phase.

*Keywords: Copper smelter, off-gas treatment, arsenic, lead.*

## THE EFFECTS OF AGING ON THE PRECIPITATION OF THE W-RICH PHASE IN THE MATRIX OF THE 92.5W-5Ni-2.5Fe POWDER METALLURGY HEAVY ALLOYS

B. T. Katavić<sup>1,a</sup>, B. R. Gligorijević<sup>1</sup>, A. B. Alij<sup>1</sup>, Z. D. Odanović<sup>2</sup>

<sup>1</sup>*Institute Goša, Milana Rakića 35, Belgrade, Serbia,*

<sup>2</sup>*IMS Institute, Bulevar Vojvode Mišića 43, Belgrade, Serbia*

<sup>a</sup>*boris.katavic@institutgosa.rs*

The precipitation behavior of W-rich phase on the specific matrix locations of Co-free and Co-containing 92.5W-5Ni-2.5Fe heavy alloys is investigated during aging of the as-quenched samples. The aging treatment is performed between 600 °C (873 K) and 800 °C (1073 K) and for aging time up to 9 hours. The average chemical composition of tungsten heavy alloys was determined by using the atomic absorption spectrophotometry (AAS) and the Leco apparatus. The Energy Dispersive X-ray (EDX) analysis was employed to analyze the chemistry of the existing phases. The changes in structure as a function of aging time and temperature have been examined by using the light microscopy (LM) and the scanning electron microscopy (SEM). The macro- and micro-hardness measurements were performed, as well. The local changes in matrix structure and various morphologies of the precipitates are observed. The aging has caused only a minor changes of the micro-hardness of the existing phases ( $\gamma$  and W-rich) as well as the macro-hardness of the investigated alloys. In the case of the Co-free 92.5W-5Ni-2.5Fe heavy alloy, at lower temperatures and for shorter time of aging, there is a dominant presence of lamellar and Widmanstätten morphology of W-rich precipitates within the  $\gamma$ -matrix grains. At higher temperatures and for longer time, there is a significant precipitation of W-rich precipitates at the matrix grain boundaries ( $\gamma/\gamma$ ). In the case of 92.5W-5Ni-2.5Fe heavy alloy micro-alloyed with Co, it is dominant precipitation of W-rich phase at the matrix grain boundaries ( $\gamma/\gamma$ ), especially at higher aging temperatures and for longer aging time.

## **ANALYSIS OF INTERMETALLIC COMPOUNDS In Al-Si FOUNDRY ALLOY**

<sup>1a</sup>Monika Tokár, <sup>1</sup>Jenő Dúl, <sup>1</sup>György Fegyverneki, <sup>2</sup>Valéria Mertinger

<sup>1</sup>*University of Miskolc, Metallurgical and Foundry Engineering Institute*

<sup>2</sup>*University of Miskolc, Physical Metallurgy, Metalforming and  
Nanotechnology Institute*

<sup>a</sup>*monika.tokar@uni-miskolc.hu*

The Al-Si alloys are the most frequently used aluminium alloys by the foundry industry. Mainly two elements are used to modify the eutectic silicon phase in these alloys, some foundries apply strontium, others modify with antimony. After the scrap recycling these elements are together in the melt, and the strontium and antimony together may be cause formation of intermetallic compounds. The intermetallic compounds can be harmful in the point of view of mechanical properties. We designed tensile test specimen according to industrial parameters, whereby we examined strength properties. In this work we studied the effects of intermetallic compounds in Al-Si foundry alloy.

## **PREVENTION OF SURFACE DEFECTS IN LOST FOAM CASTINGS**

VAHED NAJATI

*ALDA, Aluminum casting company, Tehran, Iran*

The right surface quality of castings is not only one of the customers expectancy but also important to the foundry, because it can save a lot of money if the quality is ok. The most important reason to increase the production cost is the rework on the low surface quality castings. Therefore too many researchers have studied about solving surface defects such as burn-on, penetration and vein in castings. Meanwhile more numerous of these works related to green sand mold castings and there are rarely paper about lost foam castings .That is why in this article we have investigated the effect of lost foam process parameters such as foam pattern density, pouring temperature, coating permeability and viscosity ,molten metal fluidity on the occurrence of surface defects. The other important parameter that has less notified by other researchers is foam pattern cluster drying condition that we will explain it in this study. The result of experiments represent that increase the pouring temperature, coating permeability, metal fluidity increases the burn-on defect and increase in pattern density and humidity of dried cluster increase penetration defect in castings. But there are critical ranges for most of parameters that determine the kind of surface defects and this is a novel result in lost foam technology.

*Keywords: lost foam casting, investment casting, casting defects, surface defects.*

## ALLOY FORMATION BY UNDERPOTENTIAL DEPOSITION OF Mg ON Al FROM NITRATE MELTS

Vesna S. Cvetković, Jovan N. Jovičević

University of Priština, Faculty of Sciences and mathematics  
E-mail: chupka976@hotmail.com

Magnesium has been underpotentially deposited on aluminium electrodes from magnesium nitrate and magnesium nitrate-ammonium nitrate melts at temperatures ranging from 85°C to 200°C. Electrochemical techniques used were cyclic voltammetry and potential step. Deposits were studied by electron microscopy, EDS and XRD. The electrodeposition of magnesium was performed from the melts made with magnesium hexahydrate and anhydrous magnesium nitrate. A new method for the synthesis of water free magnesium nitrate was designed to avoid the influence of water strongly bonded to magnesium cation and its influence on the magnesium deposition process. In the magnesium UPD region on Al the processes of nitrate, nitrite and water (when present) reduction take part simultaneously with magnesium UPD. The underpotential deposition of magnesium leads to  $\text{Al}_3\text{Mg}_2$ ,  $\text{Mg}_2\text{Al}_3$  and  $\text{Al}_{12}\text{Mg}_{17}$  formation. The reduction of nitrate, nitrite and water results in  $\text{O}^{2-}$  and  $\text{O}_2^{2-}$  which with Mg adatoms react to form several Mg oxides. It was established also that the surface of the three-dimensional magnesium (when deposited) has been very quickly transformed into magnesium oxide or oxi-hydroxide by the evolved oxygen,  $\text{O}^{2-}$ ,  $\text{O}_2^{2-}$  and  $\text{OH}^-$  ions in both kinds of melts.

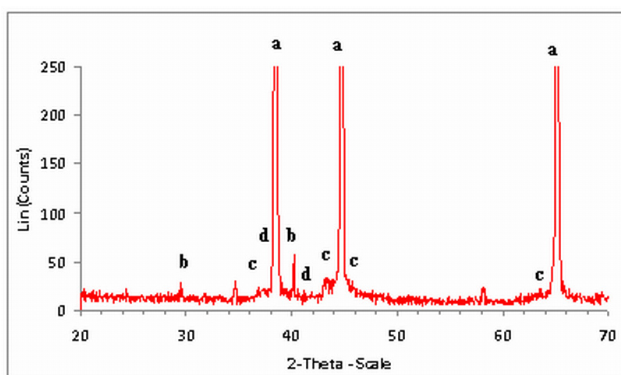


Figure 1. XRD analysis of the Al electrode after underpotential step to 0,090 V vs. Mg (duration 120 min) at 100°C: a) fcc – aluminium, c) cubic  $\text{Al}_2\text{Mg}$ , d) hexagonal  $\text{Mg}_2\text{Al}_3$ .

## **THERMOMECHANICAL ANALYSIS OF Cu-Al-Be ALLOY USED AS COUPLINGS OF OIL AND GAS PIPES**

Martins, C.E.L.<sup>1</sup>; Veloso, A.C.R.<sup>1</sup>; Gomes, R.M.<sup>2</sup>; Melo, T.A.A.<sup>2</sup>;  
Lima, S.J.G.<sup>2</sup>; Cavalcanti<sup>3,4</sup>, E.B.; Figueiredo, R.T.<sup>3,4</sup>

<sup>1</sup> *Federal University of Sergipe, Department of Mechanical Technology, Campus I, São Cristovão, Sergipe, Brazil.*

<sup>2</sup> *Federal University of Paraíba, Center for Technology, Department of Mechanical Engineering, João Pessoa, Paraíba, Brazil.*

<sup>3</sup> *Tiradentes University, Campus II, Aracaju, Sergipe, Brazil.*

<sup>4</sup> *Research and Technology Institute, Aracaju, Sergipe, Brazil  
eugenio1989@hotmail.com*

We are experiencing the process of development of the oil sector. The level of demand is increasing, requiring the investment in changes, and radically altering postures already rooted for decades. Shape-memory alloys, in particular, have been extensively studied because of their broad spectrum of applications. One quite bold application of these alloys is use of shape memory for manufacture of couplings capable of performing the union of pipes through the shape memory effect. Therefore, firstly, it is necessary to achieve thermoelastic martensitic transformation. The austenite matrix transforms during cooling into martensite which can be deformed. After this deformation the material be restored to its original form (austenite) if it is subjected to heating.

Several compositions were studied for manufacturing these couplings. However, the Cu-Al-Be presented the best alternative, because it has good mechanical strength and is stable stability at low temperatures.

In the present scenario, however, these couplings, which are in the final testing phase in an oil field, showed small cracks on the surface, as a result of stresses imposed during the process when couplings return to their original shape. In fact, these stresses can reach values of the order of 200 MPa. In this context, several studies have been conducted to solve this problem and a good alternative was adjusting the chemical composition of the couplings. It is now known that even there is no appearance of cracks the couplings will always be subject to internal stresses. Therefore, this study is aimed to evaluate the influence of residual stresses during transformation.. Therefore, it was necessary to use the following experiments: metallography, tensile testing, thermal cycling and differential scanning calorimetry (DSC). Obtained results indicate a strong influence of transformation temperatures on properties of Cu-Al-Be alloy when it was subjected to stresses.

## **A FAILURE ANALYSIS OF A HIP STAINLESS STEEL IMPLANT: CASE REPORT**

Dušan Petković<sup>1</sup>, Goran Radenković<sup>1</sup>, Miroslav Miljković<sup>2</sup>

<sup>1</sup>*Faculty of Mechanical Engineering University of Niš*

<sup>2</sup>*Center for Electron Microscopy University of Niš  
dulep@masfak.ni.ac.rs*

Although fortunately rare, failed implants can cause significant problems for both patients and surgeons due to consequences such as the need for repeated surgery, possible unwanted complications and extension of the healing period. An orthopaedic implant (total hip replacement) made of 316L stainless steel (SS) that failed prematurely was examined to determine the root cause for the fracture. The experimental work consisted of visual inspection of the sample, macroscopic and microscopic characterization of the material, hardness test, fractographic investigation of the fracture surface and adjacent areas and its chemical composition. Based on the results of the study, fatigue fracture mechanism was identified as the primary cause of the failure.

*Keywords: hip implant; failure analysis; fatigue fracture; stainless steel*

## **THERMODYNAMIC MODELLING OF THE MATERIAL PROPERTIES FOR Al-Cu-Mg ALLOYS**

Biljana V. Zlaticanin<sup>1</sup>, Mirjana V. Filipovic<sup>2</sup>

<sup>1</sup>*Faculty of Metallurgy and Technology, Podgorica, Montenegro*  
*biljana@ac.me*

<sup>2</sup>*Faculty of Technology and Metallurgy, Belgrade, Serbia*

### **Abstract**

The current paper concentrates on Al-based alloys and describes the scientific background used for the calculation of materials properties for these alloys. Aluminium alloys form one of the most widely used groups of materials in existence. The properties which can be calculated are wide ranging, including thermo-physical and physical properties. It is very useful to be able to predict materials properties and behaviour in multi-component alloys. The current work forms part of the development of a more generalized software package (JMatPro) for the calculation of wide ranging of materials properties. By JMatPro's property models a complete set of physical and mechanical properties can be calculated. The present paper describes a general methodology to calculate properties such as the fraction solid transformed, enthalpy, specific heat ( $C_p$ ) etc. for multi-component alloys.

## CHARACTERIZATION OF COPPER POWDER OBTAINED ON ALLUMINIUM CATHODE BASE

R. Markovic, J. Stevanović, G. Slavković

*Mining and Metallurgy Institute Bor, Zeleni bulevar 35, 19210 Bor  
Institute of Chemistry, Technology and Metallurgy, University of Belgrade,  
Njegoševa 12, 11001 Belgrade  
e-mail: radmila.markovic@irmbor.co.rs*

### Abstract

This paper presents the physic-chemical characteristics of electrolytic copper powder. The experiments were done on apparatus of semi-industrial size. Electrochemical deposition on aluminium cathode base has been carried out from sulphurous acidic electrolyte with follow conditions: concentration of cupric ion, ( $\text{g/dm}^3$ ): 10, 20 and 30; concentration of sulphuric acid, ( $\text{g/dm}^3$ ):  $150 \div 160$ , at working temperature of 303 K with used  $2000 \text{ A/m}^2$  cathode current density. Electrolyte flow was adjusted to be one change of cell volume for an hour. Duration of the experiment was 4 h. The results of chemical analysis on copper, oxygen, sulphate ions and moisture capacity were shown that the copper content was  $> 99.7\%$  Cu, the oxygen content was  $< 0.15\%$ , without moisture and content of sulphate ions was  $< 0.0015\%$   $\text{SO}_4^{2-}$ . The sieve analyses were shown that content of fractions lower than  $45 \mu\text{m}$  is the highest for the copper concentration of 10 and  $20 \text{ g/dm}^3$ . For  $30 \text{ g/dm}^3$ , the highest mass percentage is registered for the fraction -  $106+75 \mu\text{m}$ . After each experiment, performed analysis was shown no presence aluminium in electrolyte and powder.

## INVESTIGATIONS OF STRUCTURE OF NICRALY METALLIC COATING APPLIED BY DIAMOND JET PROCESS ON IRON-BASED SUPERALLOY A286

Milenko Rimac<sup>1</sup>, Mirsada Oruč<sup>2</sup>, Sulejman Muhamedagić<sup>2</sup>, Samir Butković<sup>3</sup>

<sup>1</sup>University of Zenica, Metallurgical Institute „Kemal Kapetanović“, Travnička cesta 7, Zenica 72 000; BiH

<sup>2</sup>University of Zenica, Faculty of Metallurgy and Materials Science, Travnička cesta 1, Zenica 72 000; BiH

<sup>3</sup>University of Tuzla, Faculty of Mechanical Engineering, Univerzitetska 4, Tuzla 75 000; BiH

E-mail: [sulejman.muhamedagic@famm.unze.ba](mailto:sulejman.muhamedagic@famm.unze.ba)

New processes of improvement of surface characteristics of A285 iron-based superalloy by applying metallic coating by Diamond Jet process.

The results of microstructural investigation of NiCrAlY metallic coating obtained by high velocity oxygen fuel (HVOF) thermal spray *process* applied by Diamond Jet method were described. Investigations of microstructure, gamma prime phase and oxide phases Al<sub>2</sub>O<sub>3</sub>, Cr<sub>3</sub>O<sub>4</sub>, and Y<sub>2</sub>O<sub>3</sub>, are conducted on specially prepared samples. The impacts of these phases on the coating properties are also described.

*Key words: Superalloy, microstructure, gamma prime phase, metallic coating*

## NATURAL FIBERS-WASTE COMPOSITES: MECHANICAL PROPERTIES PROFILES

J.M. Vázquez-Rodríguez, A.del C. Lizardo-Pérez, S.G. Gómez-Jiménez.

<sup>a</sup> *Universidad Juárez Autónoma de Tabasco. División Académica de Ingeniería y Arquitectura. Tabasco, México.  
jm670324@hotmail.com*

Recently natural fibers as rice and coconut hull have become of engineering and commercial interest for production of novel classes of Natural Fiber Composites (NFCs) and Wood Polymer Composites (WPCs). In terms of markets and applications, it is particularly attractive to the automotive industry, building and construction industry which have expressed interest in using such materials. Along with cost saving aspects and expected ecological benefits, the main motivation driving these developments is related to the mechanical property profiles of natural fibers, which indicate a substantial reinforcement potential. Combined with the low density of natural fibers, NFCs may result in lighter weight structures when compared to traditional reinforced materials. Hence, the overall objective is to provide the mechanical property profiles of NFCs of rice, coconut and bagasse fiber from sugar industry. The fiber was pre-conditioned, through a sieve, washed in distilled water and pre-dried on sunlight for five hours. The final drying process was performed in a vacuum oven at 80°C. The curing process for each NFCs was eight days, after seven days composites were de-molded and cut. Finally the eighth day measurements of the mechanical properties were made using the universal testing machine INSTRON Model 3384. The mechanical properties of tensile and three points bending were analyzed for each group of samples corresponding to a content of reinforcing material (rice, coconut and bagasse fiber from sugar industry), and compared with samples without reinforcement. The results of tensile tests showed markedly the effect of the presence of the fiber. Increasing the weight of the fiber in the material it was observed a higher elastic modulus. For samples having fiber content over 15% was noticed a decrease in mechanical properties. According to the results obtained, the materials are favorable for replacing synthetic materials, wood pellets and some traditional construction materials.

*Topics: New and advanced materials; Recycling and waste minimization*

## **THE INCREASING OF WROUGHT ALUMINIUM ALLOYS SUSTAINABILITY TOWARD HIGHER CONSUMPTION OF COST BENEFICIAL GRADES OF EXTERNAL SCRAP**

Varužan Kevorkijan

*Impol R in R d.o.o., Partizanska 38, 2310 Slovenska Bistrica, Slovenia*

The increasing of wrought aluminium alloys sustainability toward higher consumption of cost beneficial grades of external scrap is very demanding. In spite of the significant progress made in last decades in the development of pre-melt, melt and refining technologies, the recyclability of commercial wrought alloys of standard quality remain far below the level already established in cast alloys. The main reasons for that are: (i) the existence of a very narrow upper limits for maximally allowed concentrations of alloying and tramp elements in wrought aluminium alloys, which significantly reduced possibilities for using less-defined scrap as the raw material, and (ii) the fundamental thermodynamic barrier to the removal of most of elements from the melt, limiting in practice the refining procedures for wrought aluminium alloys to lowering the content of magnesium and calcium as well as the removal of inclusions and hydrogen.

The purpose of this paper is to present the activities for further increasing wrought aluminium alloys sustainability, mostly focused in: (i) formulation of wrought alloys with broader compositional tolerance limits, following the methodology called “development of alternative wrought compositions for desired properties”, (ii) developing more effective prior to melt scrap sorting and mixing procedures for achieving the standard metallurgical composition of the low grades scrap-based inputs with minimal addition of alloying elements and primary aluminium, and (iii) rigorous control and removal of inclusions.

Finally, by analysing the market prices of various grades of scrap and the total cost of their recycling, the cost of aluminium ingots made from recycled aluminium was modelled as a function of the aluminium and alloying elements content in the incoming scrap. Based on that, scrap mixtures for producing aluminium wrought alloys of standard quality from lower grades of scrap and with significant new added value were formulated and exemplified.

## THE INFLUENCE OF THE TYPE AND CONCENTRATION OF METALS ON THE ELECTRICAL CONDUCTIVITY OF PECTIN HYDROGELS

S. Šešlija<sup>1</sup>, J. Stevanović<sup>2</sup>, S. Veličković<sup>3</sup>

*1Innovation Centre of the Faculty of Technology and Metallurgy, University of Belgrade, Belgrade, Serbia, 2Institute of Chemistry, Technology and Metallurgy, Department of Electrochemistry, Belgrade, Serbia, 3University of Belgrade, Faculty of Technology and Metallurgy, Belgrade, Serbia*  
sseslija@tmf.bg.ac.rs

Traditionally, polymeric materials are used as insulators. Electroactive polymers (EAPs), a new class of materials, received recent attention from academia and industry due to their potential for applications such as biosensors, artificial muscles, actuators, corrosion protection, electronic shielding, environmentally sensitive membranes, visual displays, solar materials, and components in high-energy batteries. The commercialization of synthetic EAPs, however, is severely limited due to limitations in production and electrical properties

Partially esterified polygalacturonic acid is the main component of pectins in higher plants, and is an important constituent of the apoplastic transport system. The presence of carboxyl groups and methyl ester has a determinant influence in the physicochemical properties of those compounds, mainly in terms of complexation and gel formation. The reactivity of pectins with respect to metal ions strongly depends on the degree of esterification, content of ballast agents, and content of free and bound carboxy groups.

The purpose of this study was to examine electrical properties of pectin cross-linked with copper and zinc ions. Pectin hydrogels were formed using different copper and zinc salts:  $\text{Cu}_2\text{Cl}_2$ ;  $\text{CuCl}_2$ ;  $\text{CuSO}_4$ ;  $\text{Cu}(\text{NH}_2\text{SO}_3)_2 \cdot 2\text{H}_2\text{O}$ ;  $\text{Cu}(\text{C}_2\text{H}_3\text{O}_2)_2 \cdot 2\text{H}_2\text{O}$ ;  $\text{Ni}(\text{SO}_4) \cdot x\text{H}_2\text{O}$ ;  $\text{Ni}(\text{NO}_3)_2 \cdot 6\text{H}_2\text{O}$ ;  $\text{Ni}(\text{C}_2\text{H}_3\text{O}_2)_2 \cdot 4\text{H}_2\text{O}$ . The dependence of electrical conductivity on the concentration and type of cross-linking agent was tested. Conductivity was determined indirectly by measuring the electrical resistance of ion-polymer films, which are obtained by drying the hydrogel samples at various temperatures. The results of this research show that changes of the synthesis parameters (concentration and type of solvent, temperature) significantly affect the value of the electrical conductivity of materials.

## **STUDY OF STRUCTURE-CHEMISTRY RELATIONSHIP IN THE SYNTHESIS OF BARIUM TITANATE NANOSCALE PARTICLES THROUGH A NEWLY DEVELOPED PROCESS**

R. Ashiri

*a Department of Materials Science and Engineering, Dezful branch, Islamic Azad University, P.O. Box 313, Dezful, Iran.*

### **Abstract:**

In this research, structural evolution from sol-to-gel and from gel-to-ceramic during synthesis of nanoscale BaTiO<sub>3</sub> through a newly developed water-based sol-gel process was investigated. Moreover in-depth understanding of the relationship between the processing and the structure of the powder was elucidated. Carbonate-free BaTiO<sub>3</sub> nanopowders were prepared at lower temperature and shorter period of time. Moreover the polymorphic transformation of BaTiO<sub>3</sub> initiated at lower temperature. According to the reaction mechanism, the formation of BaTiO<sub>3</sub> in the initial stage of the interfacial reaction between BaCO<sub>3</sub> and TiO<sub>2</sub> depends on the BaCO<sub>3</sub> decomposition. In the second stage, BaTiO<sub>3</sub> formation is controlled by the barium diffusion through BaTiO<sub>3</sub> layer. The results showed that reduction in the amount of carbonate phases can result in reduction of the required time and temperature for calcination and synthesis. Moreover, fine structure of the nanopowders is an effective way of preventing the formation of secondary phases. *Keywords: A. nanostructures, B. sol-gel chemistry, C. electron microscopy, D. phase transactions, D. diffusion.*

## **CALCULATION OF THE LOADING AND RESIDUAL STRESS INTENSITY FACTOR**

A.M. Al-Mukhtar<sup>1</sup>

*Technische Universität Bergakademie Freiberg, Faculty of Geosciences,  
Geoengineering and Mining, Freiberg/Sa. Germany  
E-mail: almukhtar@hotmail.de*

This work presents the numerical and analytical calculations of the stress intensity factor (SIF). SIF presents the cracking toughness and the propagation. Therefore, the driving force which is required for the crack propagation was evaluated using SIF due to the applied load ( $K_{app}$ ) using finite element method (FEM). FE software describes the crack direction according to the applied load. Then, SIF could be calculated. In mean while, the residual stresses which are accompanying the welding process, have been considered. Therefore, SIF due to the residual stresses ( $K_{res}$ ) has been calculated using the analytical weight function method (WF) and different residual stress distributions have been adopted. The results were compared with the available literature and good agreements were shown.

*Keyword: Crack Path, Crack Propagation, Residual Stresses, Stress Intensity Factor (SIF), Welded Joints*

## ELECTROCHEMICAL BEHAVIOR OF NIOBIUM IN SOME ACID WATER SOLUTIONS

Vesna S. Cvetković<sup>1</sup>, Nevena T. Mitković<sup>1</sup>, Nataša M. Vukićević<sup>2</sup>,  
Goran P. Zebić<sup>2</sup>

<sup>1</sup>*University of Priština, Faculty of Sciences and Mathematics*

<sup>2</sup>*University of Beograd, SI Institute of Chemistry, Technology and Metallurgy*

*E-mail: chupka976@hotmail.com*

The literature on electrodeposition and dissolution of niobium from water solution is rather modest compared to the literature on the same subject from melts. The aim of this work was to examine electrochemical behavior of niobium in some acid water solutions.

Niobium water solutions were prepared applying careful dissolution of metal niobium in dilute H<sub>2</sub>SO<sub>4</sub>, HNO<sub>3</sub> and HF.

Niobium has been electrochemically deposited and dissolved using vitreous carbon electrode. Cyclic voltammetry and potential step techniques were used to obtain deposits and SEM and EDS techniques to analyze them.

It was found that from 0,025 M Nb + 0,9M H<sub>2</sub>SO<sub>4</sub> + 0,7 M HF + 0,3 M HNO<sub>3</sub> and 0,05 M Nb + 1,8 M H<sub>2</sub>SO<sub>4</sub> + 1,4 M HF + 0,6 M HNO<sub>3</sub> solutions niobium containing deposit onto mechanically fine polished vitreous carbon was formed at the potentials more negative than - 0,200 V vs. SHE. The deposits were in the form of numerous very small (order of nanometers) crystal grains, Fig.1. It appears that metal niobium was formed by reduction of Nb(IV) and/or Nb(III) ions. At the potentials more positive than - 0,110 V vs. SHE niobium was electrochemically dissolved from the vitreous carbon electrode in the same solutions and at the potentials more positive than 0,830 V vs. SHE oxides NbO<sub>2</sub> and Nb<sub>2</sub>O<sub>3</sub> were formed on the vitreous carbon electrode from Nb<sup>4+</sup> and/or Nb<sup>3+</sup> ions and oxygene or O<sup>2-</sup> ions present.

At the potentials more positive than 1,260 V vs. SHE a deposition of Nb<sub>2</sub>O<sub>5</sub> was observed, made of newly formed Nb<sup>5+</sup> from dissolution of metal Nb and oxidation of Nb<sup>4+</sup> and/or Nb<sup>3+</sup> ions.

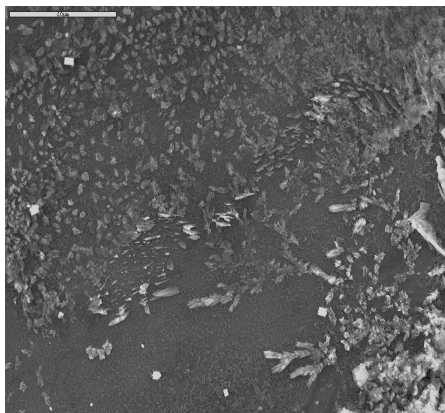


*Figure 1. SEM photograph of vitreous carbon electrode surface held 6 minutes at the potential - 0,340 V vs. SHE in the 0,05M Nb + 1,8M H<sub>2</sub>SO<sub>4</sub> + 1,4M HF + 0,6M HNO<sub>3</sub> at 410 K, magnification 1500x.*

### **Acknowledgement**

This work was supported by Ministry of Education and Science - Republic of Serbia under contract No. ON 176018

### **References**

- [1] S.V. Volkov, N.Kh. Tumanova, E.A. Babenkov, V.A. Bandur, N.I. Buryak, *Journal of Electroanalytical Chemistry*, 424 (1997) 13-17.
- [2] L.P. Polyakova, P. Taxilb, E.G. Polyakov, *Journal of Alloys and Compounds*, 359 (2003) 244–255.
- [3] O.B.Babushkina, E.O.Lomako, S.Ekres, and G.E.Nauer, The 59th Annual meeting of the International Society of Electrochemistry, from 7-12 September, Seville, Spain, 2008, SO7-P-004.
- [4] M. Mohamedi, Y. Sato, T. Yamamura, *Electrochimica Acta*, 44 (1999) 1559–1565.
- [5] C.V. D'Alkaine, L.M.M. de Souza, F.C. Nart, 34, 1 (1993) 117-127.
- [6] F. Lantelme, A. Salmi, B. Coffin, J. Claverie, Y. Le Petitcorps, *Material Science and Engineering*, B39 (1996) 202 – 207.

## **STRAIN INDUCED MELT ACTIVATION (SIMA) OF AA2014 ALLOY**

RVSM. Ramakrishna, P. Pramod Kumar

*Metallurgical and Materials Engineering, Mahatma Gandhi Institute of  
Technology, Hyderabad  
rentala.ramakrishna@gmail.com*

### **Abstract**

Strain induced melt activation (SIMA) is one of the semi-solid processing technologies performed for many aluminium wrought alloys. In the SIMA process, an alloy is subjected to cold working so as to induce stored energy and heated to temperature region between the solidus and liquidus temperatures. At this temperature recovery and recrystallization occur before liquid formation with the aid of the stored energy. Reaching the mushy zone, liquid is formed by preferential melting at grain boundaries with high energy state, and penetrates into high angle boundaries of recrystallized grains. The amount of stored energy and its distribution is the most critical factor in controlling the recovery, recrystallization kinetics and the uniformity of the resultant microstructure. The present paper essentially deals with different plastic deformations adopted on AA2014 alloy to achieve uniform refined and equi-axed globular microstructure that would result in to enhancement of properties like resistant to wear (abrasion, friction, erosion and corrosion). The alloy was cold forged and heat treated to semi solid temperature and then subjected to Microstructural analysis. Conclusions were drawn basing on the results obtained.

*Key Words: AA 2014, Cold Working, Recrystallization*

## MICROMECHANICAL PROPERTIES OF WOOD HYBRID COMPOSITES

S. Perisic, N. Aleksic, M. Zrilic, D. Trifunovic, D. Stojanovic, V. Radojevic,  
R. Aleksic

*Faculty of Technology and Metallurgy, University of Belgrade,  
Karnegijeva 4, 11120 Belgrade, Serbia  
sperisic@tmf.bg.ac.rs*

Wood-plastic composites are more resistant to degradation and dimensional stability when exposed to moisture compared to wood. Compared with the hollow plastic, wood-plastic composites are stiffer (harder) and have better dimensional stability when exposed to temperature changes. Characteristics of **these** composites may vary depending on the type, shape (form) **and** weight fraction.

This paper investigated the processing, structure and micromechanical properties of hybride wood-plastic composites, which were made by hot-pressing ("*pressure molding*"). The composite was built by using WPC granules consisting of 60% wood and 40% polyethylene PE and strenghtening layers. The strenghtening layers were glass fiber mesh in one series of samples, and metal wire mesh in the second series. The micromechanical properties were investigated by tensile and bending testing, as well as with modified hardness testing method. The Young's modulus and tensile strength, bending strength and hardness are dependent on processing paremeters and the type and the number of reinforcement layers.

*Keywords: composites, PE, wood, mechanical properties, structural properties*

## **EFFECT OF CRYSTALLOGRAPHIC ORIENTATIONS ON THE LIQUATION CRACKING TENDENCY IN LASER WELDED IN738**

S. M. Mousavizade<sup>1</sup> and Hidetoshi Fuji<sup>2</sup>

*1-Departemnt of Materials Science and Engineering, Faculty of Engineering, Sabzevar Tarbiat Moallem University, Sabzevar, Iran (Email: sm.mosavizade@hsu.ac.ir)*

*2-Joining and Welding Research Institute, Osaka University, Japan*

### **Abstract**

This paper examines the effect of crystallographic orientations on the hot crack susceptibility of IN738 nickel base superalloy during laser welding. Microstructural examination of the HAZ of laser welding showed that any GB intersecting the fusion zone had liquidation cracked or had liquidated but not cracked. Different grain boundaries in the HAZ were examined with high resolution EBSD. The GBs misorientation and also the lowest angle between 001 crystallographic directions of both adjacent grains and the normal to the grain boundary between them (only for GBs which are nearly normal to the fusion line ) were measured. This angle has been considered as a  $\theta$ . It is shown that there is a good relationship between the  $\theta$  and the cracking susceptibility. The liquated but not cracked GBs did not have a  $\theta$  angle lower than 10-20 at least in one of the grains adjacent to the GB. However, the cracked GBs did not have a low  $\theta$  angle in any of adjacent grains. Examination of this criterion for 75 cracked and uncracked GBs shows 5 exceptions. This behavior of GBs can be related to the different factors such as segregation and resolidification time of GB liquid. The GB liquid is resolidified epitaxially in planar mode, The liquid along the GB which have a low  $\theta$  angle in one or two adjacent grains is expected to be solidified faster than other GBs due to the effect of easy growth direction 001. But the liquid along the GB which have not any easy growth direction in both adjacent grains, did not resolidified fast and therefore, it remains until lower temperatures during weld cooling which is attendant with build-up of higher welding tensile stresses across the GB. Therefore, this behavior can enhance liquation cracking susceptibility.

## PROCESSING OF NANOSTRUCTURED Mg DOPED HAP/TCP BIOCERAMICS BY MICROWAVE SINGLE- AND TWO-STEP SINTERING

Dj. Veljović<sup>1</sup>, Z. Radovanovic<sup>1</sup>, E. Palcevskis<sup>2</sup>, A. Dindune<sup>2</sup>, A. Krumina<sup>2</sup>,  
R. Petrović<sup>1</sup>, Dj. Janačković<sup>1</sup>

<sup>1</sup>*Faculty of Technology and Metallurgy, University of Belgrade, Karnegijeva  
4, 11120 Belgrade, Serbia*

<sup>2</sup>*Institute of Inorganic Chemistry, Riga Technical University, Miera 34,  
Salaspils, LV-2169, Riga, Latvia  
e-mail: djveljovic@tmf.bg.ac.rs*

Magnesium ions incorporated into hydroxyapatite (HAP) structure, are of great interest for stimulation of osteoblast proliferation and affect all stages of skeletal metabolism. On the other hand, magnesium ions change microstructure and mechanical characteristics of HAP based materials. In this research, the effects of doped Mg ions on the sintering behavior, microstructure and mechanical properties of HAP based bioceramics were investigated, using one- and two-step, microwave and conventional sintering techniques.

A nanosized calcium hydroxyapatite powder doped with Mg, with a following formula ( $\text{Ca}_{9.88}\text{Mg}_{0.12}(\text{PO}_4)_6(\text{OH})_2$ ), was obtained by modified precipitation synthesis. The powder was isostatically pressed at high pressure, resulting into uniform green compacts, which were sintered: by microwave sintering technique at 1200 °C and 900 °C for 15 min, and by microwave technique in two-step (MWTSS) at different temperatures of the first step and at temperatures of the second step between 850 °C and 950 °C for 10 min. Control samples were conventionally sintered in one step at 1200 °C for 2 h and conventionally in two-step with different combination of temperatures and times of the steps.

During the sintering, doped HAP powders in all cases turned into biphasic mixtures of HAP and tricalcium phosphate ( $\beta$ -TCP). It has been shown that Mg ion, parameters and techniques of sintering significantly affect the density, microstructure (porosity and grain size), hardness and fracture toughness of processed bioceramics. A dense biphasic HAP/TCP bioceramic materials obtained by MWTSS was composed of the lowest grain size in the range of 75 nm to 150 nm (Fig. 1), possessing maximum fracture toughness (up to 1.40 MPam<sup>1/2</sup>), and hardness in the range of literature values for this kind of bioceramics. According to the obtained results, it was concluded that microwave two-step sintering could be a promising technique for the processing of Mg doped bioceramics with improved mechanical properties.

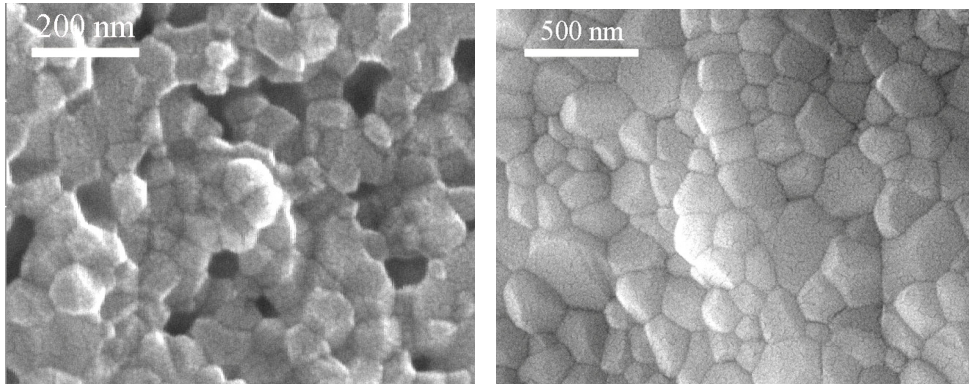


*Figure 1. Microstructures of the MWTSS sample at: a) 850 °C and b) 950 °C for 10 min*

## **THE INFLUENCE OF Mg CONTENT AND IMPURITIES OF AA5083 ALLOY ON THE PROPERTIES OF FLOW FORMED TUBES**

Milutin Nikačević<sup>1</sup>, Radović Ljubica<sup>1</sup>, Branka Jordović<sup>2</sup>

*Military Technical Institute, Belgrade, Serbia  
Faculty of Technical Science, Čačak, Serbia*

### **Abstract**

The mechanical properties and microstructure of flow formed thin-walled tubes of AA5083 alloy from two metallurgical heats are presented. The influence of the chemical composition and reduction on the surface features, and residual macro stresses were also studied. The residual macro stresses were estimated by ring method. The heat with higher content of alloying elements (Mg, Mn, Fe, Si) had higher mechanical properties of preform as well as flow formed tubes. The residual stresses were three times higher in that heat. That heat had lower spinnability and the large amount the surface defects (microcracks) on the flow formed tubes. It was attributed to the inhomogeneous material flow during deformation and presence of impurities.

*Keywords: AA5083, chemical composition, tube, flow forming, residual stress, mechanical properties*

## THE POSSIBILITY OF ALUMINUM PISTON ALLOY OBTAINED BY RHEOCASTING AND COMPOCASTING PROCESS APPLICATION IN CAVITATION CONDITIONS

M.Ćosić<sup>1</sup>, M.Dojčinović<sup>2</sup>, Z.Aćimović-Pavlović<sup>2</sup>

*1Tehnikum Taurunum College of Mechanical Engineering, Belgrade,  
Serbia,*

*e-mail: cosic.milena@gmail.com*

*2University of Belgrade, Faculty of Technology and Metallurgy, Serbia,*

*e-mail: rina@tmf.bg.ac.rs*

### **Abstract**

The cavitation resistance of hypereutectic AlSi alloy prepared via the comocasting and rheocasting process was evaluated. *Composite samples* were obtained by adding 10wt% SiC as reinforcements. Rheocasting samples were synthesized at a speed of 1500 rpm and after the stirring time of 60, 120 and 180s. The microstructure of the cast samples was characterized by optical microscopy. Ultrasonically induced cavitation test method was used in this testing. Mass loss of specimens were measured by an analytical method. The morphology of damaged surfaces of tested samples was examined using scanning electron microscopy (SEM). *It is shown that the cavitation rates of aluminum matrix composite with SiC and rheocast samples were 0.047mg/min and 0.152mg/min respectively.* According to the results, it can be concluded that the *composite* samples can be successfully applied in conditions where the cavitation resistance is needed.

*Keywords: cavitation resistance, aluminum alloy, aluminum matrix composite, rheocasting.*

## FINITE ELEMENT MODELING OF HYDRIDE COMPOSITE MATERIAL SUBJECTED TO BALLISTIC IMPACT

Nataša Tomić<sup>1</sup>, Marija Dimitrijević<sup>1</sup>, Jelena Zec<sup>1</sup>, Milorad Zrilić<sup>1</sup>, Irena Živković<sup>2</sup>, Radmila Jančić Heinemann<sup>1</sup> and Radoslav Aleksić<sup>1</sup>

*University of Belgrade, Faculty of Technology and Metallurgy, karnegijeva 4, Belgrade*

### Abstract

Hybrid composite materials are prepared to combine different properties of materials in order to stop the ballistic impact make consequences milder. First layer is ceramics in order to influence the projectile shape, induce plastic deformation to the top of the projectile, reduce speed, power and strength of the attack. Accomplishing its job ceramics is breaking and overhang projectile to composite layer that prevents further advancement of the projectile due to improved elastic properties. Samples are subjected to impact tests, to determine maximum speed, deep of penetration and fracture. FEM (finite element modeling) provides faster and realistic simulations of ballistic impact. Used software is Abaqus 6.10 CAE.

*Key words: ballistic impact, composite material, finite element modeling*

Materials subjected to ballistic impact have the aim to protect persons and goods from the sudden destruction by the projectile. The impact is important for the protection in (army) war but also in some situations where the material is subjected to the sudden collision with another object. The aim of a hybrid composite is to absorb the energy of the projectile, to deform it and to stop subject's indentation into the material. This sort of composites is usually composed of several layers each of them having a proper role (This kind of composites are made of several layers sorted with proper role ).

Faur-Csukat studied the mechanical and ballistic behavior of carbon, glass (E and S type), aramid and polyethylene fabric reinforced composites with different epoxies produced by hand lay-up method [1]. The ballistic performance of a composite focuses on the capacity of energy absorption of structures during a high-velocity impact. For a given target-projectile combination, the ballistic limit is defined as the lowest initial velocity of the projectile that will result in complete. The specimens were characterized by low and high velocity impact tests. They absorbed a significant part of the kinetic energy of the projectile. In low velocity impact tests (e.g., in drop-weight testers) the support conditions are crucial as the stress waves generated outward from the impact point have time to reach the edges of the structural element, resulting in a full-vibration response. For common epoxy composites, the transition to a stress wave dominated impact occurs at impact velocities between 10 and 20 m/s. In high velocity or ballistic impact, the response of the structural element is governed by the 'local' behavior of the material in the neighborhood of the impacted zone.

For the protection of vehicles the composite protection often has the outer surface composed of plates made of SiC. The aim of this layer is to protect the surface from the impact, to deform the bullet and to absorb the impact energy. The commercial SiC plates were subjected to mechanical and structural testing and then the corresponding data were used in the calculation of the stress distribution in the material subjected to the impact. Both the stress and deformation of the SiC plate and the bullet are studied using the Finite element calculation of stress distribution.

### Experimental

The material was subjected to characterization of the crystal structure using the XRD, to the microstructure using optical and SEM and to mechanical testing using the 3 point bending test. The obtained data gave the properties of the material that are critical for the development of the mathematical model.

The analysed specimen was approximately 4 mm high, and having good rather smooth surface. The specimen was subjected to the identification of the crystal structure using The observed phases are  $\alpha$ -SiC having the crystallographic definition 6H-SiC that represent approximately 90% of the material and the other phase is defined as 4H-SiC. For both phases the narrow diffraction peaks are identified indicating the good crystalline material. The cell parameters are in accordance to the literature data[2].

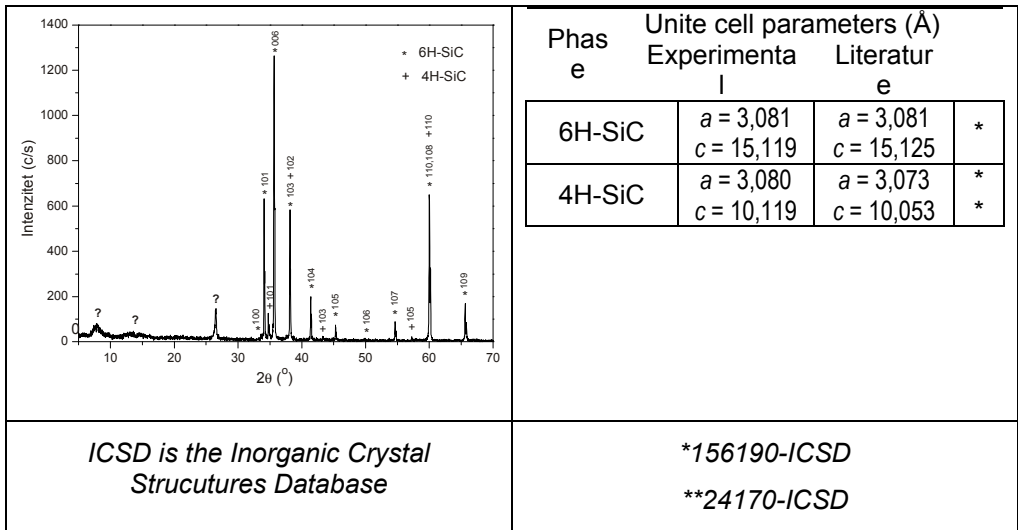


Figure 14 Diffraction pattern of the examined SiC specimen. The observed phases are  $\alpha$ -SiC having the crystallographic definition 6H-SiC that represent approximately 90% of the material and the other phase is defined as 4H-SiC.

The microstructure was examined using the optical and scanning electron microscope Jeol JSM 5800, working voltage was 20 keV. The characteristic images are given in Figure 2 showing the presence of surface defects that were

than characterized using the image analysis. The corresponding distribution of the size of surface defects is given in the same figure.

Finally, the mechanical testing gave the flexural strength gave the main value of 313 MPa having values that were ranging from 250 to 430 MPa. The data used in the numerical simulation are given in table.

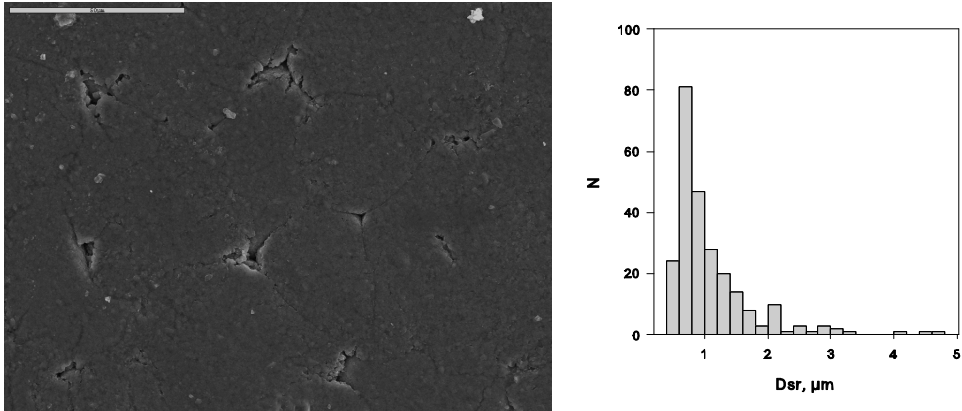


Figure 15 The surface of the specimen characterized using the SEM and the corresponding distribution of the main diameter of the defect observed.

### Finite element modeling (FEM)

Software used for finite element modeling is Abaqus CAE 6.9. Impact conditions with hard contact are modeled in Abaqus/Standard with the assumption that, at the time of impact, the two impacting surfaces instantaneously acquire the same velocity in the direction of the impact. An explicit dynamic analysis is used due to its computationally efficiency for the analysis of large models with relatively short dynamic response times and for the analysis of extremely discontinuous events or processes. Model is made of 2 parts: target and projectile. Target consists of 4 layers. Upper one is silicone carbide; next three layers are made of steel with different Young's modules. Parts are divided on hexagonal elements. Structure and assembly are shown at Figure 3

The simulation of the impact of the steel object on the surface of the material consisting of the layer of SiC is given. Velocity of impact is 200 m/s. Projectile is made of steel with following properties: density 7800 kg/m<sup>3</sup>, Young modulus 210 GPa, Poisson coefficient 0,3. First layer of target is made of silicone carbide with next properties: density 3120 kg/m<sup>3</sup>, Young modulus 410 GPa, Poisson coefficient 0,2. Next layers of steel differ in Young module, upper is with 210 GPa, lower 200 GPa and the lowest with 190 GPa. Other properties are the same with projectile. According to Figure 4 stress distribution is shown with different colors depending on level of stress in material. Stress in ceramics is 150 MPa at target. Stress in projectile is 1,8 GPa which caused deformation as it can be seen. At this stress

level the ceramic material is still not destroyed as this level is under the measured level of strength.

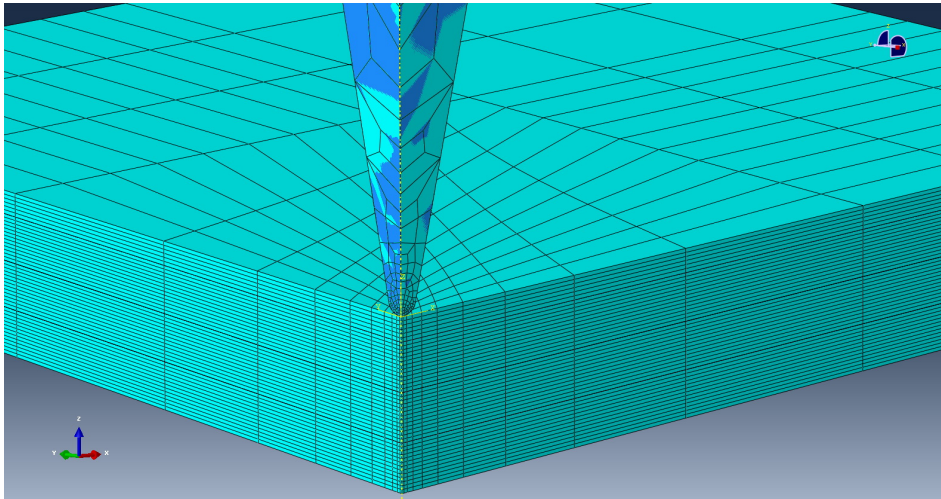


Figure 3. Hexagonal elements used to define parts in FEM model

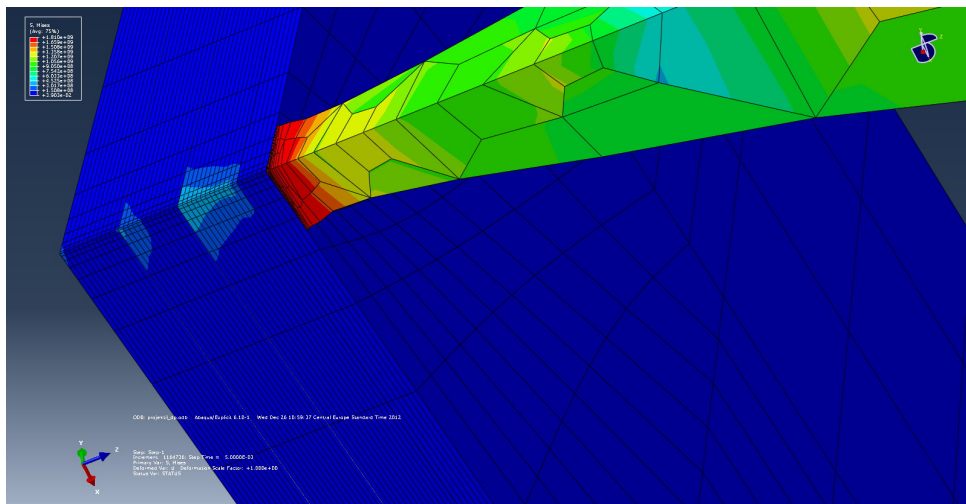


Figure 4. Deformation of projectile impacting target

## Conclusion

Material used as shield protection for vehicles is analyzed. The microstructure is crystalline and is composed of two most commonly seen phases of SiC. The lattice parameters are in accordance with the literature values. Surface is characterized with SEM and reveals the surface pores that are up to 5  $\mu\text{m}$  in diameter, but most of them is having the mean diameter under 1  $\mu\text{m}$ . Flexural strength of the material give the value of 313 MPa and this was the parameter for

the evaluation of the material behavior simulated using the FEM technique. The simulation of the impact explains the main purpose of the ceramic material layer and illustrates the deformation of the projectile in contact with the surface. The stress level in the composite material in the simulation is lower than the level indicated by flexural strengths and therefore the material exhibits only small elastic deformation up to this moment of the simulation.

### Acknowledgements

This research has been financed by the Ministry of Science and Environment of the Republic of Serbia as a part of the project TR34019.

### References

- [1] M. Colakoglu, O. Soykasap, T. Özek, Experimental and numerical investigations on the ballistic performance of polymer matrix composites used in armor design, *Appl. Compos. Mater.*, 14, 47–58 (2007).
- [2] Bakin, Andrey S. (2006). SiC materials and devices, vol. 1, edited by M. Shur, S. Rumyantsev, M. Levinshtein - Chap.: "SiC Homoepitaxy and Heteroepitaxy". World Scientific. pp. 43–76. ISBN 981-256-835-2
- [3] <http://www.3ds.com/products/simulia>
- [4] <http://abaqusdoc.ucalgary.ca/v6.9/books/exa/default.htm>

---

CIP - Каталогизација у публикацији  
Народна библиотека Србије, Београд

**CIP**

669(082)  
66.017/.018(082)

METALLURGICAL & Materials Engineering  
Congress of South-East Europe (1 ; 2013 ;  
Beograd)  
Proceedings and Book of Abstracts / First  
Metallurgical & Materials Engineering  
Congress of South-East Europe (MME SEE 2013),  
May 23-25, 2013, Belgrade, Serbia ;  
[organized by] Association of Metallurgical  
Engineers of Serbia (AMES) [and] University  
of Belgrade - Faculty of Technology and  
Metallurgy Belgrade (TMF) ; editors Endre  
Romhanji, Milan T. Jovanović, Nenad Radović.  
- Belgrade : Association of Metallurgical  
Engineers of Serbia (AMES), 2013 (Belgrade :  
Faculty of Technology and Metallurgy,  
Department of Printing Engineering). - [16],  
462 str. : ilustr. ; 24 cm

Tiraž 150. - Str. [15]: Preface / editors. -  
Bibliografija uz svaki rad.

ISBN 978-86-87183-24-7

1. Romhanji, Endre [уредник] [аутор  
додатног текста], 1952- 2. Association of  
Metallurgical Engineers of Serbia (Beograd)  
а) Металургија - Зборници б) Наука о  
материјалима - Зборници с)  
Металоперађивачка индустрија - Балканске  
државе - Зборници  
COBISS.SR-ID 198514956

---





www.prizma.rs  
e-mail: bosko.nikolic@prizma.rs

**PRIZ** nano



ULTRASONIC

PYROLYSIS ATOMIZED

GENERATOR

ULTRASONIC  
PYROLYSIS  
ATOMIZED GENERATOR



# USED FOUNDRY PLANTS

## TCT Tesic offers all types of Used Foundry Plants

- **Moulding lines**  
Automatic and semi-automatic, with flasks or flaskless
- **Induction melting furnaces**  
Medium frequency, mains frequency, crucible type or channel type
- **Green sand preparation plants**  
Complete plants or only sand mixers, moisture control unit, sand coolers
- **Coreshop equipment**  
Core shooters for cold-box or hot-box process, gasing devices, coresand preparation, regeneration plants, amine gas scrubbers
- **Shot blast machines**  
Hanger type, throughput type, tumble type
- **Lab equipment**  
Metal, chemical or sand analysis, spectrometers

## Full Service

- Dismantling, Packaging and Loading
- Forwarding, Shipping
- Erection supervision, Start-up, Training
- After sales service, Spare parts

## Contact

- Zoran Tesic
- Sudhir Gurram



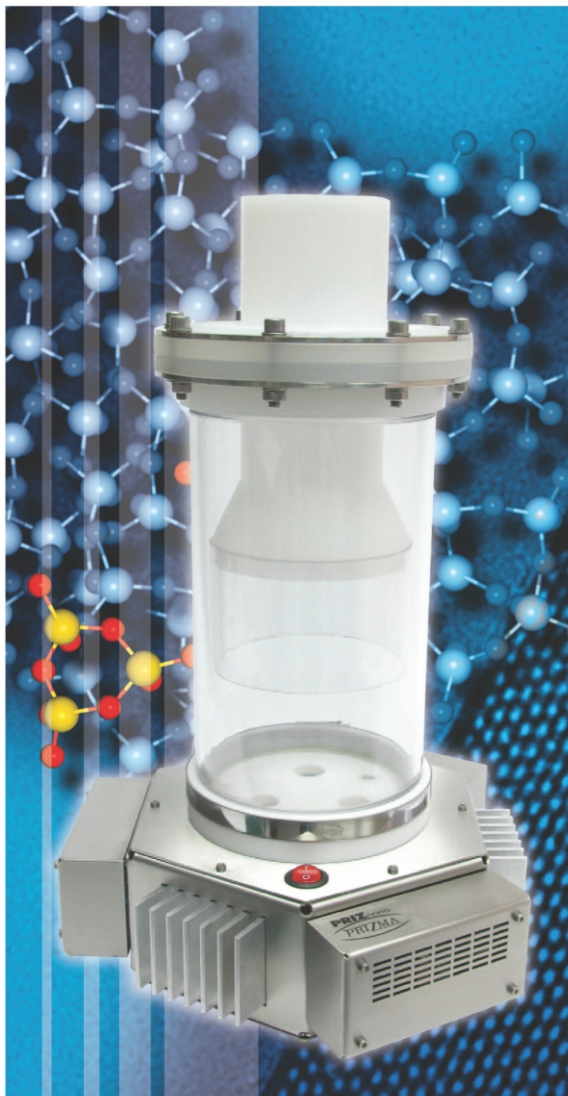
**TCT TESIC**  
Foundry Marketing & Services

Kalthofer Feld 19  
DE-58640 Iserlohn  
Germany

Fon: +49 (0)2371-77260  
Fax: +49 (0)2371-772610  
E-Mail: [info@tct-tesic.com](mailto:info@tct-tesic.com)

[www.tct-tesic.com](http://www.tct-tesic.com) • 24h Hotline +49 2371-77260





www.prizma.rs  
e-mail: bosko.nikolic@prizma.rs

**PRIZ**nano



ISO 9001 Q-1111  
ISO 13485 M-017  
ISO 14001 E-397



**ULTRASONIC**

**PYROLYSIS ATOMIZED**

**GENERATOR**

**ULTRASONIC  
PYROLYSIS  
ATOMIZED GENERATOR**



www.metalurgija.org.rs